SCHOLARLY PUBLICATIONS

A CURRENT AWARENESS BULLETIN
OF RESEARCH OUTPUT

@DTU

(27th Edition)

MARCH 2015

BY: CENTRAL LIBRARY

DELHI TECHNOLOGICAL UNIVERSITY
(FORMERLY *DELHI COLLEGE OF ENGINEERING)*
GOVT. OF N.C.T. OF DELHI
SHAHBAD DAULATPUR, MAIN BAWANA ROAD
DELHI 110042

PREFACE

This is the **Twenty seventh** Issue of Current Awareness Bulletin started by Delhi Technological University, Central Library. The aim of the bulletin is to compile, preserve and disseminate information published by the faculty, students and alumni for mutual benefits. The bulletin also aims to propagate the intellectual contribution of Delhi Technological University (DTU) as a whole to the academia.

The bulletin contains information resources available in the internet in the form of articles, reports, presentations published in international journals, websites, etc. by the faculty and students of DTU. The publications of faculty and student which are not covered in this bulletin may be because of the reason that the full text either was not accessible or could not be searched by the search engine used by the library for this purpose.

The learned faculty and students are requested to provide their uncovered publications to the library either through email or in CD, etc to make the bulletin more comprehensive.

This issue contains the information published during **March 2015**. The arrangement of the contents is alphabetical. The full text of the article which is either subscribed by the university or available in the web is provided in this bulletin.

Central Library

CONTENTS

1. A Better Error Estimation on Bala´ zs Operators, ***3.N. Deo*** and ***3.N. Bhardwaj***, Applied Mathematics, DTU

2. A Sentiment and Interest Based Approach for Product Recommendation, ***3.Vibhu Jawa*** and ***3.Varun Hasija***, Applied Mathematics, DTU

3. Antimicrobial and Immunomodulatory efficacy of extracellularly synthesized silver and gold nanoparticles by a novel phosphate solubilizing fungus Bipolaris tetramera, Faria Fatima, Preeti Bajpai, Neelam Pathak, Sarika Singh, Shivam Priya and ***3.Smita Rastogi Verma***, Biotechnology, DTU

4. Asymmetrical p-Shaped Slot Embedded Microstrip Antenna for Circular olarization, Ajay Kumar Sharma and ***6.Ashok Mittal*** and B. Venkata Ramana Reddy, Microwave and Millimeter Wave Electronics, DCE

5. Biodiesel Production from High Free Fatty Acid Feed Stocks through Transesterification, Sanjay Mohite, Sudhir Kumar, ***3.Amit Pal*** and ***3.Sagar Maji***, Mechanical Engineering, DTU

6. Biodiesel Production from Sal (Shorea Robusta) Seed Oil, ***6.H.S. Pali*** and ***3.N. Kumar***, Mechanical Engineering, DTU

7. Broadbandmid-IRsupercontinuumgenerationinAs2Se3 based chal-cogenide photonic crystal fiber:Anewdesignandanalysis, Than Singh Saini, Ajeet Kumar, Ravindra Kumar Sinha, Applied Physics, DTU

8. Bublz! : Playing with Bubbles to Develop Mathematical Thinking, Dhruv Chand, Karthik Gopalakrishnan, Nisha K K, Mudit Sinha, ***3.Shreya Sriram***, DTU

9. CARDIO-PRED: an in silico tool for predicting cardiovascular-disorder associated proteins, ***3.Prerna Jain, 3.Nitin Thukral***, ***3.Lokesh Kumar Gahlot*** and ***3.Yasha Hasija***, Biotechnology, DTU

10. Comparative Study of Speed Control of Induction Motor Using PI and Fuzzy Logic Controller, ***3.Anmol Aggarwal, 3.J. N. Rai*** and ***3.Maulik Kandpal***, Electrical Engineering, DTU

11. Design of Magnetorheological Brake using Parabolic Shaped Rotating Disc, ***3.Chiranjit Sarkar*** and Harish Hirani, Mechanical Engineering, DTU

12. Design, Analytical Analysis, Instrumentation and Flow Simulation of Sub-Sonic Open Circuit Wind Tunnel Model, ***3.Tomar Vishvendra Singh, 3.Sangwan Vipul, 3.Singh Shaktiman, 3.Singh Raj Kumar***, Agrawal Jubin, Mechanical Engineering, DTU

13. Effect of DC Link Control Strategies on Multiterminal AC-DC Power Flow, ***3.Shagufta Khan*** and ***3.Suman Bhowmick***, Electrical Engineering, DTU

14. EnTwine: Feature Analysis and Candidate Selection for Social User Identity Aggregation, Niyati Chhayax, ***3.Nikaash Puri***, Dhwanit Agarwaly, Paridhi Jainz, and Deepak Paix

15. ArticleFabrication of Al5083/B4C surface composite byfriction stir processing and its tribologicalcharacterization, ***3.Narayana Yuvaraj***, Sivanandam Aravindan and ***3.Vipin***, Mechanical Engineering, DTU

16. Finite Element Analysis of Magnetorheological Brake using ANSYS, ***3.Chiranjit Sarkar*** and Harish Hirani, Mechanical Engineering, DTU

17. Get ‘em Moles! : Improved Spelling and Pronunciation through an Educational Game, Dhruv Chand, Karthik Gopalakrishnan, Nisha K K, Mudit Sinha and ***Shreya Sriram***

18. Holmium doped lead tungsten tellurite glasses for Green Luminescent Applications, M. Venkateswarlu, Sk. Mahamuda, K. Swapna, M.V.V.K.S. Prasad, ***3.A. Srinivasa Rao***, Suman, Shakya, A. Mohan Babu, G. Vijaya Prakash, Applied Physics, DTU

19. Incorporating Information from Trusted Sources to Enhance Urban Navigation for Blind Travelers, Byung-Cheol Min, ***3.Suryansh Saxena***, Aaron Steinfeld, and M. Bernardine Dias, DTU

20. Limnological Study of Water Quality Parameters of Dal Lake, India, J.N.Sharma, ***6.Raj Shailesh Kanakiya*** and ***3.Dr.S.K.Singh***, Environmental Engineering, DTU

21. Medicinal plants, a gold mine of anticancer compounds, ***3.Asmita Das*** and ***3.Jaspreet Kaur Dhanjal***, Biotechnology, DTU

22. Methods for Improving Thermal Performance of Three Stage Vapour Compression Refrigeration Systems with Flash-Intercooler Using Energy– Exergy Analysis of Eight Ecofriendly Refrigerants, ***3.R. S. Mishra***, Kapil Chopra, V. Sahni, Mechanical Production & Industrial and Automobiles Engineering, DTU

23. Overview of Optical Techniques for Characterization of High Power Infrared Gas Lasers, Gaurav Singhal, ***7.1 Mainuddin***, R. Rajesh, M. T. Beg, R. K. Tyagi and A. L. Dawar, Electronics & Communication, DTU

24. Optimization of Vapour Compression Refrigeration Systems using Mixing of Nanomaterials, ***3.R. S. Mishra***, Mechanical Engineering, DTU

25. p38 MAPK and PI3K/AKT Signalling Cascades in Parkinson's Disease, ***3.Saurabh Kumar Jha, 3.Niraj Kumar Jha, 3.Rohan Kar, 3.Rashmi K Ambasta*** and Pravir Kumar, Molecular Neuroscience and Functional Genomics Laboratory, Biotechnology, DTU

26. Performance Characteristics of Biodiesel Blend in CI Engine using Artificial Neural Network (Karanja Oil), ***3.Harveer Singh Pali***, Mechanical Engineering, DTU

27. Performance Evaluation of Ecofriendly Refrigerants in the Low Temperature Circuit in Terms of First Law and Second Law Efficiency of Three Stages Cascade Vapour Compression Refrigeration of Biomedical Applications, ***3.R.S. Mishra***, Mechanical Engineering, DTU

28. Potential Use of LPG in A Medium Capacity Stationary HCCI Engine, ***3.Abhinav Tomar, 3.Abhinav Chandra*** and ***3.Jatin Madaan***, Mechanical Engineering, DTU

29. Preparation of carboxymethyl guar gum/silver nanocomposites film and its optical and antimicrobial properties, ***6.A. P. Gupta*** and ***6.Devendra Kumar Verma***, Applied Chemistry and Polymer Technology, DTU

30. Protein Functionalized Carbon Nanotubes-based Smart Lab-on-a-Chip, Md. Azahar Ali, Pratima R. Solanki, ***3.Saurabh Srivastava***, Samer Singh, Ved V. Agrawal, Renu John and ***3.Bansi D. Malhotra***, Biotechnology, DTU

31. Quad-Rotor Unmanned Arial Vehicle – A Review, Rajiv Chaudhary, ***3.Ranganath M. S., 3.R. C. Singh, 3.Arjav Desai, 3.Aakash Chaudhary*** and ***3.Mayank Garg***, Mechanical Engineering, DTU

32. Role of Oxidative Stress, ER Stress and Ubiquitin Proteasome System in Neurodegeneration, Niraj Kumar Jha1, Saurabh Kumar Jha1, Rohan Kar1, Rashmi K Ambasta1 and ***3.Pravir Kumar***, Biotechnology, DTU

33. Sustainability Analysis in Terms Energy and Exergy Evaluation of Two-Stage Vapour Compression Refrigeration System Using Eight Eco friendly Refrigerants, Kapil Chopra, V. Sahni and ***3.R. S. Mishra***, Mechanical Engineering, DTU

34. Thermal Analysis & Optimization of Two Stages Vapour Compression Refrigeration Systems Using Sixteen Ecofriendly Refrigerants, ***3.R. S. Mishra***, Mechanical Engineering, DTU

35. Time-domain UWB transmission model for three-dimensional environments with low-loss obstacles, ***3.Bajrang Bansal*** and ***3.Sanjay Soni***, Electronics and Communication Engineering, DTU

36. Visible, Up-Conversion and NIR (~ 1.5 μm) Luminescence Studies of Er3+ doped Zinc Alumino Bismuth Borate Glasses, K. Swapna1, Sk. Mahamuda1, M.Venkateswarlu1, ***3.A. Srinivasa Rao***, M.Jayasimhadri2, Suman Shakya3and G. Vijaya Prakash, Applied Physics, DTU

1. Vice Chancellor	***1.1. Ex Vice Chancellor***
2. Pro Vice Chancellor	***2.1. Ex Pro Vice Chancellor***
3. Faculty	***3.1. Ex Faculty***
4. Teaching-cum-Research Fellow	
5. Alumni	
6. Research Scholar	***6.1. Ex Research Scholar***
7. PG Scholar	***7.1. Ex PG Scholar***
8. Undergraduate Student	***8.1. Ex Undergraduate Student***

ISSN 1995-0802, Lobachevskii Journal of Mathematics, 2015, Vol. 36, No. 1, pp. 9–14. © Pleiades Publishing, Ltd., 2015.

A Better Error Estimation on Balázs Operators

N. Deo* **and N. Bhardwaj****

(Submitted by A. M. Elizarov)

Department of Applied Mathematics, Delhi Technological University, Shahbad Daulatpur, Main Bawana Road, Lelhi-110042, India

Received September 16, 2013

Abstract—In this paper we consider King [24] type modification of Balázs [5] operators and obtain the approximation properties of these operators. Then we show that our modified operators have a better error estimation and we also study rate of convergence as well as its Voronovskaya result.

DOI: 10.1134/S1995080215010060

Keywords and phrases: *Balázs operators, Peetre's K_2-functional, Voronovskaya result.*

1. INTRODUCTION

Let f be a real-valued continuous function on the closed unit interval $[0,1]$ of the real line and let $n \in \mathbb{N} = \{1,2,3,\dots\}$. Then n-th Bernstein polynomial of f is defined as

$$B_n(f)(x) = \sum_{k=0}^{n} \binom{n}{k} x^k (1-x)^{n-k} f\left(\frac{k}{n}\right), \quad x \in [0,1].$$

It is well known that the sequence $\{B_n(f)\}_{n\in\mathbb{N}}$ converges uniformly to f on $[0,1]$ and the Bernstein polynomials and their generalization as well as modification have an important role in approximation theory (see, for instance, [2, 4, 10, 11, 17]).

In view of these concernments, Katalin Balázs [5] introduced and studied several approximation properties of the Bernstein type rational functions defined as follows.

Let f be a real single valued function defined on $[0,\infty)$ and $n \in \mathbb{N}$, and define

$$R_n(f;x) = \frac{1}{(1+a_n x)^n} \sum_{k=0}^{n} \binom{n}{k} (a_n x)^k f\left(\frac{k}{b_n}\right), \quad x \in [0,\infty),$$

where $a = \{a_n\}_{n\in\mathbb{N}}$ and $b = \{b_n\}_{n\in\mathbb{N}}$ are suitable chosen sequence of positive real numbers, independent of x.

Let $f \in C_B[0,\infty)$ be the space of all real valued continuous bounded functions on $[0,\infty)$, equipped with the norm $||f|| = \sup_{x\in[0,\infty)} |f(t)|$. The classical Peetre's K_2-functional and the second modulus of smoothness of a function $f \in C_B[0,\infty)$ are defined respectively by $K_2(f,\delta) = \inf\{||f-g|| + \delta||g''|| : g \in W_\infty^2\}$, $\delta > 0$, where $W_\infty^2 = \{g \in C_B[0,\infty) : g', g'' \in C_B[0,\infty)\}$. From [11], there exists a positive constant C such that

$$K_2(f,\delta) \le C\omega_2\left(f,\sqrt{\delta}\right) \tag{1}$$

and

$$\omega_2(f,\sqrt{\delta}) = \sup_{0<h\le\delta} \sup_{x\in[0,\infty)} |f(x+2h) - 2f(x+h) + f(x)|.$$

*E-mail: dr_naokant_deo@yahoo.com

**E-mail: neha_bhr@yahoo.co.in

Now we consider the Lipschitz type space

$$Lip_M^*(\gamma) = \left\{ f \in C[0,\infty) : |f(t) - f(x)| \leq M|t-x|^\gamma (t+x)^{-\gamma/2}; \quad x, t \in (0,\infty) \right\},$$

where M is any positive constant and $0 < \gamma \leq 1$. The intention of this paper is to study the approximation properties of modified Balázs [5] operators and obtain better error estimation, rate of convergence and Voronovskaya result.

Lemma 1.1. [5, 12]. *Let $e_i(t) = t^i$, $i = 0, 1, 2, 3, 4$, then for $x \geq 0$ and $n \in \mathbb{N}$ we have*

$$R_n(e_0; x) = 1, \quad R_n(e_1; x) = \frac{np(x)}{b_n}, \quad R_n(e_2; x) = \frac{n(n-1)[p(x)]^2}{b_n^2} + \frac{np(x)}{b_n^2},$$

$$R_n(e_3; x) = \frac{n(n-2)}{b_n^3} \frac{(a_n x)^2 (1 + n a_n x)}{(1 + a_n x)^3} + \frac{n}{b_n^3} \frac{a_n x (1 + 2n a_n x)}{(1 + a_n x)^2},$$

$$R_n(e_4; x) = \frac{n(n-3)}{b_n^4} \frac{(a_n x)^2 \left[1 + (3n-1) a_n x + (n a_n x)^2\right]}{(1 + a_n x)^4}$$

$$+ \frac{n}{b_n^4} \frac{a_n x \left[1 + 2(3n-1) a_n x + 3(n a_n x)^2\right]}{(1 + a_n x)^3}.$$

Thus

$$p(x) = \frac{a_n x}{1 + a_n x}, \quad R_n(\varphi_x; x) = -\frac{a_n x^2}{1 + a_n x} \quad R_n(\varphi_x^2; x) = m(x) \equiv \frac{x \left[1 + n(a_n x)^3\right]}{b_n (1 + a_n x)^2},$$

where $\varphi_x(e_1) = e_1 - e_0 x$ and $a_n = b_n/n$, $b_n > 0$ is an arbitrary real number.

Agratini [1], İspir & Atakut [22] and Gupta [18] have studied and given some interesting results on the variant of Balázs operators. Many researchers have given King type modification for different operators (see, for instance, [8, 9, 13–16, 20, 21, 24–26]). Very recently, Gupta and Agarwal [19] have presented approximation properties of different operators. First author [7] studied pointwise estimate for the linear combination approximation for hybrid (Baskakov–Beta) operators by using of Ditzian–Totik modulus of smoothness.

In this paper we consider Balázs [5] operators for this type of modification. We assume that $\{r_n(x)\}$ is a sequence of real-valued continuous functions defined on $[0,\infty)$ with $0 \leq r_n(x) < \infty$, for $x \in [1, n/b_n)$ $(n/b_n \to \infty \text{ as } n \to \infty)$, $n \in \mathbb{N}$ and $n \geq 2$ then we have

$$\hat{R}_n(f; x) = \frac{1}{[1 + a_n r_n(x)]^n} \sum_{k=0}^{n} \binom{n}{k} [a_n r_n(x)]^k f\left(\frac{k}{b_n}\right), \tag{2}$$

where

$$r_n(x) = \frac{b_n}{a_n} \frac{x}{(n - b_n x)}, \quad x \neq n/b_n.$$

We obtain the following results at once.

Lemma 1.2. *Let $e_i(x) = x^i$, $i = 0, 1, 2, 3, 4$, then for $x \in [1, n/b_n)$ and $n \geq 2$, where $n \in \mathbb{N}$, we have*

$$\hat{R}_n(e_0; x) = 1, \quad \hat{R}_n(e_1; x) = x, \quad \hat{R}_n(e_2; x) = \frac{n-1}{n} x^2 + \frac{x}{b_n},$$

$$\hat{R}_n(e_3; x) = \frac{(n-1)(n-2)}{n^2} x^3 + \frac{3(n-1)}{n b_n} x^2 + \frac{x}{b_n^2}$$

and

$$\hat{R}_n(e_4; x) = \frac{(n-3)(n-2)(n-1)}{n^3} x^4 + \frac{6(n-1)(n-2)}{n^2 b_n} x^3 + \frac{7(n-1)}{n b_n^2} x^2 + \frac{x}{b_n^3}.$$

Lemma 1.3. *For $x \in [1, n/b_n)$, $n \geq 2$ where $n \in \mathbb{N}$ and $\varphi_x(t) = e_1 - e_0 x$, we have*

$$\hat{R}_n(\varphi_x; x) = 0, \quad \hat{R}_n(\varphi_x^2; x) = \lambda(x) \equiv \frac{x(1 - a_n x)}{n a_n}, \quad \hat{R}_n(\varphi_x^3; x) = \frac{2x^3}{n^2} + \frac{3(2n-1)}{n b_n} x^2 + \frac{x}{b_n^2},$$
$$\hat{R}_n(\varphi_x^4; x) = \frac{3(n-2)}{n^3} x^4 - \frac{6(n-2)}{n^2 b_n} x^3 + \frac{(3n-7)}{n b_n^2} x^2 + \frac{x}{b_n^3}.$$

The operators $\hat{R}_n$ preserve the linear functions, i.e., for $q(t) = at + b$, where a, b any real constants, we obtain $\hat{R}_n(q; x) = q(x)$. Throughout, in this paper we have taken $q(x) = \lambda(x)$ ($a_n = n^{-1/3}$, $b_n = n^{2/3}$) and $n \geq 2$, where $n \in \mathbb{N}$.

2. DIRECT ESTIMATES

In this section first we establish the following direct local approximation theorem for the modified operators $\hat{R}_n$ in ordinary approximation.

Theorem 2.1. *Let $f \in C_B[0, \infty)$, then for every $x \in [1, n/b_n)$ and for $C > 0$, $n \geq 2$, where $n \in \mathbb{N}$, we have* $\left| \left(\hat{R}_n f \right)(x) - f(x) \right| \leq C \omega_2 \left(f, \sqrt{\lambda(x)} \right)$.

Proof. Let $g \in W_\infty^2$. Using Taylor's expansion

$$g(y) = g(x) + g'(x)(y - x) + \int_x^y (y - u) g''(u) du$$

from Lemma 1.3 we have $\left(\hat{R}_n g \right)(x) - g(x) = \left(\hat{R}_n \int_x^y (y - u) g''(u) du \right)(x)$. We know that $\left| \int_x^y (y - u) g''(u) du \right| \leq (y - u)^2 ||g''||$. Therefore

$$\left| \left(\hat{R}_n g \right)(x) - g(x) \right| \leq \left(\hat{R}_n (y - u)^2 \right)(x) ||g''|| = \lambda(x) \, ||g''||.$$

By Lemma 1.2, we have

$$\left| \left(\hat{R}_n f \right)(x) \right| \leq \frac{1}{[1 + a_n r_n(x)]^n} \sum_{k=0}^{n} f\left(\frac{k}{b_n} \right) \binom{n}{k} [a_n r_n(x)]^k \leq ||f||.$$

Hence

$$\left| \left(\hat{R}_n f \right)(x) - f(x) \right| \leq \left| \left(\hat{R}_n (f - g) \right)(x) - (f - g)(x) \right| + \left| \left(\hat{R}_n g \right)(x) - g(x) \right|$$
$$\leq 2||f - g|| + \lambda(x) \, ||g''||.$$

Taking the infimum on the right side over all $g \in W_\infty^2$ and using (1), we get the required result. □

Remark 2.2. Under the same conditions of Theorem 2.1, we obtain

$$|(R_n f)(x) - f(x)| \leq C \omega_2 \left(f, \sqrt{m(x)} \right).$$

In the year 1932, Voronovskaya [27] studied asymptotic formula for Bernstein polynomials. Motivated by this work, many researchers have given Voronovskaya type results (see e.g. [3, 6, 23]). Here we compute the following Voronovskaya type result for the operators (2).

Theorem 2.3. *If a function f is such that its first and second derivative are bounded in $[0, \infty)$ then for $C > 0$ and $n \geq 2$, where $n \in \mathbb{N}$, we get*

$$\left[\left(\hat{R}_n f \right)(x) - f(x) \right] = \frac{\lambda(x)}{2} f''(x). \tag{3}$$

Proof. Applying Taylor's theorem we write that

$$f(t) - f(x) = (t - x) f'(x) + \frac{(t - x)^2}{2!} f''(x) + \frac{(t - x)^2}{2!} \xi(t, x), \tag{4}$$

where $\xi(t,x)$ is a bounded function $\forall t,x$ and $\lim\limits_{t\to x}\xi(t,x)=0$. Using (2) and (4), we obtain

$$\left(\hat{R}_nf\right)(x)-f(x)=f'(x)\hat{R}_n\left(\varphi_x,x\right)+\frac{f''(x)}{2}\hat{R}_n\left(\varphi_x^2,x\right)+\frac{1}{2}\hat{R}_n\left(\varphi_x^2,x\right)\xi(t,x).$$

From Lemma 1.3, we get

$$\left[\left(\hat{R}_nf\right)(x)-f(x)\right]=\frac{f''(x)}{2}\lambda(x)+\hat{R}_n\left(\varphi_x^2,x\right)\xi(t,x).$$

Now, we have to show that as $n\to\infty$, the value of $I=(na_n/2)\hat{R}_n\left(\varphi_x^2,x\right)\xi(t,x)\to 0$. Let $\varepsilon\geq 0$ be given since $\xi(t,x)\to 0$ as $t\to x$, then there exists $\delta>0$ such that when $|t-x|<\delta$ we have $|\xi(t,x)|<\varepsilon$ and when $|t-x|\geq\delta$, we write $|\xi(t,x)|\leq C<C(t-x)^2\delta^{-2}$. Thus, $|\xi(t,x)|\leq\varepsilon+C(t-x)^2\delta^{-2}$ for all $t,x\in[0,\infty)$ and

$$I\leq na_n\hat{R}_n\varphi_x^2(\varepsilon+C\varphi_x^2\delta^{-2}))(x)\leq E_1+E_2;$$
$$E_1=na_n\varepsilon(\hat{R}_n\varphi_x^2)(x),\quad E_2=na_nC\delta^{-2}\left(\hat{R}_n\varphi_x^4\right)(x),$$

by Lemma 1.3 and choosing ε arbitrarily as 0, we obtain E_1 and E_2 tends to 0 as $n\to\infty$. Hence $I\to 0$ as $n\to\infty$. This leads to (3). □

Our next results are error estimation followed by the rate of convergence in terms of modulus of continuity.

Theorem 2.4. *If $g\in C_B^2[0,\infty)$, then we have*

$$\left|\left(\hat{R}_ng\right)(x)-g(x)\right|\leq\frac{\lambda(x)}{2}||g||_{C_B^2}. \tag{5}$$

Proof. We have

$$g(t)-g(x)=(t-x)g'(x)+\frac{1}{2}(t-x)^2g''(\zeta), \tag{6}$$

where $t\leq\zeta\leq x$. From Lemma 1.3 and (6), we get

$$\left|\left(\hat{R}_ng\right)(x)-g(x)\right|\leq||g'||\left|\left(\hat{R}_n\varphi_x\right)(x)\right|+\frac{1}{2}||g''||\left|\left(\hat{R}_n\varphi_x^2\right)(x)\right|$$
$$\leq\frac{\lambda(x)}{2}||g''||=\frac{\lambda(x)}{2}||g||_{C_B^2}.$$

□

Remark 2.5. Under the same conditions of Theorem 2.4, we obtain

$$|(R_ng)(x)-g(x)|\leq(1/2)hg(x)||g||_{C_B^2}.$$

Theorem 2.6. *For $f\in C_B[0,\infty)$, we obtain*

$$\left|\left(\hat{R}_nf\right)(x)-f(x)\right|\leq A\left[\omega_2\left(f,\sqrt{\lambda(x)}/2\right)+\min\{1,\lambda(x)/4\}\,||f||_{C_B}\right],$$

where constant A depends on f and $\lambda(x)/2$.

Proof. For $f\in C_B[0,\infty)$ and $g\in C_B^2[0,\infty)$, we write

$$\left(\hat{R}_nf\right)(x)-f(x)=\left(\hat{R}_nf\right)(x)-\left(\hat{R}_ng\right)(x)+\left(\hat{R}_ng\right)(x)-g(x)+g(x)-f(x)$$

from (5) and Peetre K_2-functions, we get

$$\left|\left(\hat{R}_nf\right)(x)-f(x)\right|=\left|\left(\hat{R}_nf\right)(x)-\left(\hat{R}_ng\right)(x)\right|+\left|\left(\hat{R}_ng\right)(x)-g(x)\right|+|g(x)-f(x)|$$
$$\leq\left|\left|\hat{R}_nf\right|\right|||f-g||+\frac{\lambda(x)}{2}||g||_{C_B^2}+||f-g||\leq 2||f-g||+\frac{\lambda(x)}{2}||g||_{C_B^2}$$
$$=2\left\{||f-g||+\frac{\lambda(x)}{4}||g||_{C_B^2}\right\}\leq 2K_2\{f,\lambda(x)/4\}$$

$$\leq 2A\left[\omega_2\left(f,\sqrt{\lambda(x)}/2\right)+\min\left\{1,\lambda(x)/4\right\}||f||_{C_B}\right].$$

This completes the proof. □

Remark 2.7. By the same conditions of Theorem 2.6, we get

$$|(R_nf)(x)-f(x)|\leq 2A\left[\omega_2\left(f,[m(x)]^{1/2}/2\right)+\min\left\{1,m(x)\right\}||f||_{C_B}\right].$$

Theorem 2.8. *For every $f\in C[0,\infty)$, $x\in[1,n/b_n)$ and $n\geq 2$, where $n\in\mathbb{N}$, we obtain*

$$\left|\left(\hat{R}_nf\right)(x)-f(x)\right|\leq 2\omega\left(f,\delta_x\right),$$

where $\omega(f,\delta_x)$ is the modulus of continuity of f.

Proof. For $f\in C[0,\infty)$, $x\in[1,n/b_n)$ and $n\geq 2$, where $n\in\mathbb{N}$, using linearity and monotonicity of $\hat{R}_n$, we obtain, for every $\delta_x>0$, that

$$\left|(\hat{R}_nf)(x)-f(x)\right|\leq\omega(f,\delta_x)\left[1+\delta_x^{-1}\sqrt{\hat{R}_n\left(\varphi_x^2,x\right)}\right].$$

By using Lemma 1.3 and choosing $\delta_x=\sqrt{\lambda(x)}$ this completes the proof. □

Remark 2.9. For the original operator R_n defined in, we may write that, for every $f\in C[0,\infty)$

$$|(R_nf)(x)-f(x)|\leq 2\omega\left(f,\nu_x\right),\quad \nu_x=\sqrt{m(x)},\tag{7}$$

where $\omega(f,\nu_x)$ is the modulus of continuity of f. The error estimate in Theorem 2.8 is better than that of (7) for $f\in C[0,\infty)$ and $x\in[1,n/b_n)$, we get $\delta_x\leq\nu_x$.

Finally we compute rate of convergence of these operators by means of the Lipschitz class $Lip_M(\gamma)$ $(0<\gamma\leq 1)$. As usual, we say that $f\in C_B[0,\infty)$ belongs to $Lip_M(\gamma)$ if the inequality

$$|f(t)-f(x)|\leq M|t-x|^{\gamma}\tag{8}$$

holds.

Theorem 2.10. *If $f\in Lip_M(\gamma)$ and $x\in[1,n/b_n)$, we have*

$$\left|\left(\hat{R}_nf\right)(x)-f(x)\right|\leq M[\lambda(x)]^{\gamma/2}.$$

Proof. For $f\in Lip_M(\gamma)$, $x\in[1,n/b_n)$ and $n\geq 2$, where $n\in\mathbb{N}$, from inequality (8) and using the Hölder inequality with $p=2/\gamma, q=2/(2-\gamma)$, we get

$$\left|\left(\hat{R}_nf\right)(x)-f(x)\right|\leq\left(\hat{R}_n\left|f(t)-f(x)\right|\right)(x)$$

$$\leq M\left(\hat{R}_n|t-x|^{\gamma}\right)(x)\leq M\left[\left(\hat{R}_n\varphi_x^2\right)(x)\right]^{\gamma/2}\leq M[\lambda(x)]^{\gamma/2}.$$

This leads to the result. □

Remark 2.11. From Lemma 1.1, under the same conditions of Theorem 1.1 for the original operator R_n, then we have $|(R_nf)(x)-f(x)|\leq M[m(x)/2]^{\gamma/2}$ for every $f\in Lip_M(\gamma)$.

ACKNOWLEDGMENTS

The authors are grateful to the Professor N. İspir and Professor O. Duman, Ankara, Turkey for valuable suggestions for improvements in the paper. The authors are also thankful to the editor, Professor A.M. Elizarov for suggestions and special attention.

REFERENCES

1. O. Agratini, Math. Notes Miskolac **2** (1), 3–10 (2001).
2. F. Altomare and M. Campiti, *Korovkin-Type Approximation Theory and its Applications* (Walter de Gruyter, Berlin/New York, 1994).
3. G. A. Anastassiou, Stud. Univ. Babes-Bolyai Math. **58** (1), 65–73 (2013).
4. G. A. Anastassiou and S. G. Gal, *Approximation Theory* (Birkhäuser, Boston/Basel/Berlin, 2000).
5. K. Balázs, Acta Math. Acad. Sci. Hungar **26** (1-2), 123–134 (1975).
6. A. Ciupa, Int. J. Math. Math. Sci. **26**, 1–7 (2006).
7. N. Deo, Lobachevskii J. Math. **31** (1), 36–42 (2010).
8. N. Deo, Appl. Math. Comput. **218**, 10486–10491 (2012).
9. N. Deo and N. Bhardwaj, Appl. Math. Comput. **217**, 5531–5536 (2011).
10. N. Deo, M. A. Noor, and M. A. Siddiqui, Appl. Math. Comput. **201**, 604–612 (2008).
11. R. A. DeVore and G. G. Lorentz, *Constructive Approximation* (Springer, Berlin, 1993).
12. O. Doğru, Studia Univ. Babeş-Bolyai Math. **XLVII** (4), 37–45 (2002).
13. O. Doğru and M. Örkcü, Math. Comput. Modelling **50**, 1245–1251 (2009).
14. N. Deo and N. Bhardwaj, Lobachevskii J. Math. **32** (1), 16–22 (2011).
15. O. Duman, M. A. Ozarslan, and H. Aktuglu, J. Computational Analysis and Applications **10** (1), 53–59 (2008).
16. O. Duman and M. A. Özarslan, Appl. Math. Lett. **20**, 1184–1188 (2007).
17. J. L. Durrmeyer, Une formule d'inversion de la transformée de Laplace-applications à la théorie des moments, Thése de 3e cycle, Faculté des Sciences de l' Université de Paris (1967).
18. V. Gupta, Appl. Math. Comput. **199**, 823–827 (2008).
19. V. Gupta and R. P. Agarwal, *Convergence Estimates in Approximation Theory* (Springer-Verlag, New York, 2014).
20. V. Gupta and N. Deo, Math. Slovaca **61** (5), 799–806 (2011).
21. V. Gupta and O. Duman, Mat. Vesnik. **62** (4), 259–264 (2010).
22. N. Ispir and C. Atakut, Int. J. Comput. Number. Anal. Appl. **4** (3), 297–316 (2003).
23. H. Karsli, Proceedings of the Estonian Academy of Sciences **61** (1), 9–19 (2012).
24. J. P. King, Acta Math. Hungar **99**, 203–208 (2003).
25. M. A. Özarslan, O. Duman, and C. Kaanoğlu, Math. Comput. Modelling **52**, 334–345 (2010).
26. L. Rempulska and K. Tomczak, Turkish J. Math. **33**, 273–281 (2009).
27. E. Voronovskaya, C. R. Acad. Sci. URSS **79**, 79–85 (1932).

2015 17th UKSIM-AMSS International Conference on Modelling and Simulation

A Sentiment and Interest Based Approach for Product Recommendation

Vibhu Jawa
Applied Mathematics Department
Delhi Technological University
Delhi, India
vibhujawa@gmail.com

Varun Hasija
Applied Mathematics Department
Delhi Technological University
Delhi, India
warunhasija@gmail.com

***Abstract* - The growing popularity of social networks has led to abundant availability of user sentiments, making them a crucial factor in buying decisions, public opinions, and brand reputations. Rise of real-time web has provided an opportunity to utilise time-sensitive data which is available in the form of tweets on public and private Twitter streams, as the basis for product recommendation based on Sentiment analysis.**
In this paper, we propose a model working on the basics of Interest graph in conjunction with Sentiment analysis to compute the correlation between different entities and provide recommendations, which range from whom to follow on Twitter to what to buy online.

Keywords - Twitter, Interest Graph, Recommendations, Algorithm, Sentiment Analysis.

I. INTRODUCTION

The vast amount of user generated content in social media applications and its high rate of generation has given us the opportunity to build real-time recommendation systems.

Twitter provides a medium to share our ideas and experiences with the whole world instantaneously. It acts as a channel to satisfy our curiosity, thus providing for the root need of every individual to be heard as well as a sense of worth and importance. Twitter acts as an easy and a fast medium which matches human beings at their speed of their thought [1].

The growing popularity of social networks has led to abundant availability of user sentiments, making them a crucial factor in buying decisions, public opinions, and brand reputations. "Internet-Scale Interest Graph" is a representation of the relationship between people and their interests. Having that knowledge allows us to tie two remote entities with no obvious common properties and show possible, but yet unexplored connections, thus discovering various relationships and interconnections between user groups and their interests [3].

Previous attempts on providing recommendations have been based on Interest Graphs or Sentiment analysis. The main idea behind this work is to explore the conjunction of Interest graphs and Sentiment analysis, to compute the correlations and provide recommendations, which range from whom to follow on Twitter to what to buy online.

II. LITERATURE REVIEW

A. Interest Graph

Pankaj Gupta et al. [21] at Twitter, presented a service called WTF (WHO TO FOLLOW) in which they explored the implications of usage of interest graphs in their user recommendation algorithm. Other researchers have also shown affinity towards Interest Graphs over Social Graphs. "The Interest Graph is an online representation of individuals' interests, with people and interests being the nodes of the graph. Connections exist between people and interests, as well as, between interests and derived interests. The strength of the connection depends on the level of interest or relatedness between concepts and can change over time. "[4]

Interest graphs find its roots in the semantic web which is defined by Tim Berners-Lee as "web of data that can be processed directly and indirectly by machines". Semantic Web defines the relationships between people and things, where relationships are represented as "triples" [11]. Conceptually, triples can be thought of as:
"PERSON-RELATIONSHIP-THING**"**
Such as Bob likes Moto X.

There are two approaches for data collection to create interest graphs [4]:
Explicit: The user provides the information.
Implicit: The user's activity is followed and the interests are derived through it.

Explicit approach may create hindrances for the users and might make them uncomfortable about providing detailed information about their interests. Users may also exercise the option to search the required product or service directly. An example of explicit approach can be Pinterest.
Implicit approach is best explained with the help of an example- Amazon uses implicit approach for data collection. The site collects information about one's purchase history and search history and computes co-relations (the people who bought this also bought that or the people who searched this item also looked for that item).
The bottom line is to collect information about the user's interests, irrespective of the approach followed for data collection. It has been observed that explicit approach tends to generate inaccurate profile of users. Hence, it is suggested

978-1-4799-8713-9/15 $31.00 © 2015 IEEE
DOI 10.1109/UKSim.2015.26

IEEE computer society

to use the implicit approach and collect data according to real interests of the users.

Next, we find the relationship that exists between various user groups and their interests. For example, we could have a group of travel enthusiasts amongst our customers who could be interested in "camping", "mountaineering", and "hiking" etcetera. All the activities that they are interested in could have a common related interest of "Outdoor Sports". Having that knowledge allows us to tie two remote entities with no obvious common properties and show possible, but yet unexplored connections.

Visualization of the interest graph is a great way to discover various relationships and interconnections between user groups and interests.

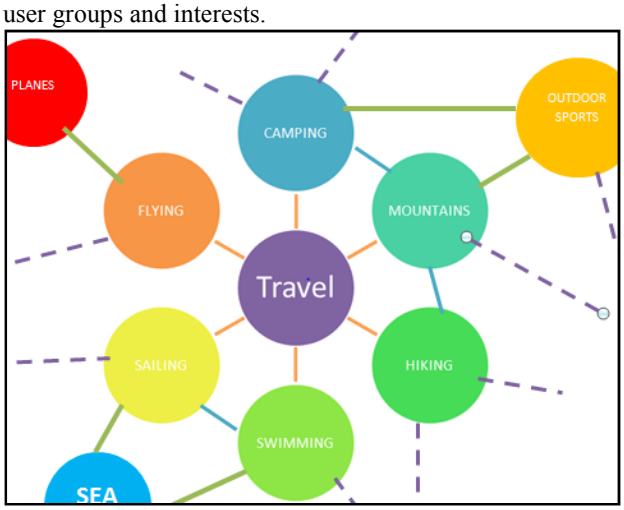

Figure 1: An example of interest graph

B. *Sentiment Analysis*

Davide Feltoni Gurini *et al.* [10] presented a technique based on a weighting function which takes into account users sentiments and then recommends them users based on it. Singh et al. [20] implemented a recommender system that incorporates sentiment classification in the case of movie recommendation.

Bing Liu defined Sentimental analysis (or opinion mining) as the study of sentiments and opinions about an entity conveyed through text [2].

Natural language processing, text analysis, and computational linguistics are being used by researchers to identify and extract relevant information in source materials. In layman terms, the purpose of sentiment analysis is to classify the product as "good or bad".

Based on level of granularities, sentiment analysis can be investigated at three levels [2]:

1. Document level: At this level, the task is to identify whether a "document" expresses a positive or a negative opinion. This type of analysis assumes that each document expresses opinions on a single entity.
2. Sentence level: At this level, the task is to identify whether each sentence expresses a positive, a negative or a neutral opinion. It can be thought of as a two-step process:
    - Subjectivity classification
    - Sentiment classification
3. Entity level/ Aspect level/ Feature level: Document level and sentence level does not tell us about WHAT people liked and WHAT they did not. Entity level is based on the fact that every opinion consists of a sentiment and a target. Hence, it performs a fine-grained analysis.

Opinions can also be divided further into regular opinions and comparative opinions. A regular opinion expresses sentiments towards a particular entity, whereas a comparative opinion compares different entities based on the attributes shared by them. [19]

Sentiment Lexicon: The most important indicators of sentiments are opinion words. These are the words which can be used to express positive or negative sentiments. For example, *"good", "awesome", "amazing"* are words expressing positive sentiments, whereas "bad", "terrible", "disgusting" express negative sentiments.

Formally, opinion is defined as a Quadruple, [2]

$$(g, s, h, t),$$

where,

- g is the opinion or sentiment target,
- s is the sentiment about the target,
- h is the opinion holder,
- t is the time when opinion was expressed.

Objective of sentiment analysis based on the above given definition can be stated as:

Given an opinion document d, discover all opinion quadruples in d and analyze those opinions to classify them as positive or negative.

III. RESEARCH LEADING TO DEVELOPMENT

"Tweets are the essence of Twitter, and while they are notionally thought of as the 140 characters of text content associated with a user's status update, there's really quite a bit more metadata there than what meets the eye." – Matthew Russell [5]. Tweets, in addition to textual content, come bundled with two subsidiary pieces of metadata i.e. *entities* and *places*. "Entities" consist of the user mentions, URLs, hashtags and media that might be associated with the tweet and "Place" is the location in real world that is attached to the tweet.

We can easily differentiate or find similarities between the most trending topic in different parts of the world using the Yahoo! GeoPlanet's WOE – Where on Earth, ID system [6].

Word frequency can be defined as the number of occurrences of a word per unit tweet.

We can derive positive or negative sentiments from the word frequency in tweets, which gives us an insight about the public opinion of the entity being observed.

For example, consider the word frequency of words obtained when searched about a topic like “SONY”

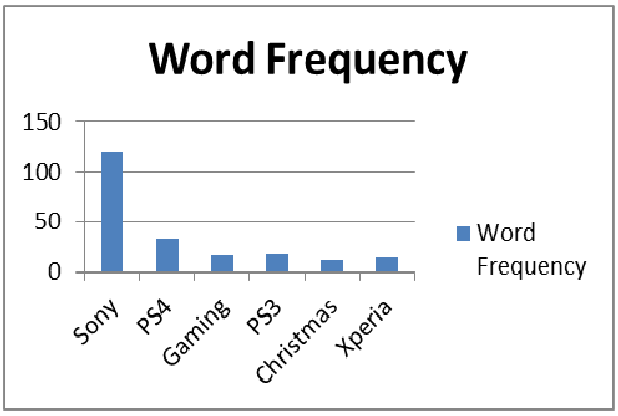

Figure 2: Word Frequency graph for "SONY"

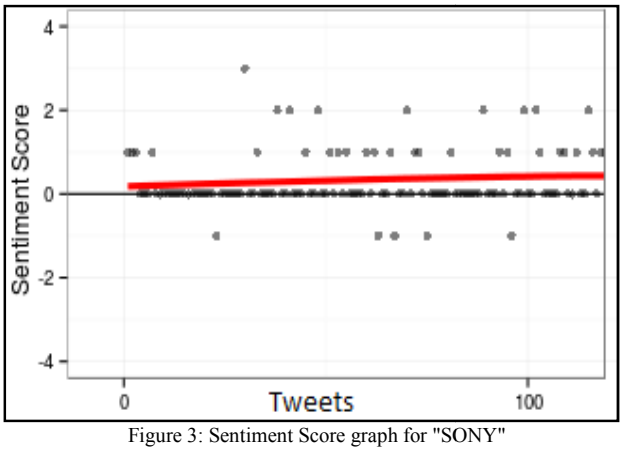

Figure 3: Sentiment Score graph for "SONY"

These graphs could suggest us which *product* is better if compared on the basis of the public sentiment procured from the tweets. Sentiment score is positive means that the entity has a positive sentimental value.

Now, we take the help of interest graphs and sentiment analysis to recommend which product is better than its counterparts or to rank different products from all over the world.

For example, we take two entities and compare them on the basis of sentiment analysis of frequently occurring words. Let the 1st and 2nd entities be “SONY” & “Samsung” respectively.

On plotting the word frequency graphs of the tweets containing “SONY” as an entity we recognize that:

1. PS4 is the most popular product,
2. Tokyo is the “Place” most popularly linked with,

Some words of sentimental value such as “great”, “good”, “unsatisfactory” etcetera are also observed. Similarly, on plotting the word frequency graph of tweets containing “Samsung” as an entity, we recorded similar results.

From these examples, we infer that, word frequency of tweets contains some important information with respect to the kind of entity we are observing:

1. If the entity is an organization, the word frequency table will contain some information about its products.
2. If the entity is a product, the word frequency table will contain some information about its parent organization, some information about its counterparts and some information about the nature of the product.
3. Information about random and latest trends in which the company is involved. Ex. “SONY server hack”.

Using interest graphs and sentiment analysis, we now provide a method that can be used for recommending a certain entity or comparing different entities based on a weighted ranking system (ranking entities on a scale of -1 to 1).

IV. PROPOSED MODEL

We propose a model of coagulation of Interest Graphs and Sentiment analysis for product recommendation.

Our model can be divided into two steps:

1. Word processing and related entity identification:

Before performing any kind of analysis, the tweets were pre-processed in which, the redundant spaces, URLS, hash tags, tweet header and references to other screen names are removed. [16]

Our algorithm creates a data frame, which contains the information for each tweet. Data frame provides a readable format of the information related with mined tweets.

For creating interest graphs, a data matrix is formed using the data frame and the row sum of each entity is calculated i.e. the number of occurrences of an entity and sorted in descending order of frequency. Then the ‘entities’ are extracted from this list and bound together into a data frame with frequencies - called cloud frame [15] with names in separate columns.

Thus, the secondary entities in descending order of relation with our primary entity are obtained.

In the interest graphs displayed below, the strength of connection of interest is depicted according to their font size.

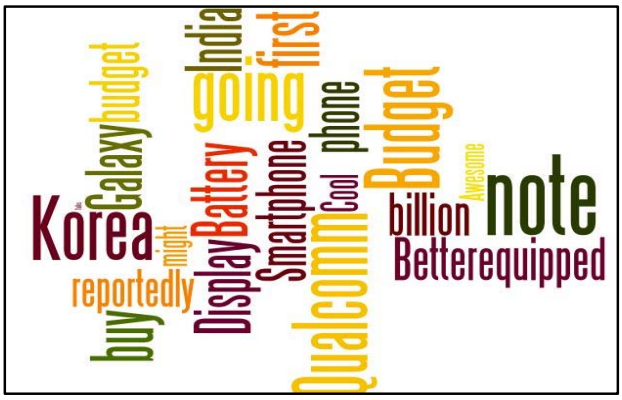

Figure 4: Interest Graph for "Samsung"

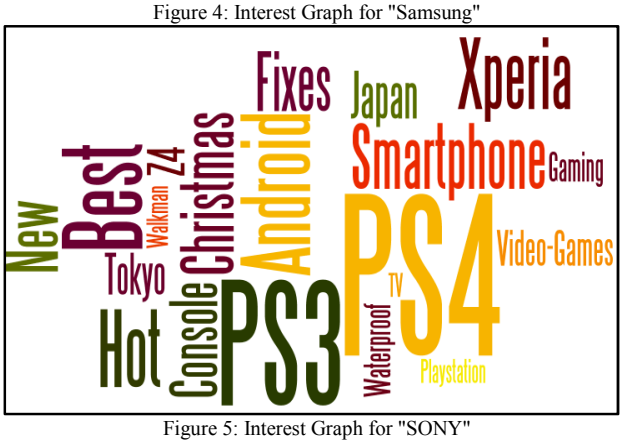

Figure 5: Interest Graph for "SONY"

Once the secondary entities are derived we calculate the sentimental value associated with each entity using the following described approach.

2. Sentiment analysis of identified entities: In our model, once the tweets are mined and cleaned, a vector of sentences is generated and "Plyr" [8] is used to handle the list. Sentences are cleaned up using R's regex-driven global substitute, "gsub" and then, converted into lower-case words.

Then, the words are compared to the dictionaries of positive & negative terms using match function and the total score is calculated by subtracting the total number of positive matches from negative matches

Sentiment Scoring Scheme: Breen's algorithm is used for calculating the sentiment score for each entity [7].

- If Score > 0, we infer that the sentence has a net 'positive opinion'.
- If Score < 0, we infer that the sentence has a net 'negative opinion'
- If Score = 0, we infer that the sentence has a net a 'neutral opinion'.

We use the opinion lexicon in English for counting the positive and negative words provided by Hu and Liu. [9]

After analyzing the sentiments, its graph is plotted. We depict the sentiments of 100 tweets in sets of four i.e. each data point shown in Figure: 6 represents the sentiment score for four tweets.

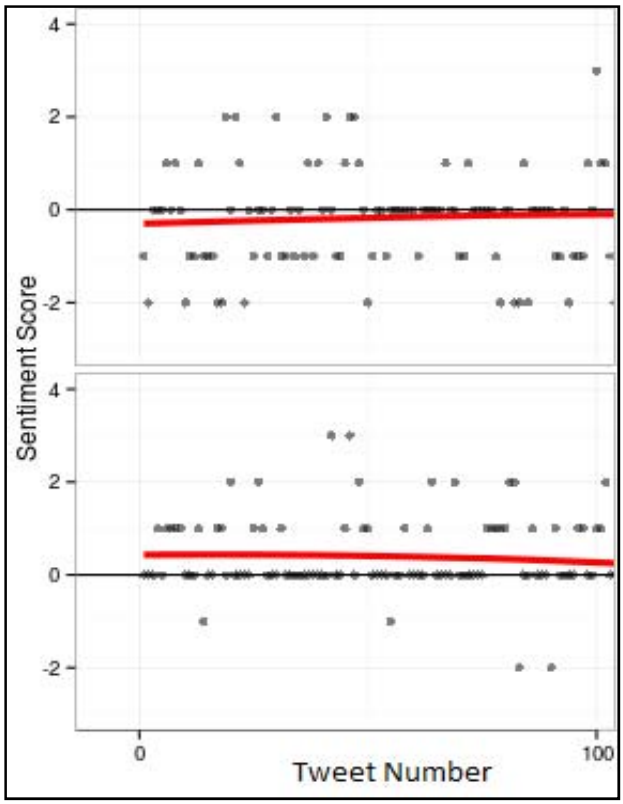

Figure 6: Sentiment Score graph for "Samsung" & "SONY"

After obtaining the sentiment score for the primary entity, our algorithm obtains the same for all the secondary entities obtained from the interest graph.

Then, our algorithm calculates the final score by inculcating both these scores using the formula given below:

$$\text{Final Score} = 0.75 * \left(Sentiment_{primary}\right) + (0.25) * \frac{1}{Total\ occurrence} * \sum_{k=1}^{n} Sentiment_k * Frequency_k$$

Where,

- *Sentiment* $_{primary}$ is the Sentiment Score of the primary entity
- *Sentiment* $_k$ is the Sentiment Score of the kth entity
- *Frequency* $_k$ is the number of occurrences of the kth entity
- *Total Occurrence* is the sum of all the occurrences of the secondary entities.

The resulting sentiment can be positive, negative or neutral. We can compare this score for multiple products and can recommend a product with the maximum positive social sentiment.

The following table depicts the differences between the average sentiment score of "Primary Entity" and the average "Commutative sentiment score" calculated by mining 30000 tweets each of Sony and Samsung.

TABLE 1. SENTIMENT SCORE FOR "SONY" & "Samsung"

Entity	Primary Entity Sentiment Score	Commutative Sentiment Score
SONY	0.56	0.61
Samsung	0.59	0.42

The commutative score of entities calculated through our algorithm show that the impact of the derived entities from the interest graph of the primary entity plays a huge role in forming the public opinion of the product and cannot be ignored. Thus, our results reinforce the notion that by integrating the techniques of sentiment analysis and Interest Graph we get a greater perception into the public opinion of the product.

The algorithm for creating interest graph is summarized below:

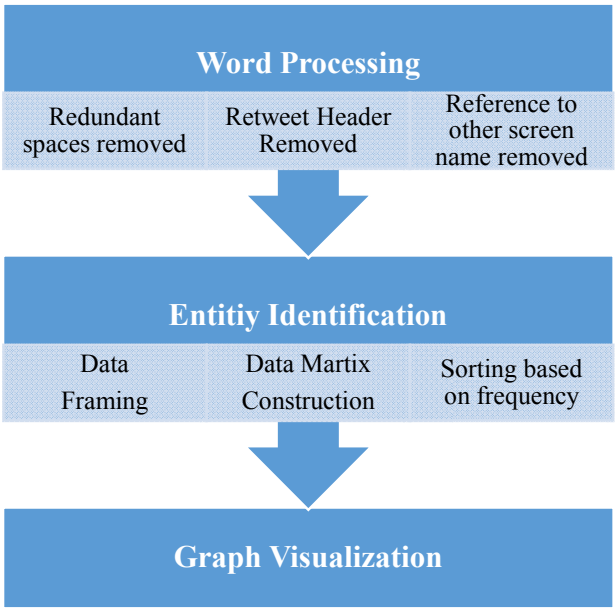

The algorithm for sentiment analysis is summarized below:

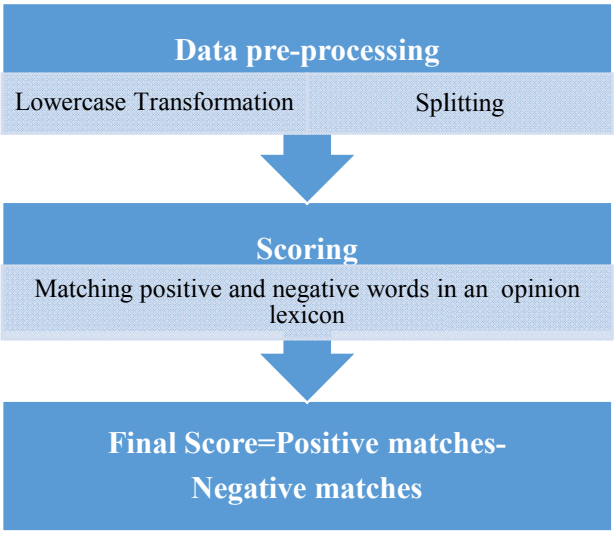

V. CONCLUSION AND FUTURE WORK

We presented a novel recommendation system, which recommends products by acquiring the public sentiment about the product and its derived entities

Thus, by integrating the techniques of sentiment analysis and Interest Graph we get a greater insight into the public opinion of the product.

This "one parent" approach can be mirrored for the derived entities for which we can develop interest graphs of all the derived entities of the parent interest graph. This recursive approach can be used to develop deeper and more correlated webs of interest graphs giving us a more extensive perception about product's social sentiment.

An alternative to allotting fixed weights to each derived entity can be allotting variable weights which are representative of real world relations to the primary entity. These variable weights would be based on the impact factor which each derived entity has on its parent entity.

ACKNOWLEDGEMENT

We would like to thank Twitter Inc. for providing an API to their service. We would also like to thank Matthew A. Russell for authoring "Mining the social web" which inspired us to work on this project.

REFERENCES

[1] Issie Lapowsky (4 October 2013). "Ev Williams on Twitter's Early Years". Inc. Inc. Retrieved 5 October 2013.
[2] Bing Liu. Sentiment Analysis and Opinion Mining, Morgan & Claypool Publishers, May 2012
[3] How the Interest Graph will shape the future of the web, By rr11 in Web, Mobile & Hardware ; April 1 2011
[4] Cygnismedia blog "what-is-interest-graph"
[5] Matthew A. Russell, Mining the Social Web: Analyzing Data from Facebook, Twitter, LinkedIn, and Other Social Media Sites, O'Reilly Media, Inc., 2011
[6] "Yahoo! WOEID Lookup". http://Zourbuth Project
[7] Gary Miner (Author), John Elder IV (Author), Thomas Hill (Author), Robert Nisbet (Author), Practical Text Mining and Statistical Analysis for Non-structured Text Data Applications. ISBN-13: 978-0123869791
[8] Hadley Wickham (2011). The Split-Apply-Combine Strategy for Data Analysis. Journal of Statistical Software, 40(1), 1-29. URL http://www.jstatsoft.org/v40/i01/.
[9] Hu and Liu, Opinion Lexicon, KDD-2004
[10] Davide Feltoni Gurini, Fabio Gasparetti,Alessandro Micarelli and Giuseppe Sansonetti "A Sentiment-Based Approach to Twitter User Recommendation".
[11] Berners-Lee, Tim (May 1, 2001). "The Semantic Web". Scientific American
[12] Hang Li ,Learning to Rank for Information Retrieval and Natural Language Processing, Second EditionOctober 2014
[13] F. Burkhardt, C. Becker-Asano, E. Begoli, R. Cowie, G. Fobe, P. Gebhard, A. Kazemzadeh, I. Steiner, T. Llewellyn: Application of EmotionML. Proceedings of the 5th International Workshop on Emotion, Sentiment, Social Signals and Linked Open Data (ES3LOD), 2014.
[14] Paul Buitelaar, Mihael Arcan, Carlos A. Iglesias, J. Fernando Sánchez, Carlo Strapparava (2013) Linguistic Linked Data for Sentiment Analysis 2nd Workshop on Linked Data in Linguistics (LDL 2013): Representing and linking lexicons, terminologies and other language data. Collocated with the Conference on Generative Approaches to the Lexicon, Pisa, Italy

[15] Kapanipathi, P., Jain, P., Venkataramani, C., & Sheth, A. P. (2014). Hierarchical Interest Graph from Tweets. *Proceedings of the Companion Publication of the 23rd International World Wide Web Conference*, 311-312.

[16] B. Sriram, D. Fuhry, E. Demir, H. Ferhatosmanoglu, and M. Demirbas. Short text classification in twitter to improve information filtering. SIGIR '10.

[17] F. Orlandi, J. Breslin, and A. Passant. Aggregated, interoperable and multi-domain user profiles for the social web. I-SEMANTICS '12

[18] Thet, Tun Thura, Jin-Cheon Na, Christopher S. G. Khoo, and Subbaraj Shakthikumar. 2009. Sentiment analysis of movie reviews on discussion boards using a linguistic approach. In Proceedings of the First International CIKM Workshop on Topic-Sentiment Analysis for Mass Opinion Measurement, pages 81–84, Hong Kong.

[19] Wilson, Theresa, Janyce Wiebe, and Rebecca Hwa. 2004. Just how mad are you? Finding strong and weak opinion clauses. In AAAI 2004, pages 761–767, San Jose, CA.

[20] V. K. Singh, M. Mukherjee, and G. K. Mehta. Combining collaborative filtering and sentiment classification for improved movie recommendations. In Proceedings of the 5th International Conference on Multi-Disciplinary Trends in Artificial Intelligence, MIWAI'11, pages 38{50, Berlin, Heidelberg, 2011. Springer-Verlag.

[21] P. Gupta, A. Goel, J. Lin, et al., "WTF: the who to follow service at twitter," in Proceedings of the 22nd International World Wide Web Conference Committee (WWW '13), pp. 505–514, 2013.+

BMC Microbiology

BioMed Central
The Open Access Publisher

This Provisional PDF corresponds to the article as it appeared upon acceptance. Fully formatted PDF and full text (HTML) versions will be made available soon.

Antimicrobial and Immunomodulatory efficacy of extracellularly synthesized silver and gold nanoparticles by a novel phosphate solubilizing fungus *Bipolaris tetramera*

BMC Microbiology (2015) 15:52

doi:10.1186/s12866-015-0391-y

Faria Fatima (fatimafaria45@gmail.com)
Preeti Bajpai (pbajpai@iul.ac.in)
Neelam Pathak (pathak_neelam@yahoo.com)
Sarika Singh (ssj3010@gmail.com)
Shivam Priya (bajn2005@gmail.com)
Smita Rastogi Verma (srsmitarastogi@gmail.com)

Published online: 27 February 2015

ISSN 1471-2180

Article type Research article

Submission date 10 September 2014

Acceptance date 18 February 2015

Article URL http://dx.doi.org/10.1186/s12866-015-0391-y

Like all articles in BMC journals, this peer-reviewed article can be downloaded, printed and distributed freely for any purposes (see copyright notice below).

Articles in BMC journals are listed in PubMed and archived at PubMed Central.

For information about publishing your research in BMC journals or any BioMed Central journal, go to http://www.biomedcentral.com/info/authors/

© 2015 Fatima *et al.*; licensee BioMed Central.
This is an Open Access article distributed under the terms of the Creative Commons Attribution License (http://creativecommons.org/licenses/by/4.0), which permits unrestricted use, distribution, and reproduction in any medium, provided the original work is properly credited. The Creative Commons Public Domain Dedication waiver (http://creativecommons.org/publicdomain/zero/1.0/) applies to the data made available in this article, unless otherwise stated.

Antimicrobial and Immunomodulatory efficacy of extracellularly synthesized silver and gold nanoparticles by a novel phosphate solubilizing fungus *Bipolaris tetramera*

Faria Fatima[1]
Email: fatimafaria45@gmail.com

Preeti Bajpai[1*]
[*] Corresponding author
Email: pbajpai@iul.ac.in

Neelam Pathak[1]
Email: pathak_neelam@yahoo.com

Sarika Singh[2*]
[*] Corresponding author
Email: ssj3010@gmail.com

Shivam Priya[3]
Email: bajn2005@gmail.com

Smita Rastogi Verma[4]
Email: srsmitarastogi@gmail.com

[1] Department of Biosciences, Integral University, Lucknow 226026, India

[2] Division of Toxicology, Central Drug Research Institute, Lucknow 226026, India

[3] Division of Environmental Carcinogenesis, Indian Institute of Toxicology Research, Lucknow 226026, India

[4] Department of Biotechnology, Delhi Technological University, Delhi, 110042, India

Abstract

Background

Particulates of nanometers size have occupied a significant area in the field of medicinal and agricultural purposes due to their large surface-to-volume ratio and exceptional physicochemical, electronic and mechanical properties. Myconanotechnology, an interface between mycology and nanotechnology is budding nowadays for nanoparticle-fabrication using fungus or its metabolites. In the present study, we have isolated and characterized a novel phosphate solubilizing fungus *B. tetramera* KF934408 from rhizospheric soil. This phosphatase releasing fungus was subjected to extracellular synthesis of metal nanoparticles by redox reaction.

Results

Silver (AgNPs) and gold nanoparticles (AuNPs) were characterized by dynamic light scattering and transmission electron microscopic analysis. The formulated AgNPs were irregular shaped with a size ranging between 54.78 nm to 73.49 nm whereas AuNPs were spherical or hexagonal, with a size of 58.4 and 261.73 nm, respectively. The nanoparticles were assessed for their antibacterial and antifungal efficacy. The results showed effective antimicrobial activity of AgNPs against *Bacillus cereus, Staphylococcus aureus, Enterobacter aeroginosa* and *Trichoderma sp*. at higher concentrations, however, AuNPs possessed only moderate antibacterial efficacy while they found no antifungal activity. Cytotoxicity analysis of nanoparticles on *J774* and *THP1* α cell lines revealed the dose dependence in case of AgNPs, while AuNPs were non-toxic at both low and high doses. Furthermore, significant elevation of intracellular ROS was observed after 4 h of incubation with both the nanoparticles. The capping of fungal proteins on the particulates might be involved in the activities demonstrated by these inert metal nanoparticles.

Conclusion

In conclusion, the findings showed that the metal nanoparticles synthesized by fungus *B. tetramera* could be used as an antimicrobial agents as well as cost effective and nontoxic immunomodulatory delivery vehicle.

Keywords

Bipolaris tetramera, Cytotoxicity, Gold nanoparticle, Immunomodulatory, Silver nanoparticle

Background

Myconanotechnology is an emerging field, where fungi can be harnessed for the synthesis of nanomaterials or nanostructures with desirable shape and size. Potential applications of myconanotechnology have fascinated microbiologists and other researchers to contribute in providing incremental solutions through green chemistry approaches for targeted drug delivery. Nanosized particles have attracted worldwide attention due to their specific properties and applications in areas such as biomedical sciences [1].

In order to meet the wide scope of nanomaterials, an overwhelming number of protocols have been exploited for their synthesis, but unfortunately, most of them are capital-intensive, inefficient in material and energy use, and often pose health hazards because of usage of toxic chemicals [2-4]. Often chemical synthesis leads to the adsorption of toxic chemical species on the surface resulting in undesirable impact on human health [5]. Therefore, there is a persistent need to develop ecofriendly methods for the preparation of nanoparticles with better applicability and limited toxicity. On the other hand, synthesis using bio-organisms (bacteria, fungi, and plant extracts) is compatible with the green chemistry principles [6]. The biosynthesized nanoparticles, are eco-friendly and biocompatible for pharmaceutical applications. Biosynthesis of nanoparticles is a kind of bottom up approach where the main reaction is the reduction / oxidation reaction. The microbial enzymes possessing high redox potential are usually responsible for the reduction of metal compounds into their respective nanoparticles. As a result, nanomaterial synthesis mediated by biological systems has attracted scientific interest across the globe.

Fungi are preferred microbes for nanostructure formulation due to their ability to produce high amount of secretory proteins [7]. Numbers of reports have showed the biological synthesis of metal nanoparticles but the potential of a phosphate solubilizing fungi *B. tetramera* has not yet been demonstrated. The present study was performed to synthesize the silver and gold nanoparticles from *B. tetramera* (GenBank: KF934408), a novel phosphate solubilizing fungus, isolated from rhizospheric region. The potential antimicrobial, cytotoxic and immunomodulatory activity of these myconanoparticles synthesized has also been evaluated.

Methods

Isolation, screening and characterization of *B. tetramera* (KF934408)

The fungus was isolated from rhizospheric soil of Kukrail forest, Lucknow, India and screened by its phosphate solubilizing ability on Pikovskaya's medium by plate assay [8]. The fungal colonies were subculture on fresh petriplates containing media and the plates were incubated in inverted position for 72 h at 28 ± 2°C and further screened by observing halo zones around the colony.

Biochemical characteristics of the fungus were tested on the basis of lacto-colony morphology, microscopic analysis of conidia, phosphate solubilization index, starch hydrolysis test and cellulose hydrolysis test according to standard protocols [9].

The fungus was further characterized at molecular level by 18S rRNA sequencing. Genomic DNA was isolated from pure culture of the isolated fungus and subjected to high–fidelity PCR using universal primers *i.e.* forward primer (5'-GGAAGTAAAAGTCGTAACAAGG-3') and reverse primer (5'-TCCTCCGCTTATTGATATGC-3') and analyzed on 1% agarose gel. The PCR product was sequenced bi-directionally using the forward and reverse primers. Homology between this 18S rRNA sequence and the strains available at the public databases (Genbank, EMBL and DDBJ) was determined using BLASTN sequence match routines. The UPGMA (Unweighted Pair Group Mathematical Average) algorithm was used to perform hierarchical cluster analysis [10]. The sequences were aligned using CLUSTALW2 program and its phylogenetic and molecular evolutionary analysis were conducted. Sequences analysis was performed by alignment of the partial 18S rRNA gene sequences to those obtained from the GenBank database, using the program BLAST (NCBI BLAST® homepage). The nucleotide sequences of 18S rRNA gene segments, determined in this study have been deposited in GenBank database under accession number KF934408.

Myco-synthesis of metal nanoparticles

The isolated fungus was grown aerobically in MGYP (Maltose glucose yeast peptone) broth comprising of malt extract (0.5%), glucose (1%), yeast extract (0.3%) and peptone (0.5%). The culture was incubated at 27°C and harvested after 120 h of growth by sieving through a plastic sieve followed by extensive washing with sterile double-distilled water. Initially, 15 g of biomass (wet weight) was transferred to 100 ml deionized water for 48 h at 27°C in an Erlenmeyer flask and agitated at 150 x rpm for release of secretory proteins. 1 mM of silver nitrate and gold tetra hydrate were added to the Erlenmeyer flasks and the reaction was allowed to proceed in dark for synthesis of silver nanoparticles (AgNPs) and gold nanoparticles (AuNPs), respectively. Time-dependent formation of silver and gold nanoparticles was observed by using ultraviolet-visible spectrophotometer (Beckman DU-20 spectrophotometer). The scanning range was 350-650 nm for AgNPs and 400-800 nm for

AuNPs at a scan speed of 420 nm/min. The data was recorded and analyzed using "UVWinlab" software.

Differential light scattering (DLS)

The suspensions of AgNPs and AuNPs were prepared in distilled water (dH_2O) by using a bath-sonicator (ULTRAsonik 57 X, 50/60 Hz, California, USA) prior to size measurements. Viscosity measurements were performed on dH_2O with the aid of a Viscometer SV-10 (A&D Instruments Ltd., UK) at 25°C and the recorded values were used in all DLS size estimations. The viscosity of dH_2O at 25°C was 0.887 centipoise. DLS size measurements were performed with the aid of a Malvern Zeta Sizer Nano ZS (Malvern Instruments, Worcestershire, UK) operating with version 5.03 of the systems Dispersion Technology Software (DTS Nano). The samples for DLS were equilibrated at 25°C for 3 min before each measurement. The refractive index (RI) of AgNP.dH_2O was 1.330 and that for AuNP.dH_2O was 1.430.

Transmission electron microscopy (TEM)

The synthesized AuNPs and AuNPs were characterized by TEM studies. The samples for TEM analysis were prepared by placing a drop of synthesized nanoparticles over gold coated negative grid followed by evaporation of the solvent [11]. TEM analysis was performed on Perkin-Elmer model, which was operated at an accelerating voltage of 1000 kV.

Antibacterial efficacy

Pure cultures of five pathogenic bacteria, namely, *Bacillus subtilis, Bacillus cereus, Staphylococcus aureus, Escherichia coli* and *Enterobacter aeroginosa* were procured from National Chemical Laboratory, Pune. Bacterial stock cultures were maintained at 4°C on nutrient agar media slants and subcultured on nutrient broth media for antibacterial analysis of NPs. The turbidity (OD_{600}) of inocula was maintained at 0.8 corresponding to ~1×10^8 CFU/ml. The antibacterial potential of both the nanoparticles was analyzed using agar well diffusion method [12]. 5 mm wells of Muller Hinton agar in diameter were prepared and filled with a range of concentrations (10 μM, 50 μM, 100 μM, 150 μM, Ab, Ab + (Ag/Au)NP). Each experiment was performed in triplicate and the average zone of inhibition, excluding well, for each case was recorded. 1 mM $AgNO_3$ and $HAuCl_4$ were used as negative controls for analyses of AgNPs and AuNPs, respectively.

Antifungal efficacy

The antifungal activity of AgNPs and AuNPs was tested against *Aspergillus niger* and *Trichoderma* sp. by agar well diffusion method [13]. Aliquot of 50 μl spores suspension (1 x 10^8 spores/ml) of each isolate was streaked in radial patterns on the surface of media plates. 5 mm wells in diameter were prepared and filled with a range of concentrations, (150 μM, 200 μM and 250 μM) of both the nanoparticles prepared. The cultured plates were incubated at 28 ± 4°C for 7 days. The average inhibition zone, excluding well, for each case was measured.

Maintenance of cell lines

Mouse macrophage cell line *J774* and human macrophage cell line *THP1 α* was procured from the National Center of Cell Sciences, Pune, India and maintained at Animal Tissue Culture facility of Central Drug Research Institute (CDRI). Cells were maintained in

Dulbecco's modified Eagle's medium (DMEM) supplemented with 10% Foetal calf serum (FCS) and 1% antibiotic-antimycotic solution, at 37°C and 5% CO_2 using standard cell culture methods.

Cytotoxicity assay

Cell viability was determined by MTT [3-(4, 5-dimethylthiazol-2-yl)-2, 5-diphenyltetrazolium bromide] conversion assay [14]. The 1 x 10^6 cells/ml were plated in 96-well culture plates and incubated with increasing concentrations of nanoparticles (10 μM, 25 μM, 50 μM, 100 μM, 150 μM and 200 μM) for 24 h at 37°C in CO_2 incubator. The MTT dye was added to each well and plate was incubated at 37°C for 4 h. The absorbance of insoluble formazan salts was assessed at 550 nm using Powerwave XS "BIOTEK, USA" spectrophotometer [15]. Data produced were used to plot a dose-reaction curve and the concentration of these metal nanoparticles required to kill 50% of cell population (IC_{50}) was determined.

$$\text{Cell viability } (\%) = \frac{\text{Mean OD}}{\text{Control OD}} \times 100$$

Intracellular reactive oxygen species estimation

Intracellular oxidative stress was estimated by using fluorescent dye 2', 7'-dichlorofluorescin di-acetate (DCFH-DA), a well accepted fluorescent marker for study of intracellular hydroperoxides [16]. The experiment was performed according to the protocol described by Goswami et al. [17] with slight modifications. Primarily, healthy confluent cells were harvested and seeded (1000 cells/well) into black bottomed 96 well plates (Nunc, Denmark) and allowed to adhere for a period of 24 h prior to exposure. For ROS quantification, both mouse and human macrophage cells were plated and distributed in triplicates. A working stock of 20 μM DCFH-DA in phosphate buffered saline (PBS) was prepared and all test concentrations, unexposed negative controls and positive controls were prepared and exposed to the cells in this working stock. The negative control consisted of the 20 μM DCFH-DA solution in PBS, whereas the positive control consisted of 1 μM hydrogen peroxide (H_2O_2) in 20 μM DCFH-DA/PBS solution. The test concentrations consisted of a continuous range of AgNPs and AuNPs. Lipopolysaccharide (1 μg/ml) was used as a mitogen for stimulation of macrophages as well as comparison of phagocytic activity of stimulated and non-stimulated macrophages. The test concentration for AgNPs/AuNPs was 10 μg/ml and the incubation period ranged from 2 h to 6 h. The rate of intracellular oxidative stress was monitored by measuring their fluorescence intensity *via* fluorometer "BIOTEK-FLX800 USA" emission at 520 nm (by 485 nm excitation).

Statistical analysis

All the experiments were conducted in triplicates and results were expressed as mean ± SD. One-way analysis of variance (ANOVA) with a Dunnett's test was performed for the multiple comparisons for normally distributed samples with homogenous variance. Statistically significant differences were set at $p < 0.05$.

Results

Screening and fungal characterization

After successive serial dilutions of rhizospheric soil, all the fungi were checked on the Pikovskaya's media for their phosphate solubilization efficiency. On Pikovskaya's medium, the transparency of the media is a primary indicator of phosphate solubilization to be visualized as halo formation in plate assay. Based on plate assay thirty-two fungal were isolated from soil samples. Among these isolated 32 fungal, 20 fungal showed the potent phosphate solubilizing activity. Among all 20, the most promising fungus isolate was FUK 29. This fungus was characterized morphologically, biochemically and at molecular level. The solubilization index of selected fungus was recorded as 3.8 cm. Further, colony morphology was analyzed on the Sabouraud agar medium (Figure 1a) and conidial pattern was analyzed microscopically after lactophenol staining (Figure 1b). Moreover, this fungus gave a negative test for starch hydrolysis while a positive test for cellulose degrading ability.

Figure 1 Morphological features of *Bipolaris tetramera* (a) Sabouraud agar plate demonstrating colonies of *Bipolaris tetramera* (b) Microscopic analysis of *Bipolaris tetramera* after lactophenol staining.

For further characterization, the genomic DNA was amplified using 18S rRNA specific primers (ITS 4 and ITS 5). An amplicon of 520 bp was observed on 1% agarose gel. The DNA sequencing of the amplified product and its BLAST analysis confirmed the fungus as *B. tetramera* (KF934408). The phylogenetic analysis (Additional file 1) revealed the fungus to belong to Pleosporacae family and the genus was *Bipolaris* (Details appended in Additional file 1).

Synthesis and size estimation of silver and gold nanoparticles

Two types of nanoparticles were synthesized from *B. tetramera.* The fungal filtrate was used as reducing and stabilizing agent for 1 mM of silver nitrate and gold tetrahydrate salts. The appearance of a brownish color in solution gave the clear indication of the formation of AgNPs in the reaction mixture while production of AuNPs was confirmed by the color change from yellow solution to pinkish violet. The color change is due to the surface plasmon resonance exhibited by the metal nanoparticles. 1 mM $AgNO_3$/$HAuCl_4$ that act as control when subjected to similar conditions did not demonstrate any color change.

Ultraviolet-visible spectrophotometric analysis

Ultraviolet-visible spectrophotometer showed no evidence of absorption in the range of 400-800 nm for the fungal extract while the fungal extract exposed to $AgNO_3$ and $HAuCl_4$ showed a distinct absorption at around 350 nm and 650 nm, with a peak at 380 nm for AgNPs (Additional file 1) and 570 nm for AuNPs (Additional file 1), respectively.

Dynamic light analysis (DLS)

DLS spectra showed an intensity of 109.4 nm for AgNPs (Additional file 1) and 73.82 nm for AuNPs (Additional file 1). The size variation is due to oxidation of metal salts into their respective nanoparticles in the presence of enzymes. This technique enables the particle size

determination by measuring the random changes in the intensity of light scattered from a suspension or solution.

Transmission electron microscopic (TEM) analyses

TEM micrographs of AgNPs depicted spherical nanoparticles while AuNPs showed three different forms *viz.,* spherical, triangular and hexagonal. This was further confirmed by the representative images recorded from the drop-coated film of the silver/gold nanoparticles uniformly dispersed on grid. The size of the silver AgNPs ranged between 54.78 nm to 73.49 nm (Figure 2a) whereas that of AuNPs ranged from 58.4 nm (spherical), 110.13 nm (triangular) and 261.73 nm (hexagonal), respectively (Figure 2b).

Figure 2 Transmission electron microscopic analysis of nanoparticles. (a) AgNPs; **(b)** AuNPs.

Antibacterial activity of AgNPs and AuNPs

The bactericidal activity of both the nanoparticles were studied using the pathogenic strains of bacteria, namely *B. subtilis, B. cereus, S. aureus, E. coli* and *E. aerogenes* using agar well diffusion method. After the incubation time, zone of inhibition (clear zones) were observed against all the test organisms with both AgNPs and AuNPs. The results recorded in centimetres for AgNPs and AuNPs are shown in Figure 3a and b, respectively.

Figure 3 Comparative analysis of antibacterial activity of nanoparticles (a) AgNP; (b) AuNP for different pathogenic bacteria. Results are presented in relative units compared with controls (Ab). Data represents the mean ± standard deviation of three individual experiments $p < 0.05$.

The comparative histogram demonstrated that the best antibacterial efficacy of AgNP was against *B. cereus* followed by *S. aureus.* Marked increase in antibacterial activity was demonstrated with increasing concentration of AgNPs (Figure 3a). In addition, the efficacy of AgNP was found to be enhanced in combination with the antibiotic tetracycline rather than alone. Similar results were observed with the AuNPs (Figure 3b).

Antifungal activity of AgNPs and AuNPs

The colloidal AgNPs inhibited the growth of the fungus (*Aspergillus niger* and *Trichoderma)* which was seeded in the Muller Hinton agar plate and formed a zone of inhibition around the central cavity. The zone of inhibition with diameter of 1 cm was recorded in case of *Aspergillus niger* and 1.2 cm in *Trichoderma* (Figure 4) where as no zones of inhibition were found in case of AuNPs, thereby indicating that AuNPs did not have any antifungal activity (data not shown).

Figure 4 Histogram showing antifungal activity of AgNP. Results are presented in relative units compared with controls. Data represent the mean ± standard deviation of the mean of three individual experiments. $p < 0.05$.

In vitro cytotoxicity assay

To determine if nanoparticles are appropriate biomaterials that produce no toxic effects, cell viability and cytotoxicity assays were performed. The results indicated significant cytotoxicity effects of nanoparticles in a dose dependent manner. These nanoparticles depicted dose-dependent cytotoxicity to *J774* and *THP1 α* cell lines. At low doses (10 µg) no cytotoxic effects were observed whereas at high doses of 100-150 µg mild cytotoxicity effects were observed which might be due to over-accumulation of metal nanoparticles inside the cell (Figure 5a and b).

Figure 5 Dose-dependent effect of nanoparticles (a) AgNPs; (b) AuNPs over cell viability using MTT assay on *J774* and *THP1 α* cells. Results are presented in relative units compared with controls. Data represent the mean ± standard deviation of the mean of three individual experiments. $p < 0.05$.

ROS level

2',7'– dichlorofluorescein emission by the macrophage cell lines incubated for various time points demonstrated that both AgNPs and AuNPs were able to generate significant ROS activity in both the cell lines indicating macrophage stimulation. The best results were obtained uptill 4 h of incubation, which declined at 6 h (Figure 6a-d). Here, the comparable ROS generation by both the nanoparticles from non-stimulated cells to mitogen-stimulated cells was observed and indicates towards the immunomodulatory capability of the synthesized metal nanoparticles. The ROS generation by AgNPs was found better when compared to AuNPs which may be due to the small size of AgNPs as these easily penetrate through the cell wall in an appreciable number than AuNPs, which are larger.

Figure 6 ROS estimation in *J774* cell lines (a and b) and *THP1 α* cell lines (c and d) after incubation with nanoparticles (1 & 3 AgNPs; (2 & 4) AuNPs at various time points (2 h, 4 h, 6 h). Results are presented in relative units compared with controls. Data represent the mean ± standard deviation of three individual experiments. $p < 0.05$.

The maximum free radical activity was obtained by the *J774* cells (Figure 6a and b) and *THP1 α* cells (Figure 6c and d) uptill 4 h of incubation with NPs.

Discussion

Phosphorous is an essential mineral nutrient, which plays an important role in plant physiological processes. Plants uses phosphorous in soluble form, thus phosphate solubilizing fungi are the important microbes, which are responsible for conversion from insoluble to soluble state. In the present study, a novel phosphate solubilizing fungal isolate, FUK 29, was isolated and subjected to characterization. The sequence of 18S rRNA of the fungal strain FUK 29 was submitted to GenBank with an accession number of (KF934408). The homology search using BLAST indicated a close genetic relation of the strain FUK 29 with the rRNA sequence of *B. tetramera* (18S: 95% similarity with the reference sequence BankIt1680597 Seq4) in NCBI database. Such a higher identical value confirmed the strain FUK 29 to be *B. tetramera*.

Myconanotechnology, an exotic branch has become a broad field of study involving chemistry, physics, engineering, computing, electronics, energy, agriculture and biomedicine.

In the realm of biomedicine, nanotechnology is widely touted as one of the next promising and important approaches to diagnose and treat various ailments [18]. Since chemical and physical methods of metal nanoparticle-synthesis are expensive and involve incorporation of toxic chemicals, the biological synthesis using bacterial, fungal and plant extract sources have been found a preferred option. This owes to their ease of availability, nontoxic nature and quicker synthesis. This prompted us to use this novel fungus *B. tetramera* for the synthesis of AgNPs and AuNPs. The recent reports indicate that the synthesis of AgNPs/AuNPs is based on the surface plasmon resonance involving color alteration [19]. The culture supernatant of selected fungi was used for the synthesis of AgNPs and it is proposed that the reduction of Ag^+ might be due to the involvement of protein components contributed by the enzyme NADH-reductase. Further, in the UV/VIS absorption, a strong peak located at 380 nm and 570 nm was observed for AgNPs/AuNPs respectively. Such type of UV-visible peak is in accordance with the previous report on assorted metal nanoparticles, which ranged between 6 to 100 nm in size [20].

Average particle size calculated from DLS data was found to be 109.4 nm for AgNP while for AuNP it is 73.82 nm. Furthermore, the SEM image of the synthesized AgNPs/AuNPs validated the formation of spherical, triangular and hexagonal nanoparticles. This indicated the reduction of Ag^+ to elemental silver (Ag) and Au^+ to elemental gold (Au). Therefore, the UV/VIS spectra showed for AgNPs/ AuNPs at 380 nm and 570 nm and the spherical images observed in this study for NPs through SEM was in agreement to those reported earlier [21]. Additionally, the synthesized nanoparticles were stable in solution over a time of three months at room temperature. Nano-silver/gold is an effective and a fast-acting microbicide against a broad spectrum of common bacteria and fungi, thus have been utilized in various processes in the medical field [22]. The similar results were obtained in the present study where both the silver and gold nanoparticles exerted high antibacterial activities along with the standard antibiotic (tetracycline) against *Bacillus cereus*. The antibacterial activity of AgNPs/AuNPs is due to the permeability of the cell membrane [23] or formation of free radicals [24] or interaction of AgNPs/AuNPs with the thiol groups of many enzymes thus inactivating them. The efficacy of AgNPs could be attributed to the fact that their larger surface area enabled them to have a better contact with the microorganisms. This is further supported by the revelation that size dependent interaction of silver nanoparticles with bacteria leads to its antibacterial activity [25]. The toxicity of silver ions, though not very clearly understood, could be either due to adhesion to the cell membrane and further penetration inside or by interaction with phosphorus containing compounds like DNA disturbing the replication process or preferably by their attack on the respiratory chain. It has also been suggested, that a strong reaction takes place between the silver ions and thiol groups of vital enzymes thus inactivating them [26]. Some studies also reported that the attachment of the nanoparticles on to the surface of the cell membrane disturbs the permeability and respiration functions of the cell [27]. Earlier experimental evidences have advocated the loss of replication ability by the DNA when treated with silver ions [28]. Beside this, the moderate antifungal activity of AgNPs against *Aspergillus niger* and *Trichoderma* was due to formation of insoluble compounds by inactivation of sulfhydryl groups in the fungal cell wall and disruption of membrane bound enzymes and lipids, which causes cell lysis [29]. The AuNPs did not possess any antifungal activity.

Metal nanoparticles can induce toxicity at various degrees. It is suggested that higher concentrations of silver nanoparticles are toxic and can cause various health problems. AgNPs were found to be significantly more toxic to *THP1 α* cells as compared to *J774* cells, which could be attributed to the intrinsic anticancer property of AgNPs. AuNPs, however, possess moderate activity. This might be due to small particle size of AgNPs with enormous

specific surface area, which facilitated further expression and dissolution of ions in comparison to AuNPs thus, potentially leading to increased toxicity. AgNPs are highly reactive and exhibit oxidative potential and ability to bind with biomolecules like proteins and DNA, resulting in creating the disturbance in the functioning of biomolecules [30]. Moreover, the maximum free radical activity was attained by the *J774* and *THP1 α* cells uptill 4 h of incubation. Analogous encapsulation efficacy and free radical generation capability of both metal nanoparticles project their use as a potential drug/vaccine delivery vehicle for macrophages as well as also indicate towards their immunomodulatory activity.

The present study also supported the notion as higher doses of silver/gold nanoparticles exhibited the cytotoxicity on both the cell lines used. The results revealed the potential use of biologically synthesized metal nanoparticles as an anti-microbicide [31], occupying its application in agriculture. Moreover, these nanoparticles can also act as immunomodulatory agent alone or in combination with established therapeutic immunomodulatory agents [32]. As these NPs are easily engulfed by the macrophages, they also pose themselves as targeted drug/vaccine delivery vehicle to macrophages thereby a boom for development of a potent chemotherapeutic vehicle for diseases involving macrophages *viz.*, leishmaniasis, tuberculosis etc [33]. Hence, care has to be taken to utilize these nanoparticles in a good, effective and efficient way, understanding its limitations and taking extreme care that it does not cause any harm to an individual or the environment. It can be believed that if utilized properly, silver nanoparticles can be a good friend, but if used haphazardly, they can become a mighty foe.

In future, the bio-conjugated nanomaterials (encapsulation) may lead to enhancement of agricultural productivity for slow release of phosphorus, from soil and fertilizers and its effective uptake by plants. As *B. tetramera* contains acid phosphatase enzyme involved in phosphate solubilization, the bio-nanoparticles prepared from them may display slow release of encapsulated enzyme and hence may enhance phosphate solubilization. The nanoparticles thus prepared may be mixed with fertilizers to enhance the uptake of phosphorus. However, this needs to be validated.

Conclusion

In the present study among all isolated and well characterized fungal species, *B. tetramera* having efficient phosphate solubilizing ability therefore the culture supernatant FUK 29 was selected for the synthesis of metal AgNPs and AuNPs. It was confirmed that the AgNPs/AuNPs formed were spherical in shape. The AgNPs/AuNPs generated showed the promising antimicrobial agent against both Gram-positive/Gram-negative bacteria and pathogenic fungi also. On the contrary, AuNPs which were found to be nontoxic in cytotoxic assays could be used as a vehicle for drug delivery. However, higher doses of silver/gold nanoparticles exhibited the cytotoxicity on both the cell lines (*J774* and T*HP1α*). The fungal strain FUK 29 used in this study is likely to provide broad-spectrum benefits such as (i) its utility in the solubilization of insoluble phosphate into soluble form, (ii) for used to generation of AgNPs/AuNPs, and (iii) its effectiveness in the implementation of infectious diseases (leishmaniasis, tuberculosis) as drug delivery vehicle as well as in the area of agriculture (antibacterial and antifungal agent).

Competing interests

The authors declare that they have no competing interests.

Authors' contributions

FF performed research and analyzed data. NP, SS, SRV and PB, designed and interpret the observations. FF wrote the paper with help from all authors. The final manuscript was read and approved by all authors.

Acknowledgements

The authors are highly thankful to Vice Chancellor, Integral University for his support and encouragement. We sincerely Ms. Himani, IIT, Kanpur for carrying out SEM/TEM analysis of nanoparticles. The grant of UGC-Maulana Azad National Fellowship is gratefully acknowledged.

References

1. Hvolbæk B, Ton J, Bieme C, Hanne F, Christensen C, Nørskov JK. Catalytic activity of Au nanoparticles. In Nano Today. 2007;2:14–8.

2. Buzea C, Blandino I, Robbie K. Nanomaterials and nanoparticles: sources and toxicity. Biointerphases. 2007;4:17–172.

3. Masinga, Petros S. Microwave-assisted synthesis of β-CD polymers incorporating N-doped carbon nanotubes and silver nanoparticles for water purification. A dissertation submitted to the Faculty of Science, University of the Witwatersrand; 2013, Johannesburg. http://hdl.handle.net/10539/12919.

4. Stark JW, Pratsinis SE. Aerosol flame reactors for manufacture of nanoparticles. Powder Tech. 2002;2:126.

5. Parashar V, Prashar R, Sharma B, Pandey AC. *Parthenium* leaf extract mediated synthesis of silver nanoparticles: a novel approach towards weed utilization. Digest J Nano Biostr. 2009;4:45–50.

6. Li H, Sun D, Lu Y, Su Y. Biosynthesis of silver and gold nanoparticles by novel sundried *Cinnamomum* camphora leaf. Nanotechnology. 2007;18:11–5.

7. Mohanpuria P, Rana NK, Yadav SK. Biosynthesis of nanoparticles: Technological concepts and future applications. J Nanopart. 2008;10:507–17.

8. Pikovskaya I. Mobilization of Phosphate in Soil in Connection With Their Vital Activities of Some Microbial Species. Microbiologiya. 1948;17:362–70.

9. Grant WD, Kamekura M, McGenity TJ, Ventosa A. Order I Halobacteriales Grant and Larsen 1989b. In D.R. Boone, R.W Calstenholz, and G.M. Garrity (eds.). Bergey's Manual of Systematic Bacteriology; 2001;1:2:294-334.

10. Dias LAS. Fundamentos e Aplicações em Plantas e Microrganismos, UFV, Viçosa Análises multidimensionais. In: Alfenas AC, editor. Eletroforese de Isoenzimas e Proteínas Afin. 1998. p. 405–73.

11. Germain V, Li JD, Ingert Z, Pileni MP. Stacking faults in formation of silver nanodisks. J Phys Chem B. 2003;107:8717–20.

12. Perez C, Pauli M, Bazerque P. An antibiotic assay by agar-well diffusion method. Acta Biologiae et Medecine Experimentaalis. 1990;15:113–5.

13. Ndukwe I, Habila J, Bello I, Adeleye E, Juss A. Phytochemical analysis and antimicrobial screening of crude extracts from the leaves, stem bark and root bark of *Ekebergia senegalensis*. Afri J Biotech. 2006;19:1792–4.

14. Mosmann F. Rapid calorimetric assay for cellular growth and survival: application to proliferation and cytotoxicity assay. J Immunol. 1983;65:55–63.

15. Lam C, James J, Mccluskey R. Pulmonary toxicity of single-wall carbon nanotubes in mice 7 and 90 days after intra-tracheal instillation. Tox Sc. 2004;77:126–34.

16. Cathcart R, Schwiers E, Ames BN. Detection of picomole levels of hydroperoxides using a fluorescent dichlorofluorescin assay. Anal Biochem. 1983;134:111–6.

17. Goswami P, Gupta S, Biswas J, Joshi N, Swarnkar S, Nath C, Singh S: Endoplasmic Reticulum Stress Plays a Key Role in Rotenone-Induced Apoptotic Death of Neurons. Mol Neurobiol 2014, 400-473. [PM:25428620].

18. Hartman K, Wilson L, Rosenblum M. Detecting treating cancer with nanotechnology. Mol Diagn Ther. 2008;12:1–14.

19. Sunkar S, Nachiyar VC. Microbial synthesis and characterization of silver nanoparticles using the endophytic bacterium *Bacillus cereus*: A novel source in the benign synthesis. Glob J of Med Res. 2012;12:2249–4618.

20. Thangapandiyan S, Prema P. Chemically fabricated silver nanoparticles enhance the activity of antibiotics against selected human bacterial pathogens. Int J Pharm Sci Res. 2012;3:1415–22.

21. Mouxing F, Qingbio L, Daohua S, Yinghua L, Ning H. Rapid preparation process of silver nanoparticles by bio-reduction and their characterization. Chinese J Chem Eng. 2006;14:114–7.

22. Wright J, Lam K, Hansen D, Burrell R. Efficacy of topical silver against fungal burn wound pathogens. Am J Infest Control. 1999;27:344–50.

23. Gavrieli Y, Sherman Y, Bensasson S. Identification of programmed cell death in situ via specific labeling of nuclear DNA fragmentation. J Cell Biol. 1992;119:493–501.

24. Hussain S, Hess K, Gearhart J, Geiss K, Schlagel. *In Vitro*: *In Vitro* Toxicity of Nanoparticles in BRL 3A Rat Liver Cells. J Toxicol. 2005;19:975–83.

25. Pal S, Tak Y, Song J. Does the antibacterial activity of silver nanoparticles depend on the shape of the Nanoparticle? A study of the gram-negative bacterium *Escherichia coli*. Appl Environ Microbiol. 2007;l 73:1712–20.

26. Liau S, Pugh DW, Russell F. Interaction of silver nitrate with readily identifiable groups: relationship to the antibacterial action of silver ions. J Lett Appl Microbiol. 1997;25:279–83.

27. Yliniemi K, Vahvaselka M. Antimicrobial activity of colloidal silver nanoparticles prepared by sol-gel method. Chem. 2008;18:199.

28. Feng Q, Chen G, Cui F, Kim T, Kim J. A mechanistic study of the antibacterial effect of silver ions on *Escherichia coli* and *Staphylococcus aureus*. J Biomed Mater Res. 2000;52:662–8.

29. Liao R, Rennie, Talbot J. Assessment of the effect of amphotericin B on the vitality of *Candida albicans*. Antimicrob Agents Chemother. 1999;43:1034–41.

30. Reidy B, Haase A, Luch A, Dawson K. Mechanisms of silver nanoparticle release, transformation and toxicity: a critical review of current knowledge and recommendations for future studies and applications. Lynch Materials. 2013;6:2295–350.

31. Dorau B, Arango R, Green F. Forest Products Society: Proceedings of the 2nd Wood-Frame Housing. Las Vegas, NV: Durabili and Disaster Issues Conference; 2004. p. 133.

32. Patra C, Bhattacharya R, Wang E, Katarya A, Dutta S, Muders M, et al. Targeted delivery of gemcitabine to pancreatic adenocarcinoma using cetuximab as a targeting agent. Cancer Res. 2008;68:1970–8.

33. Swarnakar N, Thanki K, Jain S. Effect of co-administration of CoQ10-loaded nanoparticles on the efficacy and cardio-toxicity of doxorubicin-loaded nanoparticles. RSC Advances. 2013;3:146–71.

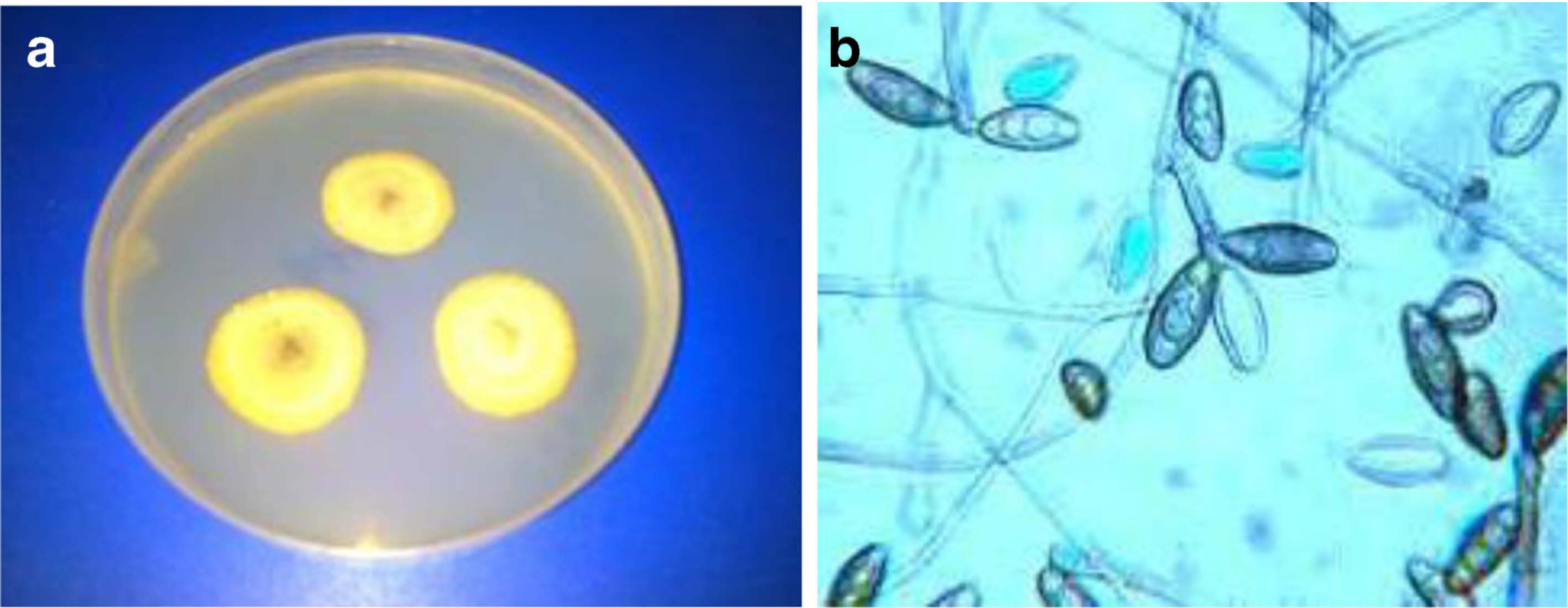
a
b

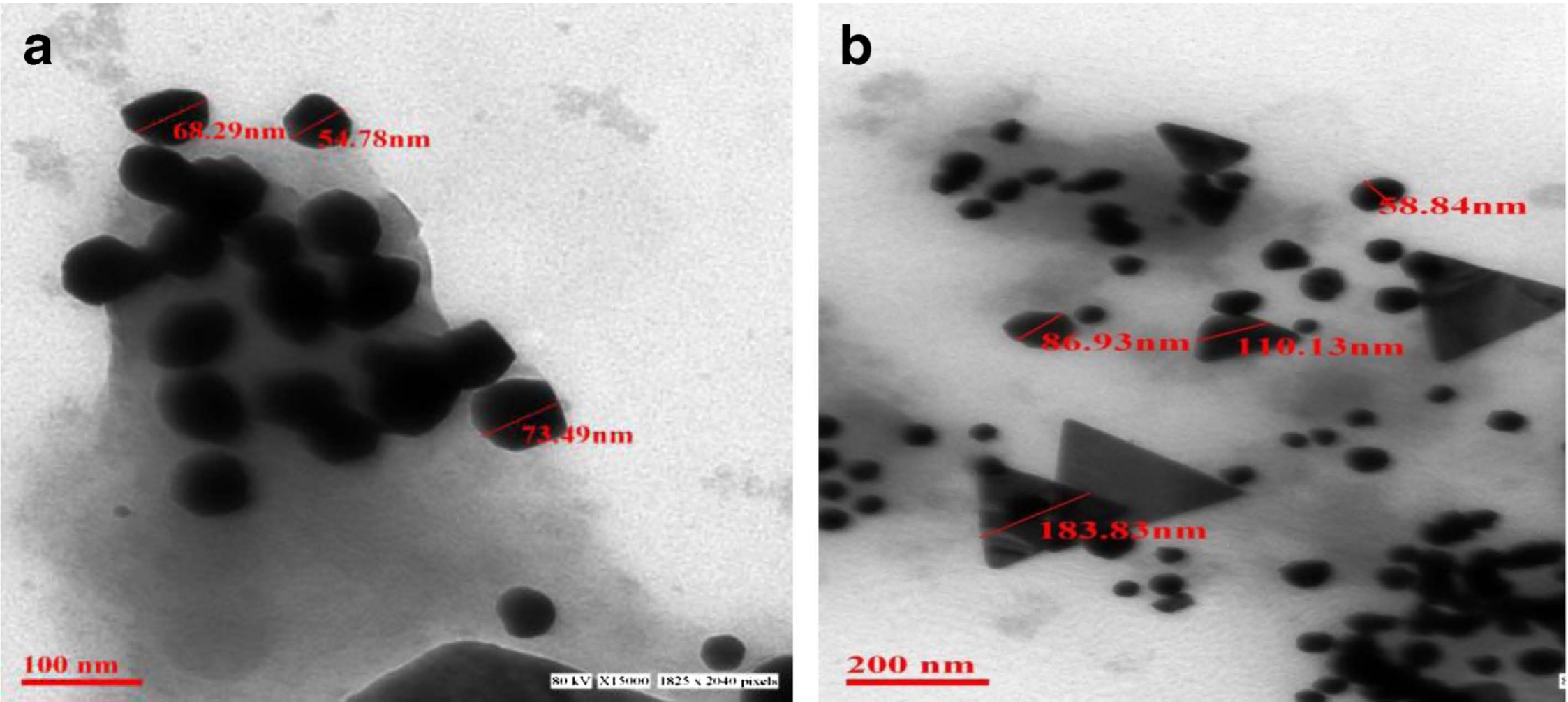
a
68.29nm
54.78nm
73.49nm
100 nm
80 kV X15000 1825 x 2040 pixels
b
58.84nm
86.93nm
110.13nm
183.83nm
200 nm

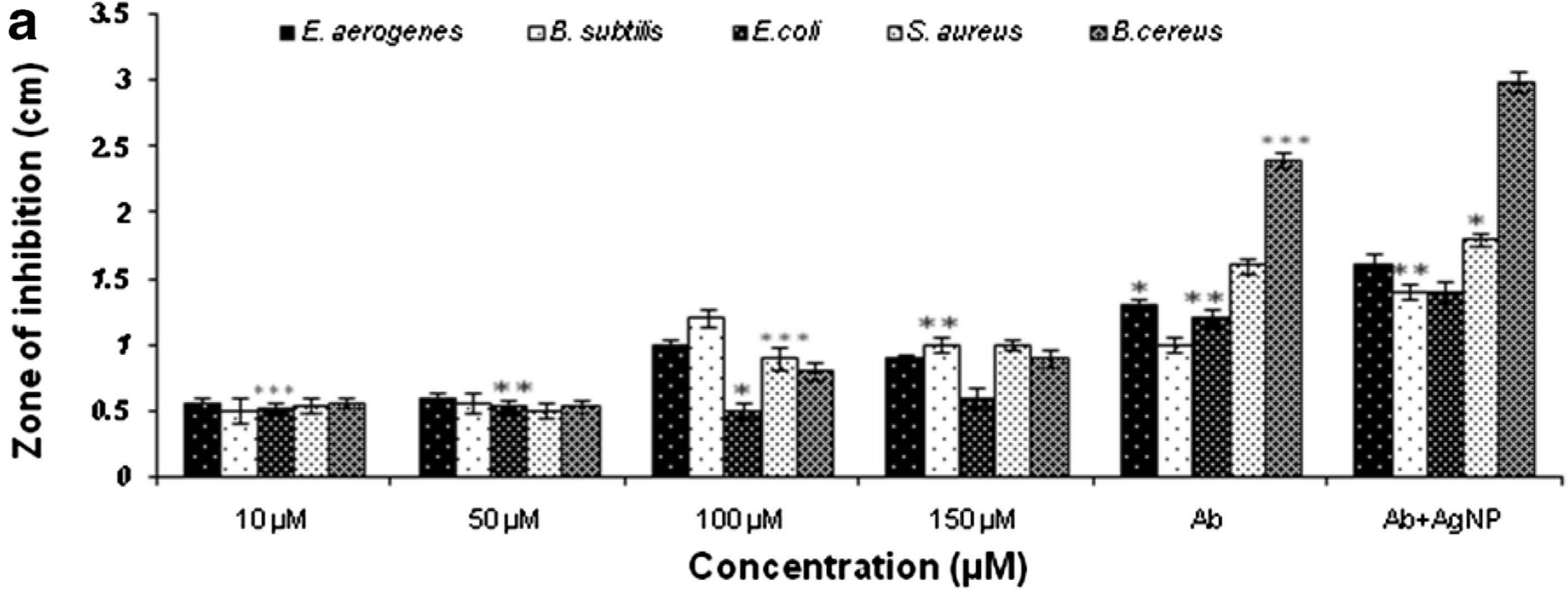
a
E. aerogenes
B. subtilis
E.coli
S. aureus
B.cereus
Zone of inhibition (cm)
3.5
3
2.5
2
1.5
1
0.5
0
10 µM
50 µM
100 µM
150 µM
Ab
Ab+AgNP
Concentration (µM)

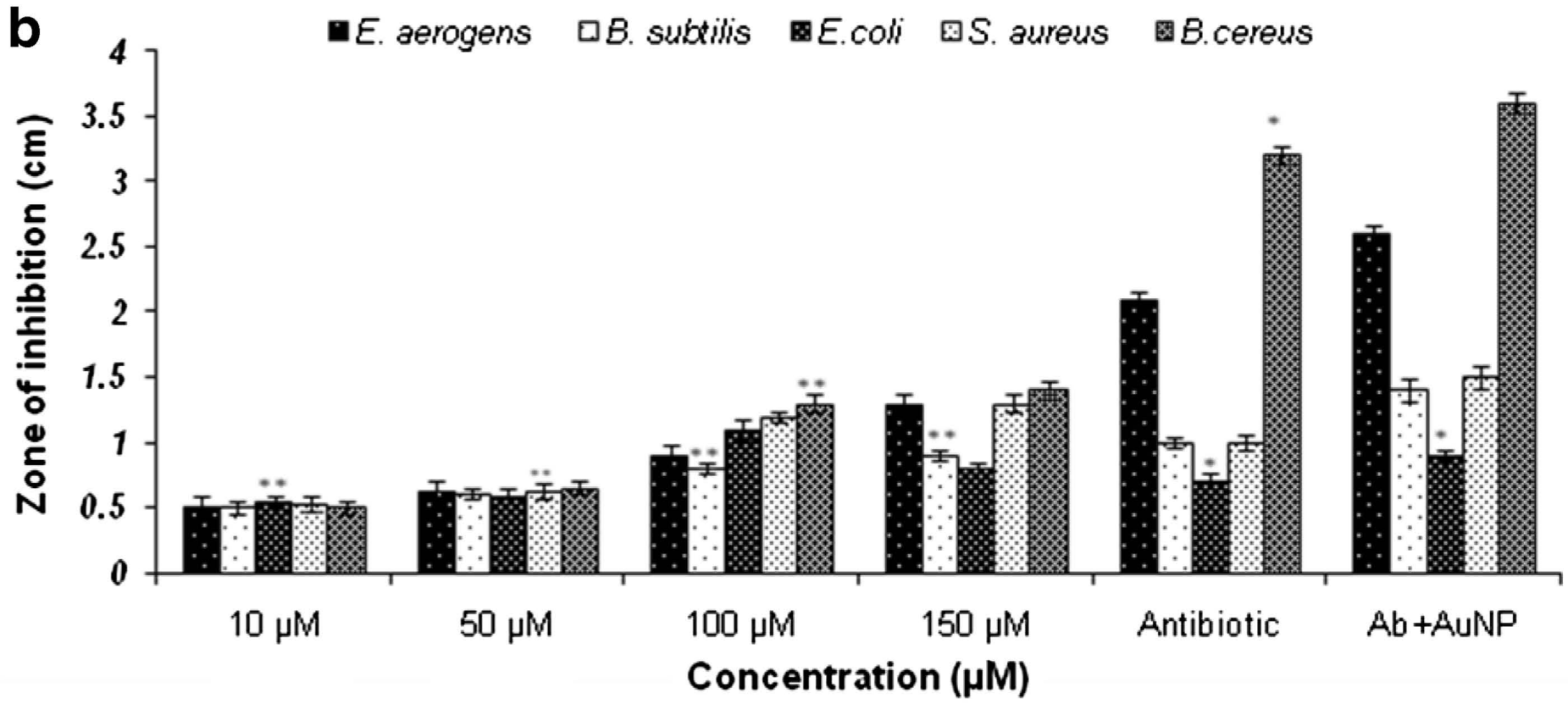
b
E. aerogens
B. subtilis
E.coli
S. aureus
B.cereus
Zone of inhibition (cm)
4
3.5
3
2.5
2
1.5
1
0.5
0
10 µM
50 µM
100 µM
150 µM
Antibiotic
Ab +AuNP
Concentration (µM)

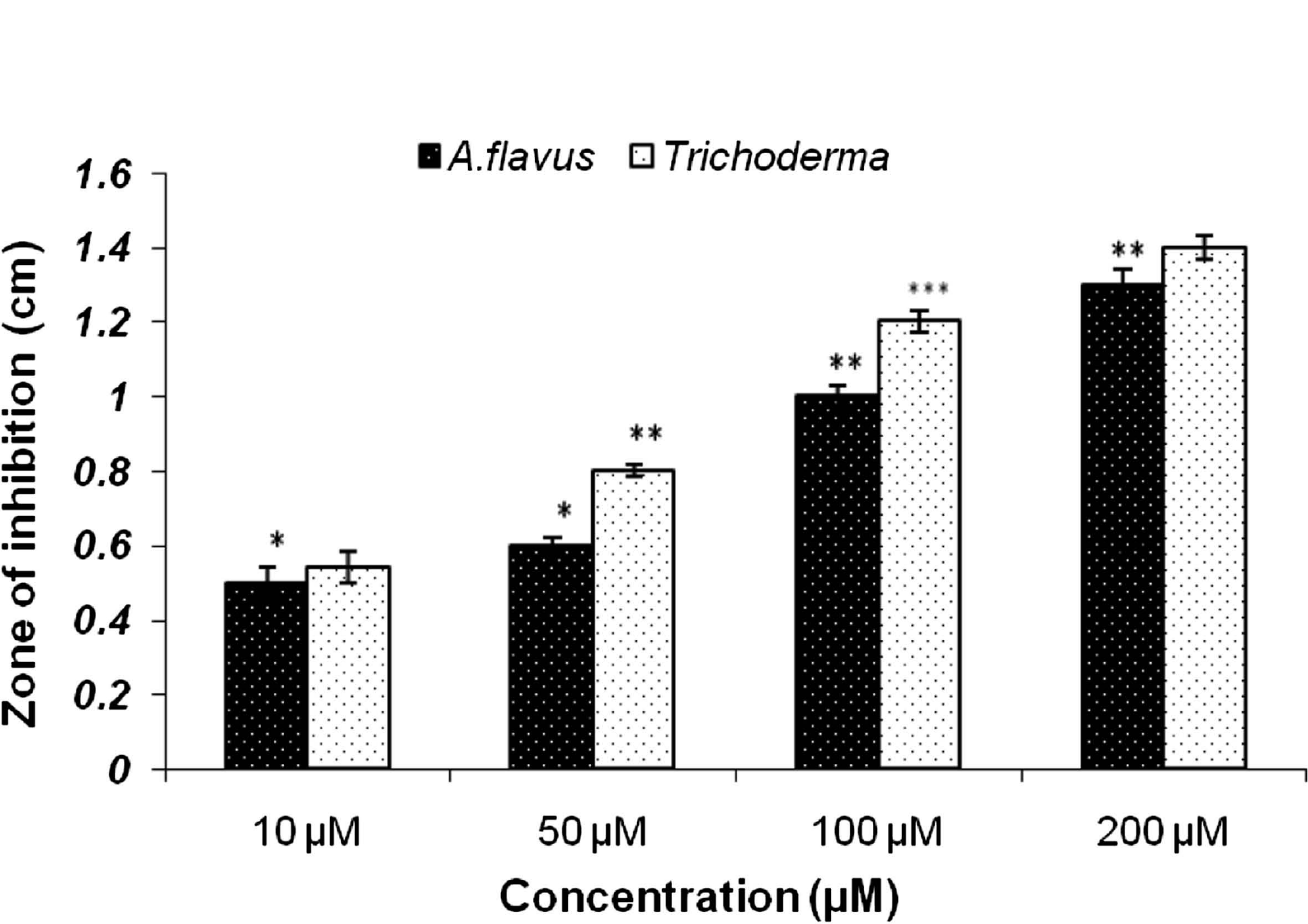
A.flavus
Trichoderma
1.6
1.4
1.2
1
0.8
0.6
0.4
0.2
0
Zone of inhibition (cm)
*
*
**
**
***
**
10 µM
50 µM
100 µM
200 µM
Concentration (µM)

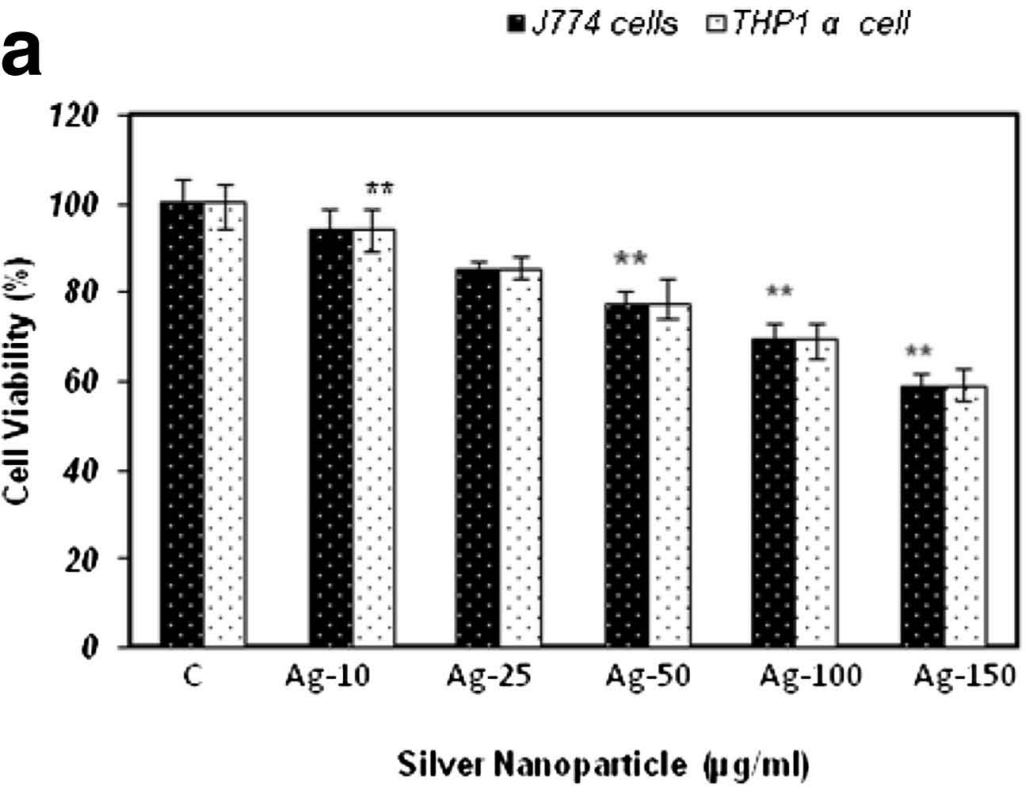
a
J774 cells
THP1 α cell
120
100
80
60
40
20
0
Cell Viability (%)
**
**
**
**
C
Ag-10
Ag-25
Ag-50
Ag-100
Ag-150
Silver Nanoparticle (µg/ml)

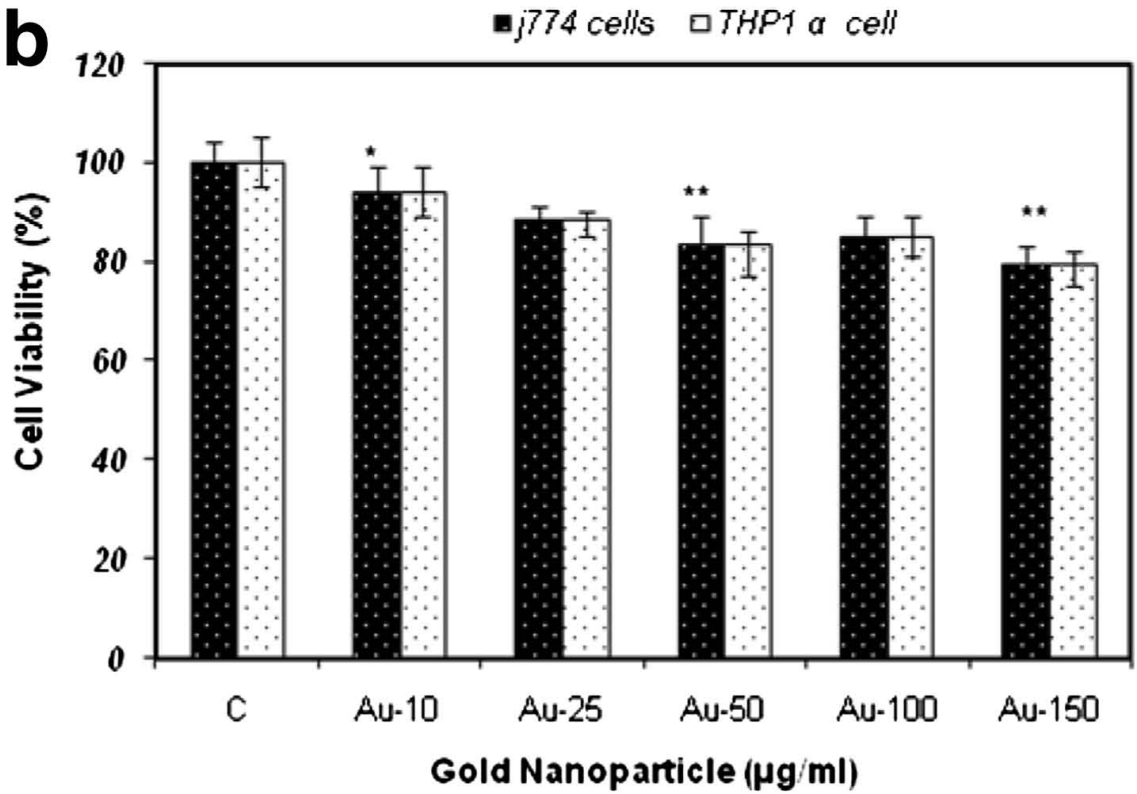
b
j774 cells
THP1 α cell
120
100
80
60
40
20
0
Cell Viability (%)
*
**
**
C
Au-10
Au-25
Au-50
Au-100
Au-150
Gold Nanoparticle (µg/ml)

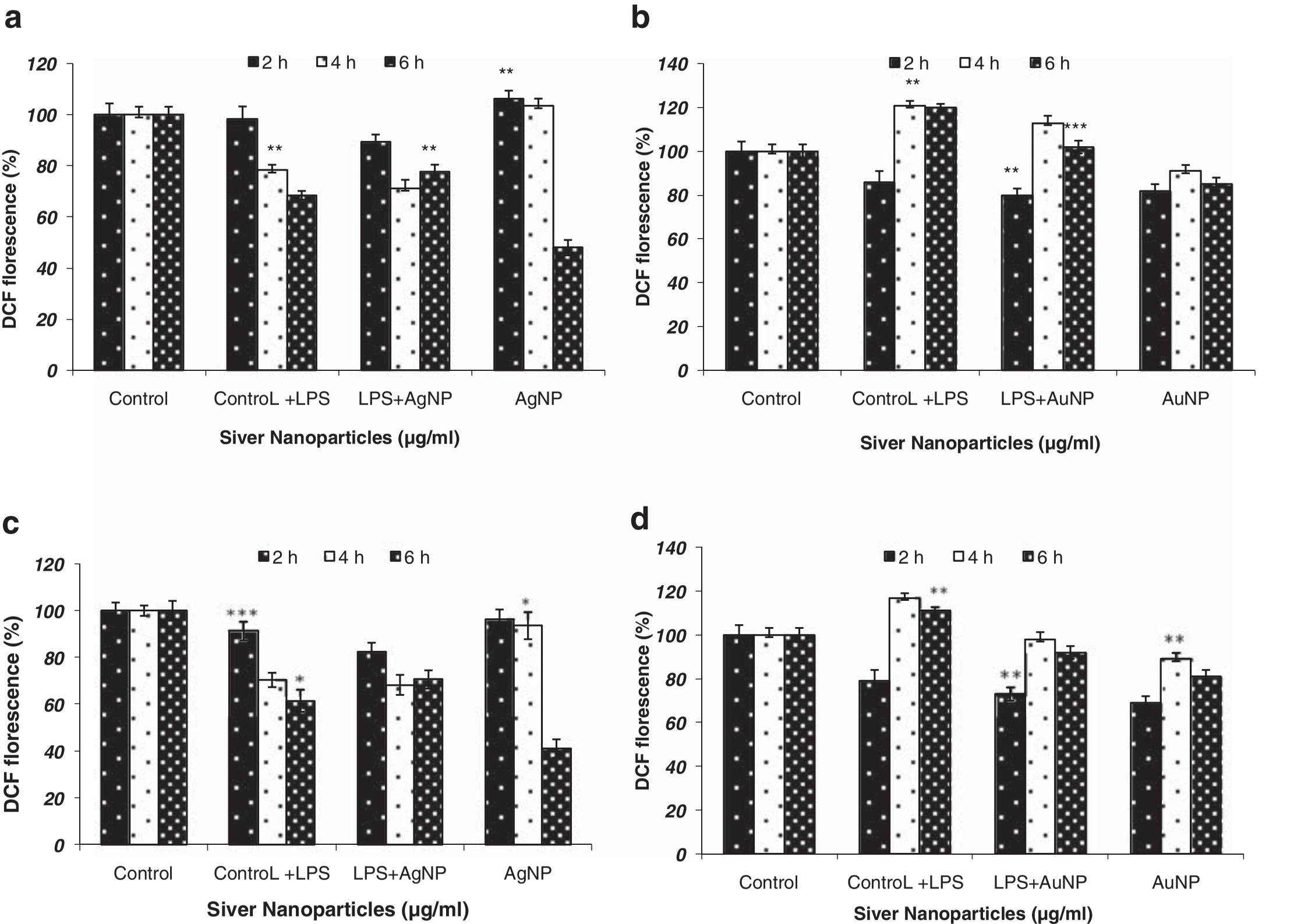
a
2 h
4 h
6 h
DCF florescence (%)
Control
ControL +LPS
LPS+AgNP
AgNP
Siver Nanoparticles (µg/ml)
b
2 h
4 h
6 h
DCF florescence (%)
Control
ControL +LPS
LPS+AuNP
AuNP
Siver Nanoparticles (µg/ml)
c
2 h
4 h
6 h
DCF florescence (%)
Control
ControL +LPS
LPS+AgNP
AgNP
Siver Nanoparticles (µg/ml)
d
2 h
4 h
6 h
DCF florescence (%)
Control
ControL +LPS
LPS+AuNP
AuNP
Siver Nanoparticles (µg/ml)

Additional files provided with this submission:

Additional file 1. Figure S1. Phylogenetic analysis of Bipolaris tetramera(KF934408). Figure S2. UV-VIS spectrophotometry of nanoparticles. Figure S3. DLS spectrum of nanoparticles (240k)
http://www.biomedcentral.com/content/supplementary/s12866-015-0391-y-s1.doc

Wireless Pers Commun
DOI 10.1007/s11277-015-2503-2

Asymmetrical π-Shaped Slot Embedded Microstrip Antenna for Circular Polarization

Ajay Kumar Sharma[1] · **Ashok Mittal**[2] · **B. Venkata Ramana Reddy**[1]

© Springer Science+Business Media New York 2015

Abstract A unique geometry of a square patch antenna with an embedded asymmetrical π-shaped slot for circular polarization is presented. The proposed structure has an aperture coupled feed which is matched over a very wide frequency band. This is accomplished by incorporating an oval shaped stub at the end of the single microstrip feed. The antenna shows a 3-dB axial ratio bandwidth of 3.9 % (2.50–2.60 GHz) with respect to the measured minimum axial ratio frequency of 2.56 GHz. The 10-dB return loss bandwidth measured is 40.23 % (2.32–3.35 GHz) with respect to 2.56 GHz. The antenna gain is >8.2 dBi in the circularly polarized band. The antenna is well suited for use in circularly polarized antennas and arrays for wireless communication.

Keywords Microstrip antenna · Circular polarization · Patch antenna · Aperture coupling

1 Introduction

Microstrip antennas with circular polarization find application in wireless, mobile and satellite communication systems. In comparison to linearly polarized antennas, the circularly polarized antennas provide more flexibility in terms of transmitter and receiver

✉ Ajay Kumar Sharma
akscrl@gmail.com

Ashok Mittal
ashok.mittal@ieee.org

B. Venkata Ramana Reddy
profbvrreddy@gmail.com

[1] School of Information and Communication Technology, Guru Gobind Singh Indraprastha University, New Delhi 110 078, India

[2] Ambedkar Institute of Advanced Communication Technologies and Research, Geeta Colony, New Delhi 110 031, India

Published online: 08 March 2015

orientations. The basic principle of operation in such antennas is that the two orthogonal field components are radiated in equal magnitude and phase quadrature. This can be achieved by exciting the antenna with a single feed or with dual feeds [1, 2]. The dual feed antenna geometries generates the circularly polarized signal using complicated feed structures like the quadrature hybrid, the ring hybrid, the Wilkinson power divider and the T-junction power splitter [1, 3, 4]. The circular polarization (or axial ratio) bandwidth generated by such geometries is large due to the inherent bandwidth of the feeding structures. However, this comes at the cost of large sized ground planes required for feed structures.

The singly fed microstrip patch geometries are the most popular configurations for circular polarization operation. These geometries provide several merits like reduced weight, less complexity and freedom from use of external hybrids and power dividers or couplers. Such geometries utilize perturbation technique [5] to generate the dual orthogonal modes required for circular polarization radiation. However, singly fed microstrip antennas suffers from inherent low (typically <1 %) 3-dB axial ratio bandwidth [1, 2].

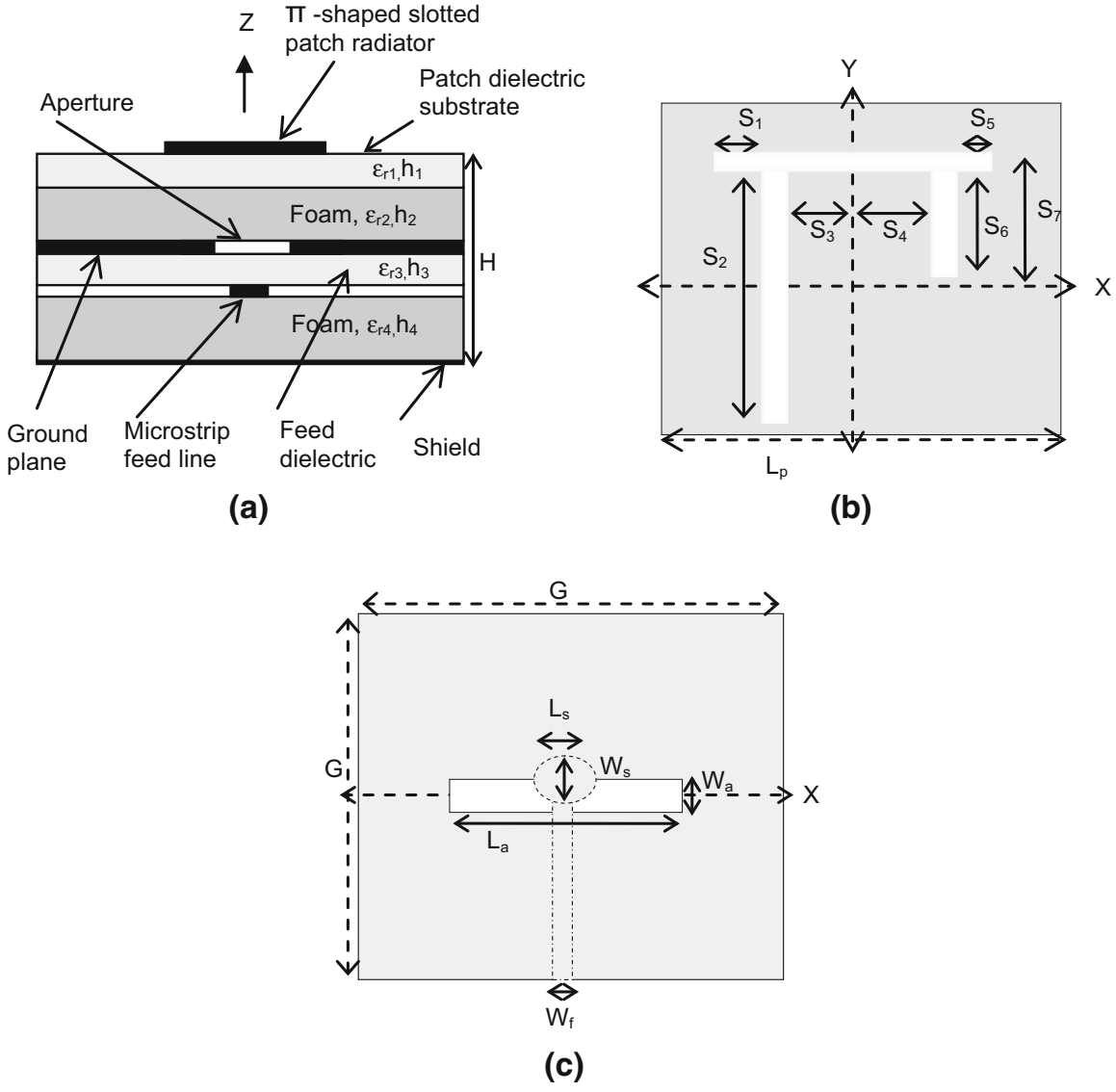

Fig. 1 Proposed π-shaped slotted patch. **a** Cross-sectional view **b** Top view **c** Microstrip feed with aperture coupling

Many geometries based on perturbation method have been reported in open literature. These include notches, truncated corners, slits, stubs and slots embedded onto the patch [5–9].

Single feed antennas with slots of different shapes embedded onto the radiating patch have emerged as popular geometries in meeting the circular polarization requirement for various applications [10–15]. The axial ratio bandwidth in these geometries ranges from <1 to 4 %. Lu et al. [10] had proposed a probe fed equilateral triangular microstrip antenna embedded with a narrow cross slot of unequal lengths for circular polarization. The 3-dB axial ratio achieved with this geometry is about 1 %. Tong et al. [11] proposed a probe fed square microstrip antenna with single layer U-slot for circular polarization operation. A thick foam layer below the patch was used for bandwidth enhancement. The 3-dB axial ratio bandwidth reported is 4 % with a 10-dB return loss bandwidth of 9 %. Nasimuddin et al. [12] proposed a C-shaped slot in square patch antenna with a single aperture coupled feed. An asymmetrical and narrow C-shaped slot was cut in the middle of a square microstrip patch for wideband circular polarization operation. The reported 10-dB return loss bandwidth is 16 % with a 3-dB axial ratio bandwidth of around 3.3 %. Nasimuddin et al. [13] had also proposed a singly fed cross shaped slotted patch antenna. A symmetric cross shaped slot was embedded along one of the diagonal axes of a square patch for circularly polarized radiation. The 3-dB axial ratio bandwidth achieved was <1 %. Lin et al. [14] proposed a X-shaped slotted square patch antenna. A cross-strip is embedded along the X-shaped slot to produce circular polarization. The 3-dB axial ratio bandwidth achieved was 1.3 % with a 10-dB return loss bandwidth of 3 %. Gautam et al. [15] proposed an arrow shaped slot embedded in the first quadrant along the diagonal axes of a

Table 1 Physical dimension (in mm) of the optimized antenna

L_p	L_a	W_a	L_s	W_s	G	H	S_1	S_2	S_3	S_4	S_5	S_6	S_7	S_w
39.5	29.7	3.5	7.4	3.2	60.0	31.6	4.5	29.0	9.0	6.5	2.5	12.2	14.0	2.0

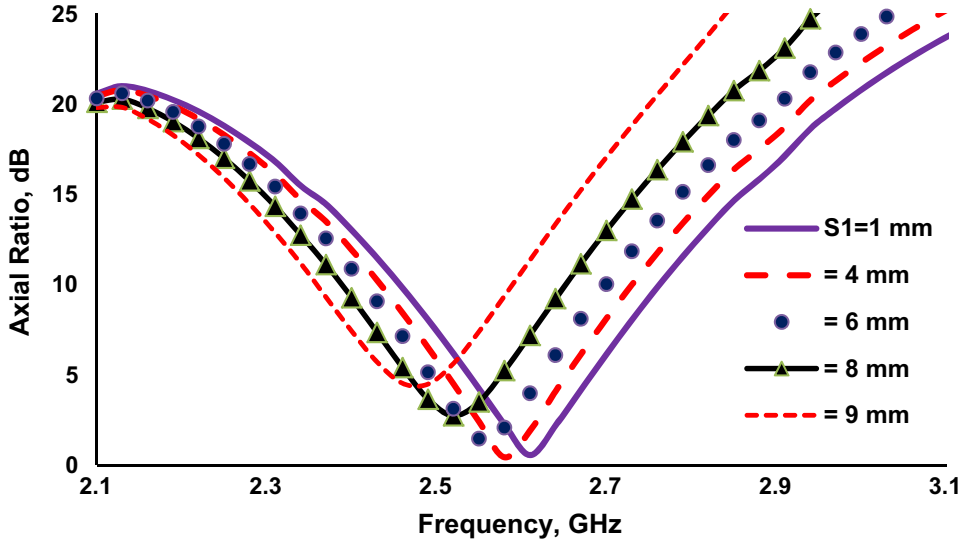

Fig. 2 Effect of S_1 on boresight axial ratio

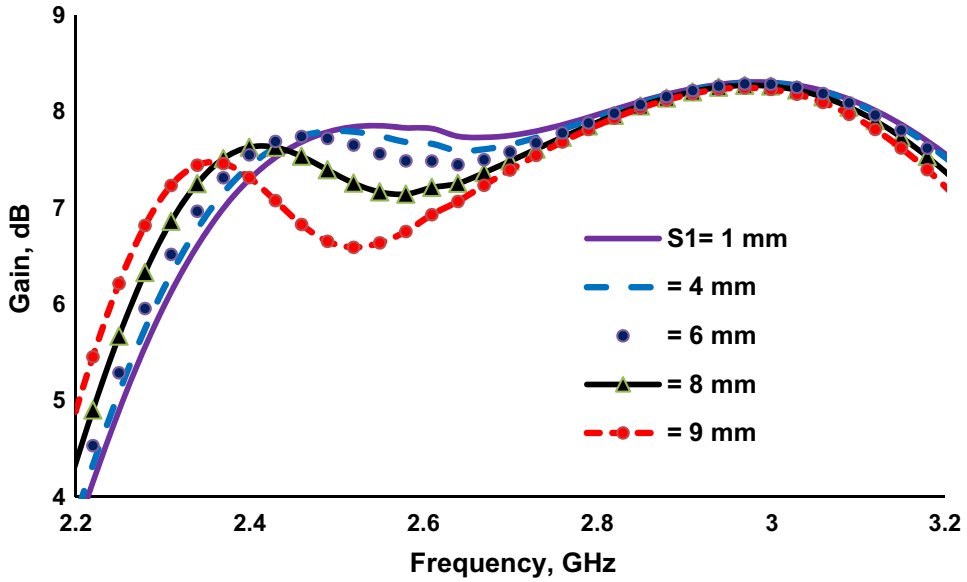

Fig. 3 Effect of S_1 on boresight gain

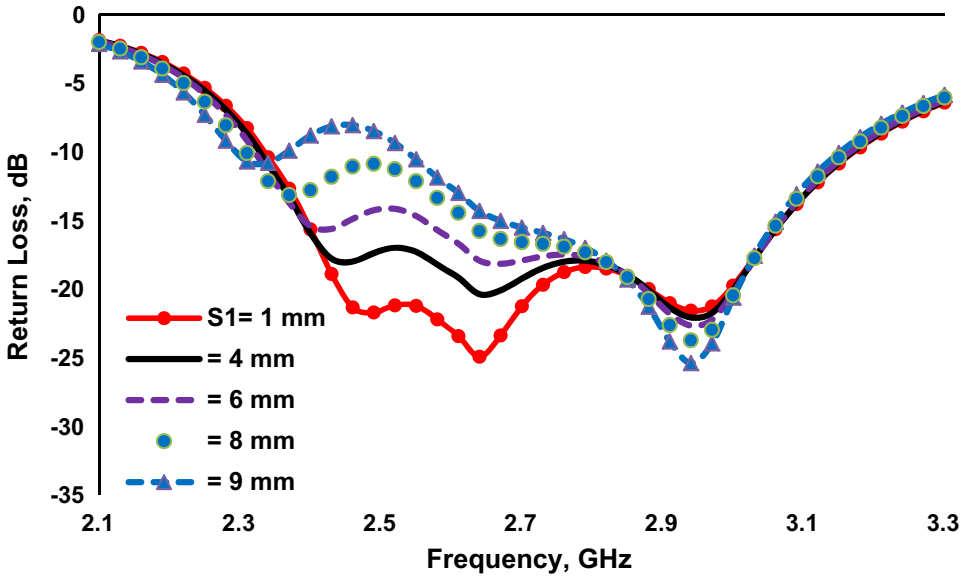

Fig. 4 Effect of S_1 on return loss

probe fed square patch antenna for circular polarization radiation. The 3-dB axial ratio bandwidth achieved was <1 % and 10-dB impedance bandwidth of the antenna was <4 %.

In this paper, a singly fed microstrip antenna embedded with a π-shaped slotted radiator for wideband circular polarization is analyzed and demonstrated. The proposed asymmetrical π-shaped slotted patch structure provides a circularly polarized radiation by slightly perturbing the antenna fields at suitable locations with respect to the feed so as to excite the dual orthogonal modes with 90° phase shift required for circular polarization. The antenna has a relatively wider axial ratio bandwidth in comparison to other singly fed circularly polarized microstrip antennas. Commercially available EM softwares, IE3D [16] and HFSS [17] were used for the design, analysis and optimization of the presented antenna.

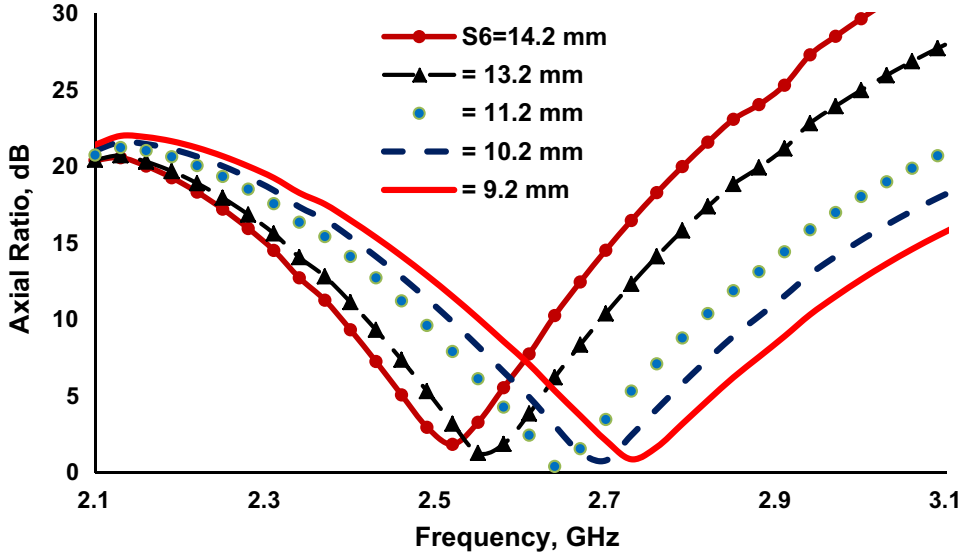

Fig. 5 Effect of S_6 on boresight axial ratio

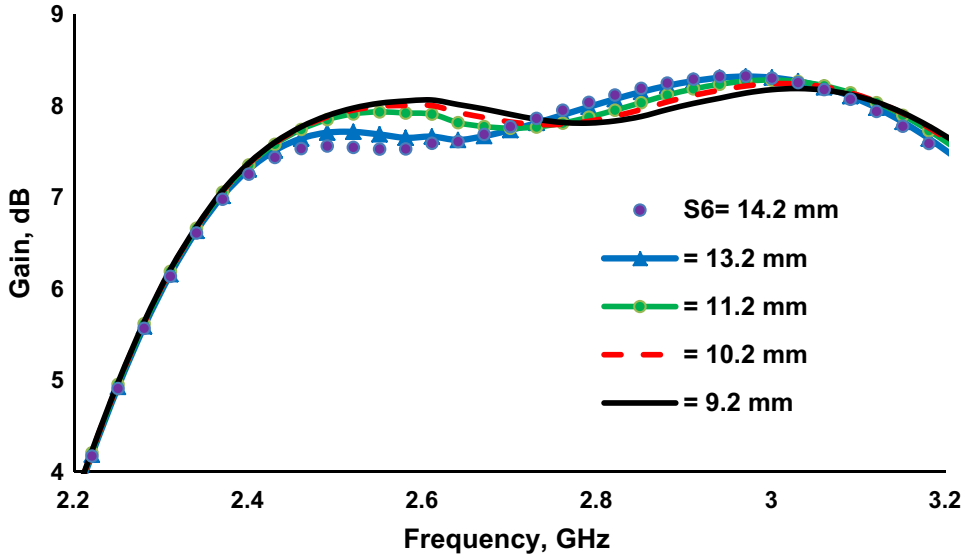

Fig. 6 Effect of S_6 on boresight gain

2 Antenna Geometry and Parametric Analysis

2.1 Antenna Geometry

The presented antenna geometry is shown in Fig. 1. The antenna cross-sectional view is shown in Fig. 1a while Fig. 1b depicts the top view of the π-shaped slotted patch antenna. The feed arrangement with aperture coupling is shown in Fig. 1c. The basic radiator is a square patch of length L_p. The radiating patch is etched on RT/Duroid 5880 substrate ($h_1 = 0.787$ mm, $\varepsilon_{r1} = 2.2$ and tan $\delta_1 = 0.0009$). The radiator distance above the ground plane is increased by using a thick foam layer from Rohacell ($h_2 = 10.0$ mm, $\varepsilon_{r2} = 1.07$ and tan $\delta_2 = 0.0002$). This is done for bandwidth enhancement. The optimized dimensions of the asymmetrical and narrow π-shaped slot embedded on the patch radiator are detailed in Table 1. An aperture coupled microstrip feed line of impedance 50 Ω and width W_f is

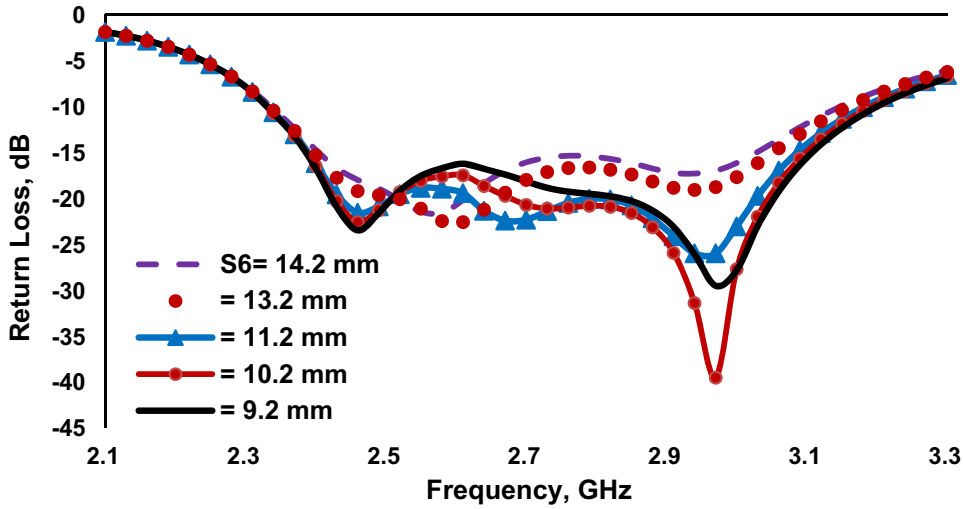

Fig. 7 Effect of S_6 on return loss

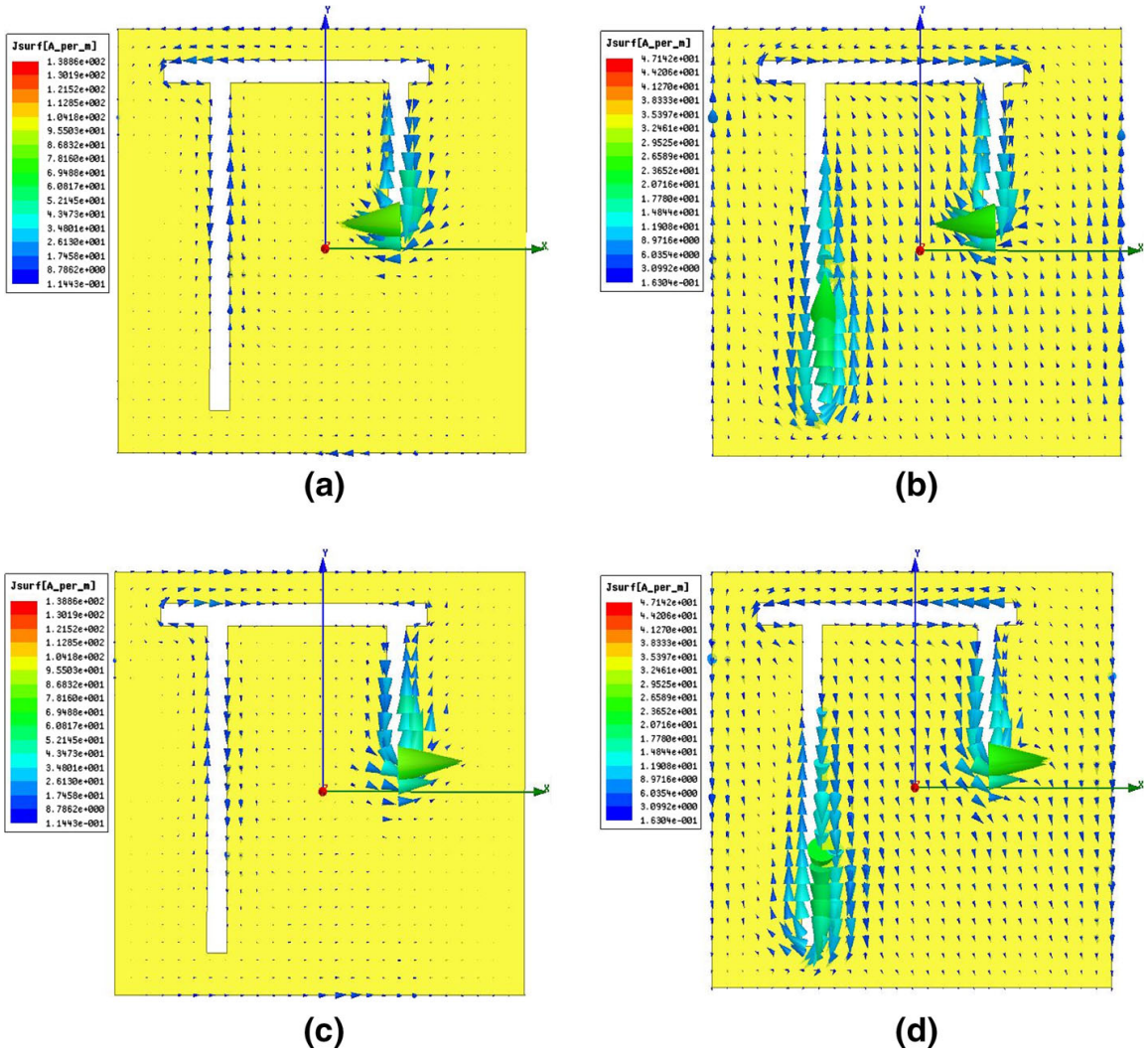

Fig. 8 Simulated current distribution at 2.6 GHz with period T **a** t = 0 **b** t = T/4 **c** t = T/2 **d** t = 3T/4

printed beneath the ground-plane to excite the π-shaped slotted patch electromagnetically. The coupling aperture and microstrip feed line are printed on the two sides of the same RT/Duroid 5880 substrate ($h_3 = 0.787$ mm, $\varepsilon_{r3} = 2.2$ and $\tan \delta_3 = 0.0009$). The feed-line open end is made oval in shape (with diagonals $W_s \times L_s$) so as to have a wide impedance match by tuning out the reactance generated by the coupling aperture. The feed is positioned in the middle of the asymmetrical π-shaped slotted radiator. A conducting back plane is used as a shield to suppress the unwanted backside radiation from the aperture and enhance the radiation in the forward direction. A foam layer ($h_4 = 18.0$ mm, $\varepsilon_{r4} = 1.07$ and $\tan \delta_4 = 0.0002$) with a conducting shield at its bottom is used for this purpose. The shield is placed at a distance of approximately 0.15 λ_0 from the aperture plane. The overall antenna size is $G \times G \times H$.

2.2 Parametric Analysis

A perturbation in the patch surface currents is created by the introduction of asymmetrical π-shaped slot in the patch radiator. Two orthogonal modes are excited by this perturbation in equal magnitude and 90° phase shift necessary for circularly polarized operation. By varying the length of different arms of the π slot, the frequency band of circular polarization operation and its sense can be adjusted. Left hand circularly polarized (LHCP)

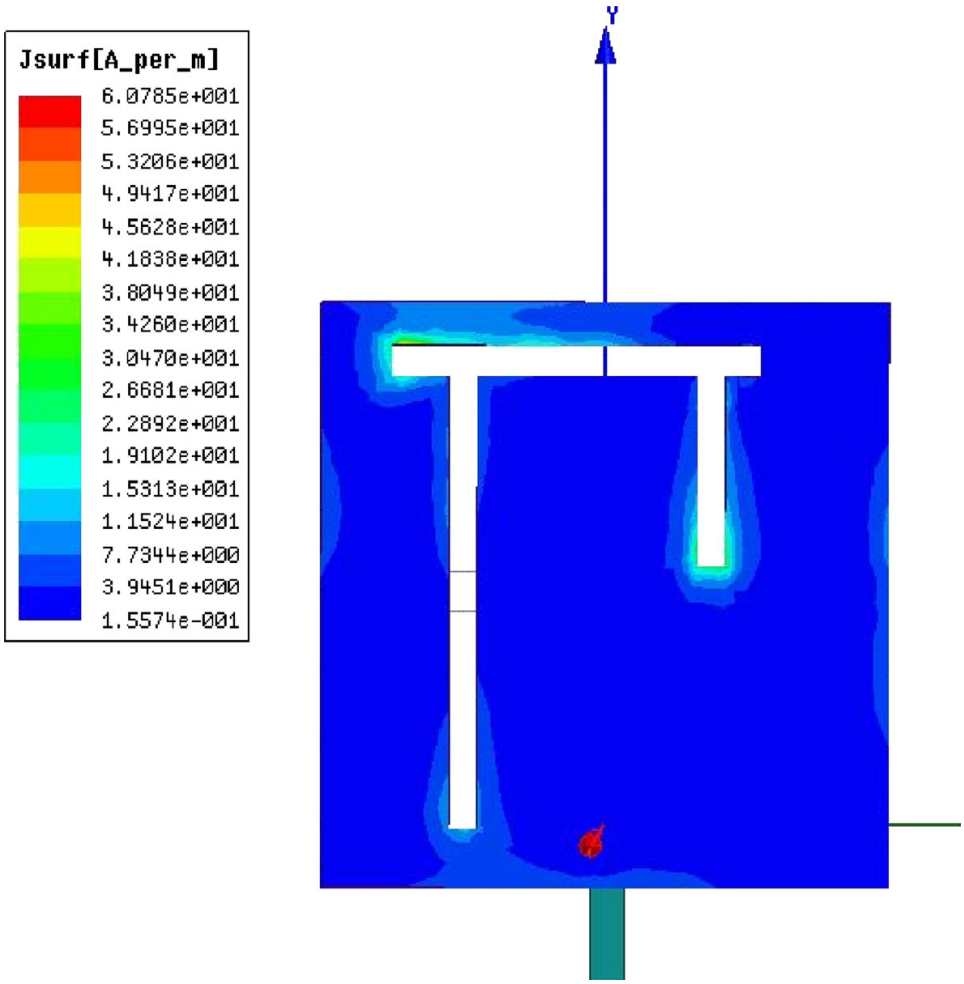

Fig. 9 Simulated average current distribution on π-shaped slotted patch at 2.6 GHz

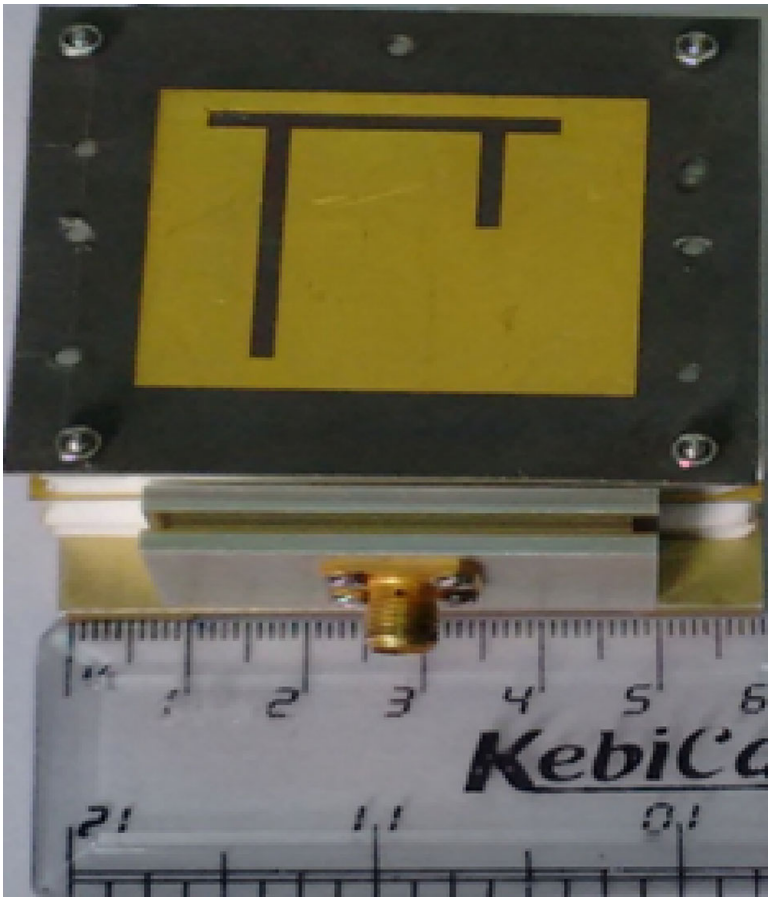

Fig. 10 Fabricated prototype antenna

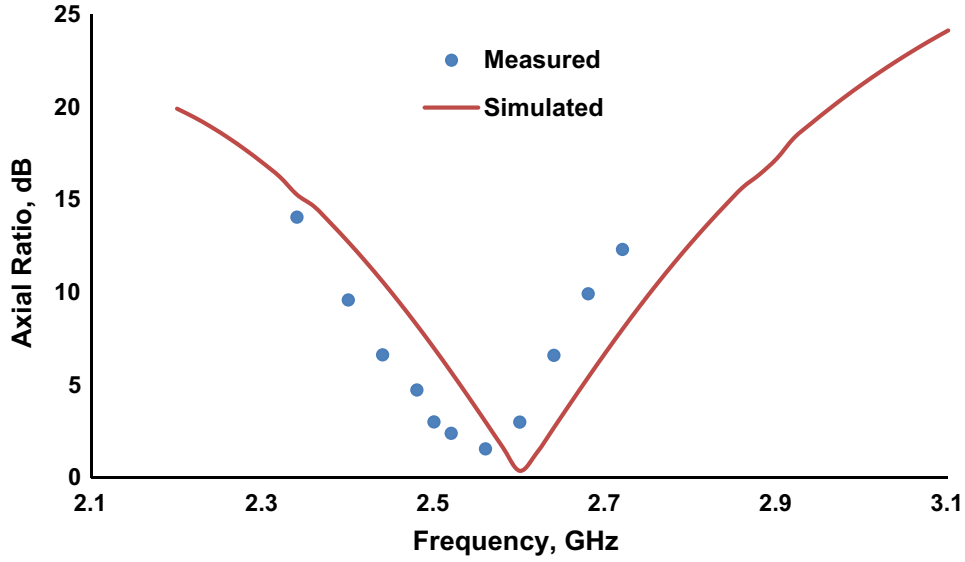

Fig. 11 Simulated and measured boresight axial ratio

wave is radiated by the antenna when $S_1 > S_5$ and $S_2 = S_6$. When $S_1 < S_5$ and $S_2 = S_6$, the antenna exhibits right hand circular polarization (RHCP). Similarly, for the case $S_2 > S_6$ and $S_1 = S_5$, the antenna radiates left hand circularly polarized radiation. The antenna radiates right hand circularly polarized radiation for $S_2 < S_6$ and $S_1 = S_5$.

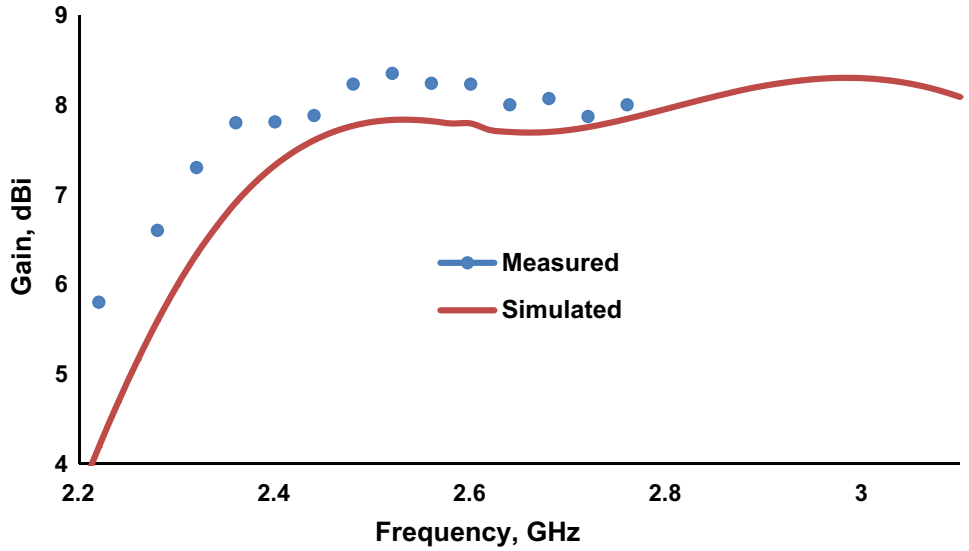

Fig. 12 Simulated and measured boresight gain

A parametric study was carried out to optimize the antenna for good axial ratio performance and to understand the slot effect on its circular polarization operation. During this study the π-shaped slot arm lengths S_1 and S_6 are varied one at an instance while other parameters remain unaltered. Figures 2, 3 and 4 depicts the effect of S_1 on antenna axial ratio, gain and return loss when its value is changed from 1 to 9 mm. Figure 2 illustrates the axial ratio at boresight with variation in S_1. It is evident from Fig. 2 that as S_1 increases the antenna generates circularly polarized radiation with a decrease in operating frequency. Thus, by adjusting S_1, the antenna circularly polarized band can be adjusted. The boresight antenna gain with different S_1 is depicted in Fig. 3. The boresight gain decreases in the circularly polarized band as S_1 increases. This is due to the increase of the gain drop in the circularly polarized band as S_1 increases. Figure 4 shows the antenna return loss with variation in S_1. As S_1 increases from 1 to 8 mm the antenna return loss increases in the circularly polarized band while the 10-dB return loss bandwidth of the antenna changes only slightly. However as S_1 is increased beyond 8 mm, the antenna match degrades significantly with visible reduction in the 10-dB return loss bandwidth.

Next, the effect of S_6 on antenna performance is studied as S_6 is varied from 14.2 to 9.2 mm. Figure 5 shows the axial ratio at boresight as S_6 is varied. As S_6 decreases the antenna generates circularly polarized radiation with an increase in operating frequency. Thus, by adjusting S_6, the operating frequency of circular polarization band can be adjusted as well. The boresight antenna gain with various values of S_6 is shown in Fig. 6. It is observed that the gain changes by about 0.5 dB with decrease in S_6. The variation in antenna return loss with S_6 is illustrated in Fig. 7. The impedance match of antenna changes as S_6 decreases, while the antenna 10-dB return loss bandwidth changing only slightly. Thus the antenna performance significantly depends on the arm S_6.

Figure 8a–d shows the direction of simulated distributed currents (at 2.6 GHz) on the π slotted patch at different time period T, from $t = 0$ to $t = 3T/4$, with an interval of T/4. From the figure, it is observed that the current of the patch travels in the clockwise direction with period T. This results in exciting a left hand circular polarization (LHCP) radiation.

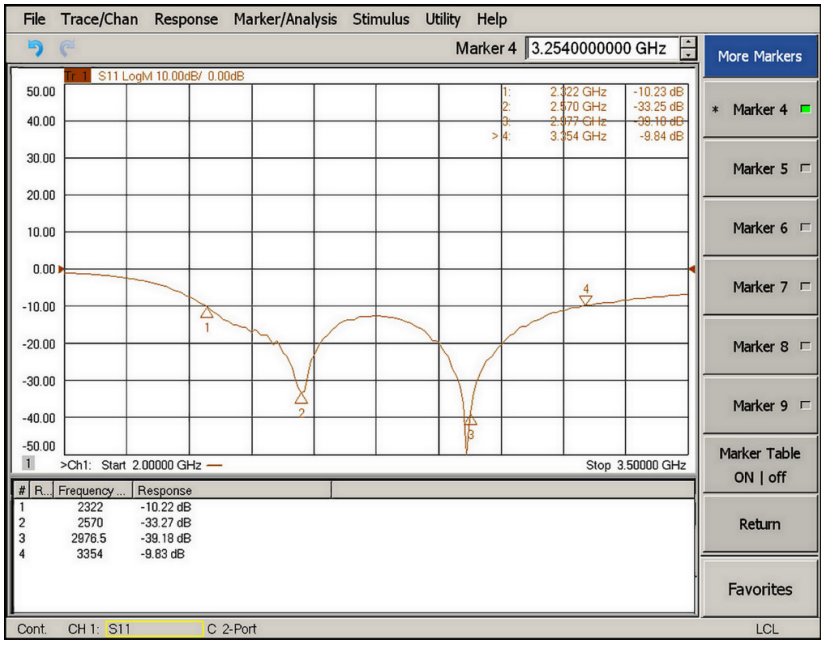

(a)

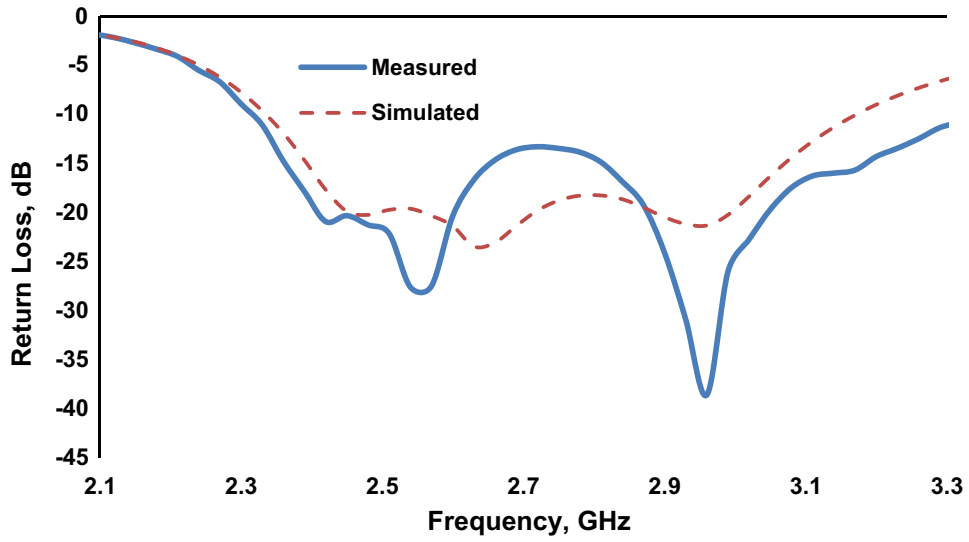

(b)

Fig. 13 **a** Screen shot of measured return loss **b** Simulated versus measured return loss

The average current distribution on the π-shaped slotted patch at the simulated axial ratio resonant frequency of 2.6 GHz is shown in Fig. 9. Strong currents are observed around the arms S_1 and S_6 as compared to arms S_2 and S_5 of the π-shaped slot.

3 Simulated, Experimental Results and Discussion

The π-shaped slotted square radiator with aperture feed was fabricated and tested for performance. The photograph of the fabricated antenna prototype is shown in Fig. 10. In the present design as $S_1 > S_5$ and $S_2 > S_6$, the antenna radiates a left hand circularly

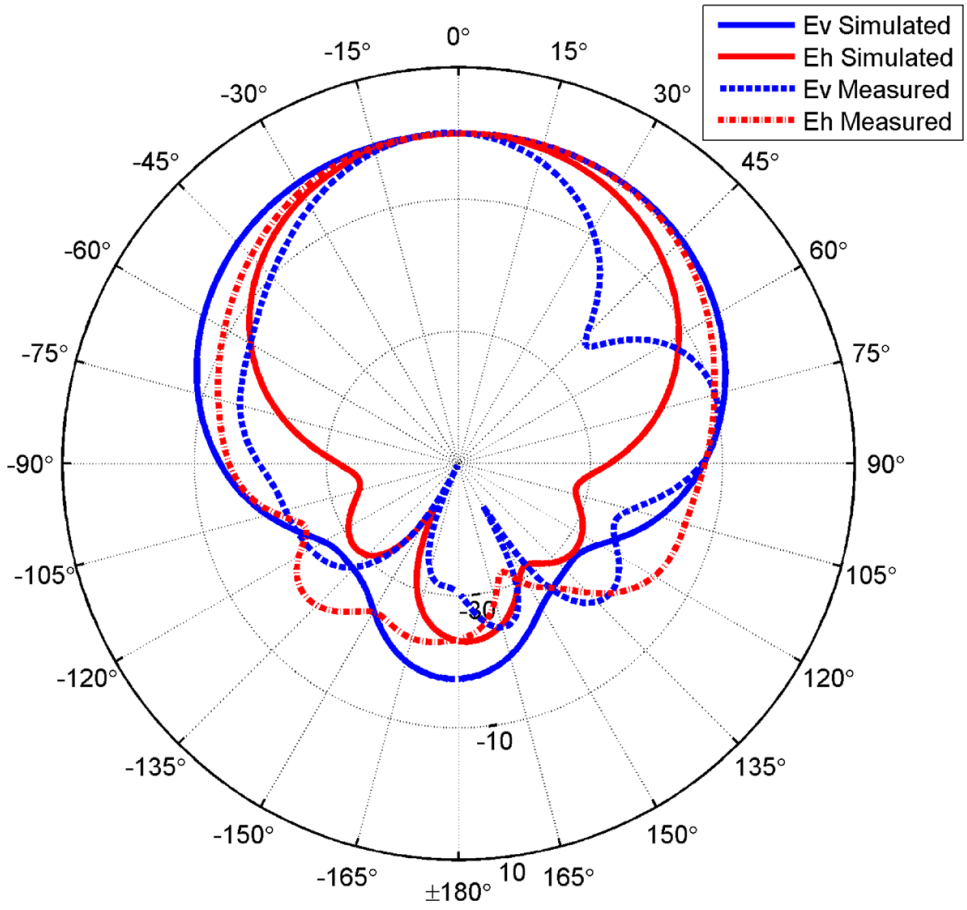

Fig. 14 Normalized measured and simulated E-vertical and E-horizontal components at 2.56 GHz in y–z plane

polarized wave. SATIMO Star Lab antenna test setup has been used for measuring the antenna radiation patterns in the two principal planes. Agilent vector network analyzer N5244A was used to measure the antenna return loss.

Figure 11 illustrates the simulated and measured axial ratio at antenna boresight. The measured minimum axial ratio frequency shows a small shift with respect to the simulated result. This is attributed to the tolerances in antenna fabrication and alignment of various layers during assembly. The minimum axial ratio (or resonance) was measured at 2.56 GHz with a value of 1.53 dB. The 3-dB axial ratio bandwidth measured in the circularly polarized band is 3.9 % (2.50–2.60 GHz) with respect to 2.56 GHz. The simulated axial ratio bandwidth was 3.5 % (2.56–2.65 GHz) with respect to axial ratio resonant frequency of 2.60 GHz. Figure 12 illustrates the simulated and measured antenna gain at boresight. The antenna gain measured over the circularly polarized band is >8.2 dBi. The variation of the gain within 3-dB axial ratio bandwidth is <0.25 dB. Figure 13a depicts the vector network analyzer screen shot of the measured return loss. This is compared with the simulated response and the comparison is shown in Fig. 13b. The simulated and measured return loss shows a good agreement except that the measured impedance bandwidth is higher by approx 7 %. The 10-dB return loss bandwidth measured is 40.23 % (2.32–3.35 GHz) against the simulated bandwidth of 32.69 % (2.32–3.17 GHz).

The normalized measured E-vertical and E-horizontal components of the antenna at 2.56 GHz in y–z ($\varphi = 90°$) and x–z ($\varphi = 0°$) planes are depicted in Figs. 14, 15. The co-polarized (LHCP) and cross-polarized (RHCP) patterns measured at 2.56 GHz are shown in Figs. 16, 17 in y–z and x–z planes. The 3-dB beamwidth measured at 2.56 GHz in y–z and x–z planes are 40° & 60° respectively.

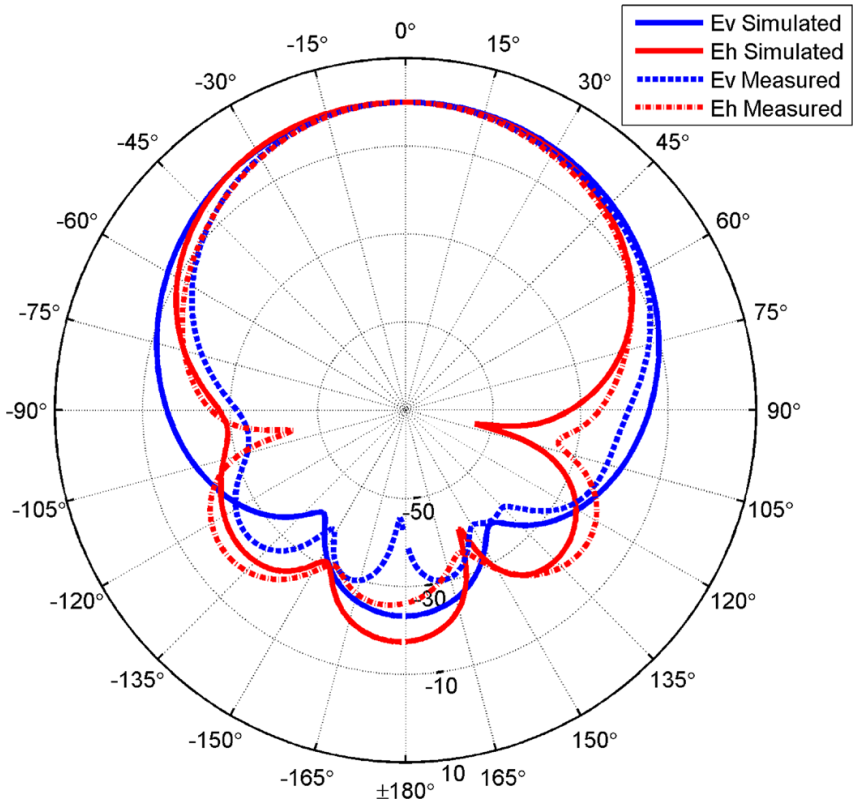

Fig. 15 Normalized measured and simulated E-vertical and E-horizontal components at 2.56 GHz in x–z plane

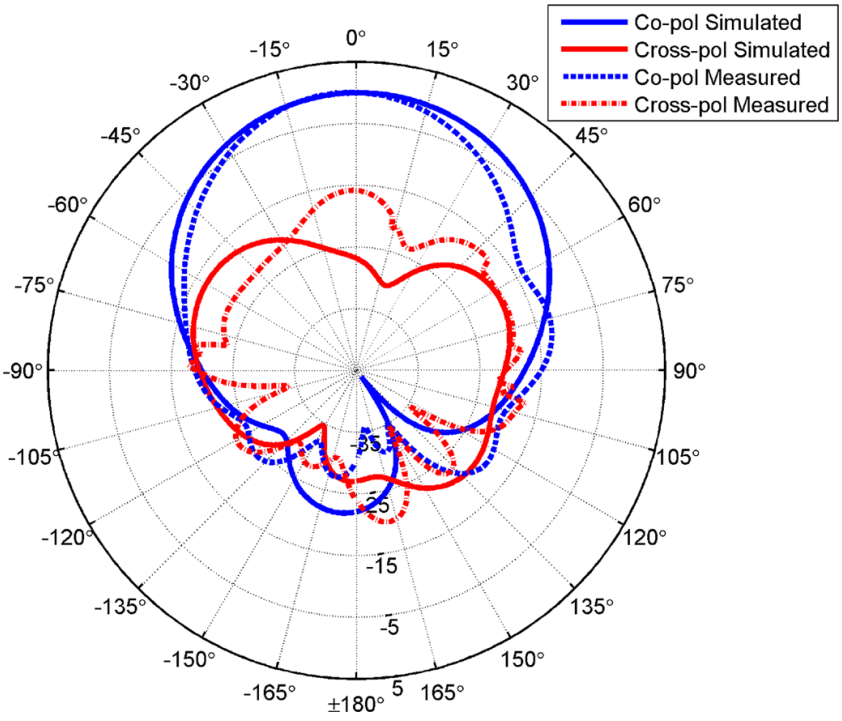

Fig. 16 Measured and simulated Co and cross polarized components at 2.56 GHz in y–z plane

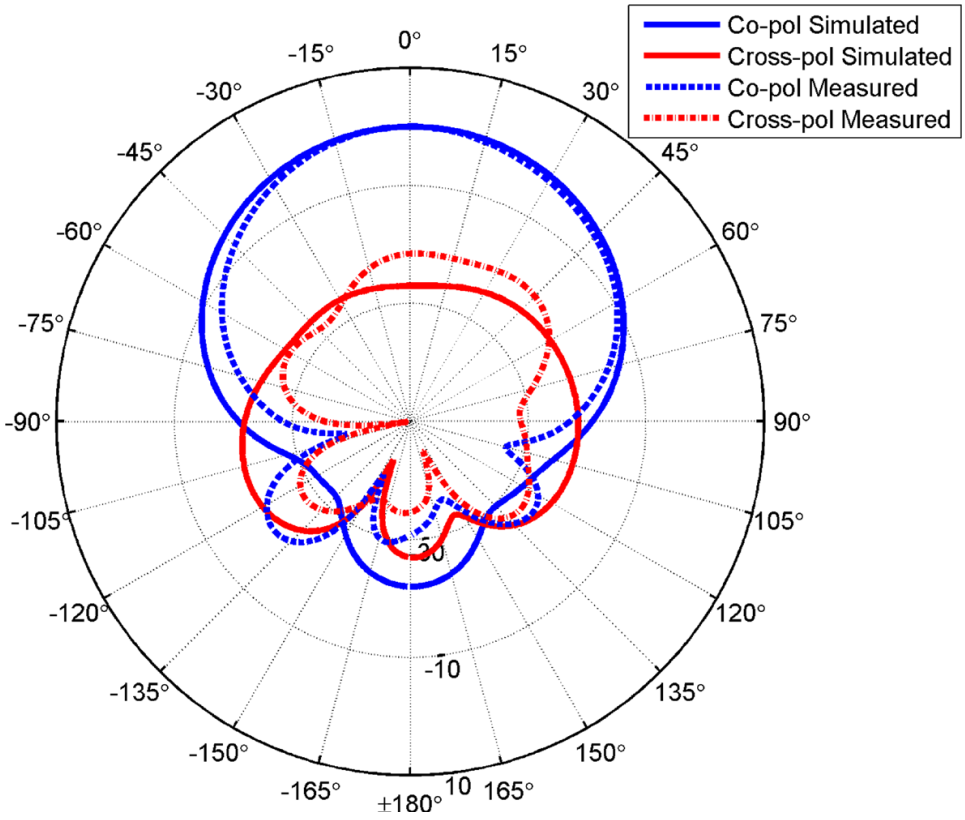

Fig. 17 Measured and simulated Co and cross polarized components at 2.56 GHz in x–z plane

4 Antenna Performance Comparisons with Existing Geometries

The measured results of the proposed antenna structure are compared with other slotted patch geometries available in literature. This comparison is shown in Table 2. The proposed antenna geometry has demonstrated very wide impedance bandwidth and higher gain in comparison to other slotted antenna geometries. Further, wideband circular polarization performance is obtained with the proposed antenna geometry.

Table 2 Proposed antenna comparison with other geometries

Antenna type	3-dB axial ratio bandwidth (%)	10-dB return loss bandwidth (%)	Gain (dBi)	Size of slotted patch ($\lambda_0 \times \lambda_0$)	Ground plane size ($\lambda_0 \times \lambda_0$)
Proposed π-shaped slot embedded antenna with aperture coupled feed	3.9	40.23	>8.2	0.34 × 0.34	0.51 × 0.51
U-slot antenna with coaxial feed [11]	3.9	9.1	8.0 (avg)	0.34 × 0.34	0.78 × 0.78
C-shaped slot antenna with aperture coupled feed [12]	3.3	16.0	6.7 (max)	0.33 × 0.33	0.48 × 0.48
Cross-shaped slotted antenna with coaxial feed [13]	0.7	2.0	>3.8	0.24 × 0.24	0.27 × 0.27
X shaped slotted patch with coaxial feed [14]	1.3	3.0	4.0 (max)	0.18 × 0.18	0.19 × 0.19
Arrowhead shaped slotted patch with coaxial feed [15]	0.9	3.8	>4.5	0.25 × 0.25	0.26 × 0.26

5 Conclusions

A wide band circularly polarized π-shaped slot embedded microstrip antenna with aperture coupled feed is analyzed, fabricated and its results presented. The circularly polarized performance of the antenna was found to greatly depend on the arm lengths S_1 and S_6 of the π shaped slot cut in the radiator. The proposed antenna showed a very wide 10-dB return loss bandwidth of 40.23 % and wide 3-dB axial ratio bandwidth of 3.9 %. A gain of more than 8.2 dBi was achieved over the circular band within 3-dB axial ratio. The antenna geometry is highly useful for circularly polarized antennas and arrays for wireless communication systems.

References

1. Garg, R., Bhartia, P., Bahl, I., & Ittipiboon, A. (2001). *Microstrip antenna design handbook*. Norwood, MA: Artech House.
2. Gupta, K. C., & Benalla, A. (1988). *Microstrip antenna design*. Norwood, MA: Artech House.
3. Targonski, S. D., & Pozar, D. M. (1993). Design of wideband circularly polarized aperture-coupled microstrip antennas. *IEEE Transactions on Antennas and Propagation, 41*(2), 214–220.
4. Karmakar, N. C., & Bialkowski, M. E. (1999). Circularly polarized aperture coupled circular microstrip patch antennas for L-band applications. *IEEE Transactions on Antennas and Propagation, 47*(5), 933–940.
5. Sharma, P. C., & Gupta, K. C. (1983). Analysis and optimized design of single feed circularly polarized microstrip antennas. *IEEE Transactions on Antennas and Propagation, 31*(6), 949–955.
6. Chen, W. S., Wong, K. L., & Wu, C. K. (2000). Inset microstripline-fed circularly polarized microstrip antennas. *IEEE Transactions on Antennas and Propagation, 48*(8), 1253–1254.
7. Ramirez, R. R., Flaviis, F. D., & Alexopoulos, N. G. (2000). Single-feed circularly polarized microstrip ring antenna and arrays. *IEEE Transactions on Antennas and Propagation, 48*(7), 1040–1047.
8. Chen, W. S., Wu, C. K., & Wong, K. L. (2001). Novel compact circularly polarized square microstrip antenna. *IEEE Transactions on Antennas and Propagation, 49*(3), 340–342.
9. Chang, F. S., Wong, K. L., & Chiou, T. W. (2003). Low-cost broadband circularly polarized patch antenna. *IEEE Transactions on Antennas and Propagation, 51*(10), 3006–3009.
10. Lu, J. H., Tang, C. L., & Wong, K. L. (1999). Single-feed slotted equilateral-triangular microstrip antenna for circular polarization. *IEEE Transactions on Antennas and Propagation, 47*(7), 1174–1178.
11. Tong, K. F., & Wong, T. P. (2007). Circularly polarized U-slot antenna. *IEEE Transactions on Antennas and Propagation, 55*(8), 2382–2385.
12. Nasimuddin., & Chen, Z. N. (2009). Aperture-coupled asymmetrical C-shaped slot microstrip antenna for circular polarization. *IET Microwaves, Antennas and Propagation, 3*(3), 372–378.
13. Nasimuddin., Qing, X., & Chen, Z. N. (2012). A compact circularly cross-shaped slotted microstrip antenna. *IEEE Transactions on Antennas and Propagation, 60*(3), 1584–1588.
14. Lin, Y. F., Lee, C. H., Pan, S. C., & Chen, H. M. (2013). Proximity-fed circularly polarized slotted patch antenna for RFID handheld reader. *IEEE Transactions on Antennas and Propagation, 61*(10), 5283–5286.
15. Gautam, A. K., Kunwar, A., & Kanaujia, B. K. (2014). Circularly polarized arrowhead-shape slotted microstrip antenna. *IEEE Antennas and Wireless Propagation Letters, 13*, 471–474.
16. IE3D Version 14.0. (2007) Zealand Software Inc: Fremont, CA.
17. HFSS Simulator ver 13.0, Ansoft: Canonsburg, PA.

Ajay Kumar Sharma was born on August 28, 1973 at New Delhi, India. He received M.E. degree with specialization in Microwave and Radar from University of Roorkee, Uttar Pradesh, India, in 1998. He is currently pursuing Ph.D. degree as a research scholar from School of Information and Communication Technologies, Guru Gobind Singh Indraprastha University, New Delhi, India. His current research involves development of wideband circularly polarized microstrip antennas. His interests include RF circuit design and active phased arrays.

Ashok Mittal was born on March 8, 1960 at New Delhi, India. He received Ph.D. degree in Microwave and Millimeter Wave Electronics from Delhi College of Engineering, New Delhi, India, in 2009. From 2001 to 2009, he worked as Member Senior Research Staff with Central Research Laboratory, Ghaziabad, Uttar Pradesh, India. Since 2009, he has been Professor with the Electronics and Communication Engineering department of Ambedkar Institute of Advanced Communication Technologies and Research, New Delhi, India. He is the author to more than 40 articles in conferences and journals. His research interests include microwave and millimeter wave circuit design, LTCC, MCM and microstrip antenna design.

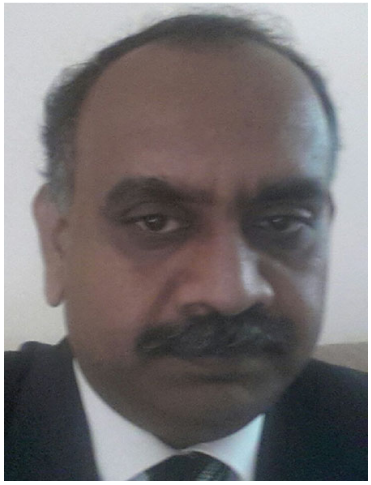

B. Venkata Ramana Reddy is currently working as Dean in School of Engineering and Technology and Professor of School of Information and Communication Technologies, Guru Gobind Singh Indraprastha University, New Delhi, India. His current research interests are wireless communication which includes mobile, Adhoc and sensor based networks, computer communication networks, VLSI circuits, microwave and optical communications and microstrip antennas. He has more than 50 publications in conferences and journals to his credit.

ISBN 978-93-5156-328-0
International Conference of Advance Research and Innovation (ICARI-2015)

Biodiesel Production from High Free Fatty Acid Feed Stocks through Transesterification

Sanjay Mohite [a], Sudhir Kumar [a], Amit Pal [b], Sagar Maji [b]
[a] Department of Mechanical Engineering, National Institute of Technology, Kurukshetra, Haryana, India
[b] Department of Mechanical Engineering, Delhi Technological University, New Delhi, India

Article Info

Article history:
Received 4 January 2015
Received in revised form
10 January 2015
Accepted 20 January 2015
Available online 31 January 2015

Keywords

Transesterification,
Biodiesel,
Feedstock,
FFA

Abstract

Transesterification is one of the most popular methods to decrease the viscosity of vegetable oils to produce biodiesel. It is the reaction of vegetable oil/ fats with an alcohol to give fatty acid alkyl esters in the presence of a catalyst with glycerol as by product. A catalyst is used to increase the rate of reaction and yield. The reaction is very much affected by the free fatty acids content in the feedstock. This paper discusses the appropriate method to produce biodiesel from the high High Free Fatty Acid (FFA) feed-stocks.

1. Introduction

There is a realization throughout the world that the petroleum resources which are non-renewable are being rapidly depleted. The growing demand for energy and gradual disappearance of fossil fuels may lead to severe energy crisis. World over researchers are looking for the renewable alternatives which is vegetable oil [1].The high viscosity of vegetable oils are the main hurdles to use it as fuel in diesel engine which causes poor fuel atomization resulting in poor combustion, ring sticking, injector coking, injector deposits, injector pump failure and lubrication oil dilution by crank case polymerization. [2-3] Biodiesel is produced as fatty acid methyl esters (FAME) from transesterification process in vegetable oils and animal fats with methanol. [4]

Feedstocks which contain triglyceride such as vegetable oils, waste oils, animal fats and waste greases can be converted into biodiesel by transesterification process. According to National Biofuel policy of India, biodiesel shall be obtained from non-edible oil seeds produced from waste, degraded and marginal lands. Biodiesel will be permitted to produce from indigenous feed-stocks [5]

2. Biodiesel Feedstocks

In developing countries, edible oils can not be used as fuel because it may cause food scarcity and other environmental problems by utilizing arable land. Therefore, non-edible vegetable oils are become more attractive for biodiesel production. Non-edible oilseed crops include Jatropha curcus, Madhuca indica (mahua), Pongamia pinnata (Karanja), Camelina sativa (Camelina),Cotton seed (Gossypium hirsutum), Cumaru, Cynara cardunculus, Abutilon muticum, neem (Azadirachta indica), jojoba (Simmondsia chinensis), Passion seed (passiflora edulis), Moringa (Moringa oleifera), Tobacco seed, rubber seed tree (Hevca brasiliensis), Salmon oil, Tall (Carnegiea gigantean), Coffee Ground (Coffea arabica), Nagchampa (Calophyllum inophyllum) , Croton megalocarpus, Pachira glabra, Aleurites moluccana, Terminalia belerica.[6]

Corresponding Author,
E-mail address: smohite001@yahoo.com
All rights reserved: http://www.ijari.org

3. Biodiesel Production Processes

Low FFA or edible feedstock can be converted to biodiesel by homogeneous basic catalytic process using sodium hydroxide or potassium hydroxide as catalyst. High yield can be obtained at normal room temperature and pressure due to low mass transfer resistance since the catalysts exist in the same liquid phase as the reactants. However, this process cannot be used for feedstocks containing high FFA content. Side reactions take place to deactivate the basic catalyst by the impurities resulting saponification with the formation of soaps and thus reducing the biodiesel yield. [7]

3.1 Transesterification Process

First step is the process of purification; any foreign materials in the oil are filtered out. Filtered oil is then heated to about 1100C to remove any moisture present in the oil. Presence of moisture will convert fatty acids into salts instead of having fatty acids of triglyceride molecule undergo transesterification. [8]

Ethanol and methanol are commonly used as alcohol in transesterification process. Methanol is more preferred over ethanol due to its high reaction rate but later one is renewable and derived from agricultural sources. Transesterification of vegetable oils produce fatty acid alkyl esters and glycerol. Glycerol is heavier than esters, its layer settle down at the bottom of reaction vessel. Monoglycerides and Diglycerides are the intermediate product in this process. [9]

3.2 Single Step Transesterification

Transesterification is one of the most popular methods to reduce viscosity of oils to produce biodiesel. For low FFA feedstock, single step transesterification is sufficient to convert the whole oil in to biodiesel. The reaction is reversible and therefore, excess alcohol is used to complete the reaction. [10] Most of the non-edible vegetable oils have

high level of free fatty acid and if free fatty acid content in the oil is more than 3% then alkali catalyzed transesterification will not be feasible. If the free fatty acid content is below 2%, alkaline transesterification is preferred. It is reported that alkaline transesterification is 4000 times faster than acid transestrification. [11]

3.3 Two Step Transesterification:

Non-edible oil feedstocks contain higher amount of impurities in the form of moisture & free fatty acids. Therefore, alkali catalyzed transesterification process is not suitable for the production of biodiesel [12]

Two step transesterification process method is used for the production of biodiesel from feedstocks containing high free fatty acids. Two step transesterification process can be used to produce biodiesel from high FFA oils. In this process, the first step is the esterification of FFA to FAME followed by a second step, alkali catalyzed transesterificaton. This technique gives high yield of biodiesel. [13]

In case of high FFA content feedstock, biodiesel is produced using two step processes. The first step consists of acid pretreatment of feedstock to bring down the FFA content followed by tranesterification with homogeneous base catalyst. [14]

Two step transesterfication processes also reduces high level of FFA to less than 1% for Mahua oil. Pretreatment of Mahua oil was carried out with 0.30-0.35 v/v methanol to oil ratio in the presence of 1% v/v H2SO4 as an acid catalyst in 1 hour reaction at 333 K. After this, biodiesel was produced by transesterification reaction using 0.25v/v methanol to oil ratio (6:1 molar ratio) and 0.7% w/v KOH as an alkaline catalyst resulting in the yield of 98% biodiesel from mahua oil. [15]

Two step processes was carried out to reduce acid value of karanja oil. The production method was studied for karanja oil containing FFA upto 20%.First step consists of acid catalyzed esterification by using 0.5% H2SO4, molar ratio 6:1 to produce methyl ester by reducing acid value and then alkali catalyzed transesterification have been carried out. The yield obtained during this two step transesterification process was 96.6-97%. [16]

Two step pretreatment process (acid esterification) was carried out to reduce acid value from 48 to 1.72 mg KOH/g with 0.40 and 0.35 v/v methanol-oil ratio and 1.0% v/v H2SO4 as catalyst at a temperature of 63(+ - 2) 0C with 1 hour reaction time for high FFA content rubber seed oil followed by transesterification using methanol oil ratio of 0.30 v/v, 0.5 w/v KOH as alkaline catalyst at 55(+-2)0C with 40 min reaction time to yield 98-99% methyl ester. [17]

4. Factors Affecting The Yield:

The Factors which affect transesterification process are the quantity and type of alcohol and catalyst, reaction temperature, pressure and time of reaction, amount of free fatty acids and water in oils. In case of presence of large quantity of free fatty acids (> 1%) in oils, the conversion is difficult since it forms soap with alkaline catalyst. The soap may prevent separation of biodiesel from glycerine. Some researchers used alternative double stage transesterification process for feedstock having higher acid value. [18-19]

4.1 Impact of Free Fatty Acids Content On Yield

Free fatty acid content in oil is one of the important factors which affect tranesterification process. [20] Sufficient yield of biodiesel can be produced with homogeneous base catalyst if the FFA content of feedstock is 0.5 wt% or less. However, the biodiesel yield reduces sharply to 6% with an increase in FFA content to 5.3 wt%. [16]

The efficiency to produce biodiesel may be determined by an important property of biodiesel feedstock i.e. fatty acid composition. The percentage and type of fatty acids composition depend upon type of plant species and their growth conditions. Non-edible oils have fatty acid composition of aliphatic compounds with a carboxyl group at the end of a straight chain.C16 and C18 fatty acids are generally present. [21]Non-edible oils generally contain high amount of free fatty acids which increase the cost of production and decrease the yield of biodiesel. [22]

Oils containing higher amount of fatty acids and water, forms large amount of soap. In case of high amount of free fatty acids, fatty acid will produce soap with reaction with base catalyst which reduces the separation of glycerin and biodiesel. There will be increase in viscosity and formation of gel due to presence of soap which decreases ester yield and inhibit the separation of glycerol. [23-24]

4.2 Effect of Catalyst Concentration and Types of Catalyst Used

Selection of the type of catalyst is one of the important parameter in transesterification reaction. It depends on the type of quality of feedstock. In general, homogeneous base catalysts are used for biodiesel production due to high yield conversion, short reaction time, lower reaction temperature and economical use. However, acid catalysts are incorporated in the production process for feedstock of high FFA content. [25]

The catalysts used for the transesterification of vegetable oils are classified as alkali, acid, enzyme or heterogeneous. Alkali catalysts like sodium hydroxide, sodium methoxide, potassium hydroxide, potassium methoxide are more effective. [26]

4.3 Effect of Molar Ratio

Methanol to oil molar ratio varied in the range of 3:1 to 12:1 for Jatropha oil and waste cooking oil and found the maximum ester conversions at molar ratio of 9:1. It was reported that further increase in molar ratio could not affect the yield amount and therefore, it was concluded that yield increased with increase in molar ratio upto 9:1. [27]

4.4 Effect of Reaction Time and Temperature

Rate of reaction is affected by reaction temperature. Transesterification reaction will be completed at room temperature, if enough time is provided. At atmospheric pressure, the reaction is conducted at 60-700C which is closer to boiling point of methanol. Removal of free fatty acids from oils is required for these reaction conditions by refining or pre-esterification. Degummed & de-acidified feedstock is used at these conditions for biodiesel production. Negative effect on the conversion is reported if the temperature exceeds beyond this limit.[28].

85% transesterification reaction was completed in 15 minutes & 97% in 3 hours using 1% KOH as catalyst. It was

observed that transesterification reaction proceeded rapidly at catalytic concentration of 1% KOH while 87% conversion was observed in 3 hours using 1.2% KOH as catalyst. It was observed that the best yield was obtained using 1% catalytic concentration of KOH [29]

5. Conclusion

Transesterification is the reaction of vegetable oil fats with an alcohol to give fatty acid alkyl esters in the presence of a catalyst with glycerol as by product. A catalyst is used to increase the rate of reaction and yield. However for high FFA vegetable oils two step transterification process seems to be more efficient and gives higher conversion yield.

References

[1] J. Janaun, N. Ellis, Perspectives on bodiesel as a sustainable fuel, Renewable & Sustainable energy reviews 14, 2010, 1312-1320
[2] A. K. Agarwal, L. M. Das, Biodiesel development and characterization for use as a fuel in compression ignition engines, J Eng Gas Turb Power, 123, 2001, 440-7
[3] A. K. Agarwal, J. Bijwe, L. M. das, Effect of biodiesel utilization on wear of vital parts in compression ignition engine, J Eng Gas Turb Power, 125, 2003, 604-11
[4] Y. Zhang, Biodiesel production from waste cooking oil: process design and technological assessment, Biores Technol, 89, 2003, 1-16
[5] G. Agoramoorthy, M. J. Hsu, S. Chaudhary, Po-Chuen Shieh, Can biofuel crops alleviate tribal poverty in India's dryland?, Applied Energy 86, 2009, S118-S124
[6] A. E. Atabani, A. S. Silitonga, I. A. Badruddin, T. M. I. Mahlia, H. H. Masjuki, S. Mekhilef, A comprehensive review on biodiesel as an alternative energy resources and its characteristics, Renewable and sustainable energy reviews 16, 2012, 2070-2093
[7] M. E. Borges, L. Diaz, Recent development on heterogeneous catalyst for biodiesel production by oil esterification and transesterificatio reaction: a review, Renewable & sustainable energy reviews, 16, 2012, 2839-49
[8] A. Demirbas, Biodiesel production from vegetable oils via catalytic and non-catalytic supertical methanol transesterification methods, Prog Energy Combust Sci 31(5-6), 2005, 466-87
[9] L. C. Meher, D. Vidya Sagar, S. N. Naik, Technical aspects of biodiesel production by transesterification – a review, Renewable and sustainable Energy Reviews 10, 2006, 248-268
[10] F. Ma, M A Hanna, Biodiesel production: a review, Bioresource Technology, 70, 1999, 1-15
[11] Soo-Young No, Inedible vegetable oils and their derivatives for alternative diesel fuels in CI engines: a review, Renewable and sustainable energy reviews 15, 2011, 131-149
[12] K. T. Lee, S. Lim, Y. L. Pang, H. C. Ong, W. T. Chong, Integration of reactive extraction with super-critical fluids for process intensification of biodiesel production: Prospects & recent advances, Progress in energy & combustion sciences 45, 2014, 54-78
[13] E. F. Aransiola, T. V. Ojumu, O. O. Oyakola, T. F. Madzimbamuto, D. I. O. Ikhu-Omoregbe, A review of current technology for biodiesel production: state of the art, Biomass & Bioenergy, 61, 2014, 276-297
[14] B. Fredman, E. H. Pryde, T. L. Mounts, Variables affecting the yield of fatty esters from transesterifed vegetable oils, J Am Oil Chem Soc 61:1638-1643:1984 doi 10.1007/BF02541649
[15] S. V. Ghatge, H. Raheman, Biodiesel production from mahua(Maduca indica) oil having high free fatty acids, Biomass Bioenergy, 28, 2005, 601-5
[16] M. Naik, L. C. Meher, S. N. Naik, L. M. Das, Production of biodiesel from high free fatty acid Karanja (Pongamia Pinnata) oil, Biomass Bioenergy: 32, 2008, 354-357, doi:10.1016/j.biombioe,2007,10.006
[17] M. Satyanarayan, C. Muraleedharan, A comparative study of vegetable oil methyl esters (Biodiesels), Energy, 2010, 1-9, DOI 10.1016/j.energy.2010.09.050
[18] A. S. Ramadhas, S. Jayaraj, C. Muraleedharan, Biodiesel production from high FFA rubber seed oil, Fuel, 84, 2005, 335-40
[19] V. Ghatge, H. Raheman, Biodiesel production from mahua oil having high free fatty acids, Biomass Bioenergy, 28, 2005, 601-5
[20] S. Dixit, S. Kanakraj, A. Rehman, Linseed Oil as a potential resource for biodiesel: A review, Renewable and Sustainable Energy Reviews, 2012, 16 4415-4421
[21] G. Knothe, S. C. Cermak, R. L. Evangelista, Biodiesel and renewable diesel: a comparison, Progress in energy and combustion science, 36(3), 2010, 364-73
[22] V. B. Borugadda, V. G. Vaibhav, Biodiesel production from renewable feedstocks:status & oppurtunities, Renewable sustainable Energy Reviews, 16, 2012, 4763-4784
[23] U. Rashid, F. Anwar, Production of biodiesel through optimized alkaline catalysed Tranesterification of rapeseed oil, Fuel, 87, 2008, 265-273
[24] A. Abbaszaadeh, B. Ghobadian, M. R. Omidkhah, G. Najafi, Current biodiesel production technologies: a comparative review, Energy Convers Manag, 63, 2012, 138-148
[25] T. Issariyakul, A. K. Dalai, Biodiesel from vegetable oils, Renewable & sustainable energy reviews, 31,2014, 446-471
[26] F. Ma, M. A. Hanna, Biodiesel production: a review, Bioresour Technol, 70, 1999, 1-15
[27] V. G. Gude, G. E. Grant, P. D Patil, S. Deng, Biodiesel Production from low cost and renewable feedstock, Cent. Eur.J.Eng, 3(4), 2013, 595-605
[28] S. Kumar, A. K. Gupta, S. N. Naik, Conversion of non-edible oil into biodiesel, JSIR, 62, 2003, 124-132
[29] L. C. Meher, S. N. Naik, L. M. Das, Methanolysis of Pongamia Pinnata (karanja) oil for production of biodiesel, JSIR, 63, 2004, 913-918

Biodiesel Production from Sal (Shorea Robusta) Seed Oil

H.S. Pali[1] , N. Kumar[2]

[1,2] *Centre for Advanced Studies and Research in Automotive Engineering, Delhi Technological University, Delhi-110042, India.*

*harvirpali@gmail.com

Abstract— **Biodiesel from renewable sources like vegetable oils, animal fats etc. are significantly evaluated as an alternative to fossil fuels. In this context, the present work deals with an underutilized vegetable oil known as "Shorea robusta" or Sal seed oil" as a potential feedstock for biodiesel production which can considerably increase the feedstock availability. The production potential of sal seed oil is a gigantic 1.5 million tons a year and the geo-climatic penetration of the plant is sub-continental with special presence in Odisha, Chhattisgarh and Madhya Pradesh. In the present work, pressure filtered Sal seed oil was transesterified sal seed methyl ester (Biodiesel) with 1:9 oil to methanol molar ratio, 0.5% by weight of catalyst (potassium hydroxide), 65°C reaction temperature and 450 rpm agitation speed leading to an ester yield of 96.8%. The results of physico-chemical properties indicated that kinematic viscosity (5.8 cSt), density (0.884 gm/cc), heating values (40.28 MJ/kg) of the Sal oil methyl ester (SOME) was well within the ASTM/EN standard limits. Oxidation stability was more than 06 hours in the biodiesel rancimat. The fatty acid profiles of SOME showed richness of saturated fatty acids like Pentadecanoic acid and Mysteric acid.**

Keywords— **Alternative fuel, biodiesel, diesel engine, sal seed oil, transesterification etc.**

I. INTRODUCTION

After the market based reforms in the year 1991, the resurgent Indian economy exhibited impressive growth. The rapid growth in the economy was coupled with improved infrastructure, mobility and industrial activity. The same may be evident from the exponential increase of automobile fleet in India from 0.3 million units in 1953 to 142 million units in 2011 with an annual growth rate of 9.9% between the years 2001-2011[1]. The rising prosperity and improving living standards resulted in higher energy demands. A significant part of this energy in India is obtained from crude oil derived products like petrol and diesel used in internal combustion engines. With no substantial diversification in energy supply, India continued to be dependent on imported crude oil to fuel its economy as it lacked oil reserves. While it's domestic crude oil production stood stagnant at less than 1000 barrels per day (BPD) in the period 2001-11, its crude oil imports increased stupendously from 2200 BPD to 3400 BPD in the same duration resulting in huge trade deficit and humongous amount of forex outflow to fund the imports [2]. Apart from this, the depletion in fossil fuel reserves, rising green house gas (GHG) emissions due to fossil fuel burning and the resultant environmental degradation as well as global warming are another area of major concern. According to the International Energy Outlook of 2011, which was published by the U.S. Energy Information Administration, the global usage of liquid fuels will increase from 85.7 million barrels per day in 2008 to 112.2 million barrels per day in 2035. In addition, the transport sector will account for 82% of the total increase in liquid fuel use, with the remaining growth attributed to the industrial sector [2]. With this projection India will be importing 100% of its total crude oil requirement by 2035 [2].

The most popular petroleum fuels in India are gasoline and diesel used as motor fuels in spark ignition and compression ignition engines respectively. Amongst them, diesel engines have proven their utility in the transportation and power sectors due to their higher efficiency and ruggedness and hence play a pivotal role in rural as well as urban Indian economy [3]. With respect to usage, diesel engines are largely favored across a wide spectrum of activities like automotive application, small and decentralized power generation, prime mover for farm and agricultural machineries, small scale industrial prime mover and so on. The same may be evident from the Ministry of petroleum, Government of India data that shows that the consumption of diesel in the year 2012 was 4.5 times higher than motor gasoline in the same period [4].Therefore, even a partial substitution of mineral diesel by any renewable and carbon neutral alternative fuel can have significant positive effect on economy

and environment in terms of reduction in carbon footprints and dependence on imported crude oil.

In the light of the above discussion, it may be stated that renewable, sustainable, efficient and cost effective alternative fuel to mineral diesel with reduced carbon footprints are one of the critical needs of the hour [5,6]. In this context, bio-origin liquid fuels like vegetable oil, animal fats etc. are long considered as suitable greener alternative to diesel. However, higher viscosity and density of crude bio-origin oils create operational problems in engines like poor fuel atomization and vaporization, injector chocking, lubricating oil dilution, increased carbon deposit, reduced efficiency etc. Therefore, vegetable oils are not recommended for direct diesel engine application. However, there are several methods like dilution, pyrolysis, transesterification and engine hardware modification etc. in which vegetable oil can be used in diesel engines. Amongst them, transesterification has been established as the best method to use vegetable oils in diesel engines. In the process of transesterification, the triglycerides of the bio-origin oils are converted in to fatty acid alkyl esters and glycerol by reacting with alcohol in presence of a suitable catalyst. Those fatty acid alkyl esters that conform to ASTM D6751 [7] or EN 14214 [8] standards are termed as biodiesel. Biodiesel is considered as a better fuel than mineral diesel on many grounds. Superior lubricity, renewable background, lack of sulfur and aromatic compounds, superior flash point and biodegradability along with reduction in regulated exhaust emissions are some of the improved characteristics of biodiesel compared to the conventional mineral diesel [9,10].

In the last decade, rising food inflation worldwide was partly attributed to the diversion of food crops for biodiesel production in many developed western countries. This phenomenon of food verses oil was critically debated in a global scale. In this context, developing countries like India cannot afford food crops or edible oils for biodiesel production especially when there is a billion plus mouths to be fed. Therefore, Indian Government decided to choose non-edible energy crops growing at drought or barren lands as the feedstock for biodiesel production. Jatropha curcas was selected as the most suitable tree born oil seed for the flagship program "National Biodiesel Mission" launched by Indian Government in 2009. However, the mission to accomplish 20% blending by 2012 was not realized on account of a number of reasons out of which lack of sufficient feedstock was cited as a major bottleneck. In the light of the above discussion, it may be stated that other potential sources of biodiesel must be explored relentlessly so that Government's biofuel policy will be supported and the feedstock base can be enlarged sufficiently to address the ever rising demand of fuels. In this context, the present research deals with the potential of biodiesel production from a still untapped non-edible oil source known as "Shorea robusta" or "sal seed oil". This is primarily a forest product with a sub-continental presence. However, it has a dominant penetration in states like Odisha, Chhatishgarah, Madhya Pradesh, east Maharashtra etc. The annual estimated production of sal seeds is around 1.5 million tonnes and the sal seed oil or fat production is around 0.18 million tonnes a year [11,12]. In the present investigation, sal seed oil is to be transesterified to produce sal oil methyl ester (SOME) and various physico-chemical properties to be evaluated and compared the corresponding ASTM/EN standards.

II. MATERIALS AND METHODS

A. SAL SEED PLANT

Shorea robusta is a large, deciduous tree up to 50 m in height. Under normal conditions the tree attains a height of 18-32 m and girth of 1.5-2 m. Bole is clean, straight and cylindrical but often bears epicormic branches. Crown is spreading and spherical. Bark is dark brown and thick, with longitudinal fissures deep in poles, becoming shallow in mature trees; provides effective protection against fire. The tree develops a long taproot at a very young age [13]. Fig.1 shows flowers and seeds of sal.

B. EXTRACTION OF NEAT SAL SEED OIL

As sal seed is a forest product, the direct access to the procurement was difficult. Therefore, the extracted sal seed oil which was in butter form was procured from some of the outlets of Odisha Forest Development Corporation in Bhubaneswar. At room temperature the oil remains in butter form. Fig.2 shows the sal seed oil butter procured for the present investigation and the oil.

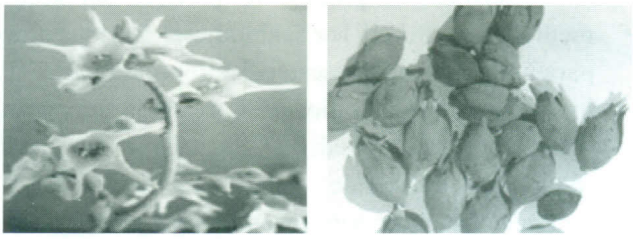

Fig. 1 Example of an unacceptable low-resolution image

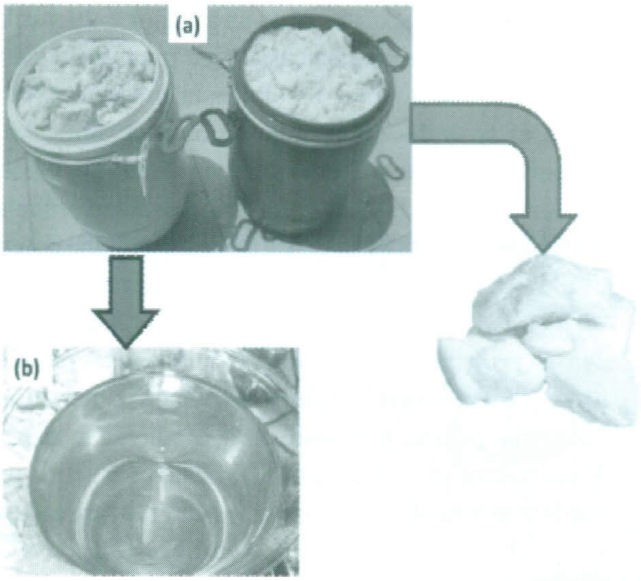

Fig. 2 (a) – Sal seed oil butter at room temperature,
(b) – sal seed oil after heating.

C. TRANSESTERIFICATION FOR PRODUCTION OF SAL SEED OIL METHYL ESTER

Biodiesel is normally produced by the transesterification process in which the triglyceride of the vegetable oil is converted in to fatty acid alkyl esters and glycerol in presence of a catalyst. The most commonly used alcohol is methanol to produce methyl esters. It is generally referred as fatty acid methyl esters (FAME) [14]. The general scheme of the transesterification reaction for FAME is presented in equation (1.1), where R is a mixture of fatty acid chains [15].

$$\begin{array}{lcl} CH_2-O-CO-R_1 & & CH_2-OH \quad R_1-COOCH_3 \\ | & \xrightarrow{\text{Catalyst}} & | \\ CH-O-CO-R_2+3CH_3OH & \leftrightarrow & CH-OH+R_2-COOCH_3 \\ | & & | \\ CH_2-O-CO-R_3 & & CH_2-OH \quad R_3-COOCH_3 \\ \text{Triglyceride} \quad \text{methanol} & & \text{Glycerol} \quad \text{methylester} \end{array} \qquad (1.1)$$

The free fatty acid contents of the sal seed oil was as low as 0.42% leading to a simple and one stage transesterification process to produce sal seed oil methyl ester (SOME) or sal biodiesel. Various process parameters for the transesterification stage were 1:9 oil to methanol molar ratio, 65°C reaction temperature, 450 rpm agitation speed, 0.5% by weight of the catalyst (potassium hydroxide) and a reaction time of 60 minutes. The ester yield was more than 96%. Fig.3 shows the SOME after water washing.

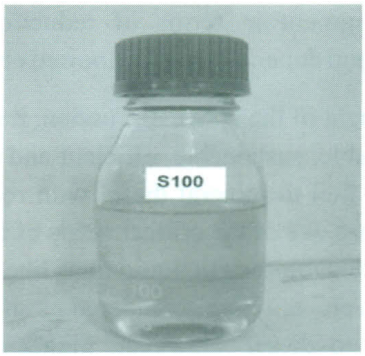

Fig. 3: – Sal seed oil methyl ester (S100)

D. PHYSICO-CHEMICAL CHARACTERIZATION

Various physico-chemical and fuel properties like density, viscosity, calorific value, cold flow properties, oxidations stability, fatty acid profiles etc. of the final SOME was determined in the laboratory. Apart from neat SOME, 5%, 10%, 15% and 20% blends of SOME in diesel named as S5, S10, S15 and S20 was also subjected to physico-chemical characterization. Fig.4 shows various test fuels for characterization. The respective equipments used for the tests were of standard quality with errors and repeatability within the permissible limits. Table 1 shows various equipments, their manufacturers and measurement standards.

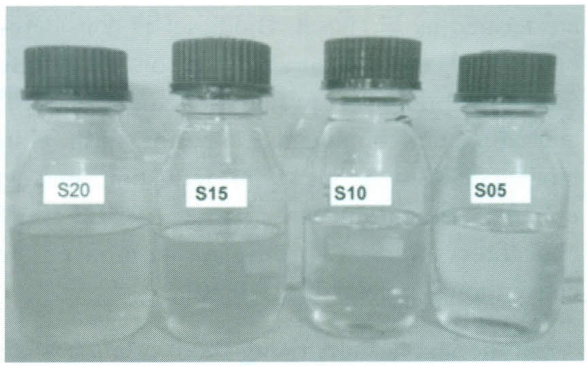

Fig. 4. SOME Blend

III. RESULTS AND DISCUSSION

As discussed earlier, the production of sal seed oil methyl ester was carried out in a single stage transesterification process. In this context, a series of initial transesterification processes are carried out and a suitable range for individual process parameters like reaction time, temperature, catalyst concentration etc. were determined corresponding to the optimum conditions. Based on the experiments and some references of earlier research work, the test matrix for transesterification stage was prepared as shown in table 2.

It may be evident that 0.25% by weight of catalyst and 60 minutes time produced the maximum ester yield of 98%. For simplicity, reaction temperature was fixed at 65°C, molar ratio was 1:9 and agitation speed was 450 rpm same for all the experiments.

A sample of fatty acid methyl ester produced form any feedstock can be termed as a biodiesel when it complies to the established international standards. Therefore, chracterisation and standardization of methyl ester samples produced in the transesterification is an integral part of biodiesel quality control. In this context, the sample of SOME produced was subjected to a comprehensive physicochmeical and fuel characterisation and the results were compared with the correpsonding ASTM/EN standards as mentioned in table 3. Moreover, the variation of significant properties like density, viscosity and heating value with increasing volume fraction of SOME in diesel was also shown in tertms of bar chat in Fig. 5. This is very much significant in terms of diesel engine application. The SOME vlume frcation was limited within 20% as per the Government of India's biofuel policy that envisages a 20% blending of alternative fuels in diesel.

TABLE I
Equipments, manufacturers and standards

S. No	Property	Equipment	Manufacturer	ASTMD6751	ASTMD6751 LIMITS
1	Kinematic viscosity	Petrotest viscometer	Anton Parr, UK	D445	1.9-6 cSt
3	Oxidative stability	873 Rancimat	Metrohm, Switzerland	D675/EN14112	3/6 hours
4	Density	U tube density meter	Anton Parr, UK	D1298/ISO12185	0.86-0.9g/cc
5	CFPP	Automatic NTL 450	Normalab, France	D6371	Not specified
6	Calorific value	Parr 6100 Bomb calorimeter	IKA, UK	Not specified	Not specified

It may be observed that a marginal reduction in density was realized after neat Sal oil was transesterified to produce SOME. Although, SOME showed 5.5% higher density than mineral diesel, but it was still well within the ISO 12185 standard limit of 0.86-0.89 g/cc. Mean while, viscosity of the neat oil was reduced drastically from 157 cSt to nearly 5.8 cSt after transesterification. Although the viscosity of the final

SOME sample was still higher than mineral diesel by a factor of 2, but it suitably conformed to ASTMD6751 standard. The heating value shown by the SOME sample was very much comparable to mineral diesel. The oxidation stability of the SOME was commendable and conformed to both D675 and EN14112 standards on account of higher composition of saturated fatty acids.

TABLE II
Test matrix for transesterification

Experiment No.	Catalyst concentration (% by original oil mass)	Reaction time (minutes)	Ester yield (%)
1	1.3	90	94
2	1.3	100	94.7
3	1.3	110	95.2
4	1.4	90	96
5	0.5	60	96.8
6	1.4	110	96.4
7	1.5	90	95.2
8	1.5	100	96.3
9	1.5	110	96.9

Table III
Various physico-chemical properties of sal seed oil, SOME and diesel

Sl No	Properties	Sal oil	SOME	Diesel
1	Density at 15°C (g/cc)	0.899	0.884	0.8239
2	Viscosity at 40°C (cSt)	157	5.88	2.956
3	Calorific value (MJ/Kg)	39.78	40.28	45.49
4	Oxidation stability (hours)	--	> 6	--

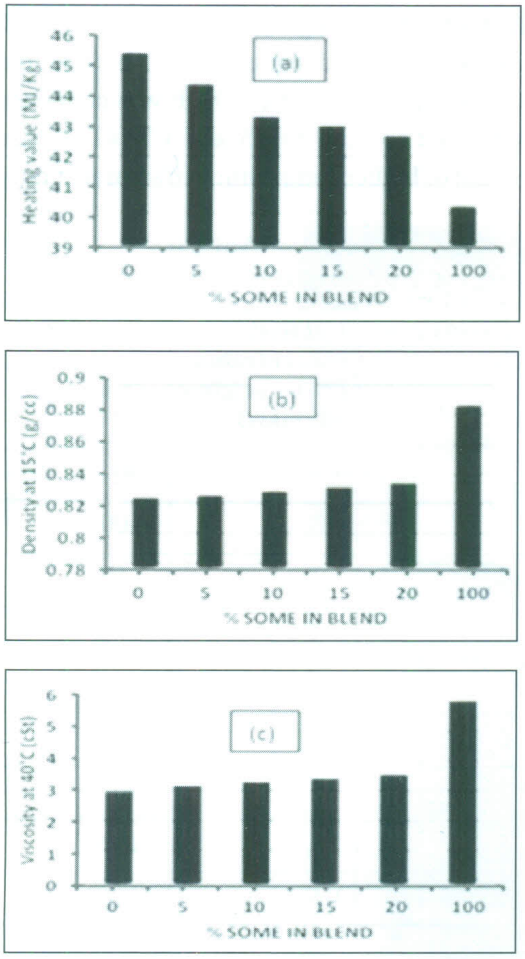

Fig. 5: (a) Variation of heating value with % blend,
(b) Variation of density % blend,
(c) Variation of viscosity with % blend

Fig. 5 shows the variation of heating value, density and viscosity with % blend. It may be observed that up to 20% blend of SOME in diesel, no significant variation in key properties was observed. Rather, the dissolved oxygen content and superior cetane rating of the SOME is supposed lead towards better combustion and enhanced efficiency. However, the viscosity of the neat SOME is very close to the upper ASTM limits.

The detailed fatty acid profile of the SOME sample was determined using high precision gas chromatography equipment. The fatty acid profile in terms f peaks is shown in Fig.6 and detailed composition is provided in the table 7.

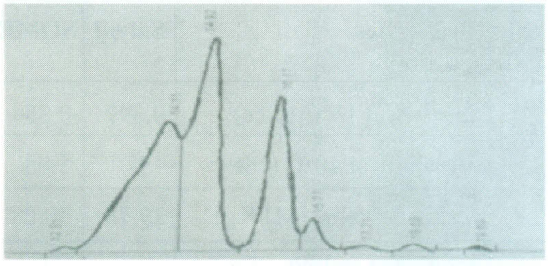

Fig. 6: Fatty acid profile of SOME in terms of peaks.

TABLE IV
Fatty acid composition of SOME

Fatty Acid	Lipid number	Weight (g/mol)	(% wt)
Lauric acid	C12:0	200.317	0.58
Mysteric acid	C14:0	228.38	37.23
Pentadecanoic acid	C15:0	242.39	36.03
Palmitic acid	C16:0	256.42	21.69
Palmitoleic acid	C16:1	192.17	3.26
Cis-10-heptadecanoic acid	C17:1	270.45	0.43
Oleic acid	C18:1	282.47	0.59
Linoleic acid	C18:2	280.45	0.15
Saturated			95.53
Unsaturated			4.43
Total			99.96

It may be easily referred from the table 7 that SOME contains nearly 95.53% saturated fatty acids and only 4.43% unsaturated fatty acids in its composition. Due to this the oil bears the form of butter at room temperature. It may be easily stated that the cold flow properties of SOME are also will be inferior. Although the cold flow properties were not evaluated in the present investigation, but the same may be studied and additives should be added to improve the cold flow properties in future studies. However, presence of saturated fat increases the storage stability of the oil manifold. The same was evident from the oxidation stability test that showed significantly low amount of peroxide formation in the biodiesel rancimat for more than 6 hours confirming to the EN standards.

IV. CONCLUSIONS

Biodiesel has enormous prospects in India as far as energy security and environmental aspects are concerned. However, the challenges to materialize the 20% blending target is also very much intriguing. In this context, exploration of new and underutilized non-edible seed oils is of paramount significance. The initiative taken in the present research work to explore sal or Shorea Robust as a biodiesel feedstock is a small step in the right direction. Biodiesel production from the sal seed oil was carried out in the present study by a transesterification process and then a comprehensive physico-chemical characterization was carried out.

- The results indicated that 0.25% by mass of catalyst (potassium hydroxide), 65°C temperature and 60 minutes time with the same 450 rpm agitation speed. The oil to methanol molar ratio was fixed at 1:9 for both the stages.
- The results of physico-chemical properties were very much encouraging with all the parameters highly accommodating with the corresponding ASTM/EN/ISO standards. The results indicated that kinematic viscosity was 5.8 cSt, density was 0.884 gm/cc and heating values was 40.28 MJ/kg.
- The fatty acid profiles of the Sal seed oil methyl ester showed the richness of Pentadecanoic acid and Mysteric acid. Besides, the saturated fatty acids account for nearly 95.53% and unsaturated fatty acids were nearly 4.43% as indicated by the gas chromatography apparatus.
- The oxidation stability of SOME was more than 6 hours conforming to the stringent EN14112 standard. The cold flow plugging point of SOME was found to be 5^0 C as compared to -9^0C exhibited by the neat diesel.

Therefore, it may be concluded that use of Sal seed oil as a feedstock for biodiesel production is feasible and practicable in Indian conditions. Concrete efforts need to be made by all the stake holders to commercialize sal biodiesel as an alternative fuel.

REFERENCES

[1] World road statistics 2011, International road federation, Geneva,

[2] International Energy Outlook 2011, Office of communications, EI-40. Washington, DC 20585: U.S. Energy Information Administration, Forrestal Building; DOE/EIA-0484, 2011.

[3] Chauhan B.S, Kumar N, Cho H.M. "Performance and emission studies on an agriculture engine on neat Jatropha oil", Journal of Mechanical Science and Technology, 24 (2), pp 529-535, 2010.

[4] Basic Statistics on Indian Petroleum & Natural Gas, Ministry of Petroleum & Natural Gas, Government of India, New Delhi, Economic Division, 2009-10.

[5] Escobar JC, Lora ES, Venturini OJ, Yanez EE, Castillo EF, Almazan O. "Biofuels: environment, technology and food security", Renewable and Sustainable Energy Reviews, 2009; 13:1275-87.

[6] Nigam PN, Singh A. Production of liquid biofuels from renewable resources. Progress in Energy and Combustion Science; 37, pp 52-68, 2011.

[7] ASTM Standard D 6751-07b. Standard specification for biodiesel fuel blend stock (B100) for middle distillate fuels. West Conshohocken, PA (USA): American Society for Testing and Materials; 2007.

[8] EN 14214. Automotive fuels – fatty acid methyl esters (FAME) for diesel engines – requirement methods. Brussels (Belgium): European Committee for Standardization; 2003.

[9] Joshi H , Moser BR, Toler J, Walker T. Preparation and fuel properties of mixtures of soybean oil methyl and ethyl esters. Biomass and bio-energy, vol. 34, , pp 14–20, 2010.

[10] Knothe G, Krahl J, Gerpen JV, editors. The biodiesel handbook. Champaign, IL (USA): AOCS Press; 2005.

[11] www.banajata.org/Sal_Seed. Data taken on 26.08.2013.

[12] Negi SS. Tannins in sal seed (Shorea robusta) and sal seed meal limit their utilization as livestock feeds. Animal Feed Science and Technology, Vol. 7, Issue 2, pp 161-183, March 1982.

[13] www.agroforestry.net. Data taken on 26.08.2013.

[14] Chopade G, Kulkarni K.S, Kulkarni A.D, Topare S. Solid heterogeneous catalysts for production of biodiesel from trans-esterification of triglycerides with methanol : a review. Acta Chimica & Pharmaceutica Indica; 2(1), pp 8–14, 2012.

[15] Park Y.M, Lee J.Y, Chung S.H, Park I.S, Lee S.Y, Kim D.K. Esterification of used vegetable oils using the heterogeneous WO3/ZrO2 catalyst for production of biodiesel. Bioresource Technology 101(1), pp 59–61,2010.

Harveer Singh Pali is a graduate from MJP Rohilkhand, Bareilly and did his Master of Technology from UPTU, Lucknow in Mechanical Engineering. Currently he is working as a Research scholar in Mechanical Engineering Department at Delhi Technological University, Delhi under the guidance of Dr. Naveen Kumar. His interest includes biofuels, renewable energy, and diesel engines.

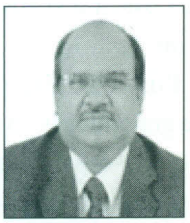

Naveen Kumar is currently a Professor of Mechanical Engineering at Delhi Technological University (Formerly Delhi College of Engineering) and has over 22 years of experience in the industry, teaching, and research. His research interests include the development of various bio-fuels and their utilization in decentralized power systems. Dr. Kumar has extensively traveled abroad and has interacted with various universities and industries in both developed and developing countries. He has executed many sponsored research projects funded by both Government and Industry. He has to his credit large number of research papers/articles.

Optics Communications 347 (2015) 13–19

Contents lists available at ScienceDirect

Optics Communications

journal homepage: www.elsevier.com/locate/optcom

Broadband mid-IR supercontinuum generation in As_2Se_3 based chalcogenide photonic crystal fiber: A new design and analysis

Than Singh Saini, Ajeet Kumar, Ravindra Kumar Sinha*

TIFAC-Center of Relevance and Excellence in Fiber Optics and Optical Communication, Department of Applied Physics, Delhi Technological University, Delhi 110042, India

ARTICLE INFO

Article history:
Received 20 December 2014
Received in revised form
21 February 2015
Accepted 24 February 2015
Available online 26 February 2015

Keywords:
Highly nonlinear photonic crystal fiber
All-normal dispersion fiber
Supercontinuum generation

ABSTRACT

A new design of a triangular-core photonic crystal fiber in As_2Se_3-based chalcogenide glass with all-normal, nearly zero flat-top dispersion has been proposed for supercontinuum generation. Simulated results indicate that ultra-broadband supercontinuum spanning 1.9–10 μm can be obtained using only 6 mm long PCF pumped with 50 femto-second laser pulses operated at 4.5 μm. In comparison to previously reported work we have obtained ultra-broadband supercontinuum spectra using relatively very low peak power of incident pulses. Proposed photonic crystal fiber structure is applicable in bio-molecular sensing and infrared spectroscopy.

© 2015 Published by Elsevier B.V.

1. Introduction

Photonic crystal fibers (PCFs) or holy fibers (HFs) are fascinating because of their unique linear and nonlinear properties such as dispersion management, high birefringence, large-mode-area with endlessly single-mode operation, high power delivery and supercontinuum generation (SCG) [1–10]. Supercontinuum (SC) is the nonlinear optical process where ultra-short pulse of laser light is evolved into the light with very broad spectral bandwidth. SCG is outcome of various nonlinear, such as self-phase modulation (SPM), cross-phase modulation (XPM), self-steepening, four-wave mixing (FWM), stimulated Raman scattering (SRS) and dispersion effects. SCG occurs when narrow-band input optical pulses undergo extreme nonlinear spectral broadening to yield spectrally continuous white light output while passing through optical fibers [1].

The applications of SC fall in different fields such as telecommunication, optical metrology, optical coherence tomography (OCT), nonlinear microscopy, cosmological studies, ultra-short pulse and frequency combs generation [11–17]. Initially, SCG in single-mode fiber was used around 1994 to obtain picosecond pulses of multiple wavelengths for wavelength division multiplexing (WDM) communication system [17]. The phenomenon of SCG was first time studied around 1970 in solid and gaseous nonlinear media by Alfano et al. [18], while supercontinuum in PCF is demonstrated by Ranka et al. in the year 2000 [19]. The progress of SCG in PCF has also been reported in several reviews [3–20,21].

In order to simulate SCG, an understanding of the media in which they are generated, is needed. PCFs in high-index non-silica glasses such as tellurite, bismuth, fluoride and chalcogenide have advantages over silica-based PCFs in various applications of highly nonlinear optical fibers and mid-infrared transmission [22–24]. Chalcogenide glasses are excellent candidates as some of its compositions have optical transparency up to 25 μm in mid-IR region [25]. In addition to broadband mid-IR transmission window, chalcogenide glasses possess very large linear and nonlinear refractive indices [26].

An experimental demonstration of SCG in the spectral range of 2.1 to 3.2 μm using hexagonal structure of As_2Se_3 chalcogenide PCF was presented by Shaw et al. [27]. Yeom et al. first time demonstrated the SCG in dispersion engineered As_2Se_3 fiber taper [28]. Hudson et al. reported experimentally the broadening of SC spectrum spanning 0.97–1.99 μm in a sulfide-based chalcogenide tapered fiber using very low pulse energy [29]. The basic elements of tapered chalcogenide optical fibers have been reviewed for supercontinuum generation [30]. Lamont et al. fabricated first time an anomalous dispersion engineered chalcogenide planar waveguide for supercontinuum genearation [31]. In the recent past, Hu et al. introduced a design procedure, which can be used to maximize the band-width of supercontinuum generation in As_2Se_3 chalcogenide PCFs, for more than 4 μm band-width of SC with input pulse at 2.5 μm [32]. A detailed comparison between the theoretical and experimental investigation of SCG in commercially available ZBLAN optical fibers have been presented in the Ref. [33].

* Corresponding author.
E-mail address: dr_rk_sinha@yahoo.com (R. Kumar Sinha).

http://dx.doi.org/10.1016/j.optcom.2015.02.049
0030-4018/© 2015 Published by Elsevier B.V.

Kubat et al. presented a numerical design optimization of ZBLAN fibers for mid-IR SC sources with spectra covering 1 – 4.5 μm regime using direct pumping with 10 ps pulses from mode-locked Yb and Er lasers [34]. In Ref. [35], the authors have experimentally demonstrated the SCG covering 0.9 – 9 μm with the help of commercially available ZBLAN fiber and commercially available chalcogenide PCF. Hudson et al. demonstrated SC spectrum spanning 1.6–5.9 μm at −20 dB level in a step-index chalcogenide fiber using an optical parametric chirped pulse amplifier at 3.1 μm [36]. Numerical modeling of broadband mid-IR SCG spanning from 3 μm to 12.5 μm has been presented in a step-index fiber pumped at 4.5 μm with 0.75 KW pump power [37].

In above mentioned works, SC have been generated in fiber structures which offer group velocity dispersion (GVD) profile in both normal and anomalous dispersion regime. If the pump wavelength lies in anomalous dispersion regime, the flatness of SC is distorted due to soliton fission for pumping with femtosecond pulses. However, the probability of soliton fission can be completely removed by designing fiber with all-normal dispersion regime [38,39]. Thus, the phenomenon of SPM and optical wave breaking leads to SCG in the fiber having all-normal dispersion. This makes the SC with very low noise. Such broad-band SC is suitable for time-resolved applications. One of the possibilities for generating SC in the normal dispersion regime is to pump the fiber far below the zero dispersion wavelength (ZDW), so that the generated spectrum does not extend into the anomalous dispersion region. However, this would require high power or very short pulses to overcome the short effective interaction length due to high value of dispersion. For obtaining the intrinsic coherent property of super continuum generation, the PCFs with all-normal and flat-top dispersion are desirable. In this regard, various efforts have been done earlier to obtain all-normal flat-top dispersion in chalcogenide PCF [40–42].

SCG in all-normal dispersion PCF has been investigated numerically using high energy femtosecond pulses to obtain coherent octave spanning SC spectra [40]. A PCF design in chalcogenide glass has been presented with all-normal flat dispersion for applications in fiber lasers, pulse compression and multi-wavelength optical sources in the mid-infrared region [41]. Recently, a numerical simulation on the coherent time-critical SCG in As_2S_3-based chalcogenide microstructured fiber with all-normal flat-top dispersion profile has been carried out for 2–5 μm spectral range [42]. Mid-IR SC spectra spanning 1.795–6.525 μm has been achieved in 8 mm length of As_2Se_3 nanofiber with input pulse energy of 100 nJ [43]. Very recently, Klimczak et al. demonstrated first experimental report of all-normal dispersion SCG spanning over an octave from 900 nm to 2300 nm in all-solid soft glass PCF using 75 fs pulses centered at 1550 nm [44].

In this paper, we report a new design of triangular-core (TC) PCF and have used the same for ultra-broadband SCG in mid-IR region. We have also investigated the effects of input pulse parameters (such as: peak power and pulse width in terms of full width at half maxima) and propagation length of fiber on evolution of SCG in proposed TC PCF. It is important to mention here that our proposed TC PCF design is able to generate ultra-broadband mid-IR SC extending from 1.9 μm to 10 μm in only 6 mm long PCF with relatively much lower peak power of 700 W, in comparison to recently demonstrated broadband mid-IR SCG extending from 2 μm to 10 μm with peak power > 5 kW at 4 μm in 6 cm long As_2Se_3 PCF [45].

A mid-IR pulsed laser operated at 4.5 μm based on praseodymium (Pr^{3+}) doped chalcogenide fiber has been considered for the formation of mid-IR SC [46]. A hyperbolic secant shaped pulse has been assumed with a temporal duration (T_{FWHM}) of 50 fs and peak power at 700 W for numerical simulation of SCG in the proposed TC PCF.

This paper is organized in five sections. Section 1 provides a brief introduction and overview of previous works on SCG in chalcogenide PCF. In Section 2, detailed description of method of analysis is given. Section 3 explains the designing of proposed TC PCF for all-normal, nearly zero flattened dispersion. Section 4 is devoted to the generation of ultra-broad band supercontinuum in proposed TC PCF. Finally, conclusions and applications of this work are summarized in Section 5.

2. Method of analysis

2.1. Linear characteristics of PCF structure

To simulate the effective index of fundamental mode propagating through proposed photonic crystal fiber, a full vectorial finite element method (FEM) based software 'COMSOL Multiphysics' has been employed. For calculating the wavelength dependent refractive index of material following Sellmeier equation has been used [41]

$$n(\lambda) = \sqrt{a + b/\lambda^2 + c/\lambda^4} \tag{1}$$

where a, b and c are coefficients. The values of coefficients are: $a=7.56$, $b=1.03\ \mu m^2$ and $c=0.12\ \mu m^4$ for As_2Se_3 based chalcogenide glass which we have used as a PCF material in this paper.

The group velocity dispersion plays an important role in SCG because it determines the extent to which different spectral components of an ultra-short pulse propagate at different phase velocities in the photonic crystal fiber. The group velocity dispersion $D(\lambda)$ is calculated from wavelength dependent effective indices of propagating mode by using the following formula

$$D(\lambda) = -\frac{\lambda}{c}\frac{d^2\mathrm{Re}(n_{eff})}{d\lambda^2} \tag{2}$$

where c is the velocity of light in free space, $\mathrm{Re}(n_{eff})$ is the real part of the effective index of mode. Both material and waveguide dispersion are included in the above equation as Sellmeier equation is taken into account while calculating n_{eff}.

The effective area of propagating mode in the PCF has been calculated using the following relation [1]

$$A_{eff} = \frac{\left(\iint_{-\infty}^{\infty} |E|^2 dx\, dy\right)^2}{\left(\iint_{-\infty}^{\infty} |E|^4 dx\, dy\right)} \tag{3}$$

2.2. Nonlinear characteristics of PCF structure

Nonlinearity in PCF is the most important parameter which must be studied more rigorously in order to get accurate results. The nonlinear coefficient γ, offered by PCF can be calculated by [1]

$$\gamma = \frac{2\pi n_2}{\lambda A_{eff}} \tag{4}$$

where, n_2 is the nonlinear refractive index of material (for As_2Se_3; $n_2 = 2.4\times10^{-17}\ m^2/W$ [47]), λ is the pump wavelength and A_{eff} is the effective area of fundamental mode. For broader supercontinuum generation (SCG) the nonlinear coefficient should be as high as possible. The value of γ can be enhanced by taking material with high nonlinear refractive index and/or by designing a PCF with smaller effective mode area.

To simulate SC, the following generalized nonlinear Schrodinger equation (GNLSE) has to be solved for output pulse envelope, $A(z, t)$ [1]

$$\frac{\partial A}{\partial z} + \frac{\alpha}{2}A - \left(\sum_{n\geq 2}\beta_n \frac{i^{n+1}}{n!}\frac{\partial^n A}{\partial t^n}\right) = i\gamma\left(1 + \frac{i}{\omega_o}\frac{\partial}{\partial t}\right)\left[A(z,t)\int_{-\infty}^{\infty} R(t')\ |A(z,t-t')|^2 dt' + i\Gamma_R(z,t)\right] \quad (5)$$

The left hand side of Eq. (5) deals with linear propagation effects while the right hand side of this deals with nonlinear effects of PCF structure. α represents the power loss in the PCF as the light travels through it. The typical value of simulated confinement loss is equal to 0.03 dB/mm at 4.5 μm wavelength. The propagation constant (β) at any frequency (ω), relative to pulse central frequency (ω_0), can be expanded as Taylor series expansion [3]

$$\beta(\omega) = \beta(\omega_0) + \beta_1(\omega_0)(\omega-\omega_0) + \frac{1}{2!}\beta_2(\omega_0)(\omega-\omega_0)^2 + \frac{1}{3!}\beta_2(\omega_0)(\omega-\omega_0)^3 + \ldots \quad (6)$$

where $\beta_n(\omega_0) = d^n\beta/d\omega^n$ first term in the right hand side of Eq. (6) gives the effective index of the propagating mode and the second and third terms are related to the group velocity and the group velocity dispersion (GVD) of the pulse respectively.

$R(t')$ is the nonlinear response function and takes account of the electronic and nuclear contributions and takes the form

$$R(t') = (1 - f_R)\delta(t' - t_e) + f_R\, h_R(t') \quad (7)$$

where, f_R is the fractional contribution of the Raman response to the total linear response. For As_2Se_3 chalcogenide glasses the fractional contribution $f_R = 0.115$ [47]. t_e is the instantaneous electronic contribution and $t_e = 1$ has been considered in the simulation. $h_R(t')$ is the Raman response function and contains information on the vibration of material molecules as light passes through the fiber.

The Raman response function $h_R(t')$ can be calculated by most common and approximate analytic form which is given by

$$h_R(t') = \frac{\tau_1^2 + \tau_2^2}{\tau_1\tau_2}\exp\left(-\frac{t'}{\tau_2}\right)\sin\left(\frac{t'}{\tau_1}\right) \quad (8)$$

where, Raman period $\tau_1 = 23.1$ fs and life time $\tau_2 = 195$ fs for As_2Se_3 based glasses [47].

The term Γ_R deals with the effect of spontaneous Raman noise. In our study, we consider the hyperbolic secant pulse which is expressed as

$$A(z=0,t) = \sqrt{P_0}\ \mathrm{sec}\, h\left(\frac{t}{t_o}\right) \quad (9)$$

where, t_0 is related to the pulse duration (i.e. full-width at half maximum (T_{FWHM})) as $t_0 = T_{FWHM}/1.7627$ and P_0 is the peak power of input pulse.

3. Design of proposed TC PCF

We present a new triangular-core photonic crystal fiber structure with four layers of air holes arranged in hexagonal pattern in As_2Se_3-based chalcogenide glass as shown in Fig. 1(a). Three air holes have been removed from the center to make triangular core of the PCF. The center to center distance of holes is taken as constant and represented by Λ. The diameter of air holes in first, third and fourth rings have been considered identical and defined by d_1, while the diameter of air holes in second ring is d_2, which is comparatively larger than d_1. To obtain the efficient SCG the structural parameters have been optimized for getting all-normal, near zero flat-top dispersion. Simulated electric field distribution of propagating mode in proposed TC PCF at 4.5 μm has been shown in Fig. 1(b).

In order to obtain efficient ultra-broad-band SC in proposed TC PCF, we have optimized the structural parameters (i.e. Λ, d_1 and d_2) for all-normal flat-top dispersion. For this purpose, initially we have simulated the effect of various values of pitch (Λ) on dispersion characteristic while keeping other parameters fixed (i.e. $d_1 = 420$ nm and $d_2 = 820$ nm) within the spectral range from 2.5 μm to 5.5 μm. This feature of structure has been shown in Fig. 2. It is to be noted that, at $\Lambda = 1$ μm the dispersion curve lies in both normal and anomalous dispersion regime and it start to shift towards normal dispersion regime on increasing the value of Λ. When $\Lambda = 1.2$ μm the dispersion curve lies in normal regime within the entire spectral range of 2.5–5.5 μm.

Now, influence of the hole diameter, d_1 (while keeping other parameters fixed; i.e. $\Lambda = 1.2$ μm and $d_2 = 820$ nm) on the dispersion characteristics of proposed structure has been illustrated in Fig. 3. It is clear from this figure that the dispersion characteristic does not change significantly on changing d_1. Therefore, it seems very difficult to get desire dispersion characteristic of structure using d_1. However, dispersion characteristic of structure can be tuned easily with air hole diameter d_2 in second ring of PCF structure. This feature of proposed structure has been illustrated in Fig. 4. The dispersion curve starts to shift toward the anomalous dispersion regime from normal dispersion regime on increasing d_2. It is to be noted that all-normal flat-top dispersion characteristic with dispersion value approximately − 2 ps/(nm km) within the spectral range from 4.4 μm to 4.8 μm can be achieved when $d_2 = 900$ nm. The above analysis and simulated results lead us to conclude that by careful choice of the structural parameter d_2 one can control and obtain the desired dispersion characteristic of

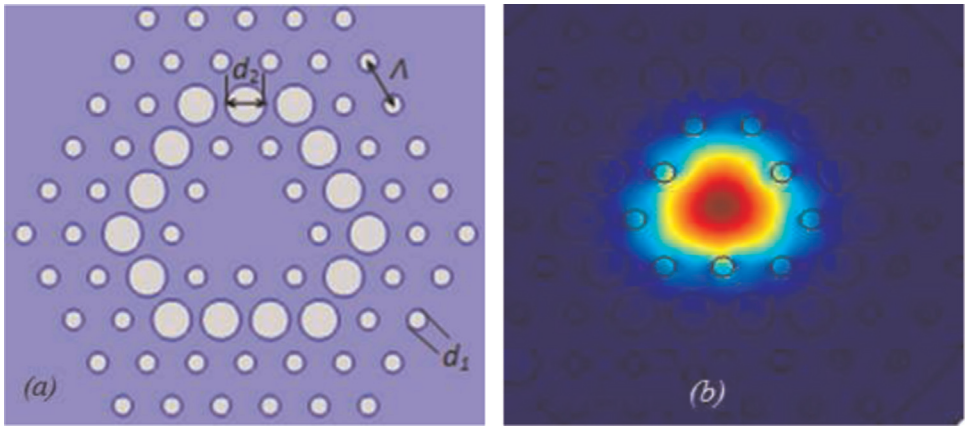

Fig. 1. (a) Transverse cross-section of proposed triangular-core PCF structure. (b) The electric field distribution of propagating mode at 4.5 μm.

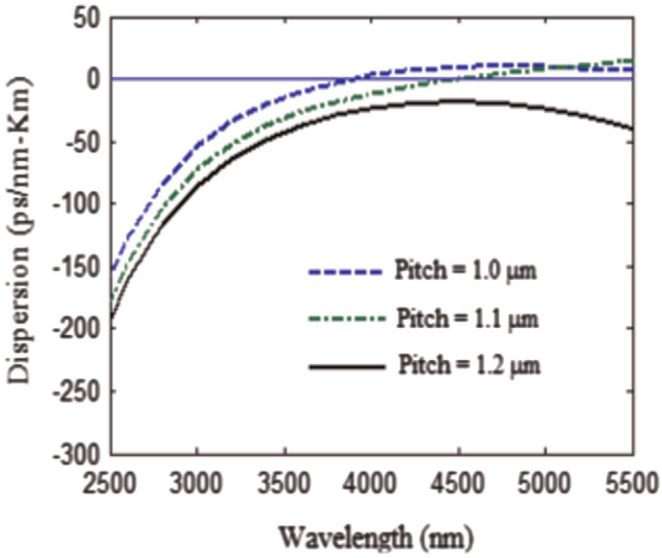

Fig. 2. Influence of the pitch (Λ) on dispersion characteristics of proposed structure while keeping other parameters fixed (i.e. d_1=420 nm and d_2=820 nm).

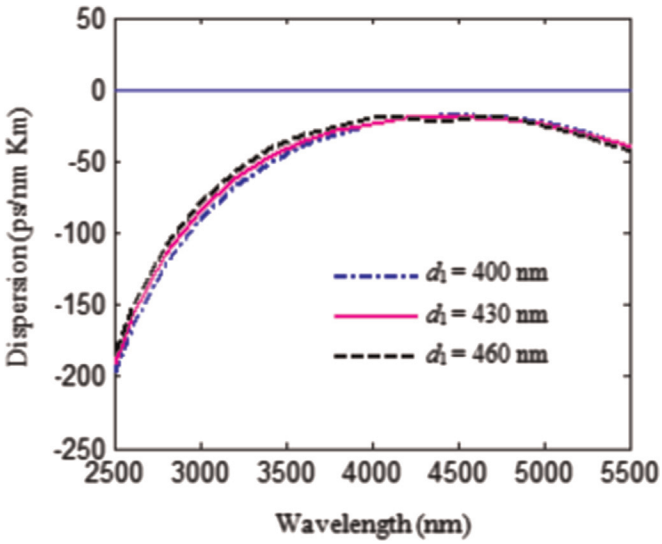

Fig. 3. Influence of the hole diameter (d_1) on dispersion characteristics of proposed structure while keeping other parameters fixed (i.e. Λ=1.2 μm and d_2=820 nm).

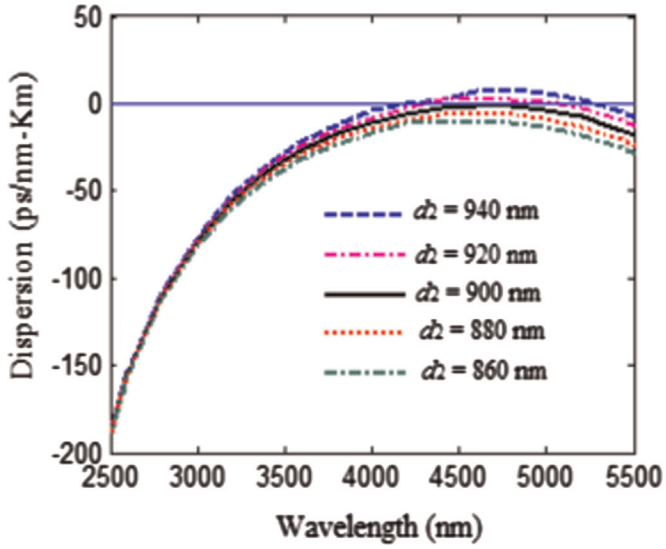

Fig. 4. Influence of hole diameter (d_2) on the dispersion characteristics of proposed structure while keeping other parameters fixed (i.e. Λ=1.2 μm and d_1=430 nm).

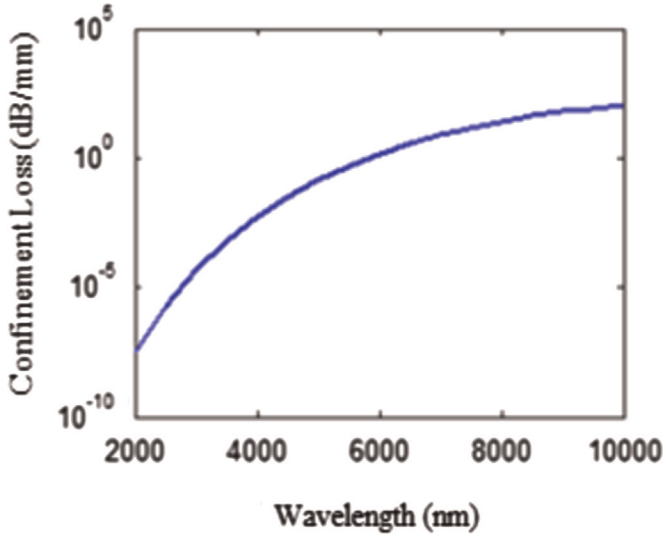

Fig. 5. The confinement loss of propagating mode of proposed TC PCF when Λ=1.2 μm, d_1=430 nm and d_2=900 nm.

proposed TC PCF.

The confinement loss of propagating mode in the spectral range of 2–10 μm is shown in Fig. 5. At pump wavelength, (i.e. 4.5 μm) the structure offers 0.03 dB/mm loss for propagating mode.

For optimized geometrical parameters (as shown in Table 1), the wavelength dependent effective mode area of propagating mode and corresponding nonlinear coefficient have been illustrated in Fig. 6. Simulated results show that the proposed TC PCF structure offers nonlinear coefficient (γ) as high as 5449 W^{-1} km^{-1} with effective mode area of 6.15 μm^2 at 4.5 μm input pulse wavelength.

From the manufacturing point of view our proposed structure can be fabricated by standard extrusion and stacking methods. For fabrication purposes it is also very important to investigate the tolerance of the proposed structure with respect to the various design parameters. After investigating the effect of small variations in the values of d_1, d_2 and Λ we have found that the magnitude of dispersion and the effective mode area of propagating mode are less sensitive to the structural parameters. As shown in Fig. 7(a and b), at 4.5 μm wavelength 1% deviations in d_1 changes the effective index value by ~0.03% and it also changes the effective mode area by ~0.56%. Similarly, 1% deviation in d_2 changes the effective index by ~0.01% and changes the effective mode area by 0.40% while, 1% deviation in Λ changes the effective index by 0.13% and changes the effective mode area by 2.31%.

Table 1
Geometrical parameters of proposed PCF.

Parameter name	Pitch	d_1	d_2
Parameter value	1.2 μm	430 nm	900 nm

4. Simulation of supercontinuum generation in proposed TC PCF

To simulate SCG in proposed PCF structure, we have to solve the generalized nonlinear Schrodinger Eq. (5) for pulse

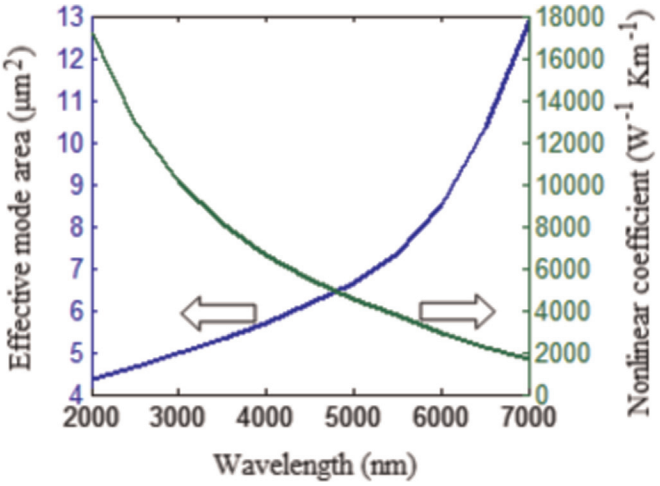

Fig. 6. The variation of effective mode area of propagating mode and corresponding nonlinear coefficient of proposed TC PCF with optimized parameters.

propagation in PCF structure. Eq. (5) represents GNLSE in time domain (TD). The drawback in implementation of this equation is that the time derivatives lead to numerical errors due to the discretization of the time window. When we write this equation in frequency domain, these derivatives vanish leaving only the discrete longitudinal step size as the source of numerical errors. In frequency domain Eq. (5) can be written as

$$\frac{\partial \tilde{A}}{\partial z} + \frac{\alpha}{2}\tilde{A} + i\tilde{A}\left(\beta(\Omega) - \beta_0 - \beta_1\Omega\right) = i\gamma\left(1 + \frac{\Omega}{\omega_0}\right) \times \left(F\left[\left(1 - f_R\right)A|A|^2 + f_R A F^{-1}[\tilde{h}_R F[|A|^2]]\right]\right) \quad (10)$$

where $\tilde{A}(z,\ \Omega)$ is the Fourier transform of $A(z,\ t)$, $\Omega = \omega - \omega_0$, F and F^{-1} stands for Fourier transform and inverse Fourier transform respectively, and $\tilde{h}_R = F(h_R(t))$. In above expression the arguments of both $\tilde{A}(z,\ \Omega)$ and $A(z,\ t)$ have been dropped. F and F^{-1} can be calculated numerically using the fast Fourier transform (FFT) and inverse fast Fourier transform (IFFT) respectively. For simulating SCG in proposed PCF structure we have solved Eq. (10) using interaction picture method in combination with conservation quantity error adaptive step-size algorithm [48].

In order to get flat, smooth and broad supercontinuum spectra we have selected pump wavelength at 4.5 μm in normal dispersion

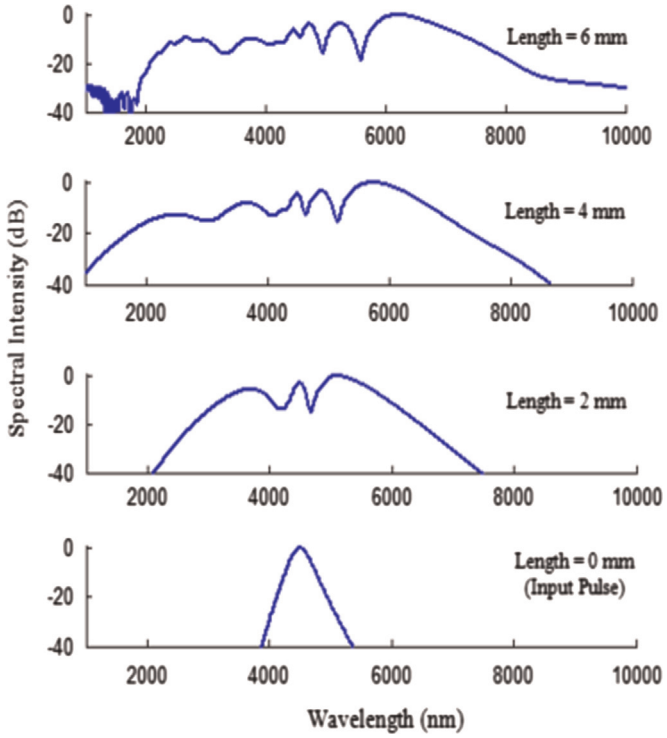

Fig. 8. Broadening of output spectra obtained at various lengths of TC PCF when peak power of incident pulse = 700 W and pulse duration (T_{FWHM}) = 50 fs.

regime with very small dispersion value of -2 ps/nm × Km for the proposed TC PCF. In our simulation, the peak power of incident pulse is 700 W with full-width at half maximum of 50 fs.

The calculated output spectra with different propagating length of PCF have been shown in Fig. 8. It has been observed that the spectral bandwidth starts to be broadened in only a few millimeter of propagation length. This feature of structure can be interpreted by comparing the nonlinear and dispersion length. The calculated values of nonlinear length ($L_{NL} = 1/\gamma P_0$) and dispersion length ($L_D = t_0^2/\beta_2$) for proposed TC PCF are 2.62×10^{-4} m and 6.49×10^{-2} m respectively at 4.5 μm pump wavelength. Since the nonlinear effect is stronger than dispersion effect, many of the new spectral components would be generated in a short length. After that the spectrum gets broadened due to the group velocity

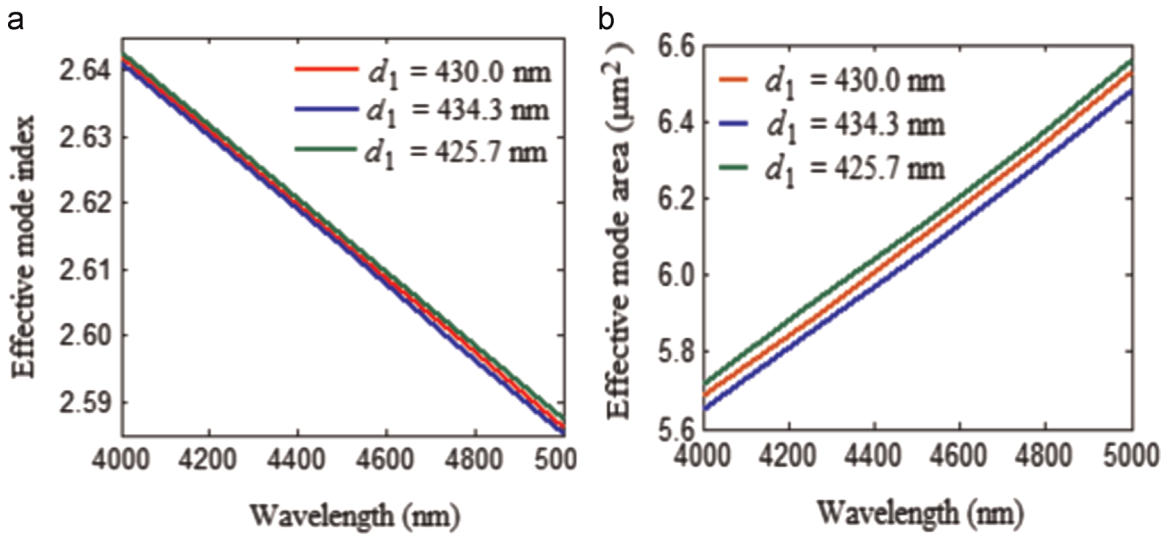

Fig. 7. Tolerance study of d_1: The effect on the effective mode index with ±1% deviation in d_1 (*a*); the effect on the effective mode area with ±1% deviation in d_1 (*b*).

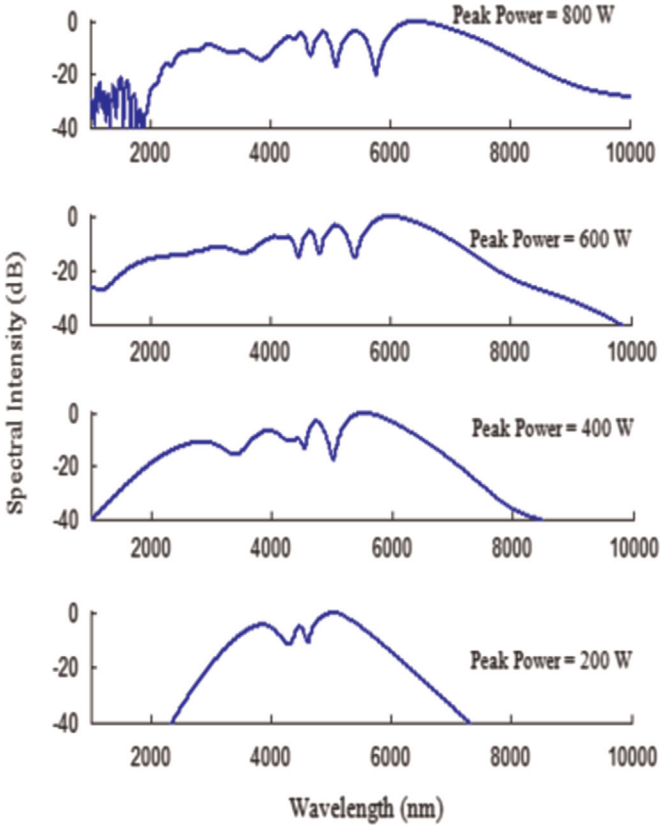

Fig. 9. Influence of input peak power on the broadening of output spectra with 50 fs incident pulse in 6 mm length of TC PCF.

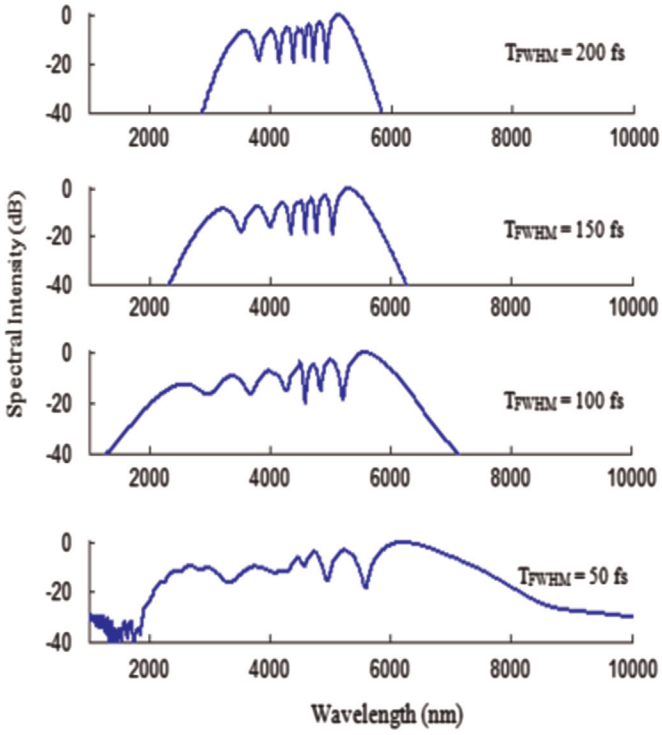

Fig. 10. Influence of full-width at half maximum (T_{FWHM}) of input pulse on the broadening of output spectra with 700 W peak power in 6 mm length of PCF.

dispersion (GVD) effect. It is to be noted that the output spectrum becomes constant in the 1.9–10 μm spectral range at the PCF length of 6 mm. In the initial phase of pulse propagation, SPM is responsible for symmetrical spectral broadening. As the PCF length is further extended, the Raman effect comes into account and extends the SC. Within 6 mm length of PCF an ultra-broadband SC extending from 1.9 μm to 10 μm at −30 dB level has been generated with 700 W peak power and 50 fs duration of input pulse. We have taken the power level −30 dB to compare our results with Ref. [45]. With further propagation the SC spectra does not change anymore.

Table 2
Optimized input pulse parameters.

Parameter name	Peak power	T_{FWHM}	Pulse shape
Parameter value	700 W	50 fs	hyperbolic secant

Fig. 9 illustrates the influence of input peak power on the bandwidth of output spectral intensity in 6 mm long PCF. The full-width at half maximum of the input pulse is fixed at 50 fs. Initially, the output spectra get broadened as the peak power of incident pulse increases. At high peak power, SPM effect dominants over dispersion effect. It has been observed that the maximum broadening in SC spectra is achieved at 700 W. Beyond this, no significant change in broadening has been observed, however, the flatness of SC spectra increases with further increase in peak power.

Finally, the influence of T_{FWHM} on the bandwidth of output spectral intensity in 6 mm long PCF has been shown in Fig. 10. The input peak power is fixed at 700 W. It is clear from figure that output spectra become narrow with increase in T_{FWHM}. This is due to SPM effect. It is to be noted that the short pulse is better to get broader SC spectra. The optimized values of input pulse are summarized in Table 2. It is to be mentioned that the coherence is also an important property of the SC spectra. However, in this paper, our focus is on the broad bandwidth of SC spectra using low pump power in a very small length of proposed TC PCF. Flatness and the coherence property is the subject of further investigation.

5. Conclusions

A new design of triangular core photonic crystal fiber with all-normal dispersion in As_2Se_3-based chalcogenide glass has been presented for ultra-broadband SCG. A flat-top dispersion curve with dispersion value approximately −2 ps/(nm × Km) in spectral range from 4.4 μm to 4.8 μm has been achieved. Proposed structure offers nonlinear coefficient as high as 5449 W^{-1} Km^{-1} at pump wavelength (i.e. 4.5 μm) with effective mode area of 6.15 μm^2. The influences of PCF length, input pulse peak power and full-width at half maximum (T_{FWHM}) on output spectral intensity have been investigated. Ultra-broadband SC spectra have been generated in a very small length of PCF with relatively low peak power of incident pulse. Simulated results indicate that the ultra-broadband SC extending from 1.9 μm to 10 μm at the −30 dB level can be generated in only 6 mm long As_2Se_3-based chalcogenide PCF with an input pulse peak power of 700 W in femtosecond regime. This new type of photonic crystal fiber can be a good candidate for generating efficient supercontinuum which is applicable for various nonlinear applications such as optical coherence tomography, pump-probe spectroscopy, metrology, nonlinear microscopy and frequency combs generation. Further, it is expected that the broadband range of the supercontinuum can be tuned and enhanced with new design of PCF.

Acknowledgments

The authors gratefully acknowledge the (*i*) initiatives and support towards establishment of the "TIFAC-Center of Relevance and Excellence" in Fiber Optics and Optical Communication at Delhi Technological University (Formerly Delhi College of Engineering) Delhi, through the "Mission REACH" program of Technology Vision-2020 of the Government of India and (*ii*). TUN-IND bilateral research project "Design, modeling and characterization of highly nonlinear fibers for all-optical high bit-rate network," funded by Ministry of Higher Education and Scientific Research of Republic of Tunisia and Department of Science and Technology, Govt. of India.

References

[1] G.P. Agrawal, Nonlinear Fiber Optics, 5th ed., Elsevier Academic Press, 2013.
[2] P. Russell, Photonic crystal fibers, Science 299 (2003) 358–362.
[3] J.M. Dudley, G. Genty, S. Coen, Supercontinuum generation in photonic crystal fiber, Rev. Mod. Phys. 78 (2006) 1135–1184.
[4] R.K. Sinha, S.K. Varshney, Dispersion properties in photonic crystal fibers, Microw. Opt. Tech. Lett. 37 (2003) 129–132.
[5] B. Dabas, R.K. Sinha, Dispersion characteristics of hexagonal and square lattice chalcogenide As_2Se_3 glass photonic crystal fiber, Opt. Commun. 283 (2010) 1331–1337.
[6] B. Dabas, R.K. Sinha, Design of highly birefringent chalcogenide glass PCF: a simplest design, Opt. Commun. 284 (2011) 1186–1191.
[7] T.S. Saini, A. Kumar, R.K. Sinha, Triangular-core large-mode-area photonic crystal fiber with low bending loss for high power applications, Appl. Opt. 53 (2014) 7246–7251.
[8] H. Ademgil, S. Haxha, Highly nonlinear birefringent photonic crystal fiber, Opt. Commun. 282 (2009) 2831–2835.
[9] S. Haxha, H. Ademgil, Novel design of photonic crystal fibers with low confinement losses, nearly zero ultraflatted chromatic dispersion, negative chromatic dispersion and improved effective mode area, Opt. Commun. 281 (2010) 278–286.
[10] S. Ghosh, R.K. Varshney, B.P. Pal, Generation of a low divergent supercontinuum for mid-IR high power delivery through a large mode area photonic bandgap fiber, Laser Phys. 23 (2013) 095105.
[11] D.J. Jones, S.A. Diddams, J.K. Ranka, A. Stentz, R.S. Windeler, J.L. Hall, S. T. Cundiff, Carrier-envelope phase control of femtosecond mode-locked lasers and direct optical frequency synthesis, Science 288 (2000) 635–639.
[12] B. Povazay, K. Bizheva, A. Unterhuber, B. Hermann, H. Sattmann, A.F. Fercher, W. Drexler, A. Apolonski, W.J. Wadsworth, J.C. Knight, P.S. Russell, M. Vetterlein, E. Scherzer, Submicrometer axial resolution optical coherence tomography, Opt. Lett. 27 (2002) 1800–1802.
[13] H.N. PaulseN, K.M. Hilligse, J. Thogersen, S.R. Keiding, J.J. Larsen, Coherent anti-Stokes Raman scattering microscopy with a photonic crystal fiber based light source, Opt. Lett. 28 (2003) 1123–1125.
[14] S. Sanders, Wavelength-agile fiber laser using group-velocity dispersion of pulsed super-continua and application to broadband absorption spectroscopy, Appl. Phys. B: Laser and Opt. 75 (2002) 799–802.
[15] S. Dupont, C. Petersen, J. Thogersen, C. Agger, O. Bang, S.R. Keiding, IR microscopy utilizing intense supercontinuum light source, Opt. Express 20 (2012) 4887–4892.
[16] A. Schliesser, N. Picque, T.W. Hansch, Mid-infrared frequency combs, Nat. Photon 6 (2012) 440–449.
[17] T. Morioka, K. Mori, S. Kawanishi, M. Saruwatari, Multi-WDM-channel GBit/s pulse generation from a single laser source utilizing LD-pumped supercontinuum in optical fibers, IEEE Photon, Technol. Lett 6 (1994) 365–368.
[18] R.R. Alfano, S.L. Shapiro, Emission in the region 4000 to 7000 < FigureObject > via four-photon coupling in glass, Phys. Rev. Lett. 24 (1970) 584.
[19] J.K. Ranka, R.S. Windeler, A.J. Stentz, Visible continuum generation in air silica microstructured optical fibers with anomalous dispersion at 800 nm, Opt. Lett. 25 (2000) 25–27.
[20] G. Genty, S. Coen, J.M. Dudley, Fiber supercontinuum sources, J. Opt. Soc. Am. B 24 (2007) 1771–1785.
[21] J.M. Dudley, J.R. Taylor, Supercontinuum Generation in Optical Fibers, Cambridge University Press, 2010.
[22] A. Barh, S. Ghosh, G.P. Agrawal, R.K. Varshney, I.D. Aggarwal, B.P. Pal, Design of an efficient mid-IR light source using chalcogenide holey fibers: a numerical study, J. Opt. 15 (2013) 035205.
[23] M. El-Amraoui, G. Gadret, J.C. Jules, J. Fatome, C. Fortier, J. Troles, Microstructured chalcogenide optical fibers from As_2S_3 glass: towards new IR broadband sources, Opt. Express 18 (2010) 26655–26665.
[24] L. Liu, G. Qin, Q. Tian, D. Zhao, W. Qin, Numerical investigation of mid-infrared supercontinuum generation up to 5 μm in single mode fluoride fiber, Opt. Express 19 (2011) 10041–10048.
[25] V. Shiryaev, M. Churbanov, Trends and prospects for development of chalcogenide fibers for mid-infrared transmission, J. Non-Cryst. Solids 377 (2013) 225–230.
[26] R.E. Slusher, G. Lenz, J. Hodelin, J. Sanghera, L.B. Shaw, I.D. Aggarwal, Large Raman gain and nonlinear phase shift in high-purity As_2Se_3 chalcogenide fibers, J. Opt. Soc. Am. B 21 (2004) 1146–1155.
[27] L.B. Shaw, V.Q. Nguyen, J.S. Sanghera, I.D. Aggarwal, P.A. Thielen, and F.H. Kung, IR supercontinuum generation in As–Se photonic crystal fiber, in: Proceedings of Advanced Solid State Photonics, paper TuC5, 2005.
[28] D.-I. Yeom, E.C. Magi, M.R.E. Lamont, M.A.F. Roelens, L. Fu, B.J. Eggleton, Low-threshold supercontinuum generation in highly nonlinear chalcogenide nanowires, Opt. Lett. 33 (7) (2008) 660–662.
[29] D.D. Hudson, S.A. Dekker, E.C. Magi, A.C. Judge, S.D. Jackson, E. Li, J.S. Sanghera, L.B. Shaw, I.D. Aggarwal, B.J. Eggleton, Octave spanning supercontinuum in an As_2S_3taper using ultralow pump pulse energy, Opt. Lett. 36 (7) (2011) 1122–1124.
[30] D.D. Hudson, E.C. Magi, A.C. Judge, S.A. Dekker, B.J. Eggleton, Highly nonlinear chalcogenide glass micro/nanofiber devices: design, theory, and octave-panning spectral generation, Opt. Commun. 285 (23) (2012) 4660–4669.
[31] M.R. Lamont, B. Luther-Davies, D. Choi, S. Madden, B.J. Eggleton, Supercontinuum generation in dispersion engineered highly nonlinear ($\gamma = 10$/W/m) As_2S_3 chalcogenide planar waveguide, Opt. Express. 16 (19) (2008) 14938–14944.
[32] J. Hu, C.R. Menyuk, L.B. Shaw, J.S. Sanghera, I.D. Aggarwal, Maximizing the bandwidth of supercontinuum generation in As_2Se_3 chalcogenide fibers, Opt. Express 18 (2010) 6722–6739.
[33] C. Agger, C. Petersen, S. Dupont, H. Steffensen, J.K. Lyngso, C.L. Thomsen, J. Thogersen, S.R. Keiding, O. Bang, Supercontinuum generation in ZBLAN fibers – detailed comparison between measurement and simulation, J. Opt. Soc. Am. B 29 (2012) 635–645.
[34] I. Kubat, C.S. Agger, P.M. Moselund, O. Bang, Mid-infrared supercontinuum generation to 4.5 μm in uniform and tapered ZBLAN step-index fibers by direct pumping at 1064 or 1550 nm, J. Opt. Soc. Am. B 30 (2013) 2743–2757.
[35] I. Kubat, C.R. Petersen, U.V. Moller, A. Seddon, T. Benson, L. Brilland, D. Mechin, P.M. Moselund, O. Bang, Thulium pumped mid-infrared 0.9–9 μm supercontinuum generation in concatenated fluoride and chalcogenide glass fibers, Opt. Express 22 (2014) 3959–3969.
[36] D.D. Hudson, M. Baudisch, D. Werdehausen, B.J. Eggleton, J. Biegert, 1.9 octave supercontinuum generation in a As_2S_3 step-index fiber driven by mid-IR OPCPA, Opt. Lett. 39 (19) (2014) 5752–5755.
[37] I. Kubat, C.S. Agger, U. Moller, A.B. Seddon, Z. Tang, S. Sujecki, T.M. Benson, D. Furniss, S. Lamrini, K. Scholle, P. Fuhrberg, B. Napier, M. Farries, J. Ward, P. M. Moselund, O. Bang, Mid-infrared supercontinuum generation to 12.5μm in large NA chalcogenide step-index fibres pumped at 4.5 μm, Opt. Express 22 (2014) 19169–19182.
[38] Y. Takushima, F. Futami, K. Kikuchi, Generation of over 140-nm-wide supercontinuum from a normal dispersion fiber by using a mode-locked semiconductor-laser source, IEEE Photon, Technol. Lett 10 (1998) 1560–1562.
[39] A. Hartung, M. Heidt, H. Bartelt, Design of all-normal dispersion microstructured optical fibers for pulse-preserving supercontinuum generation, Opt. Express 19 (2011) 7742–7749.
[40] A.M. Heidt, Pulse preserving flat-top supercontinuum generation in all-normal dispersion photonic crystal fibers, J. Opt. Soc. Am. B 27 (2010) 550–559.
[41] A. Baili, R. Cherif, M. Zghal, New design of As2Se3-based chalcogenide photonic crystal fiber for ultra-broadband, coherent, mid-IR supercontinuum generation, Proc. SPIE, 8564–856409Proc. SPIE, 8564–856409.
[42] P. Yan, R. Dong, G. Zhang, H. Li, S. Ruan, H. Wei, J. Luo, Numerical simulation on the coherent time-critical 2–5 μm supercontinuum generation in an As_2S_3 microstructured optical fiber with all-normal flat-top dispersion profile, Opt. Commun. 293 (2013) 133–138.
[43] A. Baili, R. Cherif, A. Heidt, M. Zghal, Maximizing the bandwidth of coherent, mid-IR supercontinuum using highly nonlinear aperiodic nanofibers, J. Modern Optics 61 (2014) 650–661.
[44] M. Klimczak, B. Siwicki, P. Skibinski, D. Pysz, R. Stepien, A. Heidt, C. Radzewicz, R. Buczynski, Coherent supercontinuum generation up to 2.3 μm in all-normal soft-glass photonic crystal fibers with flat all-normal dispersion, Opt. Express 22 (2014) 18824–18832.
[45] W. Yuan, 2–10 μm mid-infrared supercontinuum generation in As_2Se_3 photonic crystal fiber, Laser Phys. Lett. 10 (2013) 095107.
[46] L. Sojka, Z. Tang, D. Furniss, H. Sakr, A. Oladeji, E. Beres-Pawlik, H. Dantanarayana, E. Faber, A.B. Seddon, T.M. Benson, S. Sujecki, Broadband, mid-infrared emission from Pr^{3+} doped GeAsGaSe chalcogenide fiber optically clad, Opt. Mater. 36 (2014) 1076–1082.
[47] B. Ung, M. Skorobogatiy, Chalcogenide microporous fibers for linear and nonlinear applications in the mid-infrared, Opt. Exp. 18 (2010) 8647–8659.
[48] A.A. Rieznik, A.M. Heidt, P.G. Konig, V.A. Bettachini, D.F. Grosz, Optimum integration procedures for supercontinuum simulation, J. IEEE Photon. 4 (2012) 552–560.

Bublz! : Playing with Bubbles to Develop Mathematical Thinking

Dhruv Chand
National Institute of Technology Karnataka
Surathkal, Karnataka, India
dhruvchand@live.com

Mudit Sinha
Vellore Institute of Technology
VIT University
Chennai, Tamil Nadu, India
mudit.sinha2012@vit.ac.in

Karthik Gopalakrishnan
Indian Institute of Technology Patna
Patna, Bihar, India
karthik.cs11@iitp.ac.in

Shreya Sriram
Delhi Technological University
New Delhi, India
shreyasriram29@gmail.com

Nisha K K
National Institute of Technology Karnataka
Surathkal, Karnataka, India
nishakk94@gmail.com

Figure 1: Bublz! Start Screen

Author names are arranged in alphabetical order by last name. Copyright is held by the authors.

Abstract
We encounter mathematical problems in various forms in our lives, thus making mathematical thinking an important human ability [6]. Of these problems, optimization problems are an important subset: Wall Street traders often have to take instantaneous, strategic decisions to buy and sell shares, with the goal of maximizing their profits at the end of a day's trade. Continuous research on game-based learning and its value [2] [3] led us to ask: can we develop and improve the ability of mathematical thinking in children by guising an optimization problem as a game? In this paper, we present Bublz!, a simple, click-driven game we developed as a first step towards answering our question.

Author Keywords
Game Design; Mathematics; Reasoning; Mathematical Thinking; Strategic Thinking;

ACM Classification Keywords
K.3.1;

Introduction
A complete understanding of mathematics not only includes knowledge of mathematical concepts and principles, but also the capacity to engage in mathematical thinking: observing patterns, examining constraints, making conjectures and inferences, and so

on [5]. Mathematics is a dynamic process of "gathering, discovering and creating knowledge in the course of some activity having a purpose" [4]. Such activities or tasks typically have more than one solution strategy and involve decision-making and interpreting the reasonableness of possible actions [7].

Bublz! is a single-player game in which players are given a task of this nature in each game level. The players need to do simple arithmetic and effectively reason with numbers, which are depicted using bubbles, in order to complete the task. The only mathematical prerequisite to play the game is the ability to do addition and subtraction, which are depicted through the creation and removal/popping of bubbles respectively. We developed a fully-functioning digital prototype for the task with six levels of play using Unity 3D [8] in the Javascript and C# programming languages. The game is primarily intended to be played on a Windows computer, but it can very easily be modified and built to work on portable devices like phones and tablets as well.

Figure 2: Instructions Screen

Figure 3: Main game screen at the start of a level, showing one bubble to start making moves on

Game Play

For each of the six levels in the game, a unique triplet of positive numbers (L, D, R) is associated with the three common types of clicks done on a mouse: single left-click, double left-click and single right-click.

When a level starts, one bubble is displayed on the screen (Figure 3). A positive target number T randomly chosen from the integers between 2 and 70, both inclusive, and the triplet associated with the three types of clicks for the level, are also displayed on the screen. The player is given an initial score of 1000.

- When the player does a single left-click on a bubble, L new bubbles are created.
- When the player does a double left-click on a bubble, D new bubbles are created.
- When the player does a single right-click on a bubble, R bubbles are removed or "popped", including the bubble on which the click was done.

The player's task is to obtain T bubbles on the screen using a combination of the three types of clicks, which are the possible types of moves. To obtain the highest possible score of 1000, the player should do it in the least number of moves in which T bubbles can be obtained on the screen. With each move made beyond the least number of moves, the player's score reduces by 10. The player loses if the score becomes 0.

Feedback on performance (Figure 4) is provided to players upon completing a level to facilitate learning [1]: the number of moves in which the player obtained T bubbles, and the minimum number of moves in which the player could have obtained it, are displayed on the screen. The player can retry the same target, and also repeat the level with a different target before deciding to proceed to the next level.

Game Viewed as an Optimization Problem

The task for a player in each level is to minimize the total number of moves made in order to maximize the score – an optimization problem. Let (L, D, R) be the triplet for a given level. Let T be the displayed target. Let the number of single left-clicks, double left-clicks and single right-clicks done to create T bubbles be x, y and z respectively. In order to obtain the highest score in a given level, the total number of moves must be minimized, hence the formulation of the optimization problem is:

Minimize $N = x + y + z$, such that

$1 + Lx + Dy - Rz = T$

x, y, z are non-negative integers

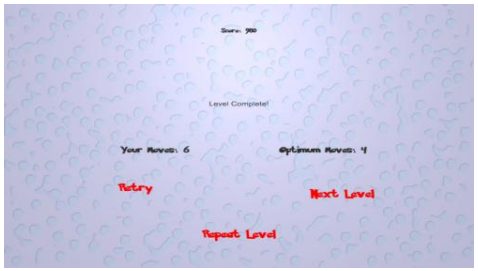

Figure 4: Score screen after finishing a level, showing the score, number of moves made, optimal number of moves, and various game options

Figure 5: Invalid move screen is displayed when an attempted move would cause the number of bubbles to go outside the range 1-150

Game Design

For each level, the triplet values (*L*, *D*, *R*) are chosen such that any positive number can be generated using a linear combination of *L*, *D* and –*R*. For example, (3, 4, 1) is a valid triplet because any positive number can be generated using a linear combination of 3, 4 and -1. This ensures that there is always at least one sequence of moves to generate *T* bubbles.

Intuition suggests more bubbles should be generated on doing a double left-click since the effort put in is twice the effort put in to do a single left-click. Hence, with the aim of making the game easy to grasp, *L* and *D* are chosen such that $D > L$.

Triplet values of higher magnitudes are chosen for higher levels to make them more difficult. For example, if the current level has (3, 4, 1) as the click triplet, the next level could have (5, 7, 4) as the click triplet. A drawback of this method is that it does not ensure higher levels would be more difficult for all possible target values. Since each level in the current prototype involves playing just one random target, some players might easily solve all levels while others struggle to progress. This can be reasonably resolved by dividing each level into several sub-levels having different targets, and allowing advancement to the next level only if the player completes all sub-levels of the current level.

To ensure that there will always be at least one bubble on the screen that can be clicked, the game prevents the player from doing a single right-click move when the number of bubbles on the screen is lesser than or equal to the value *R*. This is done by displaying an appropriate message (Figure 5). To ensure that the player doesn't unnecessarily overload the screen with bubbles by doing single/double left-clicks all the time, the game also prevents the player from making a single/double left-click move if making that move would result in the total number of bubbles on the screen exceeding a threshold value of 150. This additionally serves as a hint to the player that the target can be reached without ever exceeding 150 bubbles.

Evaluation

Our primary goal after developing the game was to evaluate our design choices through a play session with school students and get their feedback on the game. Apart from feedback to improve their gaming experience, we wanted to find out whether students would see value in the game, as a precursor to a full-fledged study on whether the game helps develop and improve mathematical thinking in players and if yes, to what degree. Hence, we organized an informal play session for about 10 middle school students from a local school in Bangalore, India, and observed while they played. The play session involved playing three successive levels of the game.

We observed several interesting things. As the play session progressed, most students who got large targets almost instantly did a double left-click as their first move. This suggests that in the course of playing the game, the students developed a mental representation associating the number of left-clicks with the number of bubbles they could generate, a positive feedback to our design decision of generating more bubbles for a double left-click than for a single left-click. The students also generally took greater time to complete higher levels and additionally reported during post-play feedback interviews that they found higher levels challenging, a positive feedback to our decision to use triplets of higher magnitudes in higher levels. No student overloaded the screen with bubbles, making the upper cap of 150 on the number of bubbles seem unnecessary. We observed the time students spent playing the game and determined their intention

to replay the game through post-play interviews. According to both factors, students showed clear motivation to play the game. They reported liking and enjoying the game. Some students wanted the game to be more visually appealing while others wanted more levels to play, which we took into account to improve the game. When asked about the game's utility to them, most students felt the game would make them "better at mathematics".

Future Work

We plan to undertake a formal study of the impact that regular play of the game has on mathematical thinking in players. One way is to study the correlation that known measures of mathematical thinking have with an edit-distance like metric that tells how close a given player's performance is at any point of time to that of an ideal player using in-game performance data. An even more interesting study would be to see whether regularly playing the game leads to improved performance on optimization problems encountered in real-life.

Acknowledgements

We thank Amy Ogan, Erin Walker and Erik Harpstead for their guidance and assistance in developing Bublz!. We thank MS Ramaiah Institute of Technology, Bangalore, India, for enabling us to play-test our game with children. We also thank Carolyn P. Rosé and Carnegie Mellon's Internship Program in Technology Supported Education, which brought us together for 15 days to conceptualize and develop the prototype for this game.

References

[1] Anderson, J. R., Corbett, A. T., Koedinger, K. R., & Pelletier, R. (1995). Cognitive Tutors: Lessons Learned. *The Journal of the Learning Sciences*, 4(2), 167-207.

[2] De Freitas, S. (2006). Learning in Immersive Worlds: A Review of Game-Based Learning. *Joint Information Systems Committee*.

[3] Kirriemuir, J., McFarlane, A. (2003). Use of Computer and Video Games in the Classroom. *DIGRA Conf*.

[4] Romberg, T. A. (1992). Perspectives on Scholarship and Research Methods. *Handbook of research on mathematics teaching and learning* (pp. 49-64).

[5] Schoenfeld, A. H. (1992). Learning to Think Mathematically: Problem Solving, Metacognition and Sense Making in Mathematics. *Handbook of research on mathematics teaching and learning* (pp. 334-371).

[6] Stacey, K. (2006). What is Mathematical Thinking and Why is it Important? *Progress report of the APEC project: Collaborative Studies on Innovations for Teaching and Learning Mathematics in Different Cultures (II)–Lesson Study focusing on Mathematical Thinking*.

[7] Stein, M. K., Grover, B. W., Henningsen, M. (1996). Building Student Capacity for Mathematical Thinking and Reasoning: An Analysis of Mathematical Tasks used in Reform Classrooms. *American Educational Research Journal*.

[8] The Unity Game Engine, http://unity3d.com/

Syst Synth Biol
DOI 10.1007/s11693-015-9164-z

RESEARCH ARTICLE

CARDIO-PRED: an *in silico* tool for predicting cardiovascular-disorder associated proteins

Prerna Jain[1] · Nitin Thukral[1] · Lokesh Kumar Gahlot[1] · Yasha Hasija[1]

Received: 4 March 2015 / Accepted: 6 March 2015
© Springer Science+Business Media Dordrecht 2015

Abstract Interactions between proteins largely govern cellular processes and this has led to numerous efforts culminating in enormous information related to the proteins, their interactions and the function which is determined by their interactions. The main concern of the present study is to present interface analysis of cardiovascular-disorder (CVD) related proteins to shed lights on details of interactions and to emphasize the importance of using structures in network studies. This study combines the network-centred approach with three dimensional studies to comprehend the fundamentals of biology. Interface properties were used as descriptors to classify the CVD associated proteins and non-CVD associated proteins. Machine learning algorithm was used to generate a classifier based on the training set which was then used to predict potential CVD related proteins from a set of polymorphic proteins which are not known to be involved in any disease. Among several classifying algorithms applied to generate models, best performance was achieved using Random Forest with an accuracy of 69.5 %. The tool named CARDIO-PRED, based on the prediction model is present at http://www.genomeinformatics.dce.edu/CARDIO-PRED/. The predicted CVD related proteins may not be the causing factor of particular disease but can be involved in pathways and reactions yet unknown to us thus permitting a more rational analysis of disease mechanism. Study of their interactions with other proteins can significantly improve our understanding of the molecular mechanism of diseases.

Keywords Interface properties · Cardiovascular-disorder · Machine learning · 3-Dimensional structure · Network analysis

Introduction

The non-modifiable major risk factors associated with CVD include advancing age, genetic predisposition, gender and ethnicity, with aging being the major risk factor. Despite of numerous studies in the cardiovascular field many unanswered questions remain as to how the genetic pathways that regulate aging in model organisms influence cardiovascular aging. A number of longevity genes and their related pathways identified in model organisms have been assessed for their role in CVD (North and Sinclair 2012). The association between genes and diseases has been well studied in the past and has been documented in various databases such as Online Mendelian Inheritance in Man (OMIM, http://omim.org/), Genetic Association Database, Disease ontology and many more. These databases not only provide genes associated with the disorders but also, insight about the common genes or essential genes which are involved in pathways and processes of multiple disorders. The human disease gene network has already established link between the genetic disorders with the genes. An important conclusion inferred from this network is that genes associated with similar disorders show higher likelihood of physical interaction

Electronic supplementary material The online version of this article (doi:10.1007/s11693-015-9164-z) contains supplementary material, which is available to authorized users.

✉ Yasha Hasija
yashahasija@gmail.com

[1] Department of Biotechnology, Delhi Technological University, Shahbad Daulatpur, Main Bawana Road, Delhi 110042, India

Published online: 14 March 2015

between their products, thus forming a hub of essential genes and their products (Goh et al. 2007).

Documentation of genes with the associated disease is not enough to understand the biological details of pathogenesis and disease progression. It is important to identify various molecules and mechanism triggering, participating and controlling the biological process. This understanding of molecular mechanism is a complex process and not much is known about the mechanism (Gonzalez and Kann 2012). Now with the tremendous increase in human interaction data, it is important to understand how any biological function is exerted over the body and this can only be made possible by the inclusion of structural details in the networks.

Undoubtedly, sequence based annotation is important in unravelling the encoded information but the finer details of the molecular mechanism within the cell is possible only with the structural information (Marini and Brandi 2010). Protein structures provide a higher resolution of information and a more sensitive approach for detecting similarities among proteins by including details about structures of the interacting proteins in the network, protein hubs and protein interfaces. Structural profile of the proteins provides the opportunities in understanding the cellular functioning in terms of structural scaffolds which facilitate the underlying molecular recognition events. Moreover, a protein's structure is more conserved than its amino acid sequence (Choura and Rebaï 2011).

Protein–protein interactions (PPI) network is a way of representing how two or more proteins interact with each other in a cell, and biological processes, are essentially interactions between multiple proteins (Zhang and Ouellette 2011) with PPI networks controlling the flow of information both within and between the cells. Network representation where proteins are nodes and interactions are edges is useful indicator of biological process and protein function (Choura and Rebaï 2011). It is well known that proteins are the main agents of biological function based on their interactions with other proteins and to other biomolecules such as DNA and RNA, mediating metabolic and signalling pathways and cellular processes. Protein interaction do not necessarily mean the physical association of proteins but can be metabolic interactions where proteins are involved in the same pathway or genetic interactions displaying co-expressed and co-regulated proteins (Gonzalez and Kann 2012). Any protein rarely acts alone but as mentioned above interacts with other protein to carry out a specific function. This pair of interacting protein forms a protein complex. The protein fragments within the complex that actually comes together and interact forms a special region called protein interface (Aung 2006). Thus, protein interaction networks are useful resources to gain knowledge about the evolution of proteins and about the different systems in which they are involved. Alteration in this network can potentially lead to various disorders because disorders are often caused by alteration in the binding sites or allosteric changes in the protein. For example, mutation in the zinc finger domain present in the oncoprotein MDM2 can disrupt the interaction of MDM2 with L5 AND L1 (ribosomal proteins) that mediates p53 degradation and leads to cancer (Zhang and Ouellette 2011). Moreover, in protein–protein network, most of the proteins have few interactions whereas some proteins may have multiple interactions, these protein are central to the stability and normal functioning of the proteins in the network for example p53, p21, p27, BRCA1, ubiquitin, calmodulin are extensively involved in different forms of cancer, and the product of these genes forms a hub. Deletion of these hub proteins, is lethal to the organism, hence it can be inferred that these proteins are encoded by essential genes and are important targets for molecular and structural studies (Choura and Rebaï 2011). In some cases, during the binding process, interactions between two proteins might involve order–disorder transitions in partially disordered regions of the interacting proteins. These unstructured or disordered regions have been found to be involved in many disease mechanisms. For instance, the cancer suppressor BRCA1 has been shown to contain intrinsically disordered regions through which it binds to several proteins (Kann 2007). Other than the interference in protein–protein interaction network, several diseases are caused due to disruption in protein-DNA interaction, protein folding mechanism, protein-RNA disruption, can enable pathogen host protein interaction or can lead to new undesired protein interactions (Gonzalez and Kann 2012).

Protein interactions are mediated by specific recognition of distinct binding regions on the surface of interacting protein. Such recognition should be of sufficient affinity to effectively bind fragments of proteins, which is decided by specificities such as interfaces. Thus, interface properties and the topology of the protein involved play an important role in deciphering their function in the network. Various studies have been carried to integrate PPI network with the structural properties. A significant work in this regard has been done in the field of cancer biology. The cancer genes were mapped onto human PPI network and the network was studied with respect to structural features such as interface properties and study showed successful results in classifying cancer and non-cancer proteins (Kar et al. 2009). A novel integrated approach was proposed named CAERUS, for identification of gene signatures to predict cancer outcomes based on domain interaction network in human proteome (Zhang and Ouellette 2011). Further, a method was developed to find sub network-based signatures by incorporating PPI networks and gene expression profiles to classify metastatic and non-metastatic tumors

(Chuang et al. 2007). Studies have shown that a molecular mechanism leading to diseases is dependent on interlinked proteins and networks, but we are far from unravelling the difference in molecular interactions in healthy and diseased organism. Mechanism of genetic malfunctioning, that leads to one or several diseases can be understood when the molecular level of the protein interactions are known. Understanding the interactions and hence binding between proteins is critical for the rational design of new therapeutic agents targeted to disrupt the interactions that cause disorders (Gonzalez and Kann 2012).

PPIs not only identify disease-associated interacting proteins but also the potential disease-associated gene candidates (genes coding for interacting proteins are putative disease causing genes). This theory has been used in the present work where all the protein associated with CVD have been retrieved and a classifier using machine learning algorithms is used to identify potential proteins which are associated with CVDs. This classifier is based on the interface properties of the interacting complexes, to differentiate CVD related proteins from non-CVD associated proteins.

Methods

The detailed protocol for the study has been mentioned below and is depicted as a flow chart in Fig. 1.

Building datasets

OMIM (OMIM, http://omim.org/) Morbid Map was used to obtain training and test sample. The training sample: consisted of two subsets; one set consisting of all the proteins associated with the cardiovascular disorders and the other set consisting of all the protein associated with diseases other than CVDs. There are a total of 124 diseases in the class of cardiovascular disorders. For each disease, concerned proteins were listed. Test sample lists polymorphic proteins which are not known to be involved in any disease. Proteins were retrieved from humsavar.txt–UniProt. It is text file describing human polymorphism and disease mutation and contains disease variants, polymorphisms and unclassified variants. In the present study, we used protein variants under polymorphism as test set (Magrane 2011).

Retrieval of the interacting proteins

Wang et al. found high quality binary PPI along with the atomic resolution interface. They combined reliable literature-curated binary interactions and well verified yeast two-hybrid interactions to produce human protein interaction network (Wang et al. 2012). Further, they structurally resolved the interfaces of these interactions using iPfam and 3did utilizing homology modelling approaches. This resulted in a human structural interaction network (hSIN). This information is stored in the database with the gene id and Pfam id. hSIN was used to determine the structurally relevant interactions to the proteins involved in the cardiovascular interactions. Gene ids for the disease associated proteins were retrieved from NCBI, and the interacting partners with reliable structure were obtained from hSIN.

Structural interaction network

Once the structurally interacting partners have been obtained, a structure interaction network was formed by using Interactome3D. It is a web service for the structural annotation of protein–protein interaction networks (Mosca et al. 2013). PDB codes with the interacting chains between proteins were retrieved.

Interface property analysis

For interface analysis, 2P2I inspector (a protein–protein interface analysis tool) was used that invokes VMD, NACCESS and SURFNET. It is a complete tool that computes the interaction properties from 3D structure of interacting complexes. The various descriptors provided by this tool includes accessible surface area (ASA), Gap Volume, percentage charged residues, secondary structure contribution, number of hydrogen bonds, number of salt bridges and number of disulphide bonds. All these parameters are important in determining the specificity and the strength of the interface. Input can be a PDB code or the PDB file along with the chains involved in the complex (Basse et al. 2013).

Balancing and building the random training dataset

Before running Weka (Hall et al. 2009), Cygwin tool was used, which is a popular GNU development tools for Microsoft Windows. With Cygwin, it is possible to easily port many Unix programs without the need for extensive changes to the source code. With Cygwin, a series of random files were created by combining the positive and negative data set. These files were then used in Weka for classification and finding the prediction probability of test or unknown dataset.

Classification analysis: algorithm and analysis

Comparison between the proteins involved in CVDs and those which are not known to be involved in these diseases

were made using interface features which describe the protein complexes. By using machine learning algorithm, an automatic classifier capable of identifying genes more likely to be involved in CVDs based on the interfacial patterns was made. Different algorithms were tested and parameters such as true positive, true negative, false positive, false negative, precision, recall and accuracy were used to determine the best algorithm. Random forest with iteration 30 was used to generate the model for prediction. Tens runs of 10-fold cross validation were performed on the classifier algorithm used. The model generated was evaluated and used to predict the likelihood of polymorphic proteins associated with CVDs.

Development of user interface

For the prediction of involvement of unknown proteins in CAD, user-friendly web interfaces was developed. XHTML and CSS was used for creating presentation layer of CARDIO-PRED, the web server used was Apache/2.4.4 (Win 32) Open SSL/0.9.8y PHP/5.4.19. For backhand, database server version 5.5.32 MySQL community server (GPL) was used. It is hosted at http://www.genomeinformatics.dce.edu/CARDIO-PRED/. The screenshots from the tool are as shown in the Fig. 2.

Results

Proteins associated with cardiovascular disorders

A total of 124 diseases under cardiovascular class of disorder were extracted from OMIM Morbid Map. Proteins associated with the specific diseases were identified from UniProt KB. For each protein interactions which are structurally relevant i.e. in which both the interacting partners have Pfam id, were considered, out of a total of 124 proteins, only 47 interactions were found to be structurally relevant (Table 1 in supplementary material). For diseases other than the CVD, a total of 1200 interactions were studied and only 400 interactions were found to be structurally relevant. In the test set, almost 1500 polymorphic proteins were studied for interactions out of which only 600 interactions were structurally relevant.

Structural interaction and interface analysis network

A network with the PDB structures mapped onto interacting proteins was obtained from Interactome3D (Fig. 3).

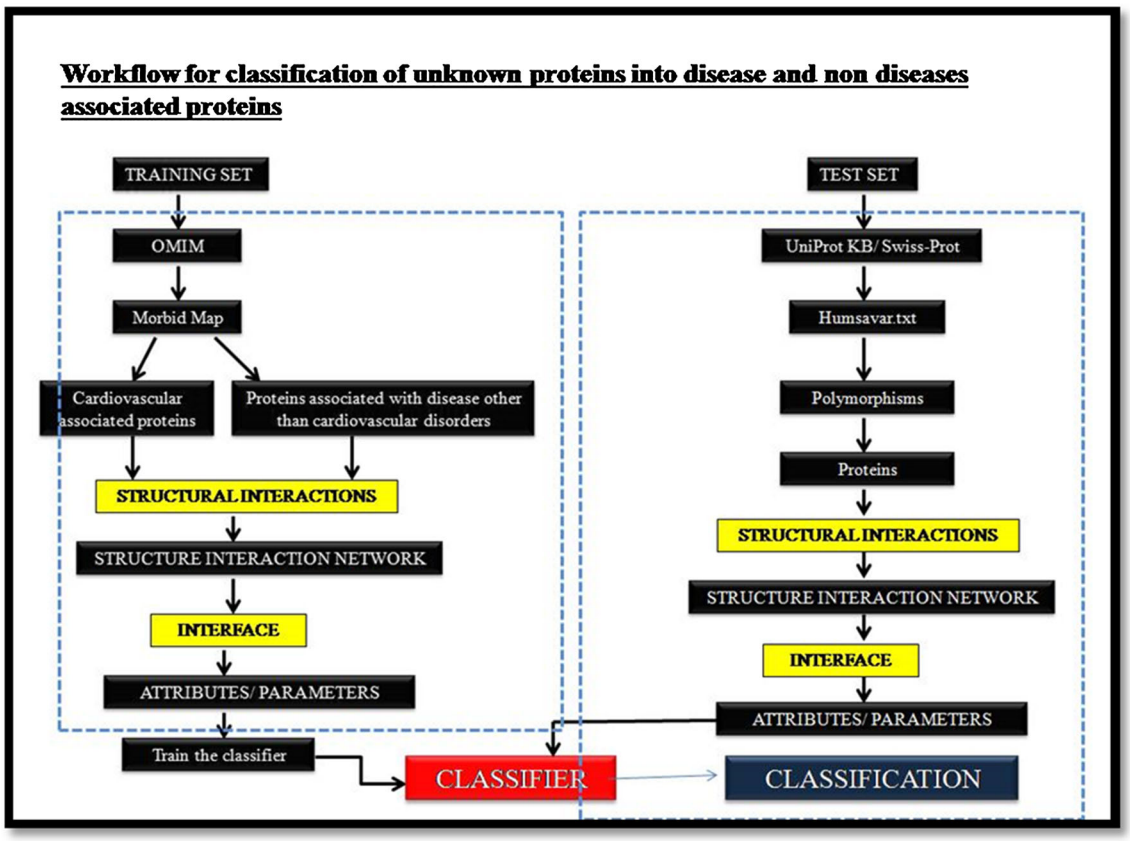

Fig. 1 Flow chart of the methodology carried out

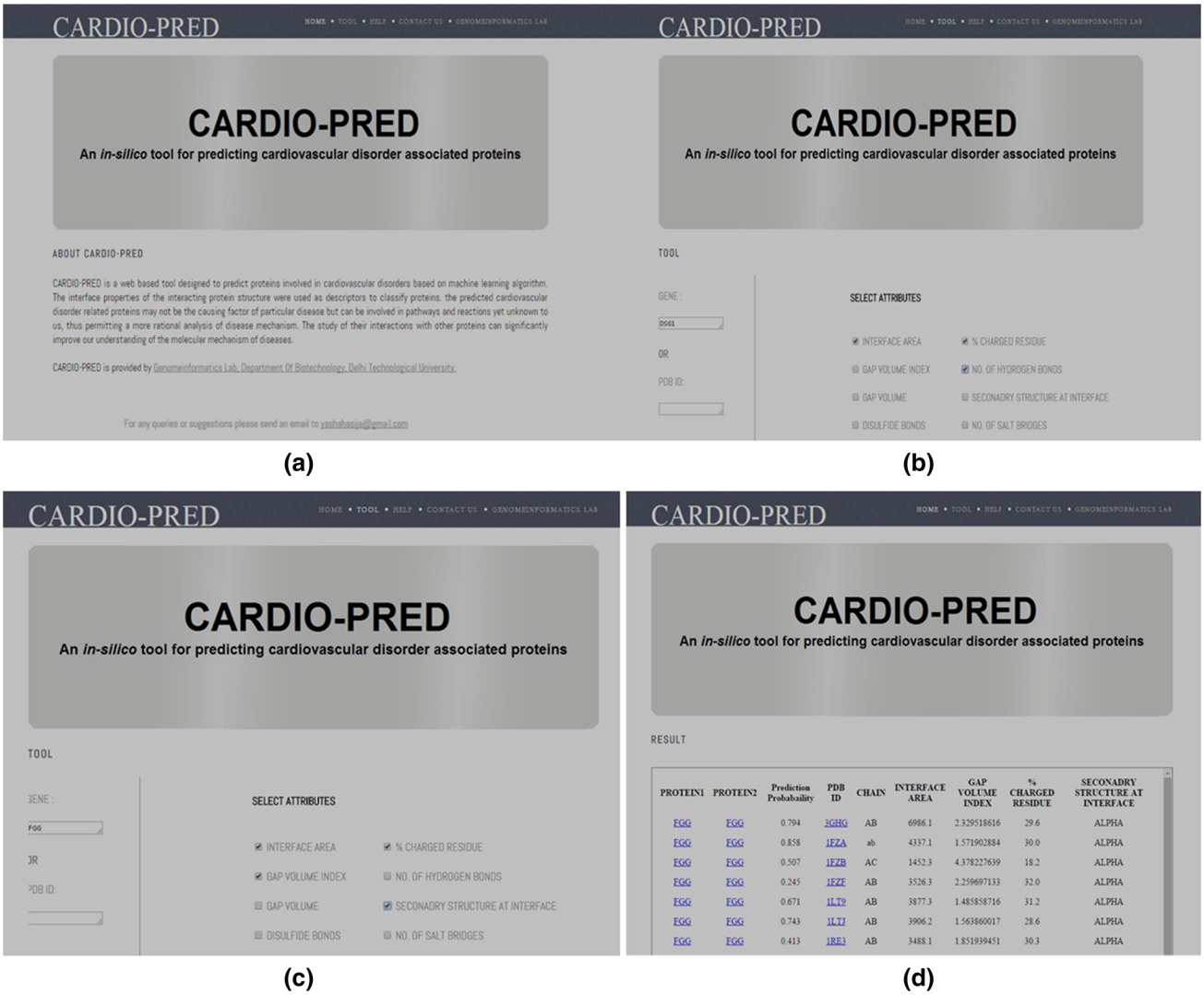

Fig. 2 Overview of CARDIO-PRED web page interface (**a**) a screenshot of home page of CARDIO-PRED, (**b**) the Tool page of CARDIO-PRED representing the attributes—interface area, % charged residues, gap volume index, no. of hydrogen bonds, gap volume, secondary structure at interface, disulphide bonds, no. of salt bridges, (**c**) an example: using "FGG"and selecting different attributes to be displayed, (**d**) result page showing the output for "FGG"

This network was generated separately for both training and the test set. A complete analysis of network helped in elucidating individual structures of proteins as well as the protein structures of interacting complexes. Along with the structures, this tool provides a detailed description of chains from both the proteins responsible for complex formation, which forms an important part of our study (Fig. 4).

A total of eight descriptors were obtained from 2P2I inspector namely accessible surface area, gap volume, gap volume index, % charged residues, number of hydrogen bonds, number of salt bridges, number of disulphide bonds and secondary structure at interface (Tables 2, 3 and 4 in supplementary materials). The parameters of interfaces for analysing interactions in the present study are as follows:

- *Accessible surface area* (*ASA*) this is the mean ASA buried by each domain of the complex.
- *Complementarity of interface—gap volume* provides a measure of complementarity and closeness of packing of the interface between two interacting proteins by measuring the volume of empty space between them (Kar et al. 2009).
- *Gap volume index* the gap volume index between two protein domains is calculated as ratio of gap volume to the interface area. It estimates the volume enclosed between any two molecules, delimiting the boundary by defining a maximum allowed distance from both interface (Kar et al. 2009).
- *Planarity* the planarity of interfaces analyzes the shape of the interface. It is defined as the rmsd of the interface

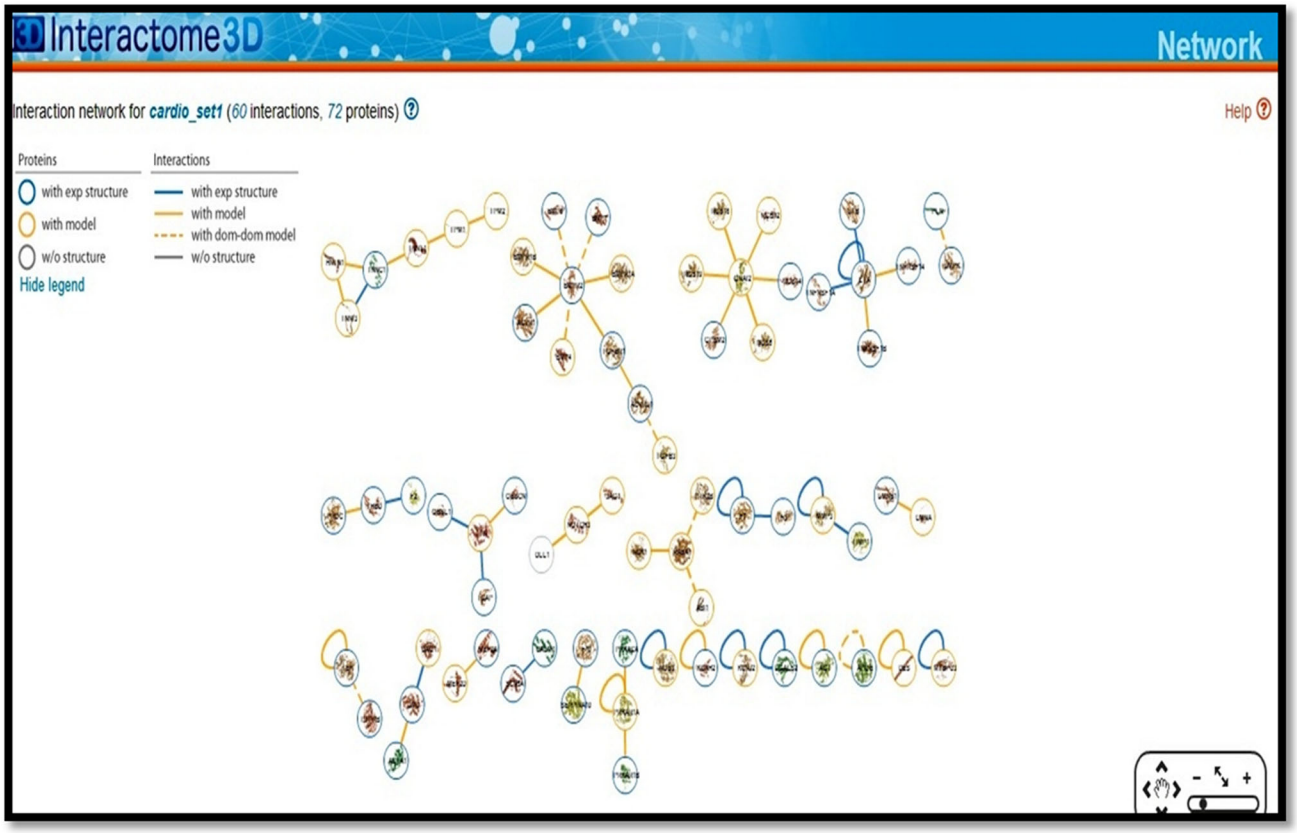

Fig. 3 Network chart of PPI with structures mapped on the network

atoms from the least-squares plane fitted through all interface atoms (Kar et al. 2009).

- *Hydrogen bonding* hydrogen bonds play key role in specificity of interactions between two proteins. The average number of hydrogen bonds is proportional to the area of subunit surfaces i.e. ASA: one bond per each 100–200 $Å^2$ (Moreira et al. 2007).
- *Number of salt bridges* the more the number of salt bridges, there will be more electrostatic interactions resulting in tighter packing within the residues.
- These descriptors were used to from the training and test sample. These files were used as input in Weka.

Classification and prediction analysis

A set of famous algorithms such as Naïve Bayes, Random Forest, J48, Random Forest with iteration 30, Bagging with Random Forest and Multilayer Perceptron were run on the dataset and comparisons were done between them (Table 1). Various statistical values were used in determining the optimum classifier for our training sample. In Fig. 5, true positive rate, true negative rate, precision, recall and accuracy-all were highest for Random Forest with iterations 30 (i.e. the number of trees were increased from 10 to 30). In the columns of false positive and false negative, Random Forest_30 scores the least. Thus, Random Forest_30 was found to be the best classifier in our dataset for the model building.

Prediction probability for test set

Predictions were made using the test sample to predict potential CVD related proteins from a set of polymorphic proteins. Further analysis of these may provide insight into yet unknown molecular mechanism various CVDs. List of all the polymorphic protein along with their prediction probability was obtained. The predicted proteins are not explicitly involved in causing CVD but may be involved in various pathways and mechanisms associated with CVDs. Table 2 shows the proteins with prediction value more than 0.8. A deep analysis of these proteins both computationally and experimentally can unravel the mechanisms not known to us. Further, the proteins listed in the table may be used to study gene prioritization by considering the proteins with the highest prediction probability as having the likelihood of being associated with cardiovascular disorders.

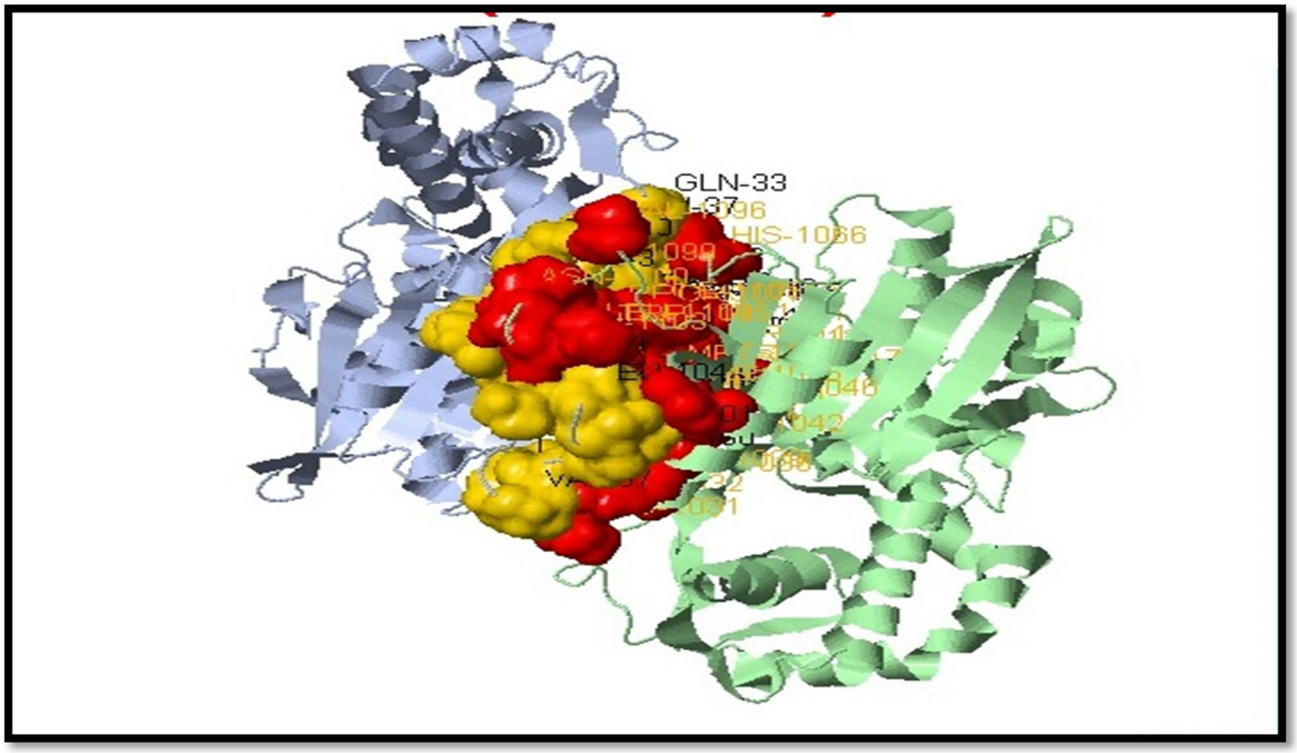

Fig. 4 Interaction between two proteins along with the interface residues

Table 1 Comparisons between different classifiers

Classifier	True positive rate	False positive rate	True negative rate	False negative rate	Precision	Recall	Accuracy (%)
Random Forest_10	0.77	0.4	0.59	0.23	0.67	0.77	68.34
Naïve Bayes	0.6	0.41	0.59	0.4	0.6	0.56	59.5
J48	0.74	0.39	0.61	0.26	0.67	0.74	67.5
Random Forest_30	0.77	0.38	0.62	0.23	0.7	0.77	69.5
Multilayer perceptron	0.71	0.41	0.6	0.28	0.65	0.71	65.5
Bagging_Random Forest	0.75	0.37	0.63	0.25	0.68	0.6	69

Discussion

Main concern of the present study was to present interface analysis of CVD related proteins to shed light on details of interactions and to emphasize the importance of using structures in network studies (Kar et al. 2009). The results obtained showed that interface properties can be used as descriptors for classifying purposes; be it two different diseases, a set of disease having same phenotypic effect from other set of disease with different phenotype, or for all the known hereditary diseases. This study provided insights into the usage of fine structural details in disorders related to cardiovascular system. A further exploration of this study can be utilized to study whether the classifier could work equally efficient when used for classifying all the inherited disease.

These results can be used as evidence when searching for candidate gene in predefined disease loci and also for predictions, to identify novel genes involved in the mechanisms. Studies have been carried out where sequence features such as cDNA, number of exons, protein size were investigated between set of genes known to be involved in hereditary disease and those not (López-Bigas and Ouzounis 2004; Adie et al. 2006). Functional annotation shared between known diseases genes had also been used to design a classifier (Rao et al. 2012). The classification based on genomic sequences have disadvantages associated with them, as algorithms which are based on functional

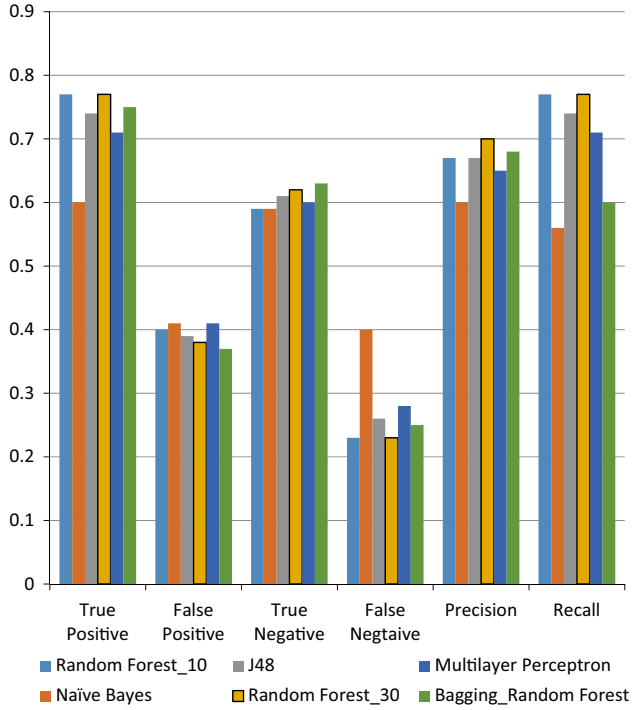

Fig. 5 Bar graph with different classifiers and the statistical values

annotations are inherently biased towards a particular known subset of genes. The present study utilized human PPI network with structural properties to compare genes involved in diseases. It is assumed that structural properties provide a much wider coverage of the understanding of mechanism of disease than sequence analysis. A promising approach for disease gene discovery is to combine all the evidences available such as PPIs, structures, sequences, transcriptional expression, functional annotation to make a classifier that would be possible to predict accurately without any ambiguities (Calvo et al. 2006).

Protein–protein interaction network provide a vast area of study in which different criteria, different features can be utilized to devise new diagnostic tool or to understand a novel mechanism. Further, new prognostic tools can be created by identification of pathways or disease sub networks that get activated only in diseases states. For instance, a recent study integrated protein networks with cancer expression profile and identified pathway that get activated only during tumor progression discriminating metastasis better than earlier described markers (Gonzalez and Kann 2012).

Drug target identification and drug design can be made more comprehensive by including disease networks and structural details, for example, structural information on allosteric site or binding site can be used to design potential drug to affect protein function. Further, rebuilding different

Table 2 Proteins predicted as potentially associated with cardiovascular disorders and their associations described

Protein 1	Protein 2	PDB ID	Prediction probability
DSG1	DSG1	3IFQ, AC	0.924
ABI1	EPS8	1GRI, AB	0.894
BCAR1	BCAR1	1OV3, AB	0.894
CASP1	CASP1	3E4C, AB	0.892
CASP1	CASP1	2H4 W, AB	0.88
ACTN2	ACTN2	1HCI, AB	0.877
CASP1	CASP1	1ICE, AB	0.868
CASP1	CASP1	1RWK, AB	0.868
CASP1	CASP1	1RWO, AB	0.868
CASP1	CASP1	1RWV, AB	0.868
CASP1	CASP1	1SC3, AB	0.868
A2 M	CELA1	3HS0, AB	0.861
ACY1	ACY1	2ZOG, AB	0.861
CAND1	CAND1	1U6G, AB	0.861
FARSA	FARSB	3L4G, AB	0.861
EGFL6	EGFL6	2BO2, AB	0.859
FGG	FGG	1FZA, ab	0.858
CASP1	CASP1	2FQQ, AB	0.846
ELANE	ELANE	1EZX, AB	0.844
CASP1	CASP1	1IBC, AB	0.841
BHMT	BHMT	1LT8, AB	0.838
CASP1	CASP1	1RWM, AB	0.827
CASP1	CASP1	1SC1, AB	0.827
DCP2	DCP2	2DSD, AB	0.827
DHPS	DHPS	1ROZ, AB	0.827
DHPS	DHPS	1RQD, AB	0.827
BCR	BCR	2B3R, AB	0.826
BHMT	BHMT	1LT7, AB	0.824
FGG	FGG	2FFD, AB	0.813
ACVR1	ACVR1	3O96, AB	0.811
CASP1	CASP1	1BMQ, AB	0.81
ABL1	ABL1	2HYY, AB	0.809
FBP1	FBP1	3KC1, AB	0.809
FBP1	FBP1	1FTA, AB	0.809
ABLIM1	ABLIM1	2DFY, CX	0.806
BCL6	BCL6	1R2B, AC	0.806
BCL6	BCL6	3LBZ, AB	0.806
ABL1	ABL1	3CS9, AB	0.803
BAIAP2	BAIAP2	1Y2O, AB	0.802
FBP1	FBP1	2VT5, AB	0.8
BAIAP2	BAIAP2	1WDZ, AB	0.799
DOCK9	CDC42	2WM9, AB	0.794
FGG	FGG	3GHG, AB	0.794
ACY1	ACY1	1Q7L, AB	0.792
ABI1	ABI1	3P8C, AD	0.791
ADA	ADA	1W1I, AB	0.79
ABL1	OSBPL5	3JV3, AB	0.782

Table 2 continued

Protein 1	Protein 2	PDB ID	Prediction probability
BIRC2	BIRC2	1I3O, AB	0.771
ADAM17	TIMP3	3CKI, AB	0.769
BDNF	BDNF	3BUK, AC	0.765
FBP1	FBP1	2JJK, AB	0.763
FECH	FECH	3HCN, AB	0.762
EMILIN1	EMILIN1	2KA3, AB	0.761
FBP1	FBP1	2WBB, AB	0.761
BFAR	BFAR	3HCU, AB	0.751
DUSP7	DUSP7	2GWO, AB	0.751
FECH	FECH	2HRC, AB	0.751
BCL6	BCL6	3E4U, AB	0.749
BLMH	BLMH	1CB5, AB	0.746
FGG	FGG	1LTJ, AB	0.743
ABCB8	ABCB8	2HYD, AB	0.742
FBP1	FBP1	3A29, AB	0.742
FBP1	FBP1	3KBZ, AB	0.742
FGG	FGG	3BVH, AB	0.742
EEA1	EEA1	1 JOC, AB	0.741
ELANE	ELANE	3KCG, HI	0.74
ELANE	ELANE	1OPH, AB	0.736
ELANE	ELANE	3F1S, AB	0.731
ELANE	ELANE	3F1S, AB	0.731
FASN	AASDHPPT	2JFK, AB	0.723
DR1	DR1	1N1J, AB	0.722
BCR	BCR	1K1F, AB	0.714
DOCK9	CDC42	2WMN, BA	0.707
ACVR1	UBXN1	2HAK, AB	0.706
BAG5	BAG5	3A8Y, AC	0.701
ABL2	ERBB3	2HCK, AB	0.697
ACAP1	ACAP1	3JUE, AB	0.693
ABI3	ABI3	2FPD, AB	0.691
BARD1	BARD1	3FA2, AB	0.689
ADH7	ADH7	1D1S, AB	0.687
FASLG	FAS	1D0G, AB	0.687
DNM1	DNM1	2X2E, AD	0.685
CADM1	CADM1	35C8, LH	0.683
ABL1	EPB41L3	2PSQ, AB	0.682
FGG	FGG	1LT9, AB	0.671
FGG	FGA	3HUS, AB	0.671
FGG	FGG	1RF0, AB	0.669
AANAT	YWHAZ	1IB1, AE	0.665
FGF9	FGFR3	1NUN, AB	0.665
ELANE	ELANE	1JMO, HA	0.661
ADH7	ADH7	1AGN, AB	0.654
ADH5	ADH5	1M6H, AB	0.653
ADH5	ADH5	1MC5, AB	0.653
ADH5	ADH5	1MP0, AB	0.653

Table 2 continued

Protein 1	Protein 2	PDB ID	Prediction probability
ABCB8	ABCB8	2IXF, AB	0.65
ACLY	ACLY	3MWE, AB	0.65
ADH5	ADH5	2FZE, AB	0.65
ADORA2A	DRD2	3ODU, AB	0.65
FASN	FASN	3HHD, AB	0.65
ECHS1	ECHS1	2HW5, EF	0.647
BDNF	BDNF	1WWW, VX	0.635
BFAR	BFAR	3EB6, AB	0.634
ACTB	ACTB	1HLU, AP	0.627
ADH1C	ADH1C	1HT0, AB	0.624
CAPN1	CAPN1	2ARY, AB	0.623
ADH5	ADH5	1M6 W, AB	0.62
ACLY	ACLY	3MWD, AB	0.618
ECHS1	ECHS1	2VRE, AB	0.618
FECH	FECH	1HRK, AB	0.618
ABL1	GRB2	3M7F, AB	0.612
BIRC2	BIRC2	3M1D, AB	0.612
ABL2	NCK1	2C0O, AB	0.608
DCTN1	DCTN1	2HKN, ab	0.602
FGG	FGG	2OYH, AB	0.599
BARD1	BARD1	2R1Z, AB	0.598
ABR	ABR	1BWN, AB	0.594
CADM1	CADM1	1S78, AB	0.592
FGG	FGG	3H32, AB	0.592
ACP6	ACP6	1CVI, AB	0.591
ADH1C	ADH1C	1U3W, AB	0.591
BIRC2	BIRC2	3MUP, AB	0.591
ABI1	EPS8	3EG1, AB	0.59
ADH5	ADH5	2FZW, AB	0.587
ADH5	ADH5	1MA0, AB	0.587
ABCD1	ABCD1	1R0Y, AB	0.582
ABR	ABL1	1DYN, AB	0.581
DNM1	DNM1	1DYN, AB	0.581
ELANE	ELANE	1H1B, AB	0.581
FBP2	FBP2	3IFA, AB	0.572
FASN	AASDHPPT	2PX6, AB	0.56
ADAM15	ADAM15	3G5C, AB	0.559
DCTN1	MAPRE1	2HKQ, AB	0.554
FASLG	TNFRSF6B	2HEY, FR	0.553
FGG	FGG	3E1I, AB	0.553
ABCD1	ABCD1	1G29, 1,2	0.552
EGLN3	EGLN3	3HQR, AS	0.545
ACVR2A	ACVR2A	3Q4T, AB	0.544
FAS	FADD	3EZQ, AB	0.544
ABCB8	ABCB8	1XF9, AB	0.541
FAU	FAU	2ZNV,AB	0.538
ABI1	NCKAP1	2V1Q, AB	0.527

Table 2 continued

Protein 1	Protein 2	PDB ID	Prediction probability
BAK1	BAK1	1BXL, AB	0.527
ABL1	NFASC	2IZV, AC	0.521
DDB1	CUL4A	2HYE, CA	0.519
BIRC2	BIRC2	3OZ1, AB	0.511
ABCD1	ABCD1	3C4 J, AB	0.51
ABLIM1	ABLIM1	2XJZ, AI	0.508
BCR	BCR	3BYI, AB	0.508
ACVR2A	ACVR2A	2QJA, AC	0.507
FGG	FGG	1FZB, AC	0.507
DDB1	DDB2	3EI4, FE	0.505
ARTN	GFRA3	2GYR, AB	0.504
DDX18	DDX18	3LY5, AB	0.504
DDX24	DDX24	3LY5, AB	0.504
ACVRL1	ACVRL1	3MY0, AM	0.5
CALM3	CALM3	2VAY, AB	0.5
CARD10	CARD10	3YGS, CP	0.499
EGFR	EGF	1NQL, AB	0.499
ADCYAP1	ADCYAP1R1	2JOD, AB	0.482
CALM3	CALM3	2X0G,AB	0.476
FASN	AASDHPPT	2JFD, AB	0.475
DCTN1	MAPRE1	1TXQ, AB	0.471
ABL2	EGFR	2K7A, AB	0.467
DVL3	DVL3	2UZC, AB	0.458
ABL2	ABL2	1D1Z, AB	0.457
ABCG2	ABCG2	2PZE, AB	0.455
BAX	bcl2l11	2K7 W, AB	0.454
ADAP1	KIF13B	3MDB, AC	0.451
CALM3	CALM3	3OXQ, AE	0.45
FASN	FASN	1XKT, AB	0.449
ACVR1	CDK14	2V55, AB	0.44
ABL1	PRICKLE3	2G2H, AB	0.439
BMP1	BMP1	1NZI, AB	0.432
ADAP1	KIF13B	3FM8, AC	0.429
BDNF	NTF3	1BND, AB	0.426
ELANE	ELANE	2R9P, EA	0.423
FBXW8	SKP1	1FQV, AB	0.415
ECHS1	ECHS1	2ZQR, AB	0.414
FGG	FGG	1RE3, AB	0.413
DVL3	DVL3	2PNT, AB	0.412
EGFL6	EGFL6	3GIS, EF	0.412
ARTN	ARTN	2GH0, CA	0.41
ABCD1	ABCD1	1Q1B, AB	0.405
BFAR	UBE2D1	3HCT, AB	0.403
DUSP7	DUSP7	2C46, CD	0.401
ABI1	EPS8	1JU5, AC	0.399
ACVR2A	ACVR2A	3KFD, AE	0.393
BARD1	BARD1	2NTE, AB	0.391

Table 2 continued

Protein 1	Protein 2	PDB ID	Prediction probability
ABCB8	ABCB8	3C41, JK	0.39
DVL3	DVL3	1N99, AB	0.386
ACVRL1	ACVRL1	3C4E, AB	0.384
BIRC2	BIRC2	2NZ7, AB	0.383
ACVR2B	ACVR2B	1NYS, AB	0.382
ECHS1	ECHS1	1HZD, AB	0.381
ABCB8	ABCB8	3G61, AB	0.376
FGG	FGB	1FIC, AB	0.374
ACVRL1	ACVRL1	3GGF, AB	0.373
BAD	BCL2L1	1G5 J, AB	0.37
BCL2A1	BCL2A1	3PK1, AB	0.37
ABI1	NCKAP1	2O88, AB	0.366
ACD	ACD	2I46, AB	0.364
BMP1	BMP1	1SZB, AB	0.359
ELANE	ELANE	1SR5, AC	0.359
BCL6	BCL6	1R28, AB	0.355
BIRC2	BIRC2	1XB0, AB	0.355
ASAP1	APC	2RQU, AB	0.351
FGG	FGG	2H43, AC	0.349
ACTB	ACTN3	3LUE, AK	0.347
BCL2A1	BCL2A1	1ZY3, AB	0.347
BCL2A1	BCL2A1	2VM6, AB	0.347
BCL6	BCL6	3BIM, AI	0.343
ADCYAP1	ADCYAP1R1	3IOL, AB	0.34
BCAR1	BCAR1	1WYX, AB	0.338
DCTN1	DCTN1	3E2U, GA	0.335
ACP5	ACP5	1FJM, AM	0.333
ACPP	ACPP	1ND6, AB	0.331
FASN	AASDHPPT	2CG5, AB	0.331
ADAM17	ADAM17	1ZXC, AB	0.328
ABL1	ASB16	2E2B,AB	0.327
DDX24	DDX24	3FE2, AB	0.324
ABL2	GRB3	2XYN, AB	0.322
ABR	ABR	1B55, AB	0.321
EHMT1	TP53	1YCS, AB	0.318
BAX	BAX	2P1L, AB	0.317
DVL3	DVL3	3GGE, BC	0.315
ABL1	ABL1	2HZI, AB	0.314
ACVR1	NKIRAS1	2H96, AF	0.314
BDNF	BDNF	1HCF, AX	0.314
ABL2	ERBB2	2D0 N, CD	0.31
ACVR1B	ACVR1B	2QJ9, AC	0.309
ELANE	ELANE	1EAW, AB	0.309
FBXW8	SKP1	1NEX, AB	0.308
ACVR1	FKBP1A	3H9R,AB	0.307
ACVRL1	ACVR2A	3H9R, AB	0.307
CAPN1	CAPN1	2NQA, AD	0.305

Table 2 continued

Protein 1	Protein 2	PDB ID	Prediction probability
BCL2	BCL2	2XA0, AB	0.294
ABL2	PLCG1	1CWE, CD	0.291
FGG	FGG	2A45, AB	0.291
ACVR1	CHN1	3MDY, AB	0.289
FBXW7	SKP1	2OVP, AB	0.284
ABL2	SRC	3N84, AG	0.283
edn1	edn1	1T7H, AB	0.283
DCTN1	MAPRE1	2HL5, AC	0.279
ACHE	ACHE	3LII, AB	0.277
DUSP7	DUSP7	1RXD, CA	0.276
FAU	FAU	3ALB, AB	0.275
BIRC2	BIRC2	3D9T, AB	0.273
ABR	ABL1	1PBW, AB	0.262
ABI1	ABL1	3SEM, AB	0.26
ABL1	HCK	1ABO, AB	0.258
ACVR1B	1NHBB	1REW, AC	0.255
BLMH	BLMH	2CB5, AB	0.253
FGG	FGG	1FZF, AB	0.245
BCL2	BCL2	2 W3L, AB	0.241
ABI1	ABI1	1JQQ, AB	0.229
ASAP1	APC	2W2W, AB	0.227
ACHE	ACHE	1VZJ, AI	0.22
DVL3	DVL3	1OBY, PA	0.22
ABI1	ABL1	1ZUY, AB	0.214
ABL1	DNM1	1U5S, AB	0.207
BIRC2	BIRC2	1TW6, AC	0.206
FGF10	FGFR3	1RY7, AB	0.197
ABCB8	ABCB8	1G9X, AB	0.19
ABCG5	ABCG5	1L7 V, AC	0.189
FBXW8	SKP1	2ASS, AB	0.189
ECT2	ECT2	3L46, AB	0.188
ABL1	SOS2	3KFA, AB	0.187
ABL1	ERBB4	1OPL, AB	0.187
FES	FES	3CBL, AB	0.187
BFAR	UBE2D3	1FBV, AB	0.186
ABI1	ABI1	1BBZ, AD	0.185
EGFR	EGF	1IVO, AC	0.182
CADM1	CADM1	1Q1 J, LH	0.173
ABCG2	ABCG2	2AWN, AB	0.165
ACY1	ACY1	1CG2, AB	0.163
ADORA2A	ADORA2A	3KJ6, AL	0.162
DCTN1	DCTN1	2HL3, AC	0.16
ACPP	ACPP	2HPA, AB	0.155
ACVRL1	ACVR2A	1B6C, AB	0.153
ABL1	ASAP1	1GCQ, AC	0.15
EML1	EML1	1P22, AB	0.149
DVL3	DVL3	3KZE, CE	0.142

Table 2 continued

Protein 1	Protein 2	PDB ID	Prediction probability
DCTN1	DCTN1	2HQH, EA	0.14
ABCD1	ABCD1	2IT1, AB	0.133
ACCS	ACCS	1AHG, AC	0.132
ABL1	ABL1	2G1T, AE	0.122
FECH	FECH	2QD1, AB	0.121
ABCB8	ABCB8	2BBS, AB	0.075
ABL1	ERBB3	2SHP, AB	0.075
ADH5	ADH5	1TEH, AB	0.075
ELK3	ELK3	1HBX, AG	0.075
BARD1	BARD1	3C5R, AB	0.065

interaction networks such as metabolic, signalling etc. prediction about hub protein can be made which are involved in various pathways for proper functioning of the cell. This knowledge can be used while designing the drugs, i.e. whether to target hub proteins or not.

The prediction of CVD associated genes is of great importance to understand the mechanism behind PPI. A lot of research efforts have gone into classifying proteins either as disease associated or not associated with a disease. Several bioinformatics strategies have been explored to develop an efficient model for this classification. Machine learning tools have been applied using different classifiers and different kinds of features/attributes based on protein sequence, structure and binding affinities. Such approaches in machine learning were used to develop the most optimal model by exploring the contribution of different attributes to interaction.

Some studies have shown the association between age-related CVDs and osteoporosis with common etiology such as increased risk of hip fracture in women. Recent studies have shown that drugs have common effect for CVDs and osteoporosis, for example bone anti-resorptive drug reduces the risk of CVDs. Similarly, positive effects of statins, antihypertensive drugs have been shown on bone mass. These studies points to the common physiopathological molecular pathways between both the diseases. Statins for example, reduces cardiovascular mortality through reduction of LDL cholesterol levels, these have also been associated to increase bone mineralization in mice and reduction of fractures. All these examples suggest a link between the vascular and skeletal systems; therefore it is the main concern to understand the exact physiopathological mechanism shared between both the diseases as well as to determine common risk factors and genetic determinants (Marini and Brandi 2010).

Conclusion

The present study aimed at identifying and distinguishing proteins based on the interface parameters of the structure involved as CVD associated and CVD non-associated. It started with genes associated with disease to the structures associated with diseases. A classifier using Random Forest with 30 iterations was used for training based on the training set which included interface properties of proteins (with their interacting partners) associated with CVDs and proteins (with their interacting partners) associated with diseases other than CVDs.

To best of our knowledge, there are no prediction servers available based on interface properties of protein structure for predicting CVD associated proteins. In the present study, we presented a Random forest based method for prediction of CVD associated proteins with the accuracy of 69.5 %. The predicted proteins/genes may not be the causing factor of particular disease but can be involved in various pathways and mechanism yet unknown to us. Study of their interactions with other proteins can significantly improve our understanding in the molecular mechanism of diseases. Generally, mutations in proteins affect the structure of protein and hence it is becoming important to shift the focus from genetic studies to molecular studies. The classifying method has been implemented to develop a web based tool, CARDIO-PRED, which is available online at http://www.genomeinformatics.dce.edu/CARDIO-PRED.

Acknowledgments The study has been supported by SERB under OYS scheme via Project File No. SR/FT/LS-96/2011.

Conflict of interest The author(s) declare that they have no competing interests.

References

Adie EA, Adams RR, Evans KL, Porteous DJ, Pickard BS (2006) SUSPECTS: enabling fast and effective prioritization of positional candidates. Bioinformatics 22(6):773–774

Aung Z (2006) Computational analysis of 3D protein structures. Doctoral dissertation, School of Computing, National Institute of Singapore

Basse MJ, Betzi S, Bourgeas R, Bouzidi S, Chetrit B, Hamon V, Morelli X, Roche P (2013) 2P2Idb: a structural database dedicated to orthosteric modulation of protein–protein interactions. Nucleic Acids Res 41:D824–D827

Calvo S, Jain M, Xie X, Sheth SA, Chang B, Goldberger OA, Spinazzola A, Zeviani M, Carr SA, Mootha VK (2006) Systematic identification of human mitochondrial disease genes through integrative genomics. Nat Genet 38(5):576–582. doi:10.1038/ng1776

Choura M, Rebaï A (2011) Structural analysis of hubs in human NR-RTK network. Biol Direct 6:49. doi:10.1186/1745-6150-6-49

Chuang HY, Lee E, Liu YT, Lee D, Ideker T (2007) Network-based classification of breast cancer metastasis. Mol Syst Biol 3:140

Goh KI, Cusick ME, Valle D, Childs B, Vidal M, Barabási AL (2007) The human disease network. Proc Natl Acad Sci 104(21):8685–8690

Gonzalez MW, Kann MG (2012) Protein interactions and disease. PLoS Comput Biol 8(12):e1002819. doi:10.1371/journal.pcbi.1002819

Hall M, Frank E, Holmes G, Pfahringer B, Reutemann P, Witten IH (2009) The WEKA data mining software: an update SIGKDD explorations 11(1)

Kann MG (2007) Protein interactions and disease: computational approaches to uncover the etiology of diseases. Brief Bioinform 8(5):333–346

Kar G, Gursoy A, Keskin O (2009) Human cancer protein–protein interaction network: a structural perspective. PLoS Comput Biol. doi:10.1371/journal.pcbi.1000601

López-Bigas N, Ouzounis CA (2004) Genome-wide identification of genes likely to be involved in human genetic disease. Nucl Acids Res 32(10):3108–3114

Magrane M, The UniProt consortium (2011) UniProt knowledgebase: a hub of integrated protein data

Marini F, Brandi ML (2010) Genetic determinants of osteoporosis: common bases to cardiovascular diseases. Int J Hypertens. doi:10.4061/2010/394579

Moreira IS, Fernandes PA, Ramos MJ (2007) Hot spots—a review of the protein–protein interface determinant amino-acid residues. Proteins 68(4):803–812

Mosca R, Céol A, Aloy P (2013) Interactome3D: adding structural details to protein networks. Nat Methods 10(1):47–53

North BJ, Sinclair DA (2012) The intersection between aging and cardiovascular disease. Circ Res 110:1097–1108

Online Mendelian Inheritance in Man, OMIM®. McKusick-Nathans Institute of Genetic Medicine, Johns Hopkins University (Baltimore, MD). http://www.omim.org/. Accessed April 2014

Rao A, Bulusu G, Srinivasan R, Joseph T (2012) Protein–protein interactions and disease, protein interactions. Dr. Jianfeng Cai (Ed.), ISBN: 978-953-51-0244-1, InTech

Wang X, Wei X, Thijssen B, Das J, Lipkin SM, Yu H (2012) Three-dimensional reconstruction of protein networks provides insight into human genetic disease. Nat Biotechnol 30(2):159–164. doi:10.1038/nbt.2106

Zhang KX, Ouellette BF (2011) CAERUS: predicting CAncER oUtcomeS using relationship between protein structural information, protein networks, gene expression data, and mutation data. PLoS Comput Biol. doi:10.1371/journal.pcbi.1001114

IOSR Journal of Electrical and Electronics Engineering (IOSR-JEEE)
e-ISSN: 2278-1676,p-ISSN: 2320-3331, Volume 10, Issue 2 Ver. I (Mar – Apr. 2015), PP 43-52
www.iosrjournals.org

Comparative Study of Speed Control of Induction Motor Using PI and Fuzzy Logic Controller

Anmol Aggarwal, J. N. Rai, Maulik Kandpal
Department of Electrical Engineering, Delhi Technological University
(Formerly Delhi College of Engineering)

Abstract:*This paper proposes the idea of using "Fuzzy Logic Technique" in estimating motor speed and controlling it for Induction motor. The Induction motor is modeled using dq axis theory. The main objective of this project is to develop a fuzzy logic based controller to control the speed of the induction motor, employing the scalar control model. The voltage and frequency input to the induction motor are to be controlled in order to obtain the desired speed response. The designed Fuzzy Logic Controllers performance is also weighed against with that of a PI controller. For V/f speed control of the induction motor, a reference speed has been set and the control architecture includes a rule base of 49 rules. These rules portray a nonchalant relationship between two inputs i.e. speed error (e), change in speed error (Δe) and an output i.e change ofcontrol (ω_{sl})*
Keywords:*InductionMotor,V/f induction motor speed control, dq axis theory, Fuzzy Logic controller, MamdaniArchitecture, Membership functions and PI controller*

I. Introduction

The induction motor is an important class of electric machines which finds wide applicability as a motor in industry and in its single phase form in several domestic applications. More than 85% of industrial motor used today are in fact induction motors. It is a singly fed motor (stator-fed). [1].
The speed of the induction motor is given by:

$$n = (1-s)\, n_s \qquad (1)$$

Where,
n=Rotor speed
s=Slip
n_s =Synchronous speed

The synchronous speed in terms of frequency is expressed as:

$$n_s = (120*f)/p \qquad (2)$$

Where,
f=Supply frequency
n=Number of poles

From equation (2) it's evident that the synchronous speed and hence the rotor speed using equation (1) can be controlled by varying supply frequency. Voltage induced in stator is given by $E_1 = K\phi f$, where K is a constant,ϕ is the air-gap flux and f is the supply frequency. Neglecting the stator voltage drop (which is hardly 10% of the supply voltage), terminal voltage $V_1 = K\phi\mathbf{f}$ .It is evident that a reduction in the supply frequency without a change in the terminal voltage causes an increase in the air-gap flux (hence shifting the operating point of the motor towards saturation).Hence we keep V/f ratio constant so as to avoid any discrepancy in motor operation. This method is also known as Scalar Control.[8][9]

II. Induction Motor-A General Overview

The stator of an induction motor is wound for three phases. Fig 1 shows the stator of an induction motor.[1]

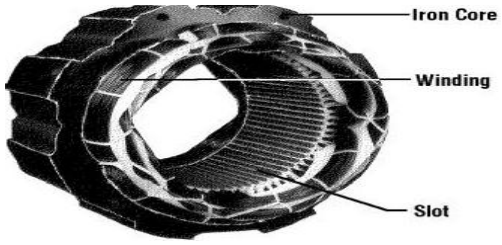

Fig1: Stator of an Induction Motor

Two types of constructions are employed for the rotor i.e. Squirrel - Cage Rotor andWoundRotor. The rotor core is of laminated construction with slots suitably punched in for accommodating the rotor winding /rotor bars. Fig 2 & Fig 3 shows squirrel cage and wound rotor respectively.[1]

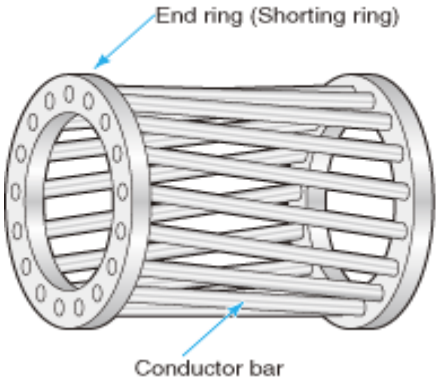

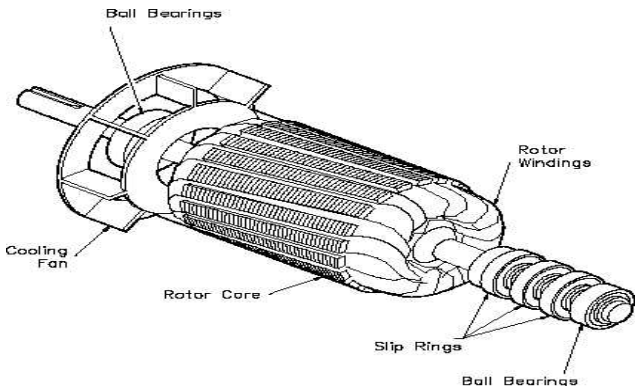

Fig2: Squirrel Cage rotor **Fig3:**Wound Rotor

Speed Control Techniques in Induction Motor

There are two basic ways of speed control, namely
(i) Slip-control for fixed synchronous speed.
(ii) Control of synchronous speed.
A stricter sorting reveals the following methods:
(i) Pole changing.
(ii) Stator voltage control.
(iii) Supply frequency control.
(iv)Eddy-current coupling.
(v) Rotor resistance control.
(vi)Slip power recovery [1][8]

III. PI Controller

The PI controller computes the controlled output by calculating the proportional and integral errors and summing these two components to compute the output.

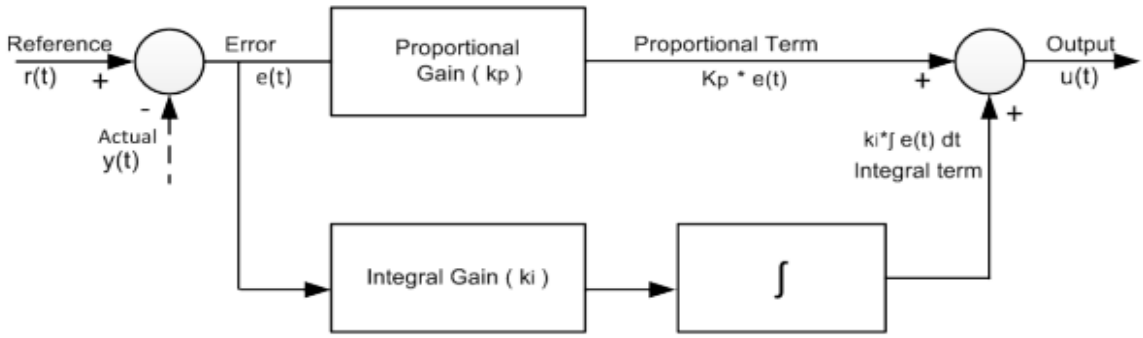

Fig 4: PI Controller block diagram.

In PI controller due to presence of the integral term, steady state error of speed is zero, making the system quite accurate. It does not require high gain as required in proportional gain controller. However it has certain drawbacks like if very fast response is desired, the penalty paid is a higher overshoot which is undesirable. The PID controller offers a very efficient solution to numerous control problems in the real world. [2][4][5].In our MATLAB model (Fig 14) we have used the inbuilt PI controller present in Simulink library of MATLAB.

IV. Fuzzy Logic Controller

Fuzzy logic control is a control algorithm based on a linguistic control strategy, which is derived from expert knowledge into an automatic control strategy. While the other control systems use difficult mathematical calculation to provide a model of the controlled plant, it only uses simple mathematical calculation to simulate the expert knowledge. Although it doesn't need any difficult mathematical calculation however it gives good

performance in a control system. Thus, it can be one of the best available answers today for a broad class of challenging control problems. [2][3][4]

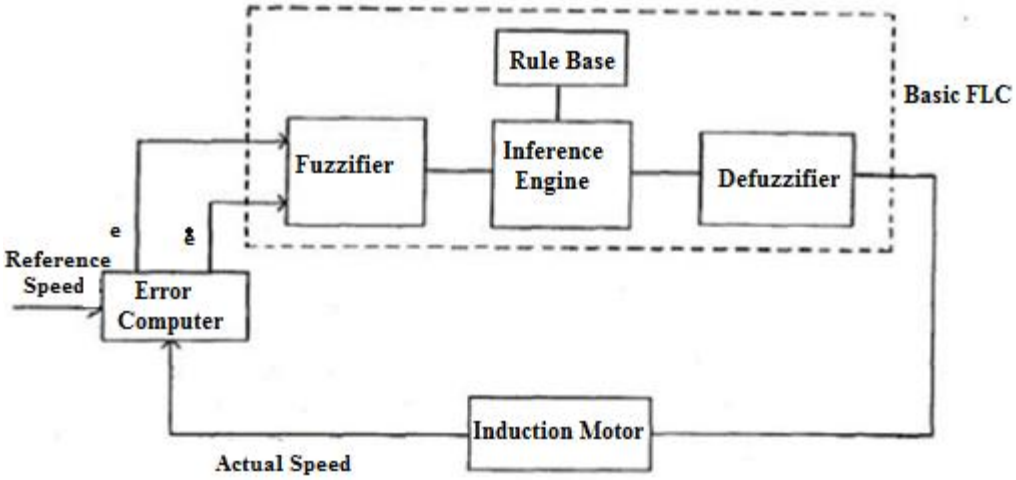

Fig 5: Block diagram of a Fuzzy Logic Controller

The fuzzifier scales and maps input variables to fuzzy sets.Inference engine with the help of rule base does the approximate reasoning and deduce the control action.Defuzzifier converts fuzzy output values to control actions.[7]

Advantage Of Using Fuzzy Technique

Fuzzy technique have gained in wide acceptance in expert systems, control units and in wide range of applications because of fast adaptation, high degree of tolerance, smooth operation, reduction in the effect of non-linearity, easy if-else logics and inherent approximation adaptability. [6]

A fuzzy logic controller (FLC) has already been proved analytically to be equivalent to a non-linear PI controller when a non-linear defuzzification method is used. Also, the result from the comparisons of conventional and fuzzy logic control techniques in the form of a FLC and fuzzy compensator showed fuzzy logic can reduce the effects of non-linearity in a DC motor and improve the performance of a controller. [2][3][4]

V. Rule Base For Speed Control Of Induction Motor

The design of a Fuzzy Logic Controller requires the choice of Membership Functions. The membership functions should be chosen such that they cover the whole universe of discourse. It should be taken care that the membership functions overlap each other. This is done in order to avoid any kind of discontinuity with respect to the minor changes in the inputs. To achieve finer control, the membership functions near the zero region should be made narrow. Wider membership functions away from the zero region provides faster response to the system. Hence, the membership functions should be adjusted accordingly. After the appropriate membership functions are chosen, a rule base should be created. It consists of a number of Fuzzy If-Then rules that completely define the behaviour of the system. These rules very much resemble the human thought process, thereby providing artificial intelligence to the system.[10]In this paper, the speed controller make use of 49 rules mentioned in the matrix below, based on which Fuzzy Logic controller operates to give the desired result.

Δe \ e	**NL**	**NM**	**NS**	**ZE**	**PS**	**PM**	**PL**
NL	NL	NL	NLM	NM	NMS	NS	ZE
NM	NL	NLM	NM	NMS	NS	ZE	PS
NS	NLM	NM	NMS	**NS**	**ZE**	PS	PMS
ZE	NM	NMS	NS	**ZE**	**PS**	PMS	PM
PS	NMS	NS	ZE	PS	PMS	PM	PLM
PM	NS	ZE	PS	PMS	PM	PLM	PL
PL	ZE	PS	PMS	PM	PLM	PL	PL

Fig 6: Rule Matrix for control output, change of control(ω_{sl})

Where,

e	Speed error	NS	Negative small
Δe	Change in speed error	Z	Zero
ω_{sl}	Change of control	PL	Positive large
NL	Negative large	PM	Positive medium
NM	Negative medium	PS	Positive small
NLM	Negative large medium	PLM	Positive large medium
NMS	Negative medium small	PMS	Positive medium small

The general considerations in the design of the controller are:

1. If both error and change in speed error are zero maintain the present control setting i.e. output=0.
2. If the error is not zero but is approaching this value at a satisfactory rate, then maintain the present controlsetting.
3. If the error is growing then change the control signal output depending on the magnitude and sign of error and change in speed error to force the error towards zero.

The typical rules of the table are read as(*shaded portion in matrix*):
IF **e=Z** AND Δe = **NS** THEN ω_{sl} = **NS**
IF **e=PS** AND Δe = **NS** THEN ω_{sl} = **ZE**
IF **e=ZE**AND Δe= **ZE**THEN ω_{sl} = **ZE**
IF **e=PS** AND Δe= **ZE**THEN ω_{sl}= **PS**

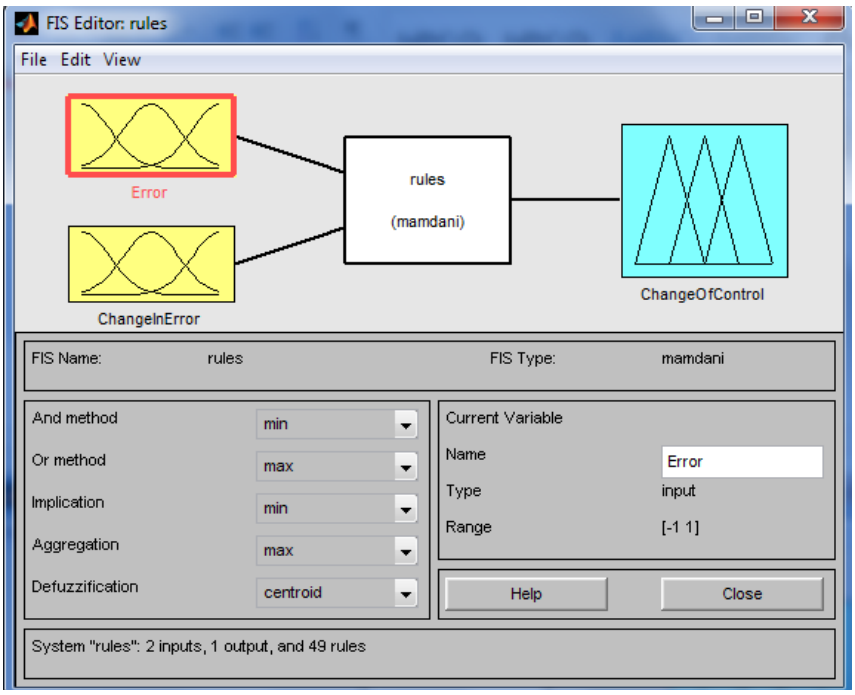

Fig 7:FIS Editor

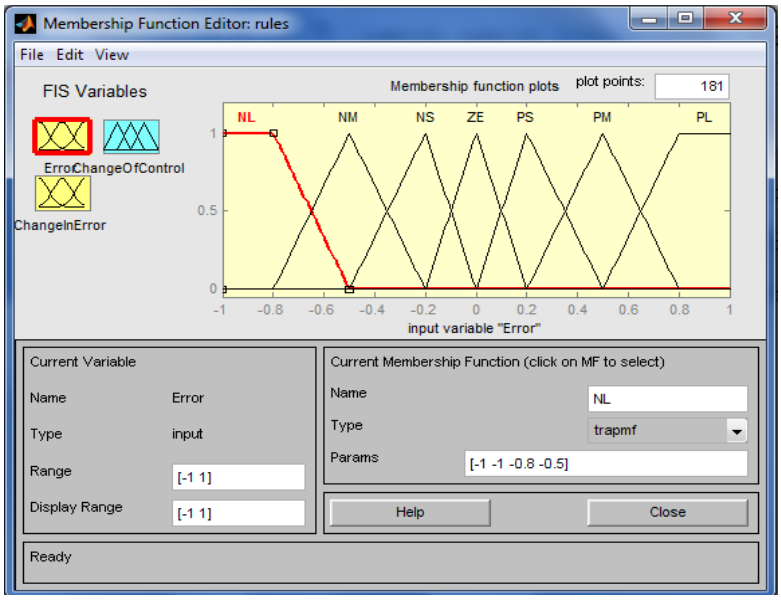

Fig 8: Membership Function for change in speed

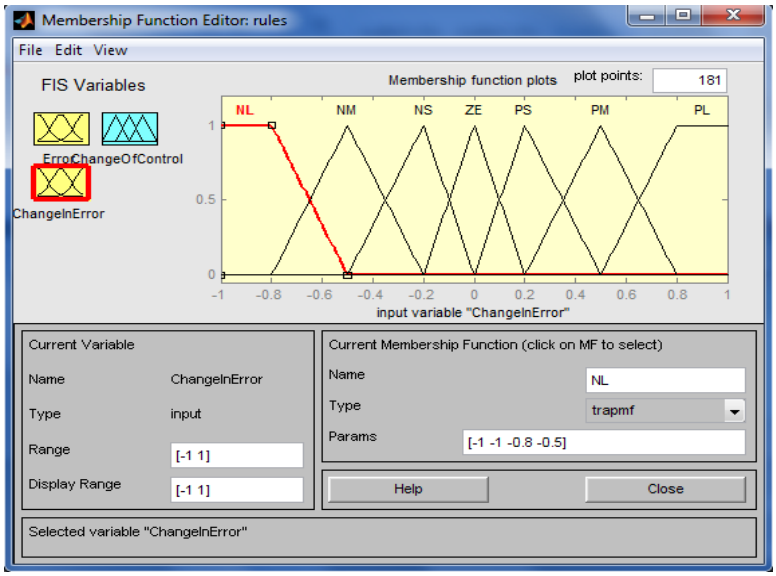

Fig 9: Membership Function for change in speed error

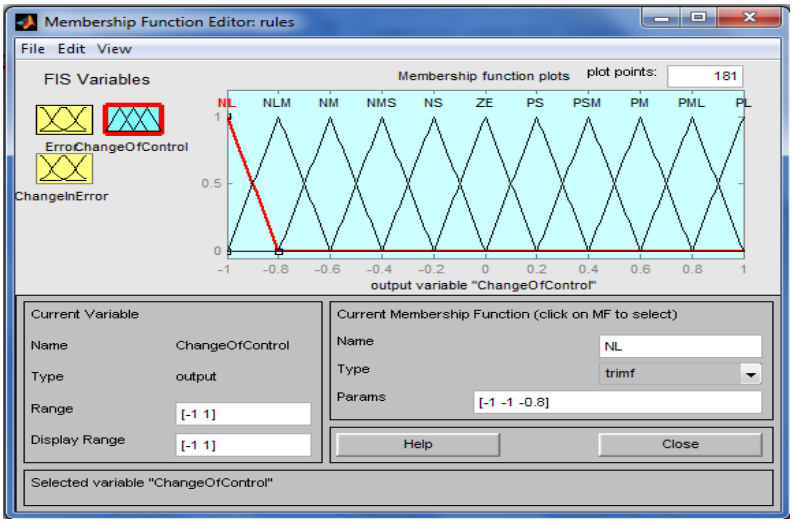

Fig 10: Membership function for output

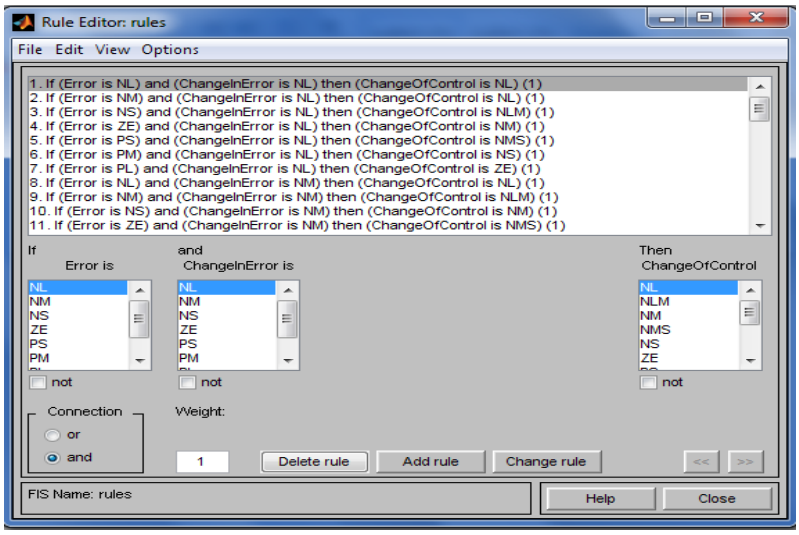

Fig 11: Rules

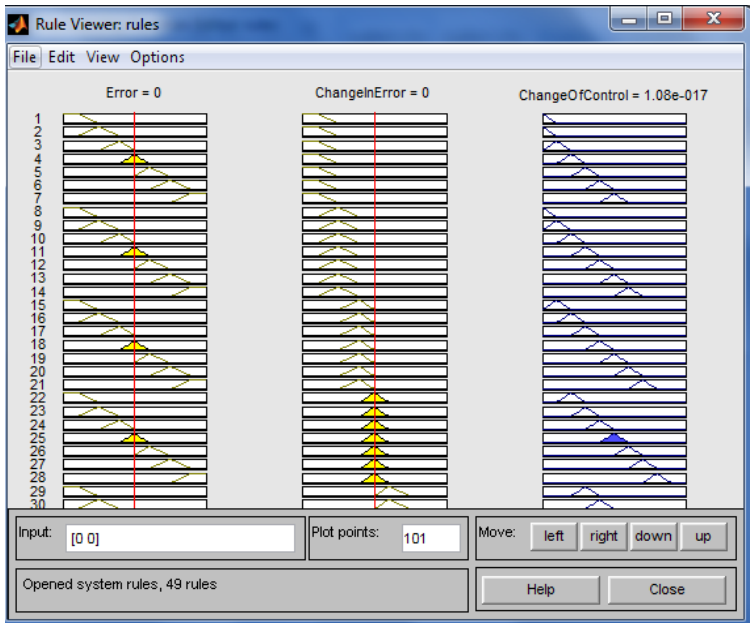

Fig 12: Rule Viewer

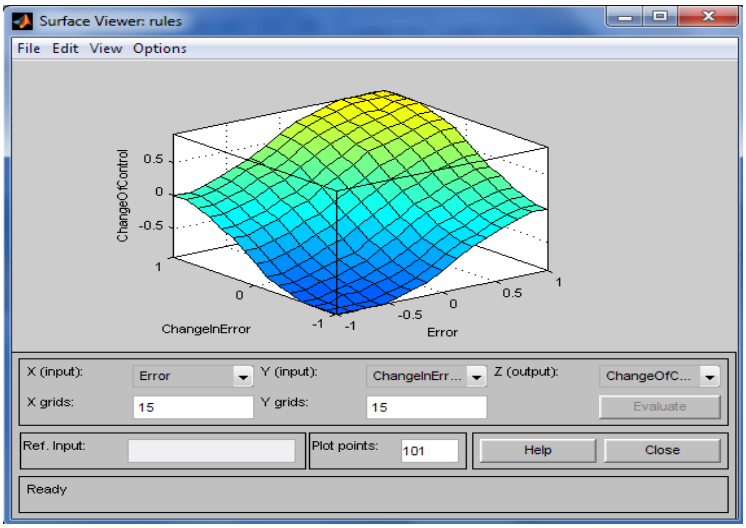

Fig13: Surface Viewer

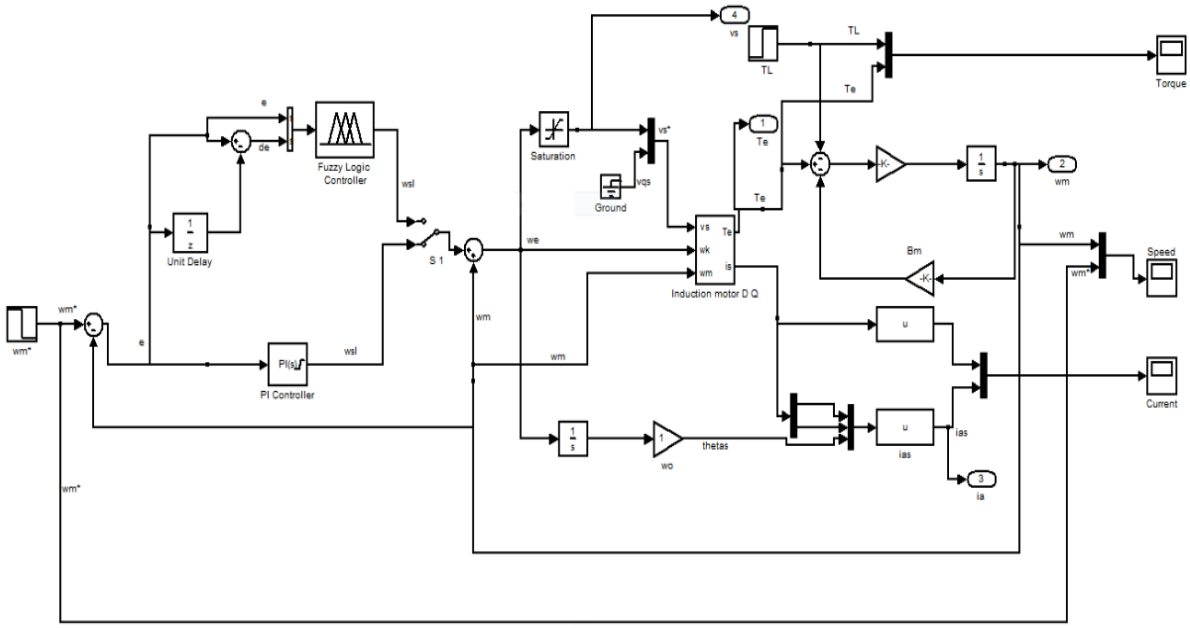

Fig14: Matlab/Simulink Model of PI Controller

As shown in the simulink diagram, "wm*" is chosen as the reference speed. The use of speed as reference signal is justified as the output of the system is speed and our aim is to control the speed of the induction motor. A tacho-generator, attached to the shaft of the induction motor, provides the current speed of the motor, "wm" which is compared with the reference speed "wm*", thus providing us with the speed error (e). This mechanism is called the feedback mechanism. The information about the instantaneous state of the output is fed back to the input which in turn is used to revise the same in order to achieve a desired output. [1]Speed error (e) is fed to the PI controller, to give an output variable. This output variable is then added to the motor speed "wm" which in turn forms the input to the V/f controller.

Electrical System Equations

$v_s=R_si_s+ d\lambda_s/dt+\omega_kM\lambda_s$ (3)

$v_r=R_ri_r+ d\lambda_r/dt+(\omega k-\omega_m)M\lambda_r$ (4)

Where the space vector $f= [f_df_q]^T$ and the $\pi/2$ rotational operator $M= \begin{bmatrix}-1 & 0\\ 0 & 1\end{bmatrix}$

Flux Linkage-Current Relations

$\lambda_s = L_si_s+L_mi_r$ (5)

$i_s= \Gamma_s\lambda_s-\Gamma_m\lambda_r$ (6)

$\lambda_r = L_m i_s+L_ri_r$ (7)

$i_r = -\Gamma_m\lambda_s+\Gamma_r\lambda_r$ (8)

$Ls = Lm +Lsl$ (9)

$Lr = Lm + Lrl$ (10)

$\Gamma_s =Lr/\Delta$ (11)

$\Gamma_r =Ls/\Delta$ (12)

$\Gamma_{rm} = Lm/\Delta$ (13)

$\Delta = L_mL_{sl} + L_mL_{rl} +L_{sl}L_{rl}$ (14)

Mechanical System Equations

$T_e = J(d\omega_{mech}/dt)+B_m\omega_{mech}+T_l$ (15)

Where,

$Te = k(\lambda_s\times i_s) = k (M\lambda_s.i_s) = k(\lambda_{ds}i_{qs} - \lambda_{qs}i_{ds})$ or, (16)

$Te = k(i_r\times \lambda_r) = kL_m (i_r\times i_s) = k(L_m/L_r)(\lambda_r\times i_s) = k\Gamma_m(\lambda_r\times\lambda_s)$ and, (17)

$\omega_{mech} = (2/p)\ \omega_m$, $k=(3/2)(p/2)$

Where,

v	Voltage space vector (V)	Γ	Inverse inductance (H^{-1})	×	Cross product
i	Current space vector (A)	f_0	Base frequency (Hz)	.	Dot product
λ	Flux linkage space vector (Wb)	ω_0	Base frequency (rad/s)	M	Rotation
R	Resistance (Ω)	ω_k	Speed of dq frame (rad/s)	s	Stator
L	Inductance (H)	ω_m	Rotor speed (rad/s)	r	Rotor
Te	Electromagnetic torque (Nm)	J	Moment of inertia ($kg.m^2$)	d	Direct axis
T_L	Load torque (Nm)	P	Number of poles	q	Quadrature axis

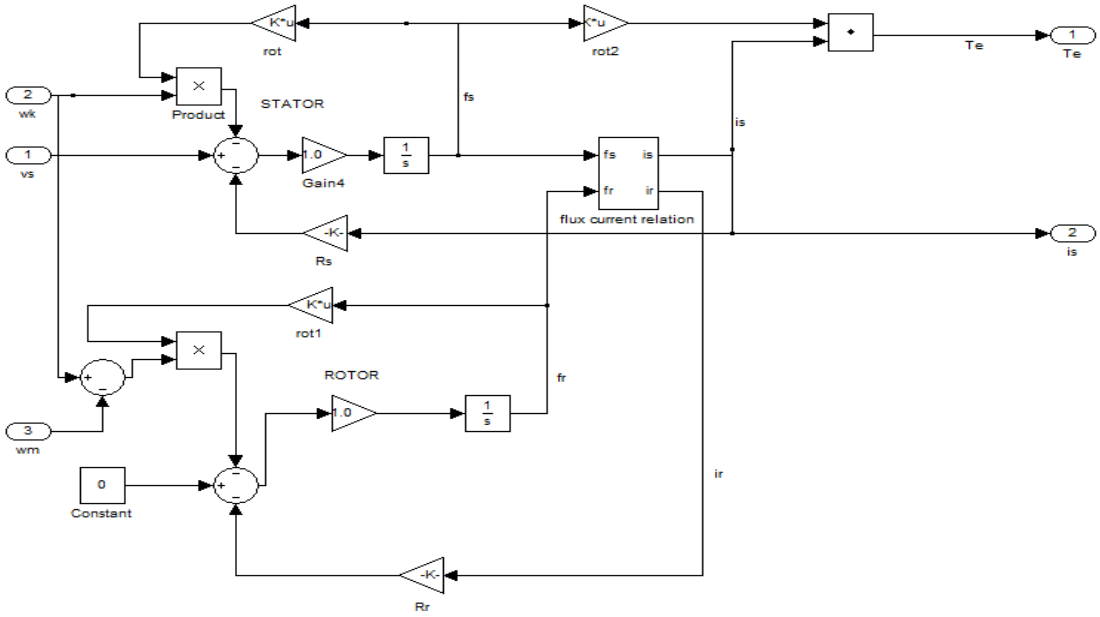

Fig15: Space vector model of Induction Motor

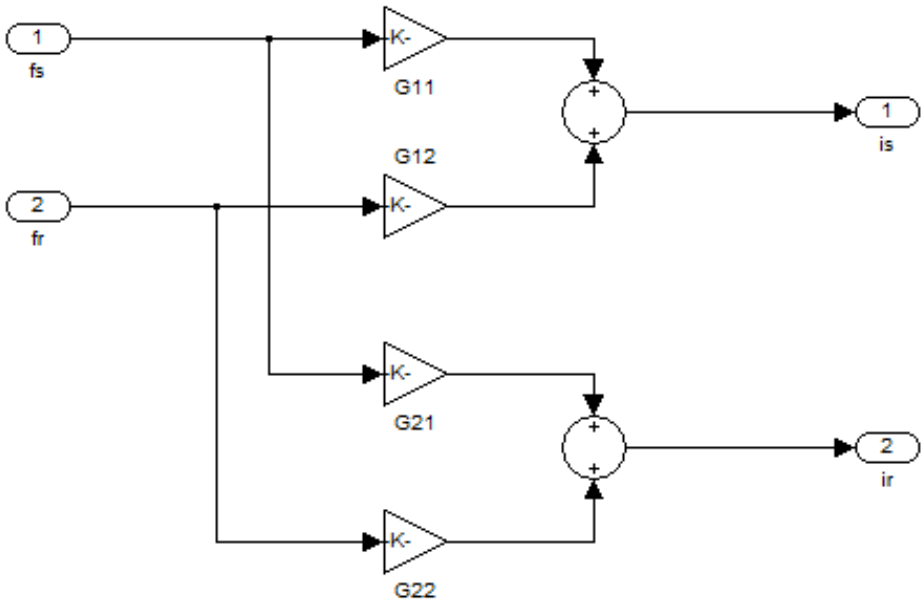

Fig16: Model for flux current relations

The space vector model of induction motor and the model for flux current relations has been modelled using equations (5) to (17).

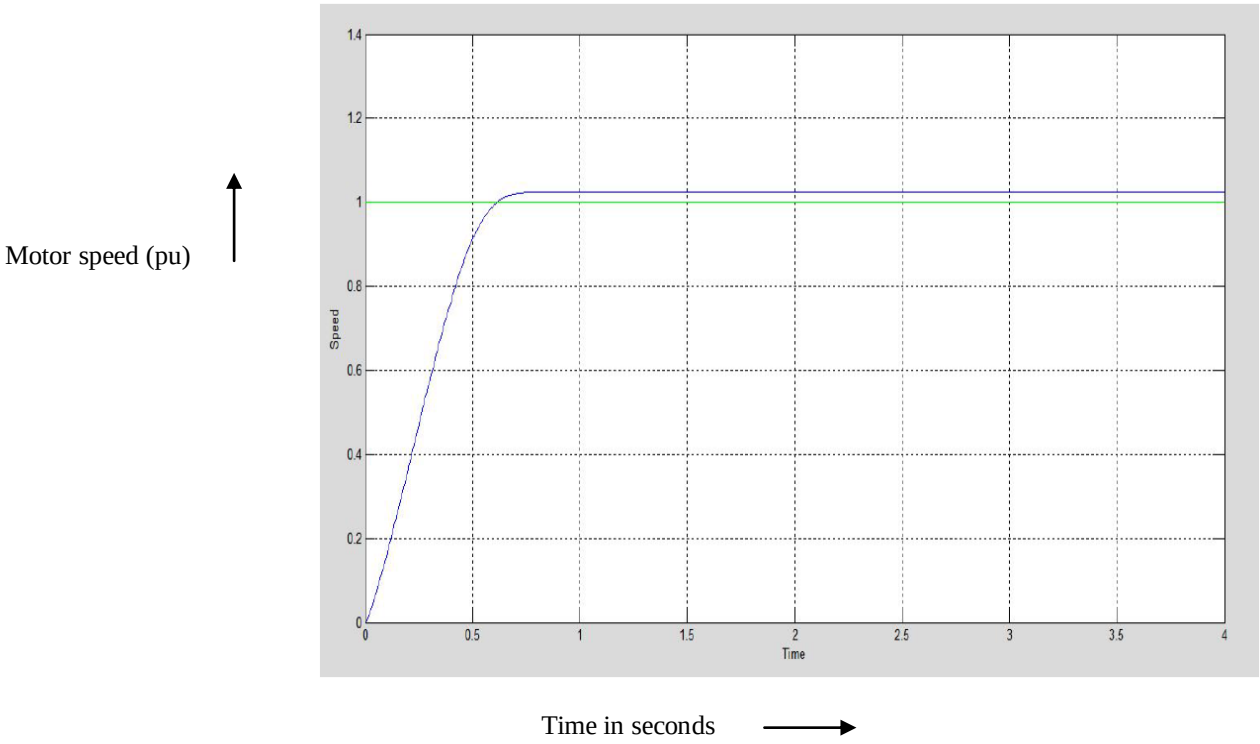

Fig 17: Speed V/S Time Response of PI controlled Induction Motor

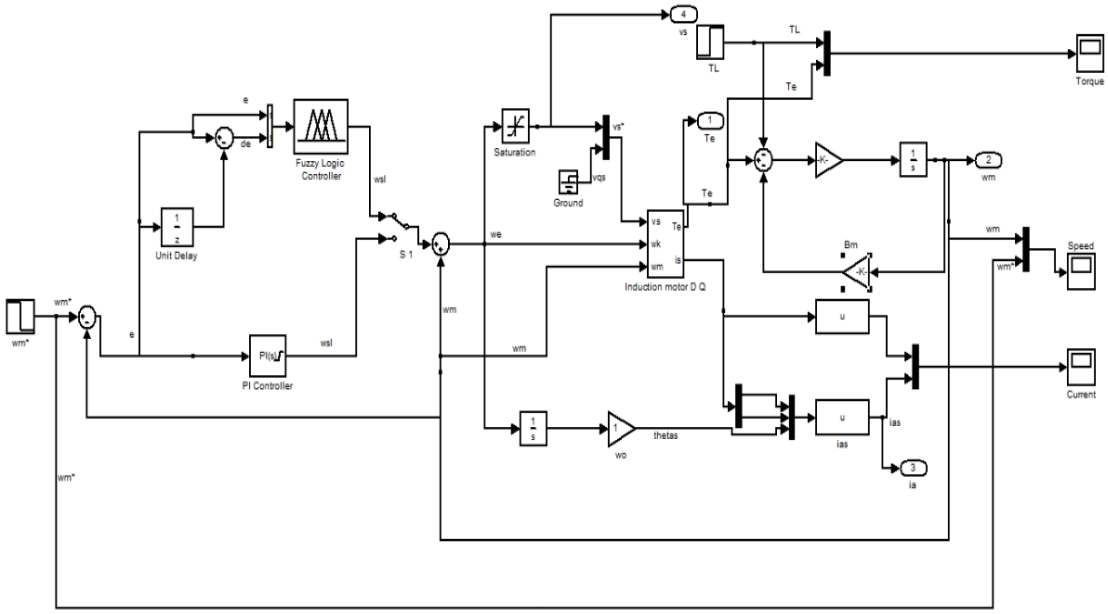

Fig18: Matlab/Simulink Model of Fuzzy Controller

The model for Fuzzy Controller works on the same principle as PI controller explained above except that the change-both e and de (Fig 18) are fed to the fuzzifier for fuzzification. The inference system then processes these two fuzzy inputs using the fuzzy control rules and the database, which are defined by the programmer based on the chosen membership function and fuzzy rule table, to give an output fuzzy variable. The fuzzy output thus obtained is defuzzified by the defuzzifier to give a crisp value.[1]

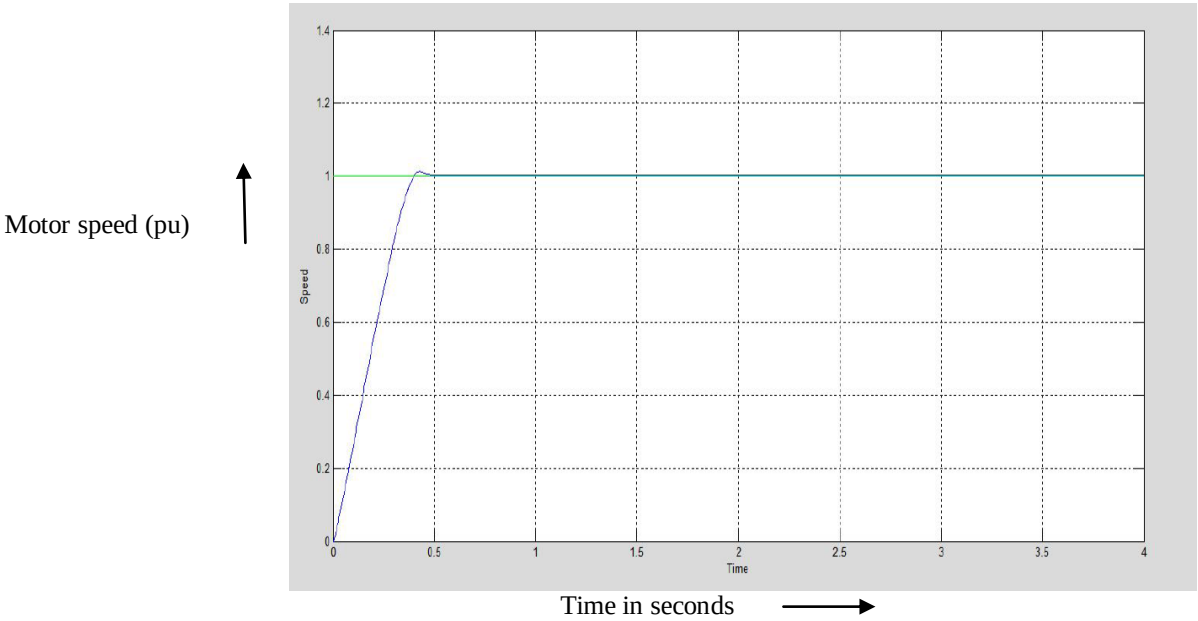

Fig 19: Speed V/S Time Response using Fuzzy logic controller

VI. Conclusion

The background of Induction Motor is studied and a study of the characteristics of induction motor is done. Graph for the speed response of induction motor using fuzzy logic controller (FLC) is successfully simulated in MATLAB and compared with graph for the speed response of Induction Motor with PI controller.It is established that fuzzy logic controller has finer performance in comparison to PI controller as steady state error (SSE) is zero in FLC whereas in PI controller the SSE is about 2%. Even the rise time in FLC is less as compared with PI controller which shows FLC have faster dynamic response as compared to designed PI controller.

Appendix-A

Specifications Of The Induction Motor

Stator Resistance = 0.050pu
Rotor Resistance = 0.030pu
Stator Leakage Inductance = 0.20 pu
Rotor Leakage Inductance = 0.02pu
Magnetizing Inductance = 6.0 pu
Base Frequency = $2*\pi*50$ rad/s
Number of Poles = 2
Moment of Inertia = 1.2pu
Viscous Friction Coefficient = $2*10^{-5}$pu

References

[1]. Electric machinery, Fitzgerald & Kingsley
[2]. Modern Control Engineering, Katsuhiko Ogata
[3]. Zimmermann, H. (2001). Fuzzy Set Theory and Its Applications. Boston: Kluwer Academic Publishers. ISBN 0-7923-7435-5
[4]. J. G. Ziegler and N. B. Nichols, "Optimum settings for automatic controllers," Trans. ASME, vol. 64, pp. 759–768, 1942.
[5]. G. Mallesham and A. Rajani, "Automatic Tuning of PID Controller using Fuzzy Logic," 8th International Conference on Development and Application Systems, Suceava, Romania, pp. 120 – 126, 2006.
[6]. PavolFedorand DanielaPerduková, "A Simple Fuzzy Controller Structure," ActaElectrotechnica et Informatica No. 4, Vol. 5, pp. 1-4, 2005.
[7]. J.-S. R. Jang, C.-T. Sun, E. Mizutani, "Neuro-Fuzzy and Soft Computing," Pearson Education Pte. Ltd., ISBN 81-297-0324-6, 1997, chap. 2, chap. 3, chap. 4.
[8]. Gopal K. Dubey, "Fundamentals of Electrical Drives", Narosa Publishing House Pvt. Ltd., 2001, chap. 6.
[9]. Yau-Tze Kao and Chang-Huan Liu, "Analysis and Design of Microprocessor-Based Vector-Controlled Induction Motor Drives," IEEE Transactions on Industrial Electronics, Vol. 39, pp. 46 – 54, 1 February, 1992.
[10]. M.Chow, A. Menozzi and F. Holcomb ,"On the Comparison of Emerging and Conventional Techniques for DC Motor Control," proc. IECON , pp. 1008-1013, 1992.

International Journal of Current Engineering and Technology
E-ISSN 2277 – 4106, P-ISSN 2347 – 5161
©2015INPRESSCO®, All Rights Reserved
Available at http://inpressco.com/category/ijcet

Research Article

Design of Magnetorheological Brake using Parabolic Shaped Rotating Disc

Chiranjit Sarkar†* and Harish Hirani‡

†Mechanical Engineering Department, Delhi Technological University, Shahbad Daluatpur, Bawana Road, Delhi – 110042, India
‡Mechanical Engineering Department, Indian Institute of Technology Delhi, Hauz Khas, New Delhi – 110016, India

Accepted 16 March 2015, Available online 18 March 2015, **Vol.5, No.2 (April 2015)**

Abstract

The aim of this paper is to enhance the braking torque of a magnetorheological brake (MRB) system. The proposed brake system consists of rotary disc with wave form boundary immersed in a MR fluid and enclosed in an electromagnet. The yield stress of the fluid varies as a function of magnetic field created by electric current passing through the electromagnet. The instantaneous increase in yield stress of fluid significantly increases the friction on the surfaces of rotating disks; thus generating a retarding braking torque. Due to the waveform boundary, a wedge shape is formed between the outer fixed casing and the disc. This wedge shape provides the extra resisting force to stop the rotation of the disc due to the shear stress of the MR fluid changed with the influence of the applied magnetic field. In the present study, the Bingham model has been used to estimate the braking torque exercised by MR brake. A parametric study considering various configurations of rotating disk and MR gap has been presented. Parabolic profile MR brake shows the large braking torque compared to circular profile of disc.

Keywords: *MR fluid, MR brake, Waveform boundary disc*

1. Introduction

Magnetorhelogical (MR) suspensions are known for dramatic change in their apparent viscosity. Due to their variable viscosity, MR fluids are used in engineering applications requiring controllable dynamic performance. One such application is magnetorheological brake in which MR fluid is treated as a brake lining material. This material does not wear-away and provides desirable friction resistance by just controlling the magnetic field passing through it. As MR brake involves electromagnetism and magnetizable friction material, this system can be named as "electromagnetic brake" (Gupta and Hirani, 2011).

A typical MR fluid consists of 20-40 volume percentage of pure-iron (purity > 99%) particles (size: Ø3-10 micrometers), suspended in a carrier liquid such as mineral oil, synthetic oil, water or glycol. A variety of proprietary additives to avoid gravitational settling, to elude wear and to promote particle suspension, are added to MR fluids. To model the behavior of MR fluids, the Bingham plastic model (Ginder and Davis, 1994) is used. MR fluids exhibit maximum yield strengths of 50-100 kPa for applied magnetic fields of 150-250 kA/m. The performance of MR-based devices is relatively insensitive to temperature over a broad temperature range (Ginder and Davis, 1994).

*Corresponding author: **Chiranjit Sarkar**

The design of MR brake starts with the maximum shear strength, τ_{max}, achievable by the available MR fluid. The control on the shear stress (between zero to τ_{max}) of MR fluid is achieved by regulating the magnitude and direction of the magnetic field. The field density is a function of permeability and saturation of materials through which magnetic field passes, brake geometry, number of turns in electromagnetic coil, and current supplied to electromagnetic coil (Sarkar and Hirani, 2015), (Sarkar and Hirani, 2013), (Sukhwani, *et al*, 2009), (Sukhwani and Hirani, 2008), (Sukhwani and Hirani, 2008), (Sukhwani, *et al*, 2008), (Hirani and Manjunatha, 2007), (Sukhwani, *et al*, 2007),(Sukhwani and Hirani, 2007), (Sukhwani, *et al*, 2006). Unfortunately, MR fluids do not show linear increment in shear strength with increase in applied magnetic field, and finally shear strength gets saturated. Therefore in the present study, the non-linear behavior of shear strength and saturation limits to estimate the braking torque exercised by MR brake have been incorporated.

2. Mathematical Modeling of MR brake using conventional disc

The braking action on MR brake is achieved due to the change in shear stress of the MR fluid in the presence of the magnetic field. The shear stress of MR fluid is modelled as the Bingham model as shown in Eq. (1)

$$\tau = \tau_o + \eta \frac{du}{dy} \quad (1)$$

Where, $\tau_o = \alpha\left(\frac{NI}{2h}\right)^{\beta}$ depends on the applied magnetic field, α and β are the constants depend on the MR fluid properties.

Figure 1 shows the schematic of MR brake. Low carbon steel is selected for the casing as well as the disc material because to magnetize the MR fluid the material of the casing and the disc should be magnetic, low carbon is the magnetic material and it is easily available. Stainless steel is selected for the shaft material; because the MR fluid at the seal should not be magnetized otherwise the seal will break. The nitrile rubber seal is good option at the low as well as at high speed.

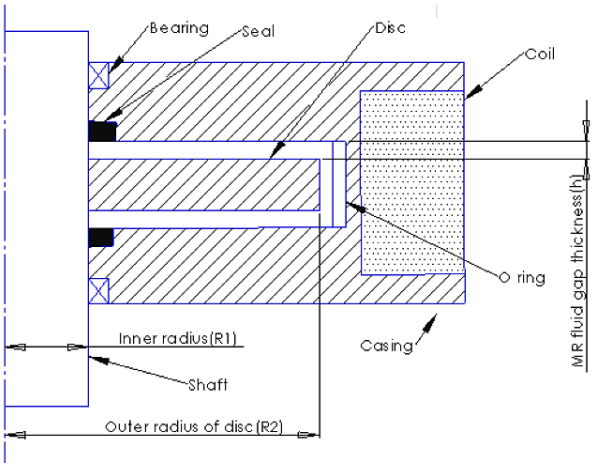

Fig.1 Schematic of MR brake with conventional disc

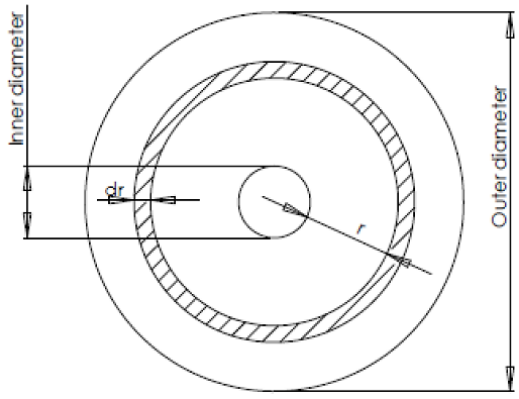

Fig.2 Geometry of conventional disc

The area of the element shown in the Figure 2 is shown in Eq. (2).

$$da = 2\pi r dr \quad (2)$$

The resisting force on the disc surface will act due to the shear stress of the MR fluid. The force acting on the element is

$$dF = \tau(2\pi r dr) \quad (3)$$

$$dF = \left(\tau_o + \eta \frac{du}{dy}\right)(2\pi r dr) \quad (4)$$

For MRF 241ES, $\alpha = 2.78\times10^{-4}\left(m/A\right)^{1.5}$ and β = 1.5.

The braking torque acting on the disc is

$$dT = \int_{R1}^{R2} h\left(\tau_o + \eta \frac{du}{dy}\right)2\pi r dr \quad (5)$$

Therefore, the total braking torque with two working surfaces is given as

$$T = 2\pi h \tau_o\left(R_2^2 - R_1^2\right) + \frac{4\pi\eta\omega}{3h}\left(R_2^3 - R_1^3\right) \quad (6)$$

3. Mathematical Modeling of MR brake using Waveform boundary disc

In finite element analysis for multi-plate MR brake (Sarkar and Hirani, 2015) estimated brake torque was approximately 300 Nm, which is lesser than the required braking torque for automotive applications. In order to enhance the braking torque, comprehensive study of MR brake is required. One way is to explore additional modes, i.e. compression, squeeze, of MR fluids. To implement compression and squeeze modes of MR fluid, there is a need to change in design of rotating disc and brake assembly. Nam and Ahn (2009) introduced waveform shaped disc in MR brake. Two such wave-formed discs, as shown in Figure 3 and Figure 4, have been explored in the present manuscript.

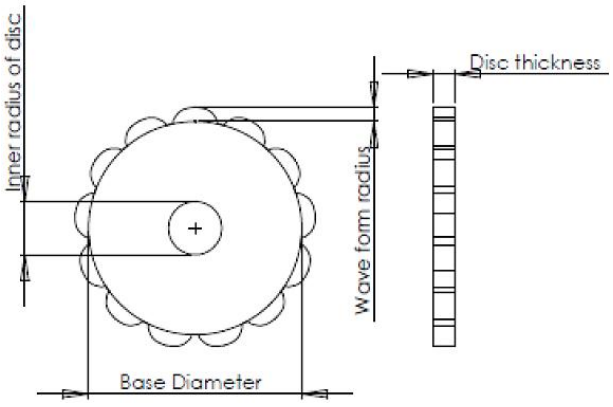

Fig.3 Disc with parabolic waveform

Due to the waveform boundary, a wedge shape is formed between the outer fixed casing and the disc. This wedge shape provides the extra resisting force to stop the rotation of the disc due to the shear stress of the MR fluid is changed with the influence of the applied magnetic field. The wedge shape and the fixed casing are shown in Figure 5.

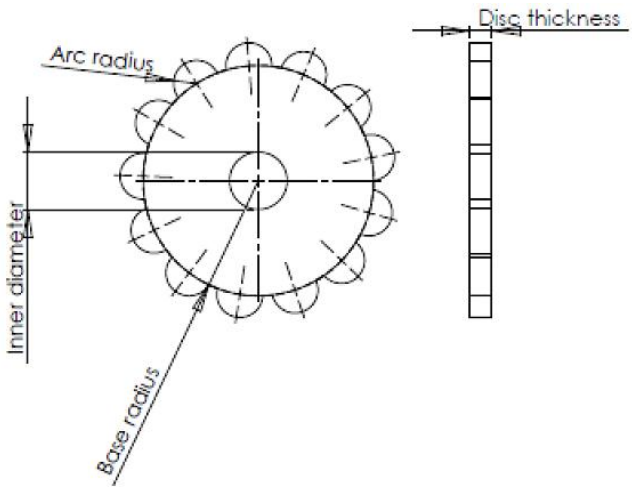

Fig.4 Disc with circular waveform

The friction force generated is given in Eq. (7).

$$F = \int_0^t \int_0^l \tau dx dz \quad (7)$$

t = thickness of the disc

l = contact length of the wave form.

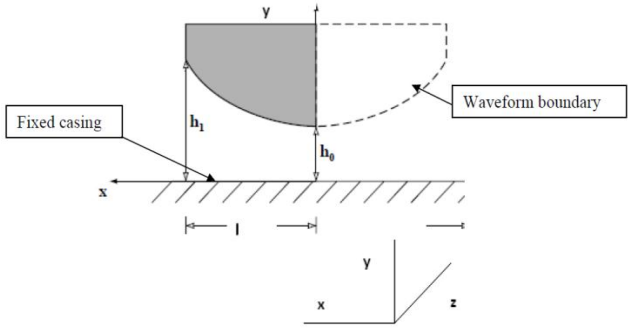

Fig.5 Schematic diagram of parabolic wedge shape

The braking action in MR brake is achieved due to change in shear stress of MR fluid in the presence of the magnetic field. The shear stress of MR fluid is modeled as the Bingham model as in Eq. (8).

$$\tau = \tau_0 + \eta \frac{du}{dy} \quad (8)$$

So the frictional force after putting the value of shear stress from Eq. (8).

$$F = \int_0^t \int_0^l \left(\tau_0 + \eta \frac{du}{dy}\right) dx dz \quad (9)$$

So the resistance force generated due to the first term of the equation.

$$F_1 = \tau_0 l t \quad (10)$$

Where, $\tau_0 = \alpha \left(\frac{NI}{2h}\right)^{\beta}$

Resistance force due to the viscosity of MR fluid is

$$F_{vis} = \int_0^t \int_0^l \eta \frac{du}{dy} dx dz \quad (11)$$

$\frac{du}{dy}$, obtained from the differentiating the velocity equation and given as

$$u = \frac{1}{2\eta}\frac{\partial p}{\partial x} y(y-h) + \frac{(y-h)U}{h} \quad (12)$$

U is the constant velocity of the disc. Then from Eq. (12)

$$\frac{du}{dy} = \frac{1}{2\eta}\frac{\partial p}{\partial x}(2y-h) - \frac{U}{h} \quad (13)$$

Then the viscous force

$$F_{vis} = \int_0^t \int_0^l \frac{1}{2\eta}\frac{\partial p}{\partial x}(2y-h) dx dz - \int_0^t \int_0^l \frac{U}{h} dx dz \quad (14)$$

The friction force will be maximum at the lower surface (y = 0) so the maximum force

$$F_{vis} = \int_0^t \int_0^l \frac{1}{2\eta}\frac{\partial p}{\partial x}(-h) dx dz - \int_0^t \int_0^l \frac{U}{h} dx dz \quad (15)$$

The film geometry for the parabolic profile is

$$h = h_0 + (h_1 - h_0)\left(1 + \frac{x}{l}\right)^2 \quad (16)$$

The film geometry for the spherical wedge profile is

$$h = h_1 - \sqrt{(h_1 - h_0)^2 - x^2} \quad (17)$$

The resisting torque has been calculated for the parabolic profile and for the circular profile by putting the value of h from the Eq. (16) into the Eq. (15) after integrating Eq. (15) and applying the boundary condition

p = 0 at x = 0 and p =0 at x = 1.

The integration of first term of Eq. (15) is

$$l_1 = \frac{h_1 - h_0}{l}(1+l) p t l$$

$$l_1 = \frac{h_1 - h_0}{l}(1+l) w$$

And $w = \frac{6U\eta l t^2}{k^2 {h_0}^2}\left(-\ln(K+1) + \frac{2K}{K+2}\right)$

Where $K = (h_1 - h_0)/h_1$then

$$l_1 = \frac{(h_1 - h_0)}{l}(1+l)\frac{6U\eta l t^2}{k^2 {h_0}^2}\left(-\ln(K+1) + \frac{2K}{K+2}\right) \quad (18)$$

The integration of the second term of the equation will be.

$$l_2 = \frac{tU\eta h_0}{\sqrt{K}}[tan^{-1}R] \quad (19)$$

Where $R = \left(1 + \frac{l}{t}\right)\sqrt{K}$

The total resisting force due to the parabolic profile

$$F_{total} = \left(l_1 + l_2 + \alpha(NI/2h)^{\beta} lt\right) \times no\,.ofarc \quad (20)$$

Braking torque from the frictional resistance force due to the waveform boundary is

$$T_{waveform} = F_{total} \times R_2$$

Total braking torque acting on the rotating disc will be the combination of the braking torque due to the waveform boundary and the braking torque due to the conventional disc (T).

Total braking torque

$$T_{total} = T_{waveform} + T \quad (21)$$

Total braking for the parabolic waveform is larger than the circular waveform, the theoretical results discussed below.

3. Results and Discussions

Considering the values of τ_o (= 56 kPa), h (= 1 mm), R_1 (= 50 mm) and ω (= 30 rad/s), the braking torque of MR brake has been estimated using Eq. (6) and plotted in Figure 6.

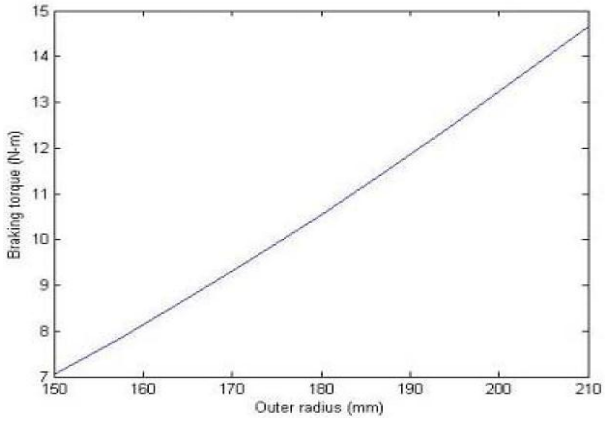

Fig.6 Braking torque of MR brake using conventional disc

It shows that the braking torque is limited to 14.5 Nm. To enhance the braking torque, analyses have been performed using waveform boundary disc.

Considering the values of τ_o (= 56 kPa), h (= 1 mm), h_o (= 8 mm), R_1 (= 50 mm) and ω (= 30 rad/s), the braking torque of MR brake has been estimated using Eq. (21). Figure 7 and Figure 8 show the braking torque at t = 10 mm and at t = 8 mm.

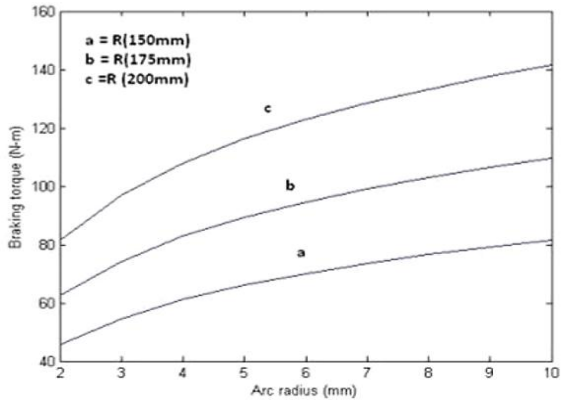

Fig.7 Braking torque with respect to focal distance of parabolic profile

Figure 7 and Figure 8 show that the braking torque is increasing as the radius of the waveform and thickness of the disc is increasing. Figure 9 and Figure 10 show the braking torque of MR brake for same thickness (t = 8 mm) for parabolic and circular profile respectively. From the Figure 9 and Figure 10 it is clear that braking torque achieved with the parabolic profile is larger than the circular profile.

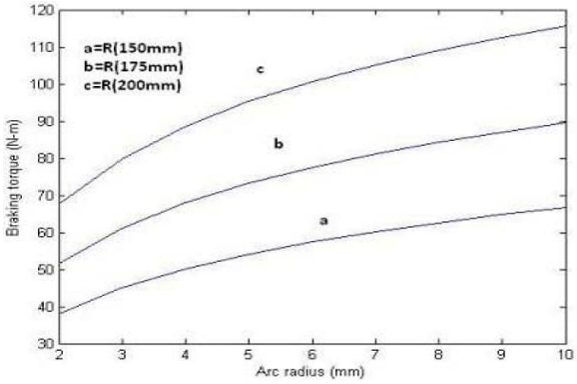

Fig.8 Braking torque with respect to focal distance of parabolic profile

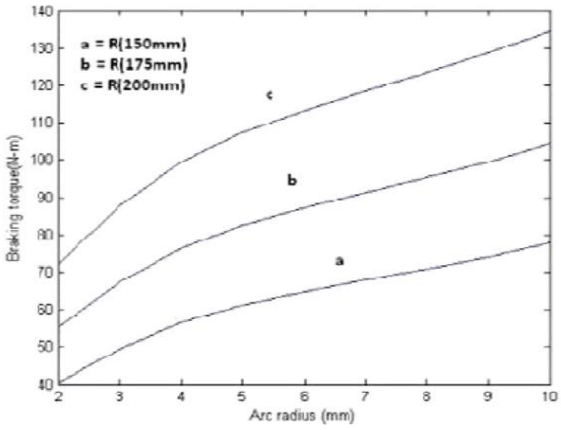

Fig.9 Braking torque with respect to arc radius of parabolic profile

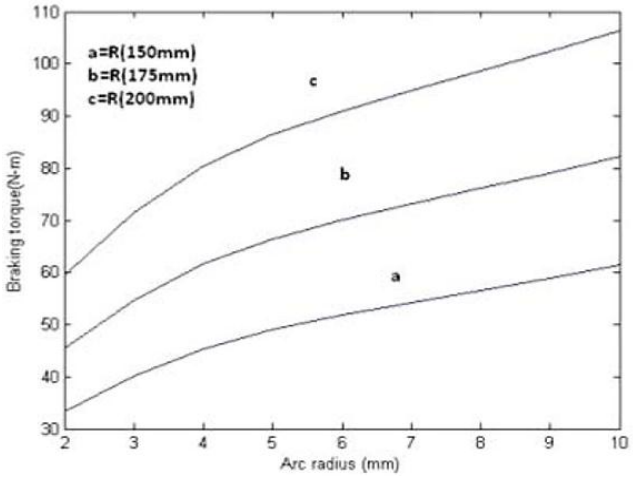

Fig.10 Braking torque with respect to arc radius for circular profile

Figure 11 and Figure 12 show the braking torque of MR brake at various MR gaps for parabolic profile and circular profile respectively.

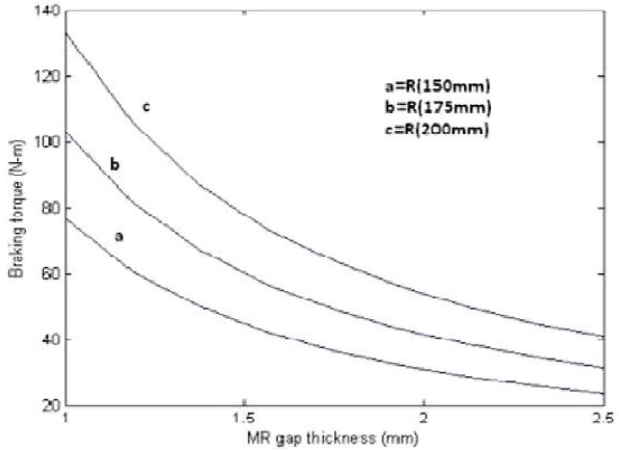

Fig.11 Braking torque with respect to MR film thickness for parabolic profile

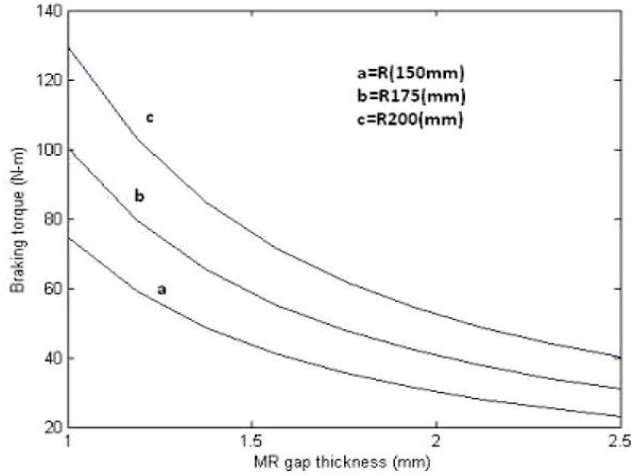

Fig.12 Braking torque with respect to MR film thickness for circular profile

From Figure 11 and Figure 12, it is clear that the braking torque is decreasing as the film thickness is increasing because due to increase in the MR gap thickness the magnetic field in the gap become weaker. Figure 13 shows the braking torque of MR brake at various input currents.

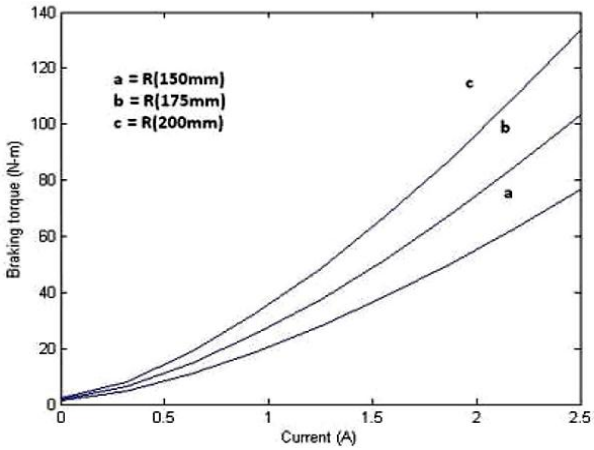

Fig.13 Braking torque with respect to applied current

From Figure 13 it is clear that braking torque is increasing as the applied current is increasing at the fixed no of coil due to the increase in the shear stress in the influence of magnetic field. At the zero value of the current there is some value of the resisting torque due to the no field viscosity of the MR fluid. The details drawing and model of fabricated MR brake with wave form boundary is shown in Figure 14.

Fig.14 Disc with waveform boundary

Conclusions

This research work has discussed the effect of different parameters on the braking torque of MR brake. The following conclusions can be made from the present research work.

- Braking torque is increasing as the radius of the waveform and thickness of the disc is increasing.
- Braking torque achieved with the parabolic profile is larger than the circular profile.

- Braking torque is decreasing as the film thickness increases.
- With increase in applied current, there is an increase in braking torque.

References

C.Sarkar, H.Hirani, (2013), Theoretical and experimental studies on a magnetorheological brake operating under compression plus shear mode, *Smart Materials and Structures*, 22, art. no. 115032.

C.Sarkar, H.Hirani, (2013), Synthesis and characterization of antifriction magnetorheological fluids for brake, *Defence Science Journal*, 63, pp. 408-412.

C.Sarkar, H. Hirani, (2013), Design of a squeeze film magnetorheological brake considering compression enhanced shear yield stress of magnetorheologicalfluid, *Journal of Physics: Conference Series*, 412, 012045.

C. Sarkar, H. Hirani, (2015), Transient thermoelastic analysis of disk brake, International Journal of Current Engineering and Technology, 5, pp. 413-418.

C. Sarkar, H. Hirani, (2015), Magnetorheological smart automotive engine mount, International Journal of Current Engineering and Technology, 5, pp. 419-428.

C. Sarkar, H. Hirani, (2015), Finite element analysis of magnetorheological brake using ANSYS, International Journal of Current Engineering and Technology, (accepted).

C. Sarkar, H. Hirani, (2015), Synthesis and characterization of nano-copper-powder based magnetorheological fluids for brake, International Journal of Scientific Engineering and Technology, 4, pp. 76-82.

C.Sarkar, H.Hirani, (2015), Effect of particle size on shear stress of magnetorheological fluids, *Smart Science,* (in press).

C. Sarkar, H. Hirani, (2015), Development of magnetorheological brake with slotted disc, *Proc. IMechE, Part D: Journal of Automobile Engineering*, (in press).

H.Hirani, C. S. Manjunatha, (2007), Performance evaluation of magnetorheological fluid variable valve, *Proc. of the Institution of Mechanical Engineers, Part D, Journal of Automobile Engineering*, 221, pp. 83-93.

J. M. Ginder, L. C. Davis,(1994), Shear Stresses in Magnetorheological fluids: Role of Magnetic Saturation, Applied Physics Letters, 65, pp. 3410-3412

T. H. Nam and K.K. Ahn, (2009), A new structure of a magnetorheologicalbrake with the waveform boundary of arotary disk", Smart Mater.Struct.18, 15029

S. Gupta, H. Hirani, (2011), Optimization of magnetorheological brake, *ASME/STLE 2011 International Joint Tribology Conference*, pp 405-406.

V.K.Sukhwani, V.Lakshmi, H. Hirani, (2006), Performance evaluation of MR brake: an experimental study, *Indian Journal of Tribology*, pp. 67-52.

V.K.Sukhwani,H.Hirani,T.Singh,(2007), Synthesis of magnetorheologicalgrease,*Greasetech India*.

V.K.Sukhwani, H.Hirani, (2007), Synthesis and characterization of low cost magnetorheological (MR) fluids, *The 14th International Symposium on: Smart Structures and Materials & Nondestructive Evaluation and Health Monitoring*, 65262R-65262R-12.

V.K.Sukhwani, H.Hirani, (2008), A comparative study of magnetorheological-fluid-brake and magnetorheological-grease-brake, *Tribology Online*, 3, pp. 31-35.

V.K.Sukhwani, H.Hirani, T.Singh, (2008), Synthesis and performance evaluation of MR grease, *NLGI Spokesman*,71.

V.K.Sukhwani, H. Hirani, (2008), Design, development and performance evaluation of high speed MR brake, *Proc. Institute Mech. Engineers., Part L, Journal of Materials: Design and Applications*, 222,pp.73-82.

V.K.Sukhwani, H.Hirani, T. Singh, (2009), Performance evaluation of a magnetorheological grease brake, *Greasetech India*, 9,pp. 5-11.

OPEN ACCESS

International
Journal
Of Modern Engineering Research (IJMER)

Design, Analytical Analysis, Instrumentation and Flow Simulation of Sub-Sonic Open Circuit Wind Tunnel Model

Tomar Vishvendra Singh[1], Sangwan Vipul[2], Singh Shaktiman[3], Singh Raj Kumar[4], Agrawal Jubin[5]

[1,2,3,4]*Department of Mechanical Engineering, Delhi Technological University, Delhi, 110042, India*
[5]*Department of Mechanical Engineering, ABES-IT, Ghaziabad, 201009, India*

ABSTRACT: *The Wind Tunnel is well known for its enormous amount of potential in Civil, Environmental, Automobile and Aeronautical applications. In today's world, Everyone's main focus is to save time, material and money which have compelled us to opt for the experimental testing on scale models, before the final product is to be shaped. The Wind Tunnel is one such platform, which provides us the appropriate desired environment conditions around the model scaled to the compatible dimensions. Therefore, to develop the favorable conditions, the design of the tunnel plays the foremost role in its proper functioning. In this paper, knowing the intricacy of the tunnel's requirements, A Sub-Sonic Open Circuit Wind Tunnel (SOWT) Model is developed and simulated, having a Mach Number (M) of 0.15. The guiding dimensions taken for the Test Chamber are: Length (L_T) = 45cm, Height (H_T) = 18cm and Width (W_T) = 24cm with maximum operating speed to be 50m/s. Using these, the secondary design parameters were estimated and the design is finalized. Moreover, the instrumentation of the Tunnel including Data Acquisition Systems (DAQs) is reviewed.*

Keywords: *Sub Sonic Open Circuit Wind Tunnel, Mach number, Boundary Layer Modeling Parameters, Model Testing and Simulation.*

I. Introduction

Today, the wind tunnel is an indispensable part of development of modern aircraft, automobile etc as no one would contemplate committing an advanced design without first measuring its stability, lift and drag properties. The utility of the wind tunnel is obvious, but it was not the first aerodynamic test device. The quest to measure drag and various aspects of aviation theory started with the very first advancement in aviation with the introduction to whirling arm. The whirling arm apparatus (4 feet long) was developed by Benjamin Robins (1707-1751), a brilliant English mathematician. It spun by a falling weight acting on a pulley and spindle arrangement having velocities of only a few feet per second at the arm tip (top speeds ranging from 3 to 6 m/s). The large amount of turbulence posed serious problems in front of experimenters like in determination of the true relative velocity between the model and air. Also, it was difficult to mount the instruments and measure the small forces exerted on the model when it was spinning at high speeds. Francis Herbert Wenham (1824–1908), a council member of the Aeronautical Society of Great Britain, addressed the issue by inventing, designing and operating the first enclosed wind tunnel in 1871. After some of the experimental studies, it was found that lift-to-drag ratios were very high as such wings could support substantial loads, making powered flight which seemed much more attainable than previously thought possible. Further research work revealed the effect of what is now known as aspect ratio: long, narrow wings, like those on modern gliders, provided much more lift than stubby wings with the same areas [1-3].

Wilbur Wright (1867-1912) and Orville Wright (1871-1948) built their first flying machine in August 1899 and then their first unpowered manned glider in 1900. However, the glider was generating far less lift and more drag than they expected. They developed a simple experiment using natural winds to compare the relative lifting forces of flat and cambered surfaces. Then they built an aerodynamic balance that showed unambiguously, which test airfoil (among the two being tested) can develop more lift. Thus for the first time "Wind Tunnel without Walls" was subjected to test. It confirmed the accepted aerodynamic design tables that they were using, were seriously in error. This helped them in rectification of the wing area, airfoil curvature. During the experimental work, they reached at conclusion that without synthesizing a well equipped wind tunnel they could not continue their work anymore as such they developed the wind tunnel in its true sense and helped themselves to trigger the flight! [1, 4]

Wind tunnels are designed for a specific purpose and speed range. Therefore, there are different types of wind tunnels and several different ways to classify wind tunnels. On the basis of Speed Regime developed in the test section relative to the speed of sound (Mach Number 'M'), Wind Tunnels are classified as subsonic (M < 0.8), transonic (0.8 < M < 1.2), supersonic (1.2 < M < 5.0), hypersonic (M > 5.0). On the basis of Tunnel Geometry, Wind tunnels are classified as Closed Circuit Wind tunnel (CCWT) and Open Circuit Wind Tunnel (OCWT) (Fig. 1). A wind tunnel that is closed and re-circulates the air through the test section is called a Closed Circuit Wind Tunnel. A wind tunnel that is open on both ends and draws air from the atmosphere into the test section is called an Open Circuit Wind Tunnel [5, 6].

(a) Closed Circuit Wind Tunnel **(b) Open Circuit Wind Tunnel**

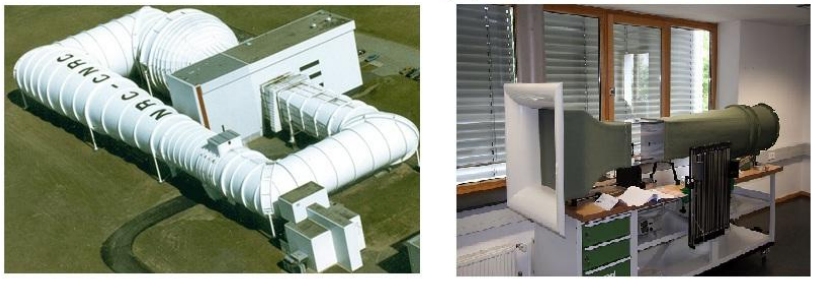

Fig. 1: Classification of Wind Tunnels on the basis of Tunnel Geometry as (a) Closed Circuit Wind Tunnel and (b) Open Circuit Wind

The OCWTs Models are used to investigate the different automotive designs by testing on scale models of cars, trucks etc. Airflow over a vehicle determines the drag forces, which in turn affects the vehicle's performance and efficiency. The three basic forces are lift, drag, and side force as measured in an axis system referenced to the direction of the vehicle. The concept of Lift and Drag can be understood with the help of airfoil. The airfoil long in the direction perpendicular to the plane of the drawing and the flow can be considered as two dimensional. The airfoil is tilted with respect to the (undisturbed) flow direction, defined by the angle of attack (AOA). The force experienced by airfoil is F_R. Decomposing the force F_R into components F_L and F_D {Given by (1) and (2)} perpendicular and parallel to the flow direction. F_L is termed as lift force and F_D is termed as drag force, the resistance to be balanced by the propulsion force generated by the engines (Fig. 2). The expressions for Lift and Drag Forces are as follows:

$F_L = 0.5\, C_L\, \rho\, A_1\, u^2$ ….(1)

$F_D = 0.5\, C_D\, \rho\, A_2\, u^2$ ….(2)

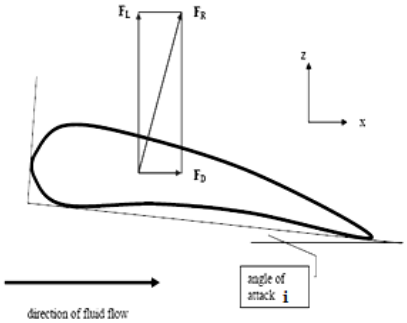

Fig. 2: Lift and Drag Forces on Airfoil subjected to fluid flow

The designer of an airplane tries to maximize C_L and to minimize C_D. C_L and C_D are dependent on the angle of attack. Usually the C_L drops sharply and C_D increases strongly at i = 15° (approx.) [7].

Wind tunnels have been used widely to simulate airflow about complete aircraft, specific aircraft components, and to conduct fundamental research concerning flow phenomena related to flight for over a century. Wind tunnels are made in different shapes and sizes, from just 30 cm long to large enough to contain a passenger airplane. The various sorts of Wind Tunnels find potential applications in estimation of pollution dispersion level near the building, investigation of wind-driven rain and building envelop, various aspects of wind loading on roofs and wind effects on towers and bridges. In Wind Engineering, wind tunnel tests are used

to measure the velocity around, and forces or pressures upon structures. Very tall buildings, buildings with unusual or complicated shapes (such as a tall building with a parabolic or a hyperbolic shape), cable suspension bridges or cable stayed bridges are analyzed in specialized atmospheric boundary layer wind tunnels. The basic idea behind all wind tunnels is universal. Depending upon the situations like thermal and hydraulic testing, it generates uniform air flows with low turbulence intensity. The aerodynamic principles of the wind tunnel work equally on watercraft, except the water is more viscous and so sets greater forces on the object being tested. External flow tunnels are used to study the external flow through the chassis climatic tunnels and used to evaluate the performance of door systems, braking systems etc. under various climatic conditions. Aero-acoustic tunnels are used in the studies of noise generated by flow and its suppression. Wind tunnel tests are also performed to measuring the air movement of the fans, Turbine Blades, Propellers etc at a specific pressure exactly [3, 8-12].

A lot of research work have been accomplished to optimize the Wind Tunnel Design and still to make it better at various levels depending upon the situations research work is still in progress. Peter et al. in their work, focused on the wind tunnel test section flow quality and its application to a numerical CCWT by studying the effects of various variables for its evaluation [8]. Diana et al. evaluated the design criteria that supported the choice of the original solution for potential application of a new large wind tunnel in Civil, Environmental and Aeronautical aspects and discussed the feasibility of a plant on the basis of experimental analysis on a 1:9 scale model [13]. Lohan [14] focused on the design and application of LSWTs having well-defined, controllable, uniform flow of air for experimental and design validation purposes. Senol and Cinar with the help of Flow Simulation Fluent 6.0 program corrected the earlier developed design of a suction-type SOWT by simulating it in computer environment [15]. Eckert et al. discussed some Aerodynamic design guidelines and computer program for estimation of SSWT performance [16]. The enormous amount of research work and experiments undertaken in wind tunnels and their importance for human life motivated the high demands that are posed on optimum design level for Wind Tunnels against the minimum cost with optimum output. This paper deals with the Sub-Sonic Open Circuit Wind Tunnel (SOWT) with negligible effect of compressibility. Following the research works and significant guidelines related to design consideration, the design for SOWT Model is developed. The Mach Number of 0.15 allows it to use for aerodynamics tests and performance of some scale models having speeds around 150 km/hr.

II. Design of Sub Sonic Open Circuit Wind Tunnel Model

The Wind tunnels cannot be perfect simulations of environmental conditions, but up to some extent they can be treated as ideal to surrounding conditions. The degree to which they are flawed is measured with the help of Reynolds Number. The SSWTs are designed to provide a well-defined, controllable, uniform flow of air for experimental and design validation purposes. These tunnels when applied as open circuit cannot be used where a very high accuracy level and precise results are required due to their inability to control air flow up to a large extent. However, with proper designs and controlled instrumentation, these tunnels can be made to produce accurate results within close limit to practical value. The major advantage associated with this tunnel is its Set-Up and Maintenance Cost, which is very small as compared to CCWT. The leading manufacturer of automobiles use the OCWTs for the Drag and performance estimation of the vehicles as with current technology & designs, these tunnels are giving results quite close to practical values under proper calibrations.

The OCWT (Fig. 3) consists of five basic parts, which are (From front to back) the Settling Chamber, the Contraction Cone, the Test Section, the Diffuser and the Drive Section. The Settling Chamber is at the very front of the wind tunnel and is made up of screens and honeycomb-shaped mesh, which straighten out the air and reduce turbulence. The Contraction Cone forces a large volume of air through a small opening in order to increase the wind velocity in the tunnel, as there is gradual decrease in area. The Test Section is the place where a model is mounted on sensors. The Diffuser is at the end of the Test Section and keeps the air running smoothly as it goes toward the back. It also increases in volume in order to slow the air down as it exits the tunnel. The Drive Section is at the very back of the wind tunnel, and it is where the fan is housed and draws air into the wind tunnel by blowing air out of it and hence reduces turbulence along with greater control of the airflow through the tunnel. The decisive characteristic of wind tunnels lies in the flow quality inside the test chamber and the overall performances.

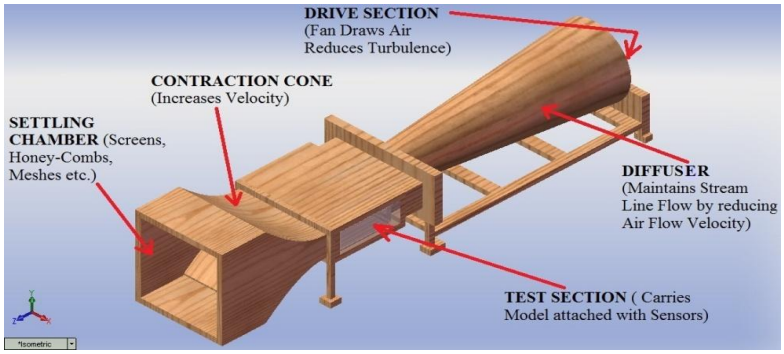

Fig. 3: Isometric View of Sub-Sonic Open Circuit Wind Tunnel Model developed Solid-Works

Three main criteria that are commonly used to define them are: maximum achievable speed, flow uniformity and turbulence level. Hence in general, the design aim of a wind tunnel is to get a controlled flow in the test chamber, achieving the necessary flow performance and quality parameters. The main specifications for a wind tunnel are the dimensions of the test section and the desired maximum operating speed. Also, it is crucial to avoid flow separation close to the walls of the contraction zone. In the subsequent sections, the design of each of the component of the Wind Tunnel is developed one by one, from the design of the Test Chamber to the Diffuser.

2.1 Test Chamber Design

The test chamber (Fig. 4) is the most delicate part of the tunnel and is also called as "The Heart of the Wind Tunnel" as it is the region for experimental study, carrying the scale model, sensors etc along with the controlled flow. Its size must be defined according to the wind tunnel main specifications, which also include the operating speed and desired flow quality. Its size and operating speed determine the maximum size of the models and the maximum achievable Reynolds number. In most of the cases, its cross-section is square in shape and its area should be decided according to the scale model which is going to be tested. The equivalent frontal area of the model should not be higher than 10% of the test chamber cross-sectional area. The width to height ratio adopted for 3-D Tests is 4:3. The Test Section Assembly is composed of the Test Section (Plexiglas) to avoid pressure loss and the Test Section Base (wooden stand and sensor mounts) [14-19].

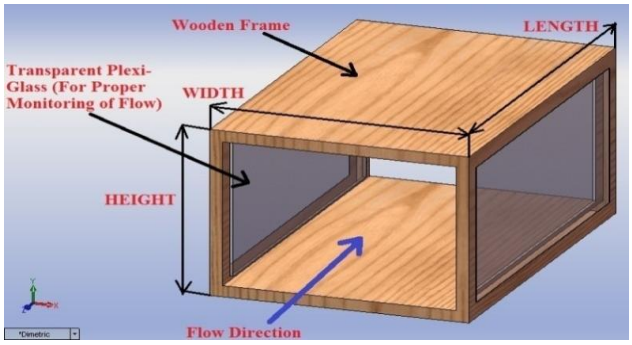

Fig. 4: Dimetric View of The Test Chamber developed using Solid-Works.

2.2 Contraction Cone Design

The Contraction Cone is the most important part in the design of a Wind Tunnel as it has the highest impact on the Test Chamber flow quality. It accelerates the flow from the Settling Chamber to the Test Chamber as such also known as 'Nozzle'. It also helps in reduction of flow turbulence and non-uniformities in the test chamber. The flow acceleration and non-uniformity attenuations mainly depend on the ratio of cross-section area of inlet to that of exit, termed as contraction ratio (**N**). Theoretically, the value of N should be as large as possible but it has an upper limit as it strongly influences the overall wind tunnel dimensions and hence its cost. For the Wind Tunnels used in civil or industrial applications, a contractions ratio between 4.0 and 6.0 may be sufficient reducing the flow turbulence and non-uniformities levels to the order of 2.0%, which is acceptable for many applications. Further with just one screen placed in the settling chamber it reduces to 0.5%. Even this is a very reasonable value for some aeronautical purposes.

$$\mathbf{N}\ (\text{Contraction Ratio}) = \frac{\text{Area at entry of C.C.}}{\text{Area at exit of C.C.}} \quad \ldots(3)$$

The second characteristic of the contraction Cone is its shape, taking into account that the contraction is rather smooth. For this 1-D (One-Dimensional) approach to the flow analysis is applied to determine the pressure gradient along it. The important point of consideration is the pressure distribution on the contraction walls, as if it has some regions with adverse pressure gradient, it may produce local boundary layer separation which can increase the turbulence level considerably, resulting in poor flow quality in the test chamber. The solution to this is to make the ratio of the radius of curvature to the flow width about the same at each end. But at the upstream end the radius of curvature cannot be too large as it leads to slow acceleration and therefore increased rate of growth of boundary-layer thickness which causes centrifugal instability in the tunnels having laminar flow. The contraction semi-angles: $\alpha/2$ and $\beta/2$ are taken to be in the order of 12º, this causes the contraction cone to possess a reasonable length and a good fluid dynamic behavior. Bradshaw et al. recommended two segments of third degree polynomial curves for deciding the exact curve (Fig. 5) for the Contraction Cone [14-20]. The polynomials are:

$y = a_W + b_W x + c_W x^2 + d_W x^3$ ….(4)

$y = a_N + b_N x + c_N x^2 + d_N x^3$ ….(5)

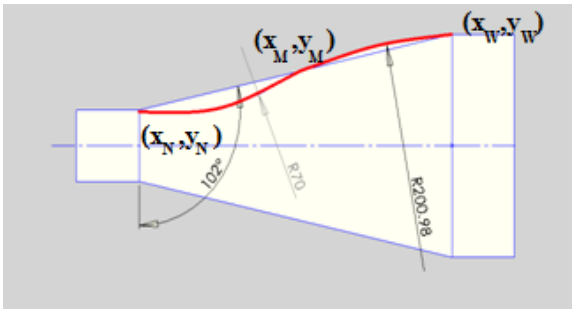

Fig. 5: Fitting Polynomial for the Contraction Cone Curve developed using Solid-Works

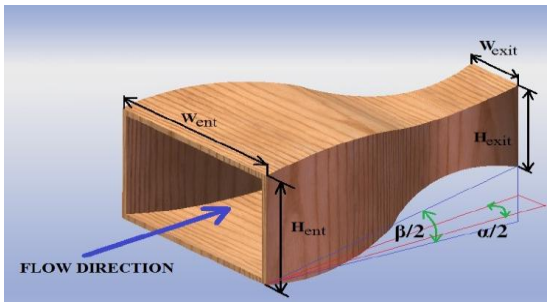

Fig. 6: Isometric View of The Contraction Cone developed using Solid-Works

The Contraction Cone developed using the above curve (Fig. 6) doesn't allow boundary layer to separate and keep boundary layer thickness within certain limit. It provides the favorable flow to the Test Chamber.

2.3 Settling Chamber Design

The Settling Chamber (Fig. 7) is the very first region designed to provide controlled high quality flow to the Contraction Cone by attenuating the various flow components responsible for turbulence. To develop high quality flow some devices like screens and honeycombs etc are installed to increase the flow uniformity and to reduce the turbulence level at the entrance of the contraction cone. They produce a relatively high total pressure loss. Honeycomb is very efficient at reducing the lateral turbulence, as the flow pass through long and narrow pipes. But the problem with Honeycombs is, it introduces axial turbulence of the size equal to its diameter which restrains the thickness of the honeycomb. To tackle this problem, Screens are introduced as they reduce longitudinal turbulence very efficiently. In this case, the problem is that in the Contraction Cone the lateral turbulence is less attenuated than the longitudinal one. Hence, to obtain better flow characteristics, a combination of Honeycombs and Screens is used. This configuration requires the honeycomb to be located upstream of 1 or 2 screens [14-21].

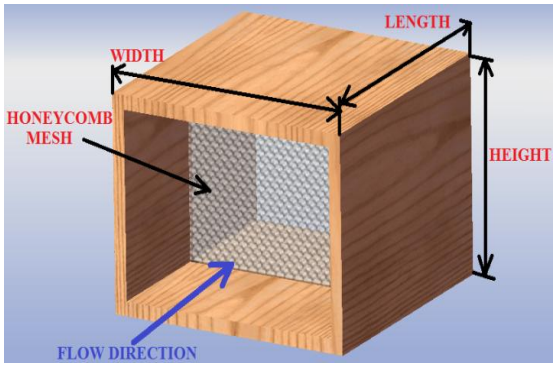

Fig. 7: Isometric View of The Settling Chamber developed using Solid-Works

2.4 Diffuser Design

The Diffuser (Fig. 8) plays an important role in controlling the flow quality inside the Test Chamber by avoiding the flow detachment as in case of flow detachment; the pressure pulsation is transmitted upstream into the test chamber, resulting in pressure and velocity non-uniformities. To avoid flow detachment, the maximum semi-opening angle in the diffuser has to be smaller than 3.5° [14-21].

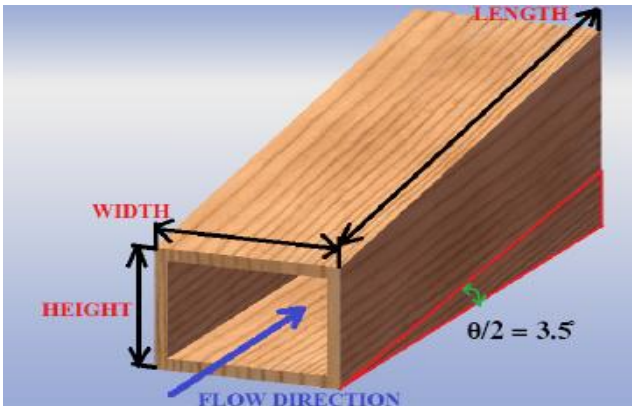

Fig. 8. Dimetric View of The Diffuser developed using Solid-Works.

III. Analysis of Sub Sonic Open Circuit Wind Tunnel Model

The Primary Design Parameters for the overall design of the Wind Tunnel include Test chamber dimensions i.e. Width (W_T), Height (H_T) and length (L_T). With the help of these parameters cross-sectional area of the Test Chamber can be calculated as $A_T = W_T.H_T$. The hydraulic diameter is given by the relation [14-21]:

$$D_T = \frac{2\,W_T\,H_T}{(W_T + H_T)} \quad \ldots.(6)$$

The Contraction ratio (N) is taken 5 for the Wind Tunnel with Mach number (M=0.15), having Maximum operating speed (V_T) to be 50 m/s. These Design variables can be summarized in the Table. 1. The dimensions for the Test Section are W_T = 24cm, H_T = 18cm, L_T = 45cm and the V_T is taken to be 50m/s which gives us the Mach Number (M) to be 0.15. So, The Designing of all other parts is done based on these dimensions with N = 5. The semi angle in the Contraction Cone (α/2) is taken as 12° and the semi angle in the Diffuser (θ/2) is taken as 3.5° . The non dimensional lengths for the Settling Chamber (l_S) and Diffuser (l_D), for Sub-Sonic Open Circuit Flow, are taken as 0.5 and 3.2 respectively. The calculated parameters are displayed in Table. 2. And the final design for this analytical analysis is represented by (Fig. 9). The total length of the SOWT is:

$$\mathbf{L_{WT} = L_S + L_C + L_T + L_D} \quad \mathbf{\ldots.(7)}$$

$$\mathbf{L_{WT} = 26.83 + 45 + 69.78 + 76.80 = 218cm}$$

Hence, $\mathbf{L_{WT}}$ is equal to **218cm.**

Table. 1: The primary and secondary design parameters required for designing of SOWT Model

PRIMARY DESIGN PARAMETERS	SECONDARY DESIGN PARAMETERS
TEST CHAMBER WIDTH (W_T)	SEMI ANGLE IN CONTRACTION CONE (A/2)
TEST CHAMBER HEIGHT (H_T)	SEMI ANGLE IN DIFFUSER (Θ/2)
TEST CHAMBER LENGTH (H_T)	SETTLING CHAMBER NON DIMENSIONAL LENGTH (L_S)
CONTRACTION RATIO (N)	DIFFUSER NON DIMENSIONAL LENGTH (L_D)
MAXIMUM OPERATING SPEED (V_T)	SETTLING CHAMBER LENGTH (L_S)
MACH NUMBER (M)	CONTRACTION CONE LENGTH (L_C)
	DIFFUSER LENGTH (L_D)

Table. 2: Secondary design Parameters of SOWT Model

Secondary Parameters	Expressions	Values
Cross-Sectional Area of the Test Chamber (A_T)	$A_T = W_T H_T$	432 cm^2
Hydraulic Diameter of the Test Chamber (D_T)	$D_T = \frac{2W_T H_T}{W_T + H_T}$	20.57 cm
Length of The Contraction Cone (L_C)	$L_C = \frac{(\sqrt{N} - 1) W_T}{2\tan(\alpha/2)}$	69.78 cm
Length of The Settling Chamber (L_S)	$L_S = \sqrt{N}\ W_T\ l_S$	26.83 cm
Length of The Diffuser (L_D)	$L_D = W_T\ l_D$	76.80 cm

Fig. 9: Isometric View of the complete model of SOWT developed using Solid-Works

IV. Instrumentation of Sub Sonic Open Circuit Wind Tunnel Model

The instrumentation of wind tunnel emphasizes on the various instruments and Data Acquisition Systems (DAQs) required by a tunnel for its proper functioning, Pressure and Flow measuring ability, Flow Visualization and Image Acquisition. In the instrumentation of the tunnel, Standard data acquisition (DAQ), Motion Control, and Image Capture hardware play a very crucial role. Data acquisition is the process of sampling signals that measure real world physical conditions and converting the resulting samples into digital numeric values that can be manipulated by a computer. Data acquisition systems convert analog waveforms into digital values for processing. The various components of data acquisition systems are Sensors (convert physical parameters to electrical signals), Signal conditioning circuitry (convert sensor signals into a form that can be converted to digital values) and Analog-to-Digital converters (convert conditioned sensor signals to digital

values). Further, various operations can be integrated to the system including Flow Visualization with Image Acquisition, Multipoint differential pressure scanning, Hot Wire Anemometry, Force and Moment measurement using internal balances, Roll, Pitch and Yaw angle measurements, and Noise and Temperature measurements.

For Pressure and Flow Measurements, measuring devices coupled with DAQs like LabVIEW and pressure scanners etc. can be used. Similarly for Force and Moment Measurements, Six-component Strain Gauge Balances can be applied. And for Flow Visualization and Image Acquisition, light sheets using Argon-ion lasers with CCD cameras and recording system can be used to capture and analyze the exact trajectory of flow particles, even sometimes incorporating IMAQ hardware and software (IMAQ vision). With such a proper design and proper instrumentation, a wind tunnel can be used for Full-model tests with sting support mechanism, Half-model testing with external balance, Two-dimensional model testing, Ground effect simulation with moving belt, Gust and cross wind simulation, Aero-acoustic testing etc. For a Wind Tunnel with $M < 0.3$, the instrumentation required is not so much complex but still it requires attention for getting accurate and precise results [22-26].

V. Simulation of Sub Sonic Open Circuit Wind Tunnel Model

Solid-Works Flow-Express is a first pass qualitative flow analysis tool which gives insight into water or air flow inside the Solid-Works model. Using this, the simulation is carried out. The constants and assumptions used in the simulation study are tabulated as (Table. 3):

Table. 3: The constants and various parameters determining the environment conditions for the simulation of SOWT Model.

CONSTANTS AND VARIOUS PARAMETERS	VALUES
Inlet Pressure	100890 Pa
Outlet Pressure	100000 Pa
External Ambient Temperature	293.20° K
Gas Constant	287 J/kg° K
Kinematic Viscosity	1.714×10^{-5} Kg/m-s
Acceleration due to gravity	9.81 m/s^{-2}
Air Density	1.2251 kg/m^3
Entrance Speed	11.335 m/s

The flow velocity simulation of the designed Wind Tunnel have been performed (using particle flow visualization) under the above mentioned environment conditions (Fig. 10). Also, the variation of flow velocity against the length of the tunnel is obtained. Fig. 11 shows the flow speed changes within the wind tunnel. The lowest flow speed is occurred at the surfaces of the entrance section, at the corners joining the settling chamber and the contraction cone, and the diffuser exit. Flow speed accelerates while passing through the contraction and it reaches the highest required value (49.118 m/s ≈ 50 m/s) in the test chamber. Also the flow rate increases throughout the contraction and remains constant throughout the test chamber. Flow rate gradually decreases as air exits from the test chamber and enters into the diffuser. Further, at the diffuser exit, it reaches the same value with the wind tunnel entrance.

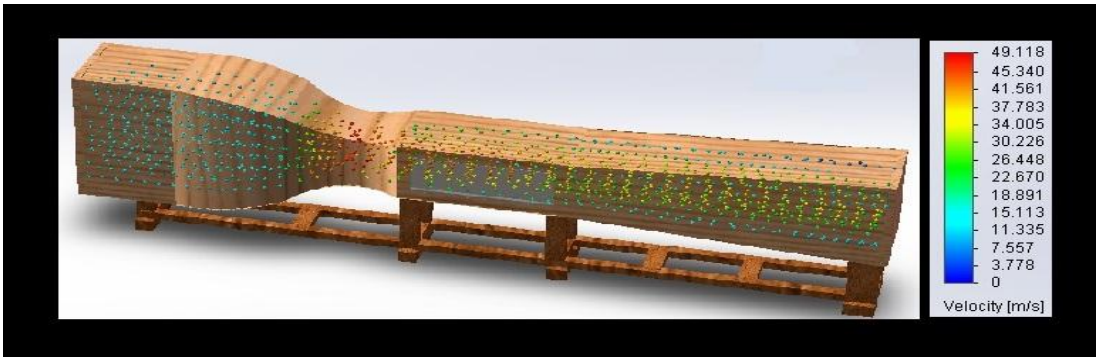

Fig. 10: Particle Flow Visualization of Air as fluid inside the SOWT, illustrating Velocity variation along the length of the Tunnel

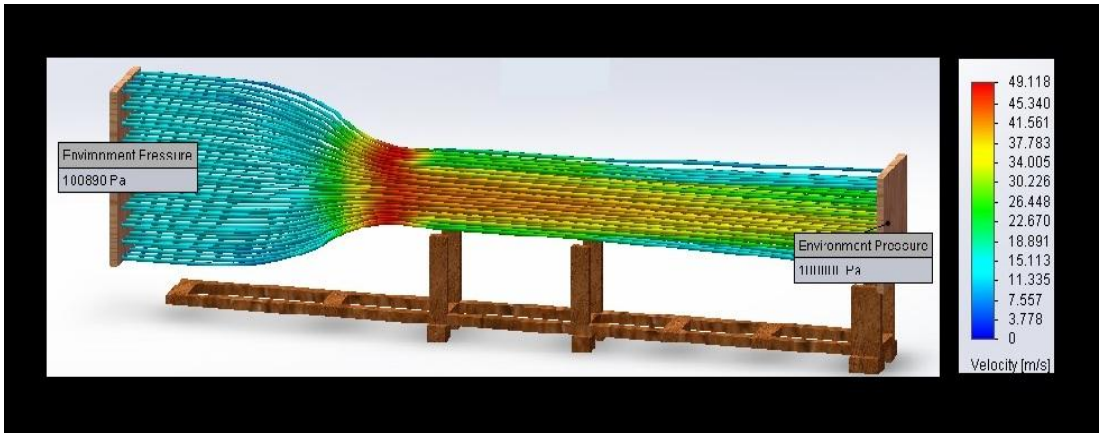

Fig. 11: Flow Velocity Variation of Air as fluid inside the SOWT along the length of the Tunnel

The graphic of static pressure distribution and velocity changes throughout the wind tunnel is shown in Fig. 12. The static pressure on the edges of the entrance section is the maximum value (100890 Pa.). It can be said that a major turbulence and counter pressure zone are created at these points. Static pressure values are closed to the each others at the settling chamber (x=2.5 ft.) and the diffuser exit (x=7 ft.). A bit of static pressure drop is occurred in the middle zone of the contraction cone. The pressure is reached to the lowest value at the test chamber exit. Since the static pressure changes are very small throughout the test chamber, it can be said that there is not any boundary layer thickening along the test chamber walls and the air flow quality is good.

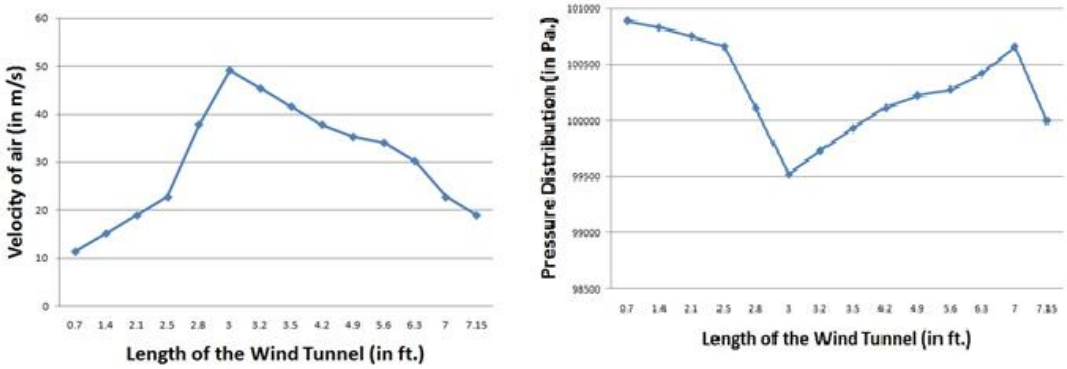

Fig. 12: Flow Velocity Variation (Quantitatively) and Pressure Distribution (Quantitatively) of Air as fluid inside the SOWT along the length of the Tunnel

VI. Conclusion

The design of Low Cost SOWT model has been generated. The main considerations like Boundary Layer Separation, Controlled Air Flow Quality, Turbulence Intensity, Stream Line Flow, Cost-Effectiveness, Design Ease and Mach Number (M = 0.15) etc were taken into the account and accordingly the model is designed. The primary design parameters of the Test Chamber were taken as the baseline and following the design guidelines, the secondary design parameters for approximately 220 cm tunnel were calculated. The Contraction Cone and the Test Chamber section were given special attention as they have direct influence on the scale model testing and the data generated. A brief insight is given to the instrumentation segment of the tunnel, especially to the various measurements and DAQs that are still playing their part in research and development concerning the various wind tunnel applications. The Velocity Variations and Static Pressure changes throughout this model were simulated. Moreover, the quantitative variation of Velocity and Pressure is plotted against the tunnel's length. With the final design, the maximum operating speed obtained at the test chamber is 49.12 m/s, quite close to desired value 50 m/s. The air flow obtained is of smooth quality with no boundary layer thickening process at the Test Chamber. Thus, the final SOWT Model design obtained can be used wherever the maximum operating velocity required is 50 m/s or 180 km/h, which generally is the case with the automobiles at high speeds.

References

[1]. Dodson, MG (2005), An Historical and Applied Aerodynamic Study of the Wright Brothers, Wind Tunnel Test Program and Application to Successful Manned Flight, US Naval Academy Technical Report, USNA-334.

[2]. Whirling Arms and the First Wind Tunnels, Wind Tunnels of NASA by Donald D. Baals and William R. Corliss, (Searched on Sept 1, 2013) http://www.grc.nasa.gov/WWW/k12/WindTunnel/history.html.

[3]. History, Origins of Wind Tunnel, NASA Aeronautics and Space Administration, http://en.wikipedia.org/wiki/Wind_tunnel (Searched on Sept 1, 2013).

[4]. Wright Brothers, National Memorial, Wind Tunnel Tests 1901, (Searched on Sept 1, 2013) http://www.cr.nps.gov/history/online_books/hh/34/hh34i.htm.

[5]. Types of Wind Tunnels, NASA Aeronautics and Space Administration, (Searched on Sept 1, 2013) http://www.grc.nasa.gov/WWW/k12/airplane/tuntype.html.

[6]. Science Buddies: How to Build a Subsonic Wind Tunnel (Searched on Sept 1, 2013) http://www.sciencebuddies.org/science-fair-projects/wind-tunnel-toc.shtml.

[7]. A Textbook of Fluid Mechanics and Hydraulic Machines, Dr. R. K. Bansal, Laxmi Publications Pvt. Ltd., New Delhi, Forces on Submerged Bodies, Page No. 657-659.

[8]. Peter Moonen, Bert Blocken, Jan Carmelieta, Indicators for the evaluation of wind tunnel test section flow quality and application to a numerical closed-circuit wind tunnel, Journal of Wind Engineering and Industrial Aerodynamics 95 (2007) 1289–1314.

[9]. Aly Mousaad, Alberto Zasso and Ferruccio Resta (2011), On the dynamics of a very slender building under winds: reponse reduction using MR dampers with lever mechanism, The Structural Design of Tall and Special Buildings.

[10]. Windless Wind Tunnels for High Altitude Tests, Popular Mechanics, February 1952, Page No-105.

[11]. J.E. Cermak, Wind tunnel for the study of turbulence in the atmospheric surface layer, Final Report Air Force Cambridge Center, Air Research and Development Command, Bedford, MA (Contract AF 19(604)-1706), 1958, 36 pages.

[12]. R.E. Whitbread, The measurement of non-steady wind forces on small-scale building models, in: Proceedings of the fourth International Conference on Wind Effects on Buildings and Structures, Heathrow, England, 1975, pages-567–574.

[13]. G. Diana, S. De Ponte, M. Falco, A. Zasso, A new large wind tunnel for civil-environmental and aeronautical applications, Journal of Wind Engineering and Industrial Aerodynamics 74-76 (1998) 553-565.

[14]. John Lohan, PhD, Article on Design and Applications of Low Speed Wind Tunnels, Department of Mechanical and Industrial Engineering, Galway-Mayo Institute of Technology (GMIT), Dublin Road, Galway, Ireland.

[15]. Serhat Senol, Ali Cinar, Design and Flow Simulation of an Open Circuit Wind Tunnel, EnginSoft International Conference 2009 1st-2nd Oct. 2009.

[16]. Eckert W. T, Mort K. W, & Jope J, Aerodynamic design guidelines and computer program for estimation of subsonic wind tunnel performance, NASA technical note / D-8243, NASA Washington, (1976).

[17]. Maskell, E. C. A theory of the blockage effects on bluff bodies and stalled wings in a closed wind tunnel, R. & M. 3400, November, (1963).

[18]. The Royal Aeronautical Society. Wind tunnels and wind tunnel test techniques, Royal Aeronautical Society London, (1992).

[19]. Mehta, R. D, & Bradshaw, P. Design Rules for Small Low-Speed Wind Tunnels, Aero. Journal, (Royal Aeronautical Society) , (1979), 73, 443.

[20]. Borger G. G., The optimization of wind tunnel contractions for the subsonic range, NASA Technical Translation / F-16899, NASA Washington, (1976).

[21]. Scheiman, J. Considerations for the installation of honeycomb and screens to reduce wind-tunnel turbulence, NASA Technical Memorandum / 81868, NASA Washington, (1981).

[22]. Gorlin, S. M, & Slezinger, I. I. Wind tunnels and their instrumentation, Israel Program for Scientific Translations Jerusalem, (1966).

[23]. Data Acquisition, (Searched on Sept 15, 2013) http://en.wikipedia.org/wiki/Data_acquisition.

[24]. Kamal Poddar, Sanjay Gupta, Instrumentation for National Wind Tunnel Facility, IIT Kanpur.

[25]. Barlow, J. B, Rae, W. H, & Pope, A. Low-speed wind tunnel testing, John Wiley & Sons New York, (1999).

[26]. Sub-Sonic Wind Tunnels and Instrumentation, www.aerolab.com, 301-776-6585 Laurel, Maryland, USA.

Effect of DC Link Control Strategies on Multiterminal AC-DC Power Flow

Shagufta Khan*
khan.shagufta7@gmail.com

Suman Bhowmick*
suman.bhowmick@dce.ac.in

* Department of Electrical Engineering, Delhi Technological University,
Delhi – 110042, India

***Abstract*—For power-flow solution of power systems incorporating multiterminal DC (MTDC) network(s), five quantities are required to be solved per converter. On the other hand, only three independent equations comprising two basic converter equations and one DC network equation exist per converter. Thus, for solution, two additional equations are required. These two equations are derived from the control specifications adopted for the DC links. Depending on the application, several combinations of valid control specifications are possible. Each combination of a set of valid control specifications is known as a control strategy. The number of control strategies increase with an increase in the number of the DC terminals or converters. It is observed that the power-flow convergence of integrated AC-MTDC power systems is strongly affected by the control strategy adopted for the DC links. This work investigates the mechanism by which different control strategies affect the power-flow convergence pattern of AC-MTDC power systems. To solve the DC variables in the Newton-Raphson (NR) power-flow model, sequential method is considered in this paper. Numerous case studies carried out on a three terminal DC network incorporated in the IEEE-300 bus test system validate this.**

Keywords- MTDC, Newton-Raphson model, control strategy, sequential method

List of symbols

S_{base}	Base MVA
$V_{ac\,base}, I_{ac\,base}, Z_{ac\,base}$	AC base voltage, AC base current and AC base impedance, respectively
$V_{dc\,base}, I_{dc\,base}, Z_{dc\,base}$	DC base voltage, DC base current and DC base impedance, respectively
n_b	Number of bridges
X_c	Commutating reactance
V_d, I_d	DC voltage and current, respectively
ϕ_R	Power factor angle at the rectifier end
ϕ_{I1}, ϕ_{I2}	Power factor angles at inverter-1 and inverter-2 ends, respectively
α_R	Firing angle of the rectifier
γ_{I1}, γ_{I2}	Extinction angles of inverter-1 and inverter-2, respectively
V_{dR}	DC voltage at the rectifier end
V_{dI1}, V_{dI2}	DC voltages at inverter-1 and inverter-2 ends, respectively
a_R	Tap ratio of the converter transformer at the rectifier end
a_{I1}, a_{I2}	Tap ratios of the converter transformers at inverter-1 and inverter-2 ends, respectively
R_d	DC link resistance
$V_i \angle \theta_i$	AC bus voltage magnitude (rms) and phase angle at i^{th} bus
$V_j \angle \theta_j$	AC bus voltage magnitude (rms) and phase angle at j^{th} bus
$V_k \angle \theta_k$	AC bus voltage magnitude (rms) and phase angle at k^{th} bus
V_{doR}	No load direct voltage at the rectifier side
V_{doI1}, V_{doI2}	No load direct voltages at inverter-1 and inverter-2 ends, respectively
P_{Di}, Q_{Di}	Active and reactive power demand at bus 'i', respectively
P_i, Q_i	Net active and reactive power injection at bus 'i', respectively
P_{dR}, Q_{dR}	Equivalent active and reactive power injection of the rectifier, respectively
P_{dI1}, P_{dI2}	Equivalent active power injections of inverter-1 and inverter-2, respectively
Q_{dI1}, Q_{dI2}	Equivalent reactive power injections of inverter-1 and inverter-2, respectively

I. INTRODUCTION

Multiterminal DC (MTDC) systems have been proven to be more versatile on account of their ability to fully exploit the economic and technical advantages of HVDC technology. Since the success of the first MTDC system "Sardinia-Corsia-Italy Scheme" in 1991, the application of MTDC systems has shown a steady increase. Further, with the rapid progress of renewable energy sources and offshore wind farms, MTDC applications are increasing. MTDC transmits bulk power from several generating stations to several load centres. It is more flexible and economical, being capable of connecting more than two asynchronous AC systems [1-4].

Now, for planning, operation and control of power systems incorporated with MTDC links, power-flow solution of such systems is required. Power-flow solution of integrated AC-MTDC systems requires five quantities to be solved per converter. These include the DC voltage, the DC current, the control angle, the converter transformer tap ratio and the converter power factor. On the other hand, only three independent equations comprising two basic converter equations and one DC network equation exist per converter. Thus, for solution, two additional equations are usually required. These two equations are derived from the control specifications adopted for the DC links. Thus, mathematically, the control specifications are used to bridge the gap between the number of independent equations and the number of unknown quantities. Control specifications usually include specified values of converter transformer tap ratio, converter control angle, DC voltage, DC current or DC power. Depending on the application, several combinations of valid control specifications are possible. Each combination of a set of valid control specifications is known as a control strategy. The number of possible control strategies increase drastically with increase in the number of the DC terminals or converters. Out of a myriad of combinations, only some control strategies are practically adopted in practice.

To carry out power-flow in AC-MTDC systems, two different algorithms have generally been reported in the literature. These are known as the unified and the sequential method, respectively. Some excellent research works on the unified and the sequential power flow method are presented in [5-19]. Unlike the unified method, the sequential method is easier to implement and poses lesser computational burden due to the smaller size of the Jacobian matrix. Consequently, in this work, only the sequential AC-DC power-flow algorithm has been considered.

In the sequential AC-DC power-flow algorithm, the AC and DC systems are solved separately in each iteration and are coupled by injecting an equivalent amount of real and reactive power at the terminal AC buses. It is observed that each different control strategy affects the sequential power flow convergence in a uniquely different manner. For standard control strategies i.e. constant DC voltage or current or power, the convergence rate can be improved by solving the DC and AC systems independently. On the other hand, for non-standard ones like constant tap ratios and

constant terminal voltage, the convergence may suffer. The mechanism by which this occurs is not been very clear and has not been exclusively addressed in the literature. This motivated the authors to investigate how different control strategies affect the power flow convergence. The work is validated by numerous case studies carried out on a three terminal DC network incorporated in the IEEE 300-bus test system. Although a large number of control strategies are possible with the three terminal DC network, however, due to a lack of space, only results corresponding to nine different control strategies are reported here.

This paper is arranged as follows: In section II, the mathematical modelling of the AC-MTDC system is presented. Section III details a few of the control strategies possible for a three terminal DC network. In Section IV, the AC-MTDC power-flow equations are presented, with the DC link powers acting as an equivalent load on the converter AC buses. Section V details the case studies carried out with a three terminal DC network incorporated in the IEEE 300-bus test system. The conclusions are presented in Section VI.

II. AC-MTDC SYSTEM MODELLING

Fig. 1 shows a typical AC power system incorporating a three terminal DC network. The DC network contains two HVDC links. The first link is connected in the branch "i - j" between any two system buses "i" and "j" of the network while the second one is connected in the branch "i - k" between system buses "i" and "k". The three converters representing one rectifier and two inverters are connected to the AC system at buses "i", "j" and "k" respectively, through their respective converter transformers. The effect of the DC links are accounted for as equivalent amount of real and reactive power injections $P_{dR}, Q_{dR}, P_{dI1}, Q_{dI1}, P_{dI2}$ and Q_{dI2} at the converters' AC terminal buses "i", "j" and "k", respectively. Although these power injections are not shown in Fig. 1, they are included in the analysis by appropriate modifications of the power flow equations as detailed later in Section IV.

Prior to the selection of variables and formulation of the equations, several basic assumptions are required which are generally accepted in the analysis of steady state DC converter operation [1-4]. These are

1. The three AC voltages at the terminal bus bars are balanced and sinusoidal.
2. The operation of the converters is perfectly balanced.
3. The direct currents and voltages are smooth.
4. The converter transformers are lossless and their magnetizing admittances are ignored.

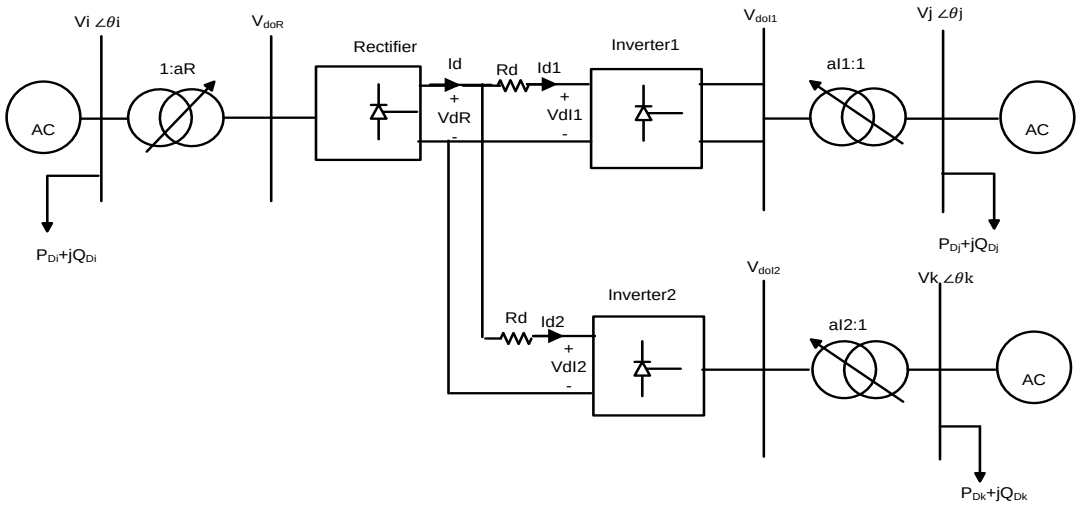

Fig. 1: Three terminal HVDC link between buses ‘i’, ‘j’ and ‘k’ of an existing power system network

Subsequently, the DC and AC equations are combined together which requires the translation of the converter equations into the per-unit system in order to use them with AC system per-unit equations. The base values for the DC system are defined in Table A.1 (Appendix-A) which culminate in the per-unit AC-DC system equations as given in Table I.

From Table I, it can be observed that twelve independent equations exist as against a total of eighteen unknowns. Thus, for a complete solution of the HVDC quantities, six quantities (two per converter) are needed to be specified. These are derived from the control specifications adopted for the DC links. Each combination of a set of valid control specifications is known as a control strategy. Theoretically, the number of possible control strategies increase drastically with increase in the number

of the DC terminals or converters. However, only a few of the possible control strategies are practically adopted in practice. This is explained in the next section.

Table I: Basic converter equations for a 3 terminal DC network in per unit system

$V_{dR} = a_R V_i \cos\alpha_R - X_c I_{dR}$	(1)
$V_{dI1} = a_{I1} V_j \cos\gamma_{I1} - X_c I_{dI1}$	(2)
$V_{dI2} = a_{I2} V_k \cos\gamma_{I2} - X_c I_{dI2}$	(3)
$V_{dR} = a_R V_i \cos\phi_R$	(4)
$V_{dI1} = a_{I1} V_j \cos\phi_{I1}$	(5)
$V_{dI2} = a_{I2} V_k \cos\phi_{I2}$	(6)
$I_{dI1} = \frac{V_{dR} - V_{dI1}}{R_d}$	(7)
$I_{dI2} = \frac{V_{dR} - V_{dI2}}{R_d}$	(8)
$I_{dR} = I_{dI1} + I_{dI2}$	(9)
$P_{dR} = V_{dR} I_{dR}$	(10)
$P_{dI1} = V_{dI1} * \left[\frac{V_{dR} - V_{dI1}}{R_d}\right]$	(11)
$P_{dI2} = V_{dI2} * \left[\frac{V_{dR} - V_{dI2}}{R_d}\right]$	(12)

III. MTDC CONTROL STRATEGIES

As already discussed in the previous section, for a three terminal DC network, a myriad of control strategies are possible. However, due to a lack of space, only nine typical control strategies are considered in this paper. These are detailed in Table II.

A. Control Strategy-1:

In this control strategy, the DC voltage and the firing angle are specified for the rectifier. On the other hand, the active powers for both the inverters are specified along with their extinction angles.

Table II: Some Control Strategies for a 3-Terminal DC link

Control Strategies	Specified Quantities		Unknown Quantities
	Include in DC load flow	Exclude in DC load flow	
1	P_{dI1}, P_{dI2}, V_{dR}	$\alpha_R, \gamma_{I1}, \gamma_{I2}$	$V_{dI1}, V_{dI2}, P_{dR}, I_{dI1}, I_{dI2}, I_{dR}, a_R, a_{I1}, a_{I2}, cos\phi_R, cos\phi_{I1}, cos\phi_{I2}$
2	P_{dI1}, I_{dI2}, V_{dR}	$\alpha_R, \gamma_{I1}, \gamma_{I2}$	$V_{dI1}, V_{dI2}, P_{dI2}, P_{dR}, I_{dI1}, I_{dR}, a_R, a_{I1}, a_{I2}, cos\phi_R, cos\phi_{I1}, cos\phi_{I2}$
3	P_{dI2}, I_{dI1}, V_{dR}	$\alpha_R, \gamma_{I1}, \gamma_{I2}$	$V_{dI1}, V_{dI2}, P_{dI1}, P_{dR}, I_{dI2}, I_{dR}, a_R, a_{I1}, a_{I2}, cos\phi_R, cos\phi_{I1}, cos\phi_{I2}$
4	I_{dI1}, I_{dI2}, V_{dR}	$\alpha_R, \gamma_{I1}, \gamma_{I2}$	$V_{dI1}, V_{dI2}, P_{dI1}, P_{dI2}, P_{dR}, I_{dR}, a_R, a_{I1}, a_{I2}, cos\phi_R, cos\phi_{I1}, cos\phi_{I2}$
5	P_{dI1}, P_{dI2}, V_{dR}	a_R, a_{I1}, a_{I2}	$V_{dI1}, V_{dI2}, P_{dR}, I_{dI1}, I_{dI2}, I_{dR}, a_R, a_{I1}, a_{I2}, cos\phi_R, cos\phi_{I1}, cos\phi_{I2}$
6	I_{dI1}, I_{dI2}, V_{dR}	a_R, a_{I1}, a_{I2}	$V_{dI1}, V_{dI2}, P_{dI1}, P_{dI2}, P_{dR}, I_{dR}, a_R, a_{I1}, a_{I2}, cos\phi_R, cos\phi_{I1}, cos\phi_{I2}$
7	P_{dI1}, I_{dI2}, V_{dR}	a_R, a_{I1}, a_{I2}	$V_{dI1}, V_{dI2}, P_{dI2}, P_{dR}, I_{dI1}, I_{dR}, a_R, a_{I1}, a_{I2}, cos\phi_R, cos\phi_{I1}, cos\phi_{I2}$
8	I_{dI1}, P_{dI2}, V_{dR}	a_R, a_{I1}, a_{I2}	$V_{dI1}, V_{dI2}, P_{dI1}, P_{dR}, I_{dI2}, I_{dR}, a_R, a_{I1}, a_{I2}, cos\phi_R, cos\phi_{I1}, cos\phi_{I2}$
9	$P_{dI1}, P_{dI2}, V_{dI1}$	$\alpha_R, \gamma_{I1}, \gamma_{I2}$	$V_{dIR}, V_{dI2}, P_{dR}, I_{dI1}, I_{dI2}, I_{dR}, a_R, a_{I1}, a_{I2}, cos\phi_R, cos\phi_{I1}, cos\phi_{I2}$

B. Control Strategy-2:

In this control strategy, the DC voltage and the firing angle are specified for the rectifier. For inverter-1, the active power is specified while the DC current is specified for inverter-2. In addition, the extinction angles of both the inverters are specified.

C. Control Strategy-3:

In this control strategy, at the rectifier terminal, the DC voltage and the firing angle are specified. The DC current is specified at inverter-1 while the active power is specified at inverter-2. Also, the extinction angles of both the inverters are specified.

D. Control Strategy-4:

In this control strategy, the DC voltage and the firing angle are specified at the rectifier end while the DC currents and the extinction angles are specified for both the inverters.

E. Control Strategy-5:

In this control strategy, the DC voltage is specified for the rectifier while the active powers are specified for both the inverters. In addition, the tap settings for all the three converter transformers are specified.

F. Control Strategy-6:

In this control strategy, the DC voltage is specified for the rectifier while the DC currents are specified for both the inverters. The tap settings for all the three converter transformers are also specified.

G. Control Strategy-7:

In this control strategy, at the rectifier terminal, the DC voltage is specified. The active power is specified at inverter-1 while the DC current is specified at inverter-2. In addition, the tap settings are specified for all the three converter transformers.

H. Control Strategy- 8:

In this control strategy, the DC voltage is specified at the rectifier terminal. For inverter-1, the DC current is specified while for inverter-2, the active power is specified. The tap settings for all the three converter transformers are also specified.

I. Control Strategy-9:

In this control strategy, the firing angle is specified for the rectifier while the DC voltage is specified for inverter-1. In addition, the values of the active powers and the extinction angles are specified for both the inverters.

IV. AC-DC POWER-FLOW EQUATIONS

As already discussed in Section I, for solving the AC-MTDC system, two additional equations per converter are required, which are derived from the control specifications adopted for the system. For the three terminal DC link considered in this paper, this translates into six specified variables. These six specified variables are divided into two subsets. The first set of specified variables is used only for the DC load flow and corresponds to specifying active power or current at all terminals except at the voltage setting terminal. In this paper, the DC load flow is solved by the Newton Raphson method.

Subsequently, for solving the AC power flow, the effects of the DC links are included in the power flow equations by injecting an equivalent amount of real and reactive power at the terminal AC

buses connected to the converters. The values of these active and reactive powers are computed using the specified variables and the variables computed from the DC power-flow. This results in appropriate modifications of the mismatch equations at the converter terminal AC buses. These are given below:

For any AC bus 'i', which is not connected to any DC link, the mismatches in the active and reactive power injections are given respectively, by

$$\Delta P_i = P_i^{sp} - \sum_{k=1}^{n} V_i V_k Y_{ik} \cos(\theta_i - \theta_k - \phi_{ik}) \tag{13}$$

$$\Delta Q_i = Q_i^{sp} - \sum_{k=1}^{n} V_i V_k Y_{ik} \sin(\theta_i - \theta_k - \phi_{ik}) \tag{14}$$

The DC network contains two HVDC links. The first link is connected in the branch 'i' and 'j' between any two buses 'i' and 'j' of the network while the second one is connected in the branch "i-k" between system buses "i" and "k". The three converters representing one rectifier and two inverters are connected to the AC system at buses "i", "j" and "k" respectively, through their respective converter transformers. The effect of the DC link can be incorporated in the AC power flow as equivalent active and reactive power injections 'P_{dR}' and 'Q_{dR}' at the rectifier bus 'i', along with 'P_{dI1}' and 'Q_{dI1}' and 'P_{dI2}' and 'Q_{dI2}' at the inverter buses 'j' and 'k', respectively. Therefore, the mismatches in the active and reactive power injections can be written as

$$\Delta P_i = P_i^{sp} - \sum_{p=1}^{n} V_i V_p Y_{ip} \cos(\theta_i - \theta_p - \phi_{ip}) - P_{dR} \tag{15}$$

$$\Delta Q_i = Q_i^{sp} - \sum_{p=1}^{n} V_i V_p Y_{ip} \sin(\theta_i - \theta_p - \phi_{ip}) - Q_{dR} \tag{16}$$

$$\Delta P_j = P_j^{sp} - \sum_{p=1}^{n} V_j V_p Y_{jp} \cos(\theta_j - \theta_p - \phi_{jp}) + P_{dI1} \tag{17}$$

$$\Delta Q_j = Q_j^{sp} - \sum_{p=1}^{n} V_j V_p Y_{jp} \sin(\theta_j - \theta_p - \phi_{jp}) - Q_{dI1} \tag{18}$$

$$\Delta P_k = P_k^{sp} - \sum_{p=1}^{n} V_k V_p Y_{kp} \cos(\theta_k - \theta_p - \phi_{kp}) + P_{dI2} \tag{19}$$

$$\Delta Q_k = Q_k^{sp} - \sum_{p=1}^{n} V_k V_p Y_{kp} \sin(\theta_k - \theta_p - \phi_{kp}) - Q_{dI2} \tag{20}$$

where

$P_{dR} = V_{dR} I_{dR}$, $Q_{dR} = P_{dR} \tan\phi_R$, $P_{dI1} = V_{dI1} I_{dI1}$, $Q_{dI1} = P_{dI1} \tan\phi_{I1}$, $P_{dI2} = V_{dI2} I_{dI2}$, $Q_{dI2} = P_{dI2} \tan\phi_{I2}$.

In the above equations, the equivalent active power injections 'P_{dR}', 'P_{dI1}' and 'P_{dI2}' are usually specified or can be very easily computed by manipulation of the specified variables. However, for the equivalent reactive power injections Q_{dR}, Q_{dI1} and Q_{dI2}, the case is different, depending on the control strategy adopted for the DC links. For control strategies 1, 2, 3, 4 and 9, ϕ_R, ϕ_{I1} and ϕ_{I2} (and hence Q_{dR}, Q_{dI1} and Q_{dI2}) can be computed by manipulation of the specified variables. However, for control strategies 5, 6, 7 and 8, ϕ_R, ϕ_{I1} and ϕ_{I2} (and hence Q_{dR}, Q_{dI1} and Q_{dI2}) are dependent on both the specified variables as well as the AC state variables, which are updated every iteration. This affects the convergence pattern. The steps involved in the computation of the active and reactive power injections for only two typical control strategies 1 and 5 are detailed in Table B.1 of Appendix-B. In control strategy 5 the reactive power injections are dependent on the AC power flow iterative process while in control strategy 1 they are independent of it. Although the steps involved in the computation of the power injections pertaining to the rest of the control strategies are not shown due to limitations of space, they can be computed in ways similar to control strategies 1 and 5.

It is important to note the conventions of the signs of the equivalent real and reactive power injections representing the DC link. It is assumed that the rectifier consumes both real and reactive power from the AC grid while the inverters supply real power and consume reactive power.

V. CASE STUDIES AND RESULTS

Numerous case studies were carried out on a three terminal DC network comprising one rectifier and two inverters incorporated in the IEEE 300-bus test system [20]. All the three converters are connected to their respective AC buses by tap changing transformers. Although a large number of control strategies are possible with the three terminal DC network, however, due to limitations of space, only results corresponding to nine different control strategies are reported here. For all the case studies, the commutating reactance and the DC link resistance were chosen as 0.1 p.u. and 0.01 p.u respectively. The number of bridges 'n_b' for all the converters was taken to be equal to 2. To minimize the reactive power requirement at the rectifier and inverter terminals and the overall system losses, the rectifier firing angles and the inverter extinction angles are kept within 5^o to 15^o and 15^o to 22^o respectively, for all the case studies. In a similar manner, the tap ratios of the converter

transformers are kept between 0.85-1.15. A convergence tolerance of 10^{-12} p.u. was uniformly adopted for all the case studies. In each of the case studies, 'NI' refers to the number of iterations taken by the algorithm to converge to the specified tolerance (10^{-12} p.u.). In general, 'NI' is representative of the degree of convergence of a power flow study.

Case Study-I: In this case study, two HVDC links are considered. The first link is incorporated between buses "25-26" and the second one between buses "25-232". The converter connected to bus no. 25 acts as a rectifier. On the other hand, both the converters connected to buses 26 and 232 act as inverters. Control strategy-1 is adopted for the control of the DC links. Corresponding to this strategy, the active power flows on the links 25-26 and 25-232 are set to 0.3 p.u and 0.1 p.u respectively. The DC voltage on the rectifier side is set at 1 p.u. The firing angle for the rectifier and the extinction angles for both the inverters are set to 5^{o} and 15^{o}, respectively. The power flow solution is shown in columns 5-8 of Table III (corresponding to Control strategy-1). The state variables pertaining to the AC and DC systems are denoted as ACSV and DCSV, respectively. From Table III, it is observed that the power flow convergence pattern in this case is similar to that of the base case power flow (without HVDC link), converging in seven iterations. This is because the power injections representing the DC links can be computed prior to the AC power flow, as elaborated from the steps given in the first column of Table B.1 (Appendix-B). This is reiterated from the convergence characteristics corresponding to the base case and case study 1, as shown in Fig. 2 and 3, respectively. The convergence characteristic plots the error (maximum absolute mismatch in p.u.) against the number of iterations 'NI'.

Case study-II: In this case study, two HVDC links are connected between buses "213-214" and "213-216". While the converter connected to bus no. 213 acts as a rectifier, both the converters connected to buses 214 and 216 act as inverters. In this case, Control strategy-2 is adopted for the control of the DC links. The rectifier end DC voltage is specified along with the firing angle. While the first inverter acts on constant power mode, the second one acts on the constant current mode. In addition, the extinction angles for both the inverters are specified. These values are detailed in columns 1-4 of Table III (corresponding to Control strategy-2). The power flow solution is detailed in columns 5-8 of

Table III. The convergence pattern is similar to that with control strategy 1, as the DC link power injections can be computed prior to the AC power flow. The steps involved in the computation of the DC link power injections (Table B.1 of Appendix-B), although similar in nature to Control strategy-1, are not shown due to limitations of space.

Table III: Study of IEEE-300 bus system with a three terminal DC network

HVDC links		**HVDC link specification**		**Power flow solution**			
Rectifier bus	Inverter buses	**Control strategy-1**		**AC terminal buses**		**HVDC variables**	
		Spec. Values		ACSV		DCSV	
25	26	P_{dI1} (p.u)	0.2	V_{25}	0.9632	V_{dI1}	0.998
						V_{dI2}	0.999
						P_{dR}	0.3005
		P_{dI2} (p.u)	0.1	θ_{25}	-2.122^0	I_{dI1}	0.2004
						I_{dI2}	0.1001
						I_{dR}	0.3005
		V_{dR} (p.u)	1	V_{26}	0.9564	a_R	1.0386
						a_{I1}	1.103
						a_{I2}	1.0441
	232	α_R (deg.)	5	θ_{26}	-3.715^0	$cos\phi_R$	0.9766
						$cos\phi_{I1}$	0.9377
		γ_{I1} (deg.)	15	V_{232}	0.9841	$cos\phi_{I2}$	0.9563
		γ_{I2} (deg.)	15	θ_{232}	-1.792^0	NI	7
		Control strategy-2		**AC terminal buses**		**HVDC variables**	
213	214	Spec. Values		ACSV		DCSV	
		P_{dI1} (p.u)	0.6	V_{213}	1.0067	V_{dI1}	0.994
						V_{dI2}	0.996
						P_{dI2}	0.4036
		I_{dI2} (p.u)	0.4	θ_{213}	-21.69^O	P_{dR}	1.0036
						I_{dI1}	0.6036
						I_{dR}	1.0036
	216	V_{dR} (p.u)	1	V_{214}	1.0087	a_R	1.0972
						a_{I1}	1.0822
						a_{I2}	1.0187
		α_R (deg.)	5	θ_{214}	-21.125^0	$cos\phi_R$	0.9053
						$cos\phi_{I1}$	0.9106
		γ_{I1} (deg.)	15	V_{216}	1.0528	$cos\phi_{I2}$	0.9286
		γ_{I2} (deg.)	15	θ_{216}	-21.39^O	NI	7
		Control strategy-3		**AC terminal buses**		**HVDC variables**	
109	146	Spec. Values		ACSV		DCSV	
		P_{dI2} (p.u)	0.1	V_{109}	0.9993	V_{dI1}	0.999
						V_{dI2}	0.996
						P_{dR}	0.1101
		I_{dI1} (p.u)	0.01	θ_{109}	5.6163^0	P_{dI1}	0.0101
						I_{dI2}	0.1001
						I_{dIR}	0.1101
	147	V_{dR} (p.u)	1	V_{146}	0.9618	a_R	1.1151
						a_{I1}	1.0871
						a_{I2}	1.1439
		α_R (deg.)	5	θ_{146}	-7.1728^0	$cos\phi_R$	0.8974
						$cos\phi_{I1}$	0.9564
		γ_{I1} (deg.)	15	V_{147}	0.9947^0	$cos\phi_{I2}$	0.878
		γ_{I2} (deg.)	15	θ_{147}	-4.9558^0	NI	7

Case study-III: In this case, two HVDC links are connected between buses “109-146” and “109-147”. The converter connected to bus no. 109 acts as a rectifier, while both the converters connected to buses 146 and 147 act as inverters. For control of the DC links, Control Strategy -3 is selected. The rectifier end DC voltage is specified along with the firing angle. While the first inverter acts on constant current mode, the second one acts on the constant power mode. In addition, the extinction angles for both the inverters are specified. These values are detailed in columns 1-4 of Table III. The power flow solution is detailed in columns 5-8 of Table III (corresponding to Control strategy-3). From Table III, it is observed that the convergence pattern obtained in this case is again similar to control strategies-1 and 2, which is expected as the power injections can be computed prior to the AC power flow.

Case study-IV: In this case study, two HVDC links are connected between buses “101-102” and “101-104”. The rectifier is connected to bus no. 101. The inverters are connected to buses 102 and 104 respectively. For control of the two DC links, Control Strategy-4 is adopted. The rectifier end DC voltage is specified along with the firing angle. Both the inverters are operated at constant current and constant extinction angle modes. The values of the specified quantities are detailed in columns 1-4 of Table IV. The power flow solution is detailed in columns 5-8 of Table IV (corresponding to Control strategy-4). It is observed that as expected, the convergence pattern is similar to that obtained with Control strategies-1 to 4 (since the DC link power injections are known before the AC power flow).

Case study-V: In this case, two HVDC links are incorporated between buses “86-87” and “86-90”. The converter connected to bus no. 86 acts as a rectifier while both the converters connected to buses 87 and 90 act as inverters. Control Strategy-5 is selected for the control of the DC links. In this strategy, the rectifier end DC voltage is specified while both the inverters are operated in the constant power mode. In addition, the tap ratios of all the three converter transformers are specified. Columns 1-4 of Table IV shows these specified values. The power flow solution is shown in columns 5-8 of Table IV (corresponding to Control strategy-5). From the power-flow solution, it is observed that unlike Control strategies-1 to 4, with this control strategy, the convergence pattern is adversely affected. This is because for this control strategy, the computation of the reactive power injections (for

the DC links) are dependent on the AC power flow variables and are updated in every iteration. This is elaborated from the steps involved in the computation of the power injections as shown in the second column of Table B.1 (Appendix-B). From Table B.1, it can be observed that the computation of the reactive power injections is dependent on the iterative process. This affects the convergence pattern. This is reiterated by comparing the convergence characteristics for this case, as shown in Fig. 4, with that of Fig. 2 and 3.

The bus voltage profile for this control strategy is shown in Fig. 5. It is observed that the bus voltage profiles undergo very slight changes at only the AC terminal buses connected to the converters.

It is important to note that due to a limitation of space, only the bus voltage profile corresponding to Control Strategy-5 is shown. This is because among all the case studies carried out, the poorest power-flow convergence pattern was observed corresponding to this Control Strategy.

Case study-VI: In this case, the two HVDC links were incorporated between buses "77-84" and "77-86". While the converter connected to bus no. 77 acts as a rectifier, both the converters connected to buses 84 and 86 act as inverters. For control of the DC links, Control Strategy-6 is adopted. In this Control Strategy, the rectifier end DC voltage is specified. On the other hand, both the inverters are operated in the constant current mode. Also, the tap ratios of all the three converter transformers are specified. While columns '1-4' of Table IV shows the values of the specified quantities, columns 5-8 details the power-flow solution (corresponding to Control strategy-6). From the power flow solution it is observed that in this case, the convergence pattern is adversely affected as in case of that with Control strategy-5. This is because the converter equivalent reactive power injections are required to be updated in every iteration of the AC power flow. This is also true for the subsequent case studies VII and VIII carried out employing Control strategies-7 and 8, respectively. Although the steps involved in the computation of the power injections with Control strategies-6 to 8 are similar to that with Control strategy-5 (second column, Table B.1, Appendix-B), they are not shown due to limitations of space.

The convergence characteristics corresponding to this case study is shown in Fig. 6. By comparing Fig. 5 and 6, the similarity in the convergence characteristics between the case studies with Control strategies 4 and 6 can be observed.

Case study-VII: In this case study, two HVDC links are incorporated between buses "68-173" and "68-174". The converter connected to bus no. 68 acts as a rectifier while both the converters connected to buses 173 and 174 act as inverters. Control Strategy-7 is selected for the control of the DC links. The first inverter is operated in the constant power mode while the second one operates in the constant current mode. In addition, the tap ratios of all the three converter transformers are specified. The specified values are given in columns 1-4 of Table V. The power flow solution is shown in columns 5-8 of Table V (corresponding to Control strategy-7). From the power-flow solution, it is observed that similar to Control strategies-5 and 6, the convergence pattern for this control strategy is adversely affected. This is expected as the reactive power injections are dependent on the iterative process of the AC power flow. This is reiterated from the convergence characteristics for this case study, as shown in Fig.7.

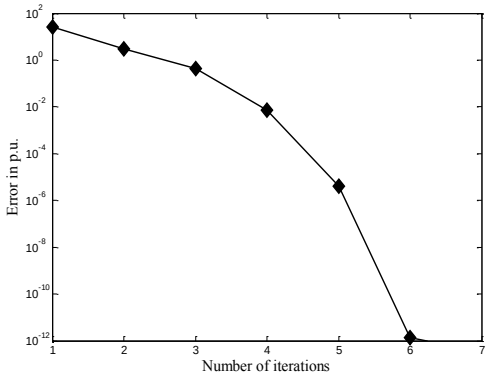

Fig. 2 Convergence characteristics for the base case power flow in IEEE-300 bus test system

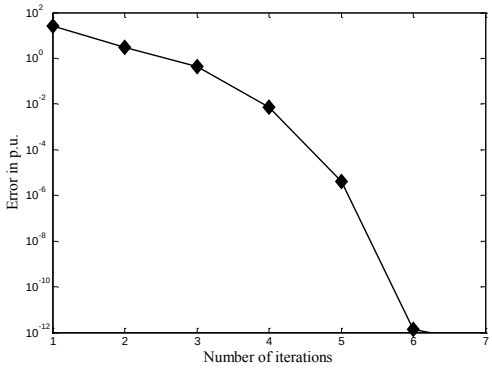

Fig. 3 Convergence characteristics for case study I of Table III with control strategy 1

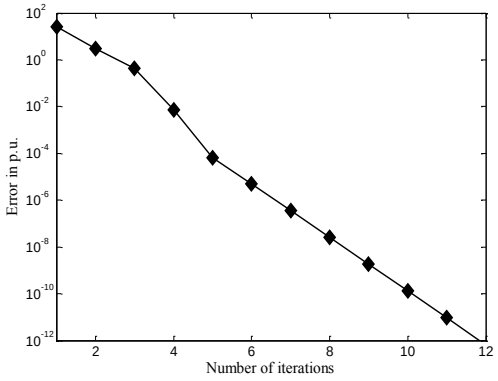

Fig. 4 Convergence characteristics for case study V of Table IV with control strategy 5

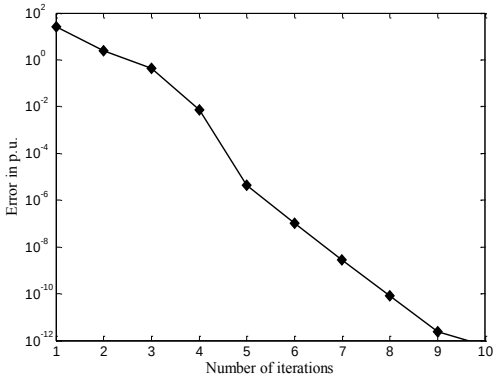

Fig. 6 Convergence characteristics for case study VI of Table IV with control strategy 6

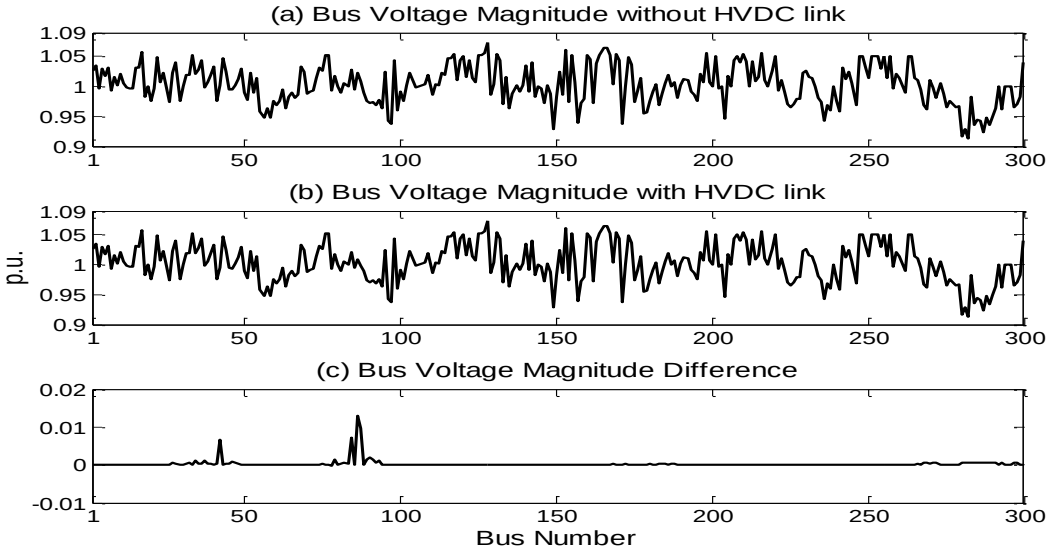

Fig. 5: Bus voltage profile for Case Study-V with control strategy-5

Case study-VIII: In this case, two HVDC links are incorporated between buses "15-31" and "15-74". The converter connected to bus no. 15 acts as a rectifier while both the converters connected to buses 31 and 74 act as inverters. Control Strategy-8 is selected for the control of the DC links. The rectifier operates in the constant voltage mode. The first and the second inverters are operated in the constant current and constant power modes, respectively. In addition, the tap ratios of all the three converter

transformers are specified. Columns 1-4 of Table V shows these specified values. The power flow solution is shown in columns 5-8 of Table V (corresponding to Control strategy-8). From the power-flow solution, it is again observed that similar to Control strategies 5-7, the convergence pattern is adversely affected by this control strategy. The convergence characteristics for this case study, as shown in Fig. 8, emphasises this fact.

Table IV: Study of IEEE-300 bus system with a three terminal HVDC network

HVDC link		**HVDC link specification**		**Power flow solution**			
Rectifier bus	Inverter buses	**Control strategy-4**		**AC terminal buses**		**HVDC variables**	
		Spec. Values		ACSV		DCSV	
101	102	I_{dI1} (p.u)	0.5	V_{101}	0.9621	V_{dI1}	0.995
						V_{dI2}	0.996
						P_{dI1}	0.3984
		I_{dI2} (p.u)	0.4	θ_{101}	-16.34^{O}	P_{dI2}	0.4975
						P_{dR}	0.9
						I_{dR}	0.9
	104	V_{dR} (p.u)	1	V_{102}	0.997	a_R	1.137
						a_{I1}	1.0851
						a_{I2}	1.0616
		α_R (deg.)	5	θ_{102}	-16.658	$cos\phi_R$	0.9139
						$cos\phi_{I1}$	0.9197
		γ_{I1} (deg.)	15	V_{104}	1.0103	$cos\phi_{I2}$	0.9286
		γ_{I2} (deg.)	15	θ_{104}	-18.43^{O}	NI	7
		Control strategy-5		**AC terminal buses**		**HVDC variables**	
86	87	Spec. Values		ACSV		DCSV	
		P_{dI1} (p.u)	0.3	V_{86}	1.007	V_{dI1}	0.997
						V_{dI2}	0.998
						P_{dR}	0.5
		P_{dI2} (p.u)	0.2	θ_{86}	-13.843	I_{dI1}	0.3009
						I_{dI2}	0.2004
						I_{dR}	0.5021
		V_{dR} (p.u)	1	V_{87}	0.996	α_R	15.266
						γ_{I1}	20.363
						γ_{I2}	17.314
	90	a_R	1.08	θ_{87}	-23.842	$cos\phi_R$	0.9187
						$cos\phi_{I1}$	0.91
		a_{I1}	1.1	V_{90}	0.9694	$cos\phi_{I2}$	0.9359
		a_{I2}	1.1	θ_{90}	-23.842	NI	12
		Control strategy-6		**AC terminal buses**		**HVDC variables**	
77	84	Spec. Values		ACSV		DCSV	
		I_{dI1} (p.u)	0.2	V_{77}	1.052	V_{dI1}	0.998
						V_{dI2}	0.999
						P_{dI1}	0.1996
		I_{dI2} (p.u)	0.1	θ_{77}	-6.815^{O}	P_{dI2}	0.0999
						P_{dR}	0.3
						I_{dR}	0.3
	86	V_{dR} (p.u)	1	V_{84}	1.0272	α_R	14.212
						γ_{I1}	17.647
						γ_{I2}	17.985
		a_R	1.01	θ_{84}	-11.694	$cos\phi_R$	0.9412
						$cos\phi_{I1}$	0.9342
		a_{I1}	1.04	V_{86}	1.02	$cos\phi_{I2}$	0.9417
		a_{I2}	1.09	θ_{86}	-12.81^{O}	NI	10

Table V: Study of IEEE-300 bus system with three terminal HVDC network

HVDC link		**HVDC link specification**		**Power flow solution**			
Rectifier Bus	Inverter Buses	**Control strategy-7**		**AC terminal buses**		**HVDC variables**	
		Spec. Values		ACSV		DCSV	
68	173	P_{dI1} (p.u)	0.5	V_{68}	1.019	V_{dI1}	0.995
						V_{dI2}	0.9995
						P_{dI2}	0.05
		I_{dI2} (p.u)	0.1	θ_{68}	-19.200	P_{dR}	0.5525
						I_{dI1}	0.5025
						I_{dR}	0.6025
		V_{dR} (p.u)	1	V_{173}	1.0363	α_R	12.373
	174					γ_{I1}	22.275
						γ_{I2}	21.965
		a_R	1.06	θ_{173}	-18.849	$cos\phi_R$	0.9256
						$cos\phi_{I1}$	0.8809
		a_{I1}	1.09	V_{174}	1.0315	$cos\phi_{I2}$	0.9228
		a_{I2}	1.05	θ_{174}	-20.83	NI	11
		Control strategy-8		**AC terminal buses**		**HVDC variables**	
15	31	Spec. Values		ACSV		DCSV	
		I_{dI1} (p.u)	0.04	V_{15}	1.0095	V_{dI1}	0.9996
						V_{dI2}	0.998
						P_{dI1}	0.2299
		P_{dI2} (p.u)	0.2	θ_{15}	-9.0928	P_{dR}	0.4299
						I_{dI2}	0.2004
						I_{dR}	0.2404
		V_{dR} (p.u)	1	V_{31}	1.0101	α_R	12.733
	74					γ_{I1}	21.787
						γ_{I2}	22.78
		a_R	1.04	θ_{31}	-11.3	$cos\phi_R$	0.9525
						$cos\phi_{I1}$	0.9249
		a_{I1}	1.07	V_{74}	1.0224	$cos\phi_{I2}$	0.9038
		a_{I2}	1.08	θ_{74}	-10.272	NI	11
		Control strategy-9		**AC terminal buses**		**HVDC variables**	
266	270	Spec. Values		ACSV		DCSV	
		P_{dI1} (p.u)	0.4	V_{25}	0.9965	V_{dR}	0.996
						V_{dI2}	0.997
						P_{dR}	0.7025
		P_{dI2} (p.u)	0.3	θ_{25}	-9.2266	I_{dI1}	0.4016
						I_{dI2}	0.3009
						I_{dR}	0.7025
	271	V_{dI1} (p.u)	1	V_{26}	0.9966	a_R	1.0437
						a_{I1}	1.1118
						a_{I2}	1.1358
		α_R (deg.)	5	θ_{26}	-9.1557	$cos\phi_R$	0.9576
						$cos\phi_{I1}$	0.9025
		γ_{I1} (deg.)	15	V_{232}	0.9362	$cos\phi_{I2}$	0.9376
		γ_{I2} (deg.)	15	θ_{232}	-7.6891	NI	6

Case study-IX: In this case, two HVDC links are incorporated between buses “266-270” and “266-271”. The converter connected to bus no. 266 acts as a rectifier while both the converters connected to buses 270 and 271 act as inverters. Control Strategy-9 is selected for the control of the DC links. In this strategy, the rectifier is operated in the constant firing angle mode. Both the inverters are operated

in constant power and constant extinction angle mode. Columns 1-4 of Table V shows these specified values. The power flow solution is shown in columns 5-8 of Table V (corresponding to Control strategy-9). From Table V, it is observed that in this case study, the convergence pattern is better than those with Control strategies 5-8. This is because the power injections representing the DC link can be computed a-priori and are independent of the iterative process of the AC power flow. This is reiterated by the convergence characteristics for this case study, as shown in Fig. 9.

The convergence patterns for the control strategies 2, 3, 4 and 9, although similar to control strategy 1, are not shown due to the limitations of space.

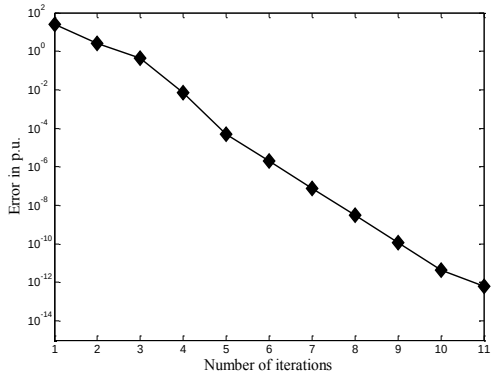

Fig. 7 Convergence characteristics for case study VII of Table V with control strategy 7

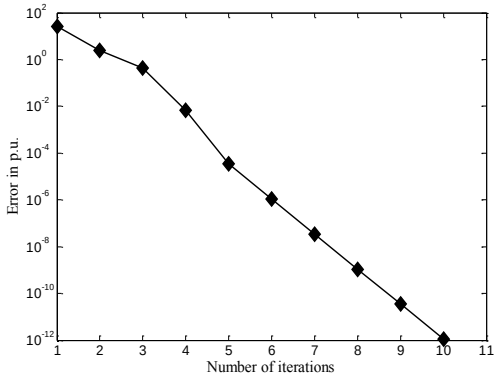

Fig. 8 Convergence characteristics for case study VIII of Table V with control strategy 8

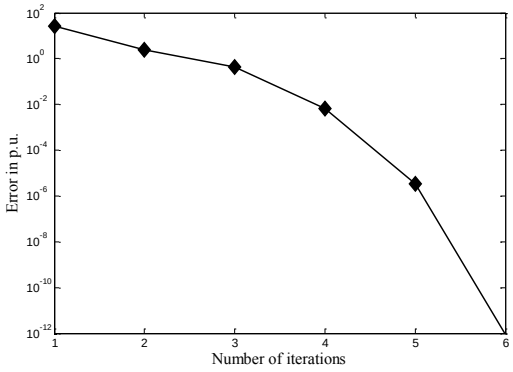

Fig. 9 Convergence characteristics for case study IX of Table V with control strategy 9

During the numerous studies carried out in the above AC-DC system, it was also observed that for a particular control strategy adopted, the power-flow convergence pattern is also affected by the values of the controlled variables corresponding to that strategy. Now, the value of the DC link power transfer is one of the most important control variables. Hence, two more case studies were conducted to observe the effect of the variation of the DC link power transfer on the power-flow convergence pattern. Since the poorest convergence pattern is observed with Control Strategy-5 (Table-IV), hence, for both of the case studies, this strategy is adopted. The details of the case studies are given below:

Case Study-X: In this case study, the power transfer over the first DC link 'P_{dI1}' is maintained to a constant value of 0.5 p.u. On the other hand, the power transfer over the second DC link 'P_{dI2}' is gradually increased from 0.08 p.u. to 0.3 p.u. The value of the specified quantities are shown in columns 3-4 of Table VI.

The power-flow solutions are detailed in columns 5-6 of Table VI. The variation of 'NI' with active power in the second DC link is shown in Fig 4. From Fig. 10, it is observed that 'NI' increases as 'P_{dI2}' is increased.

Case Study-XI: In this case study, the power transfer over the first DC link 'P_{dI1}' is gradually increased from 0.1 p.u. to 0.28 p.u. while maintaining the power transfer over the second one (P_{dI2}) to a constant value of 0.2 p.u. The specified quantities and the power-flow solutions are shown in columns 3-4 and 5-6 of Table VII, respectively. The variation of 'NI' with active power in the first DC link is shown in Fig 11. From Fig. 11, it is again observed that 'NI' increases as 'P_{dI1}' is increased.

Table VI: Study of power-flow convergence pattern with active power in the second DC link

HVDC Links		HVDC Link Specification		Power Flow Solutions	
Rectifier Bus	Inverter Buses	Control Strategy-5		AC terminal Buses	HVDC variables
85	88, 233	$P_{dI1} = 0.5$ (p.u) V_{dR} =1 (p.u) a_R =1.14 a_{I1} =1.1 a_{I2} =1.12	P_{dI2} (p.u) 0.08	$\boldsymbol{V_{85}} = 0.963\angle -18.368$ $\boldsymbol{V_{88}} = 0.99\angle -19.710$ $\boldsymbol{V_{233}} = 0.967\angle -18.23$	$V_{dI1} = 0.995$; $V_{dI2} = 0.9992$; $P_{dIR} = 0.5826$; $I_{dI1} = 0.5025$; $I_{dI2} = 0.05$; $I_{dR} = 0.5526$; $\gamma_{I1} = 16.3001$;γ_{I2}=21.7912; α_R =15.7287; $cos\phi_{I1} = 0.9137$; $cos\phi_{I2} = 0.9212$; $cos\phi_R = 0.9096$; NI=14;CT=93.294982;
			0.1	$\boldsymbol{V_{85}} = 0.9635\angle -18.36$ $\boldsymbol{V_{88}} = 0.99\angle -19.715$ $\boldsymbol{V_{233}} = 0.9674\angle -17.79$	$V_{dI1} = 0.995$; $V_{dI2} = 0.999$; $P_{dIR} = 0.6026$; $I_{dI1} = 0.5025$; $I_{dI2} = 0.1001$; $I_{dR} = 0.6026$; $\gamma_{I1} = 16.3001$;γ_{I2}=21.3669; α_R =15.133; $cos\phi_{I1} = 0.9137$; $cos\phi_{I2} = 0.922$; $cos\phi_R = 0.9105$; NI=15;CT=95.894141;
			0.15	$\boldsymbol{V_{85}} = 0.9611\angle -18.314$ $\boldsymbol{V_{88}} = 0.99\angle -19.7325$ $\boldsymbol{V_{233}} = 0.9647\angle -17.30$	$V_{dI1} = 0.995$; $V_{dI2} = 0.9985$; $P_{dIR} = 0.6528$; $I_{dI1} = 0.5025$; $I_{dI2} = 0.1502$; $I_{dR} = 0.6528$; $\gamma_{I1} = 16.3001$;γ_{I2}=20.2677; α_R =13.5279; $cos\phi_{I1} = 0.9137$; $cos\phi_{I2} = 0.9242$;$cos\phi_R = 0.9127$; NI=15;CT=93.322688;
			0.2	$\boldsymbol{V_{85}} = 0.9588\angle -18.268$ $\boldsymbol{V_{88}} = 0.99\angle -19.7537$ $\boldsymbol{V_{233}} = 0.962\angle -16.815$	$V_{dI1} = 0.995$; $V_{dI2} = 0.998$; $P_{dIR} = 0.7029$; $I_{dI1} = 0.5025$; $I_{dI2} = 0.2004$; $I_{dR} = 0.7029$; $\gamma_{I1} = 16.3001$;γ_{I2}=19.1062; α_R =11.6988; $cos\phi_{I1} = 0.9137$; $cos\phi_{I2} = 0.9263$; $cos\phi_R = 0.9149$; NI=16;CT=101.913689;
			0.25	$\boldsymbol{V_{85}} = 0.9564\angle -18.228$ $\boldsymbol{V_{88}} = 0.99\angle -19.7786$ $\boldsymbol{V_{233}} = 0.9593\angle -16.32$	$V_{dI1} = 0.995$; $V_{dI2} = 0.9975$; $P_{dR} = 0.7532$; $I_{dI1} = 0.5025$; $I_{dI2} = 0.2506$; $I_{dR} = 0.7532$; $\gamma_{I1} = 16.3001$;γ_{I2}=17.8704; α_R =9.522; $cos\phi_{I1} = 0.9137$; $cos\phi_{I2} = 0.9284$; $cos\phi_R = 0.9171$; NI=17;CT=135.807279;
			0.3	$\boldsymbol{V_{88}} = 0.99\angle -19.8072$ $\boldsymbol{V_{233}} = 0.9566\angle -15.84$ $\boldsymbol{V_{88}} = 0.99\angle -19.8072$	$V_{dI1} = 0.995$; $V_{dI2} = 0.997$; $P_{dIR} = 0.8034$; $I_{dI1} = 0.5025$; $I_{dI2} = 0.3009$; $I_{dR} = 0.8034$; $\gamma_{I1} = 16.3001$;γ_{I2}=16.544; α_R =6.602; $cos\phi_{I1} = 0.9137$; $cos\phi_{I2} = 0.9305$;$cos\phi_R = 0.9194$; NI=19;CT=118.803820;

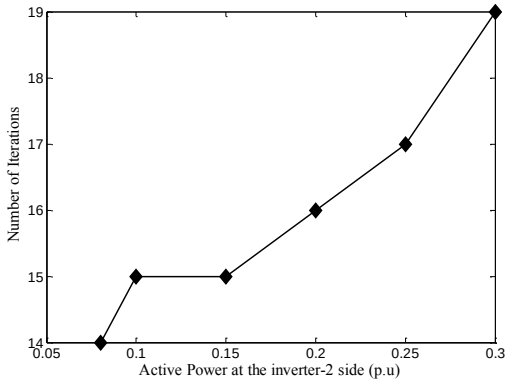

Fig. 10: Variation of 'NI' with active power in second DC link

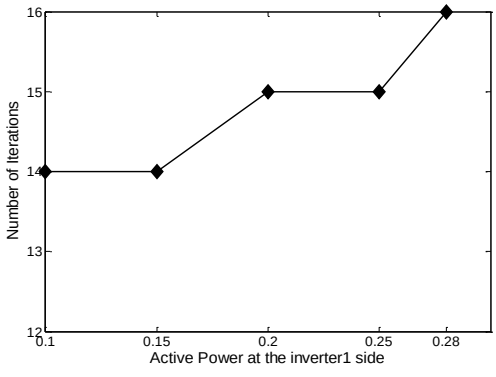

Fig. 11: Variation of 'NI' with active power in first DC link

Table VII: Study of power-flow convergence pattern with active power in the first DC link

HVDC Links		HVDC Link Specification		Power Flow Solutions	
Rectifier Bus	Inverter Buses	Control Strategy-5		AC terminal Buses	HVDC variables
85	88, 233	$P_{dI2} = 0.2$ (p.u) $V_{dR} = 1$ (p.u) $a_R = 1.08$ $a_{I1} = 1.1$ $a_{I2} = 1.1$	P_{dI1} (p.u) 0.1	$\boldsymbol{V_{85}} = 0.9831\angle -17.3494$ $\boldsymbol{V_{88}} = 0.99\angle -20.2874$ $\boldsymbol{V_{233}} = 0.9858\angle -15.9583$	$V_{dI1} = 0.999$; $V_{dI2} = 0.998$; $P_{dIR} = 0.3005$; $I_{dI1} = 0.1001$; $I_{dI2} = 0.2004$; $I_{dR} = 0.3005$; $\gamma_{I1} = 22.0973$; γ_{I2}=20.1488; α_R =14.0408; $cos\phi_{I1} = 0.9174$; $cos\phi_{I2} = 0.9203$; $cos\phi_R = 0.9418$; NI=14;CT=87.437434;
			0.15	$\boldsymbol{V_{85}} = 0.9808\angle -17.4693$ $\boldsymbol{V_{88}} = 0.99\angle -20.2093$ $\boldsymbol{V_{233}} = 0.9836\angle -16.075$	$V_{dI1} = 0.9985$; $V_{dI2} = 0.998$; $P_{dIR} = 0.3506$; $I_{dI1} = 0.1502$; $I_{dI2} = 0.2004$; $I_{dR} = 0.3506$; $\gamma_{I1} = 21.4575$; γ_{I2}=19.801; α_R =12.2691; $cos\phi_{I1} = 0.9169$; $cos\phi_{I2} = 0.9224$; $cos\phi_R = 0.9441$; NI=14;CT=87.093402;
			0.2	$\boldsymbol{V_{85}} = 0.9785\angle -17.5935$ $\boldsymbol{V_{88}} = 0.99\angle -20.1333$ $\boldsymbol{V_{233}} = 0.9815\angle -16.196$	$V_{dI1} = 0.998$; $V_{dI2} = 0.998$; $P_{dIR} = 0.4008$; $I_{dI1} = 0.2004$; $I_{dI2} = 0.2004$; $I_{dR} = 0.4008$; $\gamma_{I1} = 20.7986$; γ_{I2}=19.4495; α_R =10.1946; $cos\phi_{I1} = 0.9164$; $cos\phi_{I2} = 0.9244$; $cos\phi_R = 0.9463$; NI=15;CT=92.089820;
			0.25	$\boldsymbol{V_{85}} = 0.9762\angle -17.7218$ $\boldsymbol{V_{88}} = 0.99\angle -20.0592$ $\boldsymbol{V_{233}} = 0.9794\angle -16.3212$	$V_{dI1} = 0.9975$; $V_{dI2} = 0.998$; $P_{dIR} = 0.4510$; $I_{dI1} = 0.5025$; $I_{dI2} = 0.2004$; $I_{dR} = 0.4510$; $\gamma_{I1} = 20.1179$; γ_{I2}=19.0945; α_R =7.5728; $cos\phi_{I1} = 0.916$; $cos\phi_{I2} = 0.9246$; $cos\phi_R = 0.9485$; NI=15;CT=91.472996;
			0.28	$\boldsymbol{V_{85}} = 0.9748\angle -17.8008$ $\boldsymbol{V_{88}} = 0.99\angle -20.0158$ $\boldsymbol{V_{233}} = 0.978\angle -16.3983$	$V_{dI1} = 0.9972$; $V_{dI2} = 0.998$; $P_{dR} = 0.4812$; $I_{dI1} = 0.2808$; $I_{dI2} = 0.2004$; $I_{dR} = 0.4812$; $\gamma_{I1} = 19.6985$; γ_{I2}=18.8797; α_R =5.4231; $cos\phi_{I1} = 0.9157$; $cos\phi_{I2} = 0.9276$; $cos\phi_R = 0.9498$; NI=16;CT=99.869132;

VI. CONCLUSIONS

For power-flow solution of an integrated AC-DC system, control specifications adopted for the system bridge the gap between the number of independent equations and the number of unknown quantities. Depending on the application, several combinations of valid control specifications are possible. Each combination of a set of valid control specifications comprises a control strategy. It is observed that the power-flow convergence is strongly affected by the control strategy adopted. This work investigates the mechanism by which different control strategies affect the convergence of the iterative process. It is observed that for a majority of the possible control strategies, the equivalent power injections at the converter terminal buses are independent of the NR iterative loop. However, for others, the equivalent reactive power injections need to be computed in every NR iteration. This affects the convergence of the algorithm. This is validated by multiple case studies with application of

nine different control strategies on a three terminal DC network incorporated in the IEEE 300-bus test system.

From the case studies, it was observed that the power-flow convergence pattern for integrated AC-DC systems depend upon a number of factors. Firstly, it depends on the control strategy adopted for the DC link. Secondly, for a particular control strategy adopted, it depends upon the values of the electrical quantities specified in the control strategy. In addition, it also depends upon the location of the DC link i.e. the system buses between which the link is incorporated.

The above research work could be further extended by investigating and comparing the effects of power flow algorithms other than the sequential method. The effect of power flow based on soft computing techniques on the convergence pattern can be investigated in light of different control methodologies and computation platforms.

REFERENCES

[1] Arrillaga, J., Watson, N.R., "Computer Modelling of Electrical Power Systems", (John Wiley & Sons Ltd, 2003, 2nd edn.).

[2] Kundur, P.,"Power System Stability and Control", (Tata McGraw-Hill Publishing Co. Ltd., 2007).

[3] Wang, X.F., Song, Y.H., and Irving, M., "Modern Power Systems Analysis", (Springer, 2008).

[4] Padiyar, K.R., "HVDC Power Transmission Systems", (New Age International Publishers, 2012, 2nd edn.).

[5] Smed, T., Andersson, G., Sheble, G.B., and Grigsby, L.L., "A New Approach to AC/ DC Power Flow", *IEEE Trans. Power Syst.,* 1991, 6, (3), pp. 1238-1244.

[6] Reeve, J., Fahmy, G., and Stott, B., "Versatile load flow method for multi terminal HVDC systems", *IEEE Trans. Power Appar. Syst.* 1997, PAS-96, pp. 925-933.

[7] El- Hawary, M.E., Ibrahim, S.T., "A new Approach to AC –DC load flow Analysis", *Electric Power Research,* 1995, 33, pp. 193-200.

[8] Padiyar, K.R., Kalyanaraman, "Power Flow Analysis in MTDC-AC Systems- A New Approach", Taylor and Francis, Electric Machines and Power Systems, 1995, 23, pp. 37-54.

[9] Y.K.F.D Niebur, C.O. Nwankpa, H. Kwanty and Fischl, "Multiple Power Flow Solutions of Small Integrated AC-DC Power Systems", *IEEE Proc. Int. Symp. Circuits and Systems, Geneva, Switchgerland*, 2000, pp. 224-227.

[10] Chongru Liu, Boming Zhang, Yunhe Hou, Felix F. Wu and Yingshang Liu, "An Improved Approach for AC-DC Power flow Calculation with Multi Infeed DC Systems", *IEEE Transactions on Power Systems*, vol. 26, No. 2, May 2011, pp. 862-869.

[11] Liu, C., Bose, A., Hou, Y., "Discussion of the Solvability of HVDC Systems Power Flow with a Sequential Method", Elsevier, EPSR, 2012, 92, pp.155-161.

[12] S. Messalti, S. Belkhiat, S. Saadate and D. Flieller, "A new Approach for Load Flow Analysis Integrated AC-DC Power Systems using Sequential Modified Gauss Seidal Methods", *European Transaction on Electrical Power*, vol. 22, issue 4, May 2012, pp. 421-432.

[13] Ulas Kilic and Kursat Ayan, "Optimizing Power Flow of AC-DC Power Systems using Artificial Bee Colony Algorithms", *Electrical Power and Energy Systems 53(2013)*,pp. 592-602.

[14] Y. Sun, G.Zhang, W. Xu. J.G Mayordomo, "A Harmonically Coupled Admittance Matrix Model for AC-DC Converters, *IEEE Trans. on Power Systems*, Nov. 22, 2007, pp. 1574-1582.

[15] J. Yu, W. Yan, W. Y. Li, C.Y Chung and K.P Wong, "An Unfixed Piecewise Optimal Reactive Power Fow Model and its Algorithms for AC-DC Systems", *IEEE Trans. Power Syst.*, Vol. 23, No. 1, pp. 170-176, Feb, 2008.

[16] R. Wiget, G. Anderson, "DC Optimal Power Flow Including HVDC Grids", *IEEE Electrical Power and Energy Conference*, 2013 pp. 1-6.

[17] D. L. H. Aik, G. Anderson, "Analysis of Voltage and Power Inractions in Multi-Infeed HVDC Systems", *IEEE Trans. on Power Del.*, Vol. 28, No. 2, April 2013 pp. 816-824.

[18] U. Kilic, K. Ayan and U. Arifoglu, "Optimizing Reactive Power Flow of HVDC Systems Using Genetic Algorithms", *Electrical Power and Energy Systems*, 55(2014) pp. 1-12.

[19] M. J. Carrizosa, F.D. Navas and Gilney Damm, "Optimal Power Flow in Multi-terminal HVDC Grids with Offshore Wind Farms and Storage Devices", *Electrical Power and Energy Systems*, 65(2015) pp. 291-298.

[20] http://www.ee.washington.edu/research/pstca/

APPENDIX - A

$$V_{ac\ base} = V(line\ to\ line\ rms\ voltage) \quad (A.1)$$

$$I_{ac\ base} = \frac{S_{base}}{\sqrt{3}\ V_{ac\ base}} \quad (A.2)$$

$$Z_{ac\ base} = \frac{V_{ac\ base}}{\sqrt{3}\ I_{\ ac\ base}} \quad (A.3)$$

Table A.1: Selection of base values for the DC system

$V_{dc\ base} = k\ V_{ac\ base}$; where $k = \frac{3\sqrt{2}}{\pi}\ n_b$
$I_{dc\ base} = \frac{\sqrt{3}}{k}\ I_{ac\ base}$
$Z_{dc\ base} = k^2\ Z_{ac\ base}$
$R_{dc\ base} = \frac{3}{\pi}\ n_b\ X_{c\ base}$

APPENDIX-B

As already explained in Section-IV, for solving the AC power flow, the equivalent active and reactive power injections at the AC terminal buses connected to the converters need to be computed. The methods involved in the computation of the power injections for different control strategies are all different. However, they can be broadly categorized into two distinct ones. While in the first one the power injections are independent of the AC power flow, in the second one, they are dependent on the iterative process. Control strategies-1, 2, 3, 4 and 9 belong to the former category while Control strategies-5, 6, 7 and 8 belong to the latter. The detailed steps involved in the computation of the power injections for Control strategies-1 and 5 is shown in Table B.1 below.

From Table B.1, it can be observed that the active power injections can be computed prior to the AC power flow. It is also observed that in Control Strategy-1, the quantities ϕ_R, ϕ_{I1} and ϕ_{I2} hence the reactive power injections Q_{dR}, Q_{dI1} and Q_{dI2} can be computed prior to the AC power flow by manipulation of the specified variables. On the other hand, in Control Strategy-5, they are dependent on the AC power flow variables and thus, need to be updated every iteration.

The steps corresponding to the other control strategies can be detailed in a similar manner, and are not shown due to limitations of space.

Table B.1: Steps to compute active and reactive power injections in control strategies 1 and 5

Control Strategy-1		Control Strategy-5	
Specified quantities	Unknown quantities	Specified quantities	Unknown quantities
P_{dI1},P_{dI2}, V_{dR},α_R,γ_{I1},γ_{I2}	V_{dI1},V_{dI2},P_{dR},I_{dI1},I_{dI2},I_{dR}, a_R, a_{I1},a_{I2},$cos\phi_R$,$cos\phi_{I1}$,$cos\phi_{I2}$	P_{dI1},P_{dI2}, V_{dR},a_R,a_{I1},a_{I2}	V_{dI1},V_{dI2},P_{dR},I_{dI1},I_{dI2},I_{dR}, α_R, γ_{I1},γ_{I2},$cos\phi_R$,$cos\phi_{I1}$,$cos\phi_{I2}$
Step 1: compute V_{dI1} and V_{dI2} using DC load flow Step 2: compute $I_{dI1} = \frac{V_{dR}-V_{dI1}}{R_d}$ Step 3: compute $I_{dI2} = \frac{V_{dR}-V_{dI2}}{R_d}$ Step 4: compute $I_{dR} = I_{dI1} + I_{dI2}$ Step 5: compute $P_{dR} = V_{dR} I_{dR}$ Step 6: Compute $\cos\phi_R = \frac{V_{dR}\cos\alpha_R}{V_{dR}+X_c I_{dR}}$ Step 7: Compute $Q_{dR} = P_{dR}\tan\phi_R$ Step 8: Compute $\cos\phi_{I1} = \frac{V_{dI1}\cos\gamma_{I1}}{V_{dI1}+X_c I_{dI1}}$ Step 9: Compute $\cos\phi_{I2} = \frac{V_{dI2}\cos\gamma_{I2}}{V_{dI2}+X_c I_{dI2}}$ Step 10: Compute $Q_{dI1} = P_{dI1}\tan\phi_{I1}$ Step 11: Compute $Q_{dI2} = P_{dI2}\tan\phi_{I2}$ **Note:** P_{dI1} and P_{dI2} are specified. P_{dR}, Q_{dR}, Q_{dI1} and Q_{dI2} can be computed prior to the AC power flow and hence, are independent of the iterative loop.		Step 1: compute V_{dI1} and V_{dI2} using DC load flow Step 2: compute $I_{dI1} = \frac{V_{dR}-V_{dI1}}{R_d}$ Step 3: compute $I_{dI2} = \frac{V_{dR}-V_{dI2}}{R_d}$ Step 4: compute $I_{dR} = I_{dI1} + I_{dI2}$ Step 5: compute $P_{dR} = V_{dR} I_{dR}$ Step 6: Compute $\cos\phi_R = \frac{V_{dR}}{a_R V_i}$ **Note 1:** V_i is an AC power flow variable and is updated every iteration. Hence, $\cos\phi_R$ changes in every iteration. Step 7: Compute $Q_{dR} = P_{dR}\tan\phi_R$ Step 8: Compute $\cos\phi_{I1} = \frac{V_{dI1}}{a_{I1}V_j}$ Step 9: Compute $\cos\phi_{I2} = \frac{V_{dI2}}{a_{I2}V_k}$ **Note 2:** V_j and V_k are also AC power flow variables and are updated every iteration, along with $\cos\phi_{I1}$ and $\cos\phi_{I2}$. Step 10: Compute $Q_{dI1} = P_{dI1}\tan\phi_{I1}$ Step 11: Compute $Q_{dI2} = P_{dI2}\tan\phi_{I2}$ **Note 3:** P_{dI1} and P_{dI2} are specified. P_{dR} can be computed prior to the AC power flow. However, Q_{dR}, Q_{dI1} and Q_{dI2} depend upon ϕ_R, ϕ_{I1} and ϕ_{I2} respectively, and need to be updated every iteration.	

EnTwine: Feature Analysis and Candidate Selection for Social User Identity Aggregation

Niyati Chhaya[§],Nikaash Puri* Dhwanit Agarwal[†], Paridhi Jain[‡], and Deepak Pai[§]
*Delhi Technological University
nikaashpuri@gmail.com
[†]Indian Institute of Technology Kanpur
dhwanit@iitk.ac.in
[‡]Indian Institute of Information Technology, Delhi
paridhij@iiitd.ac.in
[§]Adobe Research India
{nchhaya,dpai} @adobe.com

***Abstract*—Organizations measure their social audience based on the number of users, fans, and followers on social media. Every social media platform has its own user identity and a single user is usually present across varied platforms. Due to the disconnected user profiles, identifying duplicate users across media is non-trivial. Hence, the audience size estimated by the marketers is often inflated. A marketer requires a complete view of a user for correct targeting and user segmentation. This view is not easily available due to the boundaries defined by the networks. In this work, we explore the feature space across social media that can be leveraged for intelligent user identity aggregation. Further, we present a two-phase unified identity creation process using our feature analysis, unsupervised candidate selection, and supervised user matching algorithms on four different social networks.**

I. Introduction

Online social networks are successful in convincing users for membership. Each of these networks then uses the registered user's information, activity, and interactions to personalize their experience. Organizations and marketers exploit this information to profile users and do targeted campaigns. The process of user profiling is restricted to information from individual networks. In reality, a user is present across different media and often relevant information about a user that can be obtained by aggregating his identity across networks is missed.

From the user's perspective, varied social networks provide platforms for different purposes. For example, Twitter [1] is a microblogging site, whereas Quora [2] is an interest–based social network. A user shares different aspects of his personality on each of these networks. Gathering this information across network identities will allow marketers to look beyond tunneled network–specific user profile. Identity of a user is protected by the network and hence, gathering a user profile across networks is not a trivial task. Further, each network comes with its own rules of identity definitions, hence adding constraints for data aggregation.

The first four authors have equal contribution
[1]www.twitter.com
[2]www.quora.com

Social media users are an important metric for organizations to estimate their reach and popularity. With companies having multiple outreach on diverse social networks, determining the size of their audience is an important use case. Current tools add unique user profiles across the networks thereby incorrectly assuming no duplicates. This generates an inflated number. In this work, we present methods of aggregating same user across networks which can be leveraged for correct reporting.

We approach the problem of user profile aggregation by first studying the feature space. We employ a statistical feature analysis approach by independently studying the available features, relevant as well as the redundant features. Further, we present a two–phased algorithm for identity aggregation exploiting both data availability using unsupervised methods and identity matching using supervised models. The main contributions of this work include feature relevancy analysis, unsupervised approach for candidate selection, and a unique pipeline that integrates a two-phased approach to building a unified user profile.

The rest of the paper is organized as follows. Section II presents the literature survey, followed by an overview of the data in section III. We then introduce our framework titled 'EnTwine', consisting of three components, feature analysis (sectionV), candidate selection (section VI), and user identification (section VII). All the analysis and experiments are presented in section VIII. The paper concludes with a discussion and insights from our work.

II. Related Work

User identity aggregation has been well explored([3], [4], [9], [13], [15]). The problem can be approached as a combination of two sub–problems: identity search and identity matching [5]. Profile features have been used for searching([4], [9], [15]) as well as ensemble approaches that use profile, network, and content features have been explored. Further, the feature selection is either heuristic or based on domain knowledge [12]. Heuristic approaches introduce limitations

and miss out on inter–feature dependencies. In this work, we explore the feature space and further try to overcome limitations introduced due to the heuristic methods. Another known problem in the space of identity search is the size of the search space. Searching the complete network for candidate identities is computationally expensive and not feasible with derived features. We attempt at addressing this issue in this paper.

For user matching, work focused on improvising identity matching techniques using syntactic and semantic profile, content, and features across networks ([12], [7], [15]) has been studied. Linear optimization has proven to be the state-of-the-art with precision of 0.9 over 10 million users across 7 networks (5 Chinese and 2 English)[7]. The aim of this paper is to focus on the complete process of studying the feature space, search-space reduction, and then matching rather than matching accuracy alone.

Datasets define the complexity of the problem. Researchers have been restrictive by choosing similar networks for the aggregation task. English networks ([5], [9], [13], [15]), German networks ([6], [14]), Chinese networks ([7]), Image-based networks ([3], [1]), Video-based networks ([4], [2]), and Location-based networks ([2]) have been explored. We look at different kinds of networks in our work, hence introducing challenges due to varying feature spaces.

III. Datasets

This section discusses the datasets collected for our work. We focus on four social networks: Twitter, a microblogging service; Facebook, a social personal connect [3]; Quora, an interest–based network; and LinkedIn, a professional network [4]. These networks vary in quality, quantity, and credibility of information. Twitter gives a users' opinions on events, Facebook is informative about the network, Quora gives interests, while LinkedIn gives a professional view of the user.

The data is not easily available. We use public API's to extract the user data. Quora does not have an API, hence we use a web crawler to gather the information. Not all users allow access to their complete data. We hence have a smaller dataset with complete features as compared to partial user data. Table I shows the size of the collected data.

TABLE I: DATASET SIZE

Social network	Partial data	Complete data
Facebook	445,743	420,000
Twitter	449,346	38,000
Linkedin	9,430	3,000
Quora	26,602	105,232

IV. EnTwine: Identity Aggregation Framework

The system has two phases: Candidate selection and User identification (refer figure 1). The novelty of this work lies in the input for Candidate selection i.e. the extensive feature analysis and the methods used for the selection process. The identification step introduces completeness to the process and allows us to understand the utility of the feature analysis and candidate selection. The system follows the following steps.

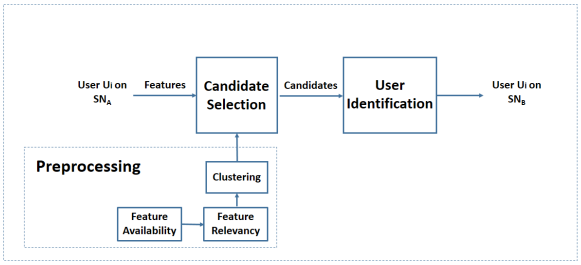

Fig. 1: EnTwine: Two-phased Identity Aggregation Framework

1) Input: Query user U_a, user identity on network SN_A, whose identity is to be aggregated along with features $F(U_a)$ (section V describes the features) and users $U_B = (U_{B1}, U_{B2}, ..U_{Bk})$ on the search network SN_B.
2) Pre–processing: Feature analysis and clustering within search network SN_B (discussed in section VI) is done on a periodic basis. Hence,the clustered network is available when we look for a query user. The clustering is done to reduce computational cost during the candidate selection step. The output from this pre–processing is available for candidate selection.
3) Candidate selection: This step refers to taking the query user U_a and finding a relevant search space for the identity in the segmented space of search network SN_B. Output here is the set of users,
$$candidate(U_a, SN_B) = U_{CB1}, U_{CB2}, ..U_{CBk}$$
such that these are likely matches for the input user. The size of $candidate(U_a, SN_B)$ is much lesser than size of SN_B.
4) User identification: This step takes in the candidates and finds the match identity for the query user on the search network. The approach for this analysis is discussed in section VII.

The algorithms involved are presented in the rest of the paper.

V. Feature Analysis

This section describes our feature space study. We focus on feature availability, relevancy, and redundancy in user–related features. Table II shows the list of features used along with the availability across networks.

A. Profile Features

Users create multiple online profiles to exploit varied services from different social networks. Profile characteristics of the user are consistent across social networks. We use these

[3] www.facebook.com
[4] www.linkedin.com

TABLE II: FEATURE SPACE ANALYSIS

Type	Raw feature	Availability				Extracted_feature
		Twitter	Facebook	Quora	LinkedIn	
Profile	Username	✓	✓	✓	✓	Jaro distance LCS distance Levenshtein distance Length difference Char Bi-gram Jaccard index Char Bi-gram Cosine similarity Entropy difference
	Name	✓	✓	✓	✓	Jaro distance LCS distance Levenshtein distance Length difference Char Bi-gram Jaccard index Char Bi-gram Cosine similarity Entropy difference
	Location	✓	-	✓	✓(area name)	Ratio of common locations Ratio of common postal codes
	Bio	✓(description)	-	✓(occupation and description)	✓(summary)	Bio length difference Bio words distribution POS tags distribution Jaccard index of bio words Cosine similarity of bio words Ratio of miss-spelled words
	Profile Image	✓	✓	✓	✓	Histogram Similarity Face similarity
	Gender	-	✓	-	-	Boolean
	Language	✓	✓(from locale)	-	-	Boolean
Content	Posts	✓(tweets)	✓(posts)	✓(questions and answers)	-	Activity distribution Device distribution Application distribution URLs distribution POS tags distribution Avg. # of multimedia shared Avg. # of words Avg. # of miss-spelled words Avg. length of words

invariant features in our work to capture the characteristic properties of the user.

1) Username and Name: Username is a unique attribute of the user. 30 to 40% of users choose similar usernames across networks [13]. Name, on the other hand, is not enforced to be unique. The value of name attribute is completely at the user's disposal, however, few social networks such as Facebook, encourage the use of real names on the network.

We extract six syntactic features for username and name. Distance metrics such as Levenshtein distance, Jaro distance, normalized longest common subsequence length, and phonetic distance are used. To capture a user's favoritism towards certain characters, Jaccard similarity coefficient between character unigrams, and cosine similarity between character bigrams is calculated. We use keyboard distance between the two usernames [15] to identify typing errors made by the user. Similar features are derived for name attribute. We have 14 features based on username and name of the user.

2) Profile Image: Users choose an image to show their identity. A comparison of profile images of the user across social networks can help in identifying if the two profiles belong to the same user. We use image histogram matching and face detection and matching to compare profile images. Histogram matching is done by comparing RGB histograms of the image, root mean squared distance is measured. In the second method, face detection is done using SIFT [8] and then detected faces are compared. Similar faces have a lower distance. Image meta–data is also used as a feature for the comparison.

3) Bio: Bio gives the user's description. The two profiles are compared on the bio attribute to understand if the user is consistent about the description across networks. Cosine similarity is used on the text after normalizing the content. We also calculate cosine similarity and Jaccard distance between bigrams. The distribution of part-of-speech tags(POS tag) [10] is also compared.

As bio is more rich in text than other profile attributes, we can extract stylistic and writing pattern of the user. We calculate average length of words used, POS tag distribution, number of digits vs. characters, and number of spelling mistakes (using Nodebox [5]). Six features are extracted in all.

4) Location: Location of a user lists the places a user posts from. Few networks like Quora allow access to the list of locations the user has been to, while few networks allow access to the most recent location of the user. To extract location, we use the 'location' attribute of the user profile or infer the same based on geo–tagged posts of the user. We compare the

[5]http://nodebox.net/code/index.php/Linguistics

unique locations of the user on different networks and check for existence of the location within the location list. Country names and postal codes are also compared.

5) Gender: Gender of a user is an invariable attribute. If the gender does not match, the possibility of two profiles belonging to the same person is low. We extract a Boolean attribute by comparing the gender across profiles, which holds true if the gender matches. For networks where gender is not accessible, user's first name is used along with Genderizer [6] to derive the value.

6) Language: User may choose to write posts in any language supported by the network. Two profiles which belong to same user are likely to have the same language preferences across networks. We extract a boolean feature which holds true if the profiles mention same language attribute.

B. Content Features

Users' interests on topics, language, writing style, and post patterns retain across multiple networks. These features rely on the users' posted content. The following content features are used in our analysis.

1) Posts: We compare bag–of–words for a sample of the users' posts on each social network and calculate the cosine similarity. Further, average length of words, distribution of part of speech tags, average number of URLs shared per post, emoticons, and sentiment distribution of the posts are also derived.

2) Post - hour of the day: User posts on the social network relative to their leisure time. A user's activity distribution reveals the time of the day while posting. Comparison of the posting behavior may help in understanding if the user is active on all networks at the same time. We extract number of posts in each hour of the day and compare the distribution extracted for different social networks. We analyze Twitter and Facebook users for this feature. We model the user's pattern based on a sample of his recent posts.

3) Device: Users access their social profiles through various devices. Social networks have applications for platforms such as iPhone, iPad, and Android. A device tag is associated with the post when a particular app is used through a specific device. We compare these device tags to trace the user across different networks. We calculate the Jaccard coefficient index for devices used.

4) Application: Social network aggregation services allow the user to access all networks through a single service (example Twitterfeed, Hootsuite). When a user posts through these services a tag is attached to the post, we use this tag to identify the services that the user uses to post on different platforms simultaneously. Jaccard coefficient index is used as the metric here.

To summarize, 33 features associated with the user profiles are extracted. Rest of this section presents the feature analysis.

[6]https://pypi.python.org/pypi/genderizer

C. Relevancy Analysis

Not all networks provide the complete set of features discussed above. Also, each network has its own way of defining a certain feature, for example on Twitter a user profile has a bio, whereas on Quora you might have an occupation. It hence becomes necessary to identify features that are comparable across user profiles. Further, some features such as gender may not be discriminating across profiles, one needs to understand the behavior of each feature based on some known aggregated profile information. We begin our analysis with feature availability. The task is to identify features available across networks. Table II summarizes this analysis. We then move on to identify comparable features. Comparability of a feature can be either approached in a heuristic manner or using domain knowledge. We use heuristics such a feature type and feature content to identify whether the features are comparable. For our analysis, we manually identify comparable features using heuristic approach. Table II also shows the comparable features.

To identify the discriminative power of a feature we define three metrics that are calculated by processing pre–labelled ground truth data. As the purpose here is to find user profiles that belong to the same user, we look at our data as a two class problem. We define the 'positive' or 'match' class representing same user's different profiles and the 'non–match' or 'negative' class representing identities that belong to different users. The metrics are defined as follows,

1) Class Majority Index: The purpose of this index is to empirically identify a threshold $CMI(Feature)$ that acts a distinguishing point for the data. For each feature, the CDF (cumulative distribution of frequency) is plotted individually for both classes. This gives us information about the distribution of the feature values. We define $CMI(Feature)$ as the intersection point of these graphs. Further, a feature is discriminative if $CMI(Feature)$ is a point that divides the data such that, majority (majority = 80%) of the data points on either side of $CMI(Feature)$ belong to the same class. For features, where this doesn't hold true, we term those as non–discriminative. Figure 2 shows the CDF curves for different metrics for username. The intersection point of the CDF curves signify the class distribution at that particular distance. The Y axis shows the CDF. As seen in the figure, Levenshtein distance is discriminative as the intersection lies 0.8 on the CDF, similarly Normalized LCS is also discriminative as $(1 - 0.8)$ is the intersection point.
2) Encroachment index: The majority index does not guarantee that the class is pure within a certain error bound. In other words, we cannot tell whether the relevant feature is discriminative enough to assure that at the extreme metric values for each class, we would get samples from one class. We define the encroachment index that signifies how deep one needs to go into the opposite class to reach one–class purity. We define

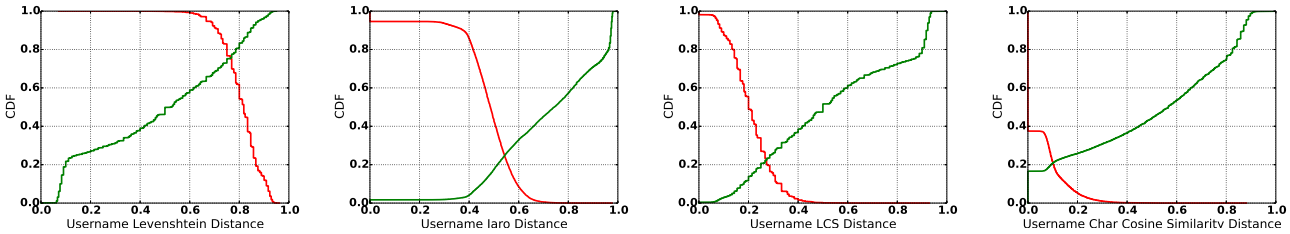

(a) Levenshtein distance (b) Jaro distance (c) Normalized LCS (d) Character cosine similarity

Fig. 2: CDF plot for username across the match (green line) and no match (red line) class using different metrics

encroachment index ($EI(F)$) for each class as

$$EI(F)_M = \frac{|min(ClassNM) - CMI(Feature)|}{|min(ClassM) - CMI(Feature)|} \quad (1)$$

where, $min(ClassNM)$ is the minimum value that the feature takes for the encroaching class, and $min(ClassM)$ is the minimum value that the feature takes for the calculating class. We do a similar thing for the other class,

$$EI(F)_{NM} = \frac{|max(ClassM) - CMI(Feature)|}{|max(ClassNM) - CMI(Feature)|} \quad (2)$$

This second index is of importance for the following reason. Say, we define a threshold above which we have 20% user–pairs of the non–match class. If we experimentally conclude that the non–match class completely encroaches into the match class. Then this means that some fraction of the number of non–match pairs had values equal to the highest (or for some metrics lowest) value of the match pair. This could be an indicator of the metric not being discriminative in our study. For some features, the range of each class might be the same but the distribution of data across classes on either side of $CMI(Feature)$ would differ. In this case we modify $EI(F)$ to capture the difference in the standard deviation and variance of the data distribution rather than just the range alone.

3) Content Impurity Index: We have still not captured the actual number of users that might overlap beyond the $CMI(Feature)$ in the opposite class. Hence, we introduce a measure that captures the proportion of users within a class region that belong to the other class. Hence, we define the content impurity index as,

$$CII(Feature) = Max(Term(M), Term(NM))$$

where,

$$Term(M) = \frac{Users[min(ClassNM, CMI(Feature)]}{Total(ClassM)}$$

$$Total(ClassM) = Users[min(ClassNM, CMI(Feature)] + Users[min(ClassM, CMI(Feature)]$$

$$Term(NM) = \frac{Users[max(ClassM, CMI(Feature)]}{Total(ClassNM)}$$

$$Total(ClassNM) = Users[max(ClassM, CMI(Feature)] + Users[max(ClassNM, CMI(Feature)]$$

MAX captures the higher impurity among the two classes. Ideally we want $CII(Feature) = 0$.
Another way to measure the metric is by comparing the data points on either side of the CMI as a Loss/Profit ratio. Here, loss is the user-pairs in the no match class (NM)above CMI. And profit is the user-pairs in the match class above this threshold (M). Consider $NM = M$, then $NM/M = 1$ and this indicates a highly impure collection. We can look at it in another way, if we were given a random pair of users having username above this threshold. The probability of this pair belonging to the match class is same as that of belonging to the no match class. A small value of NM/M indicates that the feature is relevant. Since, it implies that for a user-pair having username above that threshold, there is a high probability that they belong to the match class. Also note that, in case of skewed data (NM is very big as compared to M) we look at $NM/(NM + M)$ instead. Table III shows the relevant features based on this index.

TABLE III: MOST RELEVANT FEATURES ON THE BASIS OF NM/M

Feature	Thresh	$\frac{NM}{M}$	$\frac{NM}{(NM+M)}$
Name Leven	0.85	6.47E-05	1.850483729
Name Leven	0.8	6.88E-05	1.800351803
Name CosSim	0.9	0.004483	0.004462915
Name Phonetic	0.85	0.004741	1.850483729
Name Kbd dist	0.85	0.004743	1.850088183

TABLE IV: MOST RELEVANT FEATURES ON THE BASIS OF NM/(NM+M)

Feature	Thresh	$\frac{NM}{M}$	$\frac{NM}{(NM+M)}$
Name CosSim	0.9	0.004482922	0.004462915
Name Jaro	0.85	0.004746043	0.004723624
Name LCS	0.85	0.009492086	0.009402833
Name Jaccard	0.85	0.014238129	0.01403825
Name Jaro	0.9	0.017926402	0.017610706

All the definitions here assume that higher the value of the distance metric the users are unlikely to match. In case of features with an inverted relationship (Non–match= 0), we would need to inverse all max values to min and vice–versa.

D. Redundancy Analysis

Relevant features mark their importance on decision for a profile pair under observation. But, some features might be inter–dependent and hence give redundant information. We perform correlation–based feature redundancy tests. In this analysis we consider two features f_i and f_j among which we are trying to determine some dependancy. We plot a joint frequency distribution between each value that f_i can take and each value that f_j can take. From this joint frequency distribution we determine the joint probability distribution.

Consider for instance the following example. We calculated the joint probability distribution between gender and posts. The intuition behind this was to draw inferences of the form (do girls talk about certain topics, say Justin Bieber). This form of analysis could be used in the following ways:

1) A very high probability of the two features taking certain values would indicate high degree of correlation and suggest dependency. This could then be used in our supervised models to ensure that the models are only trained with independent features. So, say 'Female' and 'Justin Bieber' had a high probability of occurring together and 'Male' and 'football' had a high probability of occurring together. This would imply that the content of posts is dependent on the gender and hence both should not be used in conjunction in our supervised models.
2) A very high probability of certain feature values occurring together does not imply such a dependency but may still be used in the searching step of EnTwine. To understand this, consider the following example. Say that the occurrence of gender 'Female' and content 'Justin Bieber' is highly likely. This does not imply feature dependence since we have found no similar results for the gender 'Male'. Hence we cannot conclude that features gender and content are related. However, in our searching step. Say, the user profile we are looking for has a gender value of 'Female'. In such a case, we can use the results obtained above to expand the candidate set by looking for users talking about 'Justin Bieber'.

We carried out experiments for different feature combinations. However, in our experiments we did not find a high probability of occurrence of feature value pairs. This could be due to the following reasons:

1) Extending the gender example, it is possible that users of the same gender talk about similar topics rather than the same topic. To understand this, consider the following example. Different users with the gender 'male' may talk about different sports such as 'football', 'cricket', etc.. It would make more sense then to represent what users are talking about at a higher level of granularity ('sports' in this case) and then use our feature redundancy analysis. The aim then could be to make statements of the form 'Given two user profiles having the same gender, what is the probability they talk about similar things?'. Another interesting question could be 'Given that the two users talk about similar things, what is the probability that they have the same gender?'. The answers to both of these questions could be used in the searching step.
2) It could be that such dependancies require large amounts of data to present themselves. By this we mean that such patterns may only emerge on very large datasets. Hence, our dataset may have been unable to capture such dependencies.

VI. Candidate selection

We now have a list of relevant features and various measures associated with these features. Next we look at candidate selection. As explained earlier, the search network is pre–processed and segmented. We use clustering algorithms to do this. In an ideal world, the candidate space for every user profile is the aggregating network (search network). But, searching through a network is computationally expensive and in some cases the set of search user profiles might be pre–defined hence, there is no need to search the network. We would like to avoid bias introduced due to training data and hence, we focus on using clustering methods as against any classification mechanism. We start with the clustering algorithm here.

As described in section V, relevant features are name and username. These features are used for clustering. We use an approach based on Canopy clustering[11]. Canopy clustering was introduced to reduce the computational overhead in clustering and processing large scale data. This algorithm uses two thresholds to define clusters. The intuition behind this algorithm is create canopies based on two thresholds along the varied feature distances specified. In this paper we use the Jaro distance as the clustering measure. The algorithm is given as Algorithm 1 [**procedure** CANOPY-CLUSTERING].

Algorithm 1 Algorithm for Canopy Clustering

```
1: procedure CANOPY-CLUSTERING
2: U ← set of user profiles on the network
3: T1 ← loose threshold
4: T2 ← tight threshold
5: d(x, y) ← distance measure
6: for each user-profile x in U:
7:     create canopy Cx such that
           for each user-profile y in U:
               insert y into Cx if d(x, y) ¡ T1;
8: for each user-profile y selected in the previous step
       remove y from U if d(x, y) ¡ T2;
```

The algorithm when translated to our application relies on two important interpretations.

1) Identifying thresholds T_1 and T_2
2) Cluster centroid: Canopy clustering is a distribution based clustering algorithm and hence does not have an inherently defined cluster centroid. In this work, as this is an intermediate step towards matching, we need to define the cluster centroid to understand the belongingness of a given user profile.

Thresholds T_1 and T_2 are usually defined based on domain knowledge. Here, as mentioned we use Jaro distance as the similarity measure, and empirically fix $T_1 = 0.9$ and $T_2 = 0.7$ respectively. Algorithmically, this can be interpreted as two user profiles would be in the same cluster if their name (or username) has a metric value greater than T_2. Instead of relying on domain knowledge, we study the data distribution before choosing the threshold values.

Results of feature relevancy analysis are used in order to determine thresholds. Ideally, the existence of a single threshold above which all user profiles are in the match class and below which all user profiles do not match would be most suitable for the approach. However, this sort of threshold does not exist. So, 85% percentage measure is chosen in order to define thresholds. The relevancy metrics are used here.

Fig 2(b) shows the plot for username across the match and the non-match class using Jaro distance measure for user profiles on Twitter and Quora. As is clear from the plots, for close to 80% of user profiles, the jaro distance between usernames is greater than 0.56. For the no match class on the other hand, our findings show that around 80% of the user profiles in the no match class have a jaro similarity lesser than 0.56. Hence 0.56 was chosen as the threshold for comparing usernames across Twitter and Quora. A similar analysis was carried out for all pairs of networks and all metrics.

Each pair of networks have different thresholds. This follows from the fact that there are some networks where users are more likely to give their accurate name than in others. The calculated threshold in the case of Facebook and Linkedin is 0.9. This value is high as both these networks are used to maintain a friend network (Facebook) and a professional network (LinkedIn) where name is an important attribute. In case of Twitter and Facebook the threshold is lower, for our dataset the threshold is 0.8. This is lower as both of these are not used for official purposes and users might use nick names and acronyms as their name attribute.

The problem we address now is given a user profile U on social network SN_A, who is the query user, we need to identify a corresponding cluster or candidate subset for this user profile on network SN_B. Canopy clustering is applied to the search network SN_B and hence we now have a set of overlapping clusters for this network. We need to address two sub-problems.

1) Identify cluster centroid (representative center of the cluster): For numerical data, mean of all points in a cluster is used to identify the cluster center. However, for string–based data such as names and usernames, defining measures is non–trivial. Consider the following example, say we have a cluster that consists of the following usernames: Adam, Adder, Alan. We define the center of this cluster as the average frequency distribution of characters of each member of the cluster.

   In the example of Adam, Adder and Alan. The centroid would be a frequency distribution determined in the following manner
   a) Let the overall number of user profiles in the cluster be denoted by N.
   b) Select a character that appears in at least one user profile in the cluster. Say, we start with character 'a'.
   c) Count the occurrence of this character across all members of the cluster. Here 'a' appears twice in 'adam', once in 'adder' and twice in 'alan'. So five times in all.
   d) Divide this number by N to get the average representation. In this case we get (5 / 3), i.e. 1.67.
   e) Repeat steps (b)-(d) for all the characters.

   Mathematically, we consider a centroid to be equivalent to a *D*-dimensional point where *D* is equal to the cardinality of the alphabet under consideration. We are working with the English alphabet and hence *D*=26. So, figuring out the value of the i^{th} coordinate of the centroid is equivalent to determining the average frequency of the i^{th} character of the alphabet (i=1 corresponds to the character 'a' in the English alphabet). The formula for determining the value of this i^{th} coordinate is as follows:

$$C_i = \sum_{j=1}^{N} \frac{f_{ij}}{N} \tag{3}$$

   Where f_{ij} is the frequency of the i_{th} character in the j_{th} member of the cluster, N is the total number of members in the cluster
2) Distance measure of user profile U from the cluster centroid: In order to determine the appropriate cluster for the user, we compute the square of the Euclidean distance between the frequency distribution of the user profile we are looking for and each cluster representative. The minimum distance is then chosen as the suitable cluster and we get our candidate set. For example, as explained each centroid may be represented by a 26-dimensional point. The user profile for whom we have to find the cluster is also converted to a 26-dimensional representation. So Adam, would be represented as a point with a=2, d=1 and m=1. In the steps stated below, we take the example for 3-dimensional points. This can be easily extended to D-dimensional points.
   a) Say, we represent our user profile as (1,1,1). Let us have three clusters C_1, C_2, and C_3 with centroids as (1,0,1), (2,0,0) and (1,3,4) respectively.
   b) Consider cluster C_1. Compute the distance as a square difference. In this case, it would be equal to [$(1-1)^2$ + $(1-0)^2$ + $(1-1)^2$] = 1.

c) Repeat (b) for each cluster.
d) Determine the cluster that has minimum distance to our user. We call this the most suitable cluster for our user. In this case, C_1 would be our most suitable cluster.

The general formula to determine the distance between two D-dimensional points p_1 and p_2 is given as follows:

$$Distance = \sum_{i=1}^{D} (p_{i1} - p_{i2})^2 \quad (4)$$

Where p_{i1} and p_{i2} denote the value of the i^{th} coordinate for points p_1 and p_2

This searching step is repeated for each feature on which we have made clusters in SN_B. As explained in the example, we would find the most suitable cluster for user profile Adam on each feature. This would give us a set of overlapping clusters C_1, C_2, C_3, ..., C_m. We then take a union of these clusters to determine a candidate set for the Adam on SN_B.
Say C_1 had user profiles 'Amy' and 'Andy'. C_2 had 'Belford' and 'Alan' and C_3 had 'Jack' and 'Andy'. Then we take a union of all of these clusters and our final candidate set consists of the user profiles 'Amy', 'Andy', 'Belford', 'Alan', 'Jack'. Note that when we refer to user profile 'John' on SN_B we are actually referring to the user with username 'John' on SN_B. This is because on any social network, the username is guaranteed to be unique.
This approach is suitable when we have a pre–defined user profile list and it is not too large. But for larger networks, it wouldn't scale due to the space complexity of $O(n^2)$. We hence propose an alternate approach.

A. Modification to the Canopies

Canopy clustering produces overlapping clusters and is O(n^2) in both time and space complexity. We propose a modified algorithm that uses a single threshold and produces non overlapping clusters. The space complexity now decreases to $O(n)$. We also alter the searching algorithm. We introduce the concept of sibling clusters. As non–overlapping clustering tend to miss out some probable candidates. Extending this constrained set with siblings results in higher accuracy. The algorithm is given as Algorithm 2 [**procedure** MOD-CANOPIES].

Algorithm 2 Modification to the Canopies

```
1: procedure MOD-CANOPIES
2: U ← set of user-profiles on the network
3: T ← threshold
4: d(x, y) ← distance measure
5: for each user-profile x in U:
6:     create canopy C_x such that
           for each user-profile y in U,
           insert y into C_x if d(x, y) ¡ T;
7:     Remove all user profiles y added in the previous step from U.
8:     loop while U is not empty;
```

The algorithm is similar to canopy clustering and its time complexity is still O(n^2) in the worst case. However, since clusters are non-overlapping, space complexity is now $O(n)$.

The algorithm to find the candidate set corresponding to a particular user profile is modified as follows Previously, we were evaluating the closest cluster and determining the candidate set from its members. Now, we after determining the closest cluster, we determine 'siblings' of this cluster. These are clusters that are similar to the cluster. We evaluate the distance of this cluster to other clusters and define similar clusters as those which are closer than a specific threshold (after experimenting over a range of thresholds we found the best results for threshold equal to 12). We then evaluate the distance of our user profile to these siblings and expand the candidate set obtained thus far. The algorithm is stated as Algorithm 3[**procedure** MODIFIED-SEARCH]:

Algorithm 3 Modified search algorithm

```
1: procedure MODIFIED-SEARCH
2:     U ← User profile we are looking for
3:     C ← set of non overlapping clusters
4:     T ← threshold
5:     d(C_x, C_y) ← distance measure
6: for each cluster C_x in C:
7:     compute the distance d(U, C_x)
8: select cluster C_m such that
       d(U, C_m) is minimum of all distances
       computed above, this is the most suitable cluster;
9: L ← List of suitable clusters, initially empty
10: for each cluster C_x in C:
11:     if d(C_m,C_x) ¡ T then
            if d(U, C_x) ¡ T then
                append C_x to L
12: L holds our list of candidate clusters
```

After we have our candidate clusters, we take their union to get the candidate set on this feature (as explained in the previous section). We then repeat this process on each feature we have clustered and finally combine all the clusters to give our final candidate set.

In the [**procedure** MODIFIED-SEARCH] the distance measure d(C_x,C_y) is calculated in the same manner as discussed above. i.e. We represent each canopy C_x by its centroid (which as we explained earlier is nothing but a 26-dimensional point). We then calculate the square of the Euclidean distance between the points to determine their distance. We experimented with different values of threshold T to determine the most optimal one. A very small value and we would not be able to expand our candidate set since we would not find any sibling clusters. And a very large value and our candidate set would be too large making the algorithm computationally expensive. We finally set T=12.

TABLE V: CLUSTERING COMPARISON

Users	$CANOPY$		$MOD-CANOPY$	
	Success	% Success	Success	% Success
100	80	80	83	83
1000	708	70.8	706	70.6
2000	1290	65	1220	61
5000	3368	68	3176	64

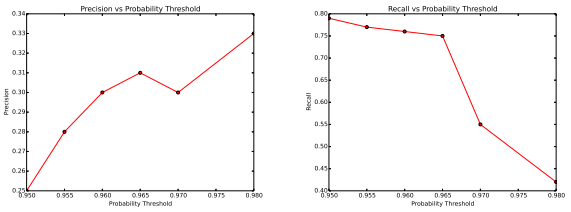

(a) Precision vs Probability threshold (b) Recall vs Probability threshold

Fig. 3: Precision and Recall for $MOD-CANOPY$

B. Comparing the Two Approaches

We present two approaches using canopy clustering. Table V shows a comparison between their performance. Success is defined as match of the user appeared in the candidate set, Failure is otherwise.

As shown in the results, the two methods are fairly close in accuracy. When we cluster on a very large dataset (15000 users), the modified method is more suitable owing to its lower space complexity. However, searching is slower. For a very small dataset, the traditional canopy clustering approach is also efficient.

VII. User Identification

In this section, we present a supervised approach that starts with a selected candidate set and helps identify a single match user for the query user. As already discussed, every network comes with its own properties hence, there is a possibility that the feature values from various sources conflict. The matching phase of our algorithm has two steps: (1) Assign match probabilities (scores) to each user in the candidate set for the query user and (2) identify the match. Figure 4 shows the process.

For task (1), the training is done with two classes, match and no match. Match class shows that two profiles belong to the same person. The no match class represents different users. Once a matching function is learned, each identity in the candidate set is compared with the known identity and assigned a match probability that signifies the confidence of matching. The goodness of the classifier is evaluated based on ROC curves and precision–recall graphs. Our experiments show that Random Forest and Naive Bayes are best suited for this framework. We use random forest for our experiments.

Next task is to pick the matched identity. One method is to pick the best matched candidate identity (with highest match probability) and declare it as the correct identity. This results in exactly one identity for the queried user. However, there is a possibility that the best match probability is low and hence the output is not the correct identity. To overcome this disadvantage, we define a threshold above which the candidate is a match. In this case, we might not get any matched identities or get multiple such identities. A fall back for option can be using human annotations to manually verify a candidate as a match. This approach relies on the goodness of the threshold. Another approach is to use human intervention to identify the correct candidate. This approach will be useful only when the candidate set is small and the human annotator is an expert. We explore both the best–pick and the threshold–approach in this work.

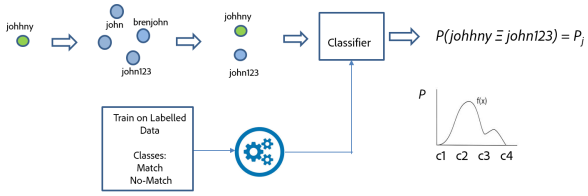

Fig. 4: User identification

A. Unified user Profile

Matched identities over a pair of networks help in creating unified view of the user. As discussed earlier, feature values of the user across networks may conflict. For instance, user has a location as 'United States' on one, while 'California' on other network. Here, the location attribute conflict syntactically but not semantically. Scenarios where user mentions name as 'John Smith' on one while 'Green Eyes' on other, the name attribute conflict syntactically and semantically. These values need to be disambiguated and the correctness of the values need to verified. As this work focuses on aggregating information and not entity or value resolution, we don't explicitly target this problem. The output of system is a unified user profile view with collated information, and we provide the user with a list of values for attributes where we don't find a single value.

VIII. Experiments

This section presents the various experiments that show comparison for different combinations of features, clustering, and classification parameters. Here, we focus on the effect of change in accuracy of the overall system rather than focusing on individual components of the system. We first present the assumptions and the dataset details, and then discuss different accuracy levels within a pair of networks and across networks.

A. Assumption and Data

We carried out a number of experiments on datasets of varying sizes across different networks. For the smaller size dataset users were split in the ratio 70:30.(i.e. 70% of the users from the positive set and 30% from the negative dataset.) The following was the data split across networks. Here M denotes the users in match class and NM denotes the users in no match class.

TABLE VI: CLASS SPLITS USED FOR DIFFERENT NETWORKS

Network-Pair	Total Users	M	NM
Quora-Linkedin	731	512	219
Facebook-Quora	1027	719	308
Facebook-Linkedin	2377	1664	713
Facebook-Twitter	2267	1587	680
Twitter-Linkedin	657	460	197
Twitter-Quora	1000	700	300

TABLE VII: CLASS SPLITS USED FOR EXPERIMENTS

Total Users	M	NM
4000	2000	2000
10000	5000	5000
20000	10000	10000
26000	13000	680

We also carried out experiments on a larger dataset as shown in Table VI and VII. These were carried out for Facebook and Twitter. In all of these experiments, we split our data evenly between the match and the non-match class. We varied the probability thresholds to see the change in precision and recall. The results for this are shown in Table VIII and IX. On increasing the threshold, precision increases and recall decreases.

TABLE VIII: EXPERIMENTAL RESULTS FOR A LARGER DATABASE (FACEBOOK AND TWITTER) USING CANOPY CLUSTERING

Total Users	Threshold	Precision	Recall
4000	0.95	0.15	0.87
4000	0.97	0.32	0.55
10000	0.95	0.14	0.91
20000	0.95	0.15	0.9
20000	0.97	0.2	0.7
20000	0.975	0.21	0.68
20000	0.98	0.24	0.62
20000	0.985	0.26	0.58
20000	0.99	0.32	0.53
26000	0.95	0.14	0.96
26000	0.97	0.2	0.69

TABLE IX: RESULTS: TWITTER AND FACEBOOK FOR $20,000$ USERS EACH USING $MOD - CANOPY$

Threshold	Precision	Recall
0.95	0.25	0.79
0.955	0.28	0.77
0.96	0.3	0.76
0.965	0.31	0.75
0.97	0.3	0.55
0.98	0.33	0.69

B. Effect of Candidate Selection

In section VI we describe the use of Canopy clustering and introduced a modification to that algorithm for this framework. Table X shows the accuracy of user aggregation with and without the candidate selection step. As seen in the table, clustering helps in improving the precision while not varying the recall. Hence, along with reduction in computational complexity we also achieve better accuracy due to the introduction of this step.

TABLE X: COMPARING ENTWINE SYSTEM WITH/WITHOUT CLUSTERING FOR A SPLIT OF 300 MATCH AND 700 NON-MATCH USERS

Users	Precision	Recall
With Clustering	0.52	0.68
Without Clustering	0.44	0.68

C. Effect of varying feature combinations

Another parameter that was varied through the experiments is the feature set. We experimented with using only name and username features and less name and username features (i.e. we applied a single metric for name and username). We compared this with the results obtained using all features. Table VIII shows the precision and recall obtained from the different feature sets used for each pair of networks. We see that the precision obtained by using all features and by using only name and username features is comparable. Though using all features gives better results. Also precision obtained using less names and usernames is slightly lower than the other two. Hence, we can conclude that name and username are clearly the most important features since, even when used alone, they give satisfactory results. However, the addition of extra features improves precision to an extent. So, these features, while not too useful by themselves, are useful in conjunction with name and username for identity aggregation.

D. Pairwise matching accuracy across networks

Every network as already mentioned has its own properties. Due to this the accuracy levels also varied for various pairs of the networks. Table XII shows these results. As seen from the table, the system achieves best recall for Facebook–Quora (0.85) and highest precision for Quora–LinkedIn. It is important to note here, that the state–of–the–art in the industry for this problem is around 20% accuracy and in academia other researchers have not attempted looking at a diversity in networks.

E. Improvement in Audience estimation

Table XI shows the results of applying EnTwine to the task of better audience estimation. As we can see, by simply adding up the users across brands we get a number of 1965 which is an inflated value, since it does not account for the same user on multiple networks. By aggregating users, we have brought that number down to 1479 unique users, which is a significant reduction and much closer to the true number.

TABLE XI: RESULTS FOR BETTER ESTIMATION

Total Users	Reduced number	Duplicate users	% Reduction	Recall
1965	1479	486	24	0.68

TABLE XII: Precision and Recall for different experiments

Network Pair	Matches	All features		Only names and username		Less name and username	
		Precision	Recall	Precision	Recall	Precision	Recall
Quora-Linkedin	512	0.67	0.71	0.71	0.72	0.55	0.71
Facebook-Quora	719	0.69	0.85	0.68	0.84	0.5	0.85
Facebook-Linkedin	1664	0.45	0.78	0.43	0.77	0.36	0.76
Facebook-Twitter	1587	0.51	0.78	0.51	0.78	0.6	0.71
Twitter-Linkedin	460	0.33	0.75	0.31	0.75	0.24	0.74
Twitter-Quora	700	0.28	0.72	0.29	0.72	0.15	0.72

IX. Conclusion

This work presents a detailed system comprising of in-depth feature analysis algorithms, candidate selection approach, and a unique framework that aims at social user identity aggregation. Through experiments and results discussed above we conclude that doing prior feature selection using relevancy metrics aids at easier profile aggregation approach. Further, we also show that having an intermediate candidate selection step reduces the computational overhead for user identification. The extensive feature analysis resulted in different relevant features through different measures. Username and Name though are most prominent across all networks and all measures. A modification of Canopy clustering was introduced to suite the application and our comparisons show that choosing between Canopy clustering and MOD-CANOPY would be a tradeoff between computational efficiency and accuracy. Finally, the last part of this paper discussed the effect of different approaches on the accuracy of the profile aggregation system.

Various explorations indicate that there is significant scope in extending this work. One direction would be further formalizing the feature space analysis while focusing more on the derived features. In this work, we have no integrated any network features. Using those would help increase the efficiency of the system. While accuracy of the system is important, applying the results for practical applications is as crucial. Research towards feature value disambiguation for aggregation of user information will help in reinforcing the results from EnTwine.

References

[1] Francesca Carmagnola and Federica Cena. User identification for cross-system personalisation.

[2] Denzil Correa, Ashish Sureka, and Raghav Sethi. Whacky!-what anyone could know about you from twitter. In *PST '12*.

[3] Oana Goga, Howard Lei, Sree Hari Krishnan Parthasarathi, Gerald Friedland, Robin Sommer, and Renata Teixeira. Exploiting innocuous activity for correlating users across sites. In *WWW'13*.

[4] Danesh Irani, Steve Webb, Kang Li, and Calton Pu. Large Online Social Footprints–An Emerging Threat. In *CSE'09*.

[5] Paridhi Jain, Ponnurangam Kumaraguru, and Anupam Joshi. @ I seek 'fb. me': Identifying Users across Multiple Online Social Networks. In *WWW'13 Companion*.

[6] Sebastian Labitzke, Irina Taranu, and Hannes Hartenstein. What your friends tell others about you: Low cost linkability of social network profiles. SNAKDD '11.

[7] Siyuan Liu, Shuhui Wang, Feida Zhu, Jinbo Zhang, and Ramayya Krishnan. Hydra: Large-scale social identity linkage via heterogeneous behavior modeling. In *SIGMOD'14*.

[8] David G Lowe. Object recognition from local scale-invariant features. In *Computer Vision, 1999*.

[9] Anshu Malhotra, Luam Totti, Wagner Meira, Ponnurangam Kumaraguru, and Virgilio Almeida. Studying User Footprints in Different Online Social Networks. *CSOSN'12*.

[10] Mitchell P Marcus, Mary Ann Marcinkiewicz, and Beatrice Santorini. Building a large annotated corpus of english: The penn treebank.

[11] Andrew McCallum, Kamal Nigam, and Lyle H Ungar. Efficient clustering of high-dimensional data sets with application to reference matching. In *SIGKDD '00*.

[12] Marti Motoyama and George Varghese. I seek you: searching and matching individuals in social networks. In *WIDM '09*.

[13] Daniele Perito, Claude Castelluccia, Mohamed Ali Kâafar, and Pere Manils. How Unique and Traceable Are Usernames? In *PETS'11*.

[14] Jan Vosecky, Dan Hong, and Vincent Y Shen. User identification across multiple social networks. In *NDT'09*.

[15] Reza Zafarani and Huan Liu. Connecting users across social media sites: a behavioral-modeling approach. In *KDD'13*.

j mater res technol. 2015;xxx(xx):xxx–xxx

Available online at www.sciencedirect.com

jmr&t Journal of Materials Research and Technology

www.jmrt.com.br

Original Article

Fabrication of Al5083/B_4C surface composite by friction stir processing and its tribological characterization

Narayana Yuvaraj[a], *Sivanandam Aravindan*[b,*], *Vipin*[a]

[a] *Department of Mechanical Engineering, Delhi Technological University, Delhi 110 042, India*

[b] *Department of Mechanical Engineering, Indian Institute of Technology, Delhi 110 016, India*

ARTICLE INFO

Article history:
Received 13 October 2014
Accepted 8 February 2015
Available online xxx

Keywords:
Friction stir processing
Boron carbide (B_4C)
Number of passes
Hardness
Wear

ABSTRACT

Improved surface properties with the retainment of bulk properties are necessary for a component for enhanced wear characteristics. Friction stir processing (FSP) is used to produce such surface composites. Fabrication of 5083 aluminum alloy with reinforced layers of boron carbide (B_4C) through FSP was carried out. Micro and nano sized B_4C particles were used as reinforcements. The friction processed surface composite layer was analyzed through optical and scanning electron microscopical studies. The number of passes and the size of reinforcement play a vital role in the development of surface composites by FSP. Mechanical properties of the friction stir processed surface composites were evaluated through micro hardness and universal tensile tests. The results were compared with the properties of the base metal. The role of reinforcement and number of passes on properties were also evaluated. Tribological performance of the surface composites is tested through pin on disk test. The surface composite layer resulted in three passes with nano particle reinforcement exhibited better properties in hardness, tensile behavior and wear resistance compared to the behavior of the base metal.

© 2015 Brazilian Metallurgical, Materials and Mining Association. Published by Elsevier Editora Ltda. All rights reserved.

1. Introduction

The aluminum based metal matrix composites provide excellent specific strength, stiffness, high hardness, wear resistance, stability at high elevated temperature [1] with additional advantages of three dimensional isotropy and affordability [2]. The Al–B_4C composites are used in the bicycle frame, bullet proof vests, armor tanks, containment of nuclear waste, neutron absorber in nuclear power plant, transportation applications, etc. owing to their high hardness, low density and excellent thermal and chemical stability [2–4]. Al–B_4C composites are fabricated by various researchers in the past few years by stir casting [5–7], casting [8–10], squeeze casting [11] and mechanical alloying [12].

However, a surface property of the material is very important to achieve longer life of mechanical components. Dispersion of the nano reinforcements in the surface to have

* *Corresponding author.*
E-mail addresses: nyuvdce@yahoo.com (N. Yuvaraj), aravindan@mech.iitd.ac.in (S. Aravindan), vipin@dce.ac.in (Vipin).

http://dx.doi.org/10.1016/j.jmrt.2015.02.006

2238-7854/© 2015 Brazilian Metallurgical, Materials and Mining Association. Published by Elsevier Editora Ltda. All rights reserved.

Please cite this article in press as: Yuvaraj N, et al. Fabrication of Al5083/B_4C surface composite by friction stir processing and its tribological characterization. J Mater Res Technol. 2015. http://dx.doi.org/10.1016/j.jmrt.2015.02.006

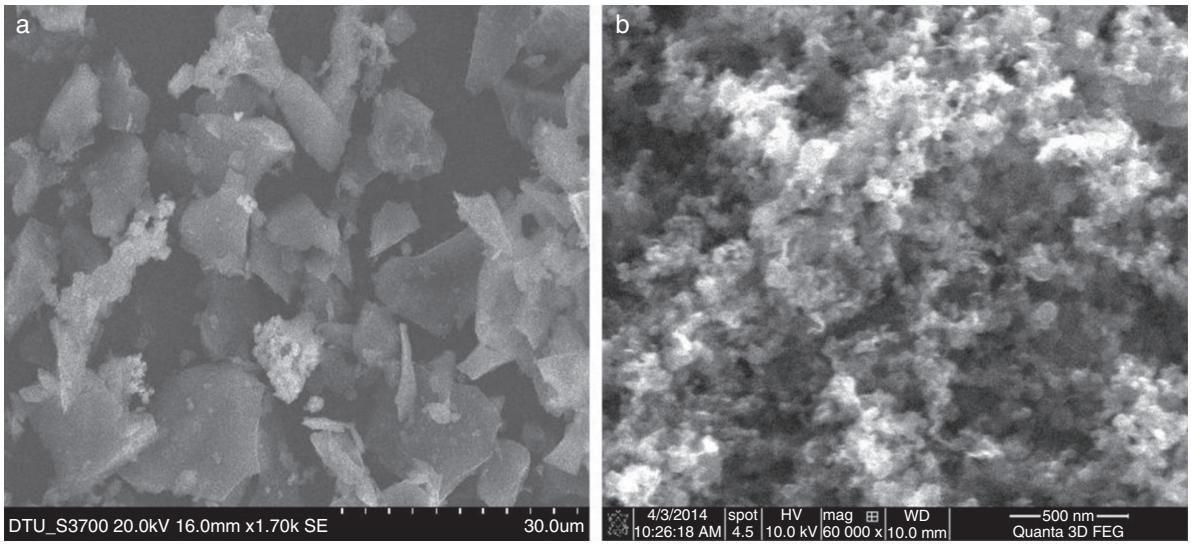

Fig. 1 – SEM micrographs of as-received (a) B_4C micro particles, (b) B_4C nano particles.

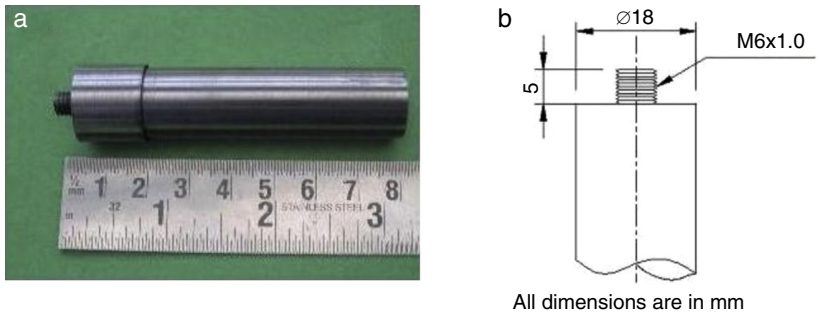

Fig. 2 – Macrograph of FSP tool.

a uniform layer is a difficult task. Existing processing techniques for processing of surface composites are based on liquid phase processing at high temperature such as laser melt treatment, electron beam irradiation and plasma spraying [13–15]. In these cases, there will be an interfacial reaction between the matrix and reinforcement, which leads to the formation of detrimental phases. The above problems can be eliminated by processing it below the melting point of substrate. The recent new surface modifying technique named Friction Stir Processing (FSP) [16] is developed by utilizing the principle of the friction stir welding (FSW). FSW was invented by the welding Institute UK in 1991 [17]. FSP is a solid state processing technique for producing a thick composite layer; the layer thickness can range from hundreds of micrometers to several millimeters. FSP is also useful to obtain a fine grained microstructure and to remove the cast defects with improved mechanical properties and wear resistance [18–20].

The successful fabrication of aluminum based metal matrix composites reinforced with particulates such as SiC

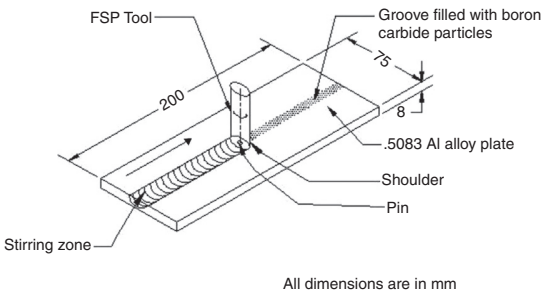

Fig. 3 – Schematic of FSP experiment.

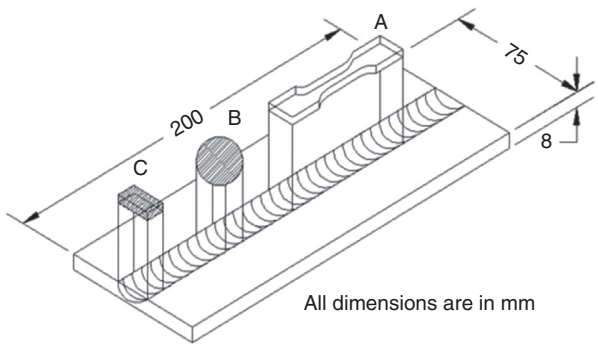

Fig. 4 – Schematic illustration of the procedure for cutting (A) tensile specimen, (B) pin specimen for wear test, (C) hardness specimen.

Please cite this article in press as: Yuvaraj N, et al. Fabrication of Al5083/B_4C surface composite by friction stir processing and its tribological characterization. J Mater Res Technol. 2015. http://dx.doi.org/10.1016/j.jmrt.2015.02.006

Table 1 – Chemical composition of base material.

Elements	Mg	Cr	Mn	Fe	Zn	Si	Ti	Cu	Ni	Al
%wt	4.162	0.064	0.554	0.191	0.029	0.230	0.049	0.051	0.023	Bal

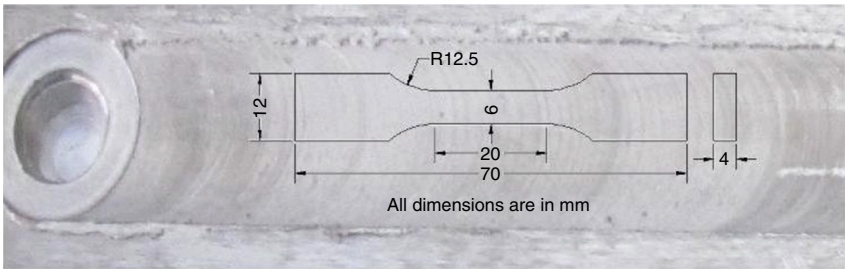

Fig. 5 – The configuration of the tensile specimen.

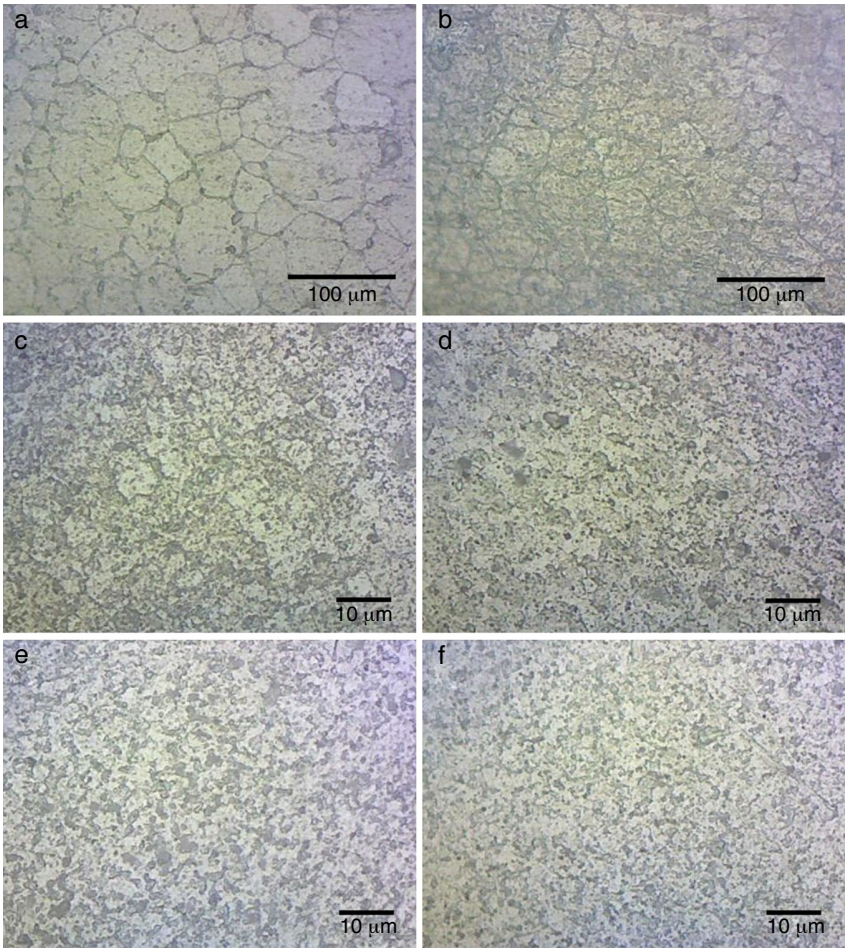

Fig. 6 – Optical micrographs of transverse cross-sectional of the FSP zone specimens (a) base material, (b) without particle one pass stir zone, (c) B_4C micro sized particle one pass, (d) B_4C micro sized particle three pass, (e) B_4C nano sized particle one pass, (f) B_4C nano sized particle three pass.

[21–24], Al_2O_3 [25–27], Si_3N_4 [28], B_4C [29,30], ZrO_2 [31] and TiO_2 [32] were reported. However, no literature is available on FSP of 5083 aluminum alloy with B_4C nano composites. The present work aims to fabricate 5083 aluminum alloy surface composite by FSP with the reinforcement of B_4C micro and nano particles. The effects of number of passes on the microstructure, micro hardness, tensile strength and wear behavior were investigated.

Please cite this article in press as: Yuvaraj N, et al. Fabrication of Al5083/B_4C surface composite by friction stir processing and its tribological characterization. J Mater Res Technol. 2015. http://dx.doi.org/10.1016/j.jmrt.2015.02.006

Table 2 – Mechanical properties of FSP composites.

Specimen	Grain size (μm)	Micro hardness (Hv)	Ultimate stress (MPa)	Total % elongation
Base material	49.85	82.6	310	26.8
Without particle one pass	18.46	107.2	331	30.0
Micro sized B_4C particle one pass	8.16	112.1	246	15.4
Micro sized B_4C particle three pass	6.52	116.4	323	11.0
Nano sized B_4C particle one pass	7.64	119.6	334	16.6
Nano sized B_4C particle three pass	3.98	124.8	360	14.9

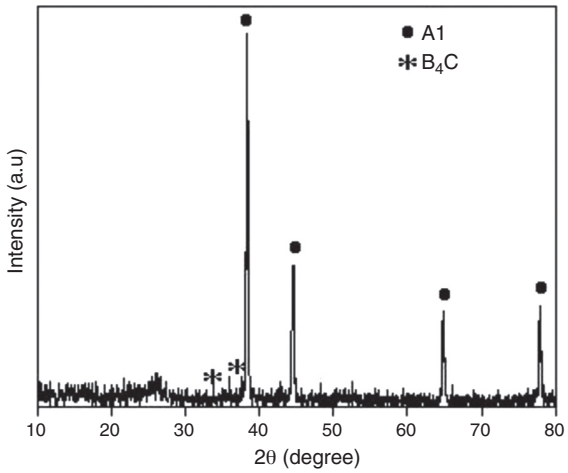

Fig. 7 – XRD of the specimens FSPed nano sized B_4C particle three passes.

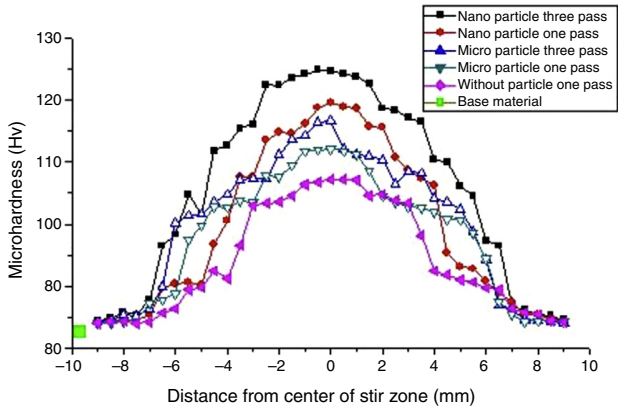

Fig. 9 – Microhardness value FSPed specimens with and without particles on the SCL.

2. Materials and methods

Al alloy of 5083-O rolled plate of 8 mm thickness was used. The chemical composition is presented in Table 1. The micron sized B_4C particles with a purity of 99% having an average particle size of 20 μm and nano size B_4C particle of 99.5% purity with the mean particle size of 30–60 nm were used as reinforcement materials. The SEM micrographs of the particles are shown in Fig. 1. These micrographs reveal the size and morphology of micro and nano level particles. The tool made of H-13 tool steel hardened to 55 HRC with a shoulder of 18 mm diameter with threaded pin diameter of M6 × 1.0 of pin length of 5 mm was used for FSP. A groove (1 mm width and 3 mm depth) was made in the middle of the workpiece and the groove was then filled with the reinforcements. A probeless FSP tool with shoulder only was initially used to prevent the escape of the particles from the FSP zone. Then the samples were subjected to various numbers of passes from one to three.

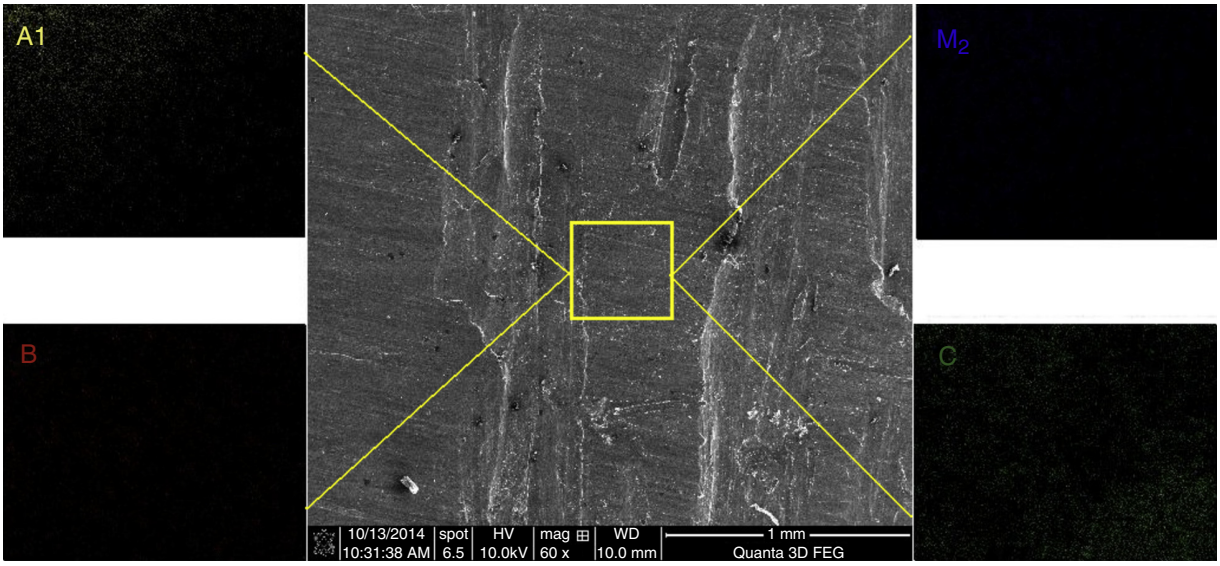

Fig. 8 – SEM micrograph and elemental composition of three pass nano FSPed specimen.

Please cite this article in press as: Yuvaraj N, et al. Fabrication of Al5083/B_4C surface composite by friction stir processing and its tribological characterization. J Mater Res Technol. 2015. http://dx.doi.org/10.1016/j.jmrt.2015.02.006

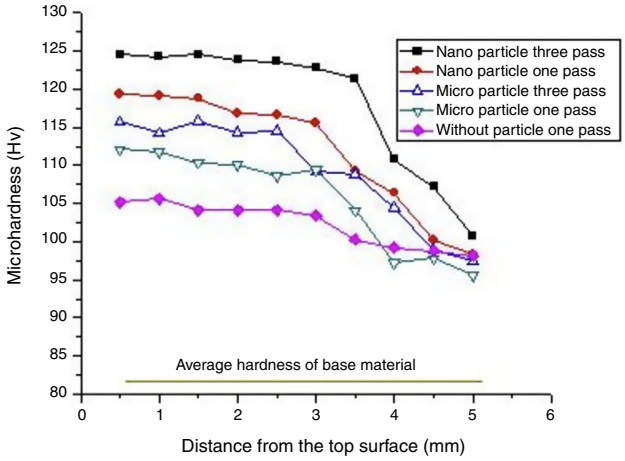

Fig. 10 – Micro hardness profile of FSPed specimens with and without particles of the cross section region (as a function of depth).

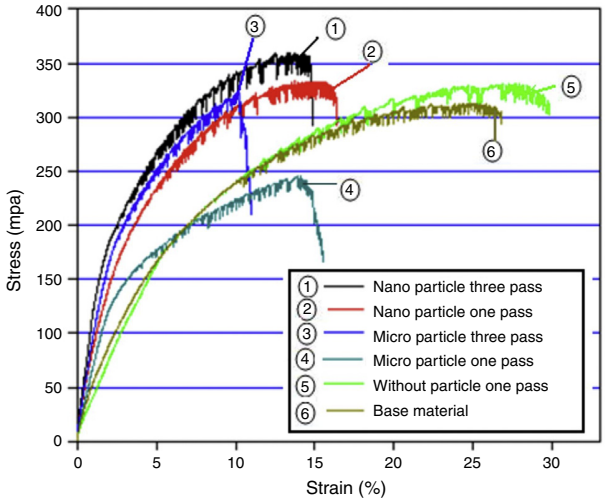

Fig. 12 – Stress–strain curves for base metal and specimens FSPed with and without particles with different passes.

An indigenously developed FSW machine (11 kW, 40 kN) was used to fabricate the surface composite layer. The specimens were clamped on the hydraulic fixture with mild steel backing plate. The constant rotational speed and transverse speed were fixed at 1000 rpm and 25 mm/min respectively after number of trials. The advancing and retreating sides of the parent metals were changed after each FSP pass. For every pass, the specimen was allowed to be cooled to the room temperature and all the experiments were carried out at room temperature. Fig. 2(a) shows the photograph of the threaded tool used for the study and Fig. 2(b) shows its dimensions. Fig. 3 shows the schematic of FSP experiment. After FSP, the samples were cut in the transverse direction and polished with different grades of emery sheets and the samples were analyzed through optical microscope. A modified Poulton's reagent (30 ml HCl, 40 ml HNO_3, 2.5 ml HF, 12 g CrO_3, and 42.5 ml H_2O) was used to study microstructure of the base metal and the stir zone of the surface composite layer (SCL). Scanning electron microscope (SEM) (Hitachi S3700) was used to examine the distribution of the reinforcement particles. XRD (BRUKER D8 ADVANCE) was used to identify the presence of phases in the Stir zone of SCL. The Vickers micro hardness (Future Tech Japan) values of the FSPed regions was measured along and perpendicular (cross section) to the processing direction using a load of 100 g with dwell time of 10 s. The tensile properties of the FSPed specimens were examined using computer controlled universal testing machine (Tinius Olsen H50KS) at a constant cross head speed of 1 mm/min in room temperature. The longitudinal tensile specimens prepared on the middle of the FSP stir zone by wire EDM as per ASTM: E8/E8M-011 standard. Figs. 4 and 5 show the size and configuration of the specimens for the tests. The wear behavior of the SCL was studied through pin on disk tribometer (make DUCOM) in room temperature condition. Wear test specimens of 10 mm diameter were cut from the middle of stirred zone of FSPed surface by wire EDM. Tribo tests were conducted as per ASTM G99-04 standard. The counterpart discs were made of EN-24 steel hardened to 58 HRC and the surface roughness (*Ra*) of 0.2 μm. A constant track diameter 100 mm was used in all the tests. Before the test, the surface of each pin was polished on 1200 grit emery paper. The wear test was conducted

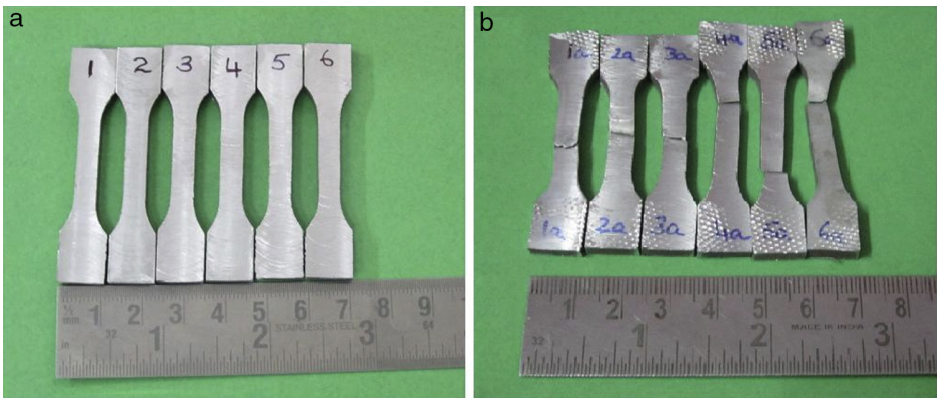

Fig. 11 – (a) Tensile specimens before tensile testing, (b) after testing.

Please cite this article in press as: Yuvaraj N, et al. Fabrication of Al5083/B_4C surface composite by friction stir processing and its tribological characterization. J Mater Res Technol. 2015. http://dx.doi.org/10.1016/j.jmrt.2015.02.006

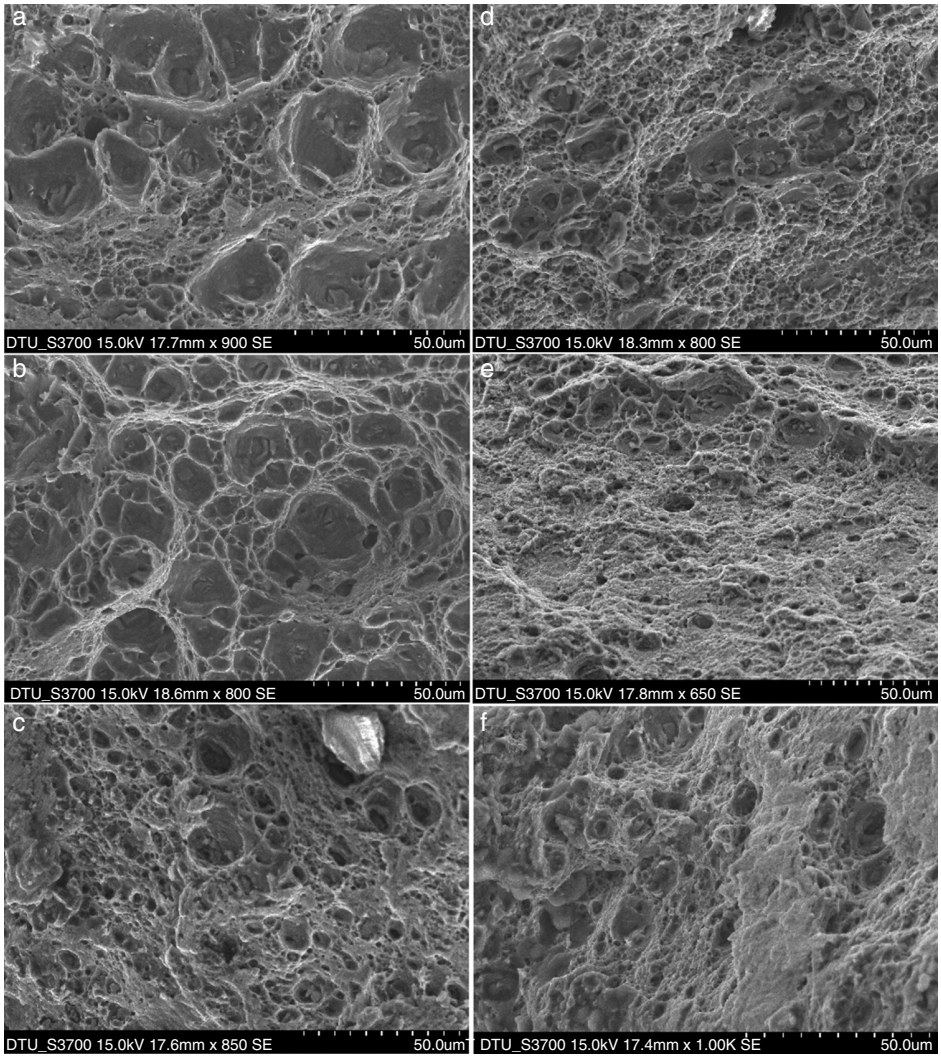

Fig. 13 – SEM fractographs of (a) base material, (b) specimen FSPed without particle one pass, (c) specimen FSPed with B_4C micro particle one pass, (d) specimen FSPed with B_4C micro particle three passes, (e) specimen FSPed with B_4C nano particle one pass, (f) Specimen FSPed with B_4C nano particle three passes.

at a sliding velocity of 2 m/s, normal force of 30 N and sliding distance of 3000 m. At every 500 m interval the samples were cleaned with acetone and weighed to an accuracy of 0.001 mg by electronic weighing balance. The applied load as well as the sliding speed were fixed in order to compare the active wear mechanisms in similar conditions. The friction coefficient between the pin specimen and disc was determined by measuring the frictional force with a stress sensor at the distance of 3000 m without stopping of the disc rotation at the same sliding velocity and normal force.

To understand the wear mechanisms the worn surfaces of the SCL and base metal were examined by SEM. The wear behavior of surface composite layer processed at single and multi (three) passes with micro and nano particles was compared with the wear behavior of base metal. FSPed surfaces without micro/nano reinforcement were also studied to have better understanding.

3. Results and discussion

3.1. *Microstructural analysis*

Microscopic observation of the SCL is shown in Fig. 6. The B_4C particles were found to be clustered in the stir zone after each FSP pass. The reinforcement particles are strengthening precipitates of Al5083 alloy that dispersed in the Al matrix. The finer grains were found in the SCL compared to the as received Al substrate, due to severe plastic deformation and dynamic recrystallization. Earlier reports also stated that the refinement of grains and uniform distribution of particles could be obtained by FSP [33]. With the increase in the number of FSP passes powder distribution becomes more homogeneous and reduced clustering of reinforcement particles is observed. Good dispersion of reinforcement occurs in the matrix and the size of the grain is also reducing. Typical XRD profile of nano

Please cite this article in press as: Yuvaraj N, et al. Fabrication of Al5083/B_4C surface composite by friction stir processing and its tribological characterization. J Mater Res Technol. 2015. http://dx.doi.org/10.1016/j.jmrt.2015.02.006

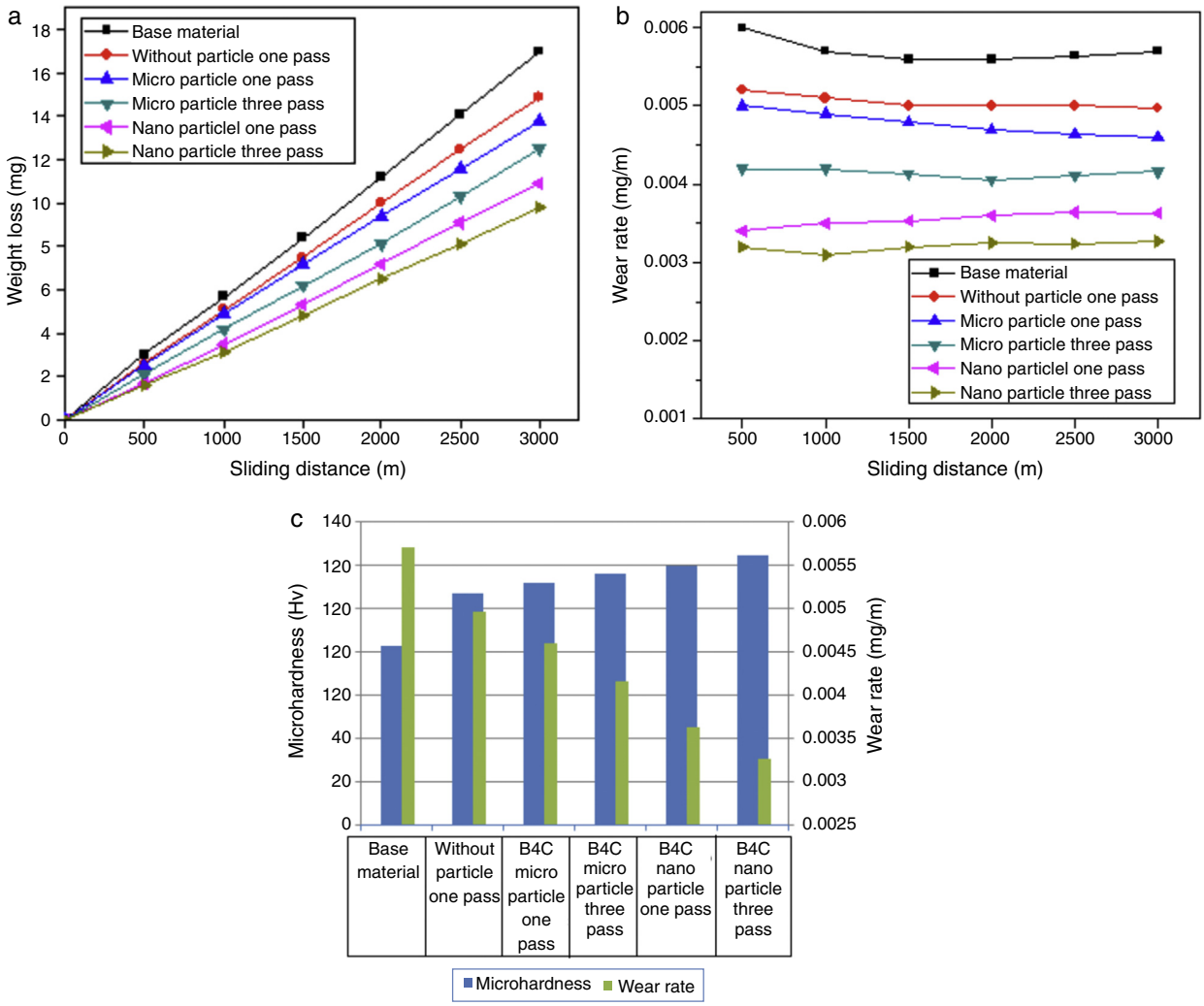

Fig. 14 – (a) Variation of weight loss with the sliding distance for base metal and specimens FSPed with and without micro and nano sized B_4C particles. (b) Variations of wear rate with the sliding distance for base metal and specimens FSPed with and without B4C micro and nano sized B4C particles. (c) Change in wear rate vs microhardness.

B_4C reinforced aluminum alloy specimen subjected to three stir passes is shown in Fig. 7. The clear peaks of aluminum and marginal peaks of B_4C are observed in the figure. Fig. 8 shows the SEM micrograph of cross section of three pass nano FSPed specimen with elemental composition.

3.2. *Hardness*

The hardness of base material was 82 Hv. For experimental purpose, the average of three hardness values was taken in all the samples. Fig. 9 show the hardness profile of specimens FSPed without particle one pass, with micro and nano sized B_4C particles one pass and three passes. The obtained data is compared with the base material. Asadi et al. [34] have reported that hardness of the FSPed AZ91/SiC nano composite is observed to be increased due to uniform dispersion of SiC particles and refinement of the grain size of the base material. Shamsipur et al. [35] have reported that the hardness value could be increased by 6.4 times for FSPed Ti/TiN composite surface layer in compare with base material due to the uniform dispersion of reinforcements. Morisada et al. [36] have revealed that FSPed nanostructured tool steel exhibited much higher hardness in compared to base material. Faraji and Asadi [37] reported that the increased number of passes FSP in AZ91/Alumina nano composite the hardness is observed to be higher than that of single pass. The second pass homogenizes the particle distribution, decreases the grain size and produces the uniform hardness profile. According to the Hall–Petch relationship, decrease in grain size increases the yield strength, which in turn increases the hardness value also. Dolatkhah et al. [22] have achieved maximum of 116 Hv hardened in FSP of 5052 Al with 50 nm SiC particles due to severe grain reduction. Shamsipur et al. [38] reported that microhardness value of Ti/SiC nano surface composite layer is 3.3 times greater than that of as received titanium substrate due to uniform dispersion of nano sized reinforcement particles after four FSP passes. Zahmatkesh and Enayati [39] have achieved higher hardness value in the stir zone of FSP in Al 2024 with Al_2O_3

Please cite this article in press as: Yuvaraj N, et al. Fabrication of Al5083/B_4C surface composite by friction stir processing and its tribological characterization. J Mater Res Technol. 2015. http://dx.doi.org/10.1016/j.jmrt.2015.02.006

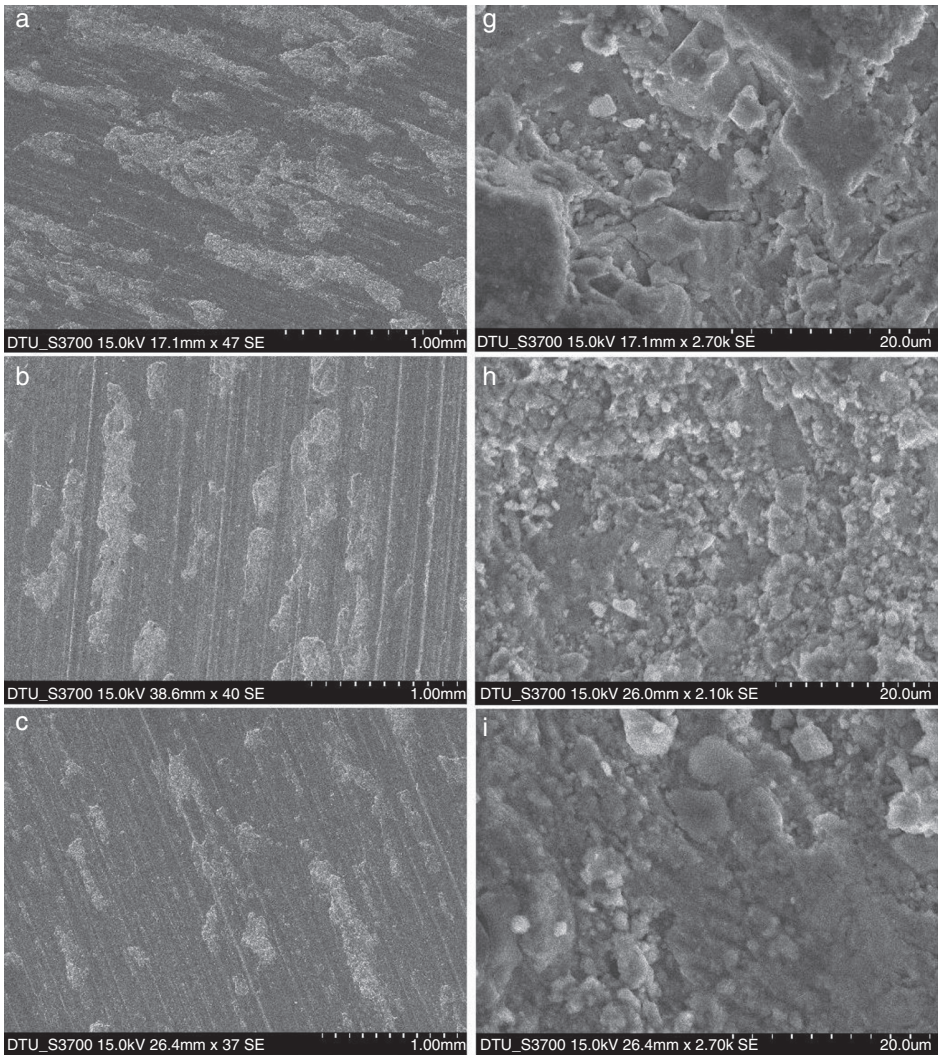

Fig. 15 – SEM micrograph of the worn out track of (a) base material, (b) specimen FSPed without particle one pass, (c) specimen B_4C micro particle one pass, and (g), (h), (i) are high magnification view of (a), (b) and (c) respectively.

nano particles than that of as received material due to uniform dispersion of Al_2O_3 particles in Al matrix. Raaft et al. [19] have reported that microhardness value of A390/Al_2O_3 and A390/graphite surface composites exhibited higher hardness than the hardness of as received material. The hardness is increased due to grain refinement of the particles and higher hardness of reinforcement particles. Shafiei-Zarghani et al. [26] reported that there is a threefold increase in hardness with passes of FSP 6082/Al_2O_3 nano reinforcements and the dispersion of nano-size Al_2O_3 in uniform manner in the Al matrix. Increase in the number of passes of many composite systems [36–40] has proved the uniformity in distribution in hardness.

The surface composite layer with nano particle three pass exhibited higher hardness compared to nano particle single pass. The hardness of the SCL depends upon fine grain size of Al matrix, fine dispersion of reinforcing particles (B_4C) in aluminum matrix and quench hardening effect due to difference in thermal contraction coefficient of aluminum matrix and B_4C reinforcing particles [40]. The above mentioned literature supports the finding of increased hardness of FSPed surfaces. The Al5083/B_4C nano FSP surface composites exhibited higher hardness when compared with the FSP of micro reinforcement particles. For example, the Al5083/B_4C nano FSP three pass and Al5083/B_4C micro three pass surface composites exhibited hardness of 134.8 Hv and 116.4 Hv respectively. The detailed hardness values are presented in Table 2.

Fig. 10 shows the cross section (depth profile) of the microhardness from processed region to the unprocessed region. Base material hardness is given in the figure. The FSP processed with nano particle three pass surface exhibited 60% increase in hardness. This increase in hardness is attributed to defects closure by friction stir process and refinement of grains. Micro particle distribution further increases its hardness and nano particle reinforcement improves the hardness. Further improvement in hardness by number of passes is certainly attributed to severe deformation of the parent material, finer grain structure and uniformity in particle distribution.

Please cite this article in press as: Yuvaraj N, et al. Fabrication of Al5083/B_4C surface composite by friction stir processing and its tribological characterization. J Mater Res Technol. 2015. http://dx.doi.org/10.1016/j.jmrt.2015.02.006

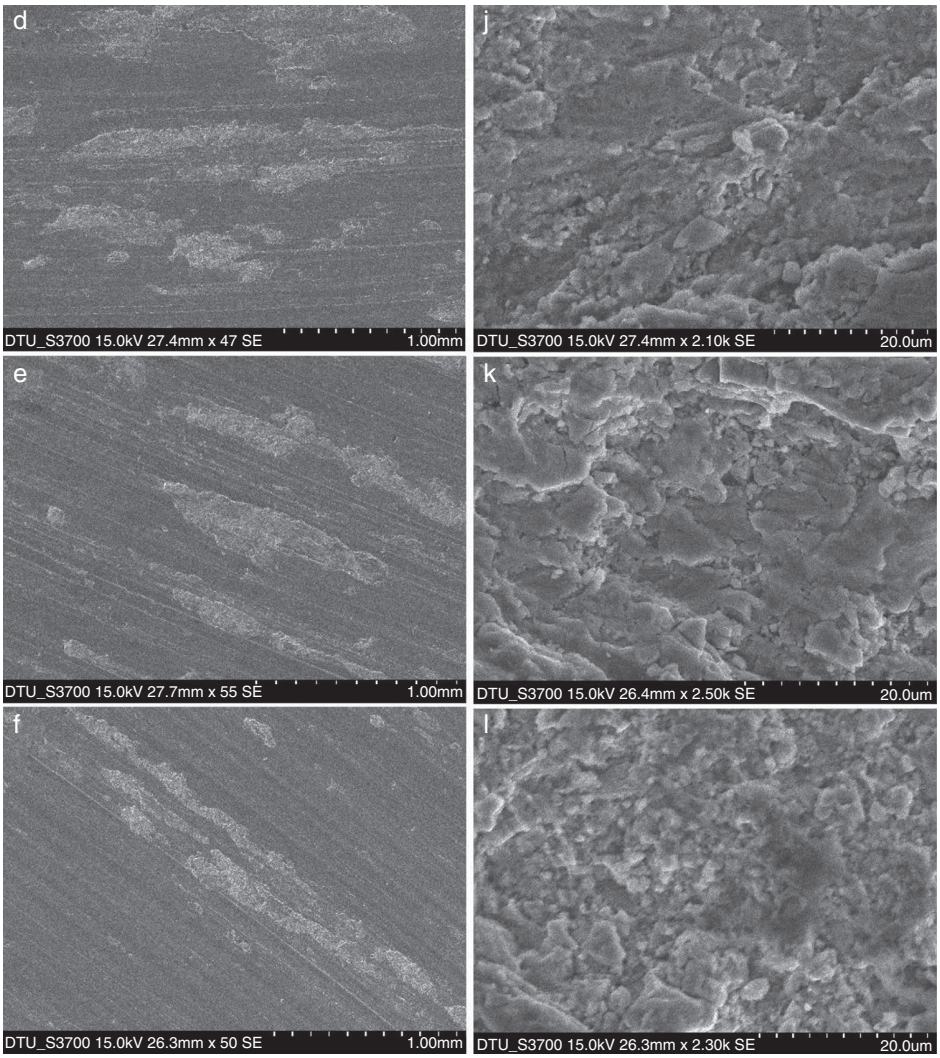

Fig. 16 – SEM micrograph of the worn out track of (d) specimen FSPed B_4C micro particle three pass, (e) specimen FSPed B_4C nano sized particle one pass, (f) specimen B_4C nano sized particle three pass and (j), (k), (l) are high magnification view of (d), (e) and (f) respectively.

3.3. *Effect on the number of passes*

The number of FSP passes reduces the clustering effect, increasing the uniformity of distribution of particles, which in turn results in improvement of mechanical and wear resistance properties. This observation in micro and nano B_4C reinforcement is supported by literature in various other material systems. Mahmoud [41] studied that FSP of A390 Al alloy with three passes and found that the hardness and wear resistance of the processed surface layer was improved and the coefficient of friction was observed to be slightly reduced when compared with the un processed material. Shafiei-Zarghani et al. [42] have reported that nano size alumina particles are more uniformly distributed in the aluminum matrix due to increasing the number of FSP passes. Alumina clusters were rarely reported. Increasing the FSP passes produces the better distribution of SiC and Al_2O_3 nano particles in the AZ91 matrix [43]. The hardness, strength, elongation and wear resistance of the composite layer are reported to be improved. After two passes, the nano sized Al_2O_3 particles are dispersed in a uniform manner in the Al matrix. Orowan strengthening can be very significant in the composites, the nano particles are well distributed in intra granularly and inter granularly. The cluster size is reduced and the integrity in the particle/matrix interface can be improved by increasing the number of passes.

3.4. *Mechanical properties*

Fig. 11(a) and (b) shows the tensile specimens before and after testing and Fig. 12 shows the result for the base material, and the processed specimens of micro and nano sized B_4C particles with one and three passes. The maximum tensile strength was achieved in the nano particles with three passes. Mechanical properties mainly depend on the fine grain size and dislocation strengthening. Restriction of movement

Please cite this article in press as: Yuvaraj N, et al. Fabrication of Al5083/B_4C surface composite by friction stir processing and its tribological characterization. J Mater Res Technol. 2015. http://dx.doi.org/10.1016/j.jmrt.2015.02.006

of grain boundaries is also influencing the tensile properties of the stirred zone material. Grain refinement is the important parameter to decide the super plastic behavior of metal [44]. FSP Al alloys forms equiaxed fine grains due to stirring the material and they exhibit excellent grain refinement. Fine grain size of nano sized FSP composites leads to a better tensile properties after the number of passes. Zohoor et al. [45] have reported that there is an increase in the strength of the Al alloy composite with the number of passes with the FSP effects on grain refinement and particle reinforcement on the Al alloy composite. FSPed Al–TiC in situ composites with two passes specimen exhibited the significant improvement of tensile properties due to homogenization, refinement of grain size and elimination of casting defects [46].

Fig. 13 shows the tensile fracture features of the specimens. Ductile fracture observed in all samples. However, a distinct difference of fracture morphologies can be observed between the as received material and FSPed composites with number of passes. The FSPed nano particles composite with three passes shows finer dimples, which are associated with finer reinforcement of nano particles in the matrix alloy. The nano sized composites with one pass FSP specimen improves the tensile properties and elongation, in three pass nano particle FSP specimen observed improved tensile properties and slightly decrease in elongation when compared with one pass nano particle FSP. The increase in dislocation density causes the reduction of elongation. The micro particle FSPed composites shows lower tensile strength compared to the nano reinforced composites and fracture morphologies show the larger dimple size with reduced ductility.

3.5. *Wear properties*

The wear behavior of the as received Al 5083 alloy, FSPed without particle one pass and FSPed with reinforcement particle (micro and nano sized B_4C particle one pass and three pass) surface composite layer (SCL) were evaluated by a pin on disc tribometer. Fig. 14(a) shows the variation of weight loss with sliding distance of the SCL samples. The weight loss of the as received material is higher than the SCL samples. The hard B_4C nano reinforcement particles exhibited the least wear amongst the tested specimens.

Fig. 14(b) shows the wear rate results. The wear rate of the as received Al5083 alloy sample is higher the SCL samples. The wear rate of the B_4C nano particle with three pass sample has less wear rate as compared to the one pass nano particle and micro particle specimen.

Reasons for better wear resistance of the SCL as compared with unprocessed matrix alloy.

1. The dispersion of hard B_4C reinforcement particles in the SCL in uniform manner, which increases hardness due to decrease in grain size in the Al matrix. These results are supported by Anwari et al. [47].
2. The fine grain size of matrix alloy due to FSP with number of passes.

Similar results were reported by Shafiei-Zarghani et al. [42] for Al–Al_2O_3 and Dolatkhah et al. [22] Al–SiC nano particles with four passes. The wear resistance of the SCL was superior

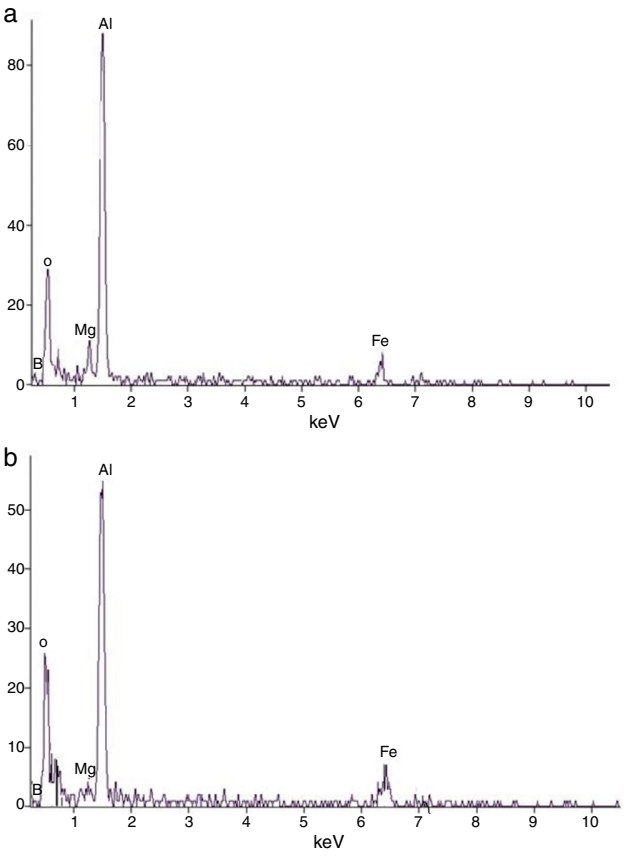

Fig. 17 – (a) EDAX of worn surface of Al–B_4C nano particle FSP specimen with three passes (b) EDAX of worn surface of Al–B_4C micro particle FSP specimen with three passes.

to the as received Al substrate due to increase in hardness and presence of hard ceramic particles and matrix refinement. Fig. 14(c) shows the change in wear rate vs microhardness. According to the Archard's equation, the wear rate is inversely proportional to the hardness of the material. Owing to the high hardness of nano particles and their bonding nature, the nano particles resist the penetration and cutting into the surface by the counter material [48–50].

Figs. 15 and 16 show the SEM micrograph of worn surface of the samples. The deep grooves occur in the base metal due to intensive material removal and plastic deformation. In nano composite with three pass specimen's shallow grooves are seen on the surface in comparison with single pass nano composite layer. Presence of ceramic particle in the FSPed composite layer prevents the wear and drastic material removal of material. Fig. 17(a) and (b) shows the EDAX of worn surface of Al–B_4C nano particle three pass FSPed specimen and Al–B_4C micro particle three pass FSPed specimen.

Fig. 18 shows the variations of friction coefficient with sliding distance of the base metal and FSPed samples. From Fig. 18(f), it is clear that the average coefficient in the three pass nano particle has the lowest value of 0.4. The friction coefficient in nano composite layer is low due to decrease in adhesive and lower abrasive wear because of higher hardness. Furthermore the presence of worn out B_4C particles acting as

Please cite this article in press as: Yuvaraj N, et al. Fabrication of Al5083/B_4C surface composite by friction stir processing and its tribological characterization. J Mater Res Technol. 2015. http://dx.doi.org/10.1016/j.jmrt.2015.02.006

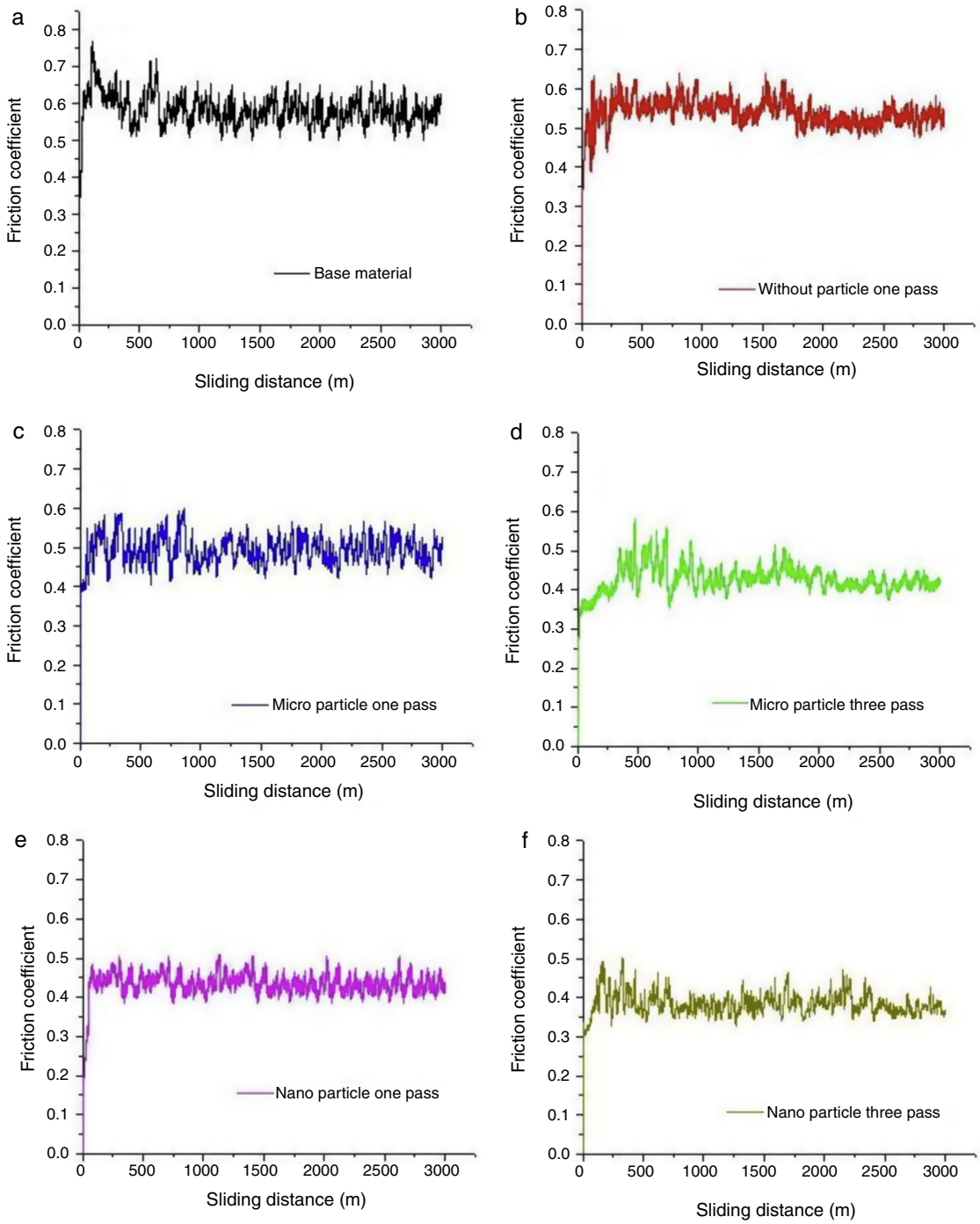

Fig. 18 – Variations of friction coefficient with sliding distance in (a) base material, (b) FSPed without particle one pass, (c) FSPed with B_4C micro particle one pass, (d) FSPed with B_4C micro particle three pass, (e) FSPed with B_4C micro particle one pass, (f) FSPed with B_4C nano particle three pass.

Table 3 – Wear test results.

Specimen	Base material	Without particle one pass	Micro sized B_4C particle one pass	Micro sized B_4C particle three Pass	Nano sized B_4C particle one pass	Nano sized B_4C particle three pass
Wear rate (mg/m)	0.0057	0.00497	0.0046	0.00416	0.00363	0.00327
Friction coefficient	0.6	0.55	0.5	0.45	0.45	0.4

Please cite this article in press as: Yuvaraj N, et al. Fabrication of Al5083/B_4C surface composite by friction stir processing and its tribological characterization. J Mater Res Technol. 2015. http://dx.doi.org/10.1016/j.jmrt.2015.02.006

lubricant is also evident from the low value of friction coefficient of nano composite layer with three passes. However, the maximum (average value) friction coefficient value of is 0.6 observed in base material. Presence of hard reinforcing material in FSPed with B_4C particles prevents adhesive wearing and material removal. Table 3 describes the wear rate of the micro and nano particle specimens with one and three passes.

4. Conclusions

Al/B_4C composites were fabricated successfully by one and three pass FSP. Effect of the reinforcing particle type and FSP passes on the microstructure, micro hardness, tensile strength and wear properties of the fabricated surface composite layer were investigated.

1. The microstructure in the FSPed specimens with nano B_4C particles three passes exhibits fine grain size, higher hardness (124.8 Hv), ultimate strength (360 Mpa) and wear rate (0.00327 mg/m) in comparison to the base material hardness (82 Hv), ultimate strength (310 Mpa) and wear rate (0.0057 mg/m).
2. By increasing the FSP passes, the distribution of nano particles in the Al matrix becomes uniform which has resulted in increased hardness, in comparison with one pass FSP nano composite.
3. The microhardness of the Al/B_4C surface nano composites is higher in comparison with B_4C micro particles. The presence of nano size B_4C particles contributes to produce ultra fine grain size.
4. The FSPed nano sized tensile specimen on the stir zone exhibited better mechanical properties than the as received Al 5083 alloy.
5. The wear properties of the Al5083 alloy were improved by addition of B_4C nano particles in comparison with B_4C micro particle, and the wear resistance of the nano SCL was higher than that of the unreinforced Al 5083 alloy.

Conflicts of interest

The authors declare no conflicts of interest.

REFERENCES

[1] Rajan TPD, Pillai RM, Pai BC. Functionally graded Al–Al3Ni in situ intermetallic composites: fabrication and microstructural characterization. J Alloys Compd 2008;453:L4–7.
[2] Miracle DB. Metal matrix composites – from science to technological significance. Compos Sci Technol 2005;65:2526–40.
[3] Kalaiselvan K, Murugan N, Siva Parameswaran. Production and characterization of AA6061–B_4C stir cast composite. Mater Des 2011;32:4004–9.
[4] Abenojar J, Velasco F, Martinez MA. Optimization of processing parameters for the Al + 10%B4C system obtained by mechanical alloying. J Mater Process Technol 2007;184:441–6.
[5] Uthayakumar M, Aravindan S, Rajkumar K. Wear performance of Al–SiC–B_4C hybrid composites under dry sliding conditions. Mater Des 2013;47:456–64.
[6] Shorowordi KM, Laoui T, Haseeb ASMA, Celis JP, Froyen L. Microstructure and interface characteristics of B_4C, SiC and Al_2O_3 reinforced Al matrix composites: a comparative study. J Mater Process Technol 2003;142:738–43.
[7] Lashgari HR, Sufizadeh AR, Emamy M. The effect of strontium on the microstructure and wear properties of A356-10%B_4C cast composites. Mater Des 2010;31:2187–95.
[8] Bradeswaran A, Elaya Perumal A. Influence of B_4C on the tribological and mechanical properties of Al 7075–B_4C composites. Composites: Part B 2013;54:146–52.
[9] Topan F, Kilicarslan A, Karaaslan A, Cigdem M, Kerti I. Processing and microstructural characterization of AA 1070 and AA 6063 matrix B_4C_p reinforced composites. Mater Des 2010;31:S87–91.
[10] Kerti I, Toptan F. Microstructural variations in cast B_4C-reinforced aluminium matrix composites (AMCs). Mater Lett 2008;62:1215–8.
[11] Toptan F, Kerti I, Rocha LA. Reciprocal dry sliding wear behavior of B_4Cp reinforced aluminium alloy matrix composites. Wear 2012;290–291:74–85.
[12] Tang F, Wu X, Ge S, Ye J, Zhuc H, Hagiwara M, et al. Dry sliding friction and wear properties of B_4C particulate-reinforced Al-5083 matrix composites. Wear 2008;264:555–61.
[13] Dubourg L, Hlawka F, Cornet A. Study of aluminium–copper–iron alloys: application for laser cladding. Surf Coat Technol 2002;151–152:329–32.
[14] Choo Seong-Hon, Lee Sunghak, Kwon Soon-Jo. Effect of flux addition on the microstructure and hardness of TiC-reinforced ferrous surface composite layers fabricated by high-energy electron irradiation. Metall Mater Trans A 1999;30(12):3131–41.
[15] Znamirowski Z, Pawlowski L, Cichy T, Czarczynski W. Low macroscopic field electron emission from surface of plasma sprayed and laser engraved TiO_2, $Al_2O_3 + 13TiO_2$ and $Al_2O_3 + 40TiO_2$ coatings. Surf Coatings Technol 2004;187:37–46.
[16] Mishra RS, Ma ZY, Charit I. Friction stir processing: a novel technique for fabrication of surface composite. Mater Sci Eng A 2003;341:307–10.
[17] Thomas WM. Friction stir welding. International Patent Application No. PCT/GB92/02203 and GB. Patent Application No.9125978.8, 1991, U.S. Patent No.5460317.
[18] Qu J, Xu H, Feng Z, Alan Frederick D, An L, Heinrich H. Improving the tribological characteristics of aluminum 6061 alloy by surface compositing with sub-micro-size ceramic particles via friction stir processing. Wear 2011;271:1940–5.
[19] Raaft M, Mahmoud TS, Zakaria HM, Khalifa TA. Microstructural, mechanical and wear behavior of A390/graphite and A390/Al_2O_3 surface composites fabricated using FSP. Mater Sci Eng A 2011;528:5741–6.
[20] Mahmoud ERI, Takahashi M, Shibayanagi T, Ikeuchi K. Wear characteristics of surface-hybrid-MMCs layer fabricated on aluminium plate by Friction Stir Processing. Wear 2010;268:1111–21.
[21] Wang Wei, Shi Qing-yu, Liu Peng, Li Hong-ke, Ting Li. A novel way to produce bulk SiCp reinforced aluminium metal matrix composites by friction stir processing. J Mater Process Technol 2009;209:2099–103.
[22] Dolatkhah A, Golbabaei P, Besharati Givi MK, Molaiekiya F. Investigating effects of process parameters on microstructural and mechanical properties of Al5052/SiC metal matrix composite fabricated via friction stir processing. Mater Des 2012;37:458–64.
[23] Salehi M, Saadatmand M, Aghazadeh Mohandesi J. Optimization of process parameters for producing

Please cite this article in press as: Yuvaraj N, et al. Fabrication of Al5083/B_4C surface composite by friction stir processing and its tribological characterization. J Mater Res Technol. 2015. http://dx.doi.org/10.1016/j.jmrt.2015.02.006

AA6061/SiC nanocomposites by friction stir processing. Trans Nonferr Metals Soc China 2012;22:1055–63.
[24] Kurt A, Uygur I, Cete E. Surface modification of aluminium by friction stir processing. J Mater Process Technol 2011;211:313–7.
[25] Mostafapour Asl A, Khandani ST. Role of hybrid ratio in microstructural, mechanical and sliding wear properties of the Al5083/Graphitep/Al_2O_{3p} a surface hybrid nanocomposite fabricated via friction stir processing method. Mater Sci Eng A 2013;559:549–57.
[26] Shafiei-Zarghani A, Kashani-Bozorg SF, Zarei-Hanzaki A. Microstructures and mechanical properties of Al/Al_2O_3 surface nano-composite layer produced by friction stir processing. Mater Sci Eng A 2009;500:84–91.
[27] Aruri D, Adepu K, Adepu K, Bazavada K. Wear and mechanical properties of 6061-T6 aluminium alloy surface hybrid composites [(SiC + Gr) and (SiC + Al_2O_3)] fabricated by friction stir processing. J Mater Res Technol 2013;2(4): 362–9.
[28] Moghaddas MA, Kashani-Bozorg SF. Effects of thermal conditions on microstructure in nanocomposite of Al/Si_3N_4 produced by friction stir processing. Mater Sci Eng A 2013;559:187–93.
[29] Maxwell Rejil C, Dinaharan I, Vijay SJ, Murugan N. Microstructure and sliding wear behavior of AA6360/(TiC + B_4C) hybrid surface composite layer synthesized by friction stir processing on aluminum substrate. Mater Sci Eng A 2012;552:336–44.
[30] Kashani-Bozorg SF, Jazayeri K. Formation of Al/B_4C surface nano composite layers on 7075 Al alloy employing friction stir processing. CP1136. In: Nanoscience and Nanotechnology International Conference on Nanoscience and Nanotechnology. 2008. p. 715–9.
[31] Shahraki S, Khorasani S, Behnagh RA, Fotouhi Y, Bisadi H. Producing of AA5083/ZrO_2 nanocomposite by friction stir processing (FSP). Metall Mater Trans B 2013;44(6): 1546–53.
[32] Khodabakhshi F, Simchi A, Kokabi AH, Nosko M, Simancik F, Svec P. Microstructure and texture development during friction stir processing of Al–Mg alloy sheets with TiO_2 nanoparticles. Mater Sci Eng A 2014;605:108–18.
[33] Mishra RS, Ma ZY. Friction stir welding and processing. Mater Sci Eng R 2005;50:1–78.
[34] Asadi P, Givi MKB, Rastgoo A, Akbari M, Zakeri V, Rasouli S. Prediciting the grain size and hardness of AZ91/SiC nanocomposite by artificial neural networks. Int J Adv Manuf Technol 2012;63:1095–107.
[35] Shamsipur A, Farshid S, Abbas Zarei-Hanzaki K-B. Production of in-situ hard Ti/TiN composite surface layers on CP-Ti using reactive friction stir processing under nitrogen environment. Surf Coat Technol 2013;218:62–70.
[36] Morisada Y, Fujii H, Mizuno T, Abe G, Nagaoka T, Fukusumi M. Fabrication of nanostructured tool steel layer by combination of laser cladding and friction stir processing. Surf Coat Technol 2011;205:3397–403.
[37] Faraji G, Asadi P. Characterization of AZ91/alumina nanocomposite produced by FSP. Mater Sci Eng A 2011;528:2431–40.
[38] Shamsipur A, Kashani-Bozorg SF, Zarei-Hanzaki A. The effects of friction-stir process parameters on the fabrication of Ti/SiC nano-composite surface layer. Surf Coat Technol 2011;206:1372–81.
[39] Zahmatkesh B, Enayati MH. A novel approach for development of surface nanocomposite by friction stir processing. Mater Sci Eng A 2010;527:6734–40.
[40] Lloyd DJ. Particle reinforced aluminium and magnesium matrix composites. Int Mater Rev 1994;39:1–23.
[41] Mahmoud TS. Surface modification of A390 hypereutectic Al–Si cast alloys using friction stir processing. Surf Coat Technol 2013;228:209–20.
[42] Shafiei-Zarghani A, Kashani-Bozorg SF, Zarei- Hanzaki A. Wear assessment of Al/Al_2O_3 nano-composite surface layer produced using friction stir processing. Wear 2011;270:403–12.
[43] Asadi P, Faraji G, Masoumi A, Besharati Givi MK. Experimental investigation of magnesium-base nanocomposite produced by friction stir processing: effects of particle types and number of friction stir processing passes. Metall Mater Trans A 2011;42A:2820–32.
[44] Cui GR, Ma ZY, Li SX. The origin of non-uniform microstructure and its effects on the mechanical properties of a friction stir processed Al–Mg alloy. Acta Mater 2009;57:5718–29.
[45] Zohoor M, Besharati Givi MK, Salami P. Effect of processing parameters on fabrication of Al–Mg/Cu composites via friction stir processing. Mater Des 2012;39:358–65.
[46] Bauri R, Yadav D, Suhas G. Effect of friction stir processing (FSP) on microstructure and properties of Al–TiC in situ composite. Mater Sci Eng A 2011;528:4732–9.
[47] Anvari SR, Karimzadeh F, Enayati MH. Wear characteristics of Al–Cr–O surface nano-composite layer fabricated on Al6061 plate by friction stir processing. Wear 2013;304:144–51.
[48] Deuis RL, Subramanian C, Yellup JM. Dry sliding wear of aluminium composites – a review. Compos Sci Technol 1997;57:415–35.
[49] Mazaheri Y, Karimzadeh F, Enayati MH. Tribological behavior of A356/Al_2O_3 surface nanocomposite prepared by friction stir processing. Metall Mater Trans A 2014;45A:2250–9.
[50] Alidokht SA, Abdollah-zadeh A, Soleymani S, Assadi H. Microstructure and tribological performance of an aluminium alloy based hybrid composite produced by friction stir processing. Mater Des 2011;32:2727–33.

Please cite this article in press as: Yuvaraj N, et al. Fabrication of Al5083/B_4C surface composite by friction stir processing and its tribological characterization. J Mater Res Technol. 2015. http://dx.doi.org/10.1016/j.jmrt.2015.02.006

International Journal of Current Engineering and Technology
E-ISSN 2277 – 4106, P-ISSN 2347 – 5161
©2015INPRESSCO®, All Rights Reserved
Available at http://inpressco.com/category/ijcet

Research Article

Finite Element Analysis of Magnetorheological Brake using ANSYS

Chiranjit Sarkar†* and Harish Hirani‡

†Mechanical Engineering Department, Delhi Technological University, Shahbad Daluatpur, Bawana Road, Delhi – 110042, India
‡Mechanical Engineering Department, Indian Institute of Technology Delhi, Hauz Khas, New Delhi – 110016, India

Accepted 06 March 2015, Available online 18 March 2015, **Vol.5, No.2 (April 2015)**

Abstract

The aim of this paper is to understand the electromagnetic action in a magnetorheological (MR) brake (MRB) system using finite element method. MR brake system consists of rotary disks immersed in a MR fluid and enclosed in an electromagnet. The torque exerted by MR fluid on the rotary disks is a function of magnetic field created by electric current passing through the electromagnet. To estimate the braking torque, under various operating conditions, an APDL code has been developed. Based on the parametric study, decisions on materials for various components of the MR brake have been made. Finally, a procedure to design a MR brake has been recommended.

Keywords:*MR fluid, MR brake, Multi disk MR Brake, Electromagnetic simulation, Finite element analysis.*

1. Introduction

In magnetorheological brake (Gupta and Hirani, 2011) torque can be magnetically manipulated by just controlling the electric current supplied to electromagnet. Such brake arrangement minimizes the number of moving links, reduces response time and increases the reliability of overall system. In addition, MR brake has advantage over conventional disk brakes, particularly in nullifying mechanical wear and providing digital control on the frictional power. It is expected that MR brake will perform smooth, jerk free operation and consume lesser power compared to eddy current or magnetic hysteresis brakes.

The design of MR brake starts with the maximum shear strength, τ_{max}, achievable by the available MR fluid (Ginder and Davis, 1994). The control on the shear stress (between zero to τ_{max}) of MR fluid is achieved by regulating the magnitude and direction of the magnetic field. The field density is a function of permeability and saturation of materials through which magnetic field passes, brake geometry, number of turns in electromagnetic coil, and current supplied to electromagnetic coil (Sarkar and Hirani, 2015), (Sarkar and Hirani, 2013), (Sukhwani, *et al*, 2009), (Sukhwani and Hirani, 2008), (Sukhwani and Hirani, 2008), (Sukhwani, *et al*, 2008), (Hirani and Manjunatha, 2007), (Sukhwani, *et al*, 2007), (Sukhwani and Hirani, 2007), (Sukhwani, *et al*, 2006). In the present study, magnetic flux density and flux path of magnetic field will be analyzed to understand the effect of magnetic and non magnetic materials using ANSYS software.

2. Electromagnetic simulation of MR brake

The geometry of MR brake is symmetric about the axis; therefore it is analysed as a 2-D axi-symmetric model as shown in Figure 1.

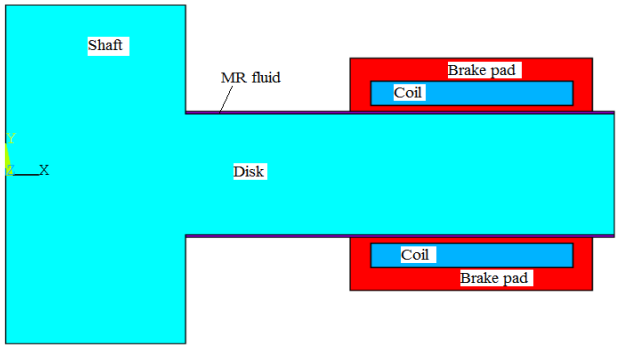

(a) Configuration 1

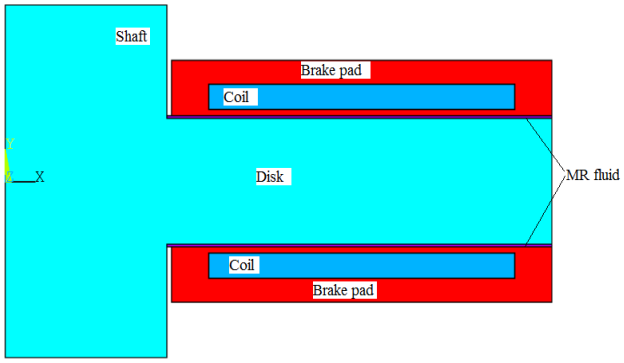

(b) Configuration 2

*Corresponding author: **ChiranjitSarkar**

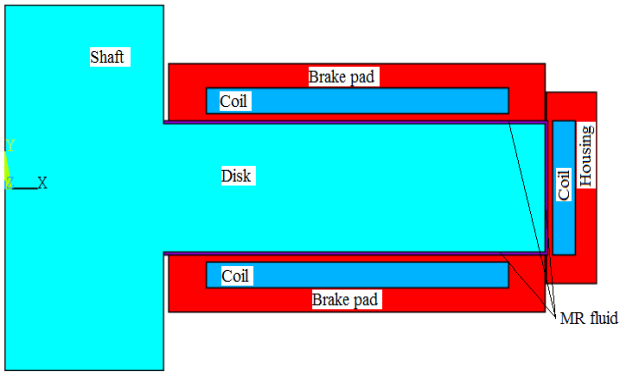

(c) Configuration 3

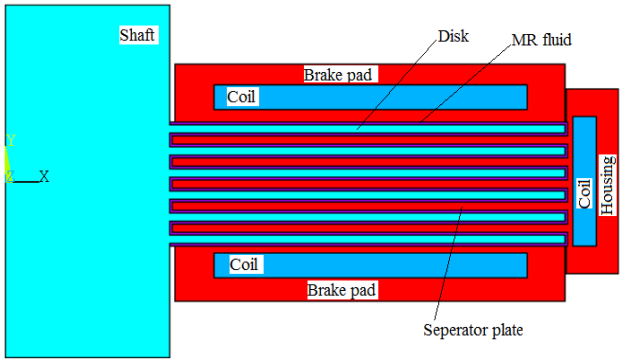

(d) Configuration 4

Fig.1 2-D Axisymmetric MR Brake in ANSYS

In Figure 1 (a) an axi-symmetric view of single disk MR brake has been shown. In this configuration it is assumed that rotating disk is mounted on the shaft with interference-fit and for FEA the shaft and rotating disk can be treated as a single component. Figure 1(b) is similar to Figure 1(a) except the changes in the brake-width and the coil area dimensions. In Figure 1 (c) additional electromagnetic coil pocketed in the housing has been shown. Figure 1 (d) shows a 2-D view of multi plate rotating disk attached to shaft and MR fluid around the rotating plates. Here brake pads and housing are stationary members. Three electromagnetic coils are shown in the figure. The details of the dimensions of four configurations are given in Sarkar and Hirani (2015). A cross sectional view of electromagnetic coil is shown in Figure 2.

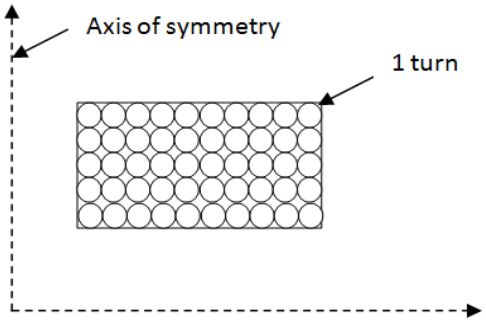

Fig.2 Axisymetric cross section of electrical coil

For given current density, one can determine the magnetic flux density at the rotary disk, MR fluid and the housing. Table 1 lists the magnetic terms used in the present electromagnetic study of MR brake.

Table1: Nomenclature used for the Magnetic Analysis

Symbols	Meaning
BSUM	Magnetic Flux Density or Magnetic Induction
JS	Current Density
B	Vector Magnetic Flux Density
N	Numbers of turns of wires
I	Current
M	Permeability of material used in the Model

In ANSYS, a static (DC) current is provided as input in the form of current density (current over the area of the coil).

$$JS = \frac{(NI)}{A}$$

To mesh the geometry of MR brake, shown in Figure 1, 2-D quadrilateral Coupled-Field-Solid elements, PLANE 13 were selected. The PLANE 13 element contains four nodes and four degrees of freedom per node. The KEYOPT (3) option was selected to use axisymmetric simulation. The PLANE 13 element can be assigned nonlinear magnetic (B-H curves) properties. SI units were set using the EMUNIT command. The value ofμ_0(free-space permeability) was kept equal to $4\pi * 10^{-7}$henries/meter. In ANSYS, the components of magnetic flux density along the x and y axes are nomenclature as $B_x$and B_y respectively. The term $B_{Sum}$is defined by

$$B_{Sum} = \sqrt{(B_x^2 + B_y^2)}$$

The values of relative permeability assigned to materials of various MR brake components are listed in Table 2.It shows MRF241ES (41% volume fraction of iron particles) and MRF336AG (36% volume fractions of iron particles) have relative permeability 8 and 5 respectively.

Table2: Relative permeability of different materials of the MR brake

Parts	Material	Relative Permeability
Shaft	Low carbon Steel/Stainless steel	100/1
Rotor plate	Low carbon steel/Iron 99.8% pure	100/5000
Housing	Low carbon steel/Iron 99.8 %pure	100/5000
Seals	Natural Rubber	1
Bearings	Low carbon steel/Stainless steel	100/1
MR fluid used	MRF 241 ES /MRF336AG	8/5

In the analysis an assumption of zero leakage from housing to the environment was made. To impose this condition, constraint of parallel direction of the magnetic flux on boundaries of housing (AZ=0) was used. By default, ANSYS uses the flux to be normal to all exterior faces. 2D magnetic static analysis (using MAGSOLV command) was performed to find the distribution of magnetic flux within the brake housing. To incorporate nonlinear B-H curve, nonlinear analysis (using NSUBST) was carried out. As nonlinear electromagnetic analysis proceeds, ANSYS computes convergence norms with corresponding convergence criteria in each equilibrium iteration. ANSYS considers a solution to be converged whenever specified convergence criteria are met. Convergence checking may be based on magnetic potential, magnetic field, or magnetic flux density. In the analysis, magnetic flux equal to 1.2 and the tolerance equal to 0.01 were selected, which means the convergence criterion for magnetic flux was kept as 0.012.

Figure 3 shows the flux lines of constant AZ (or constant radius-times-AZ for axisymmetric problems) for all four configurations.

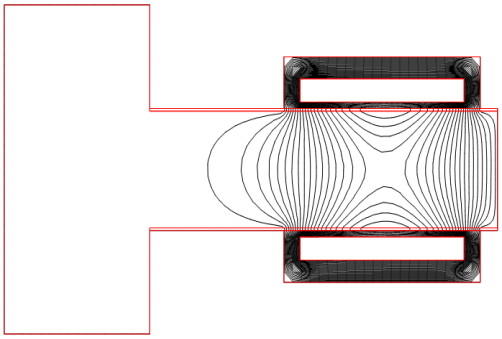

Configuration 1

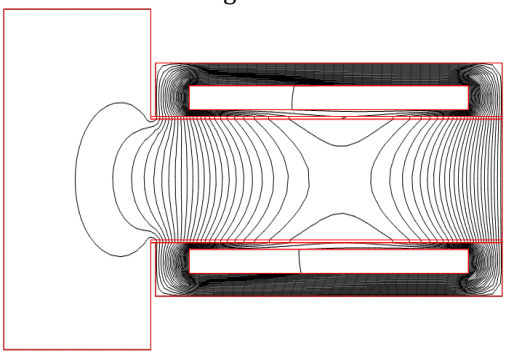

Configuration 2

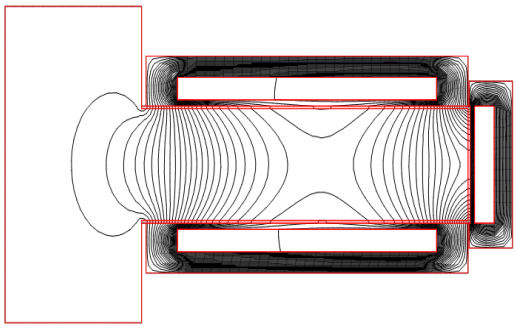

Configuration 3

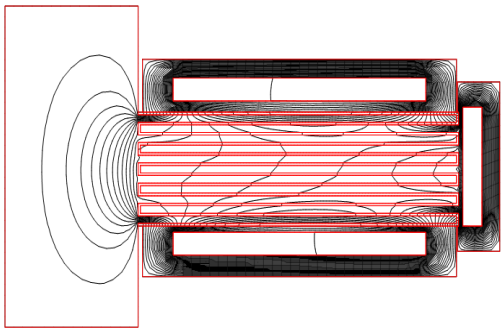

Configuration 4

Fig.32-D Flux Lines around the electrical coil

It shows that 2 D flux lines complete the path in the MR brake. The values of maximum density of 2 D flux lines (SMX) are 0.010702, 0.012923, 0.012967 and 0.012092 for configuration 1, configuration 2, configuration 3 and configuration 4 respectively. It indicates that with increase in the electromagnetic current density, maximum density of 2 D flux lines increases except in configuration 4. To justify the magnetic flux for different configurations, the vector plot of magnetic flux density using nodal solution has been plotted in Figure 4. It shows that configuration 3 has maximum magnetic flux density (SMX) of 4.08 Tesla. To observe the symmetrical magnetic flux density, ¾ expansion of the results for different configuration is shown in Figure 5. It shows the magnetic flux density is uniform along the circular direction.

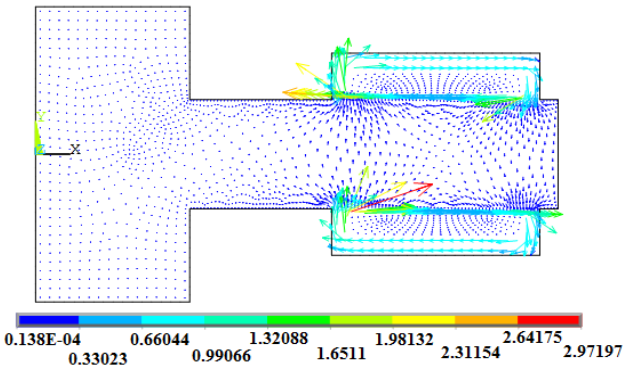

Configuration 1

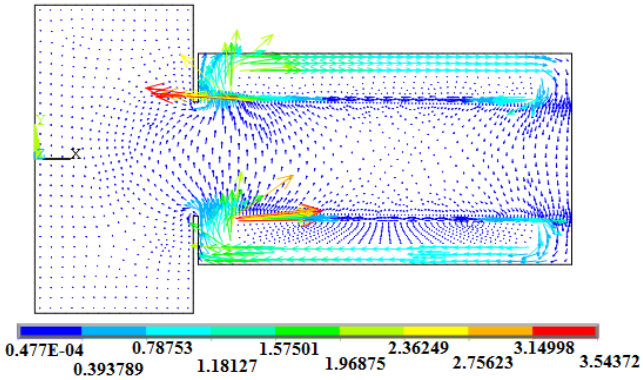

Configuration 2

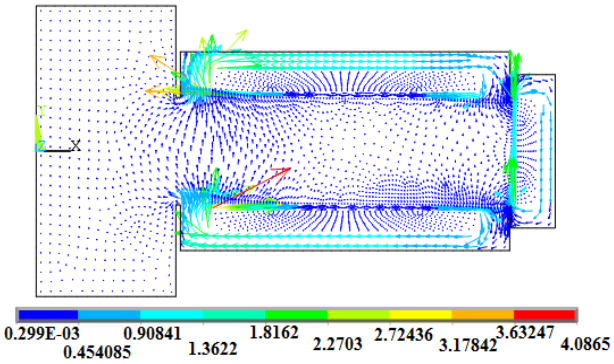

Configuration 3

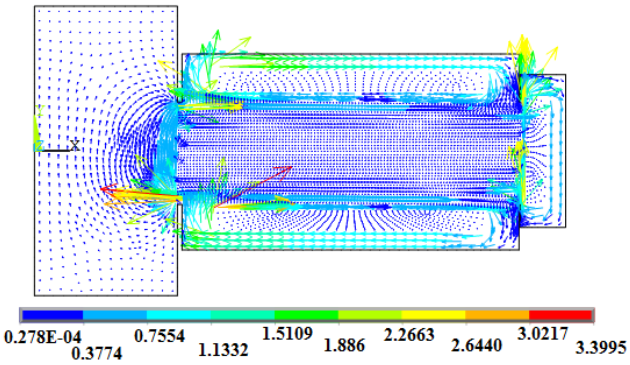

Configuration 4

Fig. 4 Nodal Solution-Magnetic Flux Density vector

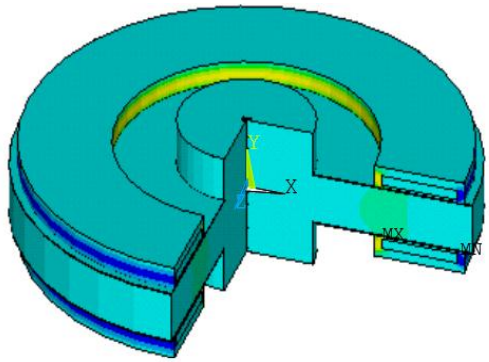

Configuration 1

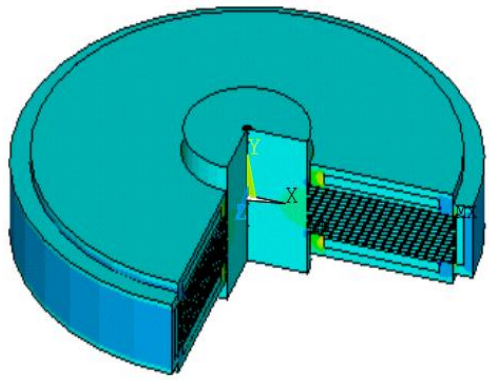

Configuration 4

Fig.5 ¾th Symmetry Expansion of MR Brake

This finite element analysis concludes that magnetic flux density is a function of radius of rotary disk. The magnetic flux densities at different nodes along the radius are different. To estimate the braking torque of MR brake, analysis of magnetic flux density at different nodes using APDL codes has been incorporated in the manuscript.

3. Estimating the Braking Torque using Finite Element Analysis

In this section, 2-D axi-symmetric analysis of a multi disk MR brake has been presented. Torque, exerted by the brake has been presented as function of MR gap and electric current supplied to electromagnet. APDL code was written for the finite element analysis.

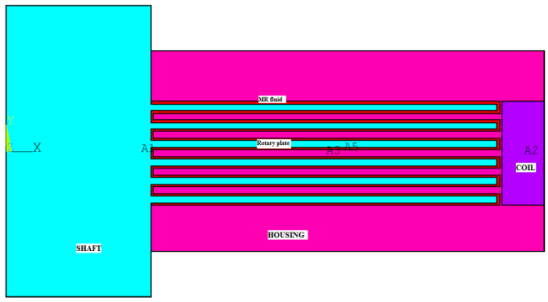

Fig.6 Simple 2D Axisymetric Model of MR Brake

A block axisymmetric model of multi disk is shown in figure 6. In this brake arrangement, MRF 336 AG is taken as MR fluid. The coilconsists of 1000turns of AWG 25 copper wire. The maximum current supplied to electromagnet was kept as 1 amp.The 2D flux lines of the multi disc brake assembly are illustrated in Figure 7.

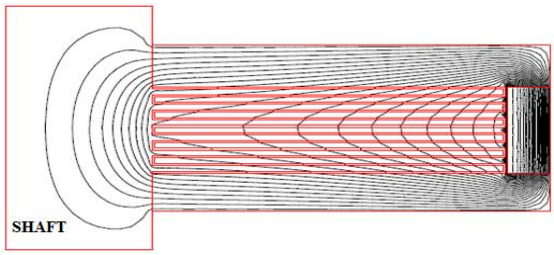

Fig.7 2D Flux Lines of multidisc assembly

It is interesting to note that flux lines are passing through the shaft. As torque is calculated along the disk, magnetic field concentration should be around the disk plate and magnetic field in the shaft should be as low as possible. Hence the shaft material should be non-magnetic material i.e. stainless steel.

Seals are required to restrict the leakage of the MR fluid. Seal is also made of non-magnetic material (i.e. Natural rubber) having permeability equal to 1. Bearing of permeability 1 is also placed to support the shaft. Figure 8 shows the multidisc assembly with the same sizes of seals and bearings.

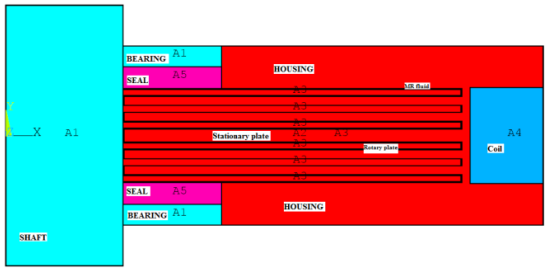

Fig.8 Modified design of Multi Disk assembly

Figure 9 shows the 2 D flux lines in the modified multi-disk brake assembly. It shows that negligible flux lines passes through the shaft, seal and bearing. Therefore, this design of MR brake is a good design as far as magnetic flux is concerned.

Figure 10 shows MR brake assembly with increase radial dimension of the disks, but maintaining overall same outer dimensions of the housing. This modification was attempted to increase the MR effect. Coil area is modified according to the number of turns of wire used.

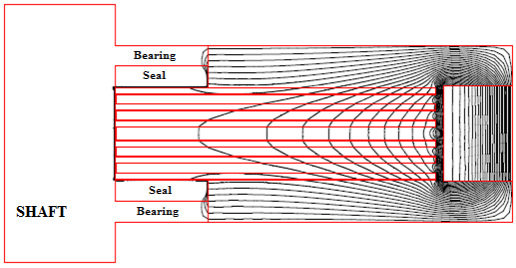

Fig.9 2 D Flux Lines of Modified Design of assembly

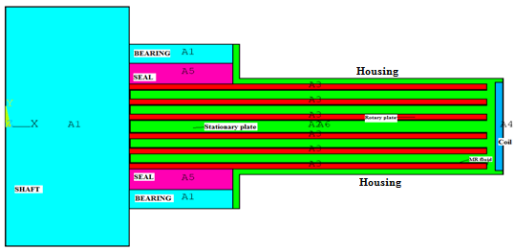

Fig.10 Modified MR Brake assembly

Figure 11 shows the 2D flux lines of the MR Brake assembly. It shows that the 2 D flux lines are more concentrated in the rotary plate of the disk which increases the magnetic flux density along the surface of the disk plate.

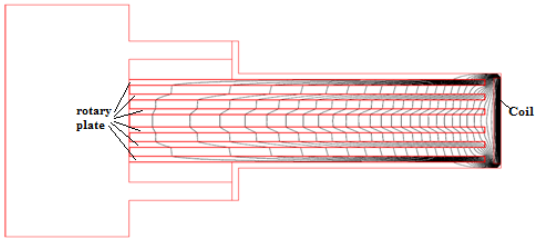

Fig.112D Flux Lines of MR Brake Assembly

Torque of the modified MR brake assembly is estimated as function of MR gap ranging from 0.25mm to 1 mm. Rotary disk plates are made of silicone steel having relative permeability equal to 5000. The housing of MR brake is made low carbon steel having the relative permeability equal to 100. Coil is made copper wire (relative permeability = 0.999994). Table 3 shows the estimation of torque at different currents up to upper limit of current 2.7 Amp in AWG 25.

Table 3 shows the saturation of torque at the higher limit of current i.e. 2.5 A and 2.7 A. Figure 12 shows that torque increases with increase in h. Considering a constraint on outer radius of housing as 210 mm and packing factor as 0.7, a new electromagnet space was designed to accommodate the 2000 turns of wire to get more magnetic fields. Figure 13 shows the MR brake design with new electromagnet space. Figure 16 shows the torque of the MR brake using different housing materials.

Table 3: Estimation of torque at different currents

I (Amp)	Torque (Nm)			
	h = 0.25mm	h = 0.50mm	h = 0.75mm	h = 1.0 mm
0.25	3.17	5.44	7.69	9.86
0.5	3.97	7.11	10.26	13.25
0.75	5.17	9.30	13.64	17.79
1.0	6.47	11.93	17.80	22.65
1.25	7.73	14.84	22.49	29.37
1.5	8.36	16.85	26.20	34.39
1.75	8.91	18.46	28.29	38.14
2.0	9.29	19.67	30.22	41.41
2.25	9.68	20.87	32.37	44.89
2.5	9.81	21.26	34.64	46.72
2.7	9.94	21.78	35.52	47.43

There is a need to understand the material requirement for MR brake housing. Low permeability of material is required to minimize the leakage of magnetic field. However, higher permeability of material is required to transmit magnetic field from housing to rotating disks. To understand this, the simulation was carried on two materials: low carbon steel (relative permeability 100) and iron 99.8% pure as housing stationary plate (relative permeability 2000-5000). Table-4 indicates the torque-estimated for different housing material.

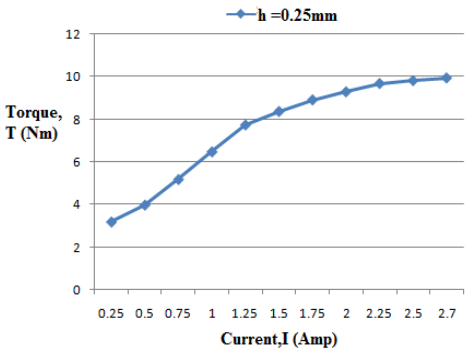

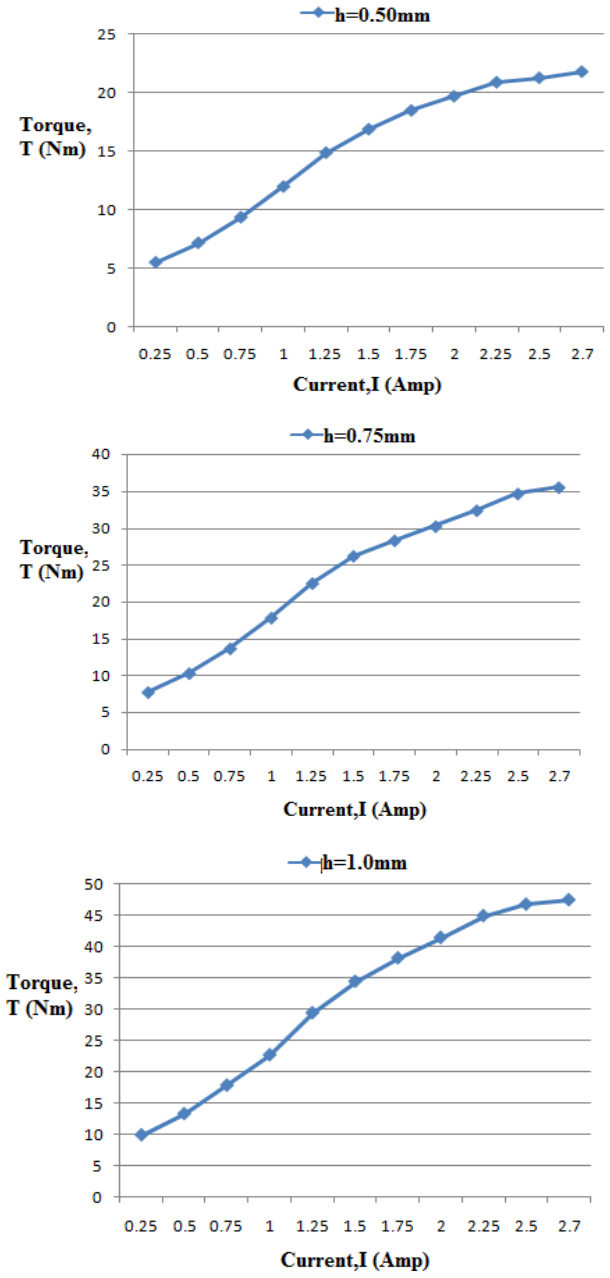

Fig.12 Torque at different MR gap, h

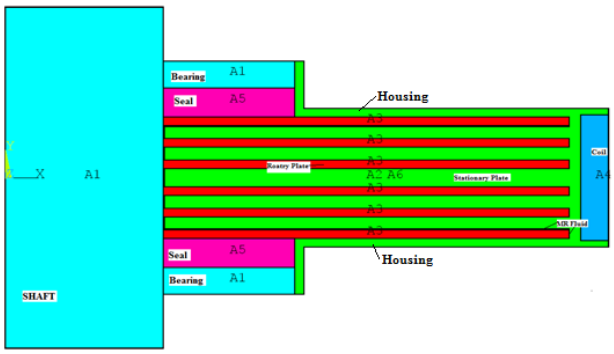

Fig.13 New design of multidisc MR brake

Finally effect of MR fluid on brake was tried by using MRF 241 ES in place of MRF-336AG MRF-336AG (Sarkar and Hirani, 2013). The maximum value of yield stress (τ_{yd}) corresponding to magnetic field intensity H = 1000kA/m (Sarkar and Hirani, 2013), for the MRF 241 ES is 69 kPa (Sarkar and Hirani, 2013). Figure 16 shows the braking torque using MRF 241 ES MR fluid.

Table 4: Estimation of torque for different housing material

Current, I (Amp)	Torque at h = 0.001m	
	Low carbon steel Housing	Iron 99.8% Housing
0.25	18.32	8.16
0.5	20.37	19.57
0.75	23.58	28.96
1.00	26.41	35.46
1.25	29.33	40.73
1.5	30.93	43.80
1.75	32.51	45.52
2	34.78	47.60
2.25	36.69	49.27
2.5	38.56	50.06

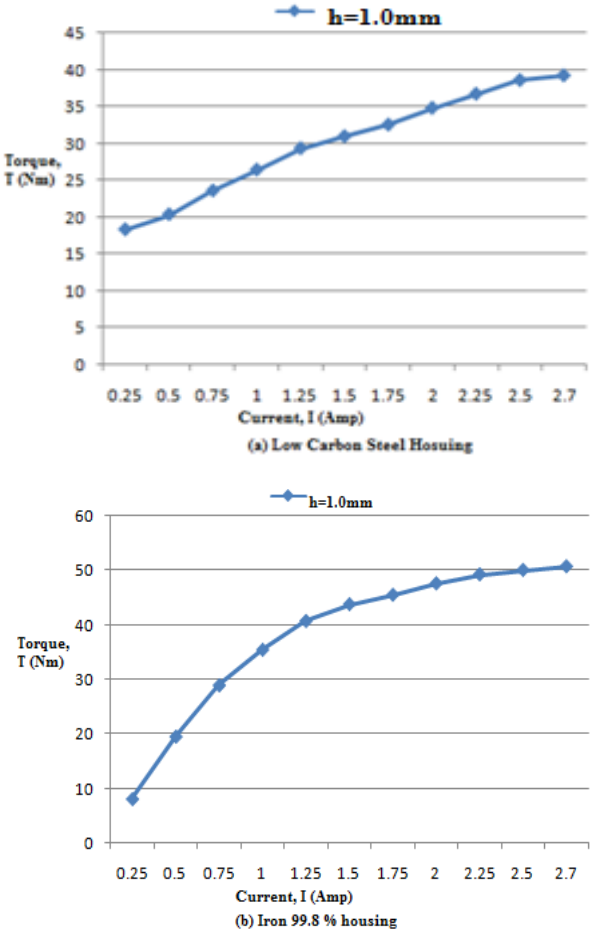

Fig.14 Effect of housing materials on the Braking Torque

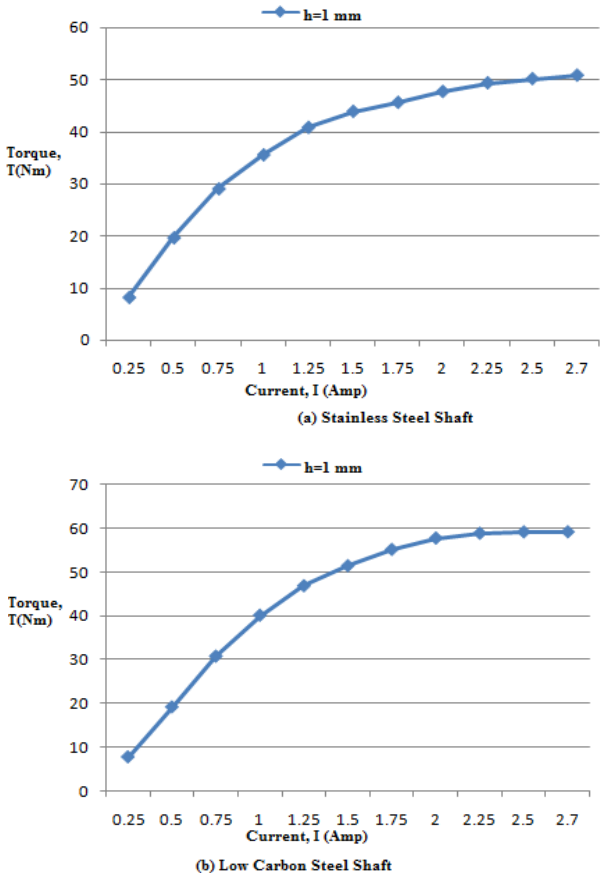

Fig. 15 Effect of shaft materials on the Braking torque

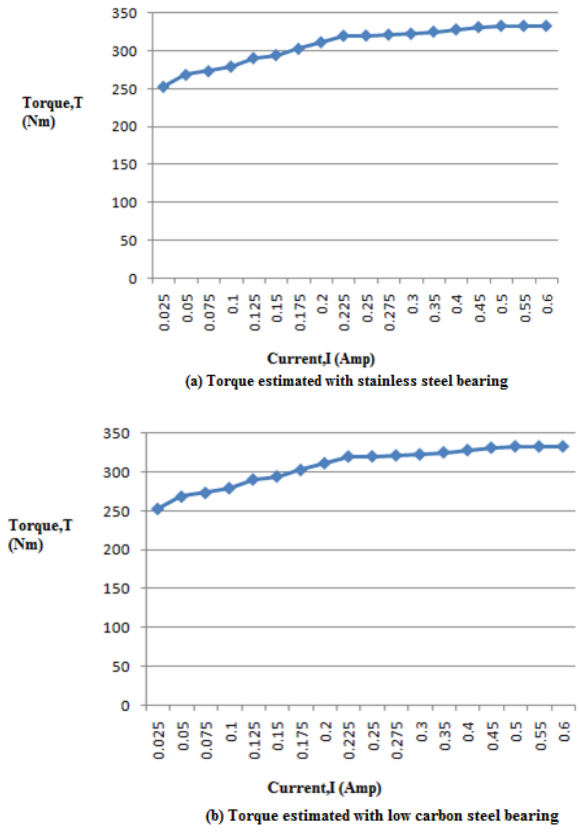

Fig.16 Torque estimated for MRF 241ES MR fluid

This figure clearly indicates that higher braking torque is possible by using MRF241 ES compared to using MRF 336 AG.

Conclusions

This research work has discussed the finite element analysis of the MR brake. The following conclusions can be made from the present research work.

- Density of 2 D flux lines in the MR brake configurations increases with increase in electromagnetic coil area.
- Non magnetic material seal (nitrile rubber) and bearing (stainless steel) restricts the passing of flux lines through them and enhances the concentrations of magnetic flux densities between disk, MR fluid and housing area. However, stainless steel bearing is costly.
- Increase in radial dimensions of the disk.
- With increase in MR gap, there is an increase in braking torque.
- Housing material with Iron 99.8% increases the braking torque as compared to Low carbon steel.Low carbon steel material of shaft increases MR effect as compared to stainless steel shaft.
- MRF241ES produces more braking torque due to high percentage of iron particles.

References

C.Sarkar, H.Hirani, (2013), Theoretical and experimental studies on a magnetorheological brake operating under compression plus shear mode, *Smart Materials and Structures*, 22, art. no. 115032.

C.Sarkar, H.Hirani, (2013), Synthesis and characterization of antifriction magnetorheological fluids for brake, *Defence Science Journal*, 63, pp. 408-412.

C.Sarkar, H. Hirani, (2013), Design of a squeeze film magnetorheological brake considering compression enhanced shear yield stress of magnetorheologicalfluid, *Journal of Physics: Conference Series*, 412, 012045.

C. Sarkar, H. Hirani, (2015), Transient Thermo Elastic Analysis of Disk Brake, International Journal of Current Engineering and Technology, 5, pp. 413-418.

C. Sarkar, H. Hirani, (2015), Magnetorheological Smart Automotive Engine Mount, International Journal of Current Engineering and Technology, 5, pp. 419-428.

C. Sarkar, H. Hirani, (2015), Design of Magnetorheological Brake using Parabolic Shaped Rotating Disc, International Journal of Current Engineering and Technology, 5, pp. 719-724.

C. Sarkar, H. Hirani, (2015), Synthesis and characterization of nano-copper-powder based magnetorheological fluids for brake, International Journal of Scientific Engineering and Technology, 4, pp. 76-82.

C. Sarkar, H. Hirani, (2015), Effect of particle size on shear stress of magnetorheological fluids, *Smart Science,* (in press).

C. Sarkar, H. Hirani, (2015), Development of magnetorheological brake with slotted disc, *Proc. IMechE, Part D: Journal of Automobile Engineering*, (in press).

H.Hirani, C. S. Manjunatha, (2007), Performance evaluation of magnetorheological fluid variable valve, *Proc. of the Institution of Mechanical Engineers, Part D, Journal of Automobile Engineering*, 221, pp. 83-93.

J. M. Ginder, L. C. Davis,(1994), Shear Stresses in Magnetorheological fluids: Role of Magnetic Saturation, Applied Physics Letters, 65, pp. 3410-3412.

S. Gupta, H. Hirani, (2011), Optimization of magnetorheological brake, *ASME/STLE 2011 International Joint Tribology Conference*, pp 405-406.

V. K. Sukhwani, V. Lakshmi, H. Hirani, (2006), Performance evaluation of MR brake: an experimental study, *Indian Journal of Tribology*, pp. 67-52.

V. K. Sukhwani, H. Hirani, T. Singh, (2007), Synthesis of magnetorheological grease, *Greasetech India*.

V. K. Sukhwani, H. Hirani, (2007), Synthesis and characterization of low cost magnetorheological (MR) fluids, *The 14th International Symposium on: Smart Structures and Materials & Nondestructive Evaluation and Health Monitoring*, 65262R-65262R-12.

V.K.Sukhwani, H.Hirani, (2008), A comparative study of magnetorheological-fluid-brake and magnetorheological-grease-brake, *Tribology Online*, 3, pp. 31-35.

V.K.Sukhwani, H.Hirani, T.Singh, (2008), Synthesis and performance evaluation of MR grease, *NLGI Spokesman*,71.

V.K.Sukhwani, H. Hirani, (2008), Design, development and performance evaluation of high speed MR brake, *Proc. Institute Mech. Engineers., Part L, Journal of Materials: Design and Applications*, 222,pp.73-82.

V. K. Sukhwani, H. Hirani, T. Singh, (2009), Performance evaluation of a magnetorheological grease brake, *Greasetech India*, 9,pp. 5-11.

Get ‘em Moles! : Improved Spelling and Pronunciation through an Educational Game

Dhruv Chand
National Institute of Technology Karnataka
Surathkal, Karnataka, India
dhruvchand@live.com

Karthik Gopalakrishnan
Indian Institute of Technology Patna
Patna, Bihar, India
karthik.cs11@iitp.ac.in

Nisha K K
National Institute of Technology Karnataka
Surathkal, Karnataka, India
nishakk94@gmail.com

Mudit Sinha
Vellore Institute of Technology
VIT University
Chennai, Tamil Nadu, India
mudit.sinha2012@vit.ac.in

Shreya Sriram
Delhi Technological University
New Delhi, India
shreyasriram29@gmail.com

Author names are arranged in alphabetical order by last name. Copyright is held by the authors.

Abstract
Get ‘em Moles! is a single-player educational game inspired by the classic arcade game Whac-A-Mole. Primarily designed for touchscreen devices, Get ‘em Moles! aims to improve English spelling and pronunciation in players by supporting learning with engaging game play. This paper describes the game, design decisions in the form of elements that support learning and engagement, preliminary results, and future work.

Author Keywords
Educational Games; Learning Technology; Game Design; English Vocabulary, English Spelling;

ACM Classification Keywords
K.3.1;

Introduction
Effective verbal communication calls for good pronunciation, and effective written communication requires a good knowledge of spelling. According to the ERIC report [3] ‘Why Teach Spelling?’, a skilled speller is both a strong reader and a strong writer. Through Get ‘em Moles!, we attempt to improve English spelling and pronunciation in players by integrating learning

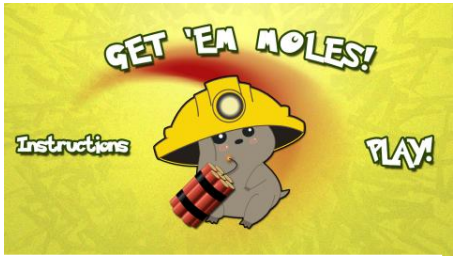

Figure 1: Get 'em Moles! Start Screen

Figure 3: Giveaway hint revealing the next letter for the word "occurrence"

with an engaging arcade gaming experience. We designed and developed a prototype of the game using the Unity 3D game engine [6] in the Javascript and C# programming languages, and compiled builds to run on the Windows Phone and Android platforms.

Learning Objectives

The game is aimed at helping children between the ages 10 and 13 with spellings and pronunciations of English words. A basic knowledge of phonetics, alphabets, and reading English are the prerequisites to play the game. A fixed word list catering to this target audience is used in the game. However, the game can be easily extended to use multiple word lists, each with a different level of difficulty. This can be useful to students from different backgrounds, for instance, to undergraduates preparing for the Graduate Record Examinations (GRE), an essential component of graduate school applications.

Through the game, we expect to achieve better English spelling and pronunciation of common to advanced words for the target age group. We also additionally expect faster typing speeds through continued usage of the QWERTY keyboard layout in the game.

Game Play

The game is a quest to defuse bombs planted by Murphy the Mole (the antagonist) under the keys of a keyboard before they detonate. This is done by typing the right spellings of words spoken by the in-game voice.

The main game screen (Figure 2) comprises of a stylized on-screen QWERTY keyboard, score meter, pause/play button, a speaker button to listen to the pronunciation of a word again, and a text area that displays letters of the word already typed in. The game play is divided into pulses of levels: each level comprises of a set of words that are served in succession. The in-game voice speaks out a word, and waits for the player to hit the letters corresponding to its spelling on the keyboard, one-by-one.

Figure 2: Main game screen showing a stylized keyboard and other components

If the player hits the correct letter, the letter turns green with a chime and the correct letter appears in the text area above. Simultaneously, the letter is spoken by the in-game voice. However, if the player does not hit any letter within a fixed period of time, some letters on the keyboard glow red and small bomb symbols appear next to them. One of these letters is correct and the rest are decoys. This provides the player a choice of possible answers to the next letter in the word as a hint. The player can use the hint and hit the correct letter, although this earns the player lesser points than hitting the correct letter without the hint. If the player does not hit any letter, the glowing letters burn up and explode after a fixed period of time, revealing Murphy the Mole under the correct letter (Figure 3). The player

Figure 4: Whac-A-Mole as a Bonus Round

is then left with no choice but to hit the correct letter and move on to the next letter of the word. This does not earn the player any points. At any stage, a wrong hit causes a wrong buzzer to sound, and turns the hit letter red to indicate a wrong choice. The correct letter is then revealed through Murphy the Mole's appearance under the correct letter.

A high score streak invokes a bonus round (Figure 4), where players get to play Whac-A-Mole and increase their overall score. The bonus round is time-limited, and fast-paced.

Game Elements Supporting Learning and Engagement

Get 'em Moles! attempts to create a multi-sensory learning environment to achieve a better rate of learning [5], by using a combination of visual and audio cues to support correct answers. The game features that support learning are as follows:

- The start of every word is accompanied with its audio pronunciation, binding the word to its pronunciation.
- Every correct hit is supported by a chime, followed by a pronunciation of that letter for further reinforcement.
- The hint system helps players navigate through common confusions, by providing a choice of possible answers.
- A giveaway hint revealing the correct letter is provided when the player doesn't hit any letter within a given delay, presumably since the player doesn't know the correct letter. This enables the player to learn and progress further.

Elements that support player engagement include features such as:

- An intuitive touch interface inspired by the popular arcade game Whac-A-Mole, with an upbeat accompanying background score.
- Sound effects and in-game audio that registers input.
- A fast-paced bonus round that adds an incentive element of gamification, and acts as an extra element of engagement.

Play Testing and Preliminary Results

We obtained feedback on the game from 5th and 6th graders from a local school in Bangalore, India, through interviews and observed the impact the game has on them through preliminary tests. Our goal was to see if the game has educational value and to get useful insights and building blocks for a more formal study evaluating and quantifying its impact.

We first gave the students a pre-test, asking them to write, on separate sheets of paper, the spellings of a set of words dictated to them. The set comprised of words that are commonly misspelled by children of their age (for example, 'weird' being spelled as 'wierd', and 'pronunciation' being spelled as 'pronounciation'). Each student then played the game, which featured a superset of the set of words from the pre-test, for about 30 minutes each on a Windows Phone device. We downloaded the pronunciations of this superset of words in advance from Google's dictionary service for our game. For a complete version having several word lists, the game can be easily modified to pre-cache the pronunciations of words via AJAX at the start of every level to provide a seamless game play. After playing

Figure 5: Play-testing session with some school students

the game, the students were interviewed to obtain feedback: they reported liking and enjoying the game. The students then took a post-test, in which the same set of words from the pre-test were dictated to them and they had to write down the spellings of the words on separate sheets of paper. Through this strategy, we wanted to see if there were instances where a word was misspelled by a student before playing the game and spelt correctly by the student after playing the game. To our delight, we did observe such instances, which serve as a preliminary ground to believe that the game has educational value.

Future Work

In our future revisions of the game, we plan to include many word lists of different levels of difficulty to target a wide range of age groups. We also plan to make the difficulty in the game adaptive, which has been shown to lead to better learning outcomes [4]. This would allow players to automatically graduate to words of greater difficulty depending on their performance. The technique of spaced repetition [2] could be used and immediate feedback [1] on performance could be provided to further facilitate learning.

We plan on undertaking a formal evaluation with a more complete version of the game to better assess its learning potential. We would like to see if our preliminary observations scale with the number of players, and repeat with a wide range of audience: young children to old people. By following the evaluation strategy described previously in combination with other strategies, and recording and analyzing the results as a whole, we hope to be able to conclude with a high degree of confidence that our game indeed achieves the impact we set out to seek.

Acknowledgements

We acknowledge Whac-A-Mole as the source of inspiration for this game. We thank Amy Ogan, Erin Walker and Erik Harpstead for their guidance in developing and evaluating Get 'em Moles!. We thank MS Ramaiah Institute of Technology, Bangalore, India, for enabling us to play-test our game with children. Finally, we thank Carolyn P. Rosé and Carnegie Mellon's Internship Program in Technology Supported Education, which brought us together for 15 days to conceptualize, develop and undertake a preliminary evaluation of the prototype for this game.

References

[1] Anderson, J. R., Corbett, A. T., Koedinger, K. R., & Pelletier, R. (1995). Cognitive Tutors: Lessons Learned. The Journal of the Learning Sciences, 4(2), 167-207.

[2] Caple, C. The Effects of Spaced Practice and Spaced Review on Recall and Retention using Computer-Assisted Instruction, *Doctoral Dissertation, North Carolina State University*, 1996.

[3] Reed, Deborah K. Why Teach Spelling? *Center on Instruction, Education Resources Information Center.* http://files.eric.ed.gov/fulltext/ED531869.pdf

[4] Sandra Sampayo-Vargas, Chris J. Cope, Zhen He, Graeme J. Byrne. The Effectiveness of Adaptive Difficulty Adjustments on Students' Motivation and Learning in an Educational Computer Game, *Computers & Education, 69,* p.452-462, Nov, 2013.

[5] Shams L., Seitz A.R. Benefits of Multisensory Learning. *Trends Cogn Sci. 2008* Nov; 12(11):411-7.

[6] The Unity Game Engine, http://unity3d.com/

Author's Accepted Manuscript

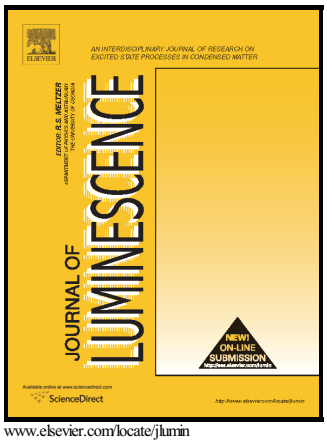

www.elsevier.com/locate/jlumin

Holmium doped lead tungsten tellurite glasses for **Green Luminescent Applications**

M. Venkateswarlu, Sk. Mahamuda, K. Swapna, M.V.V.K.S. Prasad, A. Srinivasa Rao, Suman Shakya, A. Mohan Babu, G. Vijaya Prakash

PII: S0022-2313(15)00124-6
DOI: http://dx.doi.org/10.1016/j.jlumin.2015.02.052
Reference: LUMIN13238

To appear in: *Journal of Luminescence*

Received date: 10 September 2014
Revised date: 24 February 2015
Accepted date: 26 February 2015

Cite this article as: M. Venkateswarlu, Sk. Mahamuda, K. Swapna, M.V.V.K.S. Prasad, A. Srinivasa Rao, Suman Shakya, A. Mohan Babu and G. Vijaya Prakash, Holmium doped lead tungsten tellurite glasses for **Green Luminescent Applications**, *Journal of Luminescence,* http://dx.doi.org/10.1016/j.jlumin.2015.02.052

This is a PDF file of an unedited manuscript that has been accepted for publication. As a service to our customers we are providing this early version of the manuscript. The manuscript will undergo copyediting, typesetting, and review of the resulting galley proof before it is published in its final citable form. Please note that during the production process errors may be discovered which could affect the content, and all legal disclaimers that apply to the journal pertain.

ACCEPTED MANUSCRIPT

Holmium doped Lead Tungsten Tellurite Glasses for Green Luminescent Applications

M.Venkateswarlu[1], Sk. Mahamuda[1], K. Swapna[1], M. V. V. K. S. Prasad[1], A. Srinivasa Rao*[1, 2], Suman Shakya[3], A. Mohan Babu[4] and G. Vijaya Prakash[3]

[1]Department of Physics, K L University, Green Fields, Vaddeswaram-522 502, Guntur (Dt.),, A P, India
[2]Department of Applied Physics, Delhi Technological University, Bawana Road, New Delhi-110 042, India
[3]Nanophotonics Laboratory, Department of Physics, Indian Institute of Technology-Delhi, Hauz Khas, New Delhi-110 016, India.
[4]Department of Physics, S. V. University, Tirupati-517 502, India
Corresponding author**, **E-mail: drsrallam@gmail.com, Tel: +91 85860 39007, Fax: +91 01127871023

Abstract

Lead Tungsten Tellurite (LTT) glasses doped with different concentrations of Ho^{3+} ions have been synthesised using melt quenching method and characterized to understand their visible emission characteristic futures using optical absorption and photoluminescence spectral studies. The Judd-Ofelt (JO) parameters measured from the absorption spectral features were used to evaluate radiative properties such as transition probability (A_R), branching ratio (β_R) and radiative lifetimes (τ_R) for the prominent fluorescent levels of Ho^{3+} in LTT glasses. The photoluminescence spectra recorded for all the Ho^{3+} doped LTT glasses at an excitation wavelength 452 nm gives three prominent emission transitions $^5F_4 \rightarrow {}^5I_8$, $^5F_5 \rightarrow {}^5I_8$ and $^5F_4 \rightarrow {}^5I_7$, of which $^5F_4 \rightarrow {}^5I_8$ observed in visible green region (546 nm) is relatively more intense than the other two transitions. The intensity of $^5F_4 \rightarrow {}^5I_8$ emission transition in these glasses increases up to 1mol% of Ho^{3+} ions and beyond concentration quenching is observed. Branching ratios (β_R) and emission cross-sections (σ_{se}) were evaluated for the intense emission transition $^5F_4 \rightarrow {}^5I_8$ in these glasses to understand the luminescence efficiency in visible green region (546 nm). The CIE chromaticity coordinates were also evaluated in order to understand the suitability of these glasses for visible luminescence. From the measured emission cross-sections and CIE coordinates, it was found that 1 mol% of Ho^{3+} ions in LTT glasses are most suitable for visible green luminescence in principle.

Key words

Glass, Holmium, JO Parameters, Optical properties, Luminescence,

Accepted manuscript

ACCEPTED MANUSCRIPT

1. Introduction

Glasses doped with transition metal and rare earth ions have attracted a great deal of attention because of their applications in visible and mid-infrared regions of the electromagnetic spectrum such as lasers, optical fibres, sensors, biomedical diagnostics, infrared detectors, marine optical communications, up-conversion lasers, optical data storage, atmospheric probing and high density memory storage devices [1-5]. Recently research work on tellurium based glasses increasing because of their promising technological applications in diversified fields [6-11]. Tellurium oxide (TeO_2) being a semiconductor in both crystalline and amorphous forms, with its superior physical and chemical properties, is aptly suitable for various technological devices such as ɤ-ray detectors, nonlinear optoelectronic devices and optical recording systems [12–16]. In addition to this, tellurite glasses possesses wide transmission range from 0.4 to 5 μm, high linear and non-linear refractive indices, low phonon energies (750 cm^{-1}) and high rare earth ions solubility [17]. Tellurium oxide besides being a conditional glass former can form a stable glass in presence of certain glass modifiers like tungsten trioxide (WO_3). Moreover these oxides show high thermal stability and mechanical strengths relative to other glass forming oxides and fluorides [16-21].

Tungsten based glasses can be prepared at relatively low temperatures (~750 ^oC) and also show low phonon energies (~ 800cm^{-1}) [22, 23] when compared with phosphate (~1300 cm^{-1}) borate (~ 1400 cm^{-1}) and silicate glasses (~1000 cm^{-1}) [24-26]. It is well known that the glasses with low phonon energies offer less non-radiative relaxation rates and increases the luminescent quantum efficiencies. The relatively slow crystallization rate, good transparency in a wide spectral region from visible to NIR, good mechanical strength, chemical stability and high refractive indices makes tungsten tellurium glasses as the best choice as an efficient host [27-29]. It is well known that heavy metal fluoride compounds such as PbF_2 having very less phonon energies (~340 cm^{-1}) when added to a host glass can reduce phonon energies of the host glass drastically. Moreover fluoride compounds added to a glass can react and remove the OH content present in glass and helps in reducing the phonon energies of the host glass further. Considering the aforementioned scientific patronages offered by PbF_2, WO_3 and TeO_2, we prepared Lead Tungsten Telluride (LTT) glasses using these chemicals as constituent elements to study the luminescence properties of these glasses doped with different rare earth ions. The encouraging results obtained for Pr^{3+} ions doped in LTT glasses for visible red lasers [27] prompted us to investigate Ho^{3+} ions in LTT glasses to know about their suitability for visible green luminescence.

Accepted manuscript

ACCEPTED MANUSCRIPT

Among all the trivalent rare earth ions, Ho^{3+} ion is one of the most attractive ion for spectroscopic studies, because of several electronic transitions it can give in the visible and IR regions [30-32], which have relatively long-lived $^5I_7$ level and large peak stimulated emission cross-sections [33, 34]. It has been confirmed that mid infrared laser emission of Ho^{3+} ion is in the range of 1.2 - 4.9 μm [35, 36]. The mid infrared emission of Ho^{3+} ion gives eye-safe potential laser emission at room temperature (RT) with a low threshold action that has smart applications in LIDAR and in atmospheric communication systems [37]. Moreover, the $^5F_4 \rightarrow {}^5I_8$ transition of Ho^{3+} ion is a hypersensitive transition and hence host dependent one. Therefore glasses doped with Ho^{3+} ions are the most important candidates for both visible (~547 nm) ($^5F_4 \rightarrow {}^5I_8$) and mid infrared (~2 μm) ($^5I_7 \rightarrow {}^5I_8$) regions and are useful for the development of solid state lasers in visible and mid infrared regions.

In the present work, LTT glasses doped with Ho^{3+} ions at different concentrations were prepared to study the absorption and photoluminescence spectral properties to understand the suitability of these materials for visible luminescence. From the absorption and emission spectral measurements, different radiative properties such as transition probability, radiative lifetimes, branching ratios and emission cross-sections were estimated for the observed emission transitions of Ho^{3+} ions. The CIE colour coordinates are also evaluated from the measured emission spectra to understand the utility of these glasses for green light emission.

2. Experimental

2.1. Synthesis of LTT glasses

LTT glasses doped with different concentrations of Ho^{3+} ions with chemical composition of $15PbF_2$ - $25WO_3$ - (60-x) TeO_2 – xHo_2O_3 (x=0.1, 0.5, 1.0, 1.5, 2.0 and 2.5 mol %) were prepared by using melt quenching method. The samples are referred according to the doping concentration of Ho_2O_3 as LTTHo01, LTTHo05, LTTHo10, LTTHo15, LTTHo20 and LTTHo25 glasses. 10g Batches of homogeneous mixture of starting chemicals were taken in a silica crucible and melted in an electric furnace at a temperature of 735^{o}C for 45 min. The melt was then air quenched by pouring on to a pre-heated brass mould and pressed quickly with another brass mould. The glasses thus obtained were annealed at 400 ^{o}C for about 3h to remove thermal strains. In order to measure the optical spectra, the glasses were polished (0.2 cm thickness) for optical quality.

2.2 Physical and optical measurements

The densities of Ho^{3+} ions doped LTT glasses were measured by using Archimedes's principle with water as an immersion liquid. The refractive indices of the prepared glasses

Accepted manuscript

ACCEPTED MANUSCRIPT

were measured using Brewster's angle method with He-Ne laser operating at 632 nm. Using refractive indices and densities, some other physical properties were also measured using suitable formulae [5, 38] and are given in Table 1. In the present study the physical properties are changing from glass to glass with increase in the concentration of Ho^{3+} ions, indicating the change in environment around the doped Ho^{3+} ions. The optical absorption spectra were measured for all the glass samples from 400 to 2200 nm at room temperature with a specified resolution 0.1 nm using a Jasco V-670 UV-vis-NIR spectrometer. Schimadzu RF-5301 PC Spectrofluorophotometer was used to record the photoluminescence excitation and emission spectra for all these glasses at room temperature.

3. Results and Discussion

3.1 Physical Properties

The physical properties of glassy materials play a vital role in prediction of optical properties. Density and refractive index of glass samples play an important role in evaluating the other physical properties such as Average molecular weight mean atomic volume etc. All such physical properties evaluated for the present LTT glasses are given in Table 1. Fig 1(a), shows the variation of density and refractive indices of the titled glasses with Ho^{3+} concentration. From Fig 1(a) it can be observed that the density and refractive indices of titled glasses moderately increases with the increase of Ho^{3+} ion concentration. Increase in density of the LTT glasses indicates increase in compactness of the glass by increasing the number of bridging oxygen. This leads to increase in the rigidity of the prepared glasses. Fig 1(b) shows the variation of inter atomic distance and average molecular weight with Ho^{3+} ion concentration in titled glasses. From Fig 1(b) it can be observed that the average molecular weight increases whereas inter atomic distance decreases with the increasing of Ho^{3+} ion concentration. This indicates that the atoms present in the titled glass network are more tightly packed.

3.2 FT-IR Spectral Analysis

The Fourier Transform Infrared spectrum of an un-doped Lead Tungstun Tellurite (LTT) glass in the region 400-4000 cm^{-1} is shown in Fig 2. This figure shows the characteristic IR absorption band at 3424 cm^{-1}, which is attributed to the fundamental vibrations of OH group. It is well known that, the non-radiative losses increases due to the presence of large amount of OH content in the glasses which in turn decreases the quantum efficiency of the glass materials. The low intensity of OH band observed for LTT glasses indicates the presence of less OH content. The coefficient of OH vibration (α_{OH}) at 3000 cm^{-1} is used as a measure of

Accepted manuscript

ACCEPTED MANUSCRIPT

the OH content [39]. In a glassy material, the content of OH has been estimated using the equation given in the literature [40]. The OH content estimated for the present un-doped LTT glass is 50.17 ppm (1.67 cm^{-1}), which is smaller than ZnAlBiB (65.48 ppm) [40], LBTAF (123.00 ppm) [41], GeS2 (175.5 ppm) [42] and LHG-8L (128 ppm) glasses [43]. Relatively less content of OH in these glasses signifies that these glasses are relatively good for efficient lasers with low non-radiative losses.

The peaks identified in the region 1600-3000 cm^{-1} are mainly attributed to hydrogen bonding. The vibrations observed at 894 cm^{-1} is attributed to the ν_1 vibrations of WO_4 groups & stretching vibrations of $W\text{-}O^-$ and W-O bonds in WO_4 or WO_6 units [44]. From the literature, tellurite glasses show α-TeO_2 (para tellurite) crystallization which is created by (TeO_4) Trigonal bipyramids (TBP) [45]. When glass modifiers are added into the tellurite glass network, the network will be more open and non-bridging oxygen's were formed by allowing the TeO_{3+1} and TeO_3 structural units. The peak observed at 676 cm^{-1} is due to the stretching vibrations TeO_4 trigonal bipyramid units [46]. The peak observed at 639 is due to the ν_s – TeO_{2ax} vibrations with C_{2v} symmetry. The peak observed at 589 cm^{-1}due to the stretching vibrations of TeO_{3+1} units [47]. The peaks observed at 548 and 509 cm^{-1} are due to the stretching vibrations of $PbOF_4$ and PbO_4 units. The peaks observed in the region 460 and 484 cm^{-1} are due to the stretching vibrations of Te-O-Te or Te-O-W linkages. All the band assigned from the FT-IR spectrum of an un-doped LTT glass are given in Table 2.

3.3. Absorption spectral analysis.

Fig. 3 represents the absorption spectrum of Ho^{3+} ions doped LTTHo10 glass. The spectrum exhibits nine absorption bands in the Vis-NIR regions centred at 452, 469, 476, 489, 538, 643, 890, 1153 and 1956 nm corresponding to the transitions $^5I_8 \rightarrow {}^5G_6$, $^5I_8 \rightarrow {}^3K_8$, $^5I_8 \rightarrow {}^5F_2$, $^5I_8 \rightarrow {}^5F_3$, $^5I_8 \rightarrow {}^5F_4$, $^5I_8 \rightarrow {}^5F_5$, $^5I_8 \rightarrow {}^5I_5$, $^5I_8 \rightarrow {}^5I_6$, $^5I_8 \rightarrow {}^5I_7$ respectively. The absorption spectrum shown in Fig. 3 is in consistent with the spectra reported for Ho^{3+} ions doped oxyfluoride [48], fluoride [49], tellurite [50] and fluoronidate [51] glasses. The absorption bands observed in the visible and NIR regions are attributed to the 4f–4f transitions of Ho^{3+} ions from the $^5I_8$ ground state to various excited states as presented in Table 3. The identification and assignment of energy levels are in accordance with Carnall et.al [52]. From Fig. 3 it is observed that the absorption bands $^5I_8 \rightarrow {}^5G_6$ (452nm), $^5I_8 \rightarrow {}^5F_4$ (538nm), $^5I_8 \rightarrow {}^5F_5$ (643 nm) are relatively more intense and sharp than the other transitions. The bands corresponding the transitions $^5I_8 \rightarrow {}^3K_8$ (469nm), $^5I_8 \rightarrow {}^5F_2$ (476nm), $^5I_8 \rightarrow {}^5F_3$ (489nm) are found to be very weak while the bands due to $^5I_8 \rightarrow {}^5I_5$ (890 nm), $^5I_8 \rightarrow {}^5I_6$ (1153nm) and $^5I_8 \rightarrow {}^5I_7$ (1956nm) transitions

Accepted manuscript

ACCEPTED MANUSCRIPT

are broad and weak. In general, the absorption transitions of rare earth ions are induced electric dipole in nature and magnetic dipole contribution is insignificant. However in case of Ho^{3+} ion, the transition $^5I_8 \rightarrow {}^5I_7$ (1956nm) contains some magnetic dipole contribution [50]. The pattern of absorption spectra for all the six Ho^{3+} ions doped LTT glasses remains the same and the intensity of the bands have been perceived. From these energy bands, the nephelauxetic ratio and bonding parameters have been evaluated to get an idea about the nature of Ho^{3+} ligand bond in the present work and are given in Table 3.

The nephelauxetic ratio (β) is calculated by using the following relation [53].

$$\beta = \frac{\vartheta_c}{\vartheta_a} \text{ ---------- (1)}$$

Where ϑ_c is the wave number (in cm^{-1}) of a particular transition for the rare earth ion under investigation and ϑ_a is the wave number (in cm^{-1}) for the same transition of an aqua-ion. From the average values of $\bar{\beta}$ the bonding parameter δ is calculated using the formula [53].

$$\delta = \frac{1-\bar{\beta}}{\bar{\beta}} \text{ ---------- (2)}$$

Depending on the field of environment the bonding parameter may be positive or negative indicating covalent or ionic bonding. In the present work, the positive values obtained for the bonding parameter $'\delta'$ indicates the bonding nature between Ho-O bond is covalent in nature. The experimental oscillator strengths of the absorption bands are estimated from the absorption spectra for Ho^{3+} ions doped LTT glasses using measured areas under the absorption peaks by using the expression [54, 55].

$$f_{exp} = \frac{2.303mc^2}{N\pi e^2} \int \varepsilon(\vartheta) d\vartheta \text{ ---------- (3)}$$

Where e and m are charge and mass of an electron, N is the Avogadro's number; c is the velocity of light and $\varepsilon(\vartheta)$ is the molar absorptivity of a band at a wave number ϑ (cm^{-1}). The oscillator strengths of absorption bands are calculated using JO theory with the predictable equations [56, 57].

$$f_{cal} = \left[\frac{8\pi^2 mcv}{3h(2J+1)}\right]\left[\frac{(n^2+1)^2}{9n}\right]\sum_{\lambda=2,4,6} \Omega_\lambda (\psi_J || U^\lambda || \psi'_{J'})^2 ------(4)$$

Where ν is the wave number (cm^{-1}) of the transition from ground state (ψ_J) to excited state ($\psi'_{J'}$), c is the velocity of light in vacuum, m is the rest mass of an electron and $\left|\left|U^\lambda\right|\right|^2$ doubly reduced matrix elements. The doubly reduced matrix elements were taken from the literature as they are unaffected to the environment of rare earth ions. The quality of the fit is measured by root mean square deviation (δ_{rms}) between the calculated and experimental

Accepted manuscript

ACCEPTED MANUSCRIPT

oscillator strengths by using the following equation and the measured values of f_{exp} and f_{cal} together with the r.m.s deviation are represented in Table 4. The deviation parameter δ_{rms} is calculated by using the following expression [58, 59].

$$\delta_{rms} = \left[\frac{\Sigma(f_{exp}-f_{cal})^2}{n}\right]^{1/2} \text{------ (5)}$$

Where n is the total number of transitions used in the fitting procedure. From Table 4, it is observed that, the oscillator strengths vary from glass to glass and these variations are very small.

The JO intensity parameters Ω_2, Ω_4 and Ω_6 are evaluated through least square fitting analysis using equation (4) for the present glasses are given in Table 5 along with the other reported values. Few transitions of rare earths are found to be very sensitive to the doped rare earth ion concentration and glass composition. These absorption levels show unusual intensity variations and are called as hypersensitive levels. For the Ho^{3+} ion, the transition $^5I_8 \rightarrow {}^5G_6$ is hypersensitive transitions which satisfies the selection rules such as $|\Delta S| = 0$, $|\Delta L| \leq 2$, $|\Delta J| \leq 2$ .The spectral oscillator strengths of these transitions are strongly observed by the Judd-Ofelt (Ω_2) parameter [40, 41, 60, 61]. From Table 5 [62-69], it is observed that the hypersensitive level ($^5G_6$) is appeared as more intense than other bands and significant variations were exhibited by them due to the changes in the Judd-Ofelt (Ω_2) parameter for all the glasses. In the present investigation, in all the glasses under investigation, the JO parameters follow the trend $\Omega_4 > \Omega_2 > \Omega_6$. Among all the glasses, LTTHo10 glass possesses maximum values of JO intensity parameters than other LTT glasses and other reported values [62-69]. The JO intensity parameters magnitude is mainly related with the physical and chemical properties such as viscosity and covalent character of the chemical bonds. The large values of Ω_2 parameter are the indicators of the covalent character of the chemical bonds between the glass matrix and rare earth ions [40]. The asymmetry of the sites in the neighborhood of rare earth ion also depends upon this Ω_2 parameter. If the Ω_2 parameter value is high then the degree of asymmetry around the rare earth ion will be high. Not only this, the covalency of rare earth ion-oxygen bond also becomes stronger. In the present series of glasses, LTTHo10 glass possesses maximum value of Ω_2 parameter. Therefore LTT glass with 1 mol% of Ho^{3+} ions possesses higher asymmetry and greater degree of covalency of holmium ion and oxygen bond than other reported values [62-69]. The large values of Ω_4 and Ω_6 are related to the bulk properties such as viscosity and rigidity of the glass structure.

3.4. Analysis of Emission spectra and Estimation of Radiative properties

Accepted manuscript

ACCEPTED MANUSCRIPT

It is well known that rare earth ions doped materials exhibit sharp excitation and emission bands. In order to know the excitation wavelength to record the emission spectra, we have recorded the excitation spectra for the LTTHo10 glasses by fixing the emission wavelength at 545 nm. Fig 4 shows the excitation spectrum of 1 mol % of Ho^{3+} ions doped LTT glass (LTTNd10) in the wavelength range 325 to 500 nm. As shown in Fig 4, the excitation spectra consists of five excitation bands centred at 349 nm, 419 nm, 452 nm, 473 nm, and 486 nm corresponding to the transitions $^5I_8 \rightarrow {}^5G_3$, $^5I_8 \rightarrow ({}^5G + {}^3G)_5$, $^5I_8 \rightarrow {}^5G_6$, $^5I_8 \rightarrow {}^3K_8$ and $^5I_8 \rightarrow {}^5F_3$ respectively. Among the five excitation bands observe, a band centred at 452 nm is relatively more intense than the others. By using this intense excitation wavelength, the emission spectra for all the Ho^{3+} doped LTT glasses were recorded to investigate the luminescence cha -racteristics.

Fig. 5 shows the emission spectra of Ho^{3+} ions in LTT glasses in the wavelength range 500 to 775 nm at an excitation wavelength 452 nm. The emission spectra show three bands corresponding to the transitions $^5F_4 \rightarrow {}^5I_8$ (546 nm), $^5F_5 \rightarrow {}^5I_8$ (679 nm) and $^5F_4 \rightarrow {}^5I_7$ (755 nm). Among the three emission transitions, a band corresponding to the transition $^5F_4 \rightarrow {}^5I_8$ is relatively more intense than the other bands and falls in the visible green region (546 nm). When the Ho^{3+} ions are excited to $^5F_4$ and $^5I_6$ levels radiative and non-radiative (NR) relaxations take place due to the closely spaced higher energy levels. From Fig. 5, it is clearly observed that the intensity of $^5F_4 \rightarrow {}^5I_8$ transition is higher than that of the $^5F_5 \rightarrow {}^5I_8$ transition. From Fig 5, it is also observed that the intensity of $^5F_4 \rightarrow {}^5I_8$ transition increases from 0.1 to 1.0 mol% of Ho^{3+} ion concentration and then decreases beyond showing concentration quenching. This concentration quenching observed beyond 1 mol% of Ho^{3+} ion concentration may be due to resonance energy transfer between Ho ions at higher concentrations. Fig 6 shows the energy level diagram which describes the absorption, excitation, emission (visible & NIR) and resonant energy transfer mechanisms of LTTHo10 glass. From Fig 7, it is observed that, the overlap of absorption ($^5I_8 \rightarrow {}^5F_4$) and emission ($^5F_4 \rightarrow {}^5I_8$) bands in the spectral region 520–570 nm indicates the resonant energy transfer (RET) process among the Ho^{3+} ions.

In order to check the emission performance of Ho^{3+} doped LTT glasses, the radiative parameters such as spontaneous transition probabilities (A_R), total transition probabilities (A_T), radiative lifetimes (τ_R) and luminescence branching ratios (β_R) for all the emission transitions were evaluated by using the JO parameters and are given in Table 6. All these radiative properties are evaluated by using the relevant equations given in the literature [40].

Accepted manuscript

ACCEPTED MANUSCRIPT

From Table 6 it is observed that, the LTTHo10 glass possesses maximum values for radiative transition properties. Generally the branching ratio (β_R) is a very important parameter to the laser designer, because it describes the possibility of getting stimulated emission from any particular transition [40]. The fluorescence branching ratio which characterizes and makes the transition as potential for laser emission, if its value $\beta_R \geq 0.5$. As shown in Table 6, in present study the radiative and experimental branching ratios (β_R = 0.505 & β_{exp} = 0.804) for $^5F_4 \rightarrow {}^5I_8$ emission transition are found to be maximum for LTTHo10 glass than the other LTT glasses indicating the potentiality of this glass to produce visible green luminescence.

The stimulated emission cross-section (σ_{se}) is an another significant parameter which gives the rate of energy extraction from an optical material. From the observed emission bands, the stimulated emission cross-sections (σ_{se}) are calculated using the following equation [70] and are given in Table 7.

$$\sigma_{se}(a_J, b_{J'}) = \frac{{\lambda_p}^4}{8\pi c n^2 \Delta\lambda_p} A_R(a_J, b_{J'}) \quad \text{------ (4)}$$

Where λ_p the emission is peak wavelength and $\Delta\lambda_p$is the full width at half maximum which can be calculated by integrating the intensity at the peak wavelength [71].

The large value of stimulated emission cross-section (σ_{se}) is a striking characteristic for low-threshold and high gain applications to get continuous wave laser action and it is also used to recognize the potential laser transitions of rare earth ions in any host matrix. From Table 7 it is seen that, all the transitions of LTTHo10 glass have lowest values of effective band width ($\Delta\lambda_p$). The main reason to get the lowest values of effective band width is the splitting of the transition levels and inhomogeneous broadening [40]. The decrease in effective band width values are also an indication of weak asymmetry of the ligand field. Among all the glasses, the LTTHo10 glass possess highest stimulated emission cross-section (σ_{se}) for the transition $^5F_4 \rightarrow {}^5I_8$ (546 nm). Hence LTTHo10 glass is the most suitable one to produce visible green luminescence among all the LTT glasses studied in the present investigation. There are another two important parameters namely gain band width ($\sigma_{se} \times \Delta\lambda_P$) and optical gain ($\sigma_{se} \times \tau_R$) parameter, which are used to calculate the amplification of the host in which the rare earth ions are located. For a good optical amplifier, stimulated emission cross-section (σ_{se}), gain band width ($\sigma_{se} \times \Delta\lambda_P$) and optical gain ($\sigma_{se} \times \tau_R$) parameter values should be high. From Table 7 it is observed that, the glass LTTHo10 has higher values of stimulated emission cross-section (σ_{se}), gain band width ($\sigma_{se} \times \Delta\lambda_P$) and

Accepted manuscript

ACCEPTED MANUSCRIPT

optical gain ($\sigma_{se} \times \tau_R$). Hence LTT glass doped with 1 mol% of Ho^{3+} ions is quite suitable for visible green luminescence applications and optical amplification.

3.5 Evaluation of CIE colour co-ordinates:

The colour chromaticity coordinates for the LTT glasses doped with different concentrations of Ho^{3+} ions were evaluated from the luminescence spectra using the CIE (Commission International de l'Eclairage France) system. Fig 8 presents the CIE plot with colour coordinates of the LTTHo10 glass calculated from the luminescence spectra recorded at an excitation wavelength at 452 nm. The chromaticity coordinates for the present glasses were calculated using expressions in the literature [72] and are given in Table 8. The CIE colour coordinates evaluated for the Ho^{3+} doped LTT glasses are lying in the bright green region corresponding to $^5F_4 \rightarrow {}^5I_8$ transition at 546 nm emission wavelengths.

4. Conclusions

Lead Tungstun Tellurite (LTT) glasses doped with different concentrations of Ho^{3+} ions were investigated using spectroscopic techniques such as absorption, excitation and emission to characterize and optimize the doped rare earth ions for visible emission. The photoluminescence spectra recorded for LTT glasses give three emission bands in green, red and NIR regions at 546, 679 and 755 nm corresponding to the transitions $^5F_4 \rightarrow {}^5I_8$, $^5F_5 \rightarrow {}^5I_8$ and $^5F_4 \rightarrow {}^5I_7$ respectively. The luminescence quenching observed for $^5F_4 \rightarrow {}^5I_8$ emission transition at 1 mol % of Ho^{3+} ion concentration is attributed to the RET among the excited Ho^{3+} ions. The branching ratio, stimulated emission cross-section values are found to be maximum for LTTHo10 glass than other LTT glasses. From all these studies, it is concluded that LTTHo10 glass can act as an efficient material to produce visible green emission at 546 nm. Green emission possessed by these glasses is also further confirmed by CIE chromaticity coordinates.

Acknowledgements

Two of the authors Mahamuda Shaik (SR/WOS-A/PS-53/2011) and Swapna Koneru (File No: SR/WOS-A/PS-35/2011) and are highly grateful to the Department of Science and Technology (DST), Govt. of India,, New Delhi for the financial support given to them under DST/WOS-A scheme. This work is also partly supported by High-impact Research initiative of IIT-Delhi, UK-India Education Research Initiative (UKIERI) and DST, Govt. of India, New Delhi. One of the authors, Dr. Mohan Babu is expressing his sincere thanks to ADE-BRNS (Project No.2012/34/72) and DST-SERB (Project No. SR/FTP/PS-109/2012) for their financial support to carry out this work.

Accepted manuscript

ACCEPTED MANUSCRIPT

References

[1] Kaushik Biswas, Atul D. Sontakke, R. Sen, K. Annapurna, Spectrochim. Acta Part A 112 (2013) 301-30.

[2] R. Rama Kumar, A S Rao, B C Venkata Reddy, Opt. Mater., 4 (6)(1995)723-728.

[3] K. Swapna, Sk. Mahamuda, A. Srinivasa Rao, L Rama Moorthy, J. Lumin., 39(7)(2013) 8459- 8465.

[4] M. Sreenivasulu, A.S Rao, J. Mater. Science Lett. 20(8) (2001) 737-740.

[5] A. Srinivasa Rao, B. Rupa Venkateswara Rao, M V V K S Prasad, J.V. Shanmuka Kumar, M. Jayasimhadri, J. L. Rao, R. P. S. Chakradhar., Physica B 404 (20) (2009) 3717- 3721.

[6] E. Culea, L. Pop, S. Simon, Mater. Sci. Eng. B 112(2004) 59-63.

[7] R.El –Mallawany, A. Abousehly, E. Yousef, J. Mater. Sci. Lett. 19 (2000) 409-411.

[8] D. Sushama, P. Predeep, J. App. Phys. Math.4 (2014)139-143.

[9] R. Narro-Garcia, E. F. Chillcce, L. C. Barbosa, E. dePosada, M. Arronte, E. Rodriguez, J. Lumin.134 (2013) 528-532.

[10] R. El-Mallawany, I. A. Ahmed, J. Mater Sci. 43 (2008)5131-5138.

[11] N. Sooraj Hussain, G. Hungerford, R. El-Mallawany, M. J. M. Gomes, M. A. Lopes, Nasar Ali, J. D. Santos, S. Buddhudu, J. Nanosci. Nanotechnol. 9 (2009) 3672-3677.

[12] Yannick Ledemi, Danilo Manzani, Sidney J.L. Ribeiro, Younes Messaddeq, Opt. Mater. 33 (2011) 1916-1920.

[13] R.Nayak, V. Gupta, A.L. Dawar, K. Sreenivas, Thin Solid Films 445 (2003) 118-126.

[14] Z.Y. Jiang, Z. X. Xie, X. H. Zhang, S. Y. Xie, R. B. Huang, L. S. Zheng, Inorg. Chem. Commun.7 (2004)178-181.

[15] Z. Liu T. Yamazaki, Y. Shen, T. Kikuta, N. Nakatani, Japn. J. Appl. Phys. 47(2008) 771-774.

[16] Gan Fuxi, J. Non-Cryst. Solids 184 (1995) 9-20.

[17] K. Arshak, O. Korostynska, Sensors 2 (2002) 347–355.

[18] W. Ryba - Romanowski, J. Lumin. 46 (1990) 163-172.

[19] A. A. Sidek, S. Rosmawati, Z.A. Talib, M.K. Halimah and W.M. Daud, Am. J. Appl. Sci. 6 (8), (2009) 1489-1494.

[20] D.L. Sidebottom, M.A. Hruschka, B.G. Potter, and R.K. Brow, J. Non-Cryst. Solids, 222 (1997) 282.

Accepted manuscript

ACCEPTED MANUSCRIPT

[21] B. Erariah, Mater. Bull. Sci. 33, (2010) 391–394.

[22] O. Ravi, C. Madhukar Reddy, B. Sudhakar Reddy, B. Deva Prasad Raju, Opt. Commun. 312 (2014) 263–268.

[23] I. Jlassi, H. Elhouchet, M. Ferid, C. Barthou, J. Lumin.130 (2010) 2394.

[24] Zhan G, Li-yan , Hu Li-li , Jian G Zhong- hong, Prog. Phys., 23 (2003) 473-483.

[25] I Pal,A Agarwal, S. Sanghi, Sanjay & M P Aggarwal, Ind. J. Pure & Appl.Phys.,51 (2013) 18-25.

[26] N. Chiodini and A. Paleari, G. Brambilla and E. R. Taylor, Appl. Phys. letters, 80 (2002) 4449-4451.

[27] M. Venkateswarlu, M. V. V. K. S. Prasad, K. Swapna, Sk. Mahamuda, A. Srinivasa Rao, A. Mohan Babu, D. Haranath, Ceram. Int. 40 (2014) 6261-6269.

[28] H. Nii, K. Ozaki, M. Herren, M. Morita, J. Lumin. 76-77(1998)116–119.

[29] A. Mori, Y. Ohishi, S. Sudo, Electron. Lett. 33(1997) 863–864.

[30] T. Satyanarayana, T. Kalpana, V. Ravi Kumar, N. Veeraiah, J. Lumin. 130 (2010) 498–506.

[31] Neeraj Kumar Giri , S.B. Rai, Anita Rai, Spectrochim. Acta Part A 74 (2009)1115–1119.

[32] H. Lin, D. Q. Chen, Y. L. Yu, A. P. Yang and Y. S. Wang, Opt. Lett. 36 (2011) 876 – 878.

[33] C. H. Qi, X. R. Zhang, H. F. Hu, Acta Optica Sinica 14 (1994) 583-588.

[34] L. Feng, J. Wang, Q. Tang, L. F. Liang, H. B. Liang, Q. Su, J. Lumin. 124(2007)187-194.

[35] C. J. He, X. B. Chen, Y. G. Sun, L. Chen, Chinese J. Quant. Electron. 19 (2) (2002) 109

[36] D. Lande, S. S. Orloy, A. Akella, K. Inoue, Opt. Lett. 22 (1997) 1722-1724.

[37] A. Erbit, H.P. Jenssen, Appl. Opt. 19 (1980) 1729-1730.

[38] A. S. Rao, Y. N. Ahammed, R. R. Reddy, T. V. R. Rao, ,Opt. Mater.10(1998)245-252.

[39] H. Ebendorff-Heidepriem, W. Seeber, D. Ehrt, J. Non-Cryst. Solids 163 (1) (1993) 74–80.

[40] Sk. Mahamuda, K. Swapna, P. Packiyaraj, A. Srinivasa Rao, G. Vijaya Prakash, Opt. Mater. 36 (2013) 362-371.

[41] T. Suhasini, B.C. Jamalaiah, T. Chengaiah, J. Suresh Kumar, L. Rama Moorthy, Physica B 407 (2012) 523–527.

[42] B. B. Kale, A. Jha, S.K. Apte, P.V. Adhyapak, D.P. Amalnerkar, Mater. Chem. Phys. 78(2002) 330–336.

Accepted manuscript

ACCEPTED MANUSCRIPT

[43] T.I. Suratwala, R.A. Steele, G.D. Wilke, J.H. Campbell, K. Takeuchi, J. Non-Cryst.Solids 263–264 (2000) 213–227.

[44] Ch. Srinivasa Rao, V. Ravikumar, T. Srikumar, Y. Gandhi, N. Veeraiah, J. Non-Cryst. Solids 357 (2011) 3094.

[45] R. Stegeman, C. Rivero, K. Richardson, G. Stegeman, P. Delfyett Jr., Y. Guo,A. Pope,A Schulte, T.Cardinal, P.Thomas, J.C.Champarnaud-Mesard,Opt. Expr. 13(2005)1144.

[46] Y. Dimitriev, Dimitrov. V, Arnau dov M., J.Sci.,m 18(1983)1353.

[47] Pankova M.D., Dimitriev Y., Arnaudov V., Dimitrov V., Phys. Chem Glasses,30, 260 (1989)

[48] L. Feng, J. Wang, Q. Tang, L. Liang, H. Liang, Q. Su, J. Lumin. 124 (2007) 187-194.

[49] A. Florez, S.L. Oliveira, M. Florez, L.A. Gomez, L.A.O. Nunes, J. Alloy. Comp 418(2006) 238-242.

[50] S.B. Rai, A.K. Sing, S.K. Singh, Spectrochim. Acta A 59 (2003) 3221-3226.

[51] S.L. Oliveira, M.J.V. Bell, A. Florez, L.A.O. Nunes, J. Phys. D: Appl. Phys. 39 (2006) 3230-3234.

[52] W.T.Carnall, P.R.Fields, K.Rajnak, J.Chem.Phys. 49 (1968) 4424-4442.

[53] Sk. Mahamuda , K. Swapna , M. Venkateswarlu , A. Srinivasa Rao , Suman Shakya , G.Vijaya Prakash, J. Lumin. 154(2014) 410–424.

[54] W.T. Carnall, in: K.A. Gschneidner, L.R. Eyring (Eds.), Handbook on the Physics and Chemistry of Rare Earths, vol. 3, North-Holland, Amsterdam, 1979 (Chapter 24).

[55] R. R. Jacobs, M. J. Weber, IEEE J. Quant. Electron. QE-12 (1976) 102-111.

[56] B.R. Judd, Phys. Rev. 127 (1962) 750-761.

[57] G.S. Ofelt, J. Chem. Phys. 37 (1962) 511-520.

[58] P. A. Tanner, Molec. Phys. 57 (1986) 737-754.

[59] A. Tanner, Anne De Piante, F. S. Richardson and M. F. Reid, Mol. Phys. 60 (1987) 1037-1045.

[60] J. Legendziewicze, E.Huskowskag, Argay and A Waskowskai, Inorg. Chim. Acta 95 (1984) 57-63

[61] K. Iftkar and N. Ahmad, polyhedron 4, (1985)333-342.

[62] M. Shojiya, Y. Kawamoto, K. Kadono, J. Appl. Phys. 89 (2001) 4944-4950.

[63] Mc Dugall, D.B. Hollis, M.J.P. Payne, Phys. Chem. Glasses 35 (1994) 258-259.

[64] M.J. Weber, B.H. Matsinger, V.L. Donlan, G.T. Surratt, J. Chem. Phys. 57 (1972) 562-567.

[65] L.F. Shen , B.J.Chen , E.Y.B.Pun , H.Lin ,J. Lumin. 132 (2012) 676–681

Accepted manuscript

ACCEPTED MANUSCRIPT

[66] T. Srikumar, M. G. Brick, Ch. Srinivasa Rao, N.Venkataramaiah, Y. Gandgi, N. Veeraiah, Physica B 406(2011)3592-3598.

[67] A. Speghini, M. Peruffo, M. Casarin, D.Ajo, M. Bettinelli, J. Alloy.compd. 174 (2000) 300 - 301.

[68] J.C. Boyer, F. Vertone, J.A. Capobianco, A. Speghini, M. Bettinelli, J. Appl. Phys. 93 (2003) 9461.

[69] R. Cases, M.A. Chamarro, J. Solid State. Chem. 90(1991)313-319.

[70] Sk. Mahamuda, K. Swapna, A. Srinivasa Rao, M. Jayasimhadri, T. Sasikala, K. Pavani, L. RamaMoorthy, J. Phys. Chem. Solids 74(2013)1308-1315.

[71] B. Karthikeyan, S. Mohan, M. L. Baesso, Physica B 337(2003) 249-254.

[72] N.Q. Wang, X. Zhao, C.M. Li, E. Y. B. Pun, H. Lin, J. Lumin. 130(2010) 1044-1047.

Accepted manuscript

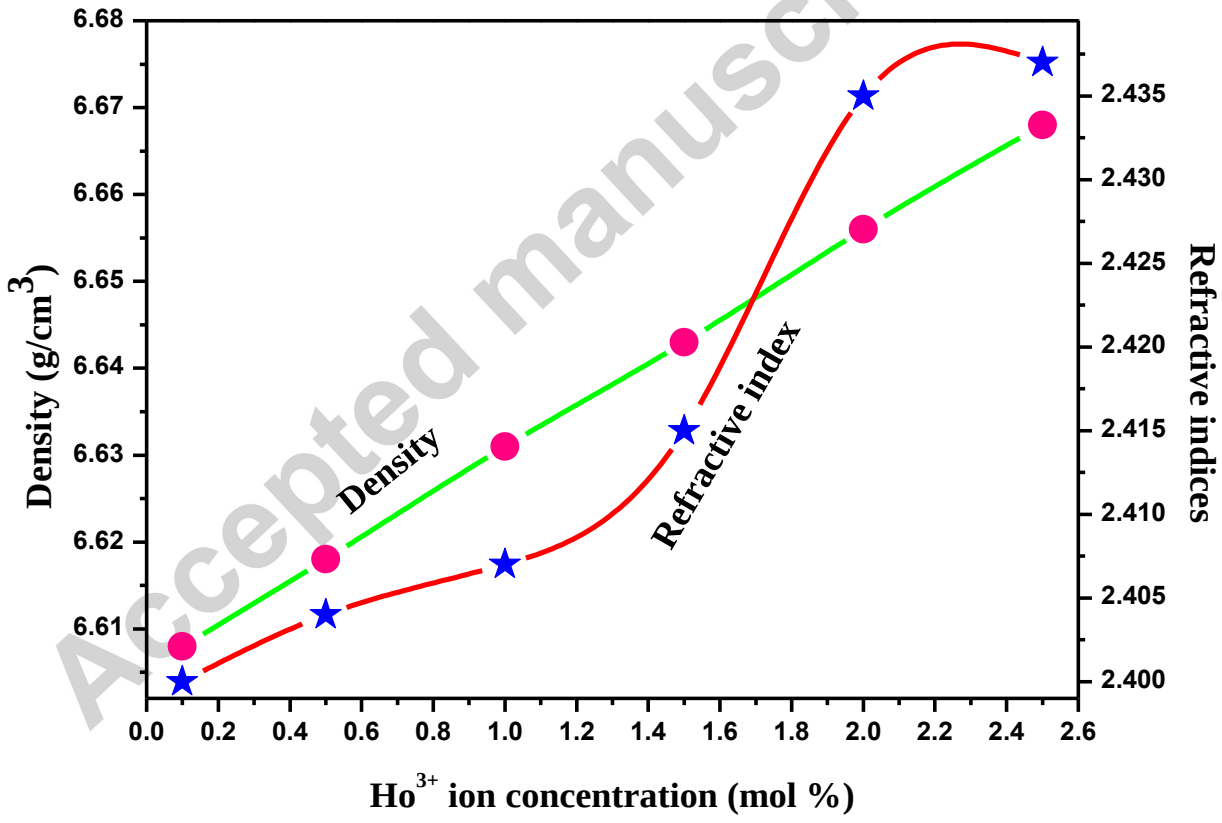

Fig 1(a): Variation of density and refractive index with Ho^{3+} ion concentration in LTT Glasses

ACCEPTED MANUSCRIPT

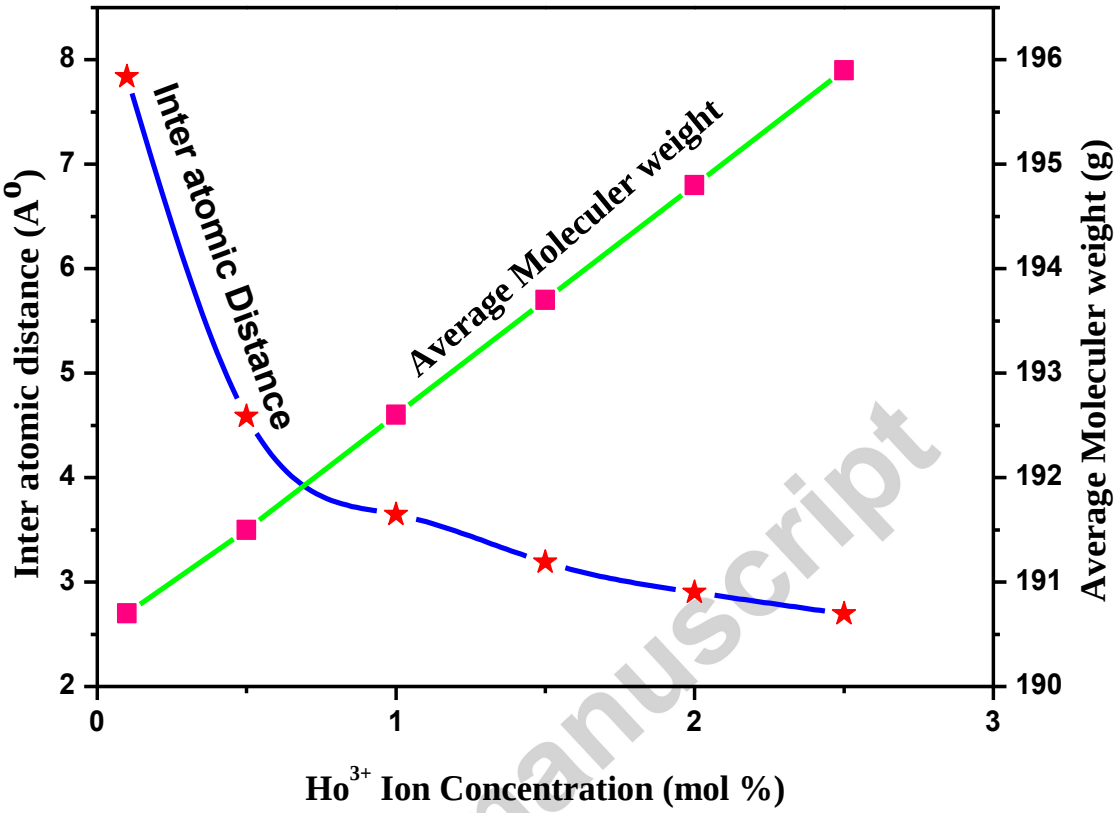

Fig 1(b): Variation of Inter atomic distance and Average Molecular Weight with Ho^{3+} ion concentration in LTT Glasses

Accepted manuscript

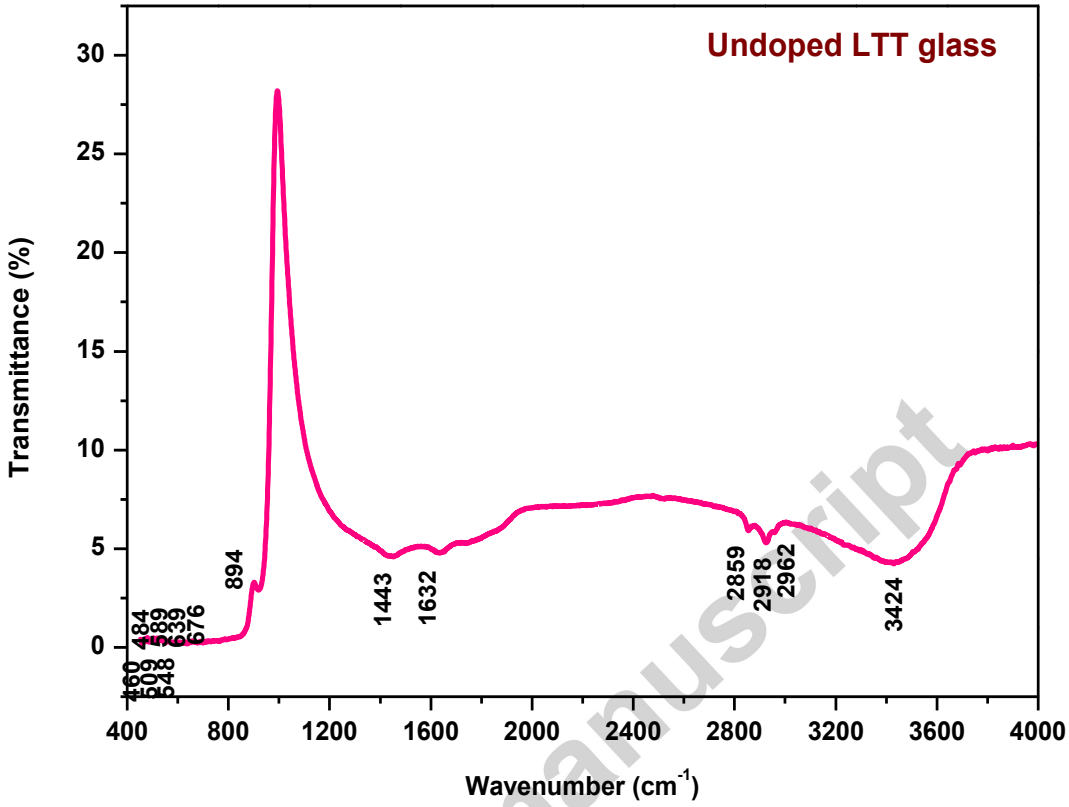

Fig 2: FT-IR spectrum of an un-doped LTT glass

Accepted manuscript

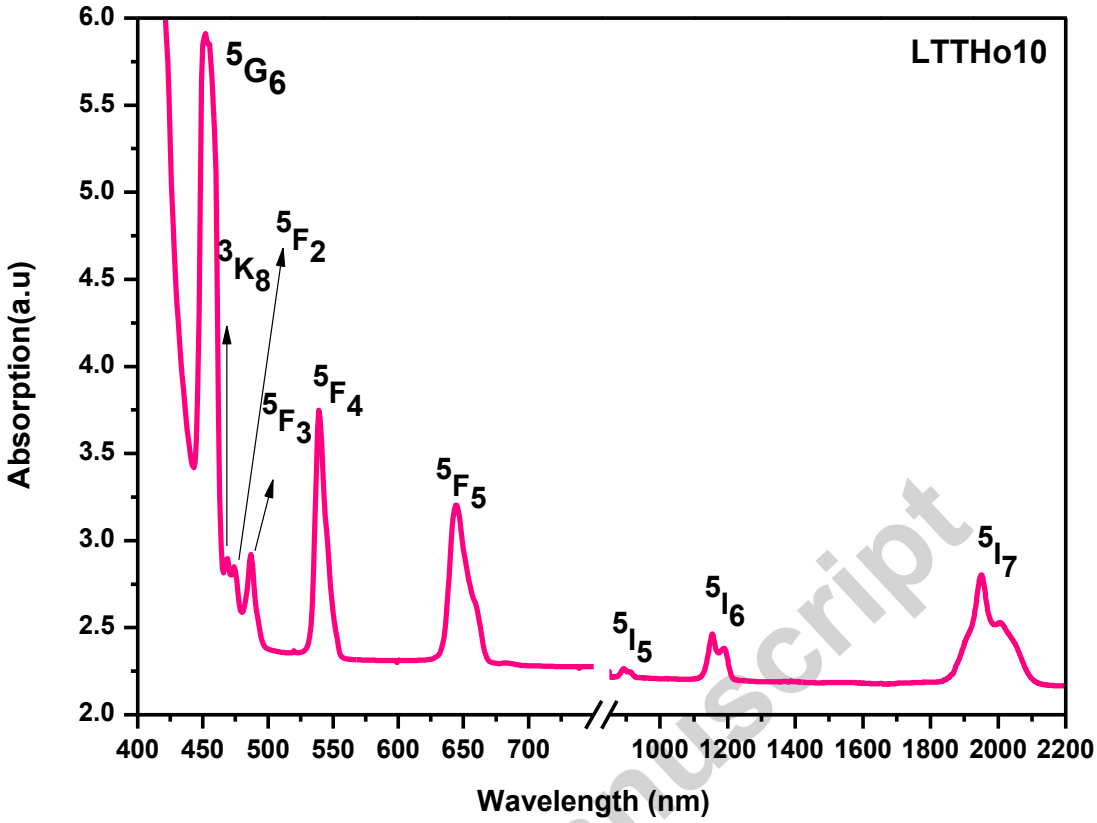

Fig 3: Optical absorption spectrum of the LTTHo10 glass

Accepted manuscript

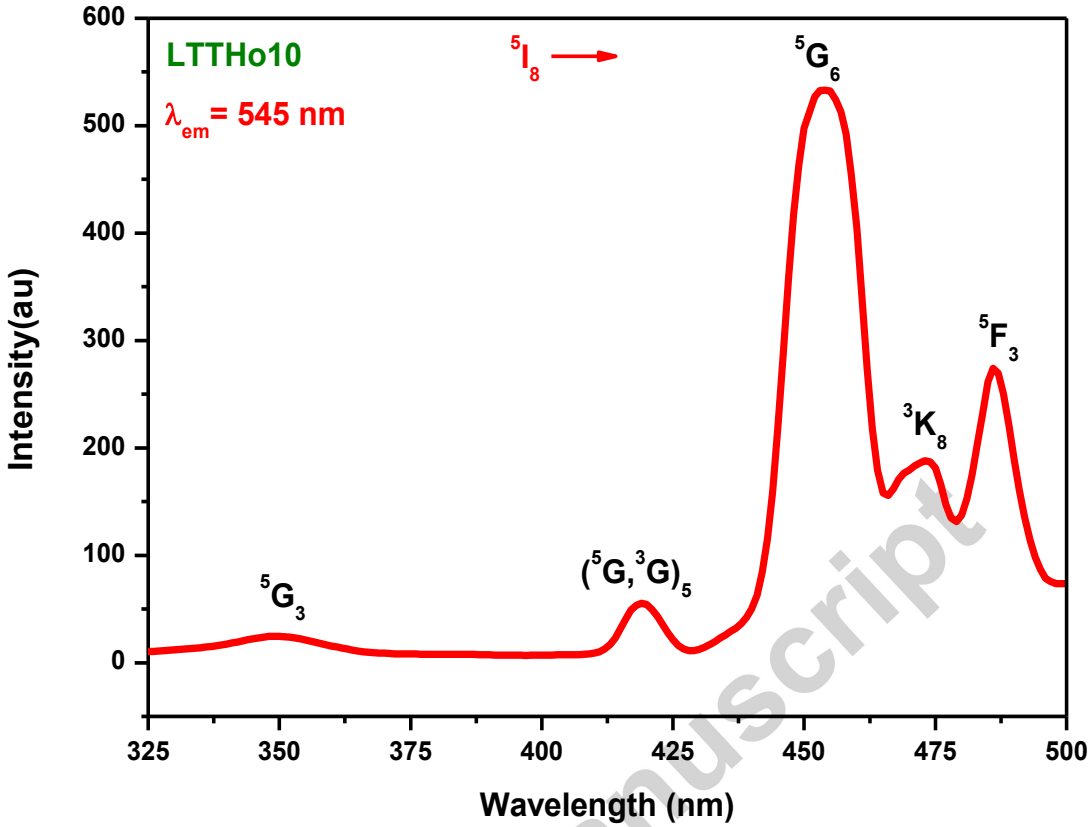

Fig 4: Excitation spectrum of the LTTHo10 glass

Accepted manuscript

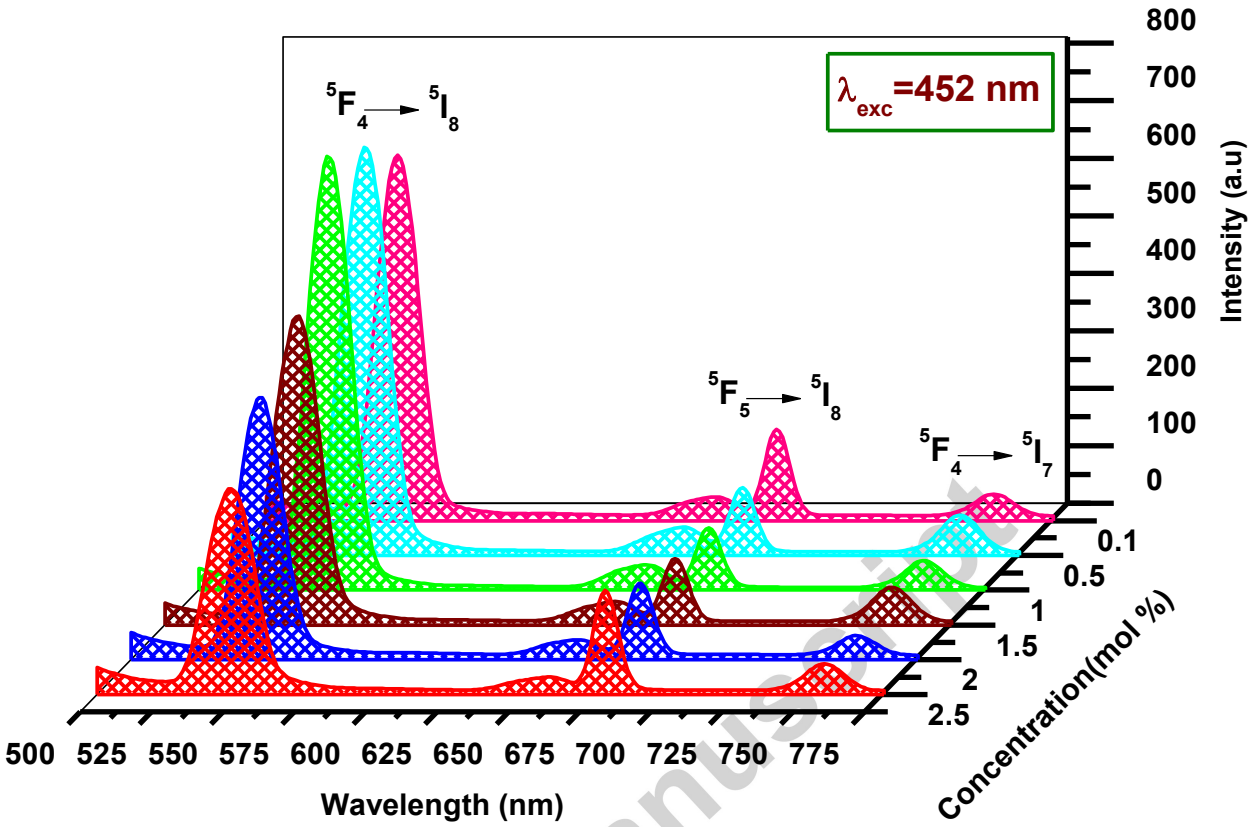

Fig 5: Emission spectra of Ho^{3+} ions in LTT glasses

Accepted manuscript

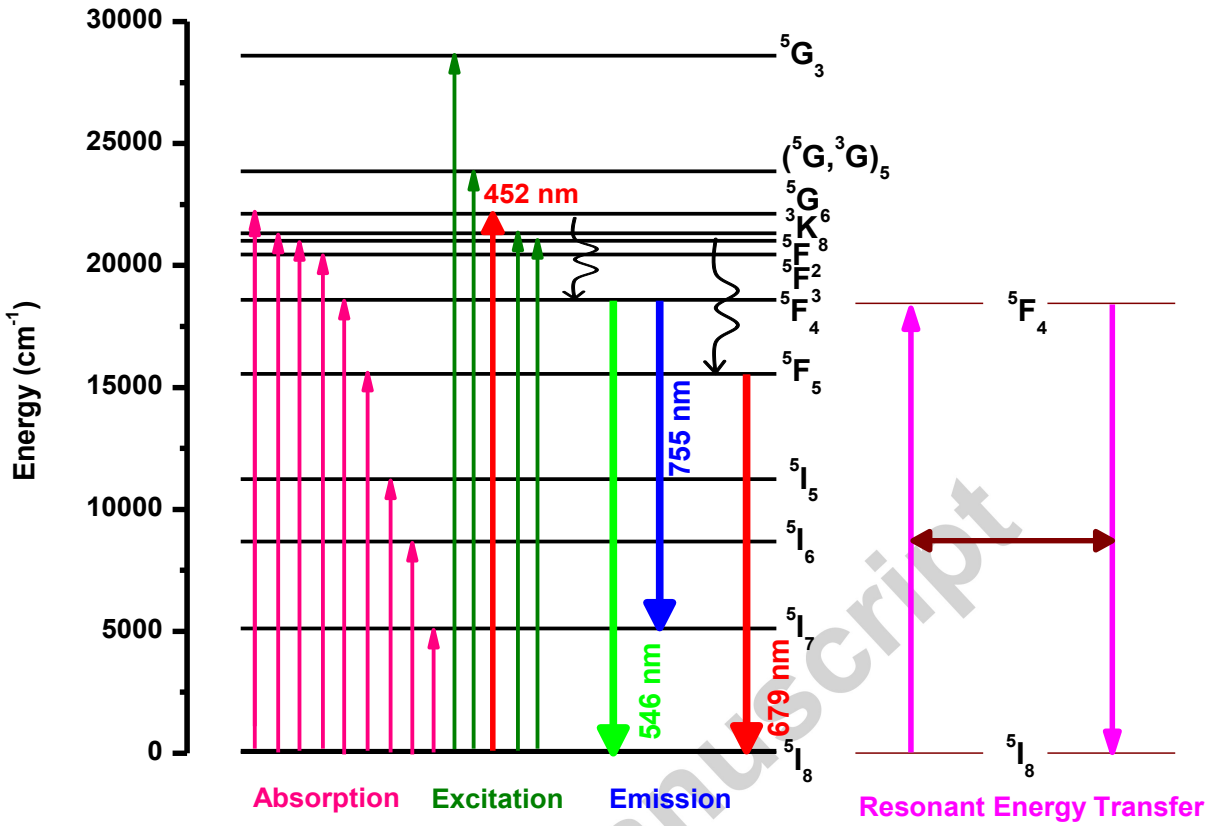

Fig 6: Energy level scheme depicting the absorption, excitation, emission and resonant energy transfer mechanism of LTTHo10 glass

Accepted manuscript

ACCEPTED MANUSCRIPT

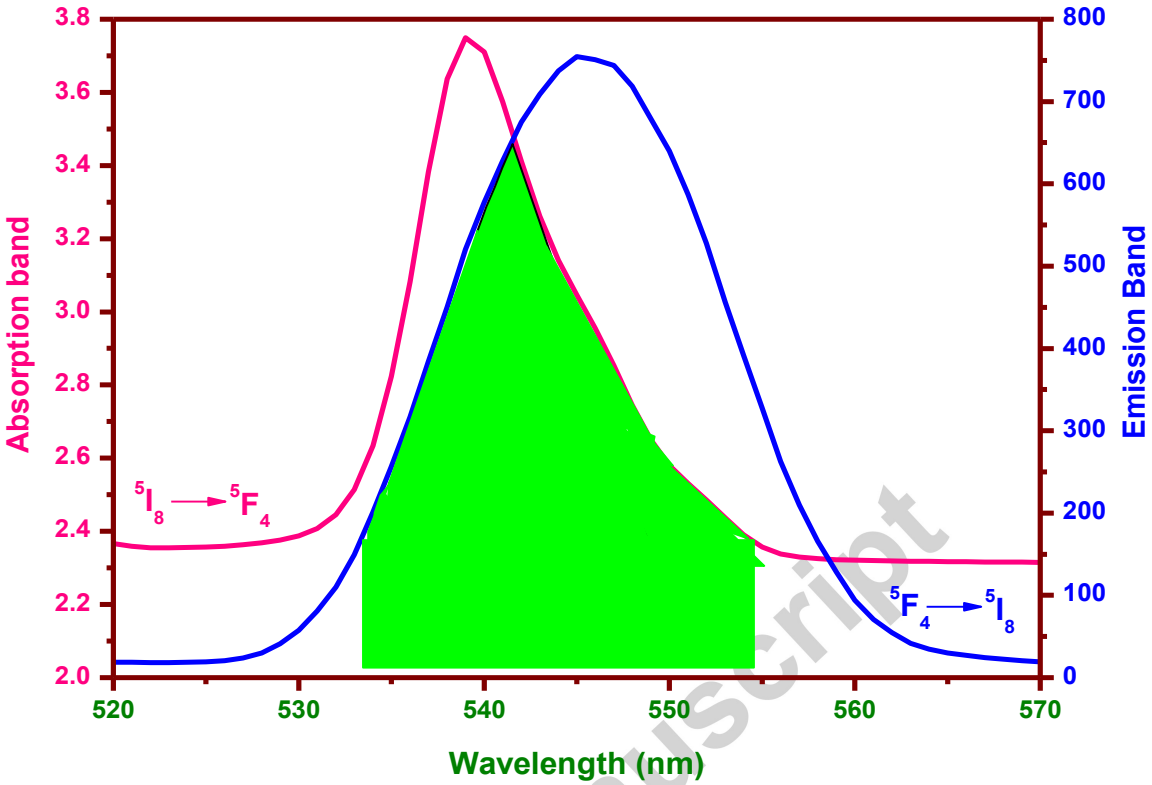

Fig 7: The overlap of absorption and emission spectra of Ho^{3+} ions in LTT glass in the spectral region from 520 to 570 nm

Accepted manuscript

ACCEPTED MANUSCRIPT

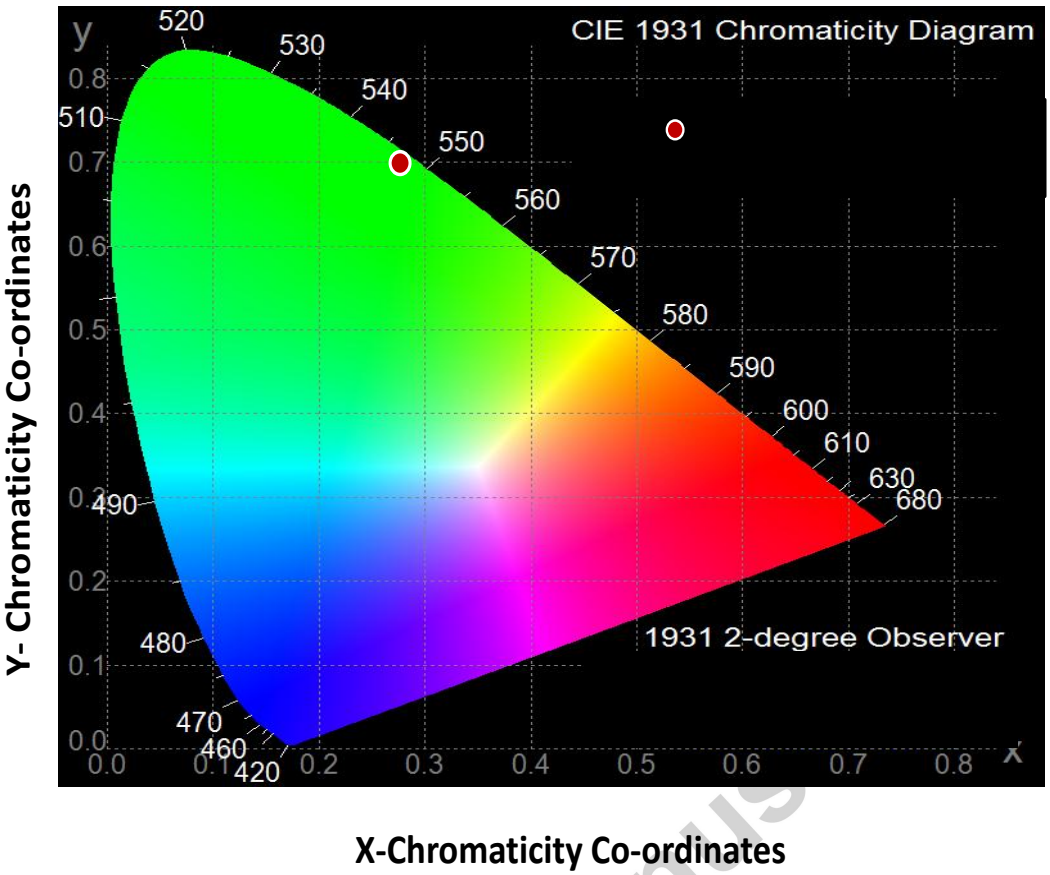

Fig 8: CIE 1931chromaticity diagram for LTTHo10 glass

Table 1:

Various physical properties of Ho^{3+} ions in LTT glasses

Physical Property	**LTTHo01**	**LTTHo05**	**LTTHo10**	**LTTHo15**	**LTTHo20**	**LTTHo25**
Refractive index (n_d)	2.400	2.404	2.407	2.415	2.435	2.437
Density, d (gm/cm^3)	6.608	6.618	6.631	6.643	6.656	6.668
Average molecular weight, $\bar{M}$(g)	190.7	191.5	192.6	193.7	194.8	195.9
Ho^{3+} ion concentration, N(10^{22} ions/cm^3)	0.208	1.040	2.072	3.096	4.113	5.123
Mean atomic volume (g/cm^3/atom)	8.875	8.880	8.886	8.893	8.898	8.905
Optical dielectric constant ($p\,\partial t/\partial p$)	4.763	4.783	4.793	4.835	4.932	4.938
Dielectric constant (ϵ)	5.733	5.783	5.793	5.835	5.932	5.938
Reflection losses (R %)	0.169	0.170	0.170	0.171	0.174	0.174
Molar refraction (R_m)(cm^{-3})	17.70	17.79	17.87	18.00	18.20	18.28
Polaron radius (r_p) (Å)	5.013	2.935	2.332	2.040	1.856	1.725
Inter-atomic distance (r_i) (Å)	7.838	4.588	3.646	3.189	2.901	2.697
Molecular electronic polarizability, α ($10^{-23}cm^3$)	7.023	1.411	0.708	0.475	0.361	0.290
Field strength ,F ($10^{15}cm^{-2}$)	1.193	3.483	5.513	7.205	8.707	10.07

Accepted manuscript

ACCEPTED MANUSCRIPT

Optical basicity ,(Λ_{th})	0.464	0.467	0.470	0.474	0.478	0.482

Accepted manuscript

Table-2

Band positions (cm^{-1}) observed in the FT-IR spectrum of an un-doped LTT glass

Band positions (cm^{-1})	**Assignments**
460	Stretching vibrations of Te-O-Te or Te-O-W linkages
484	
509	Stretching vibrations of PbO_4 units
548	Stretching vibrations of $PbOF_4$ units
589	Stretching vibrations of TeO_{3+1} units
639	ν_s – TeO_{2ax} vibrations with C_{2v} symmetry
676	Stretching vibrations TeO_4 trigonal bipyramid units
894	ν_1 vibrations of WO_4 groups / stretching vibrations of $W\text{-}O^-$ and W-O bonds in WO_4 or WO_6 units
1443	Hydrogen bonding and stretching vibrations of OH groups
1632	
2859	
2918	
2962	
3424	Stretching vibrations of OH Content

ACCEPTED MANUSCRIPT

Accepted manuscript

Table 3:

Observed band positions (cm^{-1}) and bonding parameters ($\bar{\beta}$ and δ) of Ho^{3+} ions in LTT glasses

Transition	LTTHo01	LTTHo05	LTTHo10	LTTHo15	LTTHo20	LTTHo25
$^5I_7$	5128	5134	5131	5128	5138	5131
$^5I_6$	8673	8674	8678	8677	8669	8669
$^5I_5$	11187	11058	11213	11193	11203	11223
$^5F_5$	15527	15513	15505	15501	15520	15531
$^5F_4$	18552	18564	18548	18543	18561	18554
$^5F_3$	20533	20567	20534	20563	20562	20519
$^5F_2$	--	21091	21093	21100	21090	21079
$^3K_8$	--	21349	21316	21312	21364	21321

ACCEPTED MANUSCRIPT

$^5G_6$	22026	22187	22097	22187	22187	22105
$\bar{\beta}$	0.9991	0.9987	0.9985	0.9984	0.9981	0.9979
δ	0.088	0.120	0.140	0.150	0.180	0.200

Accepted manuscript

Table 4:

Experimental (f_{exp} x 10^{-6}) and calculated (f_{cal} x 10^{-6}) oscillator strengths and rms deviation of Ho^{3+} ions in LTT glasses

Transitions	**LTTHo01**		**LTTHo05**		**LTTHo10**		**LTTHo15**		**LTTHo20**		**LTTHo25**	
from $^5I_8$→	**f_{exp}**	**f_{cal}**	**f_{exp}**	**f_{cal}**	**f_{exp}**	**f_{cal}**	**f_{exp}**	**f_{cal}**	**f_{exp}**	**f_{cal}**	**f_{exp}**	**f_{cal}**
$^5G_6$	30.1	30.1	45.0	44.9	69.7	69.6	60.2	60.1	56.4	56.3	52.6	52.5
$^3K_8$	--	9.40	0.20	5.51	0.31	9.01	0.27	7.22	0.23	3.06	0.23	5.05
$^5F_2$	--	4.40	0.57	1.65	1.01	2.73	0.88	2.16	0.99	2.19	0.75	1.43
$^5F_3$	2.57	1.96	1.74	2.89	2.79	4.80	2.27	3.79	2.67	3.85	1.75	2.51
$^5F_4$	6.02	4.44	8.30	5.62	14.6	8.98	12.0	7.23	10.7	7.16	9.52	5.29
$^5F_5$	8.27	8.54	8.96	9.81	13.8	15.2	11.2	12.4	11.3	12.1	8.68	9.75
$^5I_5$	0.63	0.39	0.99	0.53	0.71	0.86	0.57	0.69	0.51	0.69	0.41	0.48

ACCEPTED MANUSCRIPT

$^5I_6$	1.86	1.99	2.13	2.82	4.91	4.62	4.06	3.68	2.95	3.70	1.91	2.53
$^5I_7$	2.73	2.84	4.51	3.92	6.92	6.41	5.46	5.12	5.31	5.13	3.98	3.58
δ_{rms} (x10^{-6})	±0.649		±2.098		±3.604		±2.932		±1.65		±2.207	

Accepted manuscript

Table 5:

Judd-Ofelt Parameters (Ω_λ x 10^{-20}cm^2) of the Ho^{3+} ions in LTT glasses.

Glass System	Ω_2	Ω_4	Ω_6	Trend	References
LTTHo01	2.00	5.21	1.54	$\Omega_4>\Omega_2>\Omega_6$	present work
LTTHo05	4.33	5.28	2.27	$\Omega_4>\Omega_2>\Omega_6$	present work
LTTHo10	6.66	7.71	3.68	$\Omega_4>\Omega_2>\Omega_6$	present work
LTTHo15	6.01	6.52	2.96	$\Omega_4>\Omega_2>\Omega_6$	present work
LTTHo20	5.47	6.08	2.95	$\Omega_4>\Omega_2>\Omega_6$	present work
LTTHo25	5.41	5.62	1.97	$\Omega_4>\Omega_2>\Omega_6$	present work
ZrF_2-BaF_2	2.12	2.38	1.61	$\Omega_4>\Omega_2>\Omega_6$	[62]

ACCEPTED MANUSCRIPT

ZBLAN	1.90	2.09	1.56	$\Omega_4>\Omega_2>\Omega_6$	[63]
$YAlO_3$	1.82	2.38	1.53	$\Omega_4>\Omega_2>\Omega_6$	[64]
MHGHo	2.07	2.38	1.53	$\Omega_4>\Omega_2>\Omega_6$	[65]
La2O3	6.52	2.22	2.53	$\Omega_2>\Omega_6>\Omega_2$	[66]
PbO-ZnO-B2O3	2.77	2.26	1.50	$\Omega_2>\Omega_4>\Omega_6$	[67]
Fluoride	2.40	1.70	1.80	$\Omega_2>\Omega_6>\Omega_4$	[68]
HBLACs	1.53	3.19	4.93	$\Omega_6>\Omega_4>\Omega_2$	[69]

Accepted manuscript

Table 6:

Transition probabilities (A_R) (s^{-1}), luminescence branching ratios (β_R), total transition probability (A_T) (s^{-1}) and radiative lifetimes (τ_R) (μs) for the observed emission transitions of Ho^{3+} ions in LTT glasses

Transition	A_R	β_R	A_T	τ_R
LTTHo01				
$^5F_4 \rightarrow {}^5I_8$	1848.14	0.498	3705.86	269
$^5F_5 \rightarrow {}^5I_8$	795.55	0.499	1593.72	627
$^5F_4 \rightarrow {}^5I_7$	1493.21	0.402	3705.86	269
LTTHo05				
$^5F_4 \rightarrow {}^5I_8$	2743.18	0.504	5436.70	183
$^5F_5 \rightarrow {}^5I_8$	1180.83	0.505	2338.67	427
$^5F_4 \rightarrow {}^5I_7$	2216.36	0.407	5436.70	183

ACCEPTED MANUSCRIPT

LTTHo10				
$^5F_4 \rightarrow {}^5I_8$	4462.55	0.505	8821.52	133
$^5F_5 \rightarrow {}^5I_8$	1920.95	0.506	3793.72	263
$^5F_4 \rightarrow {}^5I_7$	3605,53	0.408	8821.52	133
LTTHo15				
$^5F_4 \rightarrow {}^5I_8$	3640.70	0.505	7205.63	138
$^5F_5 \rightarrow {}^5I_8$	1567.18	0.505	3098.80	322
$^5F_4 \rightarrow {}^5I_7$	2941.52	0.408	7205.63	138
LTTHo20				
$^5F_4 \rightarrow {}^5I_8$	3750.23	0.506	7412.85	140
$^5F_5 \rightarrow {}^5I_8$	1614.32	0.508	3009.04	335
$^5F_4 \rightarrow {}^5I_7$	2845.13	0.410	7412.85	140
LTTHo25				
$^5F_4 \rightarrow {}^5I_8$	2509.73	0.501	5003.39	199
$^5F_5 \rightarrow {}^5I_8$	1180.83	0.505	2048.13	464
$^5F_4 \rightarrow {}^5I_7$	2216.36	0.405	5003.39	199

Accepted manuscript

Table 7:

Emission peak wavelength (λ_P)(nm), effective band widths ($\Delta\lambda_P$)(nm), radiative and experimental branching ratios (β_R & β_{exp}), stimulated emission cross-sections (σ_{se}) (x 10^{-21}) (cm^2), gain band width (σ_{se} x $\Delta\lambda_p$) (x 10^{-28}) (cm^3) and optical gain (σ_{se} x τ_R) (x 10^{-25}) (cm^2 s) parameters for the emission transitions of Ho^{3+} ions in LTT glasses.

Spectral parameters	**LTTHo01**	**LTTHo05**	**LTTHo10**	**LTTHo15**	**LTTHo20**	**LTTHo25**
			$^5F_4 \rightarrow {}^5I_8$ (Green)			
λ_P	546	546	546	546	546	546
$\Delta\lambda_p$	13.8	11.3	8.75	10.0	11.3	11.9
β_R	0.498	0.504	0.505	0.505	0.506	0.501
β_{exp}	0.749	0.777	0.804	0.739	0.719	0.658
σ_{se}	2.75	4.97	10.4	7.36	6.63	6.27

ACCEPTED MANUSCRIPT

σ_{se} x $\Delta\lambda_p$	37.8	55.9	90.8	77.6	74.50	74.5
σ_{se} x τ_R	7.40	9.10	13.8	10.7	9.28	11.7
			$^5F_5 \rightarrow {}^5I_8$ (Red)			
λ_P	678	678	678	678	678	678
$\Delta\lambda_p$	13.8	13.8	12.5	15.0	15.6	16.3
β_R	0.499	0.505	0.506	0.505	0.508	0.505
β_{exp}	0.186	0.138	0.145	0.167	0.203	0.245
σ_{se}	2.81	4.16	7.44	5.02	4.88	3.14
σ_{se} x $\Delta\lambda_p$	38.7	57.2	93.0	75.3	76.3	51.0
σ_{se} x τ_R	17.60	17.80	19.60	16.20	16.30	14.60
			$^5F_4 \rightarrow {}^5I_7$ (Infrared)			
λ_P	755	755	755	755	755	755
$\Delta\lambda_p$	26.3	25.0	24.4	25.0	26.3	27.5
β_R	0.402	0.407	0.408	0.408	0.410	0.405
β_{exp}	0.064	0.056	0.076	0.092	0.076	0.096
σ_{se}	0.42	0.63	0.89	0.79	0.78	0.59
σ_{se} x $\Delta\lambda_p$	11.2	16.5	26.8	21.7	20.7	14.7
σ_{se} x τ_R	11.4	12.1	14.6	12.0	11.0	10.7

Accepted manuscript

Table 8:

Colour co-ordinates of Ho^{3+} ions in LTT glasses at λ_{exc} = 452 nm wavelength.

Name of the Sample	**Colour Co-ordinates**
	λ_{exc} =452 nm
LTTHo01	(0.3082, 0.6819)
LTTHo05	(0.2879, 0.7031)
LTTHo10	(0.2858, 0.7069)
LTTHo15	(0.2844, 0.7070)
LTTHo20	(0.2780, 0.7126)
LTTHo25	(03022, 0.6911)

ACCEPTED MANUSCRIPT

Highlights

1. Ho^{3+} doped LTT glasses have been synthesized using melt quenching technique.
2. From the absorption spectra, JO parameters have been evaluated using JO theory.
3. Branching ratios & Emission cross-sections were evaluated for emission transitions.
4. From the emission spectra the CIE colour co-ordinates were evaluated.
5. LTTHo10 glass was found to be more suitable for visible green luminescence.

Accepted manuscript

Incorporating Information from Trusted Sources to Enhance Urban Navigation for Blind Travelers

Byung-Cheol Min[1], Suryansh Saxena[2], Aaron Steinfeld[1], and M. Bernardine Dias[1]

***Abstract*—Dynamic changes can present significant challenges for visually impaired travelers to safely and independently navigate urban environments. To address these challenges, we are developing the NavPal suite of technology tools [1]. NavPal includes a dynamic guidance tool [2] in the form of a smartphone app that can provide real-time instructions based on available map information to guide navigation in indoor environments. In this paper we enhance our past work by introducing a framework for blind travelers to add map/navigation information to the tool, and to invite trusted sources to do the same. The user input is realized through audio breadcrumb annotations that could be useful for future trips. The trusted sources mechanism provides invited trusted individuals or organizations an interface to contribute real-time information about the surrounding environment. We demonstrate the feasibility of our solution through a prototype Android smartphone-based outdoor navigation aid for blind travelers. An initial usability study with visually impaired adults informed the design and implementation of this prototype.**

I. Introduction

The World Health Organization (WHO) estimates that 285 million people in the world are visually impaired, of whom 39 million are blind [3]. Although safe and independent mobility is a critical element of modern life, our needs assessment over the past few years [1] revealed that due to limited tools and information, traveling in unfamiliar environments can be challenging and often daunting for visually impaired people. We envision smart cities of the future that are truly accessible and navigable by everyone, including people with disabilities. These future smart cities are likely to benefit from assistive robots and a variety of other technology that could potentially enhance the safety and independence of visually impaired people during urban travel. However, smartphones are still likely to be the primary modality that connects visually impaired travelers to these other technology solutions and smart infrastructure in future smart cities.

To realize this vision of accessible smart cities, we are developing the "NavPal" suite of technology tools that combine a variety of technologies including robots, crowdsourcing, advanced path-planning and multi-modal interfaces to enhance the safety and independence of visually impaired people navigating urban environments [1], [2]. A key component of our work on accessibility and navigation is our commitment to a human-machine solution where humans and technology work together to achieve the best outcomes possible in any given scenario. In this paper, we explore three ways in which blind users can be empowered to influence their assistive navigation aids - first, by adding audio annotations for themselves to use at future times; second, by choosing to share useful information with others who invite them as trusted sources; and third, by inviting trusted sources of relevant information to influence their navigation decisions. The contribution of this work is therefore a framework to empower blind travelers to influence their technology-based navigation aids via audio breadcrumb annotations and relevant information from user-designated trusted sources.

The remaining sections of this paper are organized as follows. In section II, related work from the literature is discussed. Our system architecture and iterative design process are presented next in sections III and IV respectively. In section V, we describe our mechanism to insert audio breadcrumbs and to invite trusted sources. Sections VI and VII detail relevant use-case scenarios for audio breadcrumb annotations and trusted sources. Finally, section VIII concludes this paper with a summary of the presented work, a discussion of the strengths and limitations of our approach, and an outline of relevant future work.

II. Related Work

Assistive technologies have played an essential role in the safety and independence of people with disabilities. Long white canes, dog guides [4], and smartphones [2], [8], [9] are current assistive tools that are widely used by visually impaired people to aid in navigation. Several research efforts have also created a variety of guide robots [5], [6], [7] for this purpose.

A white cane is the most ubiquitous and universally identifiable navigation tool for visually impaired travelers and is used to detect and avoid obstacles and warn others in the path of travel [10]. A dog guide is another modality that visually impaired travelers often employ for the purpose of guidance in navigation. A white cane and dog guide have proven useful, but do not include a point-to-point navigation (route planning from a starting point to the intended destination) capability that is often necessary for visually impaired people to navigate safely and independently in unfamiliar environments.

In recent years, the use of smartphones has grown rapidly in visually impaired communities as they become more affordable and integrate several key functions needed for their daily life such as text-to-speech, gesture recognition, and localization using sensors. This follows similar trends showing rapid increases in smartphone market share [11].

[1]Byung-Cheol Min, Aaron Steinfeld, and M. Bernardine Dias are with the Robotics Institute at Carnegie Mellon University, Pittsburgh, PA 15213 USA bmin@cs.cmu.edu, steinfeld@cmu.edu, mbdias@ri.cmu.edu

[2]Suryansh Saxena was affiliated with Carnegie Mellon University when this work was done and is now with Delhi Technological University, New Delhi, Delhi, 110042 India suryansh@red-itech.com

Through the NavPal project [1], [2], [9], [13], we have been working on smartphone-based localization and navigation techniques to empower blind travelers with enhanced safety and independence when navigating indoors. Similarly, representative smartphone GPS apps targeted toward visually impaired users include BlindSquare [12] and Ariadne GPS [14]. BlindSquare is a very popular app running on the iOS platform. It uses points of interest information from Foursquare and Open Street Map and allows navigation to the point of the interest. Loadstone GPS is GPS navigation software for visually impaired users [15]. This software runs on Nokia mobile phones and uses external devices such as screen readers and a Bluetooth GPS receivers. The primary challenge for such commercial navigation solutions stems from their use of proprietary datasets to provide map information. Because of this, visually impaired users often need to pay to run those apps on their smartphones and require continuous updates on a map that often incurs additional charges. Moreover, most route planning apps are inflexible to adapt to dynamic changes, for example, blocked travel due to construction, and are not designed to be updated and refined by users.

In recent years, a growing number of research groups have shown interest in the use of crowdsourcing techniques to provide information about unfamiliar environments to enable blind travelers to navigate safely [16], [17]. Coughlan and Shen proposed a crowdsourcing approach to allow volunteers to enter information for providing guidance to blind travelers at traffic intersections [16]. The motivation of the approach is that important information such as the presence and location of walk buttons may be unavailable from some existing data sources such as Google Map, Open Street Map and other municipal/transit sources. VizWiz [17] is a smartphone app that uses a combination of image processing techniques and crowdsourcing using web workers and online social networks to allows visually impaired users to get nearly real-time answers to visual questions on their surroundings. However, as information for navigation aids is mainly from crowdsources in these approaches, it is hard for a user to have the ability to discern if the information is trustworthy and also it limits the user's options to get relevant information.

More relevant to our work is the Blind Leading the Blind project [18] that proposed the formation of online social networks where visually impaired travelers and sighted travelers collaboratively share and manage verbal route information, thus enabling visually impaired travelers to independently travel to previously unknown environments when provided with online verbal route directions. Similarly, Volkel et al. proposed a concept of sharing relevant Points of Interest (POI), such as temporary obstacles, for mobility impaired pedestrians [19]. In a similar context, Karimi et al. proposed a social navigation network, called SoNavNet, where users are connected to each other to share navigation information that is based on user experiences [20]. Although all these approaches are applicable to and are designed for empowering visually impaired persons with navigating unfamiliar environments safely and independently, they do not allow visually impaired users to invite or designate trusted individuals to and in social networks. Our previous needs assessments with visually impaired communities and orientation and mobility (O&M) experts revealed that such technologies would help maximizing advantages of using such social networks for visually impaired travelers [1].

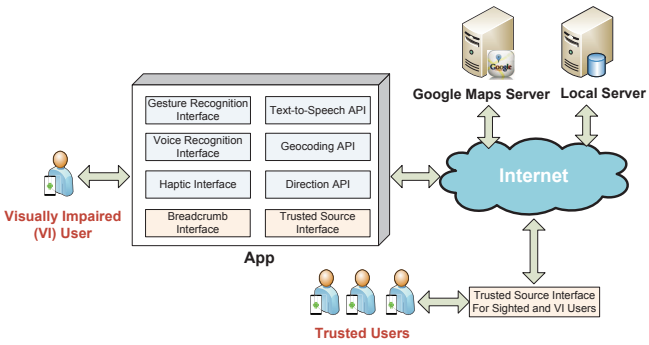

Fig. 1: System architecture of our app.

The relevant findings from our previous needs assessments are summarized as follows. First, visually impaired users prefer to invite trusted individuals and organizations to contribute information to assist their navigation. Next, visually impaired travelers wish to verbally annotate their routes on maps so they can record other information that will be useful for future trips to the same location. While different visual impairments and navigation techniques sometimes make it difficult to share entire paths or landmarks among visually impaired people in meaningful ways, most visually impaired travelers are happy to share navigation information with others who may find it useful. We address these issues in this paper via a mechanism for inviting trusted sources and inserting audio breadcrumbs.

III. System Architecture

We demonstrate the feasibility of the proposed mechanism through a prototype Android smartphone app to assist blind travelers when navigating in outdoor urban environments. The system architecture of this app is illustrated in Fig. 1. The proposed system is composed mainly of two user groups (a visually impaired user and trusted users), Android smartphone app and interfaces for the groups, servers to store data, and Internet. Through Internet data from users and trusted sources are shared and map/route/direction information are kept up-to-date.

User input to our app can be communicated in two modalities: (1) simple gestures on the touchscreen, or (2) voice input via the microphone. This multimodal input ensures that users are able to communicate with the app effectively even in a place where certain input modules do not work optimally (e.g., voice input in crowded places). The system's output to the user is communicated via synthesized speech and vibration feedback. Synthesized speech is generated by a text-to-speech (TTS) API that is available through the Google Library, and the TTS API converts text and messages displayed on the screen into voice output. A headset can allow a user to hear

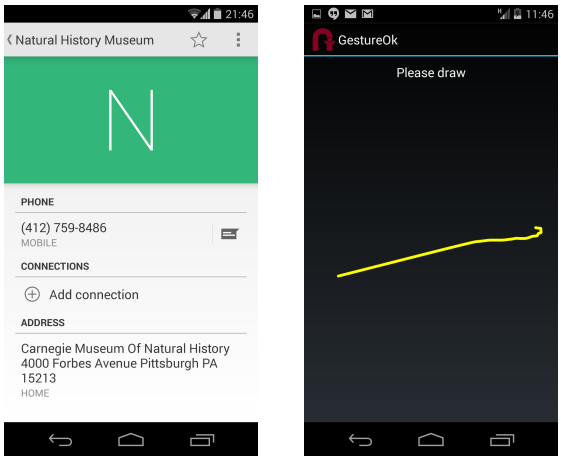

(a) Contact name and address

(b) Gesture drawn on the screen

Fig. 2: Snapshots of the contact destination and gesture input.

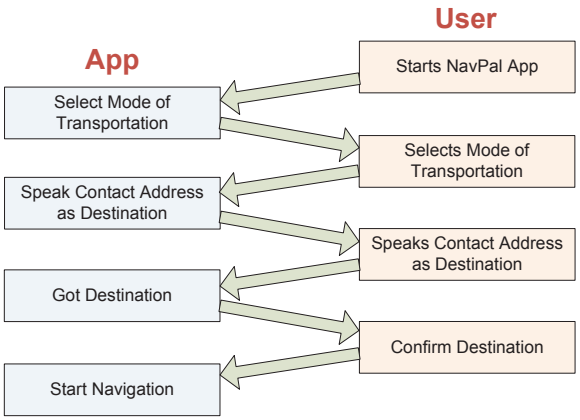

Fig. 3: Interactions between our app and the user.

voice output in noisy environments. Vibration feedback via the haptic interface is used to acknowledge user input and also to warn users about potentially problematic situations, e.g., when the user diverges from the desired path during navigation.

Our app allows the user to select a contact name and address of the place or person as the intended destination. This feature is designed to allow visually impaired users to maintain their routine when placing a call to others using their smartphones. When a destination is received from the user in the form of the contact, e.g., "Natural History Museum", a full address is then retrieved, e.g., "Carnegie Museum of Natural History 4000 Forbes Avenue Pittsburgh PA 15213", which is needed for the Geocoding API that converts this address to geographic coordinates (latitude 40.443276 and longitude -79.950082) via an HTTP request to the Google Maps server. Fig. 2 (a) shows a snapshot of this example with the contact name displayed on the top and the contact address displayed on the bottom. The Google Maps server returns an output in JSON (JavaScript Object Notation). While a route could be directly planned with text strings of the address, geographic coordinates can represent locations with a much finer resolution so we used geographic coordinates for route planning in our app. This higher resolution is greatly beneficial to blind travelers, especially when they are navigating as pedestrians. Next, a route is planned from the current position to the intended destination using a Direction API that returns multi-part directions using a series of waypoints in JSON from the Google Maps server.

Fig. 3 shows an illustration of interactions between our app and the user. The text strings displayed in the boxes on the right represent the steps in the user's interaction. The text strings displayed in the boxes on the left represent the audio messages the app returns to the user.

Starting from the top right, the user launches the app on the smartphone and receives a verbal request to select a transportation mode from choices such as walking, public transport, and car. Upon receiving the selected transportation mode, either from the gesture interface or speech interface, the app verbally announces that an input has been received. Next, the user is verbally asked to input the contact representing the desired destination. It should be noted that the address field should be filled in along with the contact name within the contact list of the smartphone device beforehand for the app to work properly. If a contact does not have an address stored beforehand, then the app will return an address as Null and ask the user to try again. The user then receives an audible message indicating the app is ready for navigation. If the user is in a location where the GPS signal is weak or unavailable, the app asks the user to change locations until the GPS signal is strong. Once the user is ready to navigate, he/she executes the relevant on-screen gesture to confirm this state and initiate navigation. While navigating with the app, the user is given audible navigational instructions at different waypoint intervals, e.g., "Head north for 20 meters and then turn left". In addition, the street name and user's direction of travel are announced at intersections. The nearby points of interest are also automatically announced to the user for better localization and orientation. If the user deviates from the desired path at a setting defined by us, e.g., 10 meters, the app directs the user to stop and plans a new path to the destination.

IV. Iterative Design with Visually Impaired Users

A. *Input via on-screen gestures*

On-screen gestures are commonly used input modalities for users who are blind or visually impaired to use a touchscreen smartphone, and thus we adopted gestures as part of our accessible interface. The literature [21], [22] shows that some gestures are easier than others for users who are blind or visually impaired. In this paper, we conducted a short usability study to determine which gestures are more effective for our app with relatively older participants (n=4) than the participants in the literature. While the average age of our participants is 63.5, the average age of blind participants (n=10) in [21] is 49.0, and ages of sighted but blindfolded

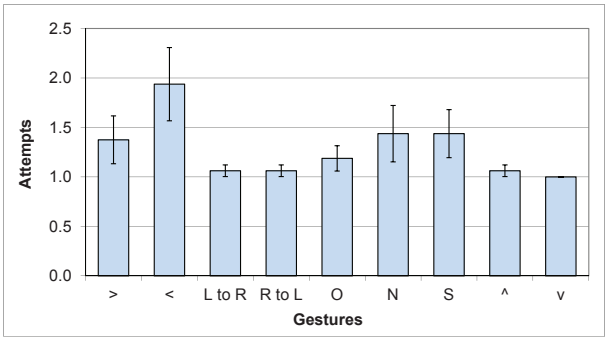

Fig. 4: Summarized results from gesture testing. Note that the lower attempts indicate that participants performed the gesutre more correctly.

participants (n=12) in [22] range between 22 and 34. Our participants' ages ranged from 61 to 66, P1, P2, and P3 are male and own iPhones or iPads, and P4 is female and owns no touchscreen devices. P1, P3, and P4 are blind and P2 is legally blind. For this usability study, we employed a Samsung Nexus S that has a 4.0-inch screen. It would be worth noting that this study would have the limitation of not gathering data on if the participants were right-handed or left-handed since that could affect performing certain gestures.

In our previous studies in [13], we conducted user studies with 8 visually impaired participants on various gestures on a touchscreen smartphone. Although we could not derive which gestures are easier or more difficult in a numerical fashion, the studies have shed on selecting the following eight gestures for the gesture testing for our app: $>$, $<$, swipe right, swipe left, O, N, S, $\wedge$, and $\vee$. First, we walked the participant through each gesture teaching them how to perform them. Then, we directed them to attempt specific gestures which the app communicated to them one at a time. Participants could have up to five attempts on each gesture so that we could discern a quantitative score for difficulty of each gesture without overly taxing the users in terms of time or frustration. Once participants performed a specified gesture correctly, they were advanced to the next gesture. Once participants completed the list of nine specified gestures, they were asked to attempt the list again in a different order. The order of gestures was randomly selected by the app to minimize any bias in performance due to gesture ordering. The test concluded once this list was completed five times (with the list of gestures presented in five different configurations) by each participant. Fig. 4 shows the average with the standard deviation of attempts for each gesture over participants. Note that the lower attempts on a vertical axis indicate that participants performed the gesture more correctly. From this figure, we can see that the most troublesome gesture was $<$, followed by N, then S, then $>$. Also, we can see that N and S which have motions in multiple directions were incorrect more often. These findings are consistent with the participant comments which reflected a greater difficulty and effort (in terms of time spent) to execute these gestures.

Fig. 4 further shows that the gestures swipe right, swipe left, $\wedge$, $\vee$, and O were the best executed gestures. However, $\wedge$ and $\vee$ were not always drawn accurately. More often than not they were executed more as L shapes following the sides of the screen. This result indicates that L shapes might be a good gesture to use since visually impaired users can follow the screen edge to write that gestures although it may require a greater effort in terms of time spent. All participants recommended using simpler gestures instead of ones that have components that go in multiple directions. Commonly recommended gestures were directional swiping with one or two fingers, which is consistent with what we discovered in past work [13], and therefore we selected those directional swiping gestures for our app as shown in Fig. 2 (b).

B. Overall accessibility of interface

Accessibility and ease of operating the app and adding data to it (via voice and gestures) are critical for visually impaired users. Therefore, we also conducted usability studies to assess the accessibility of the interface with the same four visually impaired participants. To test the accessibility of our app, the participants were first given a demo of the app interface, and were then asked to use either gestures or speech to input the transportation medium that they would use to navigate, and the contact name of the place/person to which they plan to navigate (e.g., Natural History Museum). Participants were also asked to use gestures to give system answers and feedback as requested by the app. This testing process (Test 1) was repeated twice for each participant. Furthermore, to test ease of use of the interface, participants were asked to speak an address location to annotate, and to use gestures to navigate the map and add a waypoint (Test 2). The results from these tests are summarized in Table I that shows how many were successful from the n attempts.

TABLE I: USABILITY STUDIES ON OUR APP

Participant	**Test 1**		**Test 2**
	(n=3)	**(3)**	**(2)**
P1	3	3	2
P2	1	2	2
P3	2	3	2
P4	0	2	-
Average	1.5	2.5	2

P4 was new to using a smartphone device, and thus had difficulties figuring out the gesture interaction with the device in the first attempt. But, P4 showed improvement in the second attempt. This participant was also unable to complete the latter part of the experiment due to scheduling constraints which required P4 to end the test session early.

Following these tests, we also conducted a debrief session where we collected feedback from the participants (verbally) about their experience during the quick tests, and their feedback on [a] speech recognition, [b] voice instruction, [c] gesture instruction, and [d] overall ease of use and accessibility of our app. We asked them to rate [a] to [c] in a range of 0 to 5, with 0 being very bad and 5 being excellent, and [d] in a range of 0 - 10. There was no specific reason to have these different rating ranges; but, we wanted to open up users' rating

on overall performance of the app more widely. The results are summarized in Table II.

TABLE II: USER SCORE ON OUR APP

Participant /Item	[a] Speech	[b] Voice	[c] Gesture	[d] Overall
P1	5	4	5	9
P2	5	3	5	8
P3	4	4	5	9
P4	2	4	4	6
Average	4	3.75	4.5	8

The system had difficulty understanding the speech inputs by P4 because he/she is more accustomed to typing on a physical keyboard with a talk-back feature. This caused P4 to assign a score of 2 out 5 on the speech function. However, on average, the participants liked the overall system and its features, but commonly pointed out that we would need to implement a verbosity tool for avoiding repetitive instructions. This verbosity comment is reflected in the relatively low scoring for the voice instruction feature. Also, all participants, when presented with our planned methodology for introducing audio breadcrumbs and an interface to incorporate information from trusted sources, wholeheartedly approved of the plan and indicated that it would be very helpful. Selected comments from this user feedback are shown below.

- *"The breadcrumb approach will be helpful for the user for orienting and locating in frequently visited places."* (P3)
- *"Trusted sources will be very helpful not only for outdoor navigation but also for indoor navigation. For example, trusted sources can help visually impaired users to read the room number or the direction."* (P2)

V. Audio Breadcrumbs and Trusted Sources

While most of the online map services including Google Maps provide information needed for route planning, the map rarely provides continuous information about dynamic changes, for example blocked street and sidewalk, which are often useful for blind travelers to accomplish safe and independent navigation. In addition, these solutions do not allow users to verbally annotate their routes on the maps. Addressing these shortcomings, we present a framework for incorporating information from trusted sources, and user annotations in the form of audio breadcrumbs to enhance assistive navigation aids.

The underlying motivation for a framework that incorporates input from trusted sources is enabling individuals and organizations trusted by visually impaired travelers to share their observations and information relevant to navigating unfamiliar environments via a connected network. This collaborative information sharing will ultimately empower blind travelers to navigate unfamiliar urban environments safely and independently. For example, if a street is under renovation and a trusted source traveling via this route observes this potential risk to blind travelers, he/she can report this information using the trusted sources interface. A blind traveler can then benefit from this information since the route planner can take this information into account and provide an alternative path to the destination.

Trusted sources can be relevant authorities in the locality (e.g., a policeman), property managers (e.g., a business owner), O&M experts, family and friends, or visually impaired travelers themselves. Previous studies [23] have shown that many visually impaired people prefer obtaining navigational information from other visually impaired persons because they are more likely to get information and directions that are accessible and relevant to them. Therefore, we made sure that visually impaired people can also act as trusted sources to other blind travelers. However, since there are many sighted people who are either trained or have learned to give good directions to blind travelers, we also made sure that the trusted sources interface was accessible to sighted individuals.

Furthermore, a visually impaired traveler can verbally record points of interest and reminders during a navigational experience and refer to it for future trips using the audio breadcrumb interface. The user can launch with a long tap (longer than 2 seconds) on the screen to record a message. When using this interface, the user can record a message and play it back. Examples of the message would include any potential problems encountered at that location, a waypoint identifier, or orientation information for future trips. The audio breadcrumb then appears as a waypoint on the map and as the traveler approaches the vicinity of this waypoint, the recorded information is played back to the user.

Visually impaired users are given two options when using the trusted sources interface. The first option is to use the current location as the tag for the recorded information. The second option is to specify a location other than the current location and associate it with the recorded information. If they select to use the current location, then the breadcrumb interface is launched and the same procedure described above is followed. If the user instead selects to add some other

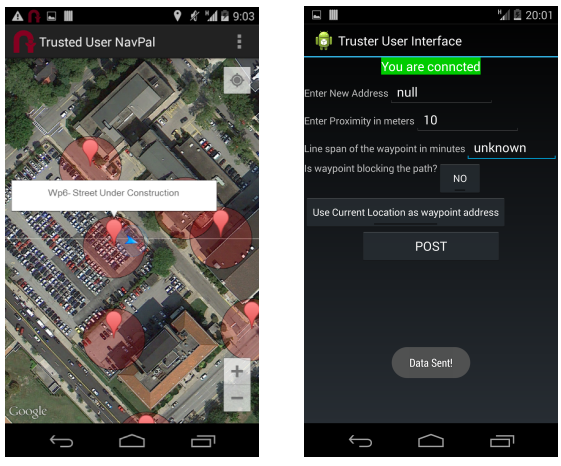

(a) Information added by a sighted trusted source

(b) Trusted source interface for sighted users

Fig. 5: A snapshot of the trusted source interface for sighted users.

position, then the app asks the user to either speak the location address or physically type the address of the waypoint via the talk-back keyboard interface. The user is then provided with the same instructions as in the scenario where the current position is selected as the waypoint tag.

For the sighted trusted users, we developed an additional app where they can simply tap the map on the screen and annotate any observed dynamic changes. Fig. 5 (a) shows a snapshot of the contributed data with an annotation "Street under construction" using the trusted source interface for sighted users shown in Fig. 5 (b). Fig. 5 (b) also shows that trusted users can specify attributes for the data such as whether or not the waypoint is an obstacle that blocks the path, the waypoint proximity (the "zone" that qualifies as having arrived at the waypoint), for example 5-10 meters, 10-15 meters, 15-20 meters, and an estimated lifetime for this entry. The estimated lifetime for a data point can be a fixed duration, or can be tagged as unknown.

Regardless of whether the trusted source is visually impaired or sighted, the information they provide is then directly sent and stored on a local server and is retrieved by our app if that source is selected as a trusted source by a user of the app. Using the trusted source interface, the blind traveler can select and designate specific contacts as trusted sourced, and thereby subscribe to all their updates. This list is stored in their Android internal memory and can be edited by selecting the setting option of this interface.

VI. Use-case Scenario for Audio Breadcrumbs

In this section we demonstrate the performance of the audio breadcrumb feature of our app by narrating the performance of the app in a relevant use-case scenario. Note however that the demonstrations were carried out by sighted users at this stage. The demonstration was conducted by physically navigating with the help of our app from the Newell Simon Hall building in the Robotics Institute at Carnegie Mellon University (in Pittsburgh, PA, USA) to the Carnegie Natural History Museum which is located a few blocks away. During this traverse we tested the performance of our app focused on the feature of adding audio breadcrumbs and verifying the app performance when the user deviates from the planned route.

The demonstration began by launching the app immediately outside Newell-Simon Hall. We selected the walking as the modality of travel, and provided verbal input "Natural History Museum" to specify the desired destination. Upon confirmation of our input, the app planned the best route for this traverse, plotted this route on the map, and incorporated relevant navigation information from all relevant sources as shown in Fig. 6. The system then started the navigation guidance process and provided the estimated time and distance to the destination, followed by the first navigation instruction. As we the navigation instructions, the app demonstrated the desired behavior by waiting until we approached the next waypoint before providing the next navigation instruction.

In order to test the breadcrumb interface, we stopped along the path near a bench shaded by a tree. We then recorded

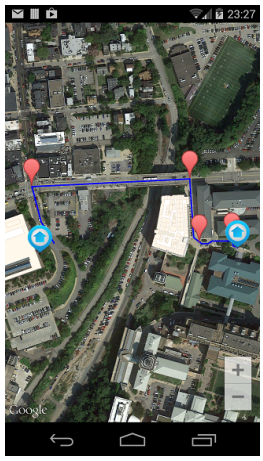

Fig. 6: Path planned connecting the origin to the destination using our app.

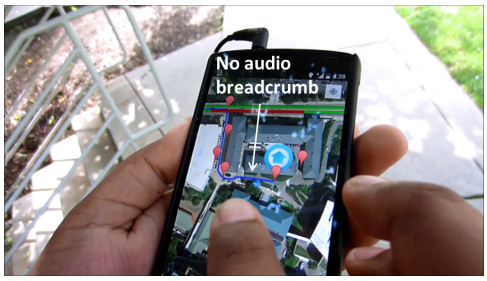

(a) Original map

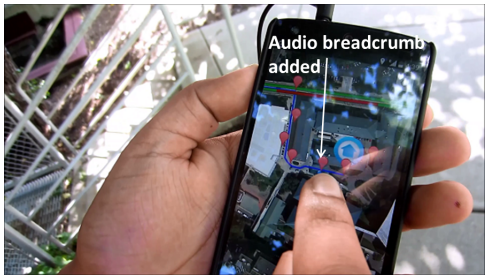

(b) Updated map

Fig. 7: Audio breadcrumb annotation - (a) The smartphone screen displaying the original map with five waypoints on the planed path; (b) The updated map with the breadcrumb added as a waypoint on the planed path

an audio breadcrumb annotation that indicated this was a good shady spot to take a seat and rest if we wished. After confirming the recorded message, the system added the audio breadcrumb as a new waypoint (shown in Fig. 7 (b)) along the originally planned route on the map (shown in Fig. 7 (a)).

To further test the performance of our app, we intentionally deviated from the recommended route near the destination waypoint. Specifically, when the system guided us to take a left turn, we intentionally took a right turn from that waypoint. The system immediately detected the deviation and provided a warning that we were moving in the wrong direction. When we continued in the incorrect direction the app asked us to stop and initiated a re-planning cycle to calculate a new route to our destination. The system re-routed after few seconds and

correctly guided us to the destination.

Finally, we further verified the functionality of the audio breadcrumb annotation by using our app to guide us back to our original location, Newell Simon Hall. Upon confirmation of the desired navigation plan, the app started instructing us to navigate back to Newell-Simon Hall. We followed the instruction to reach the intended destination. As we approached the previously added breadcrumb, the recorded data was played back. This demonstrated that the breadcrumbs interface worked as expected. A video demonstrating our app can be found at https://www.youtube.com/watch?v=h8qs86OEzxo.

VII. Use-case Scenario for Trusted Sources

In this section, similar to the previous section, we narrate the performance of our app in a relevant use-case scenario to demonstrate the performance of the app interface for trusted sources to add relevant navigation information. Similar to the previous demonstration scenario, this scenario was also executed by sighted users at this stage. In order to also show that our app performance is not location-dependent, the scenario for demonstrating the functionality of our app's interface for trusted sources was executed in Noida India. The demonstration began by physically navigating with the help of our app from the B Block Sector 26 Noida to the destination, "Kailash Healthcare Hospital" at H block sector 27. This route was chosen because a house near the destination on the route was under construction, and the sidewalk near this house was strewn with debris which could be hazardous for blind travelers. Fig. 8 shows the sites chosen for this demonstration.

When we were in the vicinity of the debris-strewn sidewalk, we launched the trusted user contribution interface and filled out attributes of the waypoint to inform blind travelers about this hazard. The first attribute was to indicate that the point of interest is not blocking the path of the user. Next, we added a waypoint proximity as 5-10 meters. Then, we recorded information for this waypoint similar to the breadcrumb approach. In this demonstration, we annotated this waypoint. The app then automatically established a connection with the local Google Application Engine (GAE) server and sent the new trusted data along with the cell phone number (CN1) which identifies the source. Next we used our app to launch a new navigation task with a second Android smartphone to demonstrate that the previously uploaded information can be correctly retrieved and played back when the navigator approaches the area. For this scenario, we pre-stored the initial phone number (CN1) as a trusted source in the contact list of the second smartphone. To add the trusted source we used speech input to select the appropriate contact from our list and tag that contact as a trusted user. Once the contact was added to the trusted source list, the app established the link with the local GAE server and retrieved information submitted by that trusted source. This in turn triggered the addition of a new waypoint on the map, which incorporated the information provided by the trusted source as shown in Fig. 9 (b). With this updated map, we started navigation and the recorded message was played back as we approached the corresponding waypoint.

(a) House under construction

(b) Debris over the sidewalk

Fig. 8: Chosen locality for demonstrating our app's interface for trusted sources to provide navigation information included (a) a house under construction and (b) a sidewalk strewn with debris which made the path hazardous for blind travelers.

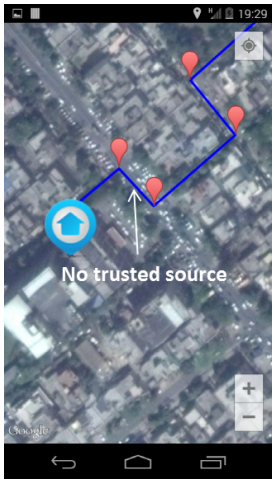

(a) Original map

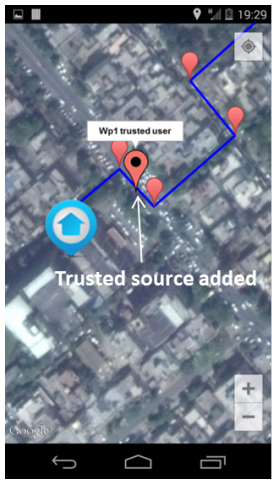

(b) Map updated with trusted source information

Fig. 9: Use-case scenario of trusted sources interface for our app - (a) shows the original map (b) shows the map updated with information from the trusted source shown as an additional waypoint

VIII. Discussion, Conclusions, and Future Work

We strive towards a vision of smarter cities that are truly accessible to everyone including people with disabilities. To realize this vision, we are developing the NavPal suite of

technology tools to empower blind and visually impaired travelers to safely and independently accomplish urban travel. In this paper we introduce two significant enhancements to the existing assistive navigation tools for this community. Namely, a mechanism for blind travelers to annotate their paths with useful information in the form of audio breadcrumbs, and a framework that allows user-designated trusted sources to provide navigation-related information that is incorporated into the route planning of the assistive tools. We developed a prototype smartphone-based navigation tool that demonstrates both of these enhancements, including a quick usability study to validate the concept and inform some aspects of the implementation. Moreover, we described detailed use-case scenarios that demonstrate the value of these enhancements.

While the demonstrated approach provides significant benefits to the target users, there are also a few limitations that must be addressed in future work. One consideration is the amount of data that the trusted sources can generate. Large amounts of data can slow down the responsiveness of the app and also could incur monetary costs depending on specific smartphone data plans. We are considering several data management strategies to address this concern. A second consideration is managing information conflicts from different trusted sources and managing information with unknown lifetimes. We can borrow strategies from the literature where a variety of technology solutions have grapples with similar issues. Other planned future work includes implementing verbosity control measures for avoiding repetitive instructions, enhancing localization accuracy, eliminating the dependence on the Google servers, and testing the app with visually impaired users.

ACKNOWLEDGMENTS

This work was sponsored by the National Science Foundation under NSF-NRI Award Number 1317989, and by the National Institute on Disability and Rehabilitation Research under the RERC-APT (grant number H133E080019). The authors also thank the participants in the user studies that informed this work, and the many members of the research team who assisted with different aspects of this work; notably Ermine Teves, Nick Hainsey, and Omar Mustardo. The Carnegie Mellon University Institutional Review Board has approved this study.

REFERENCES

[1] M. B. Dias, "NavPal: Technology Solutions for Enhancing Urban Navigation for Blind Travelers," tech. report CMU-RI-TR-21, Robotics Institute, Carnegie Mellon University, Sep. 2014.

[2] B. Kannan, N. Kothari, C. Gnegy, H. Gedaway, M. F. Dias, and M. B. Dias, "Localization, Route Planning, and Smartphone Interface for Indoor Navigation," in *Cooperative Robots and Sensor Networks*, A. Kouba and A. Khelil, Eds. Springer Berlin Heidelberg, 2014, pp. 39-59.

[3] "WHO - Visual impairment and blindness," WHO. [Online]. Available: http://www.who.int/mediacentre/factsheets/fs282/en/. [Accessed: 27-Feb-2015].

[4] "Guide Dogs of America." [Online]. Available: http://www.guidedogsofamerica.org/1/. [Accessed: 27-Feb-2015].

[5] I. Ulrich and J. Borenstein, "The GuideCane-applying mobile robot technologies to assist the visually impaired," *IEEE Transactions on Systems, Man and Cybernetics, Part A: Systems and Humans*, vol. 31, no. 2, pp. 131-136, Mar. 2001.

[6] G. Galatas, C. McMurrough, G. L. Mariottini, and F. Makedon, "eyeDog: An Assistive-guide Robot for the Visually Impaired," in *Proceedings of the 4th International Conference on PErvasive Technologies Related to Assistive Environments*, New York, NY, USA, pp. 58:1-58:8, 2011.

[7] V. Kulyukin, C. Gharpure, J. Nicholson, and G. Osborne, "Robot-assisted wayfinding for the visually impaired in structured indoor environments," *Auton Robot*, vol. 21, no. 1, pp. 29-41, Aug. 2006.

[8] P. Narasimhan, R. Gandhi, and D. Rossi, "Smartphone-based Assistive Technologies for the Blind," in *Proceedings of the 2009 International Conference on Compilers, Architecture, and Synthesis for Embedded Systems*, New York, NY, USA, 2009, pp. 223-232.

[9] N. Kothari, B. Kannan, E. D. Glasgwow, and M. B. Dias, "Robust Indoor Localization on a Commercial Smart Phone," *Procedia Computer Science*, vol. 10, pp. 1114-1120, 2012.

[10] J. A. Hesch and S. I. Roumeliotis, "An Indoor Localization Aid for the Visually Impaired," in 2007 *IEEE International Conference on Robotics and Automation*, 2007, pp. 3545-3551.

[11] A. Smith, "Nearly half of American adults are smartphone owners," *Pew Research Center's Internet & American Life Project*, 01-Mar-2012.

[12] B. Holton, "BlindSquare App for iOS: A Solution for Accessible Navigation," *AFB AccessWorld Magazine*, vol. 15, no. 7, Jul. 2014.

[13] Hend K. Gedawy, "Designing an Interface and Path Translator for a Smart Phone-Based Indoor Navigation System for Visually Impaired Users." tech. report CMU-CS-11-125, Computer Science, Carnegie Mellon University in Qatar, Dec. 2011.

[14] "An innovative app for your monility." [Online]. Available: http://www.ariadnegps.eu/. [Accessed: 27-Feb-2015].

[15] "Loadstone GPS - Free GPS Software for our Mobile Phone." [Online]. Available: http://www.loadstone-gps.com/. [Accessed: 27-Feb-2015].

[16] J. M. Coughlan and H. Shen, "Crosswatch: a System for Providing Guidance to Visually Impaired Travelers at Traffic Intersections," *J Assist Technol*, vol. 7, no. 2, Apr. 2013.

[17] J. P. Bigham, C. Jayant, H. Ji, G. Little, A. Miller, R. C. Miller, R. Miller, A. Tatarowicz, B. White, S. White, and T. Yeh, "VizWiz: Nearly Real-time Answers to Visual Questions," in *Proceedings of the 23Nd Annual ACM Symposium on User Interface Software and Technology*, New York, NY, USA, 2010, pp. 333-342.

[18] V. Kulyukin and J. Marston, "The Blind Leading the Blind: Toward Collaborative Online Route Information Management by Individuals with Visual Impairments," *AAAI Spring Symposium: Social Information Processing*, pp. 54-59, 2008.

[19] T. Völkel, R. Kühn, and G. Weber, "Mobility impaired pedestrians are not cars: Requirements for the annotation of geographical data", *ICCHP '08 Proceedings of the 11th international conference on Computers Helping People with Special Needs*, pp. 1085-1092, 2008.

[20] H. A. Karimi, B. Zimmerman, A. Ozcelik, and D. Roongpiboonsopit, "SoNavNet: a framework for social navigation networks." *Proceedings of the 2009 International Workshop on Location Based Social Networks*. ACM, pp. 81-87, 2009.

[21] S. K. Kane, J. O. Wobbrock, and R. E. Ladner. "Usable gestures for blind people: understanding preference and performance." *Proceedings of the SIGCHI Conference on Human Factors in Computing Systems*. ACM, pp. 413-422, 2011.

[22] D. McGookin, S. Brewster, and W. Jiang. "Investigating touchscreen accessibility for people with visual impairments." *Proceedings of the 5th Nordic conference on Human-computer interaction: building bridges*. ACM, pp. 298-307, 2008.

[23] J. Balata, J. Franc, Z. Mikovec, and P. Slavik, "Collaborative navigation of visually impaired," *Journal of Multimodal User Interfaces*, vol. 8, no. 2, pp. 175-185, Jun. 2014.

American International Journal of Research in Formal, Applied & Natural Sciences

Available online at http://www.iasir.net

ISSN (Print): 2328-3777, ISSN (Online): 2328-3785, ISSN (CD-ROM): 2328-3793

AIJRFANS is a refereed, indexed, peer-reviewed, multidisciplinary and open access journal published by International Association of Scientific Innovation and Research (IASIR), USA

(An Association Unifying the Sciences, Engineering, and Applied Research)

Medicinal plants, a gold mine of anticancer compounds

Asmita Das* and Jaspreet Kaur Dhanjal
Department of Biotechnology
Delhi Technological University
Shahbad Daultpur, Bawana Road, Delhi-110042, India

***Abstract**: Cancer is one of the leading causes of adult deaths worldwide. Chemotherapy, radiation therapy and surgical removal of tumors are the most common clinical approaches being used for the treatment of cancer. Today, there are more than 100 FDA approved drugs in the markets for cancer therapy. Unfortunately, the chemotherapy treatment is almost always accompanied by a varied range of short and long term adverse effects. Also the cancerous cells evolve and develop resistance against these drugs during the course of treatment to escape the process of cell death and sustain their survival. Hence, the need arises to explicate the various molecular mechanisms which get altered and support the survival of transformed cells. This would help us find novel targets highly specific to tumor cells and design drugs against them. Since natural compounds offer a potentially infinite source of chemical diversity which cannot be matched by any synthetic chemical collection or combinatorial chemistry approach, we have here discussed various possible molecular mechanisms underlying the cause of cancer and the role of various medicinal plants with anti-proliferative and chemopreventive activity.*

***Keywords**: Natural compound, cancer, anticancer, antiproliferative, chemopreventive, molecular target*

I. Introduction

Cancer is an umbrella term used to describe a variety of diseases in which cells start dividing abnormally. These cells then spread through blood and lymph system to invade other tissues of the body. There exist more than 100 different types of cancer. Depending upon the site of origin, cancer can be grouped as carcinoma (starting in the skin or tissue lining of internal organs), sarcoma (cancer of connective and supportive tissue), leukemia (staring in the blood forming tissue), lymphoma or myeloma (beginning in the immune cells) and central nervous system cancer (originating in brain or spinal cord) [1].

Cancer is one of the leading causes of adult deaths worldwide. One in every four deaths in United States is due to cancer. American Cancer Society projected an estimate of about 1,638,910 new cancer cases and 577,190 deaths from cancer in US for the year 2012. Prostate cancer is the most prevalent one among the males whereas in females breast cancer tops the chart [2]. In India the most common fatal cancers include oral, stomach and lung cancer in males and cervical, stomach and breast cancer in females [3].

The effective therapies for completely removing the cause of cancer are not yet available but efficient measures can be taken to control the growth of cancer. The traditional treatment options available for controlling cancer include chemotherapy, radiation therapy, childhood hematopoietic cell transplantation, bone marrow transplantation, surgical procedures and biological therapies for cancer. The newer technologies include hyperthermia, photodynamic therapy, gene therapy and targeted cancer therapies [1].

Chemotherapy (also described by the terms antineoplastic or cytotoxitic therapy) is a treatment that involves the use of drugs for destroying the transformed cells or slowing the growth of rapidly dividing cancerous cells. Unlike radiation and surgery, which are considered to be local treatments, chemotherapy has a systemic effect as the drug enters the circulation to encounter the cancer cells wherever they are present. More than 100 FDA approved drugs are available today to be used for the treatment of cancer. But most of the drugs have some side effects associated with their long term administration which limits their use. For example, alkylating agents used to treat various cancers including leukemia, sarcoma, multiple myloma, lymphoma, breast cancer, etc. can cause long term damage to bone marrow eventually leading to acute leukemia. Alkyl sulfonates, Triazines, Ethylenimines and Nitrosoureas are some families of drugs which belong to this category. The use of high dosages of antitumor antibiotics, another group of drugs that interfere with the enzymes essential for the process of DNA replication may cause permanent damage to the heart. Daunorubicin, Doxorubicin (Adriamycin®), Actinomycin-D and Mitomycin-C are some of the prominent antitumor antibiotics being used. Specific topoisomerase inhibitors including topotecan, irinotecan (CPT-11), etoposide (VP-16) and teniposide are also being used for the treatment of certain leukemias along with many other cancers like lung, gastrointestinal and

ovarian. Administration of inhibitors targeting topoisomerase II increases the chances of acute myelogenous leukemia (AML). This secondary leukemia may arise within 2-3 years from the time of administration. Antimitotic agents targeting the cell cycle may lead to peripheral nerve damage. Examples include Taxanes, Epothilones and vinorelbine (Navelbine®) [4].

Along with the drug specific side effect, chemotherapy is almost always accompanied by a varied range of adverse effects. Normal cells of the body which divide more rapidly like bone marrow/blood cells, cells comprising the hair follicles and the ones lining the reproductive tract and digestive tract are most likely to get damaged. The other common side effects include low RBC, WBC and platelet count, nausea and vomiting, appetite loss, constipation, diarrhea, mouth or throat sores, fatigue, heart damage, reproductive and sexual problems, damage to liver, kidney, urinary system, and much more. Permanent damage to organs, delay in development of children, nervous damage, elevated risk of secondary cancer are some of the long term adverse effects associated with the administration of these drugs [4].

Owing to the severe side effects associated with the use of these chemotherapeutic agents, the focus of the ongoing research is shifting from the drugs which have a systemic effect on the body to the therapies targeting molecules which either over express or differentially express in specific tumor or cancer cells and hence use the therapies which differentiate cancerous cells from normal cells of healthy tissues. Since these are more target specific, they often have lesser side effects as compared to the conventional chemotherapy drugs. Examples of targeted therapies include gefitinib (Iressa®), sunitinib (Sutent®), imatinib (Gleevec®) and bortezomib (Velcade®). Estrogen receptor became the first molecule of interest for molecular targeted therapy. Selective estrogen modulators (SEMs) including tamoxifen and toremifene (Fareston®) interfere with the binding of estrogen to its receptor (in ER-positive breast cancer cells) thus making it an effective approach to retard cancerous growth and proliferation. Other potential biomolecules for targeted therapies include aromatases, tyrosine kinases, serine/threonine kinases, growth factor receptors and many more enzymes which are specific for cancer cells or tissues [4].

Hormonal and immunotherapy are two more options available for cancer treatment. Hormonal therapy is generally used for the treatment of breast, prostate, and endometrial (uterine) cancers, which show growth in response to hormones found in the body. Hormonal therapy makes use of sex hormones or hormone like drugs to either prevents the body from producing the hormone or prevents the cancer cells from using the synthesized hormone. Leuprolide (Lupron®), bicalutamide (Casodex®), megestrol acetate (Megace®) and exemestane (Aromasin®) are some of the drugs which best fall in this category. Immunotherapy uses drugs which stimulate the natural immune system of a patient to recognize and attack the transformed cells. It uses two approaches: potentiating the body's own immune system (Active Immunotherapy) or using *ex vivo* created immune system components to be inserted into the patient's body to strengthen its defense mechanism (Passive Immunotherapy). Monoclonal antibody therapy such as rituximab (Rituxan®) and alemtuzumab (Campath®), Immunomodulatory drugs like thalidomide and lenalidomide (Revlimid®), the first FDA approved cancer vaccine, the Provenge® (in 2010), for instance are the examples for this group of drugs [4].

Cancer is a very active area of research. Since most of the proposed synthetic inhibitors fail to clear preclinical or clinical trial because of the drug related or drug induced toxicities, the need arises for finding natural products or their derivatives having the potential to act as inhibitors against the cancer molecular targets. Most of the natural products follow the lipinski's rule of five. Even the exceptions with high molecular weight, rotatable bonds and more stereogenic centers retain relatively low log P values. Thus, these have a higher tendency to get absorbed as compared to the conventional synthetic drugs. With the availability of more number of chiral centers [5] along with a wider distribution of molecular attributes like octanol-water partition coefficient, molecular mass and diversity of ring system, make natural products more suitable to be used as drugs [6]. Thus this review summarizes the experimental evidences of plant products being helpful in the treatment of cancer.

II. Plant Products Affecting the Molecular Basis for Cancer, the Key to New Age Cancer Therapy

The knowledge about molecular mechanism of cancer initiation, progression andmetastasis is increasing rapidly. Different signaling pathways, transcription and translationregulating factors and post-translational modification state of proteins can be developed intotherapeutic targets to treat cancer. Here we will explore various processes involved intumorogenesis and discuss about the plants with antitumor and anticancer activity.

A. Enhancement of persistent oxidative stress in cancer cells

Reactive oxygen species can be used to understand the biology of malignant neoplasia. A free radical contains unpaired electrons which either donate their electrons or accept electrons from other biological molecules of the cell in order to pair and attain a more stabilized state. This results in the initiation of a chain reaction which causes severe damage to the adjacent biological structures. Cell uses the mechanism of antioxidation to protect itself from this oxidative stress [7]. The transformed cells experience a persistent and slightly higher oxidative stress as compared to the neighboring healthy cells. There are evidences to support both the facts, firstly, that the cancer cells produce large amounts of ROS resulting in excessive oxidative stress [8] and secondly, that the natural antioxidant system of the cell gets suppressed [9, 10].

Despite the fact that the cancer cells experience more oxidative stress than the non-neoplastic cells, the stress is not sufficient to cause the cell death. These cells develop other mechanisms to combat this stress. This importunate oxidative stress provides advantage to the cancerous cells for their survival and to escape the apoptosis mechanism. It allows the constitutive activation of certain transcription factors like NF-κB and induces expression of proto-oncogenes like *c-jun, c-foc* and *c-myc*. It also causes DNA damage with modification in the base, further leading to mutations and chromosomal aberrations resulting in genome instability. Activation of cancer specific antioxidant system makes the cancer cells resistant to many chemotherapeutic agents being used for the treatment. Enhanced activity of the proteases due to the inactivation of their inhibitors, also facilitate tumor invasion and metastasis [11].

In a study conducted by Jahangir T. and Sultana S. in 2007, rats with induced renal carcinogenesis were orally administered with *Adhatoda vasica*. A significant decrease was observed in lipid peroxidation, H_2O_2 generation, xanthine oxidase (XO), blood urea nitrogen, serum creatinine, renal ODC activity and DNA synthesis leading to reduced incidence of tumors. Thus it was shown that *A. vasica* can be used as a chemopreventive agent as it reduces hyperproliferative response and carcinogenic activity induced because of Fe-NTA [12]. Many different studies report that extracts from *Aegle marmelos* ameliorate the chemical induced carcinogenesis by enhancing the antioxidant defense system. Oral administration of *A. maemelos* significantly elevates the amount of superoxide dismutase, catalase, glutathione, and vitamin C in AME-treated groups in comparison to the carcinogen-treated control [13-17]. *Aloe vera* is another promising source for chemopreventive drugs of plant origin. Saini M et al. showed that oral administration of *Aloe vera* protects the mice against skin papilloma due to the presence of various antioxidant enzymes, vitamins, minerals and polysaccharides in high concentration [18, 19]. The prophylactic effect of Aloctin I, the main lectin present in *Aloe vera* was also assayed by another group of scientists. They showed that pretreatment with the lectin regressed the tumor size probably because of its immunomodulatory activity [20]. *Alstonia scholaris*, commonly called sapthaparna was also investigated for its chemopreventive and anti-oxidant properties. On treatment with the bark extract of the plant, there was an increase in the level of reduced glutathione, superoxide dismutase and catalase along with significant decrease in lipid peroxidation. This resulted in reduced tumors with decrease in cumulative number of papillomas in carcinogen treated mice [21-23]. Inhibiting the generation of H_2O_2 in tumor cells is another way of controlling the adverse effects of oxidative stress in the transformed cells. According to a report, experiments with diacetylenic spiroketal enol ether epoxide AL-1 from *Artemisia lactiflora* in mouse with TPA-induced intracellular peroxide formation shows considerable dwindling in the tumor incidences and tumor induced biological responses. This antioxidant property of *A. lactiflora* might be attributable to the inhibition of O^{2-} generation [24]. Several *in vitro* experiments and studies on animal model suggest the efficacy of tea (*Camellia sinensis*) in the chemoprevention of cancer [25-28]. Consumption of black tea has been shown to notably decrease the micronuclei frequency and chromosomal aberrations in patients suffering from oral precancerous lesions [29]. Hossain E et al. in 2012 used the methanol extract of *Dregea volubilis* leaves to treat tumors in EAC cell lines and EAC tumor-bearing mice. They showed a decrease in tumor volume with an increase in the non-viable cell count in the infected animal model. Thus it exhibited both in vitro and in vivo antitumor activity through augmentation of antioxidant defense system of the body [30]. The seeds of *Glycine max* also emcompass some chemomodulatary potential against skin and cervical papillomas. The preventive action against the cancer is due to alteration in the levels of detoxifying and antioxidative enzymes [31]. Oral administration of ethanol extract from *Indigofera aspalathoides* in tumor bearing rats revealed a significant decrease in the levels of different enzymes- glutamate pyruvate transaminase, glutamate oxaloacetate transaminase, alkaline phosphatase, total bilirubin, gamma glutamate transpeptidase, lipid peroxidase, glutathione peroxidase and glutathione S-transferase with a simultaneous increase in superoxide dismutase and catalase levels [32, 33]. The affect of methanolic extract of *Operculina turpethum* stems on 7,12-dimethylbenz(a)anthracene induced breast cancer was investigated by Anbuselvam C et al. in female Sprague-Dawley rats. Reduce tumor weight as a consequence of low lipid peroxidation activity and increased levels of antioxidant enzymes was observed, thereby indicating its role in the protection against breast cancer [34]. *Picrorhiza kurroa*, a well known traditional herb possess a diverse set of therapeutic potentials including antioxidant and anti-neoplastic activity [35].

B. Targeting the mitochondrial stress pathway or intrinsic cell death

Many chemotherapeutic agents destroy the cancerous cells by inducing the process of apoptosis in them. The different apoptotic signaling pathways ultimately lead to mitochondrial membrane permeabilization (MMP). Involving many direct and indirect mechanisms, the intrinsic cell death or stress pathway to a maximum extent is regulated by the proteins of Bcl-2 protein family. The pro-apoptotic members of this family which include Bax, Bid, Bad, Bim, Bmf, BNIP3, NoxA, Puma translocate from the cytosol of the cell to the mitochondria and dissipate the membrane potential. In response to this change in membrane potential a number of soluble apoptogenic proteins from the intermembrane space of the mitochondria get released into the cytosol. These lethal proteins include cytochrome c, Smac/DIABLO, Htra2/Omi, AIF and endonuclease G. These in turn activate the maturation process or proteolytic cleavage of zymogens (pro-caspases) for the activation of caspases cascade. Because of this membrane permeabilization, mitochondrion loses its important metabolic and redox functions,

inner transmembrane potential and its capacity to act as Ca^{2+} storage organelle. As a consequence, the oxidative stress progressively increases and the ATP production decreases, eventually leading to the death of the cell. To keep a check on the pro-apoptotic signal transduction, a number of different proteins called anti-apoptotic proteins and metabolites are employed to locally protect the mitochondria from apoptotic events. Bcl and Bcl-X_L, the two MMP inhibitors have been reported to block the Voltage-dependent anion channels which are the prime source for release of cytochrome c from the intermembrane space into the cytosol. Figure 1 illustrates the mitochondrial cell death pathway. Thus, impairment in the balance between pro-apoptotic and anti-apoptotic proteins may result in cells with potential to divide infinitely, giving rise to a cancerous state [36].

Figure 1: Schematic representation of mitochondrial cell death pathway.

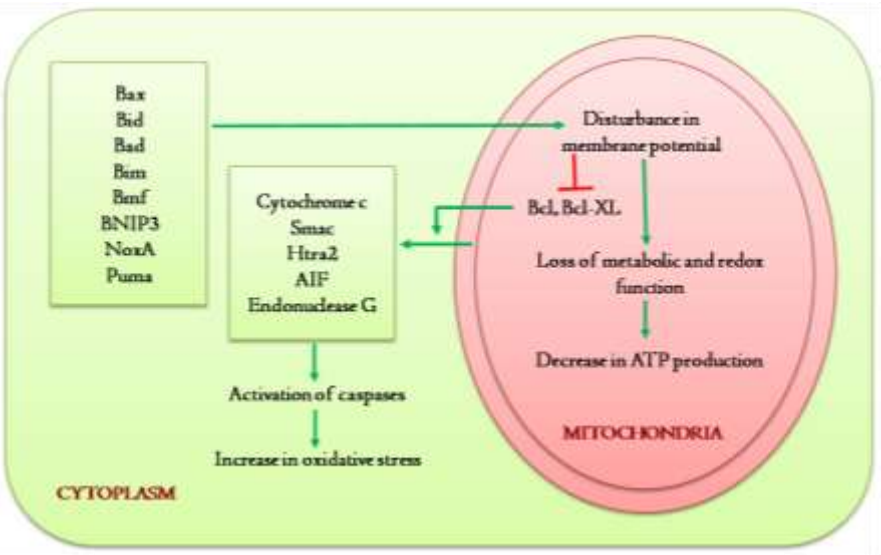

There are many medicinal plants which alter the changes that occur in the cancerous cells thereby inducing apoptosis to kill them. *Dianthus chinensis L.* is being used to treat many diseases including cancer. Nho et al. in 2012 investigated the molecular mechanism by which the ethanolic extract of this plant inhibit cell growth. He found that it selectively downregulates the anti-apoptotic proteins without altering the expression of Bax protein. Increase in the ratio of bax:bcl-2 and bax:bcl-xl leads to the activation of caspases [37]. *Panax ginseng*, another medicinal plant shows similar kind of activity. Increase in the expression of anti-apoptotic genes as a result of carcinogenic exposure got suppressed; initiating the process of apoptosis [38]. Maslinic acid is a triterpene present in high amounts in *Olea europea*. It has the potential to be used as a tumor suppressant as it was shown to induce apoptosis in the HT29 and Caco-2 colon-cancer cell lines via disturbance in the mitochondrial membrane potential with increase in the expression of Bid and Bax and decrease in the level of Bcl-2. Release of cytochrome c was characterized by the increased activity of caspases-3 [39-41]. *Betula platyphylla* is another potential anticancer plant. It shows significant radical scavenging activity and increase in cell viability against H_2O_2 along with increase in the expression of pro-apoptotic protein, Bax, thereby activating caspases-3 [42]. Some polysaccharides from *Patrinia heterophylla* could also inhibit tumor growth and induce tumor cell apoptosis by increasing the expression of p53, Bax and down regulating the expression of Bcl-2 [43].

C. Modulation of cell cycle regulators for cancer therapy

Cancer is often considered to be a disorder of impaired cell cycle. Mammalian cell cycle consists of four phases. In S phase, the cell forms a copy of its own genetic material and in M phase, the cellular components are partitioned into two daughter cells. During G1 and G2 phase the cell prepares itself and synthesises the components required for the successful completion of S and M phase respectively. In the absence of adequate mitogenic stimuli or if the cell has reached the state of terminal differentiation, it enters a non-dividing state known as G0. As soon as a cell encounters mitogenic signals, it progresses towards the G1 phase. There is a specific event in G1 phase, called Restriction Point (R), after which the cell proliferates independently of the mitogenic signals. R prevents the cell from getting through the other phases of cell cycle until it has accumulated a certain threshold of mitogen induced events. It represents a point of no return that commits cell to enter a new round of cell division. Thus there are several checkpoints which ensure that the cell does not progress to a new phase until it has completed the previous one [44].

Cyclin Dependent Kinases (CDKs), a group of serine/threonine kinases are the important factors which control the early events of the cell cycle. They form active heterodimeric complexes with their regulatory subunits, the cyclins. CDK4 and CDK6 are believed to drive cell through early G1 phase whereas CDK2 is required for the completion of G1 phase and intiation of S phase. CDK4 and CDK6 bind with D type cyclins to form active complexes while CDK2 get activated by E type cyclins in G1/S transition and A type cyclins during the

succession of S phase. CDK3 is also important in cell cycle regulation but its role is still ambiguous. These activated heterodimeric complexes act on the members of retinoblastoma protein family (including RB, p107, p130). These serve as docking sites for a variety of proteins whose function needs to be regulated tightly throughout the process of cell proliferation. RB proteins remain in bound state with E2F family of transcription factors to ensure that they remain in inactive state during M and G0 phase. The activated CDK4/6-cyclin-D complexes partially phosphorylate the RB of RB-E2F-DP complex. It enables the transcription of some genes like cyclin E. Cyclin E then pairs with CDK2 and completely phosphorylates the RB protein. This process induces the expression of E2F responsive genes that help the cell to enter S phase and initiate DNA replication. The level of CDK activity is negatively controlled by CDK kinase inhibitors. These are of two types. The INK4 family including INK4A (p16), INK4B (p15), INK4C (p18) and INK4D (p19) prevent the association of CDK4 and CDK6 to D-type cyclins thus inhibiting their activity. The three CDK inhibitors of WAF/KIP family- WAF1 (p21), KIP1 (p27) and KIP2 (p57) form heterotimeric complexes with various CDKs, mainly CDK2-cyclin-E thereby inhibiting their kinase activity [44]. Figure 2 shows the schematic representation of these important checkpoints of cell cycle that may serve as potential targets for controlling the dysregulated cell division in cancerous state.

Figure 2: Schematic representation of the cell cycle along with its important regulators

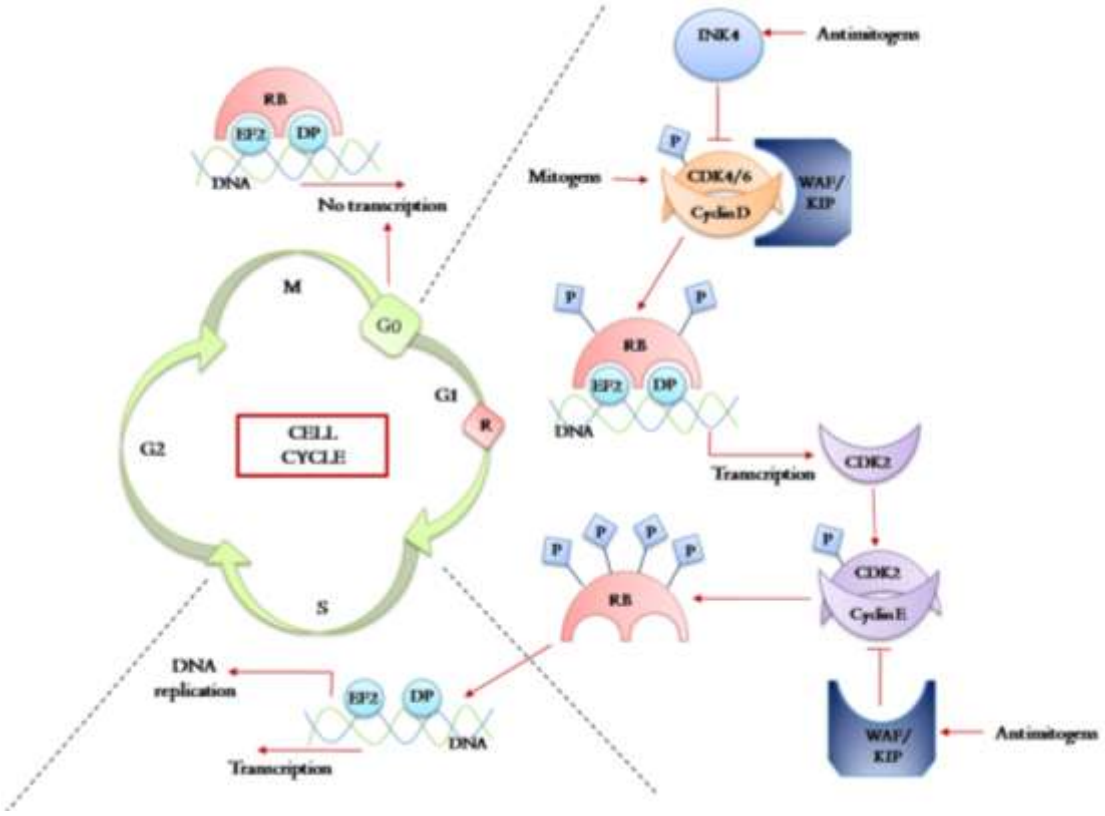

Cheng et al. in 2004 reported that the acetone extract of *Angelica sinensis* inhibits the proliferation of human cancer cells by inducing G1/S arrest and decreasing the levels of CDK4 protein, thereby activating the mechanism of apoptosis [45]. Chemopreventive and anti-cancer properties of the aqueous extract of flowers of *Butea monosperma* were investigated by G. Mathan and his colleagues. They found that treatment with this aqueous extract stimulated apoptotic cell death by accumulating cells in G1 phase which was then accompanied by decrease in the level of activated Erk1/2 and SAPK/JNK [46]. Salograviolide A, a bioactive molecule isolated from *Centaurea ainetensis* reduces the growth of colon cancer by increasing the preG1 phase which causes apoptosis, increases the Bax/Bcl-2 ratio, p53 and p21 protein levels and reduces cyclin B1 proteins [47, 48]. A family of natural products, Flavaglines from the genus *Aglaia* exhibit anti-cancer activity *by* inhibiting translation initiation. Silvestrol, one of the flavaglines, was shown to modulate the activity of eIF4A, a subunit of the eukaryotic initiation factor (eIF) 4F complex that stimulates recruitment of ribosome during translation initiation [49]. Two new bibenzyls, designated as combretastatins B-3 and B-4 where isolated from *Combretum caffrum*. It was observed that these bibenzyls possess activity against the protein tubulin which is the major component of the mitotic spindles [50]. Another chemical constituent of *Nothapodytes foetida*, 9-Methoxycamptothecin was found to have antitumour activity through topoisomerase inhibition [51]. Cell cycle analysis after treating a tumor bearing mice with a polysaccharide isolated from *Patrinia heterophylla* showed that G2/M phase specific tumor cells were accumulating and there was a relative decrease in the number of tumor cells in S phase. It was inferred

that this polysaccharide could inhibit tumor growth by inducing apoptosis [43]. Elevating the levels of CDK inhibitors is another effective approach to arrest cell cycle. *Curcuma longa Linn* was found to have beneficial effects on the early and late stages of pathogenesis by upregulating the p21 and p57 protein level, thus preventing and delaying carcinogenesis [52, 53]. A protein from *Nidus vespae* could also arrest the cell cycle at stage G1 and inhibit the mRNA expression of cyclin B, cyclin D1 and cyclin E. It suppressed cdk2 expression, but increased p27 and p21 protein expression, thus promoting apoptosis and hence has been identified as a potential drug for cancer treatment [54].

D. Activation of body's own immune system against transformed cells

NK cells are a part of the innate immune system which play a vital role in defense against pathogen infected or transformed cells. It was shown that NK cells effectively eliminate tumor cells from the circulation in mice and rats and also spontaneously kill MHC-I deficient tumor cells. Tumor cells are believed to evade T-cell response by downregulating the expression of MHC-I molecules on their surface. NK cells possess two types of receptors-activating and inhibitory. The activity of these immune cells is regulated by a balance between activating and inhibitory signals (figure 3). The ligand for inhibitory receptors are MHC-I molecules. Lack of MHC-I expression, which is very frequently observed in cancerous cells, makes them sensitive to NK cells mediated cytotoxicity. In the absence of these inhibitory signals, activating receptors of NK cells recognize stress induced ligands being expressed on the cell surface of tumors. Thus, finding ways to stimulate these cells of innate immune system have proved to be effective means of cancer therapy [55].

Figure 3: A balance between the activity of activating and Inhibitory receptors regulate the function of NK cells

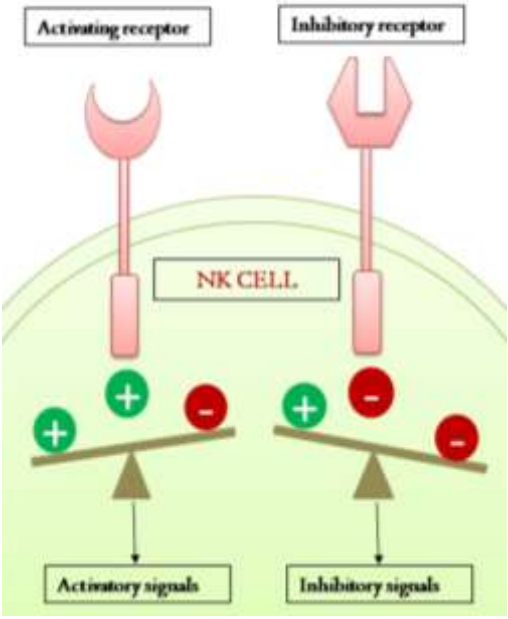

Agrimoniin, tannin contained in *Agrimonia pilosa* has the potential to augment the activity of NK cell in tumor cells. Increase in cytostatic activity and induction of antibody-dependent cell lysis were observed [56]. The sympathetic nerve of spleen has a suppressive effect on local natural killer (NK) cytotoxicity. Extract from *Lentinus edodes* was found to inhibit tumor proliferation by affecting the splenic sympathetic nerve activity [57].

E. Fatty acid synthase, a potential therapeutic target in cancer

Fatty acid synthase (FASN) is an important enzyme that performs lipogenesis in neoplastic tissues. Cancer or tumor cells require more energy for the rapid proliferation of cells. The glucose uptake increases leading to higher production of pyruvate via glycolytic pathway. This pyruvate is utilized to generate more ATP using Krebs cycle. The intermediate product, acetyl-CoA acts as a substrate for FASN enzyme. Lipogenesis leads to the production of long-chain fatty acids from acetyl-CoA and malonyl-CoA. Most of the normal cells have a low expression of FASN, which is tightly regulated by diet, hormones and growth factors. To meet the energy and lipid demands of highly proliferating cells for membrane synthesis, β-oxidation and lipid modification of proteins, they start *de novo* synthesis of fatty acids, thereof showing high expression of FASN. Many studies report an important role of FASN in tumor growth and survival. Knockdown or inhibition of this enzyme results in apoptosis of cancerous cells. It is believed that the selective anti tumor activity of FASN inhibitors might be due to the accumulation of toxic intermediate metabolites leading to cytostatic and cytotoxic effects. It has also been proposed that the over expression of FASN makes cells resistant to many chemotherapeutic agents. Thus, FASN blockage represents an attractive strategy for cancer treatment [58].

A series of compounds consisting of cylphloroglucinol derivatives, extracted from the rhizomes of *Dryopteris crassirhizoma*, has been reported to possess fatty acid synthase inhibitory activity [59].

F. Inhibiting overexpressed tyrosine kinases for cancer treatment

Tyrosine kinases (TKs) are key players involved in the modulation of growth factor signals. These enzymes transfer ϒ phosphate group from adenosine triphosphate to the target proteins and regulate a variety of cellular processes. Hyperactivation of these enzymes can cause increased cell growth and proliferation, induce antiapoptotic effect and promote angiogenesis and metastasis. Overexpression TKs like BCR-ABL, epidermal growth factor receptor (ErbB/HER) family members (EGFR), vascular endothelial growth factor receptors (VEGF), and platelet-derived growth factor (PDGF) receptors has been observed in various forms of cancer [60]. BCR-ABL, a fusion protein, is found to be constitutively expressed in many cases of chronic mylegenous leukemia and acute lymphoblastic leukemia. It dysregulates intracellular signaling with enhancement in proliferative capability and induction of resistance to apoptosis of hematopoietic stem or progenitor cells, which ultimately leads to a immense increase in number of myeloid cells [60, 61]. The transmembrane EGFR activates various downstream signaling pathways like Ras/Raf mitogen-activated protein kinase pathway and the phosphoinositol 3'-kinase/Akt pathway. Various neoplastic processes like cell cycle progression, inhibition of apoptosis, tumor cell motility, invasion and metastasis are under the control of these proteins. It also further activates vascular endothelial growth factor, a primary inducer of angiogenesis[60]. Angiogenesis is a process that remodels the existing network of blood vessels. VEGF is secreted by almost all the solid tumors [60]. Interaction of PDGF with their respective tyrosine kinase receptors: PDGFR α and β, induces cell proliferation, cell growth and differentiation. Hyperactivation of these kinases generate excess mitotic signals, transforming the normal cells to transformed cells which results in solid tumors [60].

Anti tumor activity conferred by the extract of flesh fruit of *Phaleria macrocarpa* was attributed to downregulation of a number of proteins at mRNA level which also included Vascular Endothelial Growth Factor Tyrosine Kinase, the primary angiogenesis inducer. It also significantly reduced phosphoinositide-3 (PI3)-kinase/protein kinase B (AKT) signalling with control at PI3K transcript level followed by reduction in phosphorylation of AKT. [62]. The Akt pathway/insulin like growth factor 1 receptor downstream to the activation of Epidermal Growth Factor Receptor Tyrosine Kinase was found to be downregulated byGinsenoside Rp1 from *Panax ginseng*, thus exhibiting anti-cancer activity [63].

G. Targeting mTOR having an expanding role in the pathogenesis of cancer

The mammalian target for rapamycin (mTOR) is a serine-threonine kinase that controls both cell growth and cell cycle progression. It helps the cell to respond to its changing environment and adjust accordingly. It helps the cell to grow by directly acting on the cell cycle regulators, maintaining the supply of nutrients into the cell by overproduction of nutrient transporters and promotion of angiogenesis. It primarily controls the synthesis of cyclin D1. It also increases the expression of hypoxia-inducible factor-1(HIF1) which further helps in transcription of hypoxia stress responsive genes, including various angiogenesis growth factors. The increase in nutrient transporter proteins as a consequence of mTOR activation results in greater uptake of amino acids, glucose and other nutrients which support the abnormal growth of the cells. It also helps the rapidly dividing cells to survive by activating the anti-apoptotic proteins. There are many evidences that show deregulated mTOR pathway in a number of cancers, anticipating it to be a potential target of high therapeutic value for cancer therapy [64].

Gallic acid, a natural antioxidant isolated from the fruits of *Phaleria macrocarpa* was shown to have the potential to induce apoptosis selectively in esophageal cancer cells. It resulted in downregulation of mTOR pathway, with decrease in anti-apoptosis proteins such as Bcl-2 and Xiap, increase in pro-apoptosis protein Bax, and stimulation of caspase-cascade activity in cancer cells, suggesting it to be a powerful anticancer agent [65].

H. Upregulation of p53 for controlling some specific cancers

p53 is a transcription factor which regulates the expression of many genes and microRNAs in response to cellular stress. It performs a variety of biological functions like regulation of the cell cycle, cellular differentiation, the immune response, apoptosis, senescence, DNA metabolism and angiogenesis. The main function of p53 is to act as a tumor suppressor by blocking the cell cycle progression and inducing apoptosis in stressed cells (such as in response to DNA damage). It has been observed that almost all cancers show altered p53 activity. Impairment in the p53 activity is associated with accumulation of DNA damage in the cells leading to genomic instability, a phenotype particular to cancer. Thus the concept of restoring the lost activity of p53 is an attractive approach for cancer therapy. Efficient tumor regression was observed in experimental animal models upon reactivation and modulation of wild type p53 [66].

Oldenlandia diffusa is a well-known medicinal plant being used to prevent and treat many disorders. Ursolic and oleanolic acids are the two bioactive components responsible for its antiproliferative property. These were shown to upregulate the expression of p53 protein by increased the binding of ERα/Sp1 complex to the p53 promoter region and selectively inhibiting cellular growth in ERα-positive breast cancer cells [67]. Another study reveals the proapoptotic effects of Eupatilin, an active flavones derived from *Artemisia asiatica*on human gastric cancer cells. It was found that eupatilin treatment resulted in elevated expression of p53, followed by inactivation of ERK1/2 and Akt [68]. Elevated p53 expression levels were also observed in colon-derived cancer cells upon treatment with the extracts *Centaurea ainetensis*, containing salograviolide A as the bioactive molecule [47].

Ginkgo biloba and *Patrinia heterophylla* are other examples of plants believed to have similar kind of properties with clinical significance [43, 69].

III. Conclusion

Cancer being a major global health problem has become an important and highly activearea of research. Because of overlapping nature of the underlying molecular mechanisms there isan urgent need for more work to untangle the signaling networks and focus on their tightlycontrolled regulation process by which they regulate cellular growth and proliferation. Thisknowledge would further facilitate the development of new approach towards treatment ofcancer. The new age therapy focuses on a high specificity towards tumors or cancerous cells,thus providing a broader therapeutic window with less toxicity to healthy bystander cells. Thenew targeted therapies in combination with traditional treatment methods can produce additive orsynergistic cancer therapy. We have seen that plant derived products play an important role intreatment of cancer, but only a small part of fauna has been explored for its therapeutic value.Many plant products or naturally occurring compounds are effective as targeted therapy orimmune potentiation that has the inherent capability to distinguish between tumor cells andhealthy cells. Thus, plants are expected to provide a potential gold mine of bioactive compoundsfor the development of new drugs to combat cancer.

IV. References

[1] J. Wu, K. Kandavelou, and S. Chandrasegaran, "Custom-designed zinc finger nucleases: what is next?," Cell Mol Life Sci, vol. 64, pp. 2933-44, Nov 2007.

[2] R. Siegel, D. Naishadham, and A. Jemal, "Cancer statistics, 2012," CA Cancer J Clin, vol. 62, pp. 10-29, Jan-Feb 2012.

[3] R. Dikshit, P. C. Gupta, C. Ramasundarahettige, V. Gajalakshmi, L. Aleksandrowicz, R. Badwe, R. Kumar, S. Roy, W. Suraweera, F. Bray, M. Mallath, P. K. Singh, D. N. Sinha, A. S. Shet, H. Gelband, and P. Jha, "Cancer mortality in India: a nationally representative survey," Lancet, vol. 379, pp. 1807-16, May 12 2012.

[4] American_Cancer_Society, "Chemotherapy Principles: An Indepth Discussion of the Techniques and Its Role in Cancer Treatment," American Cancer Society2011.

[5] M. Feher and J. M. Schmidt, "Property distributions: differences between drugs, natural products, and molecules from combinatorial chemistry," J Chem Inf Comput Sci, vol. 43, pp. 218-27, Jan-Feb 2003.

[6] M. L. Lee and G. Schneider, "Scaffold architecture and pharmacophoric properties of natural products and trade drugs: application in the design of natural product-based combinatorial libraries," J Comb Chem, vol. 3, pp. 284-9, May-Jun 2001.

[7] G. Bounous and J. H. Molson, "The antioxidant system," Anticancer Res, vol. 23, pp. 1411-5, Mar-Apr 2003.

[8] T. P. Szatrowski and C. F. Nathan, "Production of large amounts of hydrogen peroxide by human tumor cells," Cancer Res, vol. 51, pp. 794-8, Feb 1 1991.

[9] K. Sato, K. Ito, H. Kohara, Y. Yamaguchi, K. Adachi, and H. Endo, "Negative regulation of catalase gene expression in hepatoma cells," Mol Cell Biol, vol. 12, pp. 2525-33, Jun 1992.

[10] Y. Sun, "Free radicals, antioxidant enzymes, and carcinogenesis," Free Radic Biol Med, vol. 8, pp. 583-99, 1990.

[11] S. Toyokuni, K. Okamoto, J. Yodoi, and H. Hiai, "Persistent oxidative stress in cancer," FEBS Lett, vol. 358, pp. 1-3, Jan 16 1995.

[12] T. Jahangir and S. Sultana, "Tumor Promotion and Oxidative Stress in Ferric Nitrilotriacetate-Mediated Renal Carcinogenesis: Protection by Adhatoda vasica," Toxicol Mech Methods, vol. 17, pp. 421-30, 2007.

[13] A. Agrawal, S. Jahan, D. Soyal, E. Goyal, and P. K. Goyal, "Amelioration of chemical-induced skin carcinogenesis by Aegle marmelos, an Indian medicinal plant, fruit extract," Integr Cancer Ther, vol. 11, pp. 257-66, Sep 2012.

[14] T. H. Khan and S. Sultana, "Effect of Aegle marmelos on DEN initiated and 2-AAF promoted hepatocarcinogenesis: a chemopreventive study," Toxicol Mech Methods, vol. 21, pp. 453-62, Jul 2011.

[15] A. Agrawal, P. Verma, and P. K. Goyal, "Chemomodulatory effects of Aegle marmelos against DMBA-induced skin tumorigenesis in Swiss albino mice," Asian Pac J Cancer Prev, vol. 11, pp. 1311-4, 2010.

[16] G. C. Jagetia, P. Venkatesh, and M. S. Baliga, "Aegle marmelos (L.) Correa inhibits the proliferation of transplanted Ehrlich ascites carcinoma in mice," Biol Pharm Bull, vol. 28, pp. 58-64, Jan 2005.

[17] V. Chockalingam, S. S. Kadali, and P. Gnanasambantham, "Antiproliferative and antioxidant activity of Aegle marmelos (Linn.) leaves in Dalton's Lymphoma Ascites transplanted mice," Indian J Pharmacol, vol. 44, pp. 225-9, Mar 2012.

[18] M. Saini, P. K. Goyal, and G. Chaudhary, "Anti-tumor activity of Aloe vera against DMBA/croton oil-induced skin papillomagenesis in Swiss albino mice," J Environ Pathol Toxicol Oncol, vol. 29, pp. 127-35, 2010.

[19] G. Chaudhary, M. R. Saini, and P. K. Goyal, "Chemopreventive potential of Aloe vera against 7,12-dimethylbenz(a)anthracene induced skin papillomagenesis in mice," Integr Cancer Ther, vol. 6, pp. 405-12, Dec 2007.

[20] N. Akev, G. Turkay, A. Can, A. Gurel, F. Yildiz, H. Yardibi, E. E. Ekiz, and H. Uzun, "Tumour preventive effect of Aloe vera leaf pulp lectin (Aloctin I) on Ehrlich ascites tumours in mice," Phytother Res, vol. 21, pp. 1070-5, Nov 2007.

[21] S. Jahan, R. Chaudhary, and P. K. Goyal, "Anticancer activity of an Indian medicinal plant, Alstonia scholaris, on skin carcinogenesis in mice," Integr Cancer Ther, vol. 8, pp. 273-9, Sep 2009.

[22] B. Manjeshwar Shrinath, "Alstonia scholaris Linn R Br in the treatment and prevention of cancer: past, present, and future," Integr Cancer Ther, vol. 9, pp. 261-9, Sep 2010.

[23] G. C. Jagetia and M. S. Baliga, "Evaluation of anticancer activity of the alkaloid fraction of Alstonia scholaris (Sapthaparna) in vitro and in vivo," Phytother Res, vol. 20, pp. 103-9, Feb 2006.

[24] Y. Nakamura, N. Kawamoto, Y. Ohto, K. Torikai, A. Murakami, and H. Ohigashi, "A diacetylenic spiroketal enol ether epoxide, AL-1, from Artemisia lactiflora inhibits 12-O-tetradecanoylphorbol-13-acetate-induced tumor promotion possibly by suppression of oxidative stress," Cancer Lett, vol. 140, pp. 37-45, Jun 1 1999.

[25] J. Liu, J. Xing, and Y. Fei, "Green tea (Camellia sinensis) and cancer prevention: a systematic review of randomized trials and epidemiological studies," Chin Med, vol. 3, p. 12, 2008.

[26] K. Boehm, F. Borrelli, E. Ernst, G. Habacher, S. K. Hung, S. Milazzo, and M. Horneber, "Green tea (Camellia sinensis) for the prevention of cancer," Cochrane Database Syst Rev, p. CD005004, 2009.

[27] P. Ghosh, S. E. Besra, G. Tripathi, S. Mitra, and J. R. Vedasiromoni, "Cytotoxic and apoptogenic effect of tea (Camellia sinensis var. assamica) root extract (TRE) and two of its steroidal saponins TS1 and TS2 on human leukemic cell lines K562 and U937 and on cells of CML and ALL patients," Leuk Res, vol. 30, pp. 459-68, Apr 2006.

[28] R. Xu, H. Ye, Y. Sun, Y. Tu, and X. Zeng, "Preparation, preliminary characterization, antioxidant, hepatoprotective and antitumor activities of polysaccharides from the flower of tea plant (Camellia sinensis)," Food Chem Toxicol, vol. 50, pp. 2473-80, Jul 2012.
[29] A. Halder, R. Raychowdhury, A. Ghosh, and M. De, "Black tea (Camellia sinensis) as a chemopreventive agent in oral precancerous lesions," J Environ Pathol Toxicol Oncol, vol. 24, pp. 141-4, 2005.
[30] E. Hossain, S. Chakroborty, A. Milan, P. Chattopadhyay, S. C. Mandal, and J. K. Gupta, "In vitro and in vivo antitumor activity of a methanol extract of Dregea volubilis leaves with its antioxidant effect," Pharm Biol, vol. 50, pp. 338-43, Mar 2012.
[31] M. Singh, E. Mendez, A. R. Rao, and R. K. Kale, "Chemomodulatory potential of Glycine max against murine skin and cervical papillomagenesis," Indian J Exp Biol, vol. 49, pp. 864-70, Nov 2011.
[32] B. Rajkapoor, N. Murugesh, D. Chodon, and D. Sakthisekaran, "Chemoprevention of N-nitrosodiethylamine induced phenobarbitol promoted liver tumors in rat by extract of Indigofera aspalathoides," Biol Pharm Bull, vol. 28, pp. 364-6, Feb 2005.
[33] A. J. Christina, M. Alwin Jose, S. J. Heison Robert, R. Kothai, N. Chidambaranathan, and P. Muthumani, "Effect of Indigofera aspalathoides against Dalton's ascitic lymphoma," Fitoterapia, vol. 74, pp. 280-3, Apr 2003.
[34] C. Anbuselvam, K. Vijayavel, and M. P. Balasubramanian, "Protective effect of Operculina turpethum against 7,12-dimethyl benz(a)anthracene induced oxidative stress with reference to breast cancer in experimental rats," Chem Biol Interact, vol. 168, pp. 229-36, Jul 20 2007.
[35] V. Rajkumar, G. Guha, and R. A. Kumar, "Antioxidant and anti-neoplastic activities of Picrorhiza kurroa extracts," Food Chem Toxicol, vol. 49, pp. 363-9, Feb 2011.
[36] K. M. Debatin, D. Poncet, and G. Kroemer, "Chemotherapy: targeting the mitochondrial cell death pathway," Oncogene, vol. 21, pp. 8786-803, Dec 12 2002.
[37] K. J. Nho, J. M. Chun, and H. K. Kim, "Ethanol Extract of Dianthus chinensis L. Induces Apoptosis in Human Hepatocellular Carcinoma HepG2 Cells In Vitro," Evid Based Complement Alternat Med, vol. 2012, p. 573527, 2012.
[38] T. Varjas, G. Nowrasteh, F. Budan, E. Nadasi, G. Horvath, S. Makai, T. Gracza, J. Cseh, and I. Ember, "Chemopreventive effect of Panax ginseng," Phytother Res, vol. 23, pp. 1399-403, Oct 2009.
[39] F. J. Reyes, J. J. Centelles, J. A. Lupianez, and M. Cascante, "(2Alpha,3beta)-2,3-dihydroxyolean-12-en-28-oic acid, a new natural triterpene from Olea europea, induces caspase dependent apoptosis selectively in colon adenocarcinoma cells," FEBS Lett, vol. 580, pp. 6302-10, Nov 27 2006.
[40] F. J. Reyes-Zurita, E. E. Rufino-Palomares, J. A. Lupianez, and M. Cascante, "Maslinic acid, a natural triterpene from Olea europaea L., induces apoptosis in HT29 human colon-cancer cells via the mitochondrial apoptotic pathway," Cancer Lett, vol. 273, pp. 44-54, Jan 8 2009.
[41] F. J. Reyes-Zurita, G. Pachon-Pena, D. Lizarraga, E. E. Rufino-Palomares, M. Cascante, and J. A. Lupianez, "The natural triterpene maslinic acid induces apoptosis in HT29 colon cancer cells by a JNK-p53-dependent mechanism," BMC Cancer, vol. 11, p. 154, 2011.
[42] E. M. Ju, S. E. Lee, H. J. Hwang, and J. H. Kim, "Antioxidant and anticancer activity of extract from Betula platyphylla var. japonica," Life Sci, vol. 74, pp. 1013-26, Jan 9 2004.
[43] W. Z. Lu, G. X. Geng, Q. W. Li, J. Li, F. Z. Liu, and Z. S. Han, "Antitumor activity of polysaccharides isolated from Patrinia heterophylla," Pharm Biol, vol. 48, pp. 1012-7, Sep 2010.
[44] M. Malumbres and M. Barbacid, "To cycle or not to cycle: a critical decision in cancer," Nat Rev Cancer, vol. 1, pp. 222-31, Dec 2001.
[45] Y. L. Cheng, W. L. Chang, S. C. Lee, Y. G. Liu, C. J. Chen, S. Z. Lin, N. M. Tsai, D. S. Yu, C. Y. Yen, and H. J. Harn, "Acetone extract of Angelica sinensis inhibits proliferation of human cancer cells via inducing cell cycle arrest and apoptosis," Life Sci, vol. 75, pp. 1579-94, Aug 13 2004.
[46] G. Mathan, G. Fatima, A. K. Saxena, B. K. Chandan, B. S. Jaggi, B. D. Gupta, G. N. Qazi, C. Balasundaram, K. D. Anand Rajan, V. L. Kumar, and V. Kumar, "Chemoprevention with aqueous extract of Butea monosperma flowers results in normalization of nuclear morphometry and inhibition of a proliferation marker in liver tumors," Phytother Res, vol. 25, pp. 324-8, Mar 2011.
[47] N. El-Najjar, S. Dakdouki, N. Darwiche, M. El-Sabban, N. A. Saliba, and H. Gali-Muhtasib, "Anti-colon cancer effects of Salograviolide A isolated from Centaurea ainetensis," Oncol Rep, vol. 19, pp. 897-904, Apr 2008.
[48] A. Ghantous, A. A. Tayyoun, G. A. Lteif, N. A. Saliba, H. Gali-Muhtasib, M. El-Sabban, and N. Darwiche, "Purified salograviolide A isolated from centaurea ainetensis causes growth inhibition and apoptosis in neoplastic epidermal cells," Int J Oncol, vol. 32, pp. 841-9, Apr 2008.
[49] R. Cencic, M. Carrier, G. Galicia-Vazquez, M. E. Bordeleau, R. Sukarieh, A. Bourdeau, B. Brem, J. G. Teodoro, H. Greger, M. L. Tremblay, J. A. Porco, Jr., and J. Pelletier, "Antitumor activity and mechanism of action of the cyclopenta[b]benzofuran, silvestrol," PLoS One, vol. 4, p. e5223, 2009.
[50] G. R. Pettit, S. B. Singh, J. M. Schmidt, M. L. Niven, E. Hamel, and C. M. Lin, "Isolation, structure, synthesis, and antimitotic properties of combretastatins B-3 and B-4 from Combretum caffrum," J Nat Prod, vol. 51, pp. 517-27, May-Jun 1988.
[51] N. Liao, P. Zhang, M. Ao, J. Wang, Y. Shi, and L. Yu, "9-methoxycamptothecin from Nothapodytes foetida induces apoptosis in murine sarcoma S180 cells," Z Naturforsch C, vol. 66, pp. 471-6, Sep-Oct 2011.
[52] K. V. Rao, T. Samikkannu, K. B. Dakshayani, X. Zhang, S. S. Sathaye, M. A. Indap, and M. P. Nair, "Chemopreventive potential of an ethyl acetate fraction from Curcuma longa is associated with upregulation of p57(kip2) and Rad9 in the PC-3M prostate cancer cell line," Asian Pac J Cancer Prev, vol. 13, pp. 1031-8, 2012.
[53] J. Kim, H. L. Ha, H. B. Moon, Y. W. Lee, C. K. Cho, H. S. Yoo, and D. Y. Yu, "Chemopreventive effect of Curcuma longa Linn on liver pathology in HBx transgenic mice," Integr Cancer Ther, vol. 10, pp. 168-77, Jun 2011.
[54] C. Wang, P. Chen, H. Jin, X. Yan, L. Gan, Y. Li, S. Zhou, J. Chang, Y. Wang, G. Yang, and G. He, "Nidus vespae protein inhibiting proliferation of HepG2 hepatoma cells through extracellular signal-regulated kinase signaling pathways and inducing G1 cell cycle arrest," Acta Biochim Biophys Sin (Shanghai), vol. 40, pp. 970-8, Nov 2008.
[55] M. J. Smyth, Y. Hayakawa, K. Takeda, and H. Yagita, "New aspects of natural-killer-cell surveillance and therapy of cancer," Nat Rev Cancer, vol. 2, pp. 850-61, Nov 2002.
[56] K. Miyamoto, N. Kishi, T. Murayama, T. Furukawa, and R. Koshiura, "Induction of cytotoxicity of peritoneal exudate cells by agrimoniin, a novel immunomodulatory tannin of Agrimonia pilosa Ledeb," Cancer Immunol Immunother, vol. 27, pp. 59-62, 1988.
[57] J. Shen, M. Tanida, Y. Fujisaki, Y. Horii, K. Hashimoto, and K. Nagai, "Effect of the culture extract of Lentinus edodes mycelia on splenic sympathetic activity and cancer cell proliferation," Auton Neurosci, vol. 145, pp. 50-4, Jan 28 2009.
[58] R. Flavin, S. Peluso, P. L. Nguyen, and M. Loda, "Fatty acid synthase as a potential therapeutic target in cancer," Future Oncol, vol. 6, pp. 551-62, Apr 2010.
[59] M. Na, J. Jang, B. S. Min, S. J. Lee, M. S. Lee, B. Y. Kim, W. K. Oh, and J. S. Ahn, "Fatty acid synthase inhibitory activity of acylphloroglucinols isolated from Dryopteris crassirhizoma," Bioorg Med Chem Lett, vol. 16, pp. 4738-42, Sep 15 2006.

[60] A. Arora and E. M. Scholar, "Role of tyrosine kinase inhibitors in cancer therapy," J Pharmacol Exp Ther, vol. 315, pp. 971-9, Dec 2005.
[61] G. Vlahovic and J. Crawford, "Activation of tyrosine kinases in cancer," Oncologist, vol. 8, pp. 531-8, 2003.
[62] R. R. Tjandrawinata, P. F. Arifin, O. M. Tandrasasmita, D. Rahmi, and A. Aripin, "DLBS1425, a Phaleria macrocarpa (Scheff.) Boerl. extract confers anti proliferative and proapoptosis effects via eicosanoid pathway," J Exp Ther Oncol, vol. 8, pp. 187-201, 2010.
[63] J. H. Kang, K. H. Song, J. K. Woo, M. H. Park, M. H. Rhee, C. Choi, and S. H. Oh, "Ginsenoside Rp1 from Panax ginseng exhibits anti-cancer activity by down-regulation of the IGF-1R/Akt pathway in breast cancer cells," Plant Foods Hum Nutr, vol. 66, pp. 298-305, Sep 2011.
[64] S. H. Advani, "Targeting mTOR pathway: A new concept in cancer therapy," Indian J Med Paediatr Oncol, vol. 31, pp. 132-6, Oct 2010.
[65] A. Faried, D. Kurnia, L. S. Faried, N. Usman, T. Miyazaki, H. Kato, and H. Kuwano, "Anticancer effects of gallic acid isolated from Indonesian herbal medicine, Phaleria macrocarpa (Scheff.) Boerl, on human cancer cell lines," Int J Oncol, vol. 30, pp. 605-13, Mar 2007.
[66] K. Suzuki and H. Matsubara, "Recent advances in p53 research and cancer treatment," J Biomed Biotechnol, vol. 2011, p. 978312, 2011.
[67] G. Gu, I. Barone, L. Gelsomino, C. Giordano, D. Bonofiglio, G. Statti, F. Menichini, S. Catalano, and S. Ando, "Oldenlandia diffusa extracts exert antiproliferative and apoptotic effects on human breast cancer cells through ERalpha/Sp1-mediated p53 activation," J Cell Physiol, vol. 227, pp. 3363-72, Oct 2012.
[68] M. J. Kim, D. H. Kim, H. K. Na, T. Y. Oh, C. Y. Shin, and D. P. Y. J. Surh Ph, "Eupatilin, a pharmacologically active flavone derived from Artemisia plants, induces apoptosis in human gastric cancer (AGS) cells," J Environ Pathol Toxicol Oncol, vol. 24, pp. 261-9, 2005.
[69] J. C. Chao and C. C. Chu, "Effects of Ginkgo biloba extract on cell proliferation and cytotoxicity in human hepatocellular carcinoma cells," World J Gastroenterol, vol. 10, pp. 37-41, Jan 2004.

Volume 3, Issue 1 (2015) 94-102 ISSN 2347 - 3258
International Journal of Advance Research and Innovation

Methods for Improving Thermal Performance of Three Stage Vapour Compression Refrigeration Systems with Flash-Intercooler Using Energy– Exergy Analysis of Eight Ecofriendly Refrigerants

R. S. Mishra [a *], Kapil Chopra [b], V. Sahni [b]
[a] Department of Mechanical Production & Industrial and Automobiles Engineering, Delhi Technological University, Delhi, India
[b] Department of Mechanical Engineering, Sant Longowal Institute of Engineering & Technology, Longowal, India

Article Info
Article history:
Received 12 February 2015
Received in revised form
22 February 2015
Accepted 28 February 2015
Available online 15 March 2015

Keywords
Thermodynamic Analysis ,
Reduction in Irreversibilities,
Performance Improvement,
Energy-Exergy Analysis,
Vapour Compression Systems

Abstract

The exergy analysis is a powerful tool for finding irreversibilities occurred in the components as well as complete system. Global warming and ozone depletion is a big issues for saving our environment. In this paper using first law and second law analysis , the comparison of eight environmental friendly refrigerants on multiple stage vapour compression refrigerator with flash intercooler and individual throttle valves (system-1) and multiple stage vapour compression refrigerator with flash intercooler and multiple throttle valves (system-2) has been carried out. For eight selected refrigerants irreversibilities occurred in the system -1 is higher than the system-2 and first law efficiency (COP) and exergy efficiency of system-1is lower than sytem-2.The Exergetic performance of R600 and R717 is better in comparison of other selected ecofriendly refrigerants for both systems where as ecofriendly R125 refrigerant showed lowest thermal performances in terms of COP (energetic efficiency), and exergetic efficiency (second law efficiency) and higher irreversibilities in terms of exergey destruction ratio (EDR) . As ecofriendly R717 refrigerant is toxic in nature and restricted to limited applications and hydrocarbon R600 is slightly lower performance than R717 and 2-3% higher performance than R134a refrigerant is also flammable in nature can be used without taking of any safety precautions.Therefore R134a may also be used for practical applications. Also R134A is easily available, The performance of R1234yf (GWP four with zero ozone depletion potential) gives lower thermal performance than R134a

Nomenclature

LTE	low temperature evaporator
ITE	intermediate temperature evaporator
THE	high temperature evaporator
TR	ton of refrigeration
P	power (kJ/s)
f	flash intercooler
$\dot{Q}$	rate of heat transfer (kW)
$\dot{W}$	work rate (kW)
T	temperature (oC)
TV	throttle valve
x	dryness fraction(non-dimensional)
Φ	specific enthalpy (kJ/kg)
$\dot{\Psi}$	irreversibility rate(kW)
C	Compressor
X	exergy rate of fluid (kW)
$\dot{m}$	mass flow rate (kg/s)
S	specific entropy (kJ/kgK)
$\dot{E}P$	exergy rate of product (kW)

Subscript

e	Evaporator
c	Compressor
o	dead state
f	flash intercooler
r	Refrigerant
tv	throttle valve
lsc	liquid subcooler
k	kth component
gen	Generation
cond	Condenser

Corresponding Author,
E-mail address: rsmishra1651956@yahoo.co.in
All rights reserved: http://www.ijari.org

1. Introduction

Nowadays most of the energy utilize in cooling and air conditioning in industrial as well as for domestic applications, in addition to energy consumption, using of refrigerants in cooling and air conditioning having high GWP and ODP which are responsible for increasing global warming and ozone depletion. The primary requirements of ideal refrigerants are having good physical and chemical properties. Due to good physical and chemical properties such as non-corrosiveness, non-toxicity, non- flammability, low boiling point, Chlorofluorocarbons (CFCs) have been used over the last many decades, but hydro chloro fluoro carbons (HCFCs) and Chlorofluorocarbons (CFCs) having large amount of chlorine content as well as high global warming potential and ozone depletion potential, so after 90s refrigerants under these categories these kinds of refrigerants are almost prohibited [1].

2. Literature Review

Most of the study has been carried out for the performance evaluation of vapour compression refrigeration system using energetic analysis, but with the help of first law analysis irreversibility destruction or losses in components of system unable to determined [2-5], Therefore exergetic analysis is the advanced approach for thermodynamic performances This paper mainly deals with exergy analysis of the comparison of eight environmental friendly refrigerants on multiple stage vapour compression refrigerator with flash intercooler and individual throttle valves (system-1) and multiple stage vapour compression refrigerator with flash intercooler and multiple throttle valves (system-2) for optimizing irreversibility.

Refrigerant	**Chemical formula**	**Molecular mass (g/mol)**	**NBP (^oC)**	**T_{cri} (^oC)**	**P_{cri} (MPa)**	**ASHRAE safety code**
R410a	R-32/125	72.58	-60.9	72.5	4.95	A1
R290	$CH_3CH_2CH_3$	44.1	-42.2	96.7	4.25	A3
R600a	C_4H_{10}	58.122	-11.74	134.661	3.62	A3
R1234yf	$C_3H_2F_4$	114.04	-29.4	94.85	3.38	A2L
R600	C_4H_{10}	58.122	-0.49	151.98	3.79	A3
R134a	CH_2FCF_3	102.03	-26.1	101.1	4.06	A1
R125	C_2HF_5	120.02	-48.09	66.023	3.61	A1
R717	NH_3	17.03	-33.327	132.25	11.33	B2

Table: 1. Physical and Environmental Characteristics of Eight Ecofriendly Refrigerants Used in Vapour Compression Refrigeration System

The utility of exergy analysis (i.e. second law analysis) on vapour compression refrigeration systems is well defined because it gives the idea for improvements in efficiency due to modifications in existing design in terms of reducing exergy destructions in the components. In addition to this second law analysis also provides new thought for development in the existing system [6]. Xuan and Chen [7] carried out experimental study for replacement of R502 by mixture of HFC-161 and observed that the mixture of HFC-161 gives similar thermodynamic performances and also higher performance than using ecofriendly R404a refrigerant at lower and higher evaporative temperature respectively Cabello et al.[8] experimentally investigated the effect of condensing pressure, evaporating pressure and degree of superheating on single stage vapour compression refrigeration system using R22, R134a and R407C and observed that mass flow rate is greatly affected by change in suction conditions of compressor and found that higher compression ratio using R407C gives lower first law performance (COP) than R22 Spatz and Motta [9] focused on comparison of heat transfer and pressure drop characteristics through experimental investigation of vapour compression refrigeration system through experimental investigation in the medium temperature range for replacement of R12 using three ecofriendly refrigerants. And observed that the ecofriendly R410a gives better performance than, R404a and R290a. Han et al. [10] conducted experiments under different working conditions and concluded that R407C is a replacement of R12 in the vapour compression refrigeration system without any modification in the same system. Cabello et al [11] had studied the effect of operating parameters on COP, work input and cooling capacity of single-stage vapour compression refrigeration system and observed a great influence of performance parameters due change in suction pressure, condensing and evaporating temperatures. Arora and Kaushik [12] carried out energy and exergy analysis of vapour compression refrigeration system with liquid vapour heat exchanger for specific temperature range of evaporator and condenser. And found that the R502 is the best refrigerant than R404A and R507A, Getu and Bansal [13] had optimized the design operating parameters of R744-R717 cascade refrigeration system. using regression analysis Mohanraj et al [14] conducted experiments on domestic refrigerator and concluded that under different environmental temperatures the first law efficiency in terms of COP of system using mixture of R290 and R600a in the ratio of 45.2: 54.8 by weight indicating up to 3.6% greater than same system using R134arefrigerants, also discharge temperature of compressor with mixture of R290 and R600a is lower in the range of 8.5-13.4K than same compressor with R134a.Padilla et al [15] used energy analysis of domestic vapour compression refrigeration system with R12 and R413a and concluded that the thermal performance in terms of power consumption, and energy efficiency of R413A is better than R12.

3. Objectives of Research Investigations Objectives of Research Investigations

In this paper great emphasis put on saving of energy and using of ecofriendly refrigerants due to increase of energy crises, global warming and depletion of ozone layer. In this investigation the work input required running the vapour compression refrigeration system reduced by using compound compression and further decreased by flash intercooling between compressors. COP of system can also be enhanced by compressing the refrigerant very close to the saturation line this can be achieved by compressing the refrigerants in more stages with intermediate intercoolers. The refrigeration effect can be increase by maintaining the condition of refrigerants in more liquid stage at the entrance of evaporator which can be achieved by expanding the refrigerant very close to the liquid line. The expansion can be brought close to the liquid line by subcooling the refrigerant and removing the flashed vapours by incorporating the flash chamber in the working cycle. The evaporator size can be reduced because unwanted vapours formed are removed before the liquid refrigerant enters in the evaporator. Multi-stage vapour compression with flash intercooler and individual throttle valves (system-1) consists of three compressors arranged in compound compression, individual throttle valves, condenser and evaporators as shown in Fig.1. Multiple evaporators at different temperatures with compound compression, flash intercooler

and multiple throttle valves (system-2) consists of three compressors arranged in compound compression, multiple throttle valves, condenser and evaporators as shown in Fig.2.

3.1 First and Second Law Analysis

For carrying out energetic and exergetic analysis, computational models of system-1 and system-2 has been developed and impact of chosen refrigerants on these systems has been analyzed using computational analysis and following assumptions are made:

1. Load on the low, intermediate and high temperature evaporators are 10TR, 20 TR and 30 TR respectively.
2. Dead state temperature (T0): 25 oC
3. temperature (Tr-Te):5 oC.
4. Adiabatic efficiency of compressor: 76%.
5. Dead state enthalpy (Φ0) and entropy (s0) of the refrigerants have been calculated corresponding to the dead state temperature (T0) of 25 oC.
6. Variation in kinetic and potential energy is negligible.
7. Expansion process is adiabatic
8. Temperature of low, intermediate and high temperature evaporators are -10 oC,0 oC and 10 oC respectively.
9. Condenser temperature : 40 oC
10. Degree of sub cooling : 10 oC

Exergy at any state is given as

X= (Φ-Φ_0)-T_0 (s-s_0) (1)

Energy analysis

First law of thermodynamic gives the idea of energy balance of system.

Mass flow analysis of system-1

$$\dot{m}_{c1} = \dot{m}_{e1} = \frac{\dot{Q}_{e1}}{(\Phi_1 - \Phi_{10})} \quad (2)$$

$$\dot{m}_{e2} = \frac{\dot{Q}_{e2}}{(\Phi_3 - \Phi_9)} \quad (3)$$

$$\dot{m}_{f1} = \frac{\dot{m}_{c1}(\Phi_2 - \Phi_3)}{(\Phi_3 - \Phi_9)} \quad (4)$$

$$\dot{m}_{c2} = \dot{m}_{c1} + \dot{m}_{e2} + \dot{m}_{f1} \quad (5)$$

$$\dot{m}_{e3} = \frac{\dot{Q}_{e3}}{(\Phi_5 - \Phi_8)} \quad (6)$$

$$\dot{m}_{f2} = \frac{\dot{m}_{c2}(\Phi_4 - \Phi_5)}{(\Phi_5 - \Phi_8)} \quad (7)$$

$$\dot{m}_{c3} = \dot{m}_{c2} + \dot{m}_{e3} + \dot{m}_{f2} \quad (8)$$

Energy consumption for sytem-1

$$P_{c1} = \frac{\dot{m}_{c1}(\Phi_2 - \Phi_1)}{60} \quad (9)$$

$$P_{c2} = \frac{\dot{m}_{c2}(\Phi_4 - \Phi_3)}{60} \quad (10)$$

$$P_{c3} = \frac{\dot{m}_{c3}(\Phi_6 - \Phi_5)}{60} \quad (11)$$

Energetic efficiency of system-1

$$\mathrm{COP} = \frac{\dot{Q}_e}{P_c * 60} \quad (12)$$

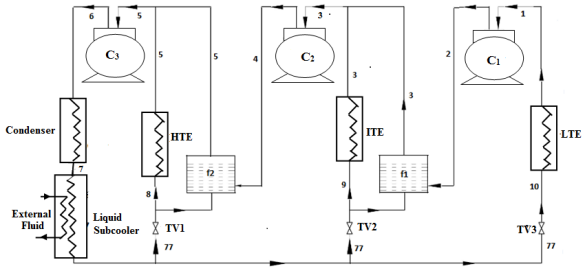

Fig: 1 Schematic Diagram of Multiple Evaporators with Compound Compression, Flash Intercooler and Individual Throttle Valves (System-1)

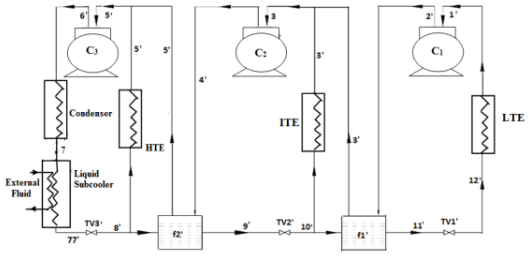

Fig: 2 Schematic Diagram of Multiple Evaporators with Compound Compression, Flash Intercooler and Multiple Throttle Valves (System-2)

Rate of exergy loss due to irreversibility $(T_o \dot{S}_{gen})$ in various components of system-1

The concept of exergy was given by second law of thermodynamics, The exergy is always decreases due to thermodynamic irreversibilityies occurred in the components as well as in the whole system. Exergy is a measure of usefulness, quality or potential of a stream to cause change and an effective measure of the potential of a substance to impact the environment [12]. Using entropy generation Concept in the three stages vapour compression refrigeration systems using flash intercooler is given below for various components Compressors

$$(T_o \dot{S}_{gen})_{c1} = \dot{W}_{c1} + \dot{m}_{c1}(X_2 - X_1) \quad (13)$$

$$(T_o \dot{S}_{gen})_{c2} = \dot{W}_{c2} + \dot{m}_{c2}(X_4 - X_3) \quad (14)$$

$$(T_o \dot{S}_{gen})_{c3} = \dot{W}_{c3} + \dot{m}_{c3}(X_6 - X_5) \quad (15)$$

$$\Psi_c = (T_o \dot{S}_{gen})_{c1} + (T_o \dot{S}_{gen})_{c2} + (T_o \dot{S}_{gen})_{c3} \quad (16)$$

Evaporators

$$(T_o \dot{S}_{gen})_{e1} = \dot{m}_{e1}(X_1 - X_{10}) - \dot{Q}_{e1}\left(1 - \frac{T_0}{T_{r1}}\right) \quad (17)$$

$$(T_o \dot{S}_{gen})_{e2} = \dot{m}_{e2}(X_3 - X_9) - \dot{Q}_{e2}\left(1 - \frac{T_0}{T_{r2}}\right) \quad (18)$$

$$(T_o \dot{S}_{gen})_{e3} = \dot{m}_{e3}(X_5 - X_8) - \dot{Q}_{e3}\left(1 - \frac{T_0}{T_{r3}}\right) \quad (19)$$

$$\Psi_e = (T_o \dot{S}_{gen})_{e1} + (T_o \dot{S}_{gen})_{e2} + (T_o \dot{S}_{gen})_{e3} \quad (20)$$

Condenser

$$\Psi_{cond} = (T_o \dot{S}_{gen})_{cond} = \dot{m}_{c3}(X_6 - X_7) - \dot{Q}_e\left(1 - \frac{T_0}{T_r}\right) \quad (21)$$

Throttle Valves

$$(T_o \dot{S}_{gen})_{tv1} = \dot{m}_{e1}(X_{77} - X_{10}) \quad (22)$$

$$(T_o \dot{S}_{gen})_{tv2} = (\dot{m}_{e2} + \dot{m}_{f1})(X_{77} - X_9) \quad (23)$$

$$(T_o \dot{S}_{gen})_{tv3} = (\dot{m}_{e3} + \dot{m}_{f2})(X_{77} - X_8) \quad (24)$$

$$\Psi_{tv} = (T_o \dot{S}_{gen})_{tv1} + (T_o \dot{S}_{gen})_{tv2} + (T_o \dot{S}_{gen})_{tv3} \quad (25)$$

Liquid subcooler

$$\Psi_{lsc} = (T_o \dot{S}_{gen})_{sc} = \dot{m}_{c3}(X_7 - X_{77}) \quad (26)$$

Flash intercoolers

$$(T_o \dot{S}_{gen})_{f1} = \dot{m}_{f1}(X_9 - X_3) + \dot{m}_{c1}(X_2 - X_3) \quad (27)$$

$$(T_o \dot{S}_{gen})_{f2} = \dot{m}_{f2}(X_8 - X_5) + \dot{m}_{c1}(X_4 - X_5) \quad (28)$$

$$\Psi_f = (T_o \dot{S}_{gen})_{f1} + (T_o \dot{S}_{gen})_{f2} \quad (29)$$

Total irreversibility destruction in system-1

$$\sum \Psi_k = \Psi_e + \Psi_c + \Psi_{cond} + \Psi_{tv} + \Psi_{lsc} + \Psi_f \quad (30)$$

$$\dot{m}_{c1'} = \dot{m}_{e1'} = \frac{\dot{Q}_{e1'}}{(\Phi_{1'} - \Phi_{12'})} \quad (31)$$

$$\dot{m}_{e2'} = \frac{\dot{Q}_{e2'}}{(\Phi_{3'} - \Phi_{10'})} + \dot{m}_{c1'}\left(\frac{x_{10'}}{1 - x_{10'}}\right) \quad (32)$$

$$\dot{m}_{f1'} = \frac{\dot{m}_{c1'}(\Phi_{2'} - \Phi_{3'})}{(\Phi_{3'} - \Phi_{10'})} \quad (33)$$

$$\dot{m}_{c2'} = \dot{m}_{c1'} + \dot{m}_{e2'} + \dot{m}_{f1'} \quad (34)$$

$$\dot{m}_{e3'} = \frac{\dot{Q}_{e3'}}{(\Phi_{5'} - \Phi_{8'})} + \dot{m}_{c2'}\left(\frac{x_{8'}}{1 - x_{8'}}\right) \quad (35)$$

$$\dot{m}_{f2'} = \frac{\dot{m}_{c2'}(\Phi_{4'} - \Phi_{5'})}{(\Phi_{5'} - \Phi_{8'})} \quad (36)$$

Power required for running the compressors

$$P_{c1'} = \frac{\dot{m}_{c1'}(\Phi_{2'} - \Phi_{1'})}{60} \quad (37)$$

$$P_{c2'} = \frac{\dot{m}_{c2'}(\Phi_{4'} - \Phi_{3'})}{60} \quad (38)$$

$$P_{c3'} = \frac{\dot{m}_{c3'}(\Phi_{6'} - \Phi_{5'})}{60} \quad (39)$$

$$\text{Energetic efficiency} = \frac{\dot{Q}_{e'}}{P_{c'} * 60} \quad (40)$$

3.2 Rate of exergy loss due to irreversibilties $(T_o \dot{S}_{gen})$ in various components of system-2

Compressors

$$(T_o \dot{S}_{gen})_{c1'} = \dot{W}_{c1'} + \dot{m}_{c1'}(X_{2'} - X_{1'}) \quad (41)$$

$$(T_o \dot{S}_{gen})_{c2'} = \dot{W}_{c2'} + \dot{m}_{c2'}(X_{4'} - X_{3'}) \quad (42)$$

$$(T_o \dot{S}_{gen})_{c3'} = \dot{W}_{c3'} + \dot{m}_{c3'}(X_{6'} - X_{5'}) \quad (43)$$

$$\Psi_{c'} = (T_o \dot{S}_{gen})_{c1'} + (T_o \dot{S}_{gen})_{c2'} + (T_o \dot{S}_{gen})_{c3'} \quad (44)$$

Evaporators

$$(T_o \dot{S}_{gen})_{e1'} = \dot{m}_{e1'}(X_{1'} - X_{12'} - \dot{Q}_{e1'}\left(1 - \frac{T_0}{T_{r1'}}\right) \quad (45)$$

$$(T_o \dot{S}_{gen})_{e2'} = \dot{m}_{e2'}(X_{3'} - X_{10'}) - \dot{Q}_{e2'}\left(1 - \frac{T_0}{T_{r2'}}\right) \quad (46)$$

$$(T_o \dot{S}_{gen})_{e3'} = \dot{m}_{e3'}(X_{5'} - X_{8'}) - \dot{Q}_{e3'}\left(1 - \frac{T_0}{T_{r3'}}\right) \quad (47)$$

$$\Psi_{e'} = (T_o \dot{S}_{gen})_{e1'} + (T_o \dot{S}_{gen})_{e2'} + (T_o \dot{S}_{gen})_{e3'} \quad (48)$$

Condenser

$$\Psi_{cond'} = (T_o \dot{S}_{gen})_{cond'} = \dot{m}_{c3'}(X_{6'} - X_{7'}) - \dot{Q}_{e'}\left(1 - \frac{T_0}{T_{r'}}\right) \quad (49)$$

Throttle Valves

$$(T_o \dot{S}_{gen})_{tv1'} = \dot{m}_{e1'}(X_{11'} - X_{12'}) \quad (50)$$

$$(T_o \dot{S}_{gen})_{tv2'} = \dot{m}_{c2'}(X_{9'} - X_{10'}) \quad (51)$$

$$(T_o \dot{S}_{gen})_{tv3'} = \dot{m}_{c3'}(X_{77'} - X_{8'}) \quad (52)$$

$$\Psi_{tv'} = (T_o \dot{S}_{gen})_{tv1'} + (T_o \dot{S}_{gen})_{tv2'} + (T_o \dot{S}_{gen})_{tv3'} \quad (53)$$

Liquid subcooler

$$\Psi_{lsc'} = (T_o \dot{S}_{gen})_{lsc'} = \dot{m}_{c3'}(X_{7'} - X_{77'}) \quad (54)$$

Flash intercoolers

$$(T_o \dot{S}_{gen})_{f1'} = \dot{m}_{f1'}(X_{10'} - X_{3'}) + \dot{m}_{c1'}(X_{2'} - X_{3'}) \quad (55)$$

$$(T_o \dot{S}_{gen})_{f2'} = \dot{m}_{f2'}(X_{8'} - X_{5'}) + \dot{m}_{c2'}(X_{4'} - X_{5'}) \quad (56)$$

$$\Psi_{f'} = (T_o \dot{S}_{gen})_{f1'} + (T_o \dot{S}_{gen})_{f2'} \quad (57)$$

Total irreversibility destruction in system-1

$$\sum \Psi_{k'} = \Psi_{e'} + \Psi_{c'} + \Psi_{cond'} + \Psi_{tv'} + \Psi_{lsc'} + \Psi_{f'} \quad (58)$$

Exergetic efficiency

$$\text{Exergetic efficiency} = \frac{\text{Exergy of cooling load of evaporat}}{\text{Compressors work}} \quad (59)$$

$$\text{Exergetic efficiency of system} - 1 = \frac{(\dot{Q}_{e1} + \dot{Q}_{e2} + \dot{Q}_{e3}) - T_o\left(\frac{\dot{Q}_{e1}}{T_{r1}} + \frac{\dot{Q}_{e2}}{T_{r2}} + \frac{\dot{Q}_{e3}}{T_{r3}}\right)}{P_c * 60} \quad 60)$$

$$\text{Rational efficiency of system} - 2 = \frac{(\dot{Q}_{e1'} + \dot{Q}_{e2'} + \dot{Q}_{e3'}) - T_o\left(\frac{\dot{Q}_{e1'}}{T_{r1'}} + \frac{\dot{Q}_{e2'}}{T_{r2'}} + \frac{\dot{Q}_{e3'}}{T_{r3'}}\right)}{P_{c'} * 60} \quad 61)$$

4. Results and Discussions

Both systems (system-1& system-2) were analytically analyzed and the variation in low, intermediate and high temperature evaporator with coefficient of performance for eight ecofriendly refrigerants in system-1 and system-2 is shown in Figs.3-5 and Figs.6-8 respectively. And it was observed that COP (energetic efficiency) of system-2 is higher than system-1. The COP of both system-1 and system-2 increase with increase in evaporator temperature for chosen refrigerants. It was also observed that R600 and R717 show better performance and R125 gives lowest thermodynamic performance in term of energetic efficiency than other refrigerants for both systems. The maximum percentage difference of COP was observed in high temperature evaporator of system-2 and system-1 is 9.59% for R125 at 15 °C, The effect of second law efficiency (exergetic efficiency) with change in temperature of low,

intermediate and high temperature evaporator of system-1 and system-2 shown by Figs 9-11and Fig.11-14 respectively.. It is also observed that second law efficiency decrease with increase in evaporator temperature. R600 and R125 have maximum and minimum second law efficiency for both systems similar to performance evaluation in terms of energetic efficiency. It was also found that temperature variation in low and intermediate evaporator put great impact on second law efficiency in comparison with high temperature evaporator, for both systems. Irreversibility in system is work required to displace the atmosphere or lost work during the process. The irreversibility analysis of system-1 and system-2 is presented by Figs.15-17 and Figs.18-20 respectively. It was experienced that irreversibility of both system-1 and system-2 increase with increase in temperature of evaporator.R125 shows maximum irreversibility, on the other hand R600 and R717 show minimum irreversibility in systems compared with other ecofriendly refrigerants. It is also observed that irreversibility in system-1 is 1.4-2.1%, 1.3-2.2% and 1.6-2.0% using R600 and 1.8-3%, 1.7-3.1%, 2.2-2.7% using R125 is lower than system-2 for low, intermediate and high temperature evaporator respectively. This marginal irreversibility differences between system-1 and system-2 could be neglected. The impact of change in condenser temperature in range of 25 ^{o}C to 45 on coefficient of performance, second law efficiency and system irreversibility is shown in Figs.21-26 for sytem-1 and system-2 using ecofriendly refrigerants. This analysis reveals that COP and second law efficiency decreases with increase in condenser temperature on the other hand exergy destruction (system irreversibility) increase with increase in condenser temperature for system-1 & sytem-2

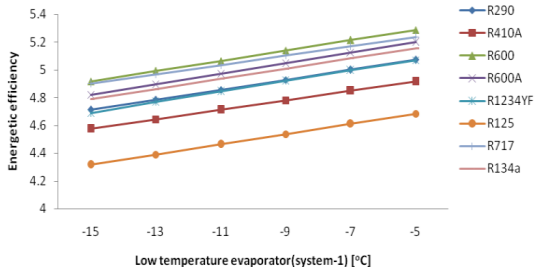

Fig: 3. Variation of Low Temperature Evaporator with Energetic Efficiency of Multiple Stage Vapour Compression Refrigerator with Flash Intercooler and Individual Throttle Valves (System-1)

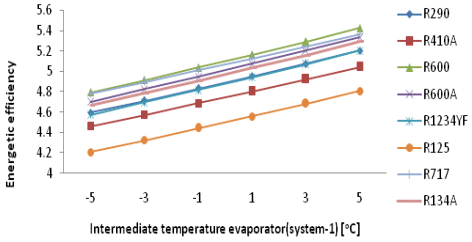

Fig: 4. Variation of Intermediate Temperature Evaporator of Multiple Stage Vapour Compression Refrigerator with Flash Intercooler and Individual Throttle Valves with Variation of Energetic Efficiency (System-1)

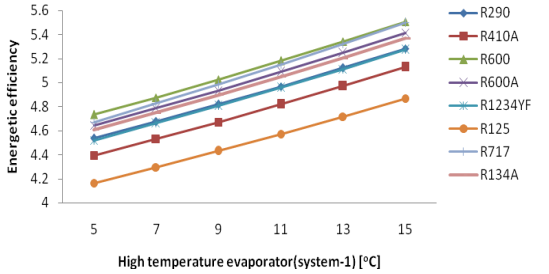

Fig: 5. Variation of High Temperature Evaporator of Multiple Stage Vapour Compression Refrigerator with Flash Intercooler and Individual Throttle Valves (System-1) With Variation of Energetic Efficiency (COP)

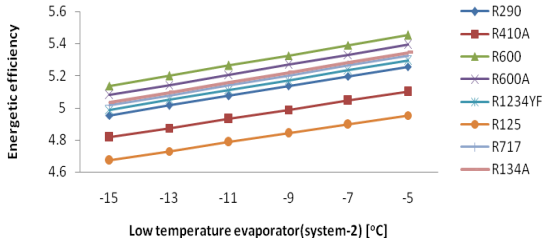

Fig: 6. Variation of Low Temperature Evaporator of Multiple Stage Vapour Compression Refrigerator with Flash Intercooler and Multiple Throttle Valves (System-2) with Variation of Energetic Efficiency (COP)

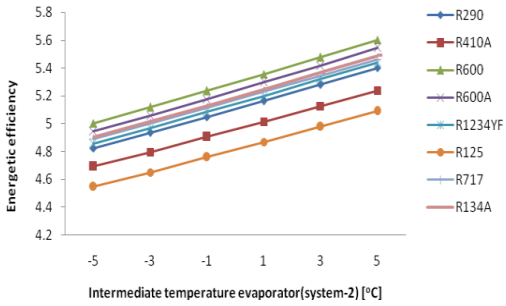

Fig: 7. Variation of Intermediate Temperature Evaporator of Multiple Stage Vapour Compression Refrigerator with Flash Intercooler and Multiple Throttle Valves (System-2) with Variation Energetic Efficiency (COP)

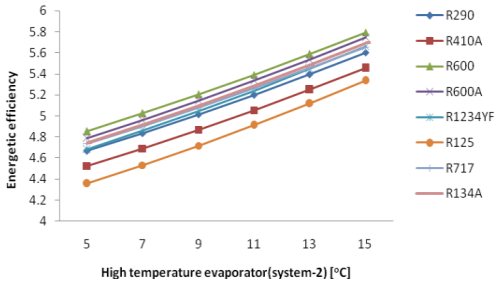

Fig: 8. Variation of High Temperature Evaporator of Multiple Stage Vapour Compression Refrigerator with Flash Intercooler and Multiple Throttle Valves (System-2) with Energetic Efficiency (COP)

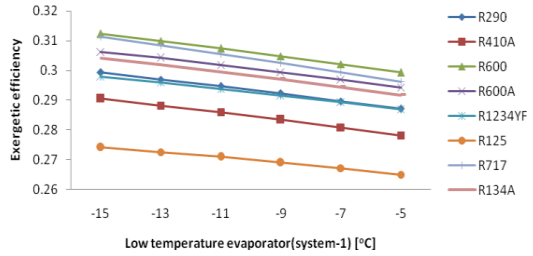

Fig: 9. Variation of Low Temperature Evaporator of Multiple Stage Vapour Compression Refrigerator with Flash Intercooler and Individual Throttle Valves (System-1) With Variation of Exergetic Efficiency

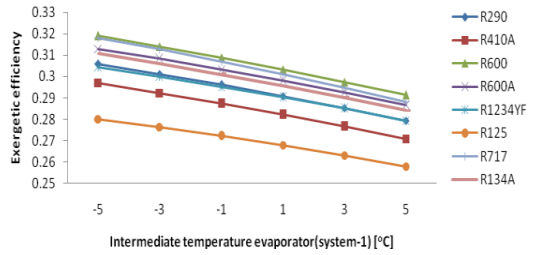

Fig: 10. Variation of Intermediate Temperature Evaporator of Multiple Stage Vapour Compression Refrigerator with Flash Intercooler and Individual Throttle Valves (System-1)With Variation of Exergetic Efficiency

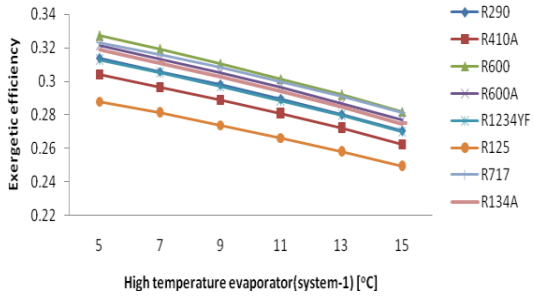

Fig: 11. Variation of High Temperature Evaporator of Multiple Stage Vapour Compression Refrigerator with Flash Intercooler and Individual Throttle Valves (System-1) with Variation of Exergetic Efficiency

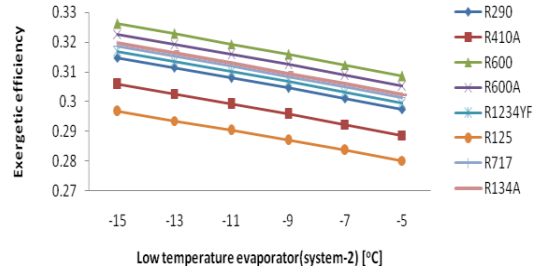

Fig: 12. Variation of Low Temperature Evaporator of Multiple Stage Vapour Compression Refrigerator with Flash Intercooler and Multiple Throttle Valves (System-2) with Variation of Exergetic Efficiency

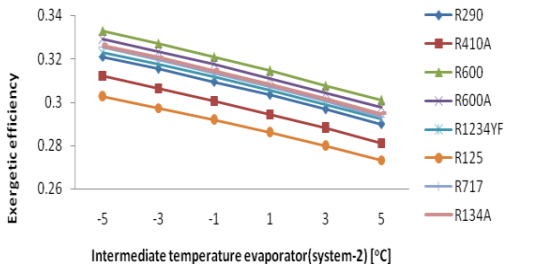

Fig: 13. Variation of Intermediate Temperature Evaporator of Multiple Stage Vapour Compression Refrigerator with Flash Intercooler and Multiple Throttle Valves (System-2) with Variation of Exergetic Efficiency

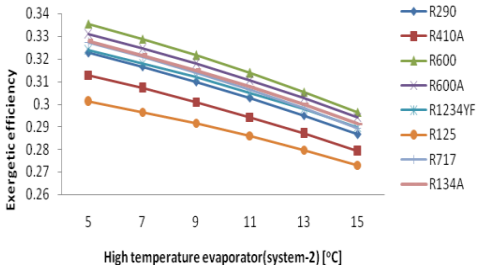

Fig: 14. Variation of High Temperature Evaporator of Multiple Stage Vapour Compression Refrigerator with Flash Intercooler and Multiple Throttle Valves (System-2) with Variation of Exergetic Efficiency

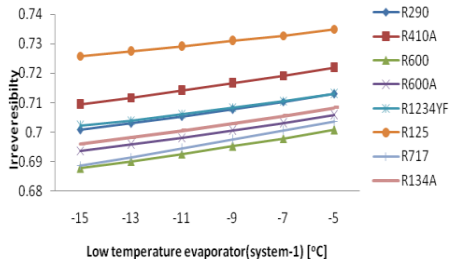

Fig: 15. Variation of Low Temperature Evaporator with Irreversibility of Multiple Stage Vapour Compression Refrigerator with Flash Intercooler and Individual Throttle Valves (Sytem-1)

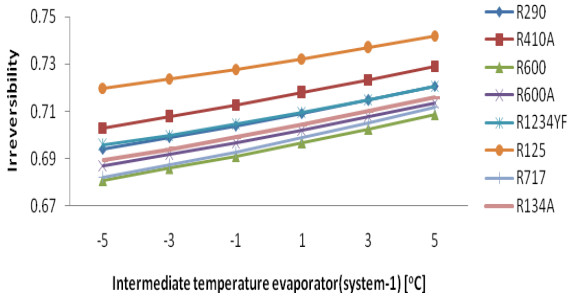

Fig: 16. Variation of Intermediate Temperature Evaporator with Irreversibility of Multiple Stage Vapour Compression Refrigerator with Flash Intercooler and Individual Throttle Valves (Sytem-1)

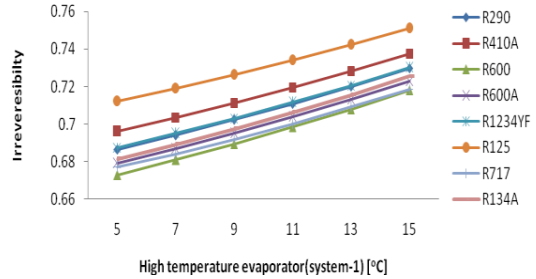

Fig: 17. Variation of High Temperature Evaporator with Irreversibility of Multiple Stage Vapour Compression Refrigerator with Flash Intercooler and Individual Throttle Valves (Sytem-1)

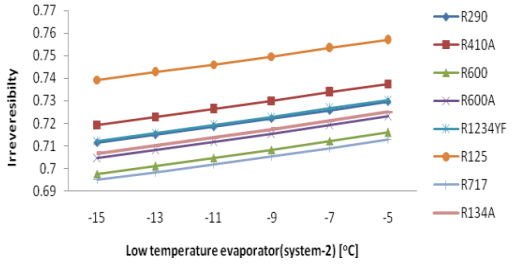

Fig: 18. Variation of Low Temperature Evaporator with Irreversibility of Multiple Stage Vapour Compression Refrigerator with Flash Intercooler and Multiple Throttle Valves (Sytem-2)

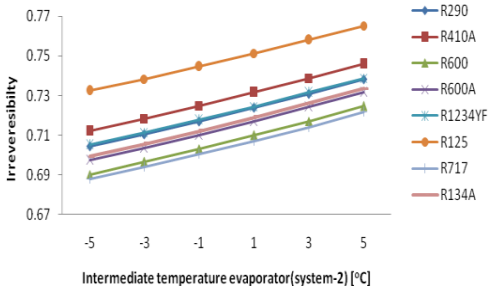

Fig:19. Variation of Intermediate Temperature Evaporator with Irreversibility of Multiple Stage Vapour Compression Refrigerator with Flash Intercooler and Multiple Throttle Valves (Sytem-2)

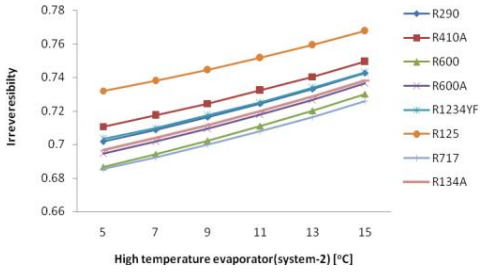

Fig: 20. Variation of High Temperature Evaporator with Irreversibility of Multiple Stage Vapour Compression Refrigerator with Flash Intercooler and Multiple Throttle Valves (Sytem-2)

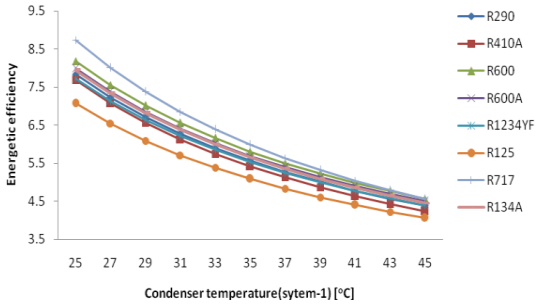

Fig: 21. Variation of Condenser Temperature with Energetic Efficiency of Multiple Stage Vapour Compression Refrigerator with Flash Intercooler and Individual Throttle Valves (Sytem-1)

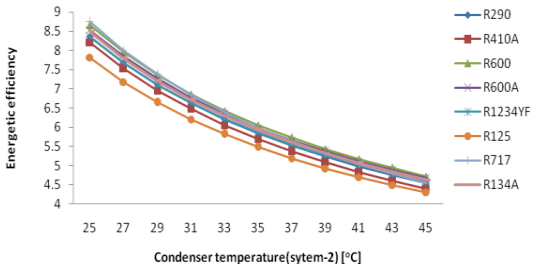

Fig: 22. Variation of Condenser Temperature with Energetic Efficiency of Multiple Stage Vapour Compression Refrigerator with Flash Intercooler and Multiple Throttle Valves (Sytem-2)

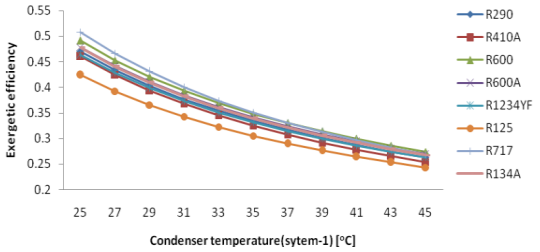

Fig: 23. Variation of Condenser Temperature with Exergetic Efficiency of Multiple Stage Vapour Compression Refrigerator with Flash Intercooler and Individual Throttle Valves (Sytem-1)

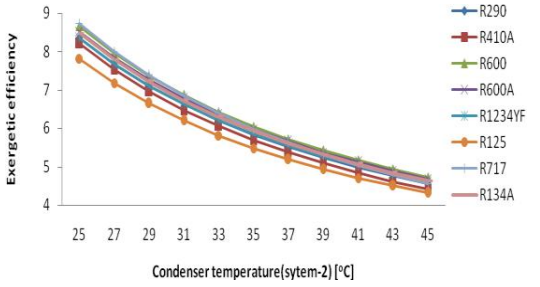

Fig: 24. Variation of Condenser Temperature with Exergetic Efficiency of Multiple Stage Vapour Compression Refrigerator with Flash Intercooler and Multiple Throttle Valves (Sytem-2)

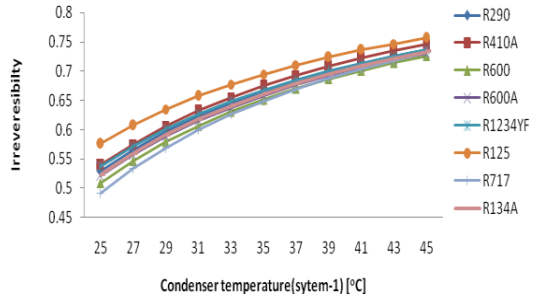

Fig: 25. Variation of Condenser Temperature with Irreversibility of Multiple Stage Vapour Compression Refrigerator with Flash Intercooler and Individual Throttle Valves (Sytem-1)

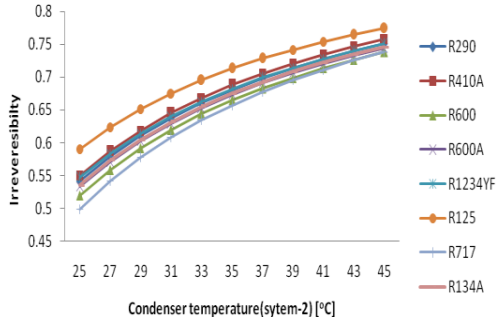

Fig: 26. Variation of Condenser Temperature with Irreversibility of Multiple Stage Vapour Compression Refrigerator with Flash Intercooler and Multiple Throttle Valves (Sytem-2)

5. Conclusions and Recommendations

Thermodynamic nalysis of multi-stage vapour compression refrigerator and flash intercooler with individual or multiple throttle valves has been done in terms of COP, second law efficiency and irreversibility destruction using eight ecofriendly refrigerants for reducing global warmingand ozone depletion by replacing R12, the following conclusions were made:

1. Energetic and exergetic performance of and multiple stage vapour compression refrigerator with flash intercooler and multiple throttle valves (system-2) is higher than multiple stage vapour compression refrigerator with flash intercooler and individual throttle valves (system-1) for selected temperature range of condenser and evaporators with eight chosen ecofriendly refrigerants.
2. For both systems R125 shows minimum thermal performance in terms of COP, second law efficiency and maximum exergy destruction ratio for finding irreversibilities occurred in the system
3. Performances of R600 and R717 better in comparison of other selected ecofriendly refrigerants for system-1 and system-2. AS R717 is toxic and limited to industrial applications, therefore R600 is recommended for both systems by taking safety precautions. Performance of R134a is slighly lesser than R600, therefore R134a can also be used for practical applications without taking of any safety precautions.
4. The maximum percentage difference of COP between system-2 and system-1 is 9.59% for R125 at 15 oC , high temperature evaporator. Irreversibility in system-1 is 1.4-2.1%, 1.3-2.2% and 1.6-2.0% using R600 and 1.8-3%, 1.7-3.1%, 2.2-2.7% using R125 is lower than system-2 for low, intermediate and high temperature evaporator respectively. This marginal irreversibility differences between system-1 and system-2 can be neglected.

References

[1] C. Stanciu, A. Gheorghian, D. Stanciu, A. Dobrovicescu, Exergy analysis and refrigerant effect on the operation and performance limits of a one stage vapour compression refrigeration system, Termotehnia, 2011, 36-42.
[2] V. S. Reddy, N. L. Panwar, S. C. Kaushik, Exergetic analysis of a vapour compression refrigeration system with R134a, R143a, R152a, R404A, R407C, R410A, R502 and R507A,Clean Techn Environ Policy, 14:47–53, 2011
[3] J. U. Ahamed, R. Saidur, H. H. Masjuki, A review on exergy analysis of vapor compression refrigeration system, Renewable and Sustainable Energy Reviews, 15, 2011, 1593–1600
[4] D. Szargut, R. Petela, Egzergia, 1965, WNT
[5] J. Szargut, D. Morris, F. Steward, Exergy analysis of thermal, chemical and metallurgical processes, New York: Hemisphere Publishing Corporation, 1998
[6] R. Saidur, H. H. Masjuki, M. Y. Jamaluddin, An application of energy and exergy analysis in residential sector in Malaysia. Energy Policy, 35, 2007, 1050–63
[7] Y. Xuan, G. Chen, Experimental study on HFC-161 mixture as an alternative refrigerant to R502. Int J Refrigeration. Article in Press
[8] R. Cabello, E. Torrella, J. Navarro-Esbr, Experimental evaluation of a vapour compression plant performance using R134a, R407C and R22 as working fluids. Int J Applied Thermal Engineering, 24, 2004, 1905-1917
[9] M. W. Spatz, S. F. Yana Motta, An evaluation of options for replacing HCFC-22 in medium temperature refrigeration systems, Int J Refrigeration, 27, 2004, 475-483
[10] X. H. Han, Q. Wang, Z. W. Zhu, G. M. Chen, Cycle performance study on R32/R125/R161 as an alternative refrigerant to R407C. Int J Applied Thermal Engineering, 27, 2007, 2559-2565
[11] R. Cabello, J. Navarro-Esbrı, R. Llopis, E. Torrella, Analysis of the variation mechanism in the main energetic parameters in a single-stage vapour compression plant, Int J Applied Thermal Engineering, 27, 2007, 167-176
[12] A. Arora, S. C. Kaushik, Theoretical analysis of a vapour compression refrigeration system with R502, R404A and R507A, Int J Refrigeration, 31, 2008, 998-1005
[13] H. M Getu, P. K Bansal, Thermodynamic analysis of an R744-R717 cascade refrigeration system. Int J Refrigeration, 31, 2008, 45-54

[14] M. Mohanraj, S. Jayaraj, C. Muraleedharan, P. Chandrasekar, Experimental investigation of R290/R600a mixture as an alternative to R134a in a domestic refrigerator. Int J Thermal Sciences, 48, 2009, 1036-1042

[15] M. Padilla, R. Revellin, J. Bonjour. Exergy analysis of R413A as replacement of R12 in a domestic refrigeration system. Int J Energy Conversion and Management, 51, 2010, 2195-2201

[16] S. A. Klein, F. Alvarado, Engineering Equation Solver, Version 7.441. F Chart Software, Middleton, WI, 2005

This article has been accepted for publication in a future issue of this journal, but has not been fully edited. Content may change prior to final publication. Citation information: DOI 10.1109/JSEN.2015.2409114, IEEE Sensors Journal

Overview of Optical Techniques for Characterization of High Power Infrared Gas Lasers

Gaurav Singhal, Mainuddin[#], R. Rajesh, M. T. Beg, R. K. Tyagi and A. L. Dawar

***Abstract*—High power lasers typically form a multidisciplinary technological area laced with innumerable challenges in its realization as a practical system. The prime amongst them are infrared gas laser sources such as Carbon-di-Oxide Gas Dynamic Laser, Hydrogen Fluoride, Deuterium Fluoride Laser and Chemical Oxygen Iodine Laser etc. Each of these laser systems is associated with a unique as well as complex active medium environment involving intense interaction between lasing and pumping species under specific gas dynamic conditions. The parameters viz. specie concentration of the lasing, pumping mediums and other by-products, medium homogeneity, individual constituent gas flow rate, pressure and temperature at critical locations and cavity Mach number are very crucial in determining the output of the gas laser system. It is essential to determine these parameters non-intrusively, with necessary precision so as to optimize these lasers especially in case of large-scale systems. Thus, the focus of this paper is to review and discuss the existing applicable optical detection methodologies ranging from the more established methods such as optical absorption/emission spectroscopy to very contemporary like Raman spectroscopy, cavity ring down spectroscopy, laser induced fluorescence/ planer laser induced fluorescence etc., which are relevant for the diagnostic needs of gas lasers.**

***Index Terms*—Gas lasers, Mach number, Optical diagnostics, Specie concentration**

I. Introduction

THE development of lasers in general and gas lasers [1-3] in particular has been a turning point in the history of science and engineering. These lasers still remains first amongst equals in terms of being scaled to high power levels on account of their excellent beam quality even at large power levels and flexible design inspite of few associated logistics issues. Hence, they are amongst the most sought after as far as high power industrial [4] as well as defense applications [5, 6] are concerned.

These lasers employ various gases and/or chemicals, which are mixed and flown through the gain region in a direction transverse to the laser beam extraction. All of these lasers require specific gas dynamic conditions for purpose of lasing and optimal power extraction. The typical cavity conditions in some of the most potent lasers are: Chemical Oxygen Iodine Laser (COIL) (λ = 1.315μm) [7, 8], laser cavity pressure P_{cavity} ~ 3 torr, Mach number (M) ~ 2; Hydrogen Fluoride/Deuterium Fluoride (HF/DF) laser (λ = 2.7-3.4μm) [9], P_{cavity} ~ 5 torr, M ~ 5; CO_2 Gas Dynamic Laser (λ = 10.6μm) [10], P_{cavity} ~ 35 torr, M ~ 5.

These lasers systems involve numerous coexistent technological aspects having substantial mutual influence along with a complex reactive lasing environment. Thus various parameters viz. specie concentration [11-13] of the lasing, pumping mediums and other by-products, medium homogeneity [14], individual constituent gas flow rate, pressure and temperature at critical locations and cavity Mach number are very crucial in determining the output of the gas laser system. It is essential to determine these parameters non-intrusively, with necessary precision to be able to optimize these lasers especially in case of large-scale systems.

The only means of effectively achieving this end is by means of customized optical techniques. In case of gas lasers, kind of applicable optical diagnostics have been grouped into three broad generic categories for ease of comprehension: (i) specie concentration/molar flow measurement, (ii) laser cavity medium characterization and (iii) laser power/pulse measurement. Table.1 summarizes these diagnostics, which are applicable for the above said three broad categories. Wherever, the diagnostics are applicable for all the three high power gas lasers viz., CO_2 GDL, HF/DF and COIL, *'All three'* has been indicated.

Researchers at various institutes like AFRL [15, 16], TRW (now Northrop Grumman) [17], Physical Sciences Inc. [18], German Aerospace [19] and Chinese Academy of Science [20] etc. have developed several customized optical based diagnostics for gas laser systems. We hereby discuss the best-suited optical diagnostics techniques (including our systems) for a host of parameters applicable to all the major high power gas lasers under the major generic classifications mentioned earlier.

Manuscript received Jul 5, 2014.

Gaurav Singhal is with Laser Science and Technology Centre, Metcalfe House, Delhi 110054, India (e-mail: singhal_g@rediffmail.com)

[#]Mainuddin is with Dept of E & C Engg. JMI, Delhi-110025, India (Corresponding author phone: 91-011-26981284; fax: 91-011-26981284; e-mail: mainuddin@jmi.ac.in)

R. Rajesh is with Naval Physical and Oceanographic Laboratory, Cochin, India (e-mail: rrthampi@rediffmail.com)

M T Beg is with Dept of E & C Engg. JMI, Delhi-110025, India (e-mail: mtbeg@jmi.ac.in)

R. K. Tyagi is with Laser Science and Technology Centre, Metcalfe House, Delhi0110054, India (e-mail: r_k_tyagi@sify.com)

A L Dawar is retired with Laser Science and Technology Centre, Metcalfe House, Delhi 110054, India (e-mail: a_l_dawar@yahoo.com).

1530-437X (c) 2015 IEEE. Personal use is permitted, but republication/redistribution requires IEEE permission. See http://www.ieee.org/publications_standards/publications/rights/index.html for more information.

This article has been accepted for publication in a future issue of this journal, but has not been fully edited. Content may change prior to final publication. Citation information: DOI 10.1109/JSEN.2015.2409114, IEEE Sensors Journal

On line estimation of specie concentration is imperative since both excess and lack of specific species lead to degradation of desired laser power levels. Further, since some of these lasers involve intensive reactive processes [21-23] which may be multiphase as well, hence determination of concentration of chemical species is not limited to lasing /pumping but may also involve intermediate reactants/ products, water vapor etc.

The second generic group pertaining to laser cavity characterization requires use of advanced customized diagnostic techniques with high sensitivity. These are required for providing critical insights into visibly complex flow fields associated with chemical gas lasers. A typical example of this is laser-induced fluorescence (LIF), planar laser induced fluorescence (PLIF) of various interacting gas streams.

This enables investigating various scales of turbulence, mixing of interacting gas streams, degree of medium uniformity, occurrence of shock waves and their interaction with mixing layers, investigation of flow separation especially in the regions of adverse pressure gradients.

The third generic group relates to laser power for which photoelectric, or calorimeter method may be used, all of which have been briefly dwelled on in the relevant sections.

Measured Parameter	Diagnostics	Gas laser
Specie concentration		
• Iodine (I_2) Conc.	a. Optical absorption b. Cavity ring down spectroscopy (CRDS)	COIL
• Chlorine Utilization (U_{Cl2})	a. Optical absorption b. CRDS	COIL
• Sulphur Hexafluoride (SF_6) conc.	Optical absorption	HF/DF
• Singlet Oxygen Yield (Y_{O2*})	a. Optical emission b. Raman spectroscopy	COIL
• Water vapor (H_2O) conc.	Optical emission	COIL
Cavity Medium characterization		
• Small signal gain	a. Probe beam method b. Voigt Profile method	All three COIL,
• Homogeneity	a. Gain Mapping b. Optical Interferometry c. Laser Induced Fluorescence (LIF) d. Planar laser Induced Fluorescence (PLIF)	All three CO_2 GDL COIL COIL
Laser power	Calorimeter	All three
Laser pulse shape	Optical emission	All three

Table.1.Summary of applicable diagnostics for different gas lasers

II. Specie Concentration Measurement

Species concentration measurements [18, 24] are critical for operation of gas lasers. The measurements ascertain whether the systems are operating at design flow rates for various species and may be utilized as a tool for troubleshooting as well. Direct Optical emission/absorption, laser diode based absorption spectroscopy, Raman spectroscopy, CRDS are the techniques for specie concentration estimation for different species involved in laser operation.

A. Optical Emission Technique

Optical emission technique utilizes the property of the species to emit light at specific wavelengths. Fig. 1 shows the typical schematic for an optical emission diagnostics.

The photodiode signal (S) is proportional to the concentration of targeted specie *[J]* and is given by the relation (1).

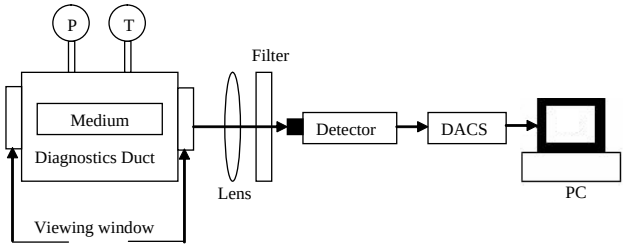

Fig.1. Schematic of optical emission diagnostics

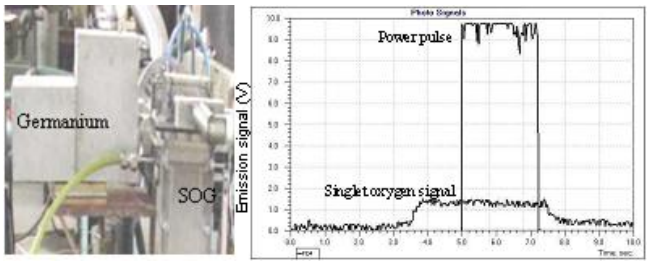

Fig.2. Singlet oxygen yield measurement system with observed emission SO signal with laser power pulse. 50 W tungsten lamp, λ= 1270 nm [25], d = 25.4 mm, A = 0.3 Vtorr^{-1}, Ge – photodiode (J16 Judson Tech., USA)

$$S = A[J] = \frac{AP_J}{kT} \quad (1)$$

Where, *'A'* is calibration constant of the detection system, *'k'* is Boltzmann constant, *'T'* is gas temperature and *'P_J'* is specie partial pressure.

Consider an example of COIL, where pumping source singlet oxygen (SO), [O_2 ($^1\Delta$)], and water vapor, H_2O, are generated during generation of SO can be measured using optical emission technique [25]. It is essential as the generated singlet oxygen may quench with itself and also with undesired water vapor, which is a reaction byproduct.

In case of SO measurement, calibration of the system is carried out by the technique suggested by Zagidullin [26] and calibration factor *'A'* given in Eq. (2) for our setup [5] is found to be ~0.33Vtorr^{-1}. Here it is also essential to take into account the effect of buffer gas dilution. Thus, the singlet oxygen yield (Y_Δ) defined as ratio of SO to total oxygen is subsequently estimated using the following relation,

$$Y_\Delta = kTS_\Delta \frac{(M_{Cl2} + M_{buffer})}{APM_{Cl2}U_{Cl}} \quad (2)$$

Where *'M_{Cl2}'* and *'M_{buffer}'* are the input chlorine and buffer gas flow rates, *'P'* is plenum pressure. Fig.2 shows the photograph of singlet oxygen measurement setup along with observed emission signal of SO superimposed with laser power pulse. In our experiments, the observed singlet oxygen yield is ~64% for peak chlorine flow rate of 1500 mmols^{-1} [12].

1530-437X (c) 2015 IEEE. Personal use is permitted, but republication/redistribution requires IEEE permission. See http://www.ieee.org/publications_standards/publications/rights/index.html for more information.

This article has been accepted for publication in a future issue of this journal, but has not been fully edited. Content may change prior to final publication. Citation information: DOI 10.1109/JSEN.2015.2409114, IEEE Sensors Journal

A similar setup has been used for water vapor fraction estimation by measuring optical emission from O_2 ($^1\Sigma$) (λ=762 nm using Si-photodiode) and O_2 ($^1\Delta$) simultaneously. The water vapor concentration is measured using an optical emission methodology suggested by Spalek *et. al* [10].This allows undertaking preventive measures to keep water vapor its fraction in the permissible range (<5%). The water vapor concentration (C_{water}) can be written as below:

$$C_{water} = C_{relative} \frac{S_\Delta^2}{S_\Sigma} \quad (3)$$

Where, S_Δ and S_Σ are the corresponding photo detector signals and $C_{relative}$ is the calibration factor and is determined using relations for water vapor saturation pressure [27].

B. Optical absorption technique

Optical absorption technique utilizes the property of the species to absorb light at specific wavelength. It basically employs a suitable light source, to generate probe beam, followed by a collimating lens and an interference filter (typically ±5 nm). The beam having passed through the medium is then collected by a detector via a focusing lens. The schematic of the setup that may be employed is shown in Fig. 4.

The concentration/ molar flow rate *'m_J'* is estimated by calculating partial pressure of gas specie (using Beer Lambert's law and perfect gas law) and substituting the expression for the partial pressure in the Dalton' law,

$$m_J = \left\{\frac{M_c kT}{\sigma_v l}\right\} \frac{\ln(I_o/I_v)}{P_{tot} - \left(kT/\sigma_v l\right)\ln(I_o/I_v)} \quad (4)$$

Where, *'I_v'* and *'I_0'*are the light intensity at frequency *'ν'* with and without gas specie respectively. *'σ_v'* is the absorption cross section, *'l'* is length of optical cell, *'k'* is the Boltzmann constant, *'T'* is the temperature of the gas, 'P_{tot}' is the measured total pressure, *'M_c'* is carrier/buffer gas molar flow rate. This concept has been detailed in earlier paper [11].

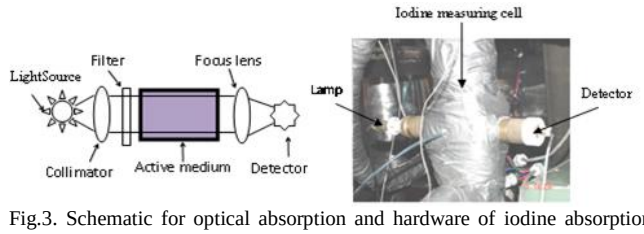

Fig.3. Schematic for optical absorption and hardware of iodine absorption diagnostics. 50 W tungsten lamp, λ= 490 nm, L = 100 mm, d = 25.4 mm, $\sigma_v = 2.1\times10^{-18}$ cm^2, Si – photo detector (RS stock no. 303-674).

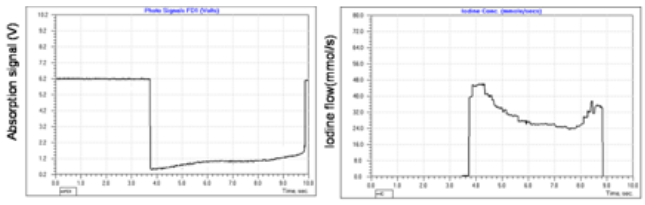

Fig.4. Temporal variation of iodine absorption signal and estimated iodine flow rates.

In context of gas lasers, the concentration/molar flow rates of iodine (λ~490nm) (refer Fig. 3) for photograph of iodine diagnostics) and chlorine (λ=330 nm) [28] in case of COIL and SF_6 (λ=115 nm) in HF/DF lasers may be estimated using optical absorption principle.

The temporal graphs for iodine absorption signal along with estimated molar flow rate are shown in Fig.4. This system has the capability to measure iodine flow rates up to 50mmols^{-1}, and it is used for continuous day-to-day optimization experiments of COIL [12, 29, 30]. Eq. (4) can be directly employed for estimating iodine flow rates.

SF_6 is the source of fluorine atoms essential for generation of HF/DF laser. SF_6 is typically chosen as a fluorine carrier since it is non-toxic, non-corrosive and safe to handle in large quantity. Since supplied SF_6 may have traces of water vapor or oxygen, hence it is appropriate to choose a source wavelength of < 140 nm as water vapor has maximum absorption at 165 nm and oxygen at 142 nm. The highest absorption coefficient for SF_6 is 10^4 m^{-1}[31] at λ = 115nm. A hydrogen argon lamp equipped with MgF_2 windows may be used as the light source coupled with a suitable interference filter. The collimated light passed through the detection cell is detected using Hamamatsu model R 268 photomultiplier tubes. Eq. (4) can subsequently be used for flow rates estimation.

C. Diode Laser based Absorption Spectroscopy

It is becoming increasingly common to employ diode laser based diagnostics especially in case of COIL gas lasers. The principles of optical absorption have already been outlined in the earlier sessions. Lately, various workers [32, 33] including Physical Sciences Inc. [34] have reported use of several of diode based diagnostics setup, which may be employed not only for COIL systems but also elsewhere in other gas lasers. An example in effect is water vapor diagnostics, where a diode laser is used to scan an individual rotovibration line of water $\nu_1+\nu_2$ band in 1.39-μm region. The laser beam is split into signal and reference beams. The system can supposedly measure water molecule densities of the order of 10^{15} cm^{-3}. Diode laser based SO diagnostic system (by PSI) measures oxygen ground state O_2 ($^3\Sigma$) density at 761.2 nm. The beam is split into a reference and a signal beam. Since the absorption signal is weak, the signal is passed 21 times through a diagnostic cell (typically 5 cm wide) in a multi pass Herriott cell configuration.

D. Raman Spectroscopy

Raman spectroscopy is a powerful experimental tool to identify and quantify the species present in the sample. Recently it is being used for diagnostics of singlet oxygen and ground state oxygen in COIL system [35]. It has several advantages over the optical emission method such as, i) allows monitoring of both singlet and ground state oxygen simultaneously in the same measurement volume, ii) experimental problems such as occurrence of dirty windows, fluctuations in source power and aerosol scattering can be ratioed out. However, major problem areas in Raman spectroscopy are due to, i) high-speed flow of mixed gases

1530-437X (c) 2015 IEEE. Personal use is permitted, but republication/redistribution requires IEEE permission. See http://www.ieee.org/publications_standards/publications/rights/index.html for more information.

This article has been accepted for publication in a future issue of this journal, but has not been fully edited. Content may change prior to final publication. Citation information: DOI 10.1109/JSEN.2015.2409114, IEEE Sensors Journal

like SO, residual chlorine and nitrogen at relatively low pressure, ii) Raman scattering cross-section of gases is extremely small. These facts make the Raman signal intensity very low and it becomes difficult to record the Raman signal even with the state of the art CCD detectors. The schematic of Raman diagnostics [36] is shown in Fig.5.

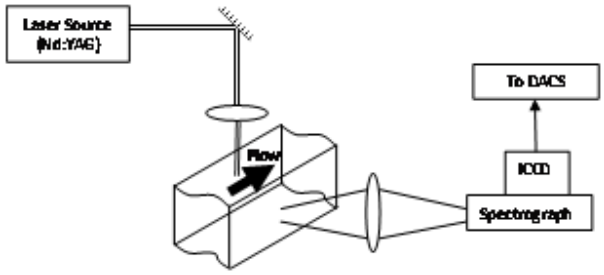

Fig.5. Schematic of Raman scattering diagnostics.

In the Raman spectroscopy, a pump laser such as frequency doubled Nd:YAG laser (Repetition rate ~10 Hz and pulse duration ~20 ns) emitting at 532 nm with pulse energy of nearly 250 mJ/ pulse may be employed. It is focused at the center of the gas flow and Raman scattering is collected perpendicular to the direction of the flow by a combination of lenses and fiber. The fiber is connected to the spectrograph with CCD detector, which records the spectra. The intensity of Raman spectrum is decided by scattered molecule structures. Typically, stokes line for ground state oxygen is at 580 nm and for singlet oxygen occurs at 577 nm. The intensity of Raman signal is directly proportional to the concentration of molecule in sample. Thus, singlet oxygen yield may be written in terms of Raman scattering cross-sections and intensities as,

$$Y = \frac{\left[I_{O_2(1\Delta)}\right]}{\left[I_{O_2(1\Delta)} + I_{O_2(3\Sigma)}\left(\frac{\sigma_{O_2(1\Delta)}}{\sigma_{O_2(3\Sigma)}}\right)\right]} \quad (5)$$

The above equation can be directly used to calculate the singlet oxygen concentration inside the SOG. Similar methodology may be used for targeted detection of various relevant species in other chemical gas lasers.

E. Cavity Ring down Spectroscopy (CRDS)

Optical absorption based concentration measurement methods are suitable for measurement of sufficiently large flow rates or concentration of gas species. However, in case of detection of certain species or gases existing in trace amounts or having a very low absorption cross-section, direct absorption spectroscopy is not suitable. A simple extension of Laser absorption spectroscopy is Cavity Ring–Down Spectroscopy (CRDS) [37, 38]. CRDS is a laser absorption technique, which takes advantage of the enhanced analytical sensitivity that is possible when making absorption measurements using extremely long path lengths. Effective path lengths of up to a few kilometers can be achieved by using a high-finesse optical cavity consisting of two high-reflectivity mirrors (R>99.9 %) to literally "bounce" a pulsed laser back and forth through the absorbing species on the order of about 10^4 times. The back and forth movement of the pulse is called ringing down. The schematic is shown in Fig. 6.

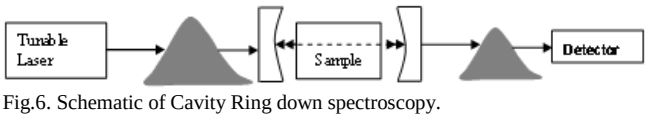

Fig.6. Schematic of Cavity Ring down spectroscopy.

The light that is transmitted through the exit mirror on each pass is measured vs. time. The leaked signal is detected through fast detector and oscilloscope. Under certain conditions, the resulting signal will decay exponentially with time. The decay time is dependent upon the reflectivity of the two mirrors, the distance between the two mirrors, the speed of light, and the molecular absorption coefficient of any absorbing species in the cavity. The exponential decay of signal directly scale with the absorption coefficient of the sample and is expressed as:

$$\alpha(\lambda) = \frac{1}{c}\left(\frac{1}{\tau(\lambda)} - \frac{1}{\tau_0}\right) \quad (6)$$

Where, τ_0 is the decay time without sample and $\tau(\lambda)$ is the decay time with sample at wavelength (λ). Thus in CRDS, by measuring the two decay times, absorption of the sample may be easily detected. CRDS is enormously sensitive. In this technique, 1m cavity length with mirrors 99.95 % reflection can safely measure concentrations up to 100 ppt.

This kind of diagnostics has been utilized for measurement of species in case of COIL such as absolute density of O_2 ($X^3\Sigma_g$) is probed by measuring the O_2 ($b^1\Sigma_g$) [v= 0] ← O_2 ($X^3\Sigma_g$) [v = 0] transition near 760 nm or trace iodine detection at 490 nm or chlorine detection at 330 nm in small-scale systems inside cavity. With the developmental focus shifting to ECOIL systems [39, 40] this technique is bound to find applications for detection of numerous trace species produced in discharge production of singlet oxygen.

III. Cavity Medium Characterization

In gas lasers, it is imperative that one is able to characterize the critical medium parameters inside the cavity. Mach number is one such parameter which influences the laser power and needs to be estimated accurately. Also small signal gain is a representation of the extent of population inversion in the cavity and it is essential that we are able to accurately quantify the gain inside the cavity. Similarly, chemical gas lasers involve mixing of multiple gas streams and a method of determining and being able to quantify a supposedly non-tangible parameter such as extent of mixing or medium homogeneity needs to be worked out. The present section discusses the measurement of these prime parameters of small signal gain, Mach number and medium homogeneity.

A. Small Signal Gain Measurement

In case of gas lasers, small signal gain (SSG) is one of the prime influences on the amount of power extracted from the system. In case of CO_2 GDL, gain medium is CO_2 molecule and lasing occurs at 10.6 μm whereas in HF/DF laser gain medium is HF or DF with lasing at 2.7 or 3.7 μm and COIL lases at 1.315 μm due to iodine atom transition. One of the simplest ways for measurement of small signal gain is to use

1530-437X (c) 2015 IEEE. Personal use is permitted, but republication/redistribution requires IEEE permission. See http://www.ieee.org/publications_standards/publications/rights/index.html for more information.

This article has been accepted for publication in a future issue of this journal, but has not been fully edited. Content may change prior to final publication. Citation information: DOI 10.1109/JSEN.2015.2409114, IEEE Sensors Journal

probe beam method and the other is the *Voigt Profile method*, which is primarily the extension of the former.

Probe Beam Method

Probe beam measurement technique [41] has been extensively used for estimation of the small signal gain in gas lasers. The technique is based on Beer-Lambert's law in which the change (basically amplification) in beam intensity is proportional to the number density of the excited atoms or the population inversion. The present discussion is taken up with reference to COIL laser but is easily extendable for the other two chemical gas lasers i.e. GDL and HF/DF laser. In case of COIL, the approach consists of employing a tunable diode laser having a peak wavelength around 1310 nm with a bandwidth of 20 nm. Since the iodine atoms also have peak absorption at 1315 nm, the diode laser output is locked to 1315 nm (emission wavelength of $I(^2P_{1/2}) \rightarrow I(^2P_{3/2})$ by passing the probe beam through a heated iodine cell (about 800–850 ^oC) and observing the peak absorption. During gain measurements, the laser is operated without resonator mirrors

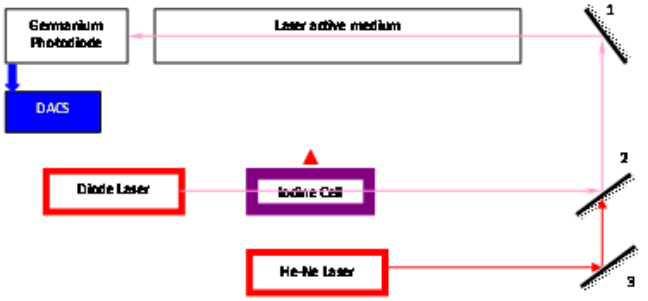

Fig.7. Schematic for gain measurement using probe beam method.

and the heated iodine cell is removed from the path of the probe beam, which is passed through the generated active medium in the laser cavity. The chord of observation in each experiment is set by a beam of He–Ne laser, which is aligned using dichroic mirror (M2) as shown in Fig. 7.

The emission signal along with the signal of the modulated probe beam is observed using a high-gain Ge photodiode. Since the diode laser has a high scanning rate (100 kHz), the photodiode signals are acquired in a data acquisition system with extremely high sampling rates. The gain can thus be directly calculated by employing the following relation [18]:

$$I_v = I_o \exp(gL) \tag{7}$$

Where, 'g' is the small signal gain, 'I_v' is the line center intensity after amplification, 'I_o' is the line center probe laser intensity entering the gain medium and 'L' is the gain length.

In case of HF/DF lasers, a probe beam at the corresponding wavelength is generated by using a suitable diode laser or generating a mini HF/DF laser by dc excitation of subsonic SF_6 followed by injection H or D for generating $HF^*(DF^*)$ [42]. An *InAs PV* detector at 300 K (Judson 512 LD) may be used for detection of amplification of probe beam. Similar measurement methodology may be employed for gain measurement in case of GDL at 10.6 μm using a small CO_2 laser [43] as the probe beam-generating source.

Voigt Profile Method

Voigt Profile, which is a combination of the Lorentz and Doppler profile, has also been used for estimation of small signal gain in case of COIL [44-46]. COIL as stated earlier operates on the strongest $I(^2P_{1/2},F=3) \rightarrow I(^2P_{3/2},F=4)$ hyperfine component of the spin orbit transition of atomic iodine at the wavelength $\lambda = 1.315$ μm. The broadening of the gain line in the uniform laminar gas stream is due to pressure broadening and Doppler broadening that results in Voigt gain line shape. The small signal gain (SSG) on this transition is equal to:

$$g = \frac{7}{12}\left[N_{I^*} - \frac{1}{2}N_I\right]\frac{A\lambda^2}{8\pi}\left(\frac{2}{\pi\Delta\upsilon}\right) \tag{8}$$

Where N_{I^*} is the concentration of excited iodine, N_I is the ground state iodine, λ is the emission wavelength and A is the Einstein stimulated emission coefficient, $\Delta\nu$ is the line width.

B. *Mach number Diagnostics*

The efficiency of gas lasers depends not only on the effective transportation of the pumping source and lasing species into the laser resonator and their proper mixing but also on the flow conditions of the active medium in the cavity. The lasing conditions inside the cavity or resonator are achieved employing supersonic nozzles, the performance of which is governed by the upstream gas flow parameters. The extent of population inversion i.e. small signal gain inside the laser resonator is a function of temperature and hence depends to a large extent on the Mach number in the cavity, which, needs to be monitored continuously during the run for performance optimization.

The typical cavity conditions for all the major high power gas lasers have already been mentioned in the introduction. However, the only word of caution is with reference to COIL, which can operate in both subsonic and supersonic regimes. Although, for high power laser systems only the latter is preferred on account of repeatability, ease of optimization and system volume.

It is ideal to employ Mach number determination unit, which can measure all Mach number whether subsonic or supersonic. Pitot static tube method [30] is a conventional non-optical method, but is flow intrusive and may disturb the flow.

The relevant optical technique is the Laser Doppler Velocimetry (LDV) [47] which is used to measure the instantaneous velocity of a flow field. In this technique a

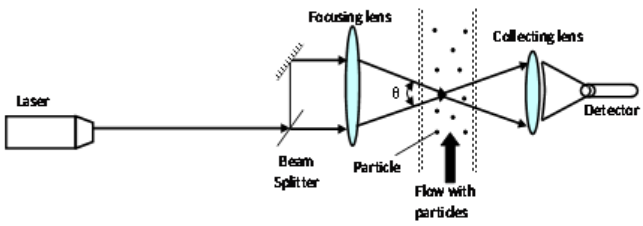

Fig.8. Schematic for Mach number using Laser Doppler Velocimetry

monochromatic laser beam is send toward the target and the reflected radiation is collected. According to the Doppler Effect, the change in wavelength of the reflected radiation is a function of the targeted object's relative velocity. Thus, the

1530-437X (c) 2015 IEEE. Personal use is permitted, but republication/redistribution requires IEEE permission. See http://www.ieee.org/publications_standards/publications/rights/index.html for more information.

This article has been accepted for publication in a future issue of this journal, but has not been fully edited. Content may change prior to final publication. Citation information: DOI 10.1109/JSEN.2015.2409114, IEEE Sensors Journal

velocity of the object can be obtained by measuring the change in wavelength of the reflected laser light. The schematic is shown in Fig. 8.

A flow is seeded with small, neutrally buoyant tracer particles that scatter light. The particles are illuminated by a known frequency of laser light. The scattered light is detected by a photomultiplier tube (PMT). The difference between the incident and scattered light frequencies is called the Doppler shift. By analyzing the Doppler-equivalent frequency of the laser light scattered (intensity modulations within the crossed-beam probe volume) by the seeded particles within the flow, the local velocity of the fluid can be determined.

It basically uses the principle of optical beating, and the particle velocity may be calculated by using the understated expression,

$$f_d = \frac{2\sin\left(\frac{\theta}{2}\right)}{\lambda} u \qquad (9)$$

Where, f_d is the Doppler shift between the incident and the scattered frequencies, λ is the wavelength of the probe beam which is typically a He-Ne laser at 632.8 nm, θ is the angle between the beams forming the probe volume and u is the fluid particle velocity.

This type of a measurement for flow velocity is possible in case of GDL, which is primarily combustion based and has sufficient particulate matter for producing Doppler scattered light. Clear gas flows without presence of any particulate matter as encountered in COIL and HF/DF flows will require introduction of tracer particles for using LDV, which is generally not a preferred methodology.

C. Medium Homogeneity

An important factor affecting the gain in gas lasers is the homogeneity of the medium. In these lasers several gases flow in the cavity e.g. CO_2, N_2, air in CO_2 GDL system, I_2, O_2, O_2 ($^1\Delta$), Cl_2, N_2 and water vapors in COIL, HF/DF, fluorine, N_2, H_2 in HF/DF laser. The proper mixing of gases is critical for achieving optimum power. In order to estimate medium homogeneity in laser chamber, suitable optical measurement techniques are required to be implemented. Mixing is one such parameter, which is apparently difficult to quantify but with its increasing importance in various flow fields, effective techniques have been developed for determining the extent of mixing between multiple gas streams.

Gain Mapping

Measurement of small signal gain using iodine scans diagnostics or Voigt profile method enables mapping the SSG data across the aperture of the resonator window in the direction transverse to the flow. The obtained data provides qualitative information regarding mixing or medium homogeneity, as the gain is high in regions where the mixing is good and poor in regions of insufficient mixing. The quantification of mixing efficiency on the basis of SSG mapping transverse to the flow direction has been suggested by Barmashenko et. al. [48, 49] in case of COIL, using the relation stated below,

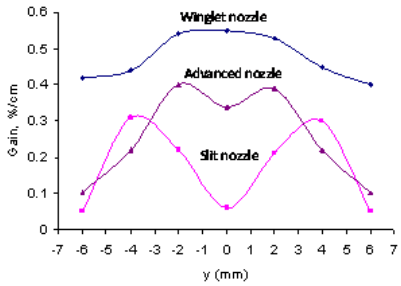

Fig.9. Gain profile transverse to both the direction of flow and to the optic axis. Gain profile is broadest for winglet nozzle. The mixing efficiencies for the slit, advanced and winglet nozzles are nearly 49 %, 60 % and 74 % [50] respectively.

$$\eta_{mix} = \frac{\int_0^H g(y)dy}{g_{\max} H}, \qquad (10)$$

Where, '$g(y)$' is the gain at certain y location, 'g_{max}' is the maximum observed gain, and 'H' is the nozzle height. The typical variation of gain for a slit nozzle, advanced and winglet nozzle cases observed in our COIL experiments is shown in Fig. 9.

The above methodology is easily extendable for GDL and HF/DF lasers by generating a transverse SSG map at various locations along the flow direction. This enables one to ascertain the distance from the nozzle throat where the medium homogeneity is the best and mixing is complete.

Laser Induced Fluorescence (LIF) / Planar-LIF (PLIF)

Laser Induced Fluorescence (LIF) and now -a- days Planar laser-induced fluorescence (planar-LIF) are both common optical measuring techniques used to measure instant whole-field concentration or temperature maps in various flow fields including supersonic flows.

LIF may be used to determine the uniformity of the lasing species in direction of the optical axis. PLIF goes a step further in providing a map of the manner of distribution of the specie being detected over a complete plane in the flow field. PLIF visualization of say the injected flow can enable identification of turbulent structures, penetration distance of the injected (secondary) flow into the primary flow, and relative concentration of the secondary to primary flows.

An example of LIF/PLIF applications is chemical lasers flow fields [51] including COIL [52-54]. In COIL, iodine molecules itself serve as a fluorescence markers. There are two options for pumping iodine molecules from X $^1\Sigma$ state to

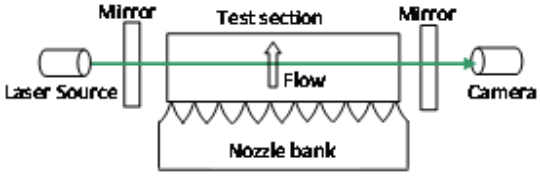

Fig.10. Laser Induced Fluorescence (LIF) schematic.

1530-437X (c) 2015 IEEE. Personal use is permitted, but republication/redistribution requires IEEE permission. See http://www.ieee.org/publications_standards/publications/rights/index.html for more information.

This article has been accepted for publication in a future issue of this journal, but has not been fully edited. Content may change prior to final publication. Citation information: DOI 10.1109/JSEN.2015.2409114, IEEE Sensors Journal

B $^3\Pi$ state, with the excited iodine molecules emitting yellow light. One methods is to use Ar-laser [52] at 514.5 nm and the other is to use Nd:YAG laser at 532 nm to pump a tunable dye laser with Rohdamine 6G emitting over a range of 559 -576 nm [55, 56]. The excited iodine molecules show peak fluorescence at 565 nm. According, to Sakurai [57] the fluorescence of iodine at cavity pressures is sustained for 1.5 μs, which is greater than the typical gating time for cameras (1 μs) allowing the cameras to take images when laser pulse is off but the fluorescence is on.

In case of LIF, the beam is passed in direction perpendicular to the flow and LIF picture is recorded by a

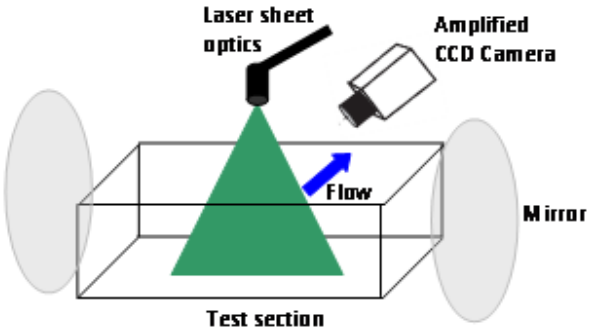

Fig.11. Schematic of Planer Laser Induced Fluorescence (PLIF)

Kodak film or some other similar manner in dark conditions with an optical filter to remove scattering radiation from the incident beam. The schematic of the same is shown in Fig. 10.

In PLIF, the beam is passed through a set of spherical and cylindrical lenses to form a laser sheet in a direction perpendicular to the flow. The PLIF images are then recorded by using an amplified CCD camera preferably perpendicular to the sheet. In case of oblique imaging applicable perspective correction may be carried out. The schematic of the same is shown in Fig. 11.

The fluorescence signal (S_f) is given as,

$$S_f = \frac{E\lambda}{hc}\frac{\chi p}{kT} L\sigma(\lambda,T)\phi(\lambda,p,T)\frac{\Omega}{4\pi}\eta \qquad (11)$$

Where, 'E' is the incident laser energy, 'λ' is the laser wavelength, 'p' is the total pressure, 'T' is the temperature, 'χ' is the mole fraction of fluorescing tracer, 'L' is the length of the illuminated volume, 'Ω' is the detector collection angle, and 'η' is the detector collection efficiency. The fluorescence quantum yield (FQY) 'ϕ' and absorption cross-section 'σ' are both photo physical parameters specific to each tracer.

In order to quantify the mixing behavior of the secondary and primary flows, histograms of the fluorescence intensity in the stack of statistically independent ensemble images are required to be created using image processing software such as DaVIS. Histograms display the probability density of the fluorescence intensity. In each image, the intensity is normalized by the maximum intensity. Initially, a high intensity secondary flow structure may be seen close to the point of injection [58]. As one moves downstream an intermediate intensity in a well mixed flow is generally observed. In other gas lasers, LIF/PLIF studies may be performed for examining medium homogeneity by seeding suitable fluorescent markers.

IV. Laser Power And Pulse Shape Measurement

Both industrial and defense applications warrant the development of gas lasers with high output laser power (ranging from few hundred watts to several hundred kW). It is important to know the overall output power and its pulse shape for the characterization of gas lasers. The reliable detection of the optical radiation is an essential element of laser technology.

Laser energy measurement can be based on calorimeter method. In calorimetric principle [59, 60], laser power is allowed to fall on a conical dump made of black anodized copper material [refer Fig.12] for maximum absorption with minimum loss. A series of K type thermocouples are fixed at the other surface of the cone for measuring the temperature rise. Since the temperature rise is proportional to the energy falling on the conical dump, the total energy (Q) is estimated

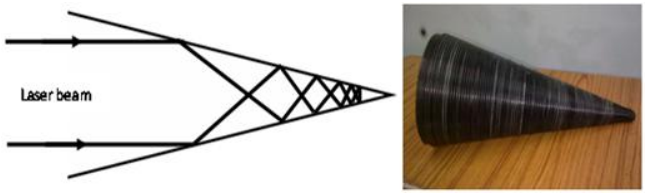

Fig.12. Calorimeter for laser power measurement.

using the relation,

$$Q = mc\Delta T \qquad (12)$$

Where, m is the mass of the calorimeter, 'c' is the specific heat capacity of the calorimeter material and 'ΔT' is the temperature rise. The calibration factor 'mc' for the calorimeter is determined beforehand in order to estimate the total energy dumped directly from measured temperature rise. It is apparent from Fig. 12 that the reflection paths lead to concentration of energy at the tip of the cone. Thus, in order to have uniform temperature rise across the entire body the thermal diffusivity of calorimeter material should be high.

The laser pulse shape and pulse duration can be observed by collecting the scattered photon from the rear mirror (reflecting mirror) of the laser by introducing a scattering medium. The pulse duration measurement is important for power estimation. In case of CO_2 GDL, laser emits at 10.6 μm, which can be detected using Mercury cadmium telluride detector. HF/DF laser wavelength is 2.7-3.7 μm, detection of which may be carried out by using InSb detector. The duration of laser is determined from FWHM of the temporal profile of the laser pulse leading to corresponding net temperature rise observed in the calorimeter enabling power output estimation.

V. Conclusions

High power lasers typically form a multidisciplinary technological area laced with innumerable challenges in its realization as a practical system. It is essential to determine various critical parameters non-intrusively, with necessary precision to be able to optimize these lasers especially in case

1530-437X (c) 2015 IEEE. Personal use is permitted, but republication/redistribution requires IEEE permission. See http://www.ieee.org/publications_standards/publications/rights/index.html for more information.

This article has been accepted for publication in a future issue of this journal, but has not been fully edited. Content may change prior to final publication. Citation information: DOI 10.1109/JSEN.2015.2409114, IEEE Sensors Journal

of large-scale systems. This paper brings out the applicable optical detection techniques for a host of parameters relevant to three prime high power candidates amongst the flowing gas laser systems viz. COIL, HF/DF and CO_2GDL. The optical diagnostics and measurement techniques applicable for optimization and performance analysis of these lasers have been discussed.

REFERENCES

[1] D. L. Carroll, "Overview of high energy lasers: Past, Present and Future", *AIAA paper*, 3102, 2011.

[2] Mainuddin, Gaurav Singhal, R K Tyagi, A K Maini, "Development of Safe Infrared Gas Lasers", *Journal of Optics and Laser Technology*,47, pp. 56-63, 2013.

[3] Jarmila Kodymova, "Overview on the chemical oxygen-iodine laser technology", SPIE, 6346, 2007.

[4] M. Endo, K. Tei, D. Sugimoto, K. Nanri, T. Uchiyama and T. Fujioka, "Development of a prototype COIL for decommissioning and dismantlement", *SPIE*, 4184, pp. 23, 2001.

[5] S.E. Lamberson, "Äirborne lasers", *SPIE*, 4184, pp. 1-6, 2001.

[6] S.E. Lamberson, H.B. Schall, Overview of Airborne lasers test program", *AIAA Paper*, 7650, 2005.

[7] W.E. McDermott, N. R. Pchelkin, D. J. Benard, R. R. Bonsek, "An electronic transition Chemical Laser", *Applied Physics Letters*, 32(8), pp. 469, 1978.

[8] S.J. Davis, W.E. McDermott, M.C. Heaven, "Atomic Iodine Lasers", *CRC Press* (NY), N4, pp. 413-448, 2007.

[9] W. H. Behrens, P. D. Lohn, "Hydrogen and deuterium fluoride chemical lasers", *CRC Press* (NY), N4, pp 341-367, 2007.

[10] W.J. Witterman, "The CO_2 Laser", *Springer*, New York, 1987.

[11] Mainuddin, M. T. Beg, Moinuddin, R. K. Tyagi, R. Rajesh, Gaurav Singhal and A. L. Dawar, "Optical spectroscopic based in-line iodine flow measurement system-an application to COIL", *Sensors and Actuators B*,109, pp. 375-380, 2005.

[12] R. Rajesh, Gaurav Singhal, Mainuddin, R. K. Tyagi and A. L. Dawar "High throughput jet singlet oxygen generator for multi kilowatt SCOIL", *Optics and Laser Technology*, 42, pp. 580-585, 2010.

[13] Manish Gupta, T. Owano, D.S. Baer, A.O'Keefe, S. Williams, "Quantitative determination of singlet oxygen density and temperature for oxygen –iodine laser applications", *Chemical Physics Letters*, 400, pp. 42-46, 2004.

[14] S.J. Davis, "Historical perspective of COIL Diagnostics", *SPIE*, 4631, pp. 66-62, 2002.

[15] P. B. Keating, C. A. Helms, B. T. Anderson, T. L. Rittenhouse, K. A. Truesdell, G. D. Hager, "Two-dimensional gain and cavity temperature maps of a small-scale supersonic COIL", *Proceedings International Conference Lasers'96*, Portland, OR, 1996.

[16] P. Keating, L. Hanko, C.A. Helms, G.P. Perram, "Absolute detection of O_2 ($a^1\Delta$) concentrations", Final Report, Weapons Lab, Air force systems command, 1992.

[17] G.Koop, J.Hartlove, C. Clendening, P.Lohn, C.C. Shih, J. Rothenflue, K.Hulick, K. Truesdell, J. Erkkila, D. Plummer, R. Walter, Airborne Laser Flight-Weighted Laser Module (FLM) and COIL Modeling support", *AIAA Paper*, 33636, 2000.

[18] S. J. Davis, W. T. Rawlins, W. J. Kessler , S. lee, A. J. R. Hunter, M. L. Silva, "Next generation diagnostics for COIL: New approaches for measuring critical parameters", *SPIE*, 5777, pp. 32-38, 2005.

[19] L.V. Von Entress- Fursteneck, J. Handke, K.M. Gruenewald, W.L. Bohn, W.O. Schall., "Supersonic COIL operation at DLR Germany", *SPIE*, 3092, pp. 706 1997.

[20] X. Du, J. Wang, "Systematic diagnostics of a chemical oxygen iodine laser device", *SPIE*, 3574, pp. 560, 1998.

[21] S. Rosenwaks, B.D. Barmashenko, K. Waichman, "A Historical Overview on the mechanism of the COIL kinetics", *SPIE*, 7751, pp. 06:1-14.

[22] A. Boreysho, V. Malkov, A. Savin, "Problems of COIL Fluid dynamics", *SPIE*, 6346, 2007.

[23] D.A. Copeland, "Transport properties for COIL", *AIAA Paper*, 2261, 2004.

[24] D.J. Benard and Pchelkin , "Measurement of $O_2(^1\Delta_g)$ content in the gaseous effluents of a chemical generator", *Review of Scientific Instruments*, 49, pp. 794, 1978.

[25] W.J. Thayer III, "Performance measurement of uniform droplet O_2 ($^1\Delta$) generator", *AIAA Paper*, 3008, 1992.

[26] M. V. Zagidullin, V. D. Nikolaev, M. I. Svitsun, V. S. Safonov, N. I. Ufimtsev, " The study of buffer gas mixing with active gas on chemical oxygen iodine laser performance with jet SOG", *SPIE*, 2702, pp. 310, 1996.

[27] O. Spalek and Jarmila Kodymova, "Singlet Oxygen Generator for Supersonic Chemical Oxygen Iodine Laser - Parametric Study and Recovery of Chemicals", *SPIE*, 2987, pp. 131, 1997.

[28] W.J. Thayer III, C.J. Fisher, "Comparison of predicted and measured output from a transverse flow uniform droplet singlet oxygen generator", *AIAA Paper*, 2454, 1994.

[29] Mainuddin, Gaurav Singhal, R. K. Tyagi, and A. K. Maini, "Diagnostics and data acquisition for chemical oxygen iodine laser", *IEEE Transactions on Instrumentation and Measurement*, 61, 6, pp. 1747-1756, 2012.

[30] Mainuddin, M. T. Beg, Moinuddin, R. K. Tyagi, R. Rajesh, Gaurav Singhal and A. L. Dawar, "Real time gas flow control and analysis for high power infrared gas lasers", *International Journal of Infrared and Millimeter Waves*, 1, pp. 91-105, Jan. 2005.

[31] C. Pradayrol, A. M. Casanovas, I. Deharo, J. P. Guelfucci and J. Casanovas, "Absorption Coefficients of SF6, SF4, SOF2 and S02F2 in the Vacuum Ultraviolet", *J. Phys. III France*, Vol. 6, pp. 603, 1996,.

[32] D. Furman, B.D. Barmashenko, S, Rosenwaks, "Diode-Laser Based absorption Spectroscopy Diagnostics of a Jet type O_2 ($^1\Delta$) generator for Chemical Oxygen Iodine Lasers", *IEEE Journal of Quantum Electronics*, 35, pp. 540- 547, 1999.

[33] K.A. Truesdell, C.A. Helms, S. Frerking, G.D. Hager, "COIL performance modeling and recent advances in diagnostic requirements", *SPIE*, 3092, pp. 676-681, 1997

[34] M. G. Allen, K. L. Carleton, S. J. Davis, W. J. Kessler, and K. R. McManus, "Diode laser- based measurements of water vapor and ground state oxygen in chemical oxygen iodine lasers", *AIAA Paper*, 2433, 1994

[35] V.T. Gylys, L.F. Rubin, "Direct measurement of O_2 ($^1\Delta$) and O_2 ($^3\Sigma$) in chemical oxygen iodine lasers with use of spontaneous Raman imaging", *Applied Optics*, 37, pp. 1026-1031, 1998.

[36] W. Zhao, F. Sang, L. Duo, F. Chen, Y. Zhang and B. Fang, "Measurement of chemical oxygen –iodine laser singlet oxygen generator parameter using Raman Spectroscopy", *SPIE*, 4631, pp. 161, 2002.

[37] G. Berden, R. Peeters, and G. Meijer, "Cavity ring-Down spectroscopy: Experimental schemes and applications", *Int. Rev. Phys. Chem*., 19, 4, pp. 565, 2000.

[38] F. Dong, Manish Gupta, "Off-axis cavity ringdown measurements of tace iodine", *Sensors and Actuators B*, 129, pp. 158-162, 2008.

[39] D. L. Carroll, B.D. Woodard, G.F. Benavides, J.W. Zimmerman, A.D. Palla, J.T. Verdeyen, W.C. Solomon, "Super- linear Enhancement of Electric Oxygen Iodine Laser", *SPIE*, 8677, 2012.

[40] G.F. Benavides, "Scientific Principles for the Electric Oxygen Iodine Laser", Thesis Dissertation, UIUC, 2013.

[41] Jarmila, Kodymova and Otomar Spalek, "A contribution of COIL Laboratory in Prague to the Chemical Oxygen-Iodine Laser research and development", *SPIE*, 4631, pp. 86, 2002.

[42] K. T. Yano, H. M. Bobitch, "Small signal gain measurement in a cw Chemical Laser", *IEEE Journal of Quantum Electronics*, Vol. 14, 1, pp. 12, 1978.

[43] J.D. Anderson Jr., "Gas Dynamic Lasers: Theory, Experiment and State of the Art", Maryland University, Report prepared for Airforce Office of Scientific Research (AFOSR), 1974.

[44] S.J. Davis, W.J. Kessler, P.B. Keating, "Progress in Development of Sensors for COIL Devices", *SPIE*, 3931, 2000.

[45] S. Rosenwaks, D. Furman, E. Bruins, B.D. Barmashenko, "Gain Diagnostic in a supersonic COIL with transonic injection of iodine", *AIAA*, 3428, 1999.

[46] V. D. Nikolaev, M. V. Zagidullin, M. I. Svistun, B. T. Anderson, R. F. Tate, G. D. Hager, "Results of Small-Signal Gain Measurements on a Supersonic Chemical Oxygen Iodine Laser With an Advanced Nozzle Bank", *IEEE Journal of Quantum Electronics*, Vol. 38, 5, pp. 421, 2005.

1530-437X (c) 2015 IEEE. Personal use is permitted, but republication/redistribution requires IEEE permission. See http://www.ieee.org/publications_standards/publications/rights/index.html for more information.

This article has been accepted for publication in a future issue of this journal, but has not been fully edited. Content may change prior to final publication. Citation information: DOI 10.1109/JSEN.2015.2409114, IEEE Sensors Journal

[47] A.A. Cenkner Jr., "Laser Doppler velocimetry measurements on supersonic mixing nozzles that employ tip jets", *AIAA Journal*, 20 (3), pp. 383-389, 1982.
[48] S. Rosenwaks, B. D. Barmashenko, E. Bruins, D. Furman, V. Rybalkin and A. Katz, "Gain and Temperature in a slit nozzle supersonic chemical oxygen iodine laser with transonic and supersonic injection of iodine", *SPIE*, 4631, pp. 11, 2001.
[49] S. Rosenwaks, V. Rybalkin, A. Katz, B. D. Barmashenko, "Diagnostic studies of Ben Gurion University High Efficiency Supersonic COIL", *AIAA*,5165, 2005.
[50] Gaurav Singhal, P. M. V. Subbarao, A. L. Dawar, M. Endo, "Computation of streamwise vorticity in a compressible flow of a winglet nozzle based COIL device", *Optics and Laser Technology*, Vol. 40, pp. 64, 2008.
[51] N.L. Rapagnani, S.J. Davis, "Laser Induced Fluorescence Measurements in Chemical Laser Flowfields", *AIAA Journal*, 1402, 1979.
[52] V. D. Nikolaev, M. V. Zagidullin, G. D. Hager, T. J. Madden, "An efficient supersonic COIL with more than 200 torr of the total pressure in the active medium", *AIAA Paper*, 2427, 2000.
[53] C. A. Noren, C. R. Truman, P. V. Vorobieff, "PLIF Flow Visualization of a Supersonic Injection COIL Nozzle", *AIAA Paper*, 5388, 2005.
[54] P. V. Vorobieff, C.R. Truman, A.M. Ragheb, G.S. Elliott, J.K. L. Woodard, D.M. King, D.L. Carroll, W.C. Solomon, "Mixing Enhancement in multi stream injection nozzles", *Experiments in Fluids*, 00348, pp. 1090, 2011.
[55] C. A. Noren, C. R. Truman, P. V. Vorobieff, "PLIF Flow Visualization and Quantitative Mixing Measurements of Supersonic Injection Nozzle", *AIAA Paper*, 2895, 2006.
[56] C. A. Noren, C. R. Truman, P. V. Vorobieff, "Quantitative Mixing Measurements of Supersonic Injection COIL Nozzle with Trip Jets", *AIAA Paper*, 3881, 2008.
[57] K. Sakurai, G. Capelle, H. P. Broida, "Measurements of Lifetimes and Quenching Cross Sections of the B $^3\Pi_{ou}$ state of iodine using tunable dye laser", *Journal of Chemical Physics*, Vol. 54 (3), pp. 1220, 1971.
[58] A.M. Ragheb, G.S. Elliott, "Low Pressure PLIF Visualization and Mixing Quantification in a Multi Stream Injection Nozzle", *AIAA Paper*, 1439, 2010.
[59] Stuart R Gunn, "Review Article: Calorimetric measurement of laser energy and power", *Journal of Physics E: Scientific Instruments*, Vol. 6, pp. 105, 1973.
[60] L.R. Smith, W.T. Russell, W.E. Case, L.A. Rasmussen, Ä calorimeter for high power cw lasers", IEEE Transactions on Instrumentation and Measurement, Vol. 21(4), pp. 434-438, 1972.

Gaurav Singhal graduated in Mechanical Engineering in 1998 from JMI, New Delhi and received Ph.D. in 2008 from IIT, Delhi. He did his post-doc research work at University of Texas at Austin during 2011-12. He is a Senior Research Scientist at Laser Science and Technology Centre (LASTEC), Delhi. His research interests include high power lasers, high speed unsteady flows, turbulent mixing, laser diagnostics, CFD techniques etc. He has more than 50 publications in international journals/ conferences.

Mainuddin received his degree in Electronics & Communication Engineering in 1994 from JMI, New Delhi and his Masters of Engineering in 2003 from Delhi College of Engineering, Delhi. He received Ph.D. in 2008 from JMI, New Delhi. He is presently working as a Professor in Department of Electronics & Communication Engineering, JMI(Central University), New Delhi. His research interests include optical diagnostics, high power lasers, data communication, optical communication and computer networks etc. He has more than 50 publications in international journals/ conferences.

R Rajesh received M.Sc degree in Physics from Madurai Kamaraj University in 1993 and obtained PhD in Physics from Jamia Millia Islamia New Delhi in 2005. His research interests are in Opto-electronics, laser based instrumentation, Spectroscopy, Optical diagnostics, Acoustic transducers and fiber optics sensor development. He has more than 20 refereed journal publications, 33 international conference papers and several technical reports in his credit.

M T Beg graduated in Electronics & Communication Engineering in 1985 from AMU, Aligarh, completed his Masters of Engineering in 1987 from Delhi University and Ph.D. in 2003 from JMI, New Delhi. He is presently working as a Professor in Department of Electronics & Communication Engineering, JMI, New Delhi. His research interests include data communication, wireless communication and computer networks etc. He has more than 50 publications in international journals/ conferences.

R. K. Tyagi received his Master of Science in Physics in 1979 from Meerut University and obtained Ph.D. in 1991 from University of Burdwan. He is a Senior Research Scientist at Laser Science and Technology Centre, New Delhi. His research interests include high power lasers, laser based ionization, nonlinear, integrated and quasi-optics.

A. L. Dawar had his post graduation in Physics in 1967 from Kurukshetra University and obtained his Ph.D. in 1974 from Delhi University. He did his post-doc research work at University of Newcastle upon Tyne and University of Glasgow during 1974-75 and 1983-84. His research interests included high power lasers, thin film, laser materials, integrated optics, EOCM, etc. He has more than 100 publications in international journals & a book on "Semiconducting Transparent Thin Films" to his credit. He retired as senior Scientist from LASTEC, Delhi in 2004.

1530-437X (c) 2015 IEEE. Personal use is permitted, but republication/redistribution requires IEEE permission. See http://www.ieee.org/publications_standards/publications/rights/index.html for more information.

Volume 3, Issue 1 (2015) 41-44 ISSN 2347 - 3258
International Journal of Advance Research and Innovation

Optimization of Vapour Compression Refrigeration Systems using Mixing of Nanomaterials

R. S. Mishra
Department of Mechanical Engineering, Delhi Technological University, New Delhi, India

Article Info

Article history:
Received 02 February 2015
Received in revised form
20 February 2015
Accepted 28 February 2015
Available online 15 March 2015

Keywords

Vapour Compression Refrigeration Systems,
Energy and Exergy Analysis,
First and Second Law Analysis,,
Irreversibility Analysis,
Efficiency Improvement,
Nano Materials

Abstract

This paper mainly deals with energy exergy analysis for finding irreversibilities in the brine cooled evaporator couped vapour compression refrigeration system using R134a ecofriendly refrigeration for reducing ozone depletion and global warming. The numerical computation was carried out using EES software on utilization of three nano particles (i.e. CuO, Al_2O_3 and TiO_2) and it was observed that thre is a improvement in the refrigerating effect, first law efficiency and second law efficiency and reduction in the the system exergety destruction ratio.

Nomenclature

COP	coefficient of performance (non-dimensional)
VCR	vapour compression refrigeration
CFC	chlorofluorocarbon
HCFC	hydrochlorofluorocarbon
Q	rate of heat transfer (kW)
W	work rate (kW)
T	temperature (K)
ED_Rational	Rational exergy destruction ratio (non-dimensional)
U_e	Evaporator Overall heat heat transfer coefficient (W/m2K)
U_k	Condenser Overall heat heat transfer coefficient (W/m2K)
E_p	exergy rate of product (W)
h	specific enthalpy (kJ/kg)
P	pressure (kPa)
IR	irreversibility (W)
E_f	exergy rate of fluid (W)
mb	Brine mass flow rate (kg/s)
s	specific entropy (kJ/kgK)
EF	exergy rate of fuel (W)
EDR	exergy Destruction Ratio non dimensional based on exergy of product
η	Exergetic efficiency (non-dimensional)
r	refrigerant, space to be cooled
ex	Exergetic

1. Introduction

The methods for finding the first law and second law efficiency of vapour compression and vapour absorption refrigeration systems are well defined in Literature [1].However highest COP indicating the better performance of the vapour compression refrigeration system. The COP of system can be enhanced either by decreasing the work of compressor by introduction of multi stages compressors or increasing the refrigeration effect. It is also possible to reduce the compressor work to considerable extent by compressing the refrigerant very close to the saturation line this can be achieved by compressing the refrigerants in more stages with intermediate inter-cooler. The refrigeration effect can be increase by maintaining the condition of refrigerants in more liquid stage at the entrance of evaporator which can be achieved by expanding the refrigerant very close to the liquid line. The expansion can be brought close to the liquid line by sub-cooling the refrigerant and removing the flashed vapours by incorporating the flash chamber in the working cycle. The evaporator size can be reduced because an unwanted vapour formed is removed before the liquid refrigerant enters in the evaporator. The use of nano particles mixing with R718 in the secondary evaporator enhances the first and second law performances in the vapour compression refrigeration systems.

Corresponding Author,
E-mail address: aj1992tech@gmail.com
All rights reserved: http://www.ijari.org

2. Vapour Compression Refrigeration Refrigeration System Using Mixing Of Nano Materials

The utility of second law analysis on vapour compression refrigeration systems is well defined because it gives the idea for improvements in efficiency due to modifications in existing design in terms of reducing exergy destructions in the components. Due to effect of global warming and ozone depletion the comparison and impact of environmental friendly refrigerants (R507a, R410a, R290, R600, R600a, R1234yf, R404a, R125, R717, R152a and R407C) on vapour compression refrigeration system is important for calculating first law and second law performance on the basis of energetic and exergetic approach. Comparison was done for different nano materials in terms of coefficient of performance, rational

efficiency and exergy destruction ratio, exergy input and exergy of product with variation of brine flow rate of water in the system. It was observed that for all considered nano materials energetic efficiency (first law efficiency) & second law efficiency (rational efficiency), and system exergy destruction and rational exergy destruction ratio of system shows minimum performance using nano copper materials.

3. Literature Review

Now a day's most of the energy utilize in cooling and air conditioning in industrial as well as for domestic applications. In addition with energy consumption, using of refrigerants in cooling and air conditioning having high GWP and ODP are responsible for global warming and ozone depletion. The primary requirements of ideal refrigerants is having good physical and chemical properties, due to good physical and chemical properties such as non-corrosiveness, non-toxicity, non- flammability, low boiling point, Chlorofluorocarbons (CFCs) have been used over the last many decades. But hydro-chloro-fluoro-carbons (HCFCs) and Chlorofluorocarbons (CFCs) having large amount of chlorine content as well as high GWP and ODP, so after 90s refrigerants under these categories are almost prohibited [1].Most of the study has been carried out for the performance evaluation of vapour compression refrigeration system using energetic analysis. But with the help of first law analysis irreversibility destruction or losses in components of system unable to determined [2], so exergetic or second law analysis is the advanced approach for thermodynamic analysis which give a additional practical view of the processes [3]. In addition to this second law analysis also provides new thought for development in the existing system [4].

Now a day, the emphasis put on saving of energy and using of ecofriendly refrigerants due to increase of energy crises, global warming and depletion of ozone layer. [5] The work input required running the vapour compression refrigeration system reduced by using compound compression and work input further decrease by flash intercooling between two compressors using of eco-friendly refrigerants[6]. These scientists did not gone through second law analysis in terms of system exergy destruction ratio used defining irreversibility calculations in various components of vapour compression system [7]. Therefore objective of the present investigations to find out the system exergy destruction ratio for finding irreversibility occurred in the components of vapour compression refrigeration systems because second law analysis is very useful for finding the irreversibility in components as well as in whole system it is a powerful tool for designing and analyzing of air conditioning and refrigeration systems

4. Summary of Literature Review And Gaps Inentified

The study of above literatures and many others not mentioned in the description presents following points-

(i) Thermodynamic analyses of different vapour compression refrigeration systems using different nano refrigerants for enhancing first and second law efficiencies.
(ii) Performance analysis for enhancing overall evaporator heat transfer coefficient, enhancing refrigerating effect, enhancing condenser overall heat transfer coefficients using alternative refrigerants of low GWP and ODP values.
(iii) The different kinds of nanoparticles are used or mixed with the refrigerants for enhancing COP and exergetic efficiency and reduction of exergy destruction ratio.

5. Research Objectives

(i) Thermodynamic analysis of simple modified vapour compression system using alternative refrigerants in the primary circuit and nano refrigerants mixed with R717 for reducing the size of evaporator by enhancing evaporator overall heat transfer coefficient, for reducing cost.
(ii) Thermodynamic analysis of vapour compression system (using alternative refrigerants) for enhancing refrigerating effect, and condenser overall heat transfer coefficient
(iii) Comparative analysis of different nano materials for enghancing first and second law performances and reducing exergy destruction ratio in the system for improving design analysis of vapour compression using alternative refrigerants and hybrid refrigeration systems using performance enhancing devices.

6. Results and Discussions

The study provides the input on the usage of nano particles mixed in R718 in the secondary evaporator circuit for a vapour compression refrigeration system, using R134a ecofriendly refrigerant in the water cooled evaporator-condenser for residential, industrial and medical applications incorporating these refrigeration systems.

Table: 1-a. Variation of Exergey of Fuel (Total Work Input) with Brine Mass Flow Rates of Vapour Compression Refrigeration Systems

Mb (Kg/sec)	Exergy_Fuel (Watts) with Copper	Exergy_Fuel (Watts) with TiO2	Exergy_Fuel (Watts) with Al2O3	Exergy_Fuel (Watts) without nano
0.007	111.0	110.3	110.70	105.10
0.008	111.7	111.0	111.4	105.9
0.009	112.2	111.5	11.90	106.6
0.010	112.6	111.9	112.3	107.10
0.011	113	112.3	112.7	107.6

From table-1a, As brine flow rate is increasing, exergy input is increasing with using mixed nano-materials R718 refrigerant in the secondary evaporator circuit as compared without nano-materials mixed with R718 maximum exergy of fuel is obtained at 0.011 brine mass flow rate. Similarly exergy of product is decreasing as increasing brine mass flow rate.as shown in Table-1b. as brine mass flow rate is increasing the refrigerating effect is increasing in the all most nano mixed R718 used in the secondary circuit of the system.

Table: 1-b. Variation of Exergey of Product with Brine Mass Flow Rates of Vapour Compression Refrigeration Systems

Mb (Kg/sec)	Exergy_ product (Watts) Copper	Exergy_ product (Watts) TiO2	Exergy_ product (Watts) Al2O3	Exergy_ product (Watts) Without nano
0.007	26.28	26.68	26.45	28.49
0.008	25.86	26.30	26.04	28.29
0.009	25.49	25.96	25.68	28.13
0.010	25.17	25.66	25.37	27.99
0.011	24.88	25.4	25.1	27.84

Table: 1-c. Variation of Refrigerating Effect with Brine Mass Flow Rates of Vapour Compression Refrigeration Systems

Mb (Kg/sec)	RE_ copper	RE_ TiO_2	RE_ $Al2O_3$	RE_ without nanomaterials
0.007	389.2	378.6	384.9	309.6
0.008	399.7	388.8	395.3	319
0.009	408.3	397.2	403.8	327
0.010	415	404.3	410.9	334
0.011	421.4	410.3	416.9	340.10

Table-2a shws the variation of condenser heat rejected with brine flow rate in the secondary circuit of evaporator and it was observed that by increasing brine mass flow rate, the heat rejected rate in the condenser is increases and similarly overall evaporator heat transfer coefficient is also increase in the larger rate and similar trends was also observed with lesser variation in the condenser overall heat transfer coefficient.as shown in Table-2(b) and Table-2(c) respectively.

Table: 2-a. Variation of Condenser Heat Rejected with Brine Mass Flow Rates of Vapour Compression Refrigeration Systems

Mb (Kg/sec)	Qcond Copper (Watts)	Qcond TiO2 (Watts)	Qcond Al2O3 (Watts)	Qcond (Watts) without nano
0.007	496.2	484.83	491.6	410.5
0.008	507.4	495.8	507.7	420.8
0.009	516.5	504.7	511.7	429
0.010	524	512.2	519.2	437
0.011	530.3	518.6	525.6	443.6

Table: 2-b. Variation of Evaporator Overall Heat Transfer Coefficient with Brine Mass Flow Rates of Vapour Compression Refrigeration Systems

Mb (Kg/sec)	Ue _copper ($w/m^{2o}C$)	Ue TiO2 ($w/m^{2o}C$)	Ue $Al2O_3$ ($w/m^{2o}C$)	Ue_ without nano Material ($w/m^{2o}C$)
0.007	1380	1239	1320.0	673.45
0.008	1401	1263.34	1342.87	700.47
0.009	1418	1284.03	1361.93	724.47
0.010	1433	1301.9	1378.26	746.05
0.011	1446	1317.55	1392.44	765.63

Table: 2-c. Variation of Condenser Overall Heat Transfer Coefficient with Brine Mass Flow Rates of Vapour Compression Refrigeration Systems

Mb (Kg/sec)	Uk _ copper ($w/m^{2o}C$)	Uk TiO2 ($w/m^{2o}C$)	Uk $Al2O_3$ ($w/m^{2o}C$)	Uk_ Without nano ($w/m^{2o}C$)
0.007	717.61	708.14	714.01	646.31
0.008	726.24	717.26	722.63	655.21
0.009	733.12	724.2	729.54	662.72
0.010	738.74	729.9	735.9	669.16
0.011	743.4	734.7	739.9	674.78

Table: 3-a. Variation of COP with Brine Mass Flow Rates of Vapour Compression Refrigeration Systems

Mb (Kg/sec)	COP_ Copper	COP_ Al_2O_3	COP_ TiO_2	COP_ without nano
0.007	3.507	3.432	3.477	2.946
0.008	3.58	3.504	3.549	3.013
0.009	3.64	3.563	3.609	3.069
0.010	3.689	3.612	3.658	3.119
0.011	3.731	3.653	3.699	3.162

Table3a. shows variation of COP of vapour compression refrigeration system with varying brine mass flow rate of using three nano particles mixed with R718 refrigerant and it was observed that the cop increases by increasing brine mass flow rate and for 0.008kg/sec improvement using nano refrigerants from 11.20% to 18.30% as compared with without nano refrigerants in secondary circuit.Table-3b shows the variation of exergetic efficiency with varing brine mass flow rate in the evaporator in the vapour compression refrigeration system using three nano particles mixed with R718 refrigerant and it was observed that the second law performance improved by increasing brine mass flow rate and for 0.008 kg/sec mass flow rates, the optimum improvement in exergetic efficiency was found to be using nano refrigerants from 16.20% to 18.3% as compared with without nano refrigerants in secondary circuit..

Table: 3-b. Variation of Exergetic Efficiency with Brine Mass Flow Rates of Vapour Compression Refrigeration Systems

Mb (Kg/sec)	ETA-II copper	ETA-II Al_2O_3	ETA-II TiO_2	ETA-II Without nano
0.007	0.3842	0.3842	o.3892	0.3298
0.008	0.4008	0.3922	0.3913	0.3372
0.009	0.4074	0.3988	0.4039	0.3436
0.010	0.4129	0.4043	0.4094	0.3491
0.011	0.4176	0.4090	0.4141	0.3540

Table: 3-c. Variation of exergy Destruction Ratio (EDR_System) with Brine Mass Flow Rates of Vapour Compression Refrigeration

Mb (Kg/sec)	EDR_ System copper	EDR_ System Al_2O_3	EDR_ System TiO_2	EDR_ System without nano
0.007	1.603	1.603	1.569	2.032
0.008	1.495	1.55	1.517	1.965
0.009	1.454	1.507	1.476	1.91
0.010	1.422	1.473	1.442	1.864
0.011	1.395	1.445	1.415	1.825

Table3a. Shows the variation of exergy Destruction ratio based on exergy output in the vapour compression refrigeration system with varying brine mass flow rate of using three nano particles mixed with R718 refrigerant and it was observed that the EDR decrease with increasing brine mass flow rate. Similar trend was observed in the rational exergey destruction which is a ratio of exergety losses in the system to the exergy of fuel. as shown in the Table-3d.

Table: 3-d. Variation of ED_Rational of System with Brine Mass Flow Rates of Vapour Compression Refrigeration Systems

M_b (Kg/sec)	EDR_ System copper	EDR_ System Al_2O_3	EDR_ System TiO_2	EDR_ System without nano
0.007	0.6158	0.6158	0.6108	0.6702
0.008	0.5992	0.6078	0.6087	0.6628
0.009	0.5992	0.6012	0.5961	0.6564
0.010	0.5871	0.5957	0.5906	0.6509
0.011	0.5824	0.6110	0.5859	0.6460

7. Conclusions

The energy and exergy analysis of vapour compression refrigeration systems using R134a ecofriendly refrigerant in primary circuit and three nano particles mixed with R718 in the secondary evaporator is carried and following conclusions are drawn.

1. The, COP, refrigerating effect, overall evaporator heat transfer coefficient, condenser heat transfer coefficient , of vapour compression refrigeration systems is increases with increasing brine mass flow rate using three nano materials and for comparison was made for three nano materials mixed in R718 gives improvement in COP by using copper oxide in the range 11.20% to 18% without nano particles and better performance was found using copper oxide nano material
2. The Second law efficiency (Exergetic efficiency) of using R134a eco-friendly refrigerant in primary evaporator circuit increases with increase in brine mass flow rate in the evaporator secondary circuit and for o.008 kg/sec , the improvement was observed using Copper oxide mixed with R718 in the secondary evaporator circuit gives better Exergetic efficiency as compared to TiO_2 nano particles mixed with R718
3. The COP improvement at brine mass flow rate of 0.008 kg/sec is to be found as 18.35% and second law efficiency improvement is 18.31% using Al_2O_3 nano materials mixed with R718 in secondary circuit as compared to without nano refrigerants. Similarly 17.72% and 17.685% improvement is observed in the second law efficiency at 0.008 kg/sec of brine mass flow rate.
4. The overall evaporator heat transfer coefficient is also increases with increasing brine mass flow rate and at 0.008 kg/sec, the is improvement 91.40% as compared with R134a ecofriendly refrigerant with copper mixed in R718as compared to without nano material and 90.57% improvement using mixed R718 with Al_2O_3 in the secondary evaporator circuit and improvement is 79.58% observed using TiO_2 nano materials mixed with R718 in secondary circuit as compared to without nano refrigerants.

References

[1] A. Arora, S. C. Kaushik, Theoretical Analysis of Vapour Compression Refrigeration System with R502, R404a, and R507a, International Journal of Refrigeration, 31, 2008, 998-1005

[2] Gaurav, R. Kumar, Performance Analysis of Household Refrigerator with Alternate Refrigerants, International Journal of Innovative Research in Science, Engineering and Technology, 3, 2014, 19-53

[3] J. Soni, R. C. Gupta, Performance Analysis of Vapour Compression Refrigeration System with R404a, R407c, and R410a, Int. J. Mech. Eng, 2, 2013, 149-165

[4] L. Jerald, A. D. Senthikumaran, Investigation on the Performance of Vapour Compression System Retrofitted With Zeotropic Refrigerant R404a, 10, 2014, 35-43

[5] M. K. Agrawal, A. G. Matani, Refrigeration System Using Different Refrigerants, International Journal of Engineering and Innovative Technology, 2, 2012, 227-275

[6] R. Cabello, E. Torrela, D. Sanchez, Comparative Evaluation of the Intermediate Systems Employed in Two Stage Refrigeration Cycles Driven by Compound Compressors, I.nt. J. Energy, 35, 2010, 1274-1280

[7] S. Mishra, V. Jain, S. S. Kachhwaha, Comparative Performance Study of Vapour Compression Refrigeration System With R22/ R134a /R410a /R407c /M20, International Journal of Energy and Environment, 2, 2011, 297-310

[8] R. S. Mishra, Methods for Improving Thermodynamic Performance of Vapour Compression Refrigeration System Using Twelve Ecofriendly Refrigerants in Primary Circuit and Nanofluid (Water-Nano Particle Based) in Secondary Circuit, International Journal of Engineering Technology and Advanced Research, 4, 2014, 878-890

[9] R. S. Mishra, Methods for improving thermodynamic performance of vapour compression refrigeration systems using thirteen ecofriendly refrigerants in primary circuit and TiO2 nano particles mixed with R718 used in secondary evaporator circuit for reducing global warming and ozone depletion

[10] R. S. Mishra, Methods for improving thermodynamic performance of vapour compression refrigeration systems using thirteen ecofriendly refrigerants in primary circuit and TiO2 nano particles mixed with R718 used in secondary evaporator circuit for reducing global warming and ozone depletion, 2015

Performance Characteristics of Biodiesel Blend in CI Engine using Artificial Neural Network (Karanja Oil)

Harveer Singh Pali
Department of Mechanical Engineering, NIET, Greater Noida, G. B. Nagar, INDIA
harvirpali@gmail.com*

***Abstract*— The rise in price and consumption of petroleum products and their effects on the industrialization and modernization of the world have been one of the key issues of the researchers. CI (Diesel) engine, one of the sectors based on the fossil fuel, is a prime issue for environmentalists and economists. To overcome this problem and as a substitute for diesel, biofuel is a better option to conserve the limited reserve of fossil fuels such as petroleum, coal and natural gas. Biodiesel, which is produced from variety of vegetable oils and animal fat through transesterification, has a lot of technical advantages over fossil fuels such as lower overall exhaust emission and toxicity, biodegradability, derivation from a renewable and domestic feedstock and negligible sulphur content. This paper deals with artificial neural network (ANN) modelling of a diesel engine using variable Karanja oil blends to predict the engine performance. To acquire data for training and testing the proposed ANN, a Single cylinder, four-stroke diesel engine was fuelled with blended diesel and operated at different engine speeds and loads. The experimental results exposed that blends of Karanja oil with diesel fuel provide better engine performance. Using some of the experimental data for training, an ANN model was developed based on standard Back-Propagation algorithm for the engine. Analysis of the experimental data by the ANN showing that there is a good correlation between the predicted data resulted from the ANN and with the measured ones. Therefore, the ANN proved to be a desirable prediction method in the evaluation of the tested diesel engine parameters.**

***Keywords*— Artificial Neural Network; b p- Brake Power; bsfc- Brake Specific Fuel Consumption; mse- Mean square Error; KO- Karanja Oil**

I. INTRODUCTION

The world is moving towards a sustainable energy era with major emphasis on energy efficiency and use of renewable energy sources. Liquid bio-origin fuels are renewable fuels coming from biological raw material and have been proved to be good substitutes for oil in transportation and agriculture sector. These fuels are gaining worldwide acceptance as solution for the problem of environmental degradation, energy security, restricting import, rural employment and agricultural economy. The most promising available biofuels market sans subsidy is ethanol, methanol, vegetable oil based fuel. Researchers are also striving to develop second generation biofuels from cellulosic materials using different conversion processes [1].

The world is getting modernized and industrialized day by day. As a result vehicles and engines are increasing, but energy sources used in these engines are limited and decreasing gradually. This situation leads to seek an alternative fuel for diesel engine. Biodiesel is an alternative fuel for the diesel engine. The esters produced from vegetables oil and animal fats are known as Biodiesel. This paper investigates the prospect of making of biodiesel from karanja oil. Karanja curcas is a renewable non-edible plant [2].

Artificial neural networks (ANN) are used to solve a wide variety of problems in science and engineering, particularly for some areas where the conventional modeling methods fail. A well trained ANN can be used as a predictive model for a specific application, which is a data-processing system inspired by biological neural system. The predictive ability of an ANN results from the training on experimental data and then validation by independent data. An ANN has the ability to re-learn to improve its performance of new available data [3].

An ANN model can accommodate multiple input variables to predict multiple output variables. It differs from conventional modeling approaches in its ability to learn about the system that can be modeled without prior knowledge of the process relationships. The prediction by a well-trained ANN is normally much faster than the conventional simulation programs or mathematical models as no lengthy iterative calculations are needed to solve differential equations using numerical methods but the selection of an appropriate neural network topology is important in terms of model accuracy and model simplicity. In addition, it is possible to add or remove input and output variables in the ANN if it is needed. The objective of this study was to develop a neural network model for predicting engine parameters like brake power, fuel consumption and torque in relation to input variables such as engine speed and biofuel blends. This model is of a great importance due to its ability to predict engine performance under varying conditions [4].

A K Aggrawal et al have analyzed the performance and emission characteristics of a compression ignition engine

fuelled with Karanja oil and its blends (10%, 20%, 50% and 75%) vis-a-vis mineral diesel. The effect of temperature on the viscosity of Karanja oil has also been investigated. Fuel preheating in the experiments – for reducing viscosity of Karanja oil and blends has been done by a specially designed heat exchanger, which utilizes waste heat from exhaust gases. A series of engine tests, with and without preheating/pre-conditioning have been conducted using each of the above fuel blends for comparative performance evaluation. The performance parameters evaluated include thermal efficiency, brake specific fuel consumption (BSFC), brake specific energy consumption (BSEC), and exhaust gas temperature. Karanja oil blends with diesel (up to 50% v/v) without preheating as well as with preheating can replace diesel for operating the CI engines giving lower emissions and improved engine performance [5].

T.K. Gogoi et al have developed that a cycle simulation model incorporating a thermodynamic based single zone combustion model to predict the performance of diesel engine. The effect of engine speed and compression ratio on brake power and brake thermal efficiency is analysed through the model. The fuel considered for the analysis are diesel, 20%, 40%, 60% blending of diesel and biodiesel derived from Karanja oil (Pongamia Glabra). The model predicts similar performance with diesel, 20% and 40% blending. However, with 60% blending, it reveals better performance in terms of brake power and brake thermal efficiency[6].

Mustafa Canakci et al have discussed that the prediction of the engine performance and exhaust emissions is carried out for five different neural networks to define how the inputs affect the outputs using the biodiesel blends produced from waste frying palm oil. PBDF, B100, and biodiesel blends with PBDF, which are 50% (B50), 20% (B20) and 5% (B5), were used to measure the engine performance and exhaust emissions for different engine speeds at full load conditions. Using the artificial neural network (ANN) model, the performance and exhaust emissions of a diesel engine have been predicted for biodiesel blends [7].

B Ghobdian et al deals with artificial neural network (ANN) modeling of a diesel engine using waste cooking biodiesel fuel to predict the brake power, torque, specific fuel consumption and exhaust emissions of the engine. To acquire data for training and testing the proposed ANN, a two cylinder, four-stroke diesel engine was fuelled with waste vegetable cooking biodiesel and diesel fuel blends and operated at different engine speeds. It was observed that the ANN model can predict the engine performance and exhaust emissions quite well with correlation coefficient (R) 0.9487, 0.999, 0.929 and 0.999 for the engine torque, SFC, CO and HC emissions, respectively. The prediction MSE (Mean Square Error) error was between the desired outputs as measured values and the simulated values were obtained as 0.0004 by the model [8].

II. EXPERIMENTAL SET UP

The experimentation was carried out on single cylinder four stroke direct injection medium speed naturally aspirated water cooled diesel engine.

A computerized automatic testing and acquisition system was installed so that the speed, fuel feed, air consumption and output torque could be controlled and the combustion process, different points pressure measurement, speed (rpm) measurement and cooling water flow measurement transported to this acquisition system could be measured as well.

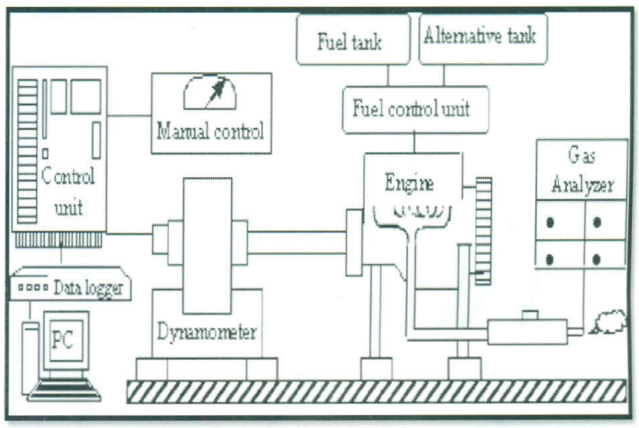

Fig.1 Experimental Setup

The data were displayed promptly on the monitor as well as stored by the computer. The schematic layout of complete experimental set up is shown in figure- 1. The basic data of the engine are given in table no. 1.

TABLE I
SPECIFICATION OF THE ENGINE

S.No.	Parameter	Specification
1	Make	Kirloskar Oil Engines Limited
2	Model	AV1
3	Type	1 Cylinder 4 Stroke
4	Bore	0.08 m
5	Engine No	10.1012/0600106
6	Stroke	0.11 m
7	Displacement	500 cc
8	Fuel	H.S.Diesel
9	Lubricating oil	SAE 30 / SAE 40
10	Rated Power	3.7 kW (5 hp)
11	Injector operating Pressure	15 MPa
12	Injector Timing	220 BTDC(Static)
13	Compression Ratio	17:1
14	Engine Speed	(1400-1600)rev/min
15	IVC	370 ABDC or (217 deg)
16	EVO	300 BBDC or (510 deg)

An engine dynamometer is used to measure the performance of the Single Cylinder Four Stroke Diesel engines. The engine is clamped on test bed and a shaft is connected to the dynamometer rotor. An electric brake dynamometer or electric generator is a device that converts mechanical energy to electrical energy. The specifications of the dynamometer are given in table no. 2.

Dynamometer was used to apply the load on the engine. The applied load causes the engine to produce a reaction torque (Newton's third law of action and reaction).

The product of the torque with the engine speed gives the output power. Figure 2 illustrates the operating principle of a dynamometer.

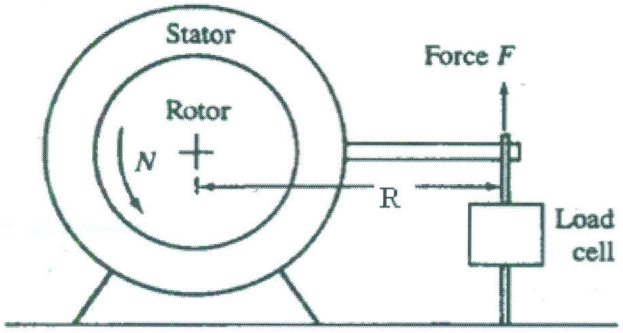

Fig. 2 Schematic diagram of Dynamometer

The rotor is coupled electromagnetically to a stator, which is supported in low friction bearings. [9]

The stator is balanced with the rotor stationary. The torque is exerted on the stator with weights. Using the notation in figure 2, if the torque exerted by the engine is T:

$$\tau = F \times R \quad \ldots\ldots\ldots\ldots\ldots \quad 1$$

The brake power (bp) delivered by the engine and absorbed by the dynamometer is the product of torque and angular speed:

$$\text{Brake Power} = 2\pi N\tau \quad \ldots\ldots\ldots\ldots\ldots \quad 2.$$

TABLE II
THE MAIN SPECIFICATION OF THE DYNAMOMETER

S.No.	PARAMETER	SPECIFICATION
1	Make	Kirloskar Brothers Limited
2	S. No.	07WKJD0015
3	Model	KBM-104
4	Type	Electric Brake air cooled
5	Output	4 KVA
6	Rated Speed	1500 rpm
7	Volt	250 V
8	Ampere	17.4 A
9	P.F.	1
10	Frequency	50 Hz
11	Arm Length	215 mm

A. Data acquisition computer set up

All computation is performed by a personal computer and a LABVIEW software customized by K.C. Engineers is shown in figure 3. A computational thread performs cycle analysis on full 720' cycles of pressure data, and makes the data available to a control thread through a status object.

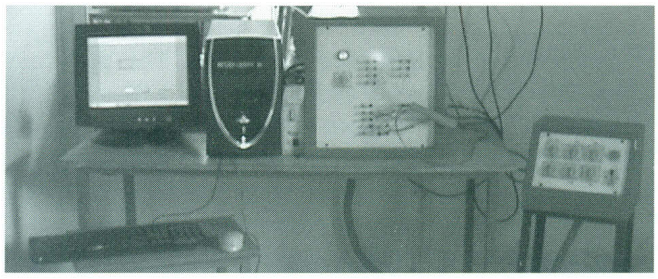

Fig. 3 Data acquisition computer set up

A Lab View data acquisition system is used to condition and log signals from all of the sensors. Analog signals are amplified and low-pass filtered using a National Instruments SCXI 1327 instrumentation amplifier. Thermocouple signals are amplified using a National Instruments SCXI 1112 thermocouple amplifier. Analog to digital conversions are performed using an eight channel, 16 bit card resident in a PC. Pulses from the flow meter are counted using a TDS 3034B digital oscilloscope and converted into flow rate using the sensor's calibration factor. Acquisition of data from the oscilloscope is also controlled through the Lab View software. Figure 4 of the LABVIEW user interface was used to set user inputs and record engine data. Data from the dynamometer is recorded in one of two modes. In the default strip chart mode, the channels are scanned once per second and the data are written in a file which provides a record of everything that happened in the course of an experiment. These data are also written on virtual indicators and strip charts displayed on a software panel to provide real-time graphical indications of the state of the experiment.

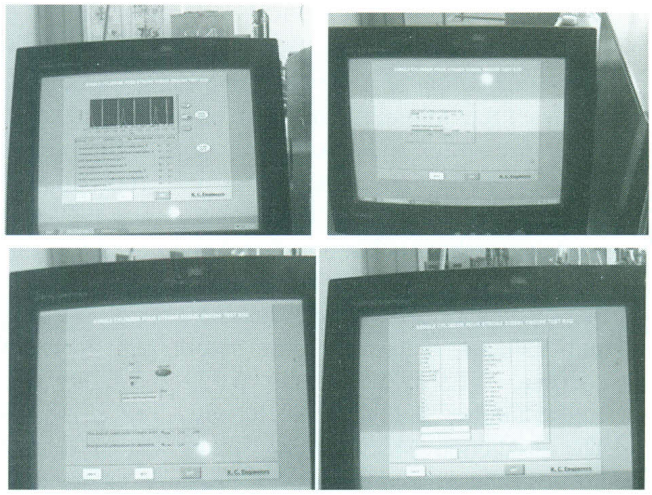

Fig. 4 LabView custom graphical user interface (GUI)

Figure 5 shows arrangement of all input cords in control panel. The interface displays the engine's speed (RPM) on a tachometer, a streaming torque chart, calculated horsepower, throttle and load settings, amount of fuel left, thermocouple temperatures, and ambient room conditions among other items.

The interface also allows the operator to control the engine's speed and torque by varying the load applied by the dynamometer. The data acquisition system also operates in the LabView environment and is integrated with the dynamometer control system. Analog signals from the torque sensor, speed sensor, and thermocouples are polled using the National Instruments 6036E data acquisition board.

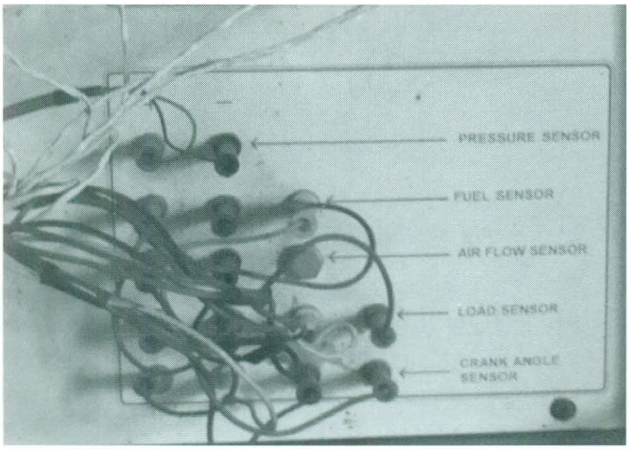

Fig. 5 Control Panel

Digital RS232 signals from the fuel scale are sent and received through the host PC's RS232 port using the LabView software. Data collection at a particular operating point is initiated by clicking a button on the user interface. Two files are created and saved to the user specified directory.

III. EXPERIMENTAL PROCEDURE

The experimental installation used in the work presented here, consists of a Kirloskar model single-cylinder engine. This is a water-cooled, direct-injection, four stroke diesel engine. A dynamometer was used to load the engine at increments of 1 kg to a maximum load of 15 kg. The reaction force and the torque were measured by means of a load cell attached to the dynamometer arrangement. The fuel supply system was modified by solenoid valve which allowed rapid switching between the diesel oil used as a standard and the test plant fuels. At each loading, the speed of the shaft was measured using a rpm sensor. The fuel was fed to the injector pump under measuring arrangement. Volumetric flow rate was measured by noting the time taken for 40 ml of fuel to flow through a graduated measuring device. The relative humidity and ambient temperature were monitored. Experimental procedure is given below step-wise [10];

- At the very outset, the essential parameters and connections are checked before starting the engine for example, cooling water supply, diesel fuel in the tank and pressure measurement etc.
- Before cranking the engine, the flow of cooling water is adjusted, level of fuel tank is checked and then tank outlet is opened. Cranking handle of engine is adjusted with the extended shaft of the crank and the lock of decompression valve is raised. Now crank the engine.
- During the cranking, after a few rotations, the lock of decompression valve is lowered, and then the engine starts functioning. This is the process to start the machine.
- Flow of water outlet and flow of exhaust outlet are checked so as to identify whether the flow is proper or not.
- If all the parameters are in appropriate condition, then the computer is switched on so that Engine software can be used for the acquisition of data from the engine setup.
- As soon as, both, the engine and the computer are connected, constant data (for engine setup) appears on the screen of the computer with two buttons (BACK and NEXT).
- Click on the NEXT button of the software, then it will show the next window of the software. Other devices like control panel, pressure transducer and loading control unit are switched on. It is also kept in mind that no key of loading control unit is switched on. This software window shows the rpm and load on the engine.
- If the data are shown properly, then we start the further process. If everything is up to the mark, then real time graph appears between pressure and crank angle.
- On the very page, all the switches of temperature displays as well as different graph displays appear. When everything is the same as stated, then NEXT button is clicked. Fuel sensor is displayed and the flow of cooling water is displayed on the page.
- The temperature displayed on engine setup is checked according to position of temperature sensor. If it is right, NEXT is clicked. Otherwise, it requires troubleshooting in temperature sensor.
- After clicking on NEXT, a new page opens and solenoid valve starts functioning with a sound. Now, the direct fuel supply of Diesel Engine is closed. This page shows fuel sensor display as well as cooling water display.
- In addition to this, cooling water flow can be edited manually according to the actual flow of rota-meters.
- Next fuel start button is clicked, and with the effect of it the solenoid valve closes.

- Two levels, TOP and BOTTOM, are seen on the page. The top level appears to be ON, whereas the bottom level is in OFF position. The fuel consumption continues from the small fuel cylinder. When the top level empties of the fuel, instantly stopwatch starts and fuel measurement process takes place from top to bottom of the fuel cylinder. As soon as the bottom empties of the fuel, then the watch stops automatically.
- NEXT button is clicked and this reveals the observation table and the calculation. Altogether the Log Reading and Next Reading switches appear.
- Clicking on the Log reading switch, reading is logged automatically for the Run No.1. Simultaneously the data are shown in the calculation table. The data (Run No.1) are saved in scroll window.
- The Detail Calculation button is clicked to get the detailed calculation step by step. Clicking on the 'Next Reading' button, it comes to the initial stage of the experiment (the experimental cycle completes at this point).
- For further runs, load is applied with Rheostat loading unit.

IV. ANN MODEL FOR SINGLE CYLINDER FOUR STROKE DIESEL ENGINE

The use of ANNs for modeling the operation of internal combustion engines is a more recent progress. This approach was used to predict the performance of diesel engines and the specific fuel consumption and fuel air equivalence ratio of a diesel engine. Basically, a biological neuron receives inputs from other sources, combines them in some way, performs generally a non-linear operation on the result, and then outputs the final result. The network usually consists of an input layer, some hidden layers, and an output layer. A popular algorithm is the back-propagation algorithm, which has different variants. Back-propagation training algorithms gradient descent and gradient descent with momentum are often too slow for practical problems because they require small learning rates for stable learning. In addition, success in the algorithms depends on the user dependent parameters learning rate and momentum constant. Faster algorithms such as conjugate gradient, quasi-Newton, and Levenberg–Marquardt (LM) use standard numerical optimization techniques. These algorithms eliminate some of the disadvantages mentioned above. ANN with back-propagation algorithm learns by changing the weights, these changes are stored as knowledge. LM method is in fact an approximation of the Newton's method. The algorithm uses the second-order derivatives of the cost function so that a better convergence behavior can be obtained. In the ordinary gradient descent search, only the first order derivatives are evaluated and the parameter change information contains solely the direction along which the cost is minimized, whereas the Levenberg–Marquardt technique extracts more significant parameter change vector. Suppose that we have a function E(X) which needs to be minimized with respect to the parameter vector x. The error during the learning is called as root-mean squared (RMS)[11].

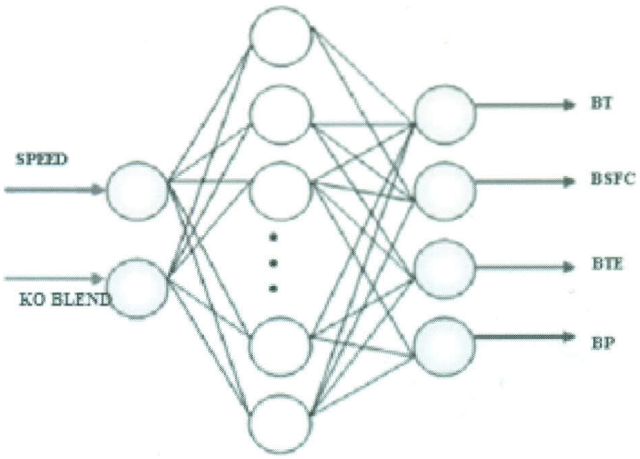

Fig. 6 Simple ANN model of the Diesel Engine

To get the best prediction by the network, several architectures were evaluated and trained using the experimental data. The back-propagation algorithm was utilized in training of all ANN models. This algorithm uses the supervised training technique where the network weights and biases are initialized randomly at the beginning of the training phase. The error minimization process is achieved using a gradient descent rule. There were two input and four output parameters in the experimental tests. The two input variables are engine speed in rpm and the percentage of biodiesel blending with the conventional diesel fuel. The four outputs for evaluating engine performance are engine torque in Nm, Specific Fuel Consumption (SFC) in l/kWh. Therefore, the input layer consisted of 2 neurons which corresponded to engine speed and levels of KO blends and the output layer had 4 neurons. The number of hidden layers and neurons within each layer can be designed by the complexity of the problem and data set. Arrangement of the model is shown in figure 6.

In this study, the number of hidden layers varied from one to two. To ensure that each input variable provides an equal contribution in the ANN, the inputs of the model were pre-processed and scaled into a common numeric range. The activation function for the hidden layer was selected to be logsig linear function suited best for the output layer. This arrangement of functions in function approximation problems or modeling is common and yields better results. However, many other networks with several functions and topologies were examined. Three criteria were selected to evaluate the networks and as a result to find the optimum one among them. The training

and testing performance (MSE) was chosen to be 0.00001 for all ANNs. The complexity and size of the network was also important, so the smaller ANNs had the priority to be selected. Finally, a regression analysis between the network response and the corresponding targets was performed to investigate the network response in more detail. Different training algorithms were also tested and finally Levenberg–Marquardt (trainlm) was selected. The computer program MATLAB 7.9, neural network toolbox was used for ANN design.

In this study, for all the networks, the learning algorithm called back-propagation was applied for the single hidden layer. Scaled conjugate gradient (SCG) and Levenberg–Marquardt (LM) have been used for the variants of the algorithm. These normalized both for the inputs and outputs are realized between the values of 0 and 1. Neurons in the input layer have no transfer function. Logistic sigmoid (logsig) transfer function has been used.

ANN was trained and tested by means of the MATLAB software on a usual PC. In order to identify the output precisely for training stage, increased number of neurons (5–8) in the hidden layer was tried. Firstly, the network was trained successfully, and then the test data were used to test the network. By means of the results deduced by the network, a comparison was carried out using the statistical methods. Errors that happened at the learning and testing stages are described as the RMS and R^2, mean error percentage values, which are defined as follows, respectively

$$R^2 = 1 - \frac{\sum_j (t_j - o_j)^2}{\sum_j (o_j)^2} \quad \ldots\ldots\ldots\ldots\ldots\ldots 3$$

$$RMS = \left(\left(\frac{1}{P}\right) \sum_j (t_j - o_j)^2 \right)^{1/2} \quad \ldots\ldots\ldots\ldots\ldots\ldots 4$$

$$\text{Mean \% Error} = \frac{1}{P} \sum_j \left(\frac{t_j - o_j}{t_j} \times 100 \right) \ldots\ldots\ldots 5$$

Where t is the target value, o is the output value, and p is the pattern. Experimental results for different fuels and biodiesel blends are used as the training and test data for the ANN. The experimentally tested fuels are PBDF, B0, and biodiesel blends with PBDF, which are 50% (B50), 20% (B20) and 10% (B10). The RMS, R^2 and the mean error percentage values were used for comparing all of them.

V. Result and Discussion

The test samples in the range of 0% to 50% blends were tested in the laboratory and show the following differences, while comparing with standard diesel.

- Figure 7 shows fuel flow rate with respect to brake power, in that the lower energy content/ unit mass of blend compared to diesel fuel resulted in increased mass flow rate. A possible explanation is that the more viscous fuel blends reduce normal injection pump leakage enough to make a significant change in the volume discharged per stroke.

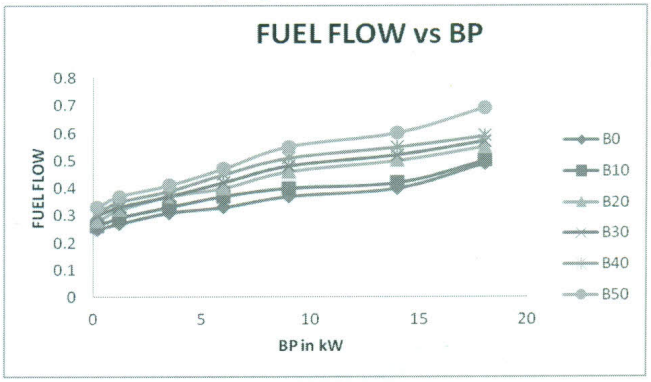

Fig. 7 Variation in fuel flow rate with Brake Power for different Blends

- Although the heating value relationship tends to reduce the specific energy input rate as blend fraction increases, the net effect is an increase in fuel heat supplied. Engine performance and emissions were influenced by basic difference between diesel fuel and (KO + DO) blends such as heating values, viscosity, density etc.
- In Figure 8, at constant speed of 1500 rpm it is observed that the brake thermal efficiency (B.T.E.) decreases with the increase in KO content in diesel. This decrease in efficiency is less, compared to the ability of the combustion system to accept the KO blends as fuel. This may be due to the high viscosity of KO content in the blends, and this may degrade fuel spray characteristics and lead to improper combustion, which result in a minor decrease in efficiency. B.T.E. decreases slightly with respect to BP at the maximum load; this may be due to a lower heat content of KO, which leads to non-uniform combustion of the fuel.

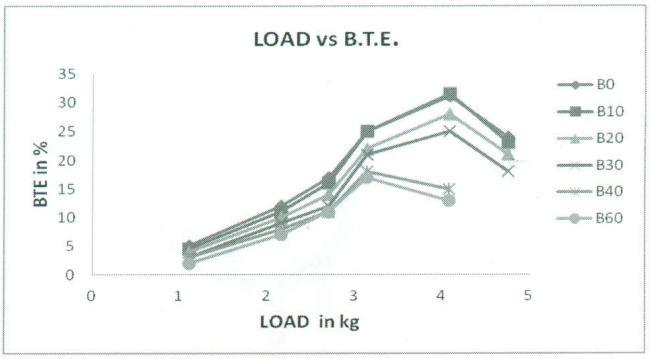

Fig. 8 BTE with Brake Power for different Blends

Considering the error values obtained from the network, we used the network to make predictions for different biodiesel blends (i.e. 50% (B50), 40% (B40), 30% (B30), 20% (B20), and 10% (B10)), other input

values (i.e. humidity, dry bulb temperature, and pressure), which are measured again, and engine speed values used for training. So, mixing ratio has been generalized. The results obtained from ANN are given in Figure 9 to Figure 12. Fuel properties, such as heating value, density and viscosity, have influences on the engine performance and emissions. Therefore, the engine brake torques, BSFC and thermal efficiencies were predicted for different biodiesel blends.

- Figure 9 and Figure 10 show variation of BSFC with respect to engine speed at full load. Due to the above reasons, it is observed that a larger amount of biodiesel is supplied to the engine compared to that of diesel. Therefore, BSFC is higher for biodiesel than diesel. Brake specific energy consumption (BSEC) is an ideal variable because it is independent of the fuel. This energy consumption is the energy input required to develop unit power which can be seen from equation 6.

$$BSFC(or\ SFC) = \frac{Q_f}{BP} \quad \text{..... 6}$$

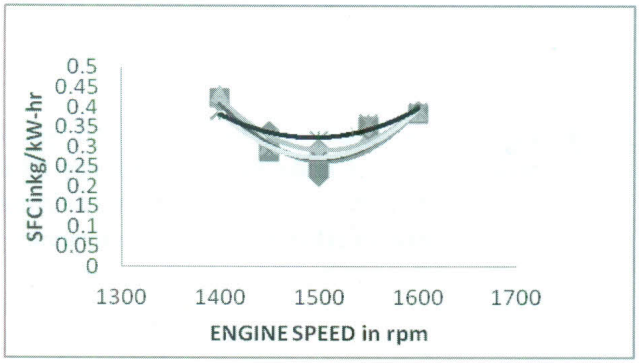

Fig. 9 Actual Performance of the BSFC with respect to engine speed for different fuel blends

Figure 9 and Figure 10 show the BSEC for biodiesel and diesel. Under almost all engine speed range, the BSEC for biodiesel is closer to that of diesel. At 1500 rpm engine speed, BSEC of biodiesel is lower than that of diesel. This small variation may be due to the combined effect of lower heating value and high density of biodiesel.

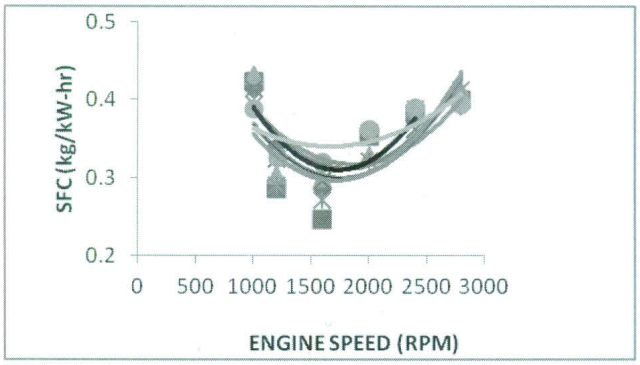

Fig. 10 The predictions of the BSFC with respect to engine speed for different fuel blends.

Figure 11 and Figure 12 also indicate the predicted brake thermal efficiencies for the different biodiesel blends if the engine was operated at different engine speeds at full load condition. Brake thermal efficiency is defined as actual brake work divided by the amount of fuel chemical energy as indicated by the fuel's lower heating value. As the figure shows, the thermal efficiency decreases with increasing ratio of the biodiesel in the fuel blend. The trends of the thermal efficiencies look similar for the brake torques for each fuel.

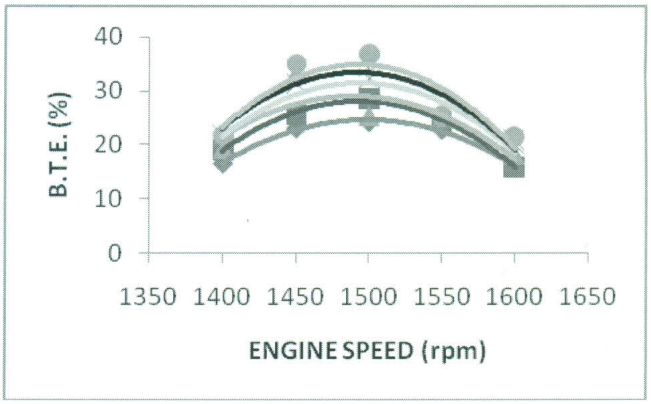

Fig. 11 The Actual Brake Thermal Efficiency with respect to engine speed for different fuel blends.

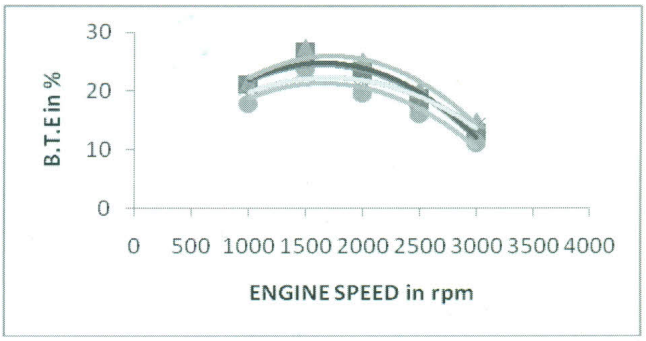

Fig. 12 The predictions of the Thermal Efficiency with respect to engine speed for different fuel blends

The predicted values for BSFC are shown also in Fig. 10. The BSFC increased with the increase of biodiesel percentage in the fuel blend. Therefore, if the engine was fuelled with biodiesel or its blends, the BSFC will increase due to the produced lower brake power caused by the lower energy content of the biodiesel. This result can be clearly seen at the higher biodiesel ratios. At the same time, for the same volume, more biodiesel fuel based on the mass flow was injected into the combustion chamber than pure diesel due to its higher density.

VI. CONCLUSIONS

An experimental investigation was conducted to explore the performance of karanja oil and its fuel blends with diesel in a direct-injection single-cylinder diesel engine and the results obtained suggest the following conclusions:

- Pure Diesel and blends of karanja and diesel oil exhibited similar performance and broadly similar emission levels under comparable operating conditions.
- An artificial neural network (ANN) was developed and trained with the collected data of this research work. The results showed that the training algorithm of Back-Propagation was sufficient enough in predicting specific fuel consumption and Brake thermal efficiency for different engine speeds and different fuel blends ratios.
- An analysis of the experimental data by the ANN exposed that there is a good correlation between the predicted data resulted from the ANN and the measured ones. Therefore, the ANN proved to be a desirable prediction method in the evaluation of the tested diesel engine parameters. There is also a priority in using artificial neural networks, since other mathematical and numerical algorithms might fail due to the complexity and multivariate nature of the problem. Generally speaking, ANN provided accuracy and simplicity in the analysis of the diesel engine performance under test.

REFERENCES

[1] A Walter, A V Ensinas, Combined production of second-generation biofuels and electricity from sugarcane residues. Energy 2010.

[2] Omkar Singh,, J P Pandey, D S Chauhan., "Challenges and Strategies for Sustainable Energy Efficiency and Envionment" organized by U.P Technical University, New Age International Publications, 2006.

[3] J Hertz, A Krogh, R G Palmer. Introduction to the theory of neural computation. Redwood City, NJ: Addison–Wesley Publishing Company; 1991.

[4] Wishart Jeffrey Daniel "Modelling, Simulation, Testing, and Optimization of Advanced Hybrid Vehicle Powertrains" A Ph.D thesis, University of Victoria, 2008.

[5] A K Agarwal, Rajamanoharan, K. Experimental investigations of performance and emissions of Karanja oil and its blends in a single cylinder agricultural diesel engine, Applied Energy 86, 106–112, 2009.

[6] T K Gogoi, D C Baruah, A cycle simulation model for predicting the performance of a diesel engine fuelled by diesel and biodiesel blends, Energy 35, 1317–1323, 2010.

[7] Mustafa Canakci, A.N.Ozsezen, Arcaklioglu,Erol, Erdil,A Prediction of performance and exhaust emissions of a diesel engine fuelled with biodiesel produced from waste frying palm oil. Expert System with Application, vol.36, pp. 9268-9280, 2009.

[8] B.Ghobdian, H. Rahimi, A.M Nikbakht, G Njaf, F. Yusaf, Diesel engine performance and exhaust emission analysis using waste cooking boidiesel fuel with artificial neural network, Renewable Energy, vol.34, pp. 976-982, 2008.

[9] John B Heywood. "Internal Combustion Engine Fundamentals"ch.-2, Mc Graw Hill International edition (Automotive Technology Sciences), Singapore, 1998.

[10] Harveer Singh Pali, "Prediction of performance parameters of blended fuelled diesel engine using ANN" M.Tech. Thesis, GBTU, Lucknow, 2010.

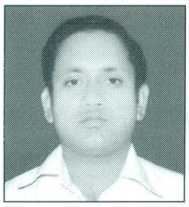

Harveer Singh Pali obtained his Bachelor of Engineering from MJP Rohilkhand, Bareilly and Master of Technology from UPTU, Lucknow in Mechanical Engineering. Currently, he is working as an Assistant Professor in NIET, Greater Noida in Dept. of Mechanical Engineering. He is also doing his doctoral research from Delhi Technological University, New Delhi under the guidance of Dr (Prof.) Naveen Kumar. Mr. Pali's areas of interest include bio-fuel, renewable energy sources, and production and utilization of Bio-Diesel oil in diesel engine to measure various characteristics like performance, combustion and emission.

ISBN 978-93-5156-328-0
International Conference of Advance Research and Innovation (ICARI-2015)

Performance Evaluation of Ecofriendly Refrigerants in the Low Temperature Circuit in Terms of First Law and Second Law Efficiency of Three Stages Cascade Vapour Compression Refrigeration of Biomedical Applications

R.S. Mishra
Department of Mechanical Engineering, Delhi Technological University, New Delhi, India

Article Info

Article history:
Received 2 January 2015
Received in revised form
10 January 2015
Accepted 20 January 2015
Available online 31 January 2015

Keywords

Three stages cascade refrigeration system, Energy –Exergy analysis, Low temperature cascade system, Irreversibility Prediction, Biomedical applications

Abstract

Biomedical preservation requires storing biological specimens like stem cells blood and organs, at a storage temperature below -95oC. ,Hence, the main aim of the current research is to conduct a thermodynamic energy and exergy analysis to determine the thermal performance of three stages / four stages cascade refrigeration systems in the high temperature condenser temperature of 70oC using R1234ze and R1234yf in high temperature circuit and varying evaporator temperature (-20 oC to 10oC) in High temperature circuit, Varying evaporator temperature in first intermediate evaporator temperature (-70oC to -90oC) circuit using R134a and R410a as ecofriendly refrigerants is investigated. For low temperature evaporator temperature(-145oC to -100 oC) using hydrocarbons (R290, R600 and R600a) , R404a and other refrigerants in low temperature evaporator circuit on system performances (i.e. overall system coefficient of performance, (first law efficiency), exergetic efficiency (second law efficiency) and system exergy destruction ratio (EDR) is investigated in three stages /four stages cascade refrigeration systems are shown in this paper

1. Introduction

Human body organ preservation requires storage temperature below -95^{o}C. For long-term storage of biological materials, temperatures below -100^{o}C are generally considered to safeguard [1] .Gnerally the temperature accuired by the single-cycle vapour compression refrigeration system arround -40^{o}C temperature, and the efficiency start deteriorate across -35^{o}C due to the vast difference between the evaporating and condensing temperatures. Thus, in order to reach a lower temperature, the utility of a cascade refrigeration system is significant [8,9] . In cascade refrigeration systems consist of at least two refrigeration systems that work independently. The two or more than refrigeration systems are connected by a cascade heat exchanger, where heat is released in the condenser low-temperature circuit (LTC) and is absorbed from the evaporator high-temperature circuit (HTC).The eco-refrigerants have good thermo physical properties and are environmentally friendly can be used for low temperature applications below -80^{o}C [3]

Hence, the main aim of the current research is to conduct a thermodynamic energy and exergy analysis to determine the thermal performance of three stages / four stages cascade refrigeration systems by varying the high temperature condenser temperature from 0^{o}C to 70^{o}C using R1234ze (GWP =6) and R1234yf (GWP=4) in high temperature circuit with zero degree centigrade evaporator temperature in High temperature circuit, and (-80^{o}C) evaporator temperature in intermediate circuit using R134a and R410a as ecofriendly refrigerants is investigated.

The effect of various ecofriendly refrigerants in the low temperature evaporator temperature (-135^{o}C) using hydrocarbons (R290, R600 and R600a) , R404a and other refrigerants in low temperature evaporator circuit is also investigated.

2. Literature Review

Several researchers [3, 4, 6, 7, 9, 10, 11, 12, 13] have evaluated the thermodynamic performance of the two-stage cascade refrigeration systems. Bhattacharyya et al. [2] studied a carbon dioxide–propane (R744–R290) optimum cascade evaporating system to define an evaporating temperature of R744 for application in heating circuits. Getu and Bansal [5] analyzed a carbon dioxide–ammonia (R744–R717) cascade system thermodynamically to determine the optimum condensing temperature of R744 in the low-temperature circuit and mass flow ratio, to give the system maximum COP in terms of sub-cooling, superheating, evaporating temperature, condensing temperature and temperature difference in the system's cascade condenser. The thermodynamic analysis of the carbon dioxide–ammonia (R744–R717) cascade system by Dopazo Alberto, et al. [4] employed both exergy analysis and energy optimization, to determine the optimum condensing temperature of R744 in the low-temperature circuit. Lee et al. [7] also analyzed a carbon dioxide–ammonia (R744–R717) cascade system thermodynamically to determine the optimum condensing temperature of R744 in the low-temperature circuit. M. Idrus Alhamid et al. [8a] also developed multilinear regression method in the two stage cascade refrigeration system using R717 refrigerant in the high temperature circuit and R744 mixed hydrocarbon blends in the low temperature circuits and obtained maximum coefficient of performance and optimum mass flow ratio of high-temperature circuit to that of low temperature circuit, and find out the optimum

Corresponding Author,
E-mail address: professor_rsmishra@yahoo.co.in
All rights reserved: http://www.ijari.org

evaporating temperature of high-temperature circuit. M. Idrus Alhamid et al. [8b] also conducted experimental studies of cascade refrigeration system using a refrigerant mixture ofCO2 and ethane on LTC and concluded their thermal performance i.e. increased cooling load, the evaporator inlet and outlet temperature difference will increased, however the pressure difference is almost constant. They obtained the COP values 0.35, 0.48, 0.60 at LTC for cooling loads of 90 Watts, 120 Watts and 150 Watts respectively.

3. Research Gaps Identified

Although lot of research work available on the two stages cascade refrigeration systems for lower temperature of circuit up to minimum temperature up to (-70^{o}C) but using ecofriendly new refrigerants such as R1234ze (of GWP six and zero ODP) and R1234yf (of GWP four and zero ODP) in three stages cascade refrigeration systems maintaining temperature below -95 ^{o}C for biomedical applications etc is not reported in literature so far. The effect of temperature overlapping in the cascade systems is also known as approach1 (Cascade condenser1-evaporator temperature1) and approach 2 (cascade condenser temperature-evaporator temperature2) and approach 3 (cascade condenser temperature3-evaporator temperature3) on system performances (i.e. overall system coefficient of performance, (first law efficiency), exergetic efficiency (second law efficiency) and system exergy destruction ratio (EDR) is also investigated in three stages cascade refrigeration systems. The results of present investigated systems are shown in this paper

4. System Description

The systems chosen for present investigation is three stages cascade vapour compression refrigeration system, which consist of R1234ze /R1234yf in high temperature evaporator circuit (HTC) while R134a/R410a in the intermediate temperature cascade circuit (ICT) and hydro-carbons and other ecofriendly refrigerants in the low temperature evaporator circuit (LTC). The performance equations using energy exergy analysis for finding irreversibilities in the system as well as components the three stages cascade vapour compression refrigeration system have been formulated and performance equations have been analysed by using EES and results for above system have been shown in Table-1 to 6 respectively.

5. Results and Discussions

The performance of three stages cascade refrigeration system using R1234ze in hot temperature evaporator circuit and R1234a in intermediate temperature circuit and six ecofriendly refrigerants in low temperature evaporator circuit are shown in presented Table-1(a) to Table 1(d) respectively. It was observed that using R1234ze in high temperature circuit gives better performance than using ecofriendly R1234yf refrigerant. It was also observed that using R134a in the intermediate temperature circuit gives better thermal performance in terms of overall system COP and exergetic efficiency (in terms of second law efficiency)than using R410a in the intermediate temperature circuit. The exergy destruction ratio is larger by using R1234yf in high temperature circuit while using R410a in the intermediate temperature circuit is also higher than using R134a in the intermediate temperature circuit.

Table: 1(a). First law performance (overall system) Exergetic Efficiency (second law efficiency) and system exergy Destruction Ratio (EDR) of Four stages cascade refrigeration system using ecofriendly R1234ze refrigerant in the high temperature evaporator circuit and ecofriendly R134a in intermediate cascade evaporator temperature circuit and six ecofriendly Refrigerants used in low temp evaporator circuit for T_{cond}= 70 ^{o}C, $T_{cascade_eva1}$= 0 ^{o}C, $T_{cascade_eva2}$= - 80 ^{o}C ,T_{eva3}= - 135 ^{o}C, Temperature overlapping (Approach1)=Approach2= 10 (^{o}C) and $Compressor_{Efficiency1}$=0.80 $Compressor_{Efficiency2}$= 0.80, $Compressor_{Efficiency3=}$ 80%

Eco friendly Refrigerant in LTC	System COP	System EDR	Exergetic Efficiency
R404a	0.2230	2.867	0.2586
Ethylene	0.2179	2.958	0.2526
Ethane	0.2241	2.848	0.2599
R290	0.2266	2.806	0.2627
R600a	0.2306	2.741	0.2673
R600	0.2299	2.752	0.2665

Table: 1(b). First law performance (overall system) Exergetic Efficiency (second law efficiency) and system exergy Destruction Ratio (EDR) of Four stages cascade refrigeration system using ecofriendly R1234yf refrigerant in the high temperature evaporator circuit and ecofriendly R134a in intermediate cascade evaporator temperature circuit and six ecofriendly Refrigerants used in low temp evaporator circuit for T_{cond}= 70 ^{o}C, $T_{cascade_eva1}$= 0 ^{o}C, $T_{cascade_eva2}$= - 80 ^{o}C , T_{eva3}= - 135 ^{o}C, Temperature Temperature -overlapping (Approach1) =Approach2= 10 (^{o}C) and $Compressor_{Efficiency1}$= 0.80, $Compressor_{Efficiency2}$= 0.80 $Compressor_{Efficiency3=}$ 0.80

Refrigerant in LTC	System COP	System EDR	Exergetic Efficiency
R404a	0.2081	3.145	0.2413
Ethylene	0.2034	3.241	0.2358
Ethane	0.2091	3.125	0.2424
R290	0.2114	3.080	0.2451
R600a	0.2150	3.011	0.2493
R600	0.2144	3.023	0.2486

Table: 1(c). First law performance (overall system) Exergetic Efficiency (second law efficiency) and system exergy Destruction Ratio (EDR) of Four stages cascade refrigeration system using ecofriendly R1234ze refrigerant in the high temperature evaporator circuit and ecofriendly R410a in intermediate cascade evaporator temperature circuit and six ecofriendly Refrigerants used in low temp evaporator circuit for T_{cond}= 70 ^{o}C, $T_{cascade_eva1}$= 0 ^{o}C, $T_{cascade_eva2}$= - 80 ^{o}C ,T_{eva3}= - 135 ^{o}C, Temperature overlapping (Approach1)=Approach2= 10 (^{o}C) and $Compressor_{Efficiency1}$=0.80, $Compressor_{Efficiency2}$= 0.80, $Compressor_{Efficiency3=}$ 80%

Eco friendly Refrigerant in LTC	System COP	System EDR	Exergetic Efficiency
R404a	0.2228	2.871	0.2583
Ethylene	0.2177	2.962	0.2524

Ethane	0.2239	2.852	0.2596
R290	0.2264	2.810	0.2625
R600a	0.2303	2.745	0.2670
R600	0.2297	2.756	0.2663

Table: 1(d). First law performance (overall system) Exergetic Efficiency (second law efficiency) and system exergy Destruction Ratio (EDR) of Four stages cascade refrigeration system using ecofriendly R1234yf refrigerant in the high temperature evaporator circuit and ecofriendly R410a in intermediate cascade evaporator temperature circuit and six ecofriendly Refrigerants used in low temp evaporator circuit for T_{cond}= 70 ^{o}C, $T_{cascade_eva1}$= 0 ^{o}C, $T_{cascade_eva2}$= - 80 ^{o}C , T_{eva3}= - 135 ^{o}C, Temperature -overlapping (Approach1) =Approach2= 10 (^{o}C) and $Compressor_{Efficiency1}$= 0.80, $Compressor_{Efficiency2}$= 0.80 $Compressor_{Efficiency3=}$ 0.80

Refrigerant in LTC	System COP	System EDR	Exergetic Efficiency
R404a	0.2079	3.149	0.2410
Ethylene	0.2032	3.245	0.2355
Ethane	0.2089	3.129	0.2422
R290	0.2114	3.084	0.2448
R600a	0.2148	3.015	0.2491
R600	0.2142	3.027	0.2483

Similarly the circuit first law efficiency COP of low temperature circuit) is significantly affecting using different ecofriendly refrigerants in the low temperature evaporator circuit used for biomedical applications. The Circuit COP using R600a is better than using other ecofriendly refrigerants. Therefore by using safety measures one can use R600a in the three stages cascade refrigeration system due to better first law and second law performances.

Table: 2(a). First law performance (overall system) Exergetic Efficiency (second law efficiency) and system exergy Destruction Ratio (EDR) of Four stages cascade refrigeration system using ecofriendly R1234ze refrigerant in the high temperature evaporator circuit and ecofriendly R134a in intermediate cascade evaporator temperature circuit and six ecofriendly Refrigerants used in low temp evaporator circuit for T_{cond}= 70 ^{o}C, $T_{cascade_eva1}$= 0 ^{o}C, $T_{cascade_eva2}$= - 80 ^{o}C , T_{eva3}= - 135 ^{o}C, Temperature -overlapping (Approach1) =Approach2= 10 (^{o}C) and $Compressor_{Efficiency1}$= 0.80, $Compressor_{Efficiency2}$=0.80, $Compressor_{Efficiency3=}$ 0.80

Refrigerant in LTC	COP_{HTC}	COP_{ITC}	COP_{LTC}
R404a	1.797	1.118	1.163
Ethylene	1.797	1.118	1.117
Ethane	1.797	1.118	1.173
R290	1.797	1.118	1.196
R600a	1.797	1.118	1.234
R600	1.797	1.118	1.228

Table: (2b). First law performance (overall system) Exergetic Efficiency (second law efficiency) and system exergy Destruction Ratio (EDR) of Four stages cascade refrigeration system using ecofriendly R1234yf refrigerant in the high temperature evaporator circuit and ecofriendly R134a in intermediate cascade evaporator temperature circuit and six ecofriendly Refrigerants used in low temp evaporator circuit for T_{cond}= 70 ^{o}C, $T_{cascade_eva1}$= 0 ^{o}C, $T_{cascade_eva2}$= - 80 ^{o}C , T_{eva3}= - 135 ^{o}C, Temperature-overlapping (Approach1) =Approach2= 10 (^{o}C) and $Compressor_{Efficiency1}$= 0.80, $Compressor_{Efficiency2}$= 0.80 $Compressor_{Efficiency3=}$ 0.80

Refrigerant in LTC	COP_{HTC}	COP_{ITC}	COP_{LTC}
R404a	1.544	1.118	1.163
Ethylene	1.544	1.118	1.117
Ethane	1.544	1.118	1.173
R290	1.544	1.118	1.196
R600a	1.544	1.118	1.234
R600	1.544	1.118	1.228

Table: 2(c). First law performance (overall system) Exergetic Efficiency (second law efficiency) and system exergy Destruction Ratio (EDR) of Four stages cascade refrigeration system using ecofriendly R1234ze refrigerant in the high temperature evaporator circuit and ecofriendly R410a in intermediate cascade evaporator temperature circuit and six ecofriendly Refrigerants used in low temp evaporator circuit for T_{cond}= 70 ^{o}C, $T_{cascade_eva1}$= 0 ^{o}C, $T_{cascade_eva2}$= - 80 ^{o}C , T_{eva3}= - 135 ^{o}C, Temperature Temperature -overlapping (Approach1) =Approach2= 10 (^{o}C) and $Compressor_{Efficiency1}$= 0.80, $Compressor_{Efficiency2}$= 0.80 $Compressor_{Efficiency3=}$ 0.80

Refrigerant in LTC	COP_{HTC}	COP_{ITC}	COP_{LTC}
R404a	1.797	1.116	1.163
Ethylene	1.797	1.116	1.117
Ethane	1.797	1.116	1.173
R290	1.797	1.116	1.196
R600a	1.797	1.116	1.234
R600	1.797	1.116	1.228

Table: (2d). First law performance (overall system) Exergetic Efficiency (second law efficiency) and system exergy Destruction Ratio (EDR) of Four stages cascade refrigeration system using ecofriendly R1234yf refrigerant in the high temperature evaporator circuit and ecofriendly R410a in intermediate cascade evaporator temperature circuit and six ecofriendly Refrigerants used in low temp evaporator circuit for T_{cond}= 70 ^{o}C, $T_{cascade_eva1}$= 0 ^{o}C, $T_{cascade_eva2}$= - 80 ^{o}C , T_{eva3}= - 135 ^{o}C, Temperature-overlapping (Approach1) =Approach2= 10 (^{o}C) and $Compressor_{Efficiency1}$= 0.80, $Compressor_{Efficiency2}$= 0.80 $Compressor_{Efficiency3=}$ 0.80

Refrigerant in LTC	COP_{HTC}	COP_{ITC}	COP_{LTC}
R404a	1.544	1.116	1.163
Ethylene	1.544	1.116	1.117
Ethane	1.544	1.116	1.173
R290	1.544	1.116	1.196
R600a	1.544	1.116	1.234
R600	1.544	1.116	1.228

As approach-1 (temperature overlapping between low temperature condenser and intermediate evaporator circuit) decreases, the first law efficiency (overall system COP) increases and also second law efficiency in terms of exergetic efficiency increases.

Table: 3(a). Effect of Approach1 on First law performance (overall system) Exergetic Efficiency (second law efficiency) and system exergy Destruction Ratio (EDR) of Four stages cascade refrigeration system using ecofriendly R1234ze refrigerant in the high

temperature evaporator circuit and ecofriendly R134a in intermediate cascade evaporator temperature circuit and six ecofriendly Refrigerants used in low temp evaporator circuit for T_{cond}= 70 ^{o}C, $T_{cascade_eva1}$= 0 ^{o}C, $T_{cascade_eva2}$= - 80 ^{o}C , T_{eva3}= - 135 ^{o}C, Temperature -overlapping (Approach1) =Approach2= 10 (^{o}C) and $Compressor_{Efficiency1}$= 0.80, $Compressor_{Efficiency2}$= 0.80 $Compressor_{Efficiency3=}$ 0.80

Effect of Approach-1	System COP	System EDR	Exergetic Efficiency
15	0.2110	3.087	0.2447
10	0.2230	2.867	0.2586
5	0.2352	2.667	0.2727
0	0.2477	2.483	0.2871

Table: 3(b). Effect of Approach1 on First law performance (overall system) Exergetic Efficiency (second law efficiency) and system exergy Destruction Ratio (EDR) of Four stages cascade refrigeration system using ecofriendly R1234yf refrigerant in the high temperature evaporator circuit and ecofriendly R134a in intermediate cascade evaporator temperature circuit and six ecofriendly Refrigerants used in low temp evaporator circuit for T_{cond}= 70 ^{o}C, $T_{cascade_eva1}$= 0 ^{o}C, $T_{cascade_eva2}$= - 80 ^{o}C , T_{eva3}= - 135 ^{o}C, Temperature-overlapping (Approach1) =Approach2= 10 (^{o}C) and $Compressor_{Efficiency1}$= 0.80, $Compressor_{Efficiency2}$= 0.80 $Compressor_{Efficiency3=}$ 0.80

Effect of Approach-1	System COP	System EDR	Exergetic Efficiency
15	0.1970	3.378	0.2284
10	0.2081	3.145	0.2413
5	0.2193	2.932	0.2543
0	0.2303	2.738	0.2675

Table: 3(c). Effect of Approach1 on First law performance (overall system) Exergetic Efficiency (second law efficiency) and system exergy Destruction Ratio (EDR) of Four stages cascade refrigeration system using ecofriendly R1234ze refrigerant in the high temperature evaporator circuit and ecofriendly R410a in intermediate cascade evaporator temperature circuit and six ecofriendly Refrigerants used in low temp evaporator circuit for T_{cond}= 70 ^{o}C, $T_{cascade_eva1}$= 0 ^{o}C, $T_{cascade_eva2}$= - 80 ^{o}C , T_{eva3}= - 135 ^{o}C, Temperature -overlapping (Approach1) =Approach2= 10 (^{o}C) and $Compressor_{Efficiency1}$= 0.80, $Compressor_{Efficiency2}$= 0.80 $Compressor_{Efficiency3=}$ 0.80

Effect of Approach-2	System COP	System EDR	Exergetic Efficiency
15	0.2109	3.090	0.2445
10	0.2228	2.871	0.2583
5	0.2339	2.672	0.2723
0	0.2472	2.489	0.2866

Table: 3(d). Effect of Approach1 on First law performance (overall system) Exergetic Efficiency (second law efficiency) and system exergy Destruction Ratio (EDR) of Four stages cascade refrigeration system using ecofriendly R1234yf refrigerant in the high temperature evaporator circuit and ecofriendly R410a in intermediate cascade evaporator temperature circuit and six ecofriendly Refrigerants used in low temp evaporator circuit for T_{cond}= 70 ^{o}C, $T_{cascade_eva1}$= 0 ^{o}C, $T_{cascade_eva2}$= - 80 ^{o}C , T_{eva3}= - 135 ^{o}C, Temperature-overlapping (Approach1) =Approach2= 10 (^{o}C) and $Compressor_{Efficiency1}$= 0.80, $Compressor_{Efficiency2}$= 0.80 $Compressor_{Efficiency3=}$ 0.80

Effect of Approach-1	System COP	System EDR	Exergetic Efficiency
15	0.1969	3.381	0.2283
10	0.2079	3.149	0.2410
5	0.2190	2.938	0.2539
0	0.2304	2.744	0.2671

As approach-2 (temperature overlapping between low temperature condenser and intermediate evaporator circuit) decreases, the first law efficiency (overall system COP) increases and also second law efficiency in terms of exergetic efficiency increases.

Table: 4(a). Effect of Approach2 on First law performance (overall system) Exergetic Efficiency (second law efficiency) and system exergy Destruction Ratio (EDR) of Four stages cascade refrigeration system using ecofriendly R1234ze refrigerant in the high temperature evaporator circuit and ecofriendly R134a in intermediate cascade evaporator temperature circuit and six ecofriendly Refrigerants used in low temp evaporator circuit for T_{cond}= 70 ^{o}C, $T_{cascade_eva1}$= 0 ^{o}C, $T_{cascade_eva2}$= - 80 ^{o}C , T_{eva3}= - 135 ^{o}C, Temperature Temperature - overlapping (Approach1) =Approach2= 10 (^{o}C) and $Compressor_{Efficiency1}$= 0.80, $Compressor_{Efficiency2}$= 0.80 $Compressor_{Efficiency3=}$ 0.80

Effect of Approach-2	System COP	System EDR	Exergetic Efficiency
15	0.2108	3.092	0.2444
10	0.2230	2.867	0.2586
5	0.2360	2.654	0.2737
0	0.2499	2.451	0.2898

Table: 4(b). Effect of Approach2 on First law performance (overall system) Exergetic Efficiency (second law efficiency) and system exergy Destruction Ratio (EDR) of Four stages cascade refrigeration system using ecofriendly R1234yf refrigerant in the high temperature evaporator circuit and ecofriendly R134a in intermediate cascade evaporator temperature circuit and six ecofriendly Refrigerants used in low temp evaporator circuit for T_{cond}= 70 ^{o}C, $T_{cascade_eva1}$= 0 ^{o}C, $T_{cascade_eva2}$= - 80 ^{o}C , T_{eva3}= - 135 ^{o}C, Temperature-overlapping (Approach1) =Approach2= 10 (^{o}C) and $Compressor_{Efficiency1}$= 0.80, $Compressor_{Efficiency2}$= 0.80, $Compressor_{Efficiency3=}$ 0.80

Effect of Approach-2	System COP	System EDR	Exergetic Efficiency
15	0.1968	3.383	0.2282
10	0.2081	3.145	0.2413
5	0.2201	2.919	0.2552
0	0.2328	2.704	0.270

Table: 4(c). Effect of Approach1 on First law performance (overall system) Exergetic Efficiency (Second law efficiency) and system exergy Destruction Ratio (EDR) of Four stages cascade refrigeration system using ecofriendly R1234ze refrigerant in the high temperature evaporator circuit and ecofriendly R410a in intermediate cascade evaporator temperature circuit and six ecofriendly Refrigerants used in low temp evaporator

circuit for T_{cond}= 70 ^{o}C, $T_{cascade_eva1}$= 0 ^{o}C, $T_{cascade_eva2}$= - 80 ^{o}C , T_{eva3}= - 135 ^{o}C, Temperature-overlapping (Approach1) =Approach2= 10 (^{o}C) and $Compressor_{Efficiency1}$= 0.80, $Compressor_{Efficiency2}$= 0.80 $Compressor_{Efficiency3=}$ 0.80

Effect of Approach-1	System COP	System EDR	Exergetic Efficiency
15	0.2106	3.092	0.2441
10	0.2228	2.871	0.2583
5	0.2358	2.658	0.2734
0	0.2497	2.455	0.2895

Table: 4(d). Effect of Approach1 on First law performance (overall system) Exergetic Efficiency (Second law efficiency) and system exergy Destruction Ratio (EDR) of Four stages cascade refrigeration system using ecofriendly R1234yf refrigerant in the high temperature evaporator circuit and ecofriendly R410a in intermediate cascade evaporator temperature circuit and six ecofriendly Refrigerants used in low temp evaporator circuit for T_{cond}= 70 ^{o}C, $T_{cascade_eva1}$= 0 ^{o}C, $T_{cascade_eva2}$= - 80 ^{o}C , T_{eva3}= - 135 ^{o}C, Temperature -overlapping (Approach1) =Approach2= 10 (^{o}C) and $Compressor_{Efficiency1}$= 0.80, $Compressor_{Efficiency2}$= 0.80 $Compressor_{Efficiency3=}$ 0.80

Effect of Approach-1	System COP	System EDR	Exergetic Efficiency
15	0.1966	3.387	0.2279
10	0.2079	3.149	0.2410
5	0.2198	2.923	0.2549
0	0.2326	2.708	0.2697

Table: 5(a). Effect of Approach1 on First law performance various circuit COPs) of Four stages cascade refrigeration system using ecofriendly R1234ze refrigerant in the high temperature evaporator circuit and ecofriendly R134a in intermediate cascade evaporator temperature circuit and six ecofriendly Refrigerants used in low temp evaporator circuit for T_{cond}= 70 ^{o}C, $T_{cascade_eva1}$= 0 ^{o}C, $T_{cascade_eva2}$= - 80 ^{o}C , T_{eva3}= - 135 ^{o}C, Temperature -overlapping (Approach1) =Approach2= 10 (^{o}C) and $Compressor_{Efficiency1}$= 0.80, $Compressor_{Efficiency2}$= 0.80 $Compressor_{Efficiency3=}$ 0.80

Effect of Approach-1	COP_{HTC}	COP_{ITC}	COP_{LTC}
15	1.797	1.018	1.163
10	1.797	1.118	1.163
5	1.797	1.228	1.163
0	1.797	1.351	1.163

Table: 5(b). Effect of Approach1 on First law performance various circuit COPs) of Four stages cascade refrigeration system using ecofriendly R1234yf refrigerant in the high temperature evaporator circuit and ecofriendly R134a in intermediate cascade evaporator temperature circuit and six ecofriendly Refrigerants used in low temp evaporator circuit for T_{cond}= 70 ^{o}C, $T_{cascade_eva1}$= 0 ^{o}C, $T_{cascade_eva2}$= - 80 ^{o}C , T_{eva3}= - 135 ^{o}C, Temperature -overlapping (Approach1) =Approach2= 10 (^{o}C) and $Compressor_{Efficiency1}$= 0.80, $Compressor_{Efficiency2}$= 0.80, $Compressor_{Efficiency3=}$ 0.80

Effect of Approach-1	COP_{HTC}	COP_{ITC}	COP_{LTC}
15	1.544	1.018	1.163
10	1.544	1.118	1.163
5	1.544	1.228	1.163
0	1.544	1.351	1.163

Table: 5(c). Effect of Approach1 on First law performance various circuit COPs) of Four stages cascade refrigeration system using ecofriendly R1234ze refrigerant in the high temperature evaporator circuit and ecofriendly R410a in intermediate cascade evaporator temperature circuit and six ecofriendly Refrigerants used in low temp evaporator circuit for T_{cond}= 70 ^{o}C, $T_{cascade_eva1}$= 0 ^{o}C, $T_{cascade_eva2}$= - 80 ^{o}C , T_{eva3}= - 135 ^{o}C, Temperature -overlapping (Approach1) =Approach2= 10 (^{o}C) and $Compressor_{Efficiency1}$= 0.80,, $Compressor_{Efficiency2}$= 0.80 $Compressor_{Efficiency3=}$ 0.80

Effect of Approach-1	COP_{HTC}	COP_{ITC}	COP_{LTC}
15	1.797	1.017	1.163
10	1.797	1.116	1.163
5	1.797	1.225	1.163
0	1.797	1.346	1.163

Table: 5(d). Effect of Approach1 on First law performance various circuit COPs) of Four stages cascade refrigeration system using ecofriendly R1234yf refrigerant in the high temperature evaporator circuit and ecofriendly R410a in intermediate cascade evaporator temperature circuit and six ecofriendly Refrigerants used in low temp evaporator circuit for T_{cond}= 70 ^{o}C, $T_{cascade_eva1}$= 0 ^{o}C, $T_{cascade_eva2}$= - 80 ^{o}C , T_{eva3}= - 135 ^{o}C, Temperature Temperature -overlapping (Approach1) =Approach2= 10 (^{o}C) and $Compressor_{Efficiency1}$= 0.80, $Compressor_{Efficiency2}$= 0.80 $Compressor_{Efficiency3=}$ 0.80

Effect of Approach-1	COP_{HTC}	COP_{ITC}	COP_{LTC}
15	1.544	1.017	1.163
10	1.544	1.116	1.163
5	1.544	1.225	1.163
0	1.544	1.346	1.163

Table: 6(a). Effect of approach2 on First law performance various circuit COPs) of Four stages cascade refrigeration system using ecofriendly R1234ze refrigerant in the high temperature evaporator circuit and ecofriendly R134a in intermediate cascade evaporator temperature circuit and six ecofriendly Refrigerants used in low temp evaporator circuit for T_{cond}= 70 ^{o}C, $T_{cascade_eva1}$= 0 ^{o}C, $T_{cascade_eva2}$= - 80 ^{o}C , T_{eva3}= - 135 ^{o}C, Temperature -overlapping (Approach1) =Approach2= 10 (^{o}C) and $Compressor_{Efficiency1}$= 0.80, $Compressor_{Efficiency2}$= 0.80 $Compressor_{Efficiency3=}$ 0.80

Effect of Approach-2	COP_{HTC}	COP_{ITC}	COP_{LTC}
15	1.797	1.118	1.055
10	1.797	1.118	1.163
5	1.797	1.118	1.289
0	1.797	1.118	1.436

Table: 6(b). Effect of approach2 on First law performance various circuit COPs) of Four stages cascade refrigeration system using ecofriendly R1234yf

refrigerant in the high temperature evaporator circuit and ecofriendly R134a in intermediate cascade evaporator temperature circuit and six ecofriendly Refrigerants used in low temp evaporator circuit for T_{cond}= 70 ^{o}C, $T_{cascade_eva1}$= 0 ^{o}C, $T_{cascade_eva2}$= - 80 ^{o}C , T_{eva3}= - 135 ^{o}C, Temperature-overlapping (Approach1) =Approach2= 10 (^{o}C) and $Compressor_{Efficiency1}$= 0.80,, $Compressor_{Efficiency2}$= 0.80 $Compressor_{Efficiency3=}$ 0.80

Effect of Approach-2	COP_{HTC}	COP_{ITC}	COP_{LTC}
15	1.544	1.118	1.055
10	1.544	1.118	1.163
5	1.544	1.118	1.289
0	1.544	1.118	1.436

Table: 6(c). Effect of approach2 on First law performance various circuit COPs) of Four stages cascade refrigeration system using ecofriendly R1234ze refrigerant in the high temperature evaporator circuit and ecofriendly R410a in intermediate cascade evaporator temperature circuit and six ecofriendly Refrigerants used in low temp evaporator circuit for T_{cond}= 70 ^{o}C, $T_{cascade_eva1}$= 0 ^{o}C, $T_{cascade_eva2}$= - 80 ^{o}C , T_{eva3}= - 135 ^{o}C, Temperature -overlapping (Approach1) =Approach2= 10 (^{o}C) and $Compressor_{Efficiency1}$= 0.80, $Compressor_{Efficiency2}$= 0.80, $Compressor_{Efficiency3=}$ 0.80

Effect of Approach-2	COP_{HTC}	COP_{ITC}	COP_{LTC}
15	1.797	1.116	1.055
10	1.797	1.116	1.163
5	1.797	1.116	1.289
0	1.797	1.116	1.436

Table: 6(d). Effect of approach2 on First law performance various circuit COPs) of Four stages cascade refrigeration system using ecofriendly R1234yf refrigerant in the high temperature evaporator circuit and ecofriendly R410a in intermediate cascade evaporator temperature circuit and six ecofriendly Refrigerants used in low temp evaporator circuit for T_{cond}= 70 ^{o}C, $T_{cascade_eva1}$= 0 ^{o}C, $T_{cascade_eva2}$= - 80 ^{o}C , T_{eva3}= - 135 ^{o}C, Temperature-overlapping (Approach1) =Approach2= 10 (^{o}C) and $Compressor_{Efficiency1}$= 0.80, $Compressor_{Efficiency2}$= 0.80 $Compressor_{Efficiency3=}$ 0.80

Effect of Approach-2	COP_{HTC}	COP_{ITC}	COP_{LTC}
15	1.544	1.116	1.055
10	1.544	1.116	1.163
5	1.544	1.116	1.289
0	1.544	1.116	1.436

Table: 7(a). Variation of high temperature evaporator temperature on First law performance (overall system) Exergetic Efficiency (second law efficiency) and system exergy Destruction Ratio (EDR) of Four stages cascade refrigeration system using ecofriendly R1234ze refrigerant in the high temperature evaporator circuit and ecofriendly R410a in intermediate cascade evaporator temperature circuit and R404a ecofriendly Refrigerants used in low temp evaporator circuit for T_{cond}= 70 ^{o}C, $T_{cascade_eva1}$= 0 ^{o}C, $T_{cascade_eva2}$= - 80 ^{o}C , T_{eva3}= - 135 ^{o}C, Temperature-overlapping (Approach1) =Approach2= 10 (^{o}C) and $Compressor_{Efficiency1}$= 0.80, $Compressor_{Efficiency2}$= 0.80 $Compressor_{Efficiency3=}$ 0.80

HTC Evap. Temp.	System COP	System EDR	Exergetic Efficiency
-20	0.2081	3.145	0.2413
-15	0.2137	3.036	0.2478
-10	0.2181	2.955	0.2528
-5	0.2211	2.901	0.2564
0	0.2228	2.871	0.2583
1	0.2230	2.868	0.2585
2	0.2231	2.866	0.2586
3	0.2231	2.866	0.2587
4	0.2231	2.866	0.2587
5	0.2230	2.867	0.2586
6	0.2229	2.869	0.2584
7	0.2227	2.873	0.2582
10	0.2218	2.889	0.2571

Table: 7(b). Variation of high temperature evaporator on First law circuits performance of Four stages cascade refrigeration system using ecofriendly R1234ze refrigerant in the high temperature evaporator circuit and ecofriendly R410a in intermediate cascade evaporator temperature circuit and R404a ecofriendly Refrigerant used in low temp evaporator circuit for T_{cond}= 70 ^{o}C, $T_{cascade_eva1}$= 0 ^{o}C, $T_{cascade_eva2}$= - 80 ^{o}C , T_{eva3}= - 135 ^{o}C, Temperature-overlapping (Approach1) =Approach2= 10 (^{o}C) and $Compressor_{Efficiency1}$= 0.80, $Compressor_{Efficiency2}$= 0.80 $Compressor_{Efficiency3=}$ 0.80

HTC Evap. Temp.(^{o}C)	COP_{HTC}	COP_{ITC}	COP_{LTC}
-20	1.068	1.635	1.163
-15	1.215	1.482	1.163
-10	1.382	1.346	1.163
-5	1.575	1.225	1.163
0	1.797	1.116	1.163
1	1.846	1.095	1.163
2	1.896	1.075	1.163
3	1.948	1.055	1.163
4	2.001	1.036	1.163
5	2.056	1.017	1.163
6	2.113	0.9977	1.163
7	2.172	0.9791	1.163
10	2.361	0.9252	1.163

Table: 8(a). Variation of low temperature evaporator temperature on First law performance (overall system) Exergetic Efficiency (second law efficiency) and system exergy Destruction Ratio (EDR) of Four stages cascade refrigeration system using ecofriendly R1234ze refrigerant in the high temperature evaporator circuit and ecofriendly R410a in intermediate cascade evaporator temperature circuit and R404a ecofriendly Refrigerants used in low temp evaporator circuit for T_{cond}= 70 ^{o}C, $T_{cascade_eva1}$= 0 ^{o}C, $T_{cascade_eva2}$= - 80 ^{o}C , T_{eva3}= - 135 ^{o}C, Temperature-overlapping (Approach1) =Approach2= 10 (^{o}C) and $Compressor_{Efficiency1}$= 0.80, $Compressor_{Efficiency2}$= 0.80 $Compressor_{Efficiency3=}$ 0.80

LTC Evaporator Temperature (^oC)	System COP	System EDR	Exergetic Efficiency
-145	0.1851	3.068	0.2458
-140	0.2036	2.958	0.2526
-135	0.2228	2.871	0.2583
-130	0.2425	2.805	0.2628
-125	0.2626	2.757	0.2662
-120	0.2832	2.726	0.2684
-115	0.3042	2.710	0.2696
-110	0.3256	2.709	0.2696
-105	0.3473	2.721	0.2687
-100	0.3693	2.747	0.2669

Table: 8(b). Variation of low temperature evaporator on First law circuits performance of Four stages cascade refrigeration system using ecofriendly R1234ze refrigerant in the high temperature evaporator circuit and ecofriendly R410a in intermediate cascade evaporator temperature circuit and R404a ecofriendly Refrigerant used in low temp evaporator circuit for T_{cond}= 70 ^oC, $T_{cascade\ _eva1}$= 0 ^oC, $T_{cascade_eva2}$= - 80 ^oC , T_{eva3}= - 135 ^oC, Temperature-overlapping (Approach1) =Approach2= 10 (^oC) and $Compressor_{Efficiency1}$= 0.80, $Compressor_{Efficiency2}$=0.80 $Compressor_{Efficiency3=}$ 0.80

LTC Eva. Temp. (^oC)	COP_{HTC}	COP_{ITC}	COP_{LTC}
-145	1.797	1.116	0.8548
-140	1.797	1.116	0.9972
-135	1.797	1.116	1.163
-130	1.797	1.116	1.358
-125	1.797	1.116	1.589
-120	1.797	1.116	1.868
-115	1.797	1.116	2.209
-110	1.797	1.116	2.634
-105	1.797	1.116	3.179
-100	1.797	1.116	3.901

Table: 9(a). Variation of low temperature evaporator temperature on First law performance (overall system) Exergetic Efficiency (second law efficiency) and system exergy Destruction Ratio (EDR) of Four stages cascade refrigeration system using ecofriendly R1234ze refrigerant in the high temperature evaporator circuit and ecofriendly R410a in intermediate cascade evaporator temperature circuit and R404a ecofriendly Refrigerant used in low temp evaporator circuit for T_{cond}= 70 ^oC, $T_{cascade\ _eva1}$= 0 ^oC, $T_{cascade_eva2}$= - 80 ^oC , T_{eva3}= - 135 ^oC, Temperature-overlapping (Approach1) =Approach2= 10 (^oC) and $Compressor_{Efficiency1}$= 0.80, $Compressor_{Efficiency2}$= 0.80 $Compressor_{Efficiency3=}$ 0.80

ITC Eva. Temp (^oC)	System COP	System EDR	Exergetic Efficiency
-70	0.2250	2.833	0.2609
-75	0. 2243	2.845	0.2601
-80	0.2228	2.871	0.2583
-85	0.2205	2.912	0.2556
-90	0.2174	2.967	0.2520

References

[1] A. Handbook, Refrigeration System and Applications, American Society of Heating, Refrigerating, and Air-Conditioning Engineer, Inc., Atlanta, Georgia, 2006.

[2] S. Bhattacharyya, S. Mukhopadhyay, A. Kumar, R. K. Khurana, J. Sarkar, Optimization of a CO2–C3H8 cascade system for refrigeration and heating.

Table: 9(b). Variation of intermediate evaporator temperature-2 on First law circuits performance of Four stages cascade refrigeration system using ecofriendly R1234ze refrigerant in the high temperature evaporator circuit and ecofriendly R410a in intermediate cascade evaporator temperature circuit and R404a ecofriendly Refrigerant used in low temp evaporator circuit for T_{cond}= 70 ^oC, $T_{cascade\ _eva1}$= 0 ^oC, $T_{cascade_eva2}$= - 80 ^oC , T_{eva3}= - 135 ^oC, Temperature-overlapping (Approach1) =Approach2= 10 (^oC) and $Compressor_{Efficiency1}$= 0.80, $Compressor_{Efficiency2}$= 0.80 $Compressor_{Efficiency3=}$ 0.80

ITC Evap. Temp. (^oC)	COP_{HTC}	COP_{ITC}	COP_{LTC}
-70	1.797	1.401	0.9601
-75	1.797	1.25	1.055
-80	1.797	1.116	1.163
-85	1.797	0.9974	1.289
-90	1.797	0.8919	1.436

6. Conclusions

The following conclusions have been drawn from present investigations.

(i) The use of R1234ze refrigerant has GWP =6) gives better thermal performance than using R1234yf (GWP=4) in the high temperature circuit although both refrigerants have zero ozone depletion potential.

(ii) By using R410a in the intermediate temperature circuit the thermal performance decreases and system exergy destruction (EDR) is increases as compared with using R134a in the intermediate temperature circuit (iii) by using safety measures , the use of R600a hydrocarbon gives better thermal performances than other hydrocarbons such as R290 and R600 and other ecofriendly refrigerants (R404a, ethane and ethylene etc) (iii)By decreasing intermediate evaporator-2 temperature the lower temperature circuit efficiency increases while intermediate circuit efficiency decreases

(iii) By decreasing lower evaporator temperature, the first law efficiency (system COP) and second law efficiency (exergetic efficiency) decreases while system exergy destruction ratio (EDR) increases .Also lower temperature circuit efficiency decreases.

(iv) By increasing high temperature evaporator temperature form (-20^oC to 10^oC) the first law efficiency (system COP) and second law efficiency (exergetic efficiency) increases while system exergy destruction ratio (EDR) decreases The optimum temperature of evaporator is found to be 3 to 4 where optimum second law efficiency of system came out to be 25.87%

(v) By decreasing intermediate evaporator-2 temperature, the first law efficiency (system COP) and second law efficiency (exergetic efficiency) decreases while system exergy destruction ratio (EDR) increases

International Journal of Refrigeration, 28, 2005, 1284–1292.

[3] N. Cox, Working towards more environmentally friendly Refrigerant Blends. 12th European Conference, Milano, Italy, 2007

[4] J. A. Dopazo, J. Fernandez-Seara, J. Sieres, F. J. Uhi, Theoretical Analysis of a CO2-NH3 Cascade Refrigeration System for Cooling Applications At Low Temperatures, Applied thermal engineering, 29, 2009, 1577-1583

[5] H. M. Gettu, P. K. Bansal, Thermodynamic Analysis of an R744-R717 Cascade Refrigeration system. International Journal of Refrigeration 2008; 31, 45-54

[6] J. H. Kim, J. M. Cho, M. S. Kim, Cooling performance of several CO2/propane mixtures and glide matching with secondary heat transfer fluid. International Journal of Refrigeration, 31, 2008 800-806

[7] T. S. Lee, C. H. Liu, T. W. Chen, Thermodynamic Analysis of Optimal Condensing Temperature of Cascade-Condenser In CO2/NH3 Cascade Refrigeration Systems. International Journal of Refrigeration, 29, 2006, 1100-1108

[8] Nasruddin, D. R. B. Syaka, Thermodynamics Analysis of Refrigerant Selection in Cascade Refrigeration System, International Conference of Saving Energy in Refrigeration and Air-Conditioning. Departemen Teknik Mesin Fakultas Teknik-Universitas Indonesia,

[9] NIST, Thermodynamics and transport properties of refrigerants and refrigerant mixtures database (REFPROP). REFPROP. ver 8.0, U.S. Department of commerce, Gaithersburg, 2007

[10] Niu, Boulian, Zhang, Yufeng, Experimental Study of the Refrigeration Cycle Performance for R744/R290 Mixtures. International Journal of Refrigeration, 30, 2007, 37-42

[11] L. Rahadiyan, Study of Propane and Ethane Characteristics in Cascade Refrigeration System, Thesis, Department of Mechanical and Precision Engineering. The Graduate School of Gyeongsang National University, Gyeongsang, 2007.

[12] J. Wu, M. Gong, Y. Zhang, Refrigerant mixtures used in the lower temperature stage of two-stage cascade refrigeration systems. USPTO

OPEN ACCESS

International
Journal
Of Modern Engineering Research (IJMER)

Potential Use of LPG in A Medium Capacity Stationary HCCI Engine

Abhinav Tomar[1], Abhinav Chandra[2], Jatin Madaan[3]
[1,2,3] *Department of Mechanical Engineering, Delhi Technological University, Delhi, 110042, India.*

ABSTRACT: *Internal combustion engines are extensively used in every field of life in today's world. Diesel engines being more efficient are preferred in the industrial and transportation sector in comparison to spark ignition engines for their higher efficiency, versatility and ruggedness. The major emissions of diesel engines are oxides of nitrogen (NOx), particulate matter (PM), carbon dioxide (CO2), carbon monoxide (CO). Among these emissions, oxides of nitrogen (NOx) and the particulate matter are the reasons of serious concern. For reduction of oxides of nitrogen (NOx) and particulate matter simultaneously, the use of Homogeneous Charge Compression Ignition (HCCI) have provided a sustainable solution in the present scenario.*

This paper presents the findings of an experimental investigation into the operation of a compression ignition (CI) engine in homogeneous charge compression ignition (HCCI) mode using LPG as the main fuel and diesel as pilot injection. Factors that were investigated include engine performance and emission characteristics and based on the results, LPG was found to be a possible fuel for operation of a CI engine in HCCI mode.

A methodology using a small pilot quantity of diesel fuel injected during the compression stroke to improve the power density and operation control is carried out for an HCCI engine based on a stationary, constant RPM, water cooled diesel engine. The objective of this study is to investigate the performance and emission characteristics of HCCI engine fuelled with LPG and help understand the viability of LPG as an alternative fuel in diesel engines for use in the automotive industry.

Keywords: *LPG , Homogeneous Charge Compression Ignition (HCCI). Performance Characteristics, NOx Emissions,*

I. INTRODUCTION

Oil accounts for 33.1% of global energy consumption. Global oil consumption grew by a below-average 0.6 million barrels per day (b/d), or 0.7%, to reach 88 million b/d [1]. In the present scenario of energy crisis and global warming, energy demand is exponentially increasing due to ever increasing number of vehicles employing internal combustion engines [2]. There is a growing need to decrease this consumption; Indian transport sector majorly consists of Diesel engines which carries many disadvantages such as more fuel consumption, lower power with higher level of harmful emissions. The excessive dependency on these Internal Combustion engines is forcing the automotive sector to utilize the technically advanced combustion technique to compensate with current demand.

Ever-increasing stringent legislations imposed by emission regulatory organizations on NOx emissions from engines make achieving near zero NOx emission combustion strategies more challenging. Hence, in-cylinder NOx reduction methods such as low temperature combustion are being widely studied. Homogeneous Charge Compression Ignition (HCCI) combustion is a reliable method that has been found to produce ultra-low NOx levels and near zero soot emissions and to provide equal or greater fuel conversion efficiencies compared to that of conventional Direct Injection (DI) diesel combustion [3, 4].

There is no direct control over the combustion timing in an HCCI engine, unlike the Diesel and Otto engines which use injection timing and spark timing respectively to control the start of combustion. Recently a lot of researches have been performed to investigate the potential control methods such as the inlet air heating [5, 6], variable compression ratio (VCR) [7, 8], variable valve actuation (VVA) [9, 10] and EGR rates [11, 12]. Moreover many studies also focused on the effects of different fuel physical and chemical properties, for instance the octane number and the cetane number, using the primary reference fuels and fuel additives [13, 14, 15, 16]. Within these attempts, attracting progresses have been reported, to some extent, about gaining control of the HCCI combustion process. In a HCCI engine, the fuel is injected into the (preheated) air in the intake manifold, to create a homogeneous charge. The charge is then further heated during the compression

stroke to get auto-ignition, close to Top Dead Centre (TDC). With HCCI, there is no direct control over the ignition timing. The ignition timing can only be controlled indirect. By adjusting the operating parameters correctly, ignition will occur near TDC [17]. The auto-ignition timing in an HCCI engine is dependent on many parameters including equivalence ratio, pilot injection timing, fuel composition and properties, compression ratio, intake pressure and temperature, and external and internal EGR. The overall efficiency of the engine depends strongly on the combustion timing and duration. The homogeneous mixing of the fuel and air before the combustion, opposite to that in diesel engines, reduces the level of soot particles in the exhaust leading to cleaner combustion. HCCI provides up to a 30-percent fuel savings, while meeting current emissions standards. In regards to gasoline engines, the emission of throttle losses improves HCCI efficiency [18]. Recent research has shown that the use of two fuels with different reactivity's can help solve some of the difficulties of controlling HCCI ignition and burn rates. RCCI or Reactivity Controlled Compression Ignition has been demonstrated to provide highly efficient, low emissions operation over wide load and speed ranges [19].

HCCI engines do present some technical challenges that have so far kept them from widespread commercialization. The main hurdles are combustion timing control, low specific power output, high emissions of hydrocarbon (HC) and carbon monoxide (CO), and difficulty to start when cold [20]. These are formidable technical challenges for transportation applications, due to the fast transients required to meet the road load and due to the size restrictions inside a vehicle. However, for stationary applications, these issues are not nearly as challenging, because a stationary engine runs predominantly at a constant speed and the load changes relatively slowly. Under these conditions, combustion control becomes much more tractable. External components (e.g. a burner and heat exchanger for starting the engine can easily be installed in stationary engines, since size restrictions are typically not as strict as for transportation applications [21].

Liquefied Petroleum Gas (LPG) accounts for 16.8% of global energy consumption by 2011 end with production increased to 35.9% in less than 20 years [1]. As LPG has a low auto ignition temperature it is more likely that it will cause HCCI mode of ignition and is quite prone to knocking.

HCCI engines can operate on gasoline, diesel fuel, and most alternative fuels [22]. Further, on using LPG as a fuel in HCCI engine results in even lower levels of NOx and other particulate emissions are observed. LPG is made by liquefying petroleum gas (which is mainly composed of butane and propane), to less than 1% of the volume it occupies at standard atmospheric pressure. It is stored and distributed in hard containers in the liquid form with a pressure of 200–248 bar (2,900–3,600 psi), usually in cylindrical or spherical shapes. Being a gaseous fuel, LPG mixes easily and evenly in air, thus producing a homogeneous mixture essential for working of HCCI engine along-with increasing the life of lubricating oils, as LPG does not contaminate and dilute the crankcase oil. As LPG is less likely to ignite on hot surfaces, since it has a high auto-ignition temperature around 450 °C and a narrow range (5–15%) of flammability, therefore a methodology using a small pilot quantity of diesel fuel injected during the compression stroke to improve the power density and operation control is implemented, thus helping the homogeneous mixture of LPG and air to combust without altering the compression ratio of the engine or installing a spark plug inside the combustion chamber.

In present study the Compression Ignition engine is used which is modified to LPG-Diesel HCCI engine in which Diesel works on pilot-injection (volumetric ratio of 1/10) and LPG as the main fuel. Combustion control is carried out by LPG and its quantity varies at different loads. The objective is to investigate the performance and emission characteristics. This technique reduces NOx by 40.53% at 40% load and increases at 80% and 100% load. Kerosene when used as an alternative for diesel in HCCI engines at high compression ratio, higher BTE was observed with low exhaust emissions.

It is proposed that a small (<20% of fuel energy) pilot injection of a fuel (diesel) with high volatility and low auto-ignition temperature will act to initiate combustion of a premixed liquefied petroleum gas charge in an HCCI engine. The pilot fuel is injected shortly before TDC to burn as a stratified charge or a diffusion jet, and not as a homogeneous mixture. As such, it will cause a relatively slow rise in the cylinder pressure and temperature and cause the homogeneous natural gas charge to auto-ignite at an appropriate timing. The pilot injection is used to lower the variation in IMEP at the lean limit, as well as prevent misfiring of the engine at marginal conditions. It can also be used to control the combustion timing in an HCCI engine and increase the efficiency of fuels like liquefied petroleum gas that have very high reaction rates. With HCCI, cycle-to-cycle variations of combustion are very small since combustion initiation takes place at many points at the same time. HCCI has no flame propagation; instead the whole mixture burns close to homogeneous at the same time.

Till now the study in this field resulted into the engines used for power generation, but here the engine optimized for this use is an engine used in rural area as a transport unit so if we can control the combustion of this technology with emission control it could result into its commercialization.

II. LITERATURE REVIEW

Diaz, p.m. et al. [23] did an experimental study on emission characteristics on a single cylinder engine, he blended reformer gas (RG) with different mass% with LPG, formed a lean preheated mixture which worked under the limit of misfiring and knocking which is 10-20 bar/CAD. Reformer gas mainly increased the maximum cylinder pressure and thus NOx increased when mass% RG is more than 60% and is reduced before it. Junjun Ma et al. [24] did experimental study on n-heptane diesel HCCI and concluded that NOx emissions decreases at low premixed ratios and increases at high premixed ratios, this is due to the diffusive combustion and increased peak pressure.

P. Saisirirat et al. [25] concluded that in HCCI combustion the usage of alcohol resulted into cooler flame and lover OH radicals, constant volume was kept hand in hand with pressure which is maintained at 20 and 40 bar to attain these conditions. S. Swami Nathan et al. [26] ran single cylinder diesel engine working on biogas-diesel HCCI and tested its performance and emissions where NOx emissions were decreased when the lean air-fuel mixture is given intake charge of 135 C thus less is the work done by compression to ignite fuel thus fuel burned evenly at multiple points and combustion control is done by adjusting amount of diesel injected with a constant supply of biogas, BTE was maximum at 135 C temperature as the expansion ratio of biogas is greater than diesel. Kimura S et al. [27] are continuously interested in developing a better understanding 0f the mechanism of HCCI combustion over a wide range of operating conditions. This study is motivated by the need to improve combustion efficiency and performance of current used engines and to reduce harmful pollutants emissions generated in the combustion. As a result many studies took place. Magnus Christensen et al. [28] used a Volvo TD100 Diesel engine was converted for HCCI operation with the capability of variable compression ratios, intake air preheating, air/fuel equivalence ratio and intake boost pressure. It was found that the level of intake charge preheating needed to accomplish ultra-lean HCCI combustion could be drastically reduced almost to the point of elimination with increasing inlet pressure (boost). The idea of charge dilution from excess air inducted from boost (creation of extremely lean charge) aids in the problematic nature of the speed of the combustion caused by the chemical reaction rates.

Rakesh Kumar Maurya et al. [29] did an experimental study where an HCCI engine was operated with a fixed compression ratio of 16.5 and fixed engine speed of 1500 RPM fuelled with ethanol. The results are reported with respect to λ (the excess air ratio {1/λ= Φ}) instead of equivalence ratio. In this study it was determined that at lower intake temperatures a richer mixture ($\Phi = 0.5$ or $\lambda = 2$) could be ignited without causing engine knock, as the intake temperature was increased at the same rich equivalence ratio knock was encountered. However it was found that the lean operational range (up to $\Phi = 0.18$ or $\lambda = 5.5$) could be extended with increases in intake temperature. John E. Dec et al. [30] resulted maximum IMEP to 16.34 bar with no knock and intake pressure ringing at 3.25 bar. Noguchi et al. conducted a spectroscopic analysis on HCCI combustion in an opposed piston, two-stroke engine. They measured high levels of CHO, HO2, and O radicals within the cylinder prior to auto ignition, which demonstrated that pre-ignition chemical reactions had occurred and these reactions contributed to the auto ignition. After auto ignition took place, H, CH, and OH radicals were detected, which were indicative of high-temperature chemical reactions. In a traditional SI engine, these radical species are only associated with end-gas auto ignition, namely knock, which confirmed the similarities between the reactions of HCCI and knock in an SI engine.

III. FUEL PROPERTIES

Table 1: Properties of LPG

S.No.	Constituents	Value
1.	Molecular weight	4409
2.	Carbon content (wt %)	8172
3.	Hydrogen content (wt %)	1828
4.	Carbon: hydrogen ratio by weight	447
5.	Density of liquid at 15ºC (kg/l)	510
6.	Boiling point of liquid at atm. pres. (ºC)	-421
7.	Density of gas at 15ºC & atm. pres. (kg/m3)	186
8.	Volume ratio of gas: liquid at STP*	274:1
9.	Vapour pressure at 20ºC (kPa abs.)	710
10.	Net calorific value at 25ºC (MJ/kg)	460
11.	Wobbe number (kcal/Nm3)	19000
12.	Limits of flammability in air (vol% gas)	22 – 10
13.	Limits of flammability in oxygen (vol% gas)	2 – 50
14.	Max. flame temperature in air (ºC)	1930

15.	Max. flame temperature in oxygen (ºC)	2740
16.	Max. flame speed in 25 mm tube (cm/sec)	82
17.	Air required for combustion at STP (m3/kg LPG)	1210
18.	Air: gas vol. ratio for combustion at STP	225
19.	O2 vol. for combustion at STP (m3/kg fuel)	256

These properties of LPG is quite useful in controlling the combustion as this gas has flammability entirely different from the other fuels which brings changes in the type of combustion and temperature program which is followed with low peak in pressure and gives low harmful emissions with similar power output.

IV. EXPERIMENTAL SETUP

The engine used for the study is Kirloskar Make, single cylinder, 4-stroke, constant speed, vertical, water cooled, direct injection, 5.2 kW diesel engine, Table 2. The engine was coupled to a swinging field separating exciting type DC generator and loaded by electrical resistance. Exhaust gas temperature was measured by an iron–constantan thermocouple. Fuel consumption was measured by U-tube manometer. The engine was started with standard diesel fuel and warmed up. The warm up period ends when the cooling water temperature is stabilized. Then the fuel consumption and different exhaust emission like NO_x, HC, CO, CO_2 and smoke were measured.

Table 2: Engine Specifications

Make	Kirloskar
Ignition Type	Compression Ignition
Type of Cooling	Water Cooled
Injection Type	Direct Injection
Number of cylinders	1
Bore (mm)	87.5
Stroke (mm)	110
Cycle	4-stroke
Compression Ratio	17.5
Rated Power (HP)	5.2kW @1500 rpm
Swept Volume (cc)	661

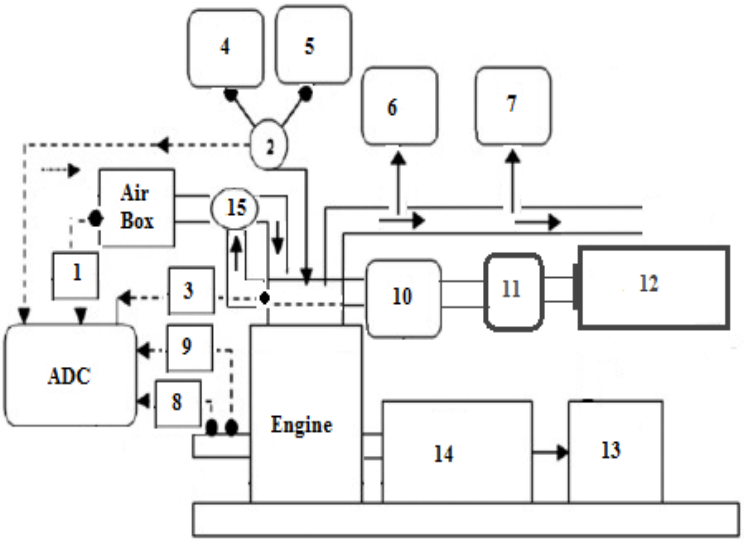

1. Air flow sensor 2. Fuel flow sensor 3. Pressure sensor
4. Diesel tank 5. Biodiesel tank 6. AVL Digas Analyser
7. AVL Smoke meter 8. RPM sensor 9. Crank angle encoder
10. LPG Vaporiser 11. Multivalve 12. LPG cylinder
13. Load Cell 14. Eddy Current Dynamometer 15. Venturie

Figure 1: Experimental Setup

The LPG is induced into the combustion chamber by installing a LPG gas kit (including a LPG cylinder, a multivalve, a vaporiser along-with a battery, lambda controller) along-with a venturi in the intake manifold just after the air filter. It assures proper mixing of the air and LPG and hence forming a homogenous and a lean air/fuel mixture before combustion. The quantity of the diesel entering the combustion chamber is controlled through the help of the diesel governor ensuring on pilot quantity of diesel entering the chamber enough for starting the combustion process of the lean mixture.

V. EXPERIMENTAL PROCEDURE

In order to achieve HCCI the engine was initially hand started same likely the normal diesel engine with a steady and constant rpm program with no load condition or the Brake Mean Effective Pressure (BMEP) was maintained constant to 1 bar, then steadily the diesel consumption is minimised from the governor followed with the flow of LPG in the intake manifold with a constant ratio with diesel to maintain the steady rpm at 1500 and controlled combustion state. The intake was given a constant charge of 300 F. The limitations found in this operational working are misfire (at high LPG flow rates followed by low diesel flow rate) and Knocking (at low LPG flow rate followed by high diesel flow rate). Thus the misfire and knocking is controlled by injecting a controlled and appropriate amount of fuel and feasible combustion state is obtained followed with the stabilization.

Data points were recorded at steady state operating conditions. Engine speed for the tests was held constant at 1500 RPM. Data sets were taken at different loads of 0%, 20%, 40%, 60%, 80%, 100%(full load i.e. 5.2kW).

Each data set contained numerous points as:
-Amount of diesel consumption in 60 sec.
-NOx emissions
-CO emissions
-HC emissions
-smoke opacity
- λ value
-exhaust temperature
-voltage and current
The data sets were first taken without LPG Induction i.e. engine operating fully on diesel fuel and then repeated with LPG fuel along with pilot diesel injection as HCCI.

VI. RESULTS AND DISCUSSIONS

6.1 Brake Thermal Efficiency (BTE):

Fig .2 shows relationship between brake thermal efficiency (BTE) and brake mean effective pressure (BMEP). In all the three cases BTE increases with increase in BMEP. It is found that brake thermal efficiency of the engine when run on LPG-HCCI mode (with diesel pilot injection) is more than that when run on diesel alone at all loads. Power available at the crankshaft increases with increase in the load due to increase richness of the air fuel mixture but as with increase in the load mass flow rate also increases, so on the whole the outcome being increase in thermal efficiency. Also, as the loss of energy increases at higher loads the Brake thermal efficiency decreases at higher loads. Except for the engine loads that are very close to the maximum load (in the range 90–100%), this analysis combined with the analysis of the BSFC (Fig.2) may suggest that the higher the engine load, the better is its performance in terms of fuel consumption and thermal efficiency, as shown by some investigations [31].

6.2 Brake Specific Fuel Consumption:

Fig .3 shows relationship between brake specific fuel consumption and brake mean effective pressure. Brake specific fuel consumption (BSFC) is a measure of the fuel efficiency of an engine. It is the rate of fuel consumption divided by the power produced. It may also be thought of as power-specific fuel consumption. BSFC decreases with increase in brake mean effective pressure in all the three cases as seen in the Fig.3, due to the increment in the value of BTE for higher loads. BSFC, being inversely proportional to Brake Thermal Efficiency, is highest for neat diesel mode, and lowest for normal pilot diesel assisted LPG-HCCI mode. To give the same power output i.e. to run on the same load range for different modes the engine starts to consume larger volume of fuel for diesel mode and LPG-HCCI water injection mode than normal pilot diesel assisted LPG-HCCI mode. With increase in the load, Brake specific fuel consumption will decrease. All these results agree with the literature [32, 33, 34].

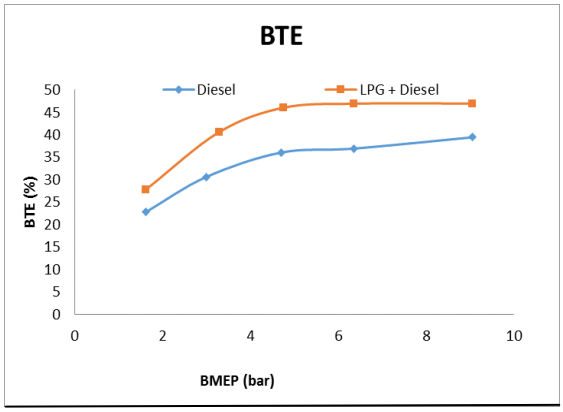

Figure 2: BTE vs BMEP

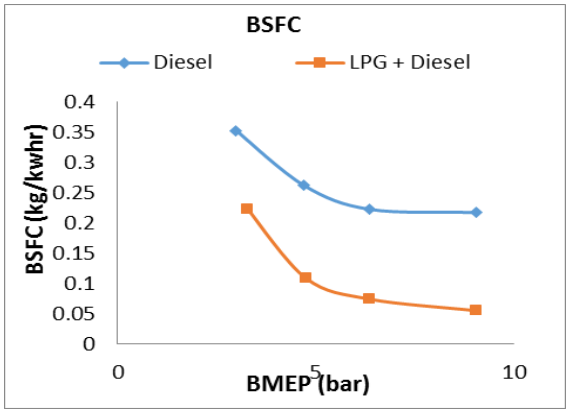

Figure 3: BSFC vs BMEP

6.3 Nitrogen Oxides (NOx):

Fig.4 depicts the NOx versus the BMEP values for various load ranges for neat diesel mode, LPG-HCCI mode. NOx formation is highly sensitive to temperature in the combustion chamber. The NOx formation rate is governed by the Zeldovich Mechanism [35]. Homogeneous charge in combination with lean mixtures of LPG gives low maximum temperature as LPG storage is in high pressured liquid form and when mixed with normal air the temperature is maintained to <273 K which when enters the combustion chamber lower its temperature to a great extent and much lower NOx are observed.

HCCI combustion is well known for its ultra-low NOx and soot emission. Thus it is considered in this study that the NOx and soot emissions are mainly due to the diffusive combustion of direct injection. The formation of Nitrogen Monoxide and Nitrogen Dioxide can be divided into thermal route, prompt route, N_2O route and fuel-bound nitrogen route [36]. The major NOx formation route in IC engine combustion is the thermal route [37]. The thermal NO route is the major constituent to the NOx emission and can be described with the following three elementary reactions called as extended Zeldovich mechanism

Eq. 1-3:

$O+N_2$®NO+N (1)

$N + O_2$®NO+O (2)

N+OH®NO+H (3)

It is evident from the Fig.4 that NOx is reduced dramatically with the pilot diesel aided HCCI mode engine running on LPG along-with exhibiting an increasing trend in NOx levels at higher loads, just as in a neat diesel engine. This reason being the trade-off relationship between the reduction of NOx during HCCI combustion and the increase of NOx during diffusive combustion. On one hand, the LPG undergoing HCCI combustion produces nearly no NOx so that increasing premixed ratio would reduce the overall NOx. On the other hand, the heat release prior to the diffusive combustion raised the in-cylinder temperature that offset the NOx decrease. Therefore at higher loads (above 85% load) the NOx emissions are greater

6.4 Hydrocarbons (HC):

Fig.5 shows relationship between hydrocarbon formation and brake mean effective pressure for different loads (0%,20%, 40%, 60%, 80% and full load (5.2KW)). Hydrocarbon formation results from unburned carbon presence inside engine. The HC emissions mainly originate from the HCCI combustion since the prototype engine run is a diesel engine and without varying its compression ratio the complete combustion of LPG cannot take place and hence unburned HCs are emitted. The low combustion temperature prevents NOx formation, but the combustion temperature becomes too low to fully oxidize the fuel completely. This low combustion temperature results in high emissions of unburned hydrocarbons. During no load condition, unburned carbon is present inside the engine which go on to produce hydrocarbons when engine is run on diesel pilot injection assisted LPG, in great amount as compared to when run on diesel alone. The increase in HC can also partly be explained by incomplete vaporization of the fuel when the humidity of the inlet air becomes very high. Further as load increases, hydrocarbon formation decreases rapidly when engine is run on LPG (with diesel pilot injection) for both modes with and without water injection as higher temperature is achieved.

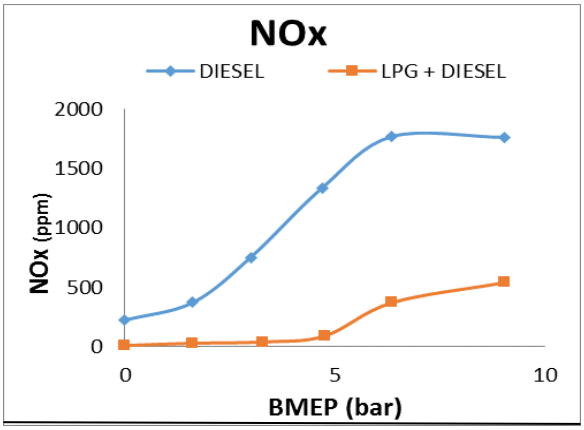

Figure 4: NOx vs BMEP

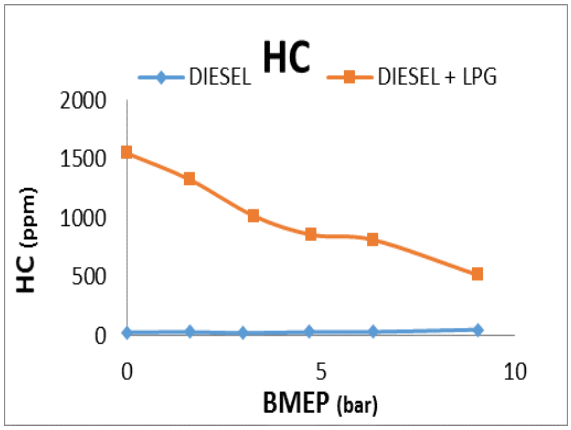

Figure 5: Hydrocarbons vs BMEP

6.5 Carbon Dioxide (CO_2):

Fig 6 shows relationship between carbon dioxide and brake mean effective pressure. In this present study the CO_2 is found to be increase gradually with the increase in the load for diesel fuel but this pattern was not found to be uniform throughout the investigation. At the same time, at maximum load the CO_2 measured is lower in HCCI-LPG mode as compared to the diesel because of the complete combustion of the butane.

6.6 Smoke Opacity:

Fig.7 shows relationship between smoke opacity (%) and brake mean effective pressure for different loads (0%, 20%, 40%, 60%, 80% and full load (5.2KW)). Smoke opacity increases with increase in the amount of unburned carbon. Unburned carbon will go on to form soot which will result in smoke formation. It is found when brake mean effective pressure approaches from 0 to 3 bar, smoke opacity increases exponentially in case when engine is run on diesel whereas it increases first then decreases in case when run on LPG (with diesel pilot injection). Amount of unburned carbon formed by LPG is more than that formed by diesel when brake mean effective pressure increases from 0 to 3.

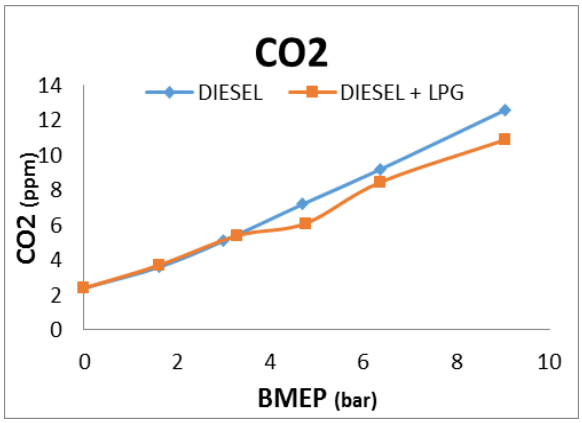

Figure 6: CO2 vs BMEP

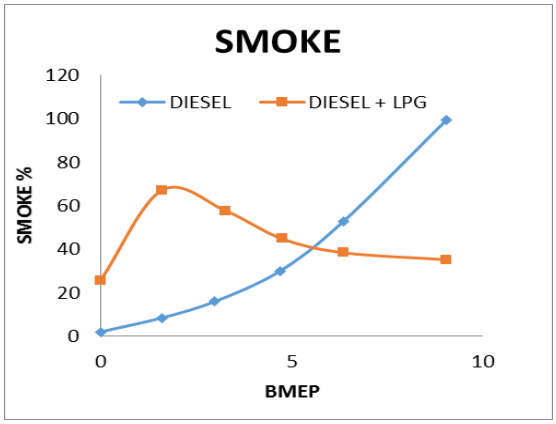

Figure 7: Smoke Opacity vs BMEP

VII. CONCLUSIONS

NOx emissions decreased at low premixed ratios with the pilot diesel aided HCCI engine running on LPG. Generally the NOx formation in HCCI could be dramatically reduced in comparison with the prototype diesel engine. Note that the specific NOx levels continue to be high at high loads and further combustion enhancements is needed to make the LPG fuelled HCCI engine practical. Smoke opacity in HCCI mode decreases with increasing load. Overall smoke opacity in HCCI mode is quite low as compared with diesel mode. Extreme low levels of smoke opacity are attained at brake mean effective pressure being above 3 bar, when the engine is operated on HCCI mode. The change of carbon monoxide with premixed ratio mainly depends upon the premixed equivalence ratio which exceeds the critical value when the unburned hydrocarbon increases linearly with the premixed ratio due to the incomplete oxidation at the boundary layer and in the

crevices. Higher Brake Thermal Efficiency was obtained at all loads and offers 20-25% overloads in HCCI mode in comparison to 10% in conventional diesel operation.

REFERENCES

[1]: BP statistical review of world energy June 2012.

[2]: Sahil Gupta Manish V Naveen Kumar Dhruv Gupta , Performance and emission Characteristics of a CI engine fuelled with Mahua oil with cold EGR, ICEF2013-19147

[3] Duret P, Gatellier B, Monteiro L, Miche M, Zima P, Maroteaux D, et al. Progress in diesel HCCI combustion within the European SPACE LIGHT project. SAE paper 2004-01-1904; 2004.

[4] Sjoberg M, Dec JE. An investigation of the relationship between measured intake temperature, BDC temperature, and combustion phasing for premixed and DI HCCI engines. SAE paper 2004-01-1900; 2004.

[5] Göran Haraldsson, Per Tunestål, Bengt Johansson, HCCI closed-loop combustion control using fast thermal management, SAE 2004-01-0943.

[6] UweWangner, Razvan Anca, Amin Velji, Ulrich Spicher, An experimental study of homogeneous charge compression ignition (HCCI) with various compression ratios, intake air temperatures and fuels with port and direct fuel injection, SAE 2003-01-2293.

[7] Thomas W. Ryan III, Timothy J. Callahan, Darius Mehta, HCCI in a variable compression ratio engine-effect of engine variables, SAE 2004- 01-1971.

[8] Jari Hyvonen, Goran Haraldsson, Bengt Johansson, Operating range in a multi-cylinder HCCI engine using variable compression ratio, SAE 2003- 01-1829.

[9] Petter Strandh, Johan Bengtsson, Rolf Johansson, Bengt Johansson, Variable valve actuation for timing control of a homogeneous charge compression ignition engine, SAE 2005-01-0147.

[10] Fredrik Agrell, Hans-Erik Ångström, Bengt Eriksson, Jan Wikander, Johan Linderyd, Transient control of HCCI through combined intake and exhaust valve actuation, SAE 2003-01-3172.

[11] Xing-cai Lü, Wei Chen, Zhen Huang, A fundamental study on the control of the HCCI combustion and emissions by fuel design concept combined with controllable EGR, Part 1: The basic characteristics of HCCI combustion, Fuel 84 (2005) 1074–1083.

[12] Xing-cai Lü, Wei Chen, Zhen Huang, A fundamental study on the control of the HCCI combustion and emissions by fuel design concept combined with controllable EGR, Part 2: Effect of operating conditions and EGR on HCCI combustion, Fuel 84 (2005) 1084–1092.

[13] Salvador M. Aceves, Daniel Flowers, Joel Martinez-Frias, Robert Dibble, Fuel and additive characterization for HCCI combustion, SAE 2003-01-0184.

[14] Shigeyuki Tanaka, Ferran Ayala, James C. Keck, John B. Heywood, Twostage ignition in HCCI combustion and HCCI control by fuels and additives, Combustion and Flame 132 (2003) 219–239.

[15] Daisuke Kawano, Hiroyoshi Naito, Hisakazu Suzuki, Effects of fuel propertiesbon combustion and exhaust emissions of homogeneous charge compressionbignition (HCCI) engine, SAE 2004-01-1966.

[16] Lucien Koopmans, Elna Strömberg, Ingemar Denbratt, The influence ofbPRF and commercial fuels with high octane number on the auto-ignition timing of an engine operated in HCCI combustion mode with negative valve overlap, SAE 2004-01-1967.

[17] Homogeneous Charge Compression Ignition with Water Injection Magnus Christensen and Bengt Johansson Division of Combustion Engines, Lund Institute of Technology

[18] Baumgarten, Carsten (2006). Mixture Formation in Internal Combustion Engines: Mixture Formation in Internal Combustion Engines. Birkhäuser. pp. 263–264. ISBN 3-540-30835-0.).

[19] Zhao, Fuquan; Thomas W. Asmus, Dennis N. Assanis, John E. Dec, James A. Eng, Paul M. Najt (2003). Homogeneous Charge Compression Ignition (HCCI) Engines: Key Research and Development Issues. Warrendale, PA, USA: Society of Automotive Engineers. pp. 11–12. ISBN 0-7680-1123-X.)

[20] Epping, K., Aceves, S.M., Bechtold, R.L., and Dec, J.E., 2002, "The Potential of HCCI Combustion for High Efficiency and Low Emissions," SAE Paper 2002-01-1923.

[21] Martinez-Frias, J., Aceves, S.M., Flowers, D., Smith, J.R., and Dibble, R., 2000, "HCCI Engine Control by Thermal Management," SAE Paper 2000-01-2869.

[22] Dec, John E.; Kathy Epping, Salvador M. Aceves, Richard L. Bechtold (2002). "The Potential of HCCI Combustion for High Efficiency and Low Emissions". Society of Automotive Engineers. 2002-01-1923)

[23]: Diaz, P.M. and B. Durga Prasad, American Journal of applied sciences 9 (7): 1030-1036, 2012.

[24] Junjun Ma, Xingcai Lu, Libin Ji, Zhen Huang, International Journal of Thermal sciences 47 (2008) 1235-1242.

[25] P. Saisiririat, C. Togbe, S. Chanchaona, Proceeding of the combustion institute 33 (2011) 3007-3014.

[26] S. Swami Nathan, J.M. Mallikarjuna, A. Ramesh, Energy Conversion Management 51 (2010) 1347-1353.

[27] Kimura S, A.O, Ogava H, New combustion effect and ultra clean combustion small DI engines SAE 1999(3681).

[28] Magnus Christensen, Bengt Johansson, Per Amn-us, Fabian Mauss, "Supercharged Homogeneous Charge Compression Ignition", SAE Paper 980787, 1998.

[29] Rakesh Kumar Maurya, Avinash Kumar Agarwal, "Experimental investigation on the effect of intake air temperature and air-fuel ratio on cycle-to-cycle variations of HCCI combustion and performance parameters", Applied Energy, 2011, 1153- 1163.

[30] John E. Dec, Yi Yang, "Boosted HCCI for High Power without Engine Knock and with Ultra-Low NOx Emissions – using Conventional Gasoline", SAE Paper 2010-01-1086, 2010.
[31] Agarwal D, Agarwal AK. Performance and emissions characteristic of jatropha oil (preheated and blends) in a direct injection compression ignition engine. Applied Thermal Engineering 2007;27:2314–23.
[32] Agarwal D, Agarwal AK. Performance and emissions characteristic of jatropha oil (preheated and blends) in a direct injection compression ignition engine. Applied Thermal Engineering 2007;27:2314–23.
[33] Vaitilingom G. Huiles ve´ge´ tales-biocombustible diesel. Ph.D. Thesis, University of Orleans, France, 1992.
[34] Agarwal AK. Biofuels (alcohols and biodiesel) applications as fuels for internal combustion engines. Progress in Energy and Combustion Science 2007;33:233–71.
[35]. J.B. Heywood: "Internal Combustion Engine Fundamentals", McGraw-Hill, New York, 1989.
[36] Warnatz, J., U. Maas and R.W. Dibble, 2006.Combustion: Physical and Chemical Fundamentals, Modeling and Simulation, Experiments, Pollutant Formation. 4th Edn., Springer Verlag, Berlin Heidelberg New York, ISBN-10: 3540259929, pp:378.
[37] Internal Combustion Engine, Heywood, 1988

ISSN NO. 2320-5407

Journal homepage: http://www.journalijar.com

INTERNATIONAL JOURNAL OF ADVANCED RESEARCH

RESEARCH ARTICLE

Preparation of carboxymethyl guar gum/silver nanocomposites film and its optical and antimicrobial properties

A. P. Gupta and Devendra Kumar Verma*

Department of Applied Chemistry and Polymer Technology, Delhi Technological University (Formerly Delhi College of Engineering), Shahabad, Daulatpur, Bawana Road, Delhi -110042, India.

Manuscript Info

Manuscript History:

Received: 15 December 2014
Final Accepted: 29 January 2015
Published Online: February 2015

Key words:

Corresponding Author

Abstract

Carboxymethyl guar gum/silver nanocomposites (CMGG/Ag NC) film was prepared by solution castings method. The aim of this paper was to study optical and antimicrobial activity of the film. The formation of nanocomposites film was confirmed by using SEM, TEM and XRD analysis. Optical properties of the film were tested by UV-Vis and Photoluminescence spectroscopy (PL) respectively. Antimicrobial activity of the CMGG/Ag NC film was studied against gram positive (*Bacillus subtilis*) and gram negative *(Escherichia coli*) bacteria by Kirby-Bauer method. It was found that a little amount of CMGG/Ag NC film was sufficient to inhibit pathogens. The result concludes that such prepared silver nanocomposites film may be effective in medical and clinical applications.

Copy Right, IJAR, 2015,. All rights reserved

1. Introduction

Modern technologies continuously need new materials with special combination of properties [1]. We need such a material which could be environmental friendly, cost effective, easy forming and storing for long duration, less time consuming with desirable properties. Polymers and nanotechnology have increased the tremendous applications for obtaining these desirable materials. Nanocomposites are one of such material. Polymer nanocomposites are the materials, in which at least one of the components becomes less than 100 nm in one dimension. Due to the similarity in size between nanomaterial's and most biological molecules and structures, nanoparticles can be highly beneficial to use both in vivo and vitro biomedical research and applications [2]. Silver nanocomposites have been used in a lot of antimicrobial and wound healing applications [3-7]. Because of the very fine antibacterial activity of silver nanoparticles [8] many scientist have found that silver-containing materials can be used in medicine to reduce infections as well as to prevent bacteria colonization on prostheses [9], catheters [10-11], vascular grafts [12], dental materials [13], stainless steel materials [14] and human skin [15-16]. Beside from antibacterial abilities, research has revealed that silver ions can also destroy viruses, fungi, protozoa and even cancer cells [17].

This paper is the second part of my previous paper. CMGG/Ag NC were synthesized by my previous paper method [18]. In this paper CMGG/Ag nanocomposites film was prepared by solution casting method to test its antimicrobial and optical properties, so that it might be used in antimicrobial film in medical applications. CMGG is an anionic semi-synthetic guar gum derivative [19]. The polysaccharide backbone is similar to guar gum which is a galactomannan. Among the guar gum derivatives, CMGG is very important because it covers a wide range of industrial applications and has a good film forming property [20].

Although there are a lot of techniques for the synthesis of silver nanoparticles like reduction, thermal decomposition, radiation assisted, electrochemical, sonochemical, microwave assisted process and recently via green chemistry route [21]. But Green synthesis process have some extra benefits over conventional methods like low cost, ecofriendly, large scale synthesis and no need to use high temperature and pressure and toxic chemicals. Especially for medical applications Ag nanoparticles should be made by green synthesis process. So in this research article CMGG/Ag nanocomposite has been synthesized by the green synthesis process. Ultimately the aim of this research

article basically was to prepare CMGG/Ag NC film by solution casting method and to test it's optically property as well as antimicrobial activity against gram positive (*Bacillus subtilis*) and gram negative *(Escherichia coli*) bacterial.

2. Experimental

2.1 Materials

Silver nitrate ($AgNO_3$) was purchase from Merck Germany. Carboxymethyl guar gum was obtained from Hariom gum industry, Gujarat, India. All aqueous solutions were made using doubled distilled (DD) water. All the chemicals were used as they were received, without any purification.

2.2 Synthesis of CMGG/Ag NC

Silver nanoparticles have been synthesized by reduction process as shown in my previous paper [18]. For the synthesis of CMGG/Ag NC, CMGG was used as reducing and stabilizing agent. A fixed CMGG concentration solution was prepared in 10 ml DD water with constant stirring at room temperature. Then the temperature of this solution was raised from (70 to 90) ^oC. Then 10 ml of 15 mM silver nitrate solution was added drop wise, with continuous stirring. After addition of silver nitrate, colour of the solution start to change from colour less to a clear brownish solution within short period. This confirms the formation of silver nanoparticles. Solution was kept in same position for 100min for complete reduction of silver nitrate to silver nanoparticles.

2.3 Preparation of CMGG/Ag NC film

CMGG/Ag NC film was prepared by solution casting method. The viscous CMGG/Ag NC solution was poured in Teflon plate. Then it was dried in oven at 30^OC for overnight. After 24 hours of drying, a fine thin CMGG/Ag NC film was obtained **Fig. 6.** Such obtained film was stored in the desiccators up to further testing.

2.4. Characterization of CMGG/Ag NC film.

CMGG/Ag NC film was characterized by using different techniques. Scanning Electron Microscope (SEM) (HITACHI-S-3700), Transmission electron microscopy (TEM) and XRD (BRUKER D8-ADVANCE) were used to find out the size and shape of silver nanoparticles in the CMGG matrix. UV (UV- Parkin Elmer Lambda -750), Photoluminiscence (PL-fluroLog–made by horiba-3, Horiba Jobin Yvon) testing were done for testing silver nanocomposites optical properties.

2.4.1 Antimicrobial testing

Antimicrobial activity of CMGG/AgNPs NC film was tested by using the disc diffusion or Kirby-Bauer method [22]. Luria Broth (LB) media was used for growth of the bacterial. The inhibition zones were measured after 24 hours of incubation at 37^oC. CMGG/Ag NC films synthesized by various concentration of silver nitrate solution (2.5mM, 5mM, 10mM and15mM) has been tested against gram positive (*Bacillus subtilis*) and gram negative *(Escherichia coli*) bacterial.

3. Results and discussion

3.1 Morphology and optical property of CMGG/Ag NC film.

Recorded UV-Vis spectrum of the CMGG/AgNC film formed by solution casting method agrees well with the result of Ref. [18]. An absorbance band was found between the Ag NPs Surface Plasmon Resonance (SPR) bands (350 to 450 nm). This confirms the presence of silver nanoparticles in the CMGG/Ag NC film. Further XRD analysis of the CMGG/Ag NC film was also tested **Fig. 1**. XRD spectrum was matched with JCPDS file no 01-1164. This confirms present of Ag metal in CMGG/Ag NC film in face central cubic lattice structure. Photoluminescence spectrum is shown in F**ig. 2**. The PL emission spectrum was obtained in visible region (400-600) nm with peak position 435nm. This PL emission in visible region may be due to excitation of electrons from occupied d bands into states above the Fermi level [22].

Morphology of the AgNPs in CMGG/Ag NC film was investigated by using SEM and TEM analysis **Fig. (3,4).** From the SEM image **Fig. 3**, it is clear that some particles are present in the film. Further the TEM image of the CMGG/Ag NC film confirms the formation of Ag nanoparticles in less than 20nm size with spherical shape **Fig. 4**. This also confirms the formation of CMGG/Ag NC film.

3.2 *Antimicrobial activity of CMGG/Ag NC film.*

The antimicrobial activity of CMGG/Ag NC film was tested against gram positive and gram negative bacteria, by using Kirby-Bauer method. This method has been found suitable for determining susceptibility and standard zones of inhibitions by many scientists [23]. According to this method, Luria Broth (LB) media was used for growing gram positive (*Bacillus subtilis*) and gram negative *(Escherichia coli*) bacterial. After this CMGG/Ag NC films prepared from different concentration of silver nitrate solutions (I = 2.5mM, II = 5mM, III = 10mM and IV = 15mM) were cut in a circular shape with same size. Then these films were put in the inoculated plates and stored for 24hours at 37^{o}C in incubator. Then zones of inhibition were measured by scale. Inhibition zone created by CMGG/Ag NC films against gram positive (*Bacillus subtilis*) and gram negative *(Escherichia coli*) bacterial are shown in **Fig. 5**. Inhibition zones diameter (in millimetres) around the different CMGG/Ag nanocomposites film was also found out **Table 1**. It was found that a CMGG/Ag NC film made from very little amount of $AgNO_3$ (2.5mM) was sufficient to inhibit both bacterial growth with 20mm of inhibition zone.

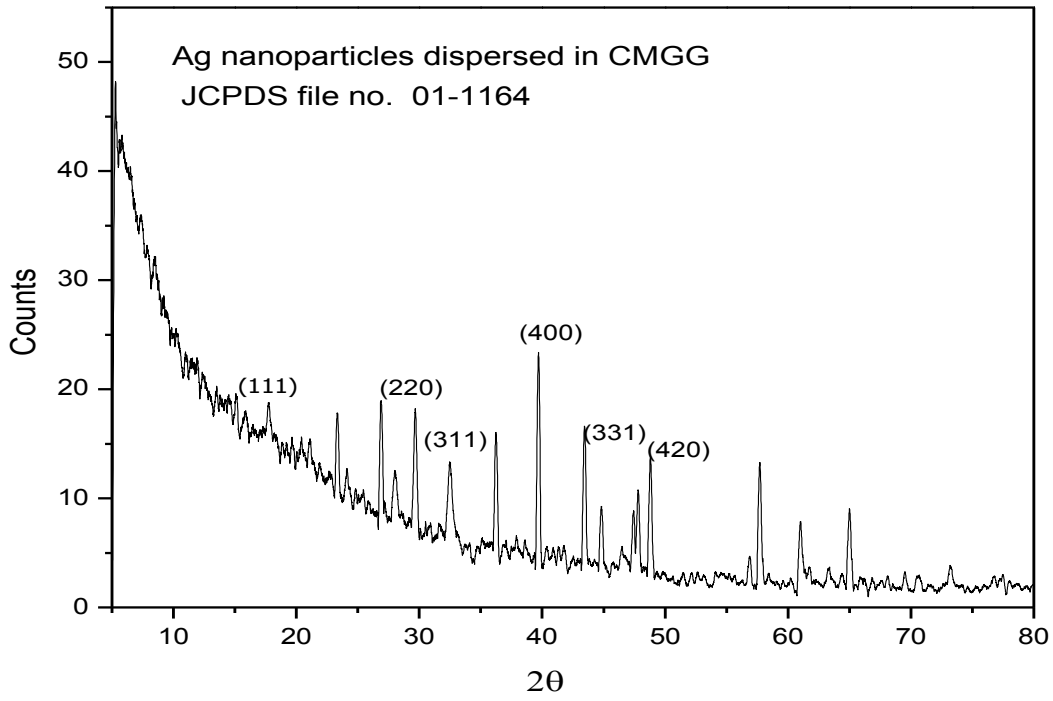

Fig. 1. XRD spectrum of CMGG/Ag nanocomposites film

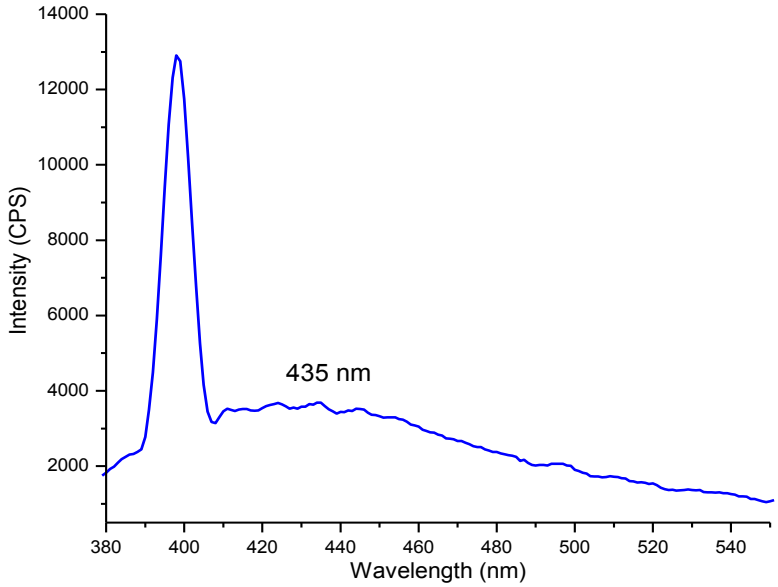

Fig. 2. Photoluminescence spectrum of CMGG/Ag NC film

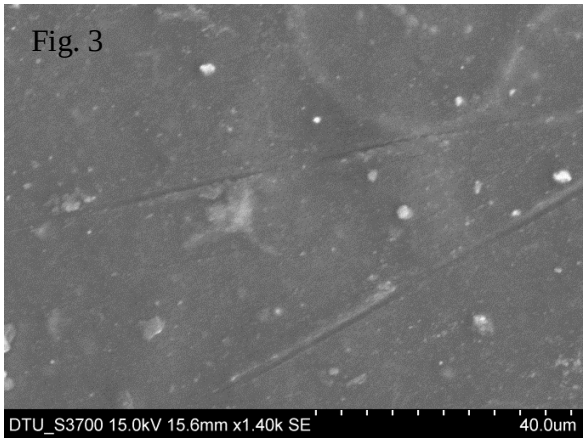

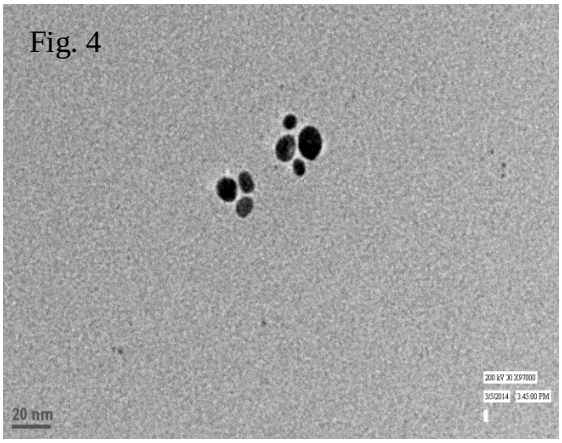

Fig. (3,4). SEM and TEM images of CMGG/Ag nanocomposites film.

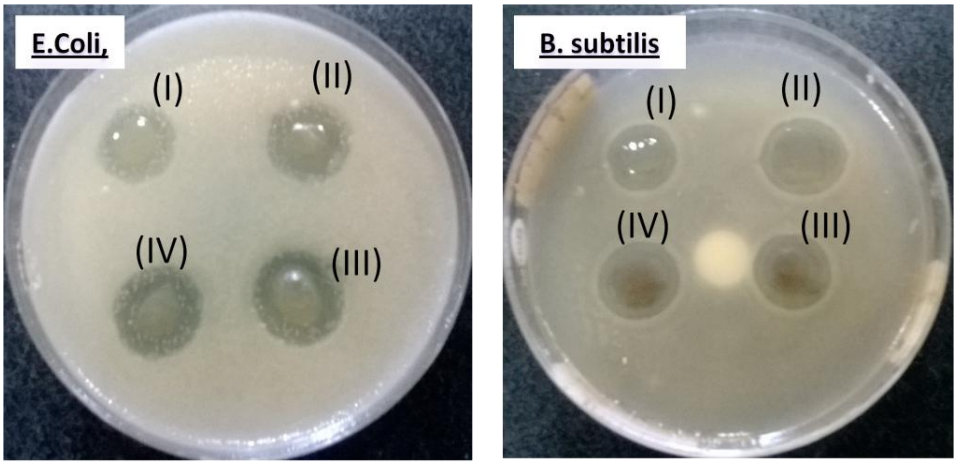

Fig. 5. Inhibition zones against various bacteria with different CMGG/Ag nanocomposites films synthesized by various concentrations of $AgNO_3$ solutions (I = 2.5 mM, II = 5 mM, III = 10 mM and IV = 15 mM).

S. No	Concentration (mM) of $AgNO_3$ used	Inhibition (mm) zones against various bacteria after 24 hours	
		E. Coli	B. subtilis
1.	2.5	20	20
2.	5.0	21	20
3.	10	22	22
4.	15	22	22

Table 1. Inhibition zones (mm) against E. coli and B. subtilis bacteria with CMGG/Ag NC films made by various concentrations of $AgNO_3$.

Fig.6. CMGG/Ag nanocomposites film

4. Conclusions

CMGG/Ag NC film has been prepared successfully by solution casting method. Size of the Ag nanoparticles in the film was found less than 20nm which was confirmed by TEM. Nanocomposite film was found very effective against gram positive (*Bacillus subtilis*) and gram negative *(Escherichia coli*) bacteria. Because this nanocomposites film has been synthesized by green method and no toxic material has been used, so this film may be very effective for medical and clinical applications. This film may also be used for the storage of Ag nanoparticle for long duration.

Acknowledgements

Authors are grateful to the Jitendra Singh, Lab Technician, Delhi Technological University, Delhi, India for helping in antimicrobial testing.

References

[1] Tamboli M S, Kulkarni M V, Patil RH, Gade WN, Navala SC and Kale BB 2012 *Colloids and surfaces B Biointerfaces.* **92** 35.
[2] Singh M, Singh S, Prasad S and Gambhir I S 2008 *Digest Journal of Nanomaterials and Biostructures*, **3(3)** 115.
[3] Balogh L, Swanson D R, Tomalia D A, Hagnauer G L and McManus A T 2001 *Nano Letter*, **1(1)** 18.
[4] Schrand A M, Braydich-Stolle L K, Schlager J J, Dai L and Hussain S M 2008 *Nanotechnology*. **19** 235104.
[5] Ciobanu C, Gavriliu S, Lungu M, Gavriliu L and Ciobanu L C 2009 *The Open Chemical and Biomedical Methods Journal*. **2** 86.
[6] Hettiarachchi M A and Wickramarachchi PASR 2011 *J. Sci. Univ. Kelaniya*. **6** 65.
[7] Chellamani K P, Sundaramoorthy P, Sureshram T 2012 *International Journal of Emerging Technology and Advanced Engineering* **2(11)** 176.
[8] Panacek A, Kvitek L, Prucek R, Kolar M, Vecerova R, Pizurova N, Sharma V K, Nevecna Tand Zboril R 2006 *J. Phys. Chem. B.* 110 (33) 16248.
[9] Roldán M V, Frattini A L, Sanctis O A and Pellegrini N S 2005 *Anales AFA* **17** 212.
[10] Yin H, Yamamoto T, Wada Y and Yanagida S 2004 *Materials Chemistry and Physics* **83** 66.
[11] Zhu Z, Kai L and Wang Y 2006 *Materials Chemistry and Physics* **96** 447.
[12] Edelstein A S, Cammarata R C 1996 *Nanomaterials, synthesis, properties and applications*, (Bristol and Philadelphia Publishers, Bristol).
[13] Maillard M, Giorgo S and Pileni MP 2002 *Adv. Mater*. **14(15)** 1084.

[14] Mock J J, Barbic M, Smith D R, Schultz D A and Schultz S 2002 *J. Chem. Phys*. **16(15)** 6755.
[15] Duran N, Marcato P L, Alves O L and De Souza G I (2005) *J. Nanobiotechnology* **3(8)** 1.
[16] Guzmán M G, Dille J and Godet S 2009 *Int. J. Chemical and Biol. Eng.* **2(3)** 104.
[17] Sung H J, Yun H H and Sung C Y 2005 *J Material Sci.* **40(20)** 5413.
[18] Gupta A P and Verma D K 2014 *Adv. Nat. Sci.: Nanosci. Nanotechnol.* **5** 035018.
[19] Gong H, Liu M, Chen J, Han F, Gao C and Zhang B 2012 *Carbohydrate Polymers*, **88(3)**1015.
[20] Gupta A P and Verma D K 2014 *Int. J. Biol. Macromol.* **68** 247.
[21] Geethalakshmi R and Sarada D V L 2010 *Int. J. Eng. Sci. and Tech.* **2(5)** 970.
[22] Vasireddy R, Paul R and Mitra A K 2012 *Nanomaterials and Nanotechnology*. **2(8)**1.
[23] Lawrence W, Barry AL, O'toole R, Sherris J C (1972) *Applied Microbiology* **24(2)** 240.

ACS APPLIED MATERIALS & INTERFACES

Research Article

www.acsami.org

Protein Functionalized Carbon Nanotubes-based Smart Lab-on-a-Chip

Md. Azahar Ali,[†,‡] Pratima R. Solanki,[§] Saurabh Srivastava,[†,∥] Samer Singh,[§] Ved V. Agrawal,[†] Renu John,[‡] and Bansi D. Malhotra*[,∥]

[†]Biomedical Instrumentation Section, Materials Physics & Engineering Division, CSIR-National Physical Laboratory, Dr. K. S. Krishnan Marg, New Delhi 110012, India

[‡]Department of Biomedical Engineering, Indian Institute of Technology Hyderabad, Ordnance Factory Estate, Yeddumailaram, Hyderabad, Andhra Pradesh 502205, India

[§]Special Centre for Nano Sciences, Jawaharlal Nehru University, New Delhi 110067, India

[∥]Department of Biotechnology, Delhi Technological University, Main Bawana Road, Delhi 110042, India

Supporting Information

ABSTRACT: A label-free impedimetric lab on a chip (*i*LOC) is fabricated using protein (bovine serum albumin) and antiapolipoprotein B functionalized carbon nanotubes–nickel oxide (CNT–NiO) nanocomposite for low-density lipoprotein (LDL) detection. The antiapolipoprotein B (AAB) functionalized CNT–NiO microfluidic electrode is assembled with polydimethylsiloxane rectangular microchannels (cross section: 100 × 100 μm). Cytotoxicity of the synthesized CNTs, NiO nanoparticles, and CNT–NiO nanocomposite has been investigated in the presence of lung epithelial cancer A549 cell line using MTT assay. The CNT–NiO nanocomposite shows higher cell viability at a concentration of 6.5 μg/mL compared to those using individual CNTs. The cell viability and proliferation studies reveal that the toxicity increases with increasing CNTs concentration. The X-ray photoelectron spectroscopy studies have been used to quantify the functional groups present on the CNT–NiO electrode surface before and after proteins functionalization. The binding kinetic and electrochemical activities of CNT–NiO based *i*LOC have been conducted using chronocoulometry and impedance spectroscopic techniques. This *i*LOC shows excellent sensitivity of 5.37 kΩ $(mg/dL)^{-1}$ and a low detection limit of 0.63 mg/dL in a wide concentration range (5–120 mg/dL) of LDL. The binding kinetics of antigen–antibody interaction of LDL molecules reveal a high association rate constant (8.13 M^{-1} s^{-1}). Thus, this smart nanocomposite (CNT–NiO) based *i*LOC has improved stability and reproducibility and has implications toward in vivo diagnostics.

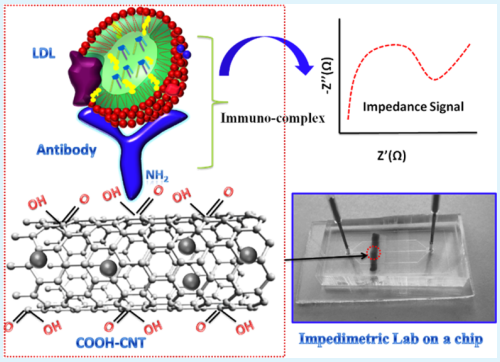

KEYWORDS: *label-free immunosensor, lab-on-a-chip, impedance, cytotoxicity, low density lipoprotein, antiapolipoprotein B*

1. INTRODUCTION

The unique physical, chemical, and electronic properties of nanomaterials have been extensively explored for application in biomedical diagnostics including lab on a chip (LOC), biosensors, implantable medical devices (e.g. in situ monitoring) and bioimaging.[1−3] Low-dimensional LOC, field-effect transistor-based biosensors, and bioelectronic devices based on carbon nanotubes (CNTs), graphene, and metal oxide/silicon nanowires have exceptional merits for point-of-care diagnostics and prognosis.[4−6] Sharf et al. have utilized CNTs for development of field effect transistor-based biosensor to obtain the improved bioelectronic interface.[7] The high conductivity, mechanical strength, and tunable functionality in conjugation with biomolecules, and electrochemical and good tribological characteristics of CNTs make it the promising candidate for fabrication of an ultrasensitive LOC for biomolecules detection.[8−10] Napier et al. have reported the electrochemical oxidation of DNA wrapped CNTs.[9]

The electrochemical properties of the CNTs can perhaps be enhanced by incorporating metal oxides nanoparticles such as nickel oxide, manganese oxide, and so on.[11] Ali et al. reported dispersion of CNTs in the presence of nickel oxide to obtain an efficient microfluidic biosensor for esterified cholesterol detection.[12] The nanostructured nickel oxide (nNiO) provides large surface-to-volume ratio, high electrocatalytic behavior, and biocompatibility and does not degrade on exposure to protein, enzyme, smRNA or DNA, antibody, and so on.[13] The nNiO provides high isoelectric point (IEP ∼ 10.8) that can be helpful for the immobilization of an antibody (IEP ∼ 4.5) via

Received: December 21, 2014
Accepted: February 26, 2015

ACS Publications © XXXX American Chemical Society

DOI: 10.1021/am509002h
ACS Appl. Mater. Interfaces XXXX, XXX, XXX−XXX

electrostatic interactions or attachment with other nanomaterials like CNTs that have a negative electrokinetic surface potential.[14] The nNiO can be used to obtain enhanced electrochemical characteristics in the presence of mediator or redox probe due to bulk conduction, tunneling, and enhanced surface scattering of electrons arising due to high density of electronic states. It has been reported that CNTs perhaps provide an electronic path for transport of the charge carriers in the electrode surface from electrolyte solution. Besides this, the integrated LOC possesses remarkable characteristics over the conventional biosensor devices due to reduced consumption of reagents/samples, power consumption and compact size.[15,16] The electrochemical impedance change in electrode interface can be directly related to the concentration of bound target.[17] The high surface-to-volume ratio of electrochemical LOC has been found to result in shorter assay times as well as label -free detection of specific biomolecules. The integrated LOC may perhaps be utilized for multiplex analysis of biorecognition events.[18] On the basis of label-free detection, several detection strategies have been implemented for highly effective signal transduction of the biorecognition events via microfluidic platforms. Ali et al. have fabricated an immunosensor based on surface plasmon resonance (SPR) and electrochemical detection system using CdS quantum dots for monitoring LDL molecules.[19] This immunosensor shows the sensitivity of 98.5 Ω/(mg/dl)/cm^2 and limit of detection is found to be as 16.03 mg/dl. The kinetics of antibody−antigen interactions of LDL molecules and their detection have been investigated using self-assembled monolayer of 4-aminothiophenol by Matharu et al.[20] Thus, a higher sensitive and miniaturized device for lipid molecules (low density lipoprotein, triglycerides, etc.) quantification is currently a major concern for point-of-care (POC) diagnostics.

CNTs have recently been used for development of biosensors/LOC, drug delivery systems, in vivo and in vitro biodistribution, and toxicity effect.[21−23] CNTs coupled with a metal oxide can play an important role for multimodal bioimaging.[8] However, the biocompatibility and cytotoxicity effect of CNTs are currently major limitations for the development of nanomaterials-based in vivo diagnostics devices. The toxicity associated with CNTs when they come in direct contact with body fluid has remained a cause of concern for biological applications.[24−26] At the molecular level, it is important to understand the nature of interaction between a biosystem with a nanostructured material including CNTs. Ryoo et al. have described the mammalian cellular (NIH-3T3 fibroblast cells) response in the presence of CNTs/graphene.[27] It has been found that these nanomaterials show good performance for bioapplication including in situ monitoring of biomolecules, especially for implantable devices without inducing remarkable deleterious effects. Davoren et al. have investigated the in vitro cell viability of single walled carbon nanotubes on human A549 lung cells to evaluate the metabolic, lysosomal and mitochondrial activity.[28] Mooney et al. have tracked the intracellular movement of CNTs through the cytoplasm to a nuclear location of human mesenchymal stem cells and investigated the effects on cellular metabolic activity, proliferation and differentiation.[29] However, the cytotoxicity effect of metal oxide integrated CNTs hybrid nanomaterial is still unexplored for application to POC devices. Thus, there is urgent requirement to conduct a systematic investigation relating to toxicity of the hybrid nanomaterials that may be in contact with human cells for in vivo and in situ measurements, such as in cell-based biosensors, LOC or implantable devices for biomolecule detection.

Estimation of low-density lipoprotein (LDL) cholesterol in human serum is urgently required via POC diagnostics.[30] Lipoproteins are known to play a vital role toward the transport of cholesterol in the bloodstream and are catabolized in the liver and kidneys, and in peripheral tissues via receptor-mediated endocytosis mechanisms. These lipoproteins are mainly synthesized in the liver and intestines, and are assembled at the cell membranes from cellular lipids and exogenous lipoproteins or apolipoproteins. They can be categorized by the electrophoretic mobility on agarose gels into pre-13, and 13 lipoproteins, corresponding to LDL, very-low-density lipoprotein, intermediate-density lipoprotein, and high-density lipoprotein, respectively. During cholesterol transportation, the interaction of apolipoprotein with sulfated glycosaminoglycans results in cholesterol accumulation in the arterial walls. This may cause plaque formation through arteries walls and make them less flexible, causing various heart and vascular diseases, such as atherosclerosis, and accompanying immune-inflammatory response.[31] Nuclear magnetic resonance spectroscopy, ultracentrifugation, gel filtration, electrophoresis, Friedewald equation, and affinity chromatography are the conventional techniques currently used to estimate concentration of LDL molecules.[30] However, for general clinical use, these methods are expensive, time-consuming, and necessitate invention of alternative strategies. Apolipoprotein B can play an important role in receptor recognition via antigen−antibody interactions.

In this study, we demonstrate the fabrication of an impedimetric lab on a chip (*i*LOC) for label-free detection of LDL molecules. In this *i*LOC, the immunoelectrode has been fabricated using antiapolipoprotein B (AAB) and bovine serum albumin (BSA) functionalized carbon nanotubes-nickel oxide (CNT−NiO) nanocomposite deposited onto indium−tin oxide (ITO) substrate. The proteins conjugated CNT−NiO electrode has been characterized and quantified using spectroscopic and microscopic techniques. In addition, the cytotoxicity effect of NiO nanoparticles, CNTs, and CNT−NiO composite in the presence of human lung epithelial cancer cell (A549) using MTT assay has been investigated.

2. EXPERIMENTAL SECTION

2.1. Chemicals. The SU8−100 negative photoresist and Shipley 1811 positive photoresist for polydimethylsiloxane (PDMS) microchannels and ITO electrode fabrication, respectively, are procured from Microchem (Newton, MA). The $Ni(NO_3)_2$ (nickel nitrate) and KOH (potassium hydroxide) have been procured from Sigma-Aldrich (St. Louis, MO). LDL antiapolipoprotein B-100 (AAB), *N*-hydroxysuccinimide (NHS), *N*-ethyl-N0-(3-(dimethylamino)propyl carbodiimide) (EDC) and bovine serum albumin (BSA) are purchased from Sigma-Aldrich (St. Louis, MO). Five milligrams (5 mg) of lyophilized LDL powder is used to dissolve in 1 mL of deionized water with 150 mM NaCl of pH 7.4 and 0.01% ethylene diaminetetra acetic acid. Then, 50 mM phosphate buffer saline (PBS) of pH 7.4 is used to prepare the BSA (2 mg/mL) and AAB (1 mg/mL) solutions containing 150 mM NaCl. Deionized water has been obtained from the Millipore water purification system.

2.1. Fabrication of LOC. Details of soft lithographic technique for PDMS microchannels and ITO electrode fabrication have been reported earlier.[32] We carried out a slight modification in PDMS microchannels and ITO electrode to decrease the channel size. In brief, the soft lithographically has been utilized to fabricate the PDMS microchannels having height, length, and width of 100 μm, 2 cm, and 100 μm, respectively. On the other hand, the indium tin oxide (ITO)

DOI: 10.1021/am509002h
ACS Appl. Mater. Interfaces XXXX, XXX, XXX−XXX

Scheme 1. Schematic Representation of the Lab-on-a-Chip Fabrication For LDL Detection

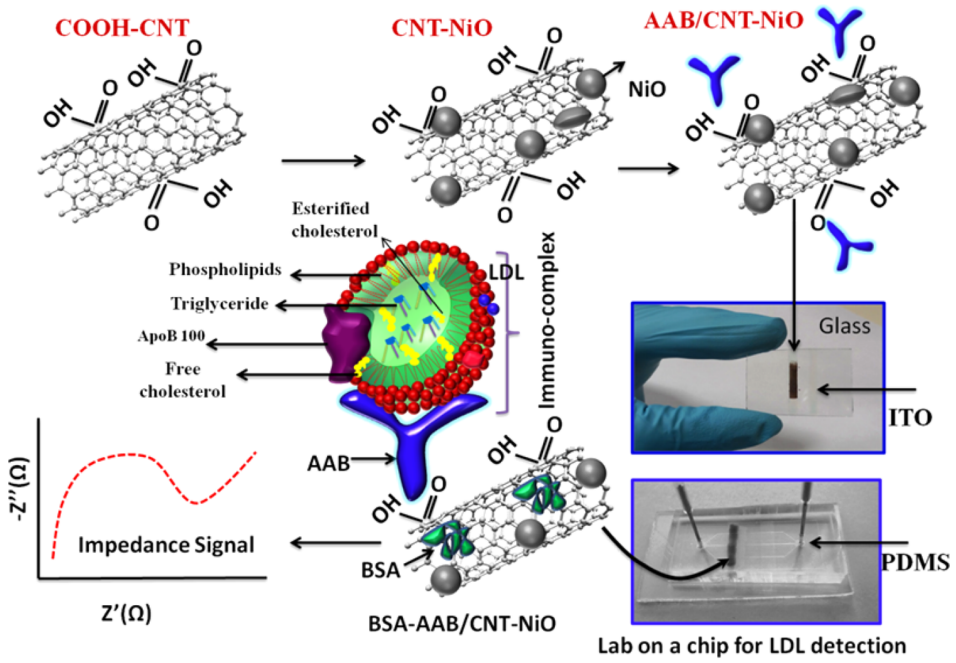

electrode on glass substrate (size; 2 mm × 2.6 cm) has been fabricated using photolithographic technique followed by wet chemical etching as shown in Figure S1 (Supporting Information). Prior to use, the ITO is cleaned with acetone and methanol. A small amount of positive photoresist (Shipley 1811) is coated onto ITO substrate and allowed to spin at 3000 rpm for 20 s. The photoresist/ITO substrate is soft baked using a hot plate for 1 min to remove the solvent. The UV radiation is used to expose this photosensitive substrate followed by an optical mask. After UV exposure, the photoresist/ITO substrate is developed using a developer solution for 10 s. The developed substrate is then dipped into the ITO etchant (zinc dust + HCL solution 15%) to etch the ITO on glass substrate from the exposed region. The remaining photoresist on ITO is washed out by acetone. This ITO electrode on glass is again cleaned with acetone via sonication (15 min) and with deionized water several times. These clean ITO electrodes are hydrolyzed using the mixture of $H_2O/H_2O_2/NH_3$ (5:1:1) at 70 °C for 1 h.

To synthesize CNTs and functionalize these with acid, we performed chemical vapor deposition in the presence of a mixture of ferrocene acting as a catalyst and toluene as a hydrocarbon source as described in literature.[12] Ali et al. have described the synthesis of NiO nanoparticles and the in situ synthesis of nanocomposite with CNTs.[12] During the NiO synthesis, CNTs (0.2%) are added into $Ni(OH)_2$ solution at a pH of 10.1. Owing to strong electrostatic interactions, CNTs bind with NiO nanoparticles. This thick gel-like CNT−$Ni(OH)_2$ solution is selectively deposited onto ITO electrode via dip coating technique. The modified substrate is dried at ∼110 °C for about 1 h and annealed at 450 °C for about 2 h to obtain CNT−NiO composite matrix on ITO surface. Then, 15 μL of AAB solution is spread onto the CNT−NiO surface via physical adsorption followed by EDC-NHS coupling chemistry and kept for 4 h in a humid chamber (4 °C). The carboxylic (−COOH) groups on CNT−NiO surface can undergo an amidation reaction with $-NH_2$ groups of the proteins (AAB). The covalently conjugated protein (AAB) molecule provides a strong covalent (C−N) bond formed between −COOH group of CNT−NiO and $-NH_2$ group of AAB that has been confirmed via X-ray photoelectron spectrometry (XPS) and Fourier transform infrared spectroscopy (FT-IR) studies. BSA molecules are used to block the nonspecific sites of AAB functionalized CNT−NiO surface. The fabricated PDMS slab is sealed with glass substrate containing ITO electrode and BSA−AAB/CNT−NiO/ITO immunoelectrode. A syringe pump maintains the constant flow rate (1.0 μL/min) to transport PBS and LDL solution through this chip. An Ag/AgCl wire introduced in the outlet of the microchannel worked as a reference electrode while bare ITO acted as the counter electrode. The fabricated BSA−AAB/CNT−NiO/ITO-based electrode LOC is kept at 4 °C when not in use. Scheme 1 shows the fabrication of LOC and the functionalization of BSA−AAB onto CNT−NiO surface for the detection of LDL molecules.

2.3. Instrumentation. The synthesized CNTs, NiO nanoparticles, and CNT−NiO nanocomposite have been characterized using transmission electron microscopy (TEM, JEOL JEM-2000 EX) and scanning electron microscopy (SEM, Zeiss, EVO, 40). To investigate the protein (AAB) functionalization on CNT−NiO, we utilized X-ray photoelectron spectrometry (XPS, Thermo Scientific, Multilab 2000, with an alpha 110 hemispherical electron energy analyzer and an X-ray source) and Fourier transform infrared spectroscopy (FT-IR, PerkinElmer, Model 2000). The electrochemical activity of this *i*LOC for LDL detection has been conducted using an electrochemical workstation (Model AUT-84275) in the presence of phosphate buffer saline (50 mM, pH 7.4) containing 5 mM $(Fe(CN)_6)^{3-/4-}$ as a redox species.

2.4. Cell Proliferation Study. The effect of CNTs, NiO nanoparticles or CNT−NiO nanocomposite on human cell line has been studied using methyl thiazol tetrazolium (MTT) assay and bright field microscopy (Figure 1). The lung epithelial cancer cell line A549 is used as a test cell line. The A549 cells are procured from NCCS, Pune, India. The cells are maintained in a complete growth medium (10% FBS containing Rosewell Park Memorial Institute; RPMI-1640) at 37 °C under humidified 5% CO_2 environment. For assay, the cells are plated at 5×10^3 cell/well in 96-well tissue-culture plate and are allowed to attach for 24 h. The next day, medium on the plated cells is replaced with fresh growth medium supplemented with CNTs, NiO, or CNT−NiO nanocomposite. The nanoparticles of NiO, CNTs (1 mg/mL) or their composite comprising of NiO and CNTs in 49:1 ratio are dispersed in deionized water by continuous sonication. This suspension is kept at room temperature for 1 h to allow the nondispersed material to settle down. Prior to the addition of dispersed nanoparticles to the growth medium, the nanoparticles are again dispersed by sonication using a sonicator bath at room temperature (10 min at 40 W). The dispersed nanoparticles are

DOI: 10.1021/am509002h
ACS Appl. Mater. Interfaces XXXX, XXX, XXX−XXX

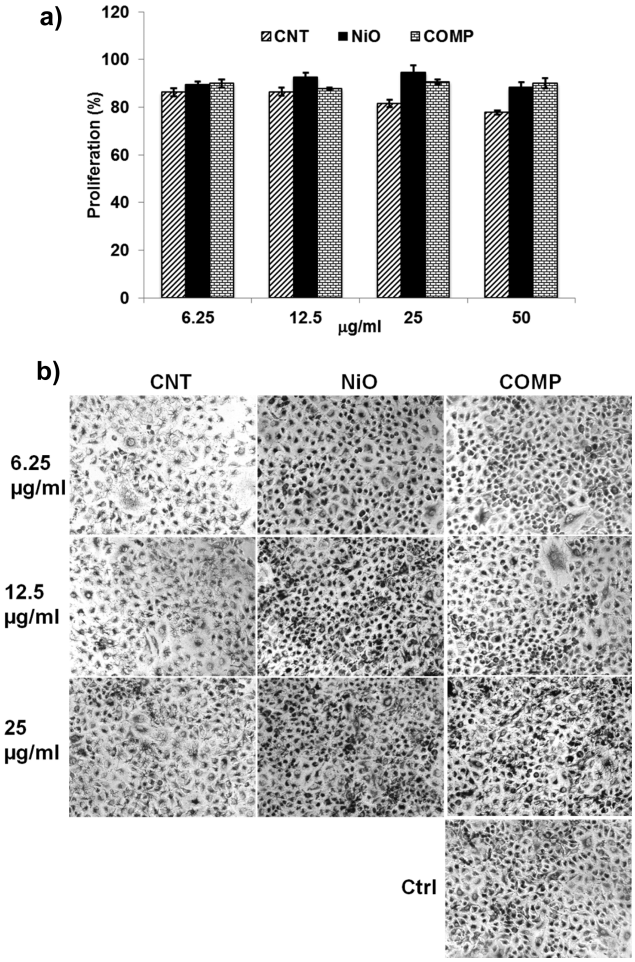

Figure 1. (a) CNT−NiO composite has reduced toxicity compared to that of CNTs alone. The A549 cells plated at 5×10^3 cells per well in 96-well tissue culture plate are exposed to growth medium containing indicated concentration of nanoparticles for 24 h. The cells are treated with MTT for 1 h and then relative reduction of MTT to formazon by cells is calculated. The relative reduction of MTT is presented as % proliferation with respect to cells not exposed to any nanoparticles (Ctrl). The error bars show average deviation. (b) CNTs exposure significantly attenuates the ability of A549 cells to reduce MTT dye to formazon as compared to NiO or CNT−NiO composite. A549 cells exposed to indicated concentration of CNTs, NiO or CNT−NiO composite (COMP) for 24 h are incubated in the presence of 1 mg/mL MTT for 1 h. The cells are imaged using Nikon eclipse microscope at 100× magnification.

added to the cell growth medium at a final concentration of 50, 25, 12.5, and 6.25 μg/mL.

The medium on cells is replaced with MTT containing RPMI-1640 medium after 24 h. The cells are further incubated for 1−2 h at 37 °C to allow reduction of MTT dye to formazan crystals. The cells are also observed under the inverted microscope prior to MTT addition and 1−2 h later before solubilization of cells with dimethyl sulfoxide (DMSO). The cells are solubilized in 100 μL of DMSO, followed by absorbance measurement at 540 nm. The absorbance value gives a measure of the cell proliferation. The relative proliferation is calculated with respect to cells that are not exposed to any kind of nanoparticles. In each experiment, every treatment group is replicated in three independent wells. Each experiment is repeated three times, and the average proliferation is calculated. A representative experiment is displayed where error bars represent ± average deviation.

3. RESULTS AND DISCUSSION

3.1. Effect of Cytotoxicity. The results of MTT assay reveal that the NiO nanoparticles and CNT−NiO nanocomposite have much reduced influence on the well being of A549 cells and consequently the ability of cells to reduce MTT to formazon at all the concentrations has been investigated as compared to CNTs alone (Figure 1a). The relative % proliferation is estimated with respect to growth of the control cells (Ctrl) that are not exposed to any nanoparticles. Though the MTT assay (Figure 1a) does not show much difference among the cells exposed to CNTs, NiO nanoparticles or CNT−NiO composite up to 12.5 μg/mL concentration, further increase in the concentration shows incremental detrimental effect in case of CNTs whereas others appear to have very little effect. The toxicity of CNTs is more evident from the pattern of formazon crystal formation in CNTs exposed cells as compared to the NiO nanoparticles or CNT−NiO composite exposed cells. The CNTs exposed cells progressively show more diffused formazon crystal formation and appearance of extracellular debris with increase in CNTs concentration while NiO nanoparticles and CNT−NiO composite exposed cells are relatively unaffected in the investigated concentration range (Figure 1b).

3.2. X-ray Photoelectron Microscopy (XPS) Studies. The surface functionalization of AAB on CNT−NiO surface has been confirmed by XPS studies. The functional groups including −O-C═O, C−C, C−OH, C−O, C═O, O−C═O, $-NH_2$ of CNT−NiO film before and after AAB immobilization have been quantified. The XPS wide scan spectra of CNT−NiO films shows C 1s and O 1s peaks in both the curves (Figure 2i,ii). The C 1s peak position and the relative atomic percentage of various functional groups present in CNT−NiO/ITO and AAB/CNT−NiO/ITO electrodes are shown in Table S1 (Supporting Information). In curve (ii), an additional peak at 401 eV is attributed to N 1s of AAB functionalization on CNT−NiO surface. In spectra b, the prominent C−C peak observed at 284.6 eV is due to graphitic (sp^2) nature of CNTs. The additional photoemission at higher binding energies is attributed to the presence of carbon atoms bonded to other functional groups. A peak seen at 285.6 eV can be ascribed to photoelectrons emitted from carbon atoms with the sp^3 configuration. The deconvoluted peaks at 286.5 and 288.5 eV arise due to the carboxylic acid functionalization such as −C−O, and −O−C═O, respectively. These results indicate the functinalization of the CNTs by −O−C═O. After AAB immobilization (curve c), the peak positions of these groups are slightly changed and an additional peak at 287.7 eV appears due to amide functionalization (−N−C═O− groups). The covalent surface functionalization of AAB perhaps results in shift of the binding energies. In curve (d), the peak seen at 399.0 eV is assigned to the core-level electron of N 1s. The binding energy peak at ∼400 eV corresponds to the formation of an amide linkage on the CNTs. The binding energy peak at 400.4 eV is due to the presence of amide nitrogen (CO−NH) in lipid molecules and the peak at 401.5 eV is ascribed to the presence of ≡N species. The atomic concentration for O−C═O is found to be as 6.2% for CNT−NiO electrode that decreases to 1.7% due to AAB incorporation. This reduced amount of the O−C═O groups is perhaps utilized for binding of -NH_2 groups of lipid molecules.

3.3. Fourier Transform Infrared Spectroscopy (FT-IR) Studies. The FT-IR spectrum of the various electrodes is

DOI: 10.1021/am509002h
ACS Appl. Mater. Interfaces XXXX, XXX, XXX−XXX

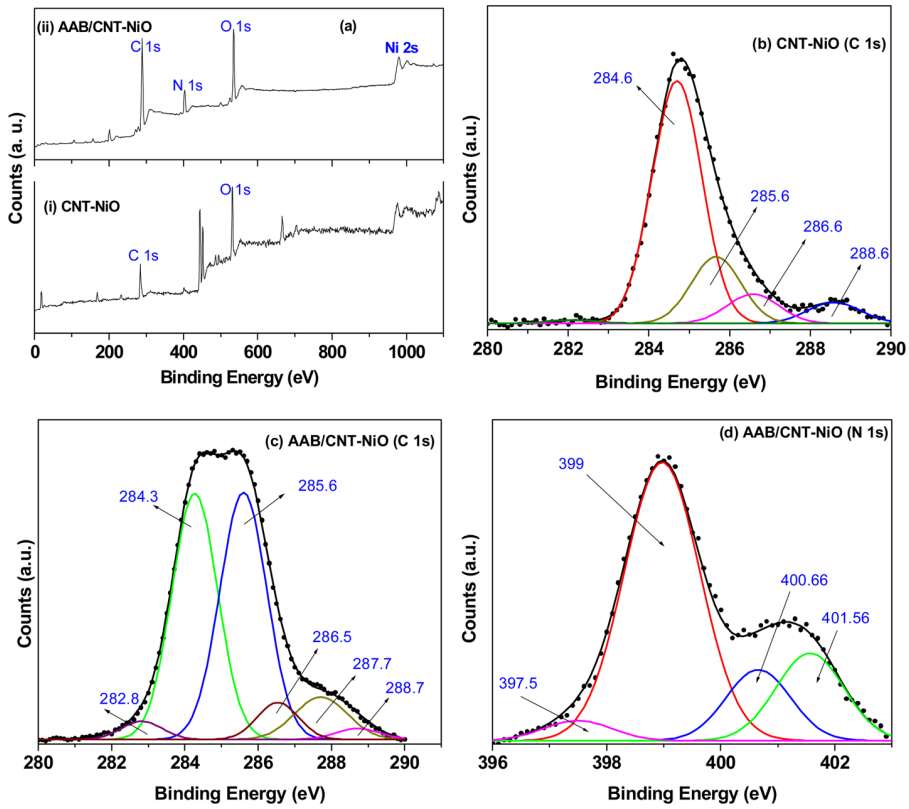

Figure 2. (a) Wide-scan XPS spectra of electrodes, (b) C 1s spectra of CNT−NiO electrode, (c) C 1s spectra of AAB functionalized CNT−NiO electrode, (d) and N 1s spectra of AAB functionalized CNT−NiO electrode.

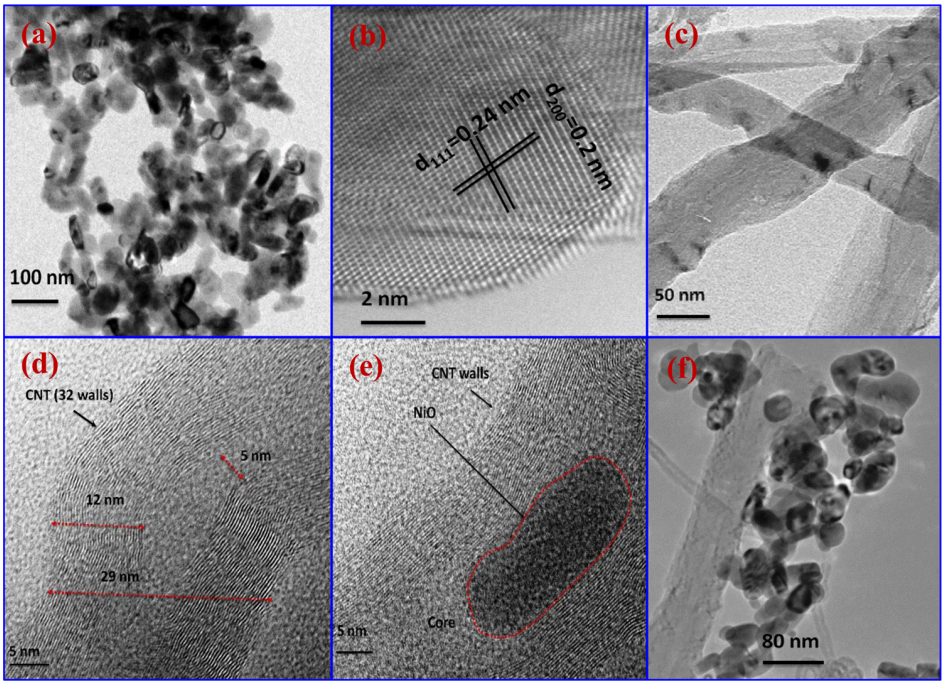

Figure 3. TEM image of (a) NiO nanoparticles, (b) lattice fringes of NiO nanoparticles (high-resolution TEM image), (c) CNTs, and (d) high-resolution image of individual CNT. (e) TEM image of elongated NiO nanoparticle with single CNT and (f) CNT modified with NiO nanoparticles.

shown in the Figure S2 (Supporting Information). The absorption peak at 503 cm^{-1} (spectra a) in the fingerprint region corresponds to Ni−O vibration band. The characteristic absorption peaks seen at 2839 and 2917 cm^{-1} are attributed to CH stretching of COOH−CNTs. The band seen at 1562.5 cm^{-1} arises due to the C═C stretching that forms the

DOI: 10.1021/am509002h
ACS Appl. Mater. Interfaces XXXX, XXX, XXX−XXX

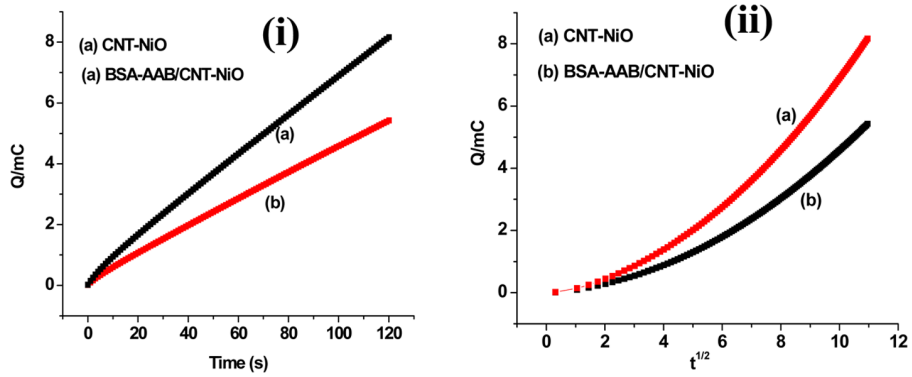

Figure 4. (i) Chronocoulometry studies of the fabricated LOC before and after protein immobilization and (ii) show the plot between charge (Q) and $t^{1/2}$.

framework of the CNT sidewall. The bands observed in the range of 2500−3000 cm^{-1} wavenumber result from the carboxylic acid O−H stretching. The absorption bands seen at ∼1000−2500 cm^{-1} are assigned to the O−C═O symmetric and asymmetric stretching vibrations and the C−O stretching vibration indicating CO_2 absorption on the CNT−NiO film. After immobilization of BSA−AAB onto CNT−NiO/ITO electrode surface (spectra b), the peak found at 850 cm^{-1} is assigned to the aromatic C−H bending. The peak at 1040 cm^{-1} is due to C−OH stretching vibration. The band seen at 3300 cm^{-1} is attributed to the OH stretching on the film surface. The bands seen at 1248 and 1650 cm^{-1} are due to amide III and amide I groups of BSA−AAB proteins molecules.

3.4. Morphological Studies. To observe the morphological features such as shape, size, and crystallinity of NiO, CNTs, and their composite, we have used both SEM and TEM techniques. The SEM image (Figure S3a, Supporting Information) shows an overview of the NiO nanoparticles. On addition of CNTs in NiO nanoparticles (Figure S3b, Supporting Information), it can be seen that the NiO nanoparticles are attached with majority of the carbon nanotubes (size: a few microns), which are well-dispersed on the electrode surface. These CNTs and NiO nanoparticles bind via electrostatic interactions resulting from opposite surface charges. In the case of protein (BSA and AAB) immobilized COOH-functionalized CNT−NiO electrode (Figure S3c, Supporting Information), a coating of proteins appears on the electrode surface. The dotted line indicates the separation of CNT−NiO electrode before and after proteins immobilization. The pore structure of CNT−NiO electrode is uniformly filled by BSA and AAB molecules due to strong covalent interactions between them.

The high-resolution TEM image (Figure 3a) shows that the shape of NiO is elongated and is uniformly distributed. It appears that some of the nanoparticles are spherical. The size of these NiO nanoparticles is estimated to be <90 nm. The highly crystalline nature of nanostructured NiO exhibits two dominant (111) and (200) planes with lattice spacing of 0.24 and 0.2 nm, respectively (Figure 3b). The micron size of CNTs with diameter <100 nm can be seen in Figure3c. The higher resolution image of CNTs, shows its inner core diameter and outer diameter (Figure 3d) as 5 and 29 nm, respectively. It can be clearly seen that the CNTs are multiwalled having 32 walls. It appears that elongated NiO nanoparticles are occupied on the core of CNTs (Figure 3e). Figure 3f exhibits that the NiO nanoparticles are attached on the edges of CNTs on the electrode surface.

3.5. Chronocoulomerty Studies. To measure the electrode surface areas, we carried out studies relating to diffusion coefficients, charges with respect to time, the mechanisms, and rate constants of chemical reactions coupled to electron transfer reactions, the chronocoulometry (CC) for various electrodes at the same step potential (1.0 V) in PBS containing ferro/ferri cyanide mediator, as shown in Figure 4i. Typical CC plots (charge-time) for CNT−NiO/ITO electrode and BSA−AAB/CNT−NiO/ITO bioelectrode (Figure 4ii) indicate charge-time dependence for linear diffusion control. It has been observed that the BSA−AAB/CNT−NiO immunoelectrode shows a fewer charge each time as compared to that of CNT−NiO/ITO electrode. The analysis of the chronocoulometric data is based on the Anson equation (eq 1) which defines the charge-time dependence for linear diffusion control:

$$Q = 2nFACD^{1/2}\pi^{1/2}t^{1/2} \quad (1)$$

where, Q represents the charge (coulombs). A plot of Q vs $t^{1/2}$ referred to as the Anson plot, where the slope (a) can be determined by the following:

$$a = 2nAFCD^{1/2}/\pi^{1/2} \quad (2)$$

where n and A represent the number of electrons transferred and the real electrochemical surface area of the electrode (cm^2), respectively. F is the Faraday constant (96 485 coulombs/mol). The concentration of the mediator is denoted by C, and the diffusion coefficient of the mediator (cm^2/s) and time (s) are denoted by D and t, respectively. Therefore, the real electrochemical surface area of the electrode (A_{ec}) can be calculated from the slope in eq 3, provided the other four parameters (n, F, C, and D) are known.

$$A = a/(2nFCD^{1/2}/\pi^{1/2}) \quad (3)$$

The values of diffusion coefficient (D) of the mediator for the CNT−NiO/ITO electrode and BSA−AAB/CNT−NiO/ITO bioelectrode are found to be 6.29×10^{-9} and 2.82×10^{-9} cm^2/s. The electrochemical active surface area (A_{ec}) is found to be as 1.9×10^{-2} and 2.0×10^{-2} cm^2 for the CNT−NiO/ITO electrode and BSA−AAB/CNT−NiO/ITO bioelectrode, respectively. Fragkou et al. have reported the magnitude of electrochemical surface area as 0.08 cm^2 for screen printed carbon electrode (bulk electrode).[33] Fotouhi et al. have estimated the electrochemical surface for CNT-carbon paste

DOI: 10.1021/am509002h
ACS Appl. Mater. Interfaces XXXX, XXX, XXX−XXX

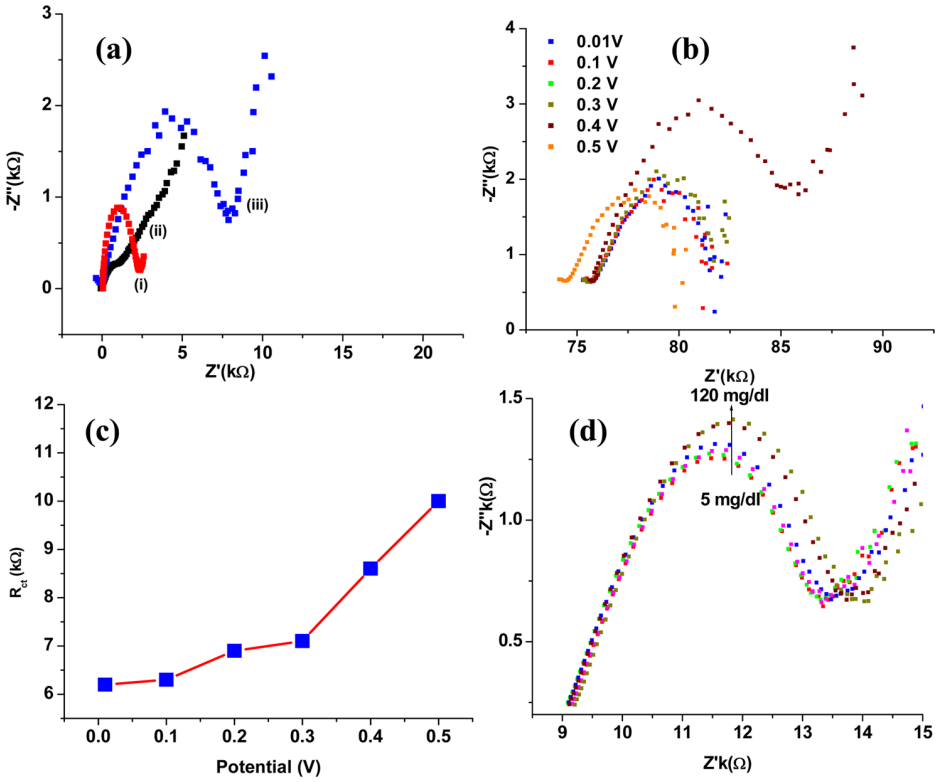

Figure 5. (a) The EIS spectra of the proposed LOC before and after BSA−AAB immobilization, (b) potential studies of the *i*LOC using EIS measurements, (c) plot between charge transfer resistance (R_{ct}) and potential, (d) EIS response of the *i*LOC (BSA−AAB/CNT−NiO) as a function of LDL concentration.

electrode as 0.9 cm^2.[34] Thus, these results reveal a reasonable agreement with those reported in literature for nanostructures. Figure S4i (Supporting Information) shows potential-dependent chronocoulometric response recorded for the BSA−AAB/CNT−NiO/ITO bioelectrode at different potentials (1.0−5.0 V). It has been found that the observed charge-time response increases with increasing potential. Again, we have recorded CC curves at different flow rates (0.01−15 μL/min), as shown in Figure S4ii (Supporting Information). The Q vs $t^{1/2}$ plot for different flow rates (Figure S4iii, Supporting Information) and slope of chronocoulometric curves vs flow rates are shown in the inset of Figure S4iii (Supporting Information). At a flow rate of 1.0 μL/min, the slope value is found to decrease, after which it increases to saturated value perhaps due to increased fluid velocity.[35]

3.6. Electrochemical Impedance Spectroscopy (EIS) Studies. To investigate the nature of antigen−antibody interaction, we conducted the impedance analysis by applying a small sinusoidal AC signal as a function of frequency (0.01−10^5 Hz) at fixed bias potential. In the EIS measurements, the equivalent circuit model consists of the electrolyte (R_s), in series with the capacitance of the dielectric layer (C_{dl}), the charge-transfer resistance (R_{ct}), and the Warburg impedance (Z_w). In the EIS measurements (Figure 5a), the R_{ct} value of nNiO/ITO electrode (i) is found to be 2.3kΩ, which is higher compared to that of the CNT−NiO electrode (2.4 kΩ). This is due to incorporation of CNTs in the nNiO matrix, wherein CNTs play a significant role toward the improved electrochemical conductivity for redox conversation. At the electrode surface, the CNT−NiO nanocomposite acts as a mediator for electron transfer due to the decreased electron tunneling distance from the redox probe $[Fe(CN)_6]^{3-/4-}$ in bulk solution to electrode resulting in decreased R_{ct}. The C_{PE} value of CNT−NiO/ITO is found to be higher (10.0 μF) compared to that of the bioelectrode (4.6 μF) due to the BSA−AAB incorporation onto CNT−NiO/ITO surface. After the BSA−AAB immobilization, R_{ct} value of the CNT−NiO/ITO electrode (iii) increases to 11.2 kΩ. This is attributed to the covalent interaction of proteins with the CNT−NiO molecules, which in turn impedes the ions transfer from bulk solution to electrode. The insulating characteristics of antibody and BSA on CNT−NiO/ITO transducer surface perhaps contribute toward the blocking of charge transfer through the diffusion layer. Thus, the charge transfer resistance after proteins immobilization is increased drastically. The results of cyclic voltammetry (CV) are shown in Figure S5 (Supporting Information). In CV curves, the electrochemical current for CNT−NiO electrode is found to be higher than that of nNiO electrode. CNTs provide electrochemical conduction paths for electrons generated during the redox processes resulting in enhanced electrochemical current.

The kinetic parameters such as the heterogeneous electron transfer rate constant (k_0) and the time constant (τ) of the *i*LOC have been evaluated to investigate the interfacial interactions of biomolecules at electrode/analyte interface. The k_0 and τ of the CNT−NiO/ITO electrode have been calculated before and after the proteins immobilization using the relations, $k_0 = RT/n^2F^2AR_{ct}C$ and $\tau = R_{ct}C_{dl} = 1/2\pi f_{max}$, respectively, where T is the temperature, R is the gas constant, n is the electron transfer constant of the redox couple, F is Faraday constant, A is the effective area of the electrode, and C is the concentration of the redox couple in the bulk solution.

DOI: 10.1021/am509002h
ACS Appl. Mater. Interfaces XXXX, XXX, XXX−XXX

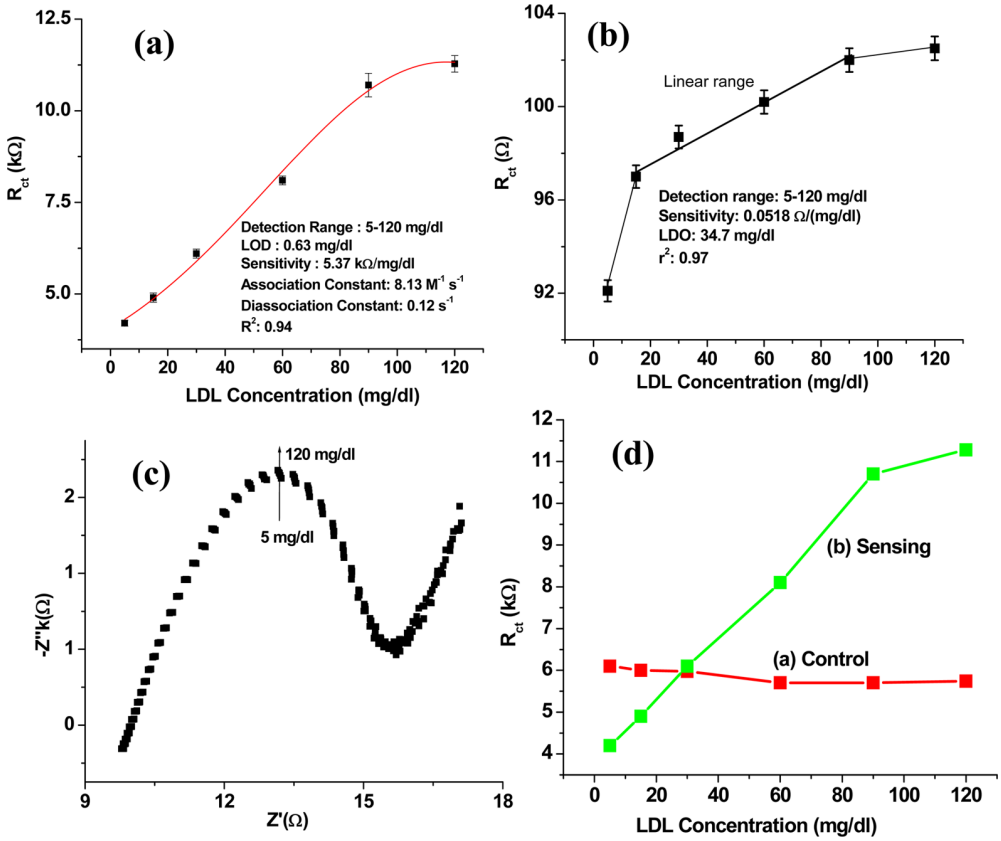

Figure 6. (a) Linear plot between the charge transfer resistance (R_{ct}) and LDL concentration of the BSA−AAB/CNT−NiO immunosensor, (b) sensor calibration plot for BSA−AAB/nNiO-based immunosensor, (c) EIS response of the *i*LOC by varying LDL concentration without BSA−AAB immobilization (control studies), and (d) comparison plot of LDL sensing and control experiment using CNT−NiO-based immunoelectrode.

The values of k_0 are 1.4×10^{-8} and 23.0×10^{-8} cm/s for the CNT−NiO/ITO electrode and BSA−AAB/CNT−NiO/ITO bioelectrode, respectively. The immobilization of proteins on the CNT−NiO surface leads to sluggish charge transfer rate constant resulting in the generation of low capacitance at the electrode surface. The value of τ after protein immobilization estimated to be as 5.15×10^{-2} is attributed to slow diffusion of the $[Fe(CN)_6]^{3-/4-}$ ions through interface layer compared to that of the unimmobilized CNT−NiO/ITO (2.4×10^{-2}) electrode. The surface coverage (θ) can be calculated using the relation; $\theta = 1 - R_{ct(electrode)}/R_{ct(bioelectrode)}$, where θ is the fraction of the occupied binding sites. The $R_{ct(electrode)}$ and $R_{ct(bioelectrode)}$ are the surface specific charge transfer resistance of CNT−NiO/ITO electrode and BSA−AAB/CNT−NiO/ITO bioelectrode, respectively. The value of θ is estimated to be 0.8, indicating more than 80% surface coverage of the CNT−NiO/ITO electrode by BSA−AAB molecules. Considering 80% surface coverage, the number of molecules per unit area is estimated to be as 1.15×10^{-10} mol/cm^2 or 6.94×10^{13} molecules/cm^2. Figure 5b shows EIS spectra of *i*LOC as a function of potential (0.01−0.5 V). It can be seen that at low potential, the EIS spectra exhibits the low charge transfer resistance. At higher potential such as 0.5 V, the *i*LOC shows a higher value of charge transfer resistance, as shown in Figure 5c. Thus, this potential (0.5 V) has been used to conduct the impedance response analysis.

The impedimetric response of the *i*LOC (BSA−AAB/CNT−NiO/ITO bioelectrode) has been measured as a function of low density lipoprotein (LDL) concentration [5−120 mg/dl] in PBS containing $[Fe(CN)_6]^{3-/4-}$ with incubation time of about 5 min (Figure 5d). The various LDL concentrations have been injected into the inlet of the microchannel by a syringe pump. The BSA molecules block the nonspecific site of AAB/CNT−NiO/ITO immunoelectrode. The variation of R_{ct} or blocking properties of the BSA−AAB/CNT−NiO/ITO bioelectrode occurs due to presence of antigen−antibody interactions at electrode/electrolyte interface. The magnitude of charge transfer resistance (R_{ct}) value increases linearly on addition of LDL concentration (Figure 6a). The presence of the insulating layer of LDL molecules on BSA−AAB/CNT−NiO/ITO bioelectrode surface inhibits diffusion of the redox species to the electrode resulting in increased diameter of EIS response. In addition, negatively charged LDL molecules may block the electron transfer of the $[Fe(CN)_6]^{3-/4-}$ redox probe resulting in increased impedance. The glycine solution (0.2 M, pH 2.4) is treated for about 2 min for regeneration of the *i*LOC. The variation of R_{ct} with LDL concentration (5−120 mg/dl) is given by

$$R_{ct}(\Omega) = -0.66(\text{k}\Omega) + 5.3\ \text{k}\Omega\ \text{mgdl}^{-1} \times \text{LDL concentration} \quad (4)$$

The sensitivity of this *i*LOC is obtained to be as 5.3 kΩ/(mg/dl) with regression coefficient (r^2) as 0.94. It has been found that the impedimetric LOC exhibits improved characteristics such as low detection limit of 0.63 mg/dl (Figure 6a). It may be noted that Ali et al. have utilized protein−conjugated CdS quantum dots for estimation of LDL molecules and found

DOI: 10.1021/am509002h
ACS Appl. Mater. Interfaces XXXX, XXX, XXX−XXX

the sensitivity and detection limit of this biosensor as 98.5 Ω $(mg/dl)^{-1}$ and 16.03 mg/dl, respectively.[19] Thus, integration of this CNT−NiO biomaterial-based *i*LOC device provides improved sensitivity and a low detection limit for LDL detection. This is attributed to covalent functionaliztion of the BSA−AAB with CNT−NiO matrix on transducer surface. The values of association and dissociation constant of this *i*LOC estimated to be as 8.13 M^{-1} s^{-1} and 0.12 s^{-1}, respectively, indicate that LDL molecules have higher affinity toward this protein immobilized CNT−NiO based bioelectrode. Using reduced graphene oxide, association and dissociation constants for LDL have been found to be as 1.66 M^{-1} s^{-1} and 0.6 s^{-1}, respectively.[31] It can be noted that the dissociation constant of this chip is higher as compared to the value reported in literature.[36] The higher value of the association constant reveals that CNT−NiO matrix has a good affinity toward LDL molecules. This may perhaps be due to the nanocomposite formation of CNTs with NiO enabling functionalization of the antibodies for LDL cholesterol detection with superior performance as compared to that based on reduced graphene oxide.[31] The sensing performance using only nNiO has been carried out for detection of LDL molecules (Figure S6, Supporting Information). It has been found that the sensitivity of CNT−NiO-based immunosensor is much higher [5.37 kΩ $(mg/dL)^{-1}$] than that based on nNiO alone [0.0518 Ω $(mg/dL)^{-1}$]. The limit of detection for nNiO-based immunosensor is higher (34.8 mg/dl) than that of CNT−NiO immunosensor (0.63 mg/dL). The lower detection limit of this CNT−NiO smart material for detection of LDL molecules may perhaps be due to available functional groups of CNTs as compared to that of nNiO immunosensor.

A control study of this proposed *i*LOC has been conducted for LDL detection using EIS method (Figure 6c). The EIS measurements have been carried out using CNT−NiO transducer chip. The observed changes in the R_{ct} values in the presence of LDL concentration are not significant as shown in Figure 6d. This may perhaps be due to the lesser affinity of LDL molecules with CNT−NiO electrode. Thus, AAB functionalized CNT−NiO immunoelectrode is highly specific, resulting in the observed changes in the impedance values.

The stability of this biochip has been evaluated for 100 days. This chip shows an excellent stability of up to 60 days with 95% response of R_{ct} value, after which the response decreases to 78%. The BSA−AAB/CNT−NiO immunoelectrode is stored at 3 °C when not in use. The reproducibility of the working electrode has been investigated under similar conditions. The changes in impedance (R_{ct}) values for electrodes used in the chip are negligible, as indicated by the relative standard deviation (RSD) of 3.44%. To determine selectivity of the *i*LOC for LDL (90 mg/dl) detection, we performed EIS studies by incorporating other analytes including triglyceride (150 mg/dl), free cholesterol (150 mg/dl), and total cholesterol (150 mg/dl). We have observed a low RSD of 4.3%, indicating negligible interference with other analytes, which in turn indicates that this biochip exhibits good selectivity and stability.

4. CONCLUSIONS

An impedimetric biochip has been fabricated using functionalized CNT−NiO for LDL detection. The covalent immobilization of BSA−AAB on CNT−NiO-based LOC surface has been confirmed by XPS and FT-IR studies. The XPS studies reveal that 4.5% of O−C═O groups present in the CNT−NiO electrode are utilized to bind with amine groups of BSA−AAB molecules. This covalent immobilization of specific protein molecules results in higher sensitivity and a low detection limit for LDL detection. We have evaluated the binding kinetics of antigen−antibody interaction in the sensor surface. In addition, this LOC is found to be highly selective, has a good stability and a wide detection range of 5−120 mg/dl within the physiological range of LDL. The cytotoxicity studies of CNTs, NiO, and CNT−NiO composite have been performed in the presence of human lung epithelial cancer cells using MTT assay. The electron microscopic studies of the CNT−NiO composite in this LOC shows integration of NiO nanoparticles with COOH-functionalized CNTs. The cytotoxicity test indicates that a CNT−NiO composite-based biochip is a better and safer choice for this application. The CNT−NiO composite provides a biocompatible and favorable environment due to high surface-to-volume ratio resulting in enhanced loading capacity of AAB. The application of CNT−NiO composite not only improves the electrochemical impedance characteristics for LDL detection but results in enhanced loading capacity of proteins. The high sensitivity combined with specificity of LDL-AAB binding toward LDL detection using CNT−NiO is an interesting platform that can be used to detect other biomolecules. This *i*LOC requires a minute amount of sample, indicating that this miniaturized compact device has high potential for application as point-of-care diagnostics.

■ ASSOCIATED CONTENT

Supporting Information

Photolithographic process for fabrication of patterned ITO electrode, FT-IR studies, SEM studies, electrochemical studies (chronocoulometric, cyclic voltammetry, and impedance), and a Table containing results of XPS measurements. This material is available free of charge via the Internet at http://pubs.acs.org.

■ AUTHOR INFORMATION

Corresponding Author

*E-mail: bansi.malhotra@gmail.com. Tel.: 91 11 27871043, ext. 1609. Lab Tel.: 91 11 27294668. Fax: 91-11-27871023.

Notes

The authors declare no competing financial interest.

■ ACKNOWLEDGMENTS

We thank Director NPL, New Delhi, India, for the facilities. M.A.A. is thankful to CSIR, India, for the award of Senior Research Fellowships. The financial support received from Department of Science and Technology, India (Grant No. DST/TSG/ME/2008/18), and Indian Council of Medical Research, India (Grant No. ICMR/5/3/8/91/GM/2010-RHN), is gratefully acknowledged.

■ REFERENCES

(1) Yang, W.; Ratinac, K. R.; Ringer, S. P.; Thordarson, P.; Gooding, J. J.; Braet, F. Carbon Nanomaterials in Biosensors: Should You Use Nanotubes or Graphene? *Angew. Chem., Int. Ed.* **2010**, *49*, 2114−2138.

(2) Medina-Sánchez, M.; Miserere, S.; Merkoçi, A. Nanomaterials and Lab-on-a-Chip Technologies. *Lab Chip* **2012**, *12*, 1932−1943.

(3) Wang, Y.-F.; Liu, G.-Y.; Sun, L.-D.; Xiao, J.-W.; Zhou, J.-C.; Yan, C.-H. Nd^{3+}-Sensitized Upconversion Nanophosphors: Efficient in Vivo Bioimaging Probes with Minimized Heating Effect. *ACS Nano* **2013**, *7*, 7200−7206.

(4) Crevillén, A. G.; Pumera, M.; González, M. C.; Escarpa, A. Towards Lab-on-a-Chip Approaches in Real Analytical Domains based

DOI: 10.1021/am509002h
ACS Appl. Mater. Interfaces XXXX, XXX, XXX−XXX

on Microfluidic Chips/Electrochemical Multi-Walled Carbon Nanotube Platforms. *Lab Chip* **2009**, *9*, 346−353.
(5) Craighead, H. Future Lab-on-a-Chip Technologies for Interrogating Individual Molecules. *Nature* **2006**, *442*, 387−393.
(6) Misewich, J.; Martel, R.; Avouris, P.; Tsang, J.; Heinze, S.; Tersoff, J. Electrically Induced Optical Emission from a Carbon Nanotube FET. *Science* **2003**, *300*, 783−786.
(7) Sharf, T.; Kevek, J. W.; DeBorde, T.; Wardini, J. L.; Minot, E. D. Origins of Charge Noise in Carbon Nanotube Field-Effect Transistor Biosensors. *Nano Lett.* **2012**, *12*, 6380−6384.
(8) Choi, J. H.; Nguyen, F. T.; Barone, P. W.; Heller, D. A.; Moll, A. E.; Patel, D.; Boppart, S. A.; Strano, M. S. Multimodal Biomedical Imaging with Asymmetric Single-Walled Carbon Nanotube/Iron Oxide Nanoparticle Complexes. *Nano Lett.* **2007**, *7*, 861−867.
(9) Napier, M. E.; Hull, D. O.; Thorp, H. H. Electrocatalytic Oxidation of DNA-Wrapped Carbon Nanotubes. *J. Am. Chem. Soc.* **2005**, *127*, 11952−11953.
(10) Lin, Y.; Taylor, S.; Li, H.; Fernando, K. S.; Qu, L.; Wang, W.; Gu, L.; Zhou, B.; Sun, Y.-P. Advances toward Bioapplications of Carbon Nanotubes. *J. Mater. Chem.* **2004**, *14*, 527−541.
(11) Periasamy, A. P.; Yang, S.; Chen, S.-M. Preparation and Characterization of Bismuth Oxide Nanoparticles-Multiwalled Carbon Nanotube Composite for the Development of Horseradish Peroxidase based H_2O_2 Biosensor. *Talanta* **2011**, *87*, 15−23.
(12) Ali, M. A.; Srivastava, S.; Solanki, P. R.; Reddy, V.; Agrawal, V. V.; Kim, C.; John, R.; Malhotra, B. D. Highly Efficient Bienzyme Functionalized Nanocomposite-based Microfluidics Biosensor Platform for Biomedical Application. *Sci. Rep.* **2013**, *3*, 2661.
(13) Salimi, A.; Sharifi, E.; Noorbakhsh, A.; Soltanian, S. Immobilization of Glucose Oxidase on Electrodeposited Nickel Oxide Nanoparticles: Direct Electron Transfer and Electrocatalytic Activity. *Biosens. Bioelectron.* **2007**, *22*, 3146−3153.
(14) Lewis, J. A. Colloidal Processing of Ceramics. *J. Am. Ceram. Soc.* **2000**, *83*, 2341−2359.
(15) Daw, R.; Finkelstein, J. Insight: Lab on a Chip. *Nature* **2006**, *442*, 367−418.
(16) Stone, H. A.; Stroock, A. D.; Ajdari, A. Engineering Flows in Small Devices: Microfluidics toward a Lab-on-a-Chip. *Annu. Rev. Fluid Mech.* **2004**, *36*, 381−411.
(17) Ruan, C.; Yang, L.; Li, Y. Immunobiosensor Chips for Detection of *Escherichia coli* O157:H7 using Electrochemical Impedance Spectroscopy. *Anal. Chem.* **2002**, *74*, 4814−4820.
(18) Carlborg, C. F.; Gylfason, K. B.; Kaźmierczak, A.; Dortu, F.; Polo, M. B.; Catala, A. M.; Kresbach, G.; Sohlström, H.; Moh, T.; Vivien, L. A Packaged Optical Slot-Waveguide Ring Resonator Sensor Array for Multiplex Label-free Assays in Labs-on-Chips. *Lab Chip* **2010**, *10*, 281−290.
(19) Ali, M. A.; Srivastava, S.; Pandey, M. K.; Agrawal, V. V.; John, R.; Malhotra, B. D. Protein−Conjugated Quantum Dots Interface: Binding Kinetics and Label-Free Lipid Detection. *Anal. Chem.* **2014**, *86*, 1710−1718.
(20) Matharu, Z.; Bandodkar, A. J.; Sumana, G.; Solanki, P. R.; Ekanayake, E. M.; Kaneto, K.; Gupta, V.; Malhotra, B. Low Density Lipoprotein Detection based on Antibody Immobilized Self-Assembled Monolayer: Investigations of Kinetic and Thermodynamic Properties. *J. Phys. Chem. B* **2009**, *113*, 14405−14412.
(21) Lacerda, L.; Bianco, A.; Prato, M.; Kostarelos, K. Carbon Nanotubes as Nanomedicines: from Toxicology to Pharmacology. *Adv. Drug Delivery Rev.* **2006**, *58*, 1460−1470.
(22) Kostarelos, K. The Long and Short of Carbon Nanotube Toxicity. *Nat. Biotechnol.* **2008**, *26*, 774−776.
(23) Al Faraj, A.; Cieslar, K.; Lacroix, G.; Gaillard, S.; Canet-Soulas, E.; Crémillieux, Y. In Vivo Imaging of Carbon Nanotube Biodistribution using Magnetic Resonance Imaging. *Nano Lett.* **2009**, *9*, 1023−1027.
(24) Jia, G.; Wang, H.; Yan, L.; Wang, X.; Pei, R.; Yan, T.; Zhao, Y.; Guo, X. Cytotoxicity of Carbon Nanomaterials: Single-Wall Nanotube, Multi-Wall Nanotube, and Fullerene. *Environ. Sci. Technol.* **2005**, *39*, 1378−1383.
(25) Magrez, A.; Kasas, S.; Salicio, V.; Pasquier, N.; Seo, J. W.; Celio, M.; Catsicas, S.; Schwaller, B.; Forró, L. Cellular Toxicity of Carbon-based Nanomaterials. *Nano Lett.* **2006**, *6*, 1121−1125.
(26) Zhang, Y.; Ali, S. F.; Dervishi, E.; Xu, Y.; Li, Z.; Casciano, D.; Biris, A. S. Cytotoxicity Effects of Graphene and Single-Wall Carbon Nanotubes in Neural Phaeochromocytoma-Derived PC12 Cells. *ACS Nano* **2010**, *4*, 3181−3186.
(27) Ryoo, S.-R.; Kim, Y.-K.; Kim, M.-H.; Min, D.-H. Behaviors of NIH-3T3 Fibroblasts on Graphene/Carbon Nanotubes: Proliferation, Focal Adhesion, and Gene Transfection Studies. *ACS Nano* **2010**, *4*, 6587−6598.
(28) Davoren, M.; Herzog, E.; Casey, A.; Cottineau, B.; Chambers, G.; Byrne, H. J.; Lyng, F. M. In Vitro Toxicity Evaluation of Single Walled Carbon Nanotubes on Human A549 Lung Cells. *Toxicol. In Vitro* **2007**, *21*, 438−448.
(29) Mooney, E.; Dockery, P.; Greiser, U.; Murphy, M.; Barron, V. Carbon Nanotubes and Mesenchymal Stem Cells: Biocompatibility, Proliferation and Differentiation. *Nano Lett.* **2008**, *8*, 2137−2143.
(30) Lopes-Virella, M. F.; Stone, P.; Ellis, S.; Colwell, J. Cholesterol Determination in High-Density Lipoproteins Separated by Three Different Methods. *Clin. Chem.* **1977**, *23*, 882−884.
(31) Ali, M. A.; Kamil Reza, K.; Srivastava, S.; Agrawal, V. V.; John, R.; Malhotra, B. D. Lipid−Lipid Interactions in Aminated Reduced Graphene Oxide Interface for Biosensing Application. *Langmuir* **2014**, *30*, 4192−4201.
(32) Ali, M. A.; Solanki, P. R.; Patel, M. K.; Dhayani, H.; Agrawal, V. V.; John, R.; Malhotra, B. D. A Highly Efficient Microfluidic Nano Biochip based on Nanostructured Nickel Oxide. *Nanoscale* **2013**, *5*, 2883−2891.
(33) Fragkou, V.; Ge, Y.; Steiner, G.; Freeman, D.; Bartetzko, N.; Turner, A. P. Determination of the Real Surface Area of a Screen-Printed Electrode by Chronocoulometry. *Int. J. Electrochem. Sci.* **2012**, *7*, 6214−6220.
(34) Fotouhi, L.; Fatollahzadeh, M.; Heravi, M. M. Electrochemical Behavior and Voltammetric Determination of Sulfaguanidine at a Glassy Carbon Electrode Modified with a Multi-Walled Carbon Nanotube. *Int. J. Electrochem. Sci.* **2012**, *7*, 3919−3928.
(35) Mulchandani, P.; Chen, W.; Mulchandani, A. Flow Injection Amperometric Enzyme Biosensor for Direct Determination of Organophosphate Nerve Agents. *Environ. Sci. Technol.* **2001**, *35*, 2562−2565.
(36) Matharu, Z.; Arya, S. K.; Sumana, G.; Gupta, V.; Malhotra, B. Self-Assembled Monolayer for Low Density Lipoprotein Detection. *J. Mol. Recognit.* **2008**, *21*, 419−424.

DOI: 10.1021/am509002h
ACS Appl. Mater. Interfaces XXXX, XXX, XXX−XXX

ISBN 978-93-5156-328-0
International Conference of Advance Research and Innovation (ICARI-2015)

Quad-Rotor Unmanned Arial Vehicle – A Review

Rajiv Chaudhary, Ranganath M. S., R. C. Singh, Arjav Desai, Aakash Chaudhary, Mayank Garg
Department of Mechanical Engineering, Delhi Technological University, Delhi, India

Article Info

Article history:
Received 4 January 2015
Received in revised form
10 January 2015
Accepted 20 January 2015
Available online 31 January 2015

Keywords

Modeling,
Quad-Rotor,
Unmanned Arial Vehicle

Abstract

A review has been performed on modelling and control of Quad-Rotor unmanned arial vehicles (UAVs) based on earlier published works.This research develops a thorough understanding of the system's behaviour, whereas it can be used as case study, for experimenting with control techniques and other abilities developed. The main objective is to arrive at a complete and as realistic as possible conclusion, that too without unnecessary complexity, by using simulation model in Mat lab/Simulink, allowing further immediate use of the quad rotor in future studies.

1. Introduction

In the recent years, especially due to advances in Micro-Electromechanical Systems (MEMS), electrical energy accumulators, actuators and smaller integrated micro-controlled boards, the number of studies are growing in UAVs such as the quad-rotor and related autonomous aerial robots, not only by universities and research institutions for private civilian applications but also for military purposes. It is mainly due to the inherent characteristics of such aircraft, namely high maneuvering at low translational speeds and in small volumes while being able to carry significant payload, thus making them especially adequate for aerial surveillance and monitoring tasks.

The main advantage of rotating-wing over fixed-wing aircraft is the ability of hovering and omni-directional movement. A drawback is, however, relatively higher power consumption during the flight. Even inside the rotating-wing aircraft classification, a quad-rotor is much simpler and easier to build in comparison to a classical helicopter, since the rotors' rotational axis is fixed and there are no moving parts, like aerodynamic control surfaces. Nevertheless, the rotational speed of each rotor needs to be independently controlled in order to achieve the control goals of such a highly unstable open-loop system, which makes it a challenging control engineering problem.

2. Literature Review

An extensive literature review has been done for this study. Bouabdallah [2004a] presented a system model with DC motors and by using the Lyapunov Function's non-linear control technique approach for stabilizing the aircraft's orientation (Euler angles), compare the real system's behaviour with a respective simulation. Bouabdallah et al. [2004b] extended their work on the OS4 project as they compared classical PD and PID controllers for orientation stabilization with modern LQ adaptive optimal control, despite realizing that the latter one yielded only average results, due to modeling imperfections. Stepaniak [2008] made a detailed identification work of his built system and model derivation, besides discussing hardware implementation aspects. Despite not focusing on the control loops design, whereby classical control theory was used, his work turned out to be one of the main references hereby used.

Tayebi and McGilvray [2006], on the other hand, performed a thorough and advanced study on control techniques for attitude stabilization of a quadrotor. It was used quaternions for attitude representation, Lyapunov stability's criterion and a PD2 feedback structure, with which a model-independent PD controller was compared, achieving with both configurations global asymptotic stability and disturbance rejection in similar fashion. Their experimental results were obtained from a modified version of the Draganflyer III aircraft. Kim [2007] made an interesting performance comparison among four control techniques: LQR, LQR with gain scheduling, feedback linearization and sliding mode control. They experimentally verified that LQR with gain scheduling presented more robustness in light of modeling uncertainties whereas for an accurately modeled system a better performance was achieved with the sliding mode approach. A meticulous study of usually otherwise disregarded effects such as blade flapping and propeller modeling was done by Pounds [2004]. In fact, the theoretical model for the propeller thrust and torque discussed in their paper was employed in this present work. Later on, Pounds [2006] gave continuity to their work on the X-4 flyer Mark II quad-rotor implementation (Fig. 1.1a) by designing a discrete-time PID control law to their model including the very fast blade flapping dynamics. The closed-loop behavior, though, turned out to be poor at higher rotor angular speeds (! > 450 rad/s), approaching an unstable behavior, which was attributed to high-frequency noise from the rotors interfering with the accelerometer readings.

Hamel [2002] employed the non-linear Lyapunov functions and the back stepping approach allied to quaternion attitude representation for designing non-linear attitude stabilization controllers. Although presenting a minute theoretical study and proof-based mathematical derivations, their proposal unfortunately was not accompanied by experimental results. Castillo [2004] proposed a real-time non-linear nested saturation control scheme based on Lyapunov's stability criterion, where each system state is sequentially stabilized following a priority

Corresponding Author,
E-mail address: rajiv_ch@rediffmail.com
All rights reserved: http://www.ijari.org

rule, hence allowing a wider stability region and therefore more aggressive manoeuvring while maintaining good disturbance rejection capability. Later on, Castillo et al. [2005] compared the performance of their non-linear control with a linear one such as LQR, which presents stability issues when the system is taken far away from its operation point used for the controller design. Martinez [2007] performed an extensive identification experimental study on a commercial Dragonfly XProquadrotor, including blade flapping and torsion investigations besides windtunnel tests to identify the aircraft's aerodynamic characteristics. Since his work didn't extend to the design of control loops, its use for this project was limited as another reference for cross-checking the basics aircraft modeling hereby dealt with.

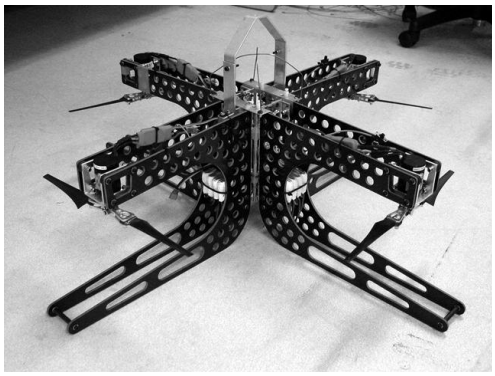

Fig: 1. STARMAC I

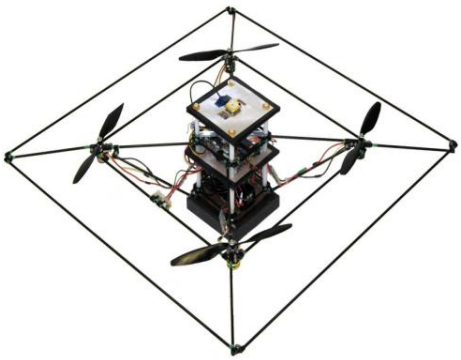

Fig: 2. X-4 Flyer Mark II

Voos [2009] applied feedback linearization in a nested control loop structure where theinner loop contains the attitude dynamics and the outer, the position one. Their experimental results were obtained also with a Dragon flyer real model. However, the dynamics of the DC motors used in the rotors was not considered in their work. *Hoffmann [2007]* focused their study on the aerodynamic effects on the quad-rotor's airframe when operating significantly far from the hover regime, at higher translational speeds, while also considering the very fast dynamics of blade flapping. Their theoretical results were experimented on the STARMAC II vehicle. *Rong Xu and ¨Umit ¨Ozg¨uner [2006]* presented a new design method for the flight control of an autonomous quadrotor helicopter based on sliding mode control. Due to the under-actuated property of a quadrotor helicopter, the controller can make the helicopter move three positions (x, y, z) and the yaw angle to their desired values and stabilize the pitch and roll angles. A sliding mode control is proposed to stabilize a class of cascaded under- actuated systems. The global stability analysis of the closed-loop system is presented. The advantage of sliding mode control is its insensitivity to the model errors, parametric uncertainties and other disturbances. Simulations show that the control law robustly stabilizes a quadrotor. A quadrotor is an under-actuated system with four independent inputs and six coordinate outputs. In this paper we present a new approach using sliding mode control to stabilize a quadrotor helicopter. A quadrotor system can be divided into a fully-actuated subsystem and an under-actuated subsystem.

Eduardo Rondon, Luis-Rodolfo Garcia-Carrillo and Isabelle Fantoni (2010) addressed the hover flight and speed regulation of a quad-rotor rotorcraft to perform autonomous navigation. For this purpose, a vision system was developed which estimates the altitude, the lateral position and the forward speed of the engine during flights. The visual information allows the construction of control strategies for different kinds of flying modes: hover flight, forward flight at constant speed. A hierarchical control strategy is developed and implemented. The local stabilization of the vehicle is proven. Experimental autonomous flight was successfully achieved which validates the visual algorithm and the control law. Image-based navigation arises as an attractive solution, small low cost cameras attached to the vehicle provide detailed information about the UAV motion and the environment structure. Due to this interaction between the sensor with its surroundings, new techniques can be developed permitting the vehicle to navigate within clustered environments. In recent years, vision has become an ”ideally” to UAVs. The overall system consists of the rotorcraft, the down- ward looking camera attached to the vehicle, and the road model. The road zone is computed by a combination of line detection and color segmentation processes. Once the road information has been extracted, position and altitude estimates can be built. We consider the camera moving with respect to a rigid scene for pseudo speeds determination. *Samir Bouabdallah and Roland Siegwart* in their research came up with the conclusion that varying the rotor speeds, one can change the lift force and create motion. Thus, increasing or decreasing the four propeller’s speeds together generates vertical motion. Changing the 2 and 4 propeller’s speed conversely produces roll rotation coupled with lateral motion. Pitch rotation and the corresponding lateral motion result from 1 and 3 propeller’s speed conversely modified as described in Fig. 1. Yaw rotation is more subtle, as it results from the difference in the counter-torque between each pair of propellers. In spite of the four actuators, the Quadrotor is still an underactuated and dynamically unstable system. It is well known that the VTOL systems are dynamically unstable and thus very hard to control the system natural response to an initial roll (or pitch) angular speed excitation. The system gains mechanical energy, starts to oscillate and tends to amplify rapidly these oscillations.

The research done by *Robbert van Ginkel, Iris Meerman and Timo Mulder [2005]* describes an autonomous landing procedure for the Parrot AR.Drone 2.0 quad- copter. An autonomous landing is defined as a landing with correct orientation on a predefined target marker without human

intervention. The landing procedure should be initiated after first recognition of the specified landing location and until then manual control is assumed. The landing procedure can also be broken down into three steps: moving into horizontal position, orienting the direction the drone is facing and decreasing altitude while maintaining orientation and location until the surface has been reached. The first step in the process is that of colour segmentation. The target is red, therefore any object in the photo that is not red can be ex- cluded. To find the target in the image, contours are gen- erated of all red areas in the image. After all the contours in the image have been found, the contour that best matches the shape of the target marker is selected. After the image has been processed the actua- tion module, which is implemented as a movement function in our 'landing Platform' plugin, processes its results and generates the according movement.The review methods and technologies that have been applied in aerial robotics. The paper presents several unmanned aerial vehicle platforms. Then summarizes different control techniques including both control architectures and control methods. Furthermore, computer vision techniques for aerial robotics are briefly considered. Finally, the paper presents systems and projects involving multiple autonomous aerial and ground systems. In the last decades many autonomous and tele-operated vehicles for field robotics applications have been developed, including wheeled, tracked and legged vehicles. However, in many cases, ground vehicles have significant inherent limitations to access to the desired locations due to the characteristics of the terrain and the presence of obstacles that cannot be avoided. In these cases aerial vehicles is the natural way to approach the objective to get information or even to perform some actions such as the deployment of instrumentation. Then, aerial robotics seems a useful approach to perform tasks such as data and image acquisition of targets and affected areas, localization of targets, tracking, map building and others. Unmanned aerial vehicles (UAV) have been used for military applications but also are useful for many civilian applications such as terrain and utilities inspection, disaster monitoring, environmental surveillance, search and rescue, law enforcement, aerial mapping, traffic surveillance, and cinematography. In the last years UAVs improved their autonomy both in energy and information processing. However, the development of autonomous aerial robotic vehicles involves many problems related to limited payload, safety requirements, flight endurance and others. This paper reviews some significant developments in aerial robotics.

Knowledge Based Control Methods: As far as the research in control methods is concerned different approaches can be used. Thus, fuzzy logic has been applied to control the Yamaha's helicopter at the Tokyo Institute of Technology, which demonstrated autonomous capabilities and also person–machine interfaces including voice command (Sugeno, Griffin, & Bastian, 1993). Fuzzy logic with rules generated by the observation of ahuman pilot and consultation with helicopter experts is the approach used in Cavalcante and coworkers (1995). In Montgomery, Fagg, and Bekey (1995) the behaviours of the control architecture proposed in the USC architecture are implemented as PD control loops with gains tuned by trial and error. In Montgomery and Bekey (1998), the ''teaching by showing'' approach is presented. In this work the controller is generated by using training data gathered while a human teacher controls a system until the synthesized controller can also control the system to meet predefined performance criteria. In Buskey, Wyeth, and Roberts (2001) learning is based on the direct mapping of sensor inputs to actuator control via an artificial neural network. Then, the neural network controller was used for the helicopter hovering. The analysis of the pilot's execution of aggressive manoeuvres from flight test data is the base of the method presented in Gavrilets, Frazzoli, Mettler, Piedmonte, and Feron (2001) to develop a full non-linear dynamic model of a helicopter. This model will be used in the design of new control systems for autonomous helicopters.

Learning Based Control Methods: On the other hand, several methods have been applied for model-based control of UAVs. Modelling the UAV dynamics is a main issue. The full model of a helicopter involving the flexibility of the rotors and fuselage and the dynamics of the actuators and the combustion engine is very complex. Then, in most cases, the helicopter is considered as a rigid body with inputs forces and torques applied to the centre of mass and outputs the position and linear velocities of the centre of mass, as well as the rotation angles and angular velocities. Furthermore, the relations between the control inputs of the helicopter and the above mentioned forces and torques should be considered in the model. In general, these relations involve the consideration of the aerodynamics of the fuselage and the effect of stabilizers. However, at low speeds these effects can be ignored (Koo &Sastry, 1998). In Kim and Tilbury (2004) a mathematical model and experimental identification of a model helicopter is presented. The model of the interactions between the stabilizer flybar and the main rotor blade is also included showing its effects in the stability of the model helicopter. The identification of the parameters is performed on a SISO basis using a specially built stands to restrict the motion of the helicopter to one degree of freedom. It should be noted that the identification from input–output data, collected when a human pilot is controlling the vehicle, is difficult because it is not possible to study the individual effect of each control input (the pilot has to apply more than one input to maintain the stability).

Commercially Available Quadrotors: Quadrotor implementations and studies do not limit themselves to the academic environment. Especially in the last decade, several commercially available models have appeared in the market, with a variety of models stretching from mere entertainment up to serious applications. For example, the German company Microdrones GmbH was established in 2005 and since then has been developing such UAVs for tasks such as aerial surveillance by police forces, inspection services of power lines, monitoring of nature protection areas, photogrammetry, and archaeology research, among others. A picture of the quadrotor is illustrated below. Another manufacturer of such aircraft is the Canadian Draganfly Innovations. Their quadrotor models portfolio stretches from the Draganyer X4, with 250 g of payload capacity up to the Draganflyer X8, illustrated in Fig. 1.3 (b), featuring a 8-rotor design, with payload capacity of 1000 g and GPS position hold function. Still another relevant manufacturer of quadrotors, among other products, is the

French company Parrot. Their A R. Drone model, pictures in Fig. 1.3(c) with a surrounding protective frame, is comparable in size to the md4-200 of Microdrone, however it can fly only for approximately 12 minutes, reaching a top speed of 18 km/h. It was designed for entertainment purposes, including video-gaming and augmented reality, and can be remote-controlled by an iPhone remotely through a Wi-Fi network.

(a) md 4- 20

(b) Dragon flyer X8

(c) The AR Drone

Fig: 3. Commercially Available Quad-rotors

3. Conclusion

The review performed on modeling and control of Quad-Rotor unmanned areal vehicles (UAVs) based on earlier published workshas been found useful to arrive at a complete and as realistic as possible conclusion, that too without unnecessary complexity, by using simulation model in Matlab / Simulink, allowing further immediate use of the quadrotor in future studies. The research studies have shown successfully how various components work and interact so that the resulting system is completely autonomous. This research develops a thorough understanding of the system's behaviour, whereas it can be used as case study, for experimenting with control techniques and other abilities developed.

References

[1] S. Bouabdallah, P. Murrieri, R. Siegwart, Design and control of an indoor micro quadrotor. Robotics and Automation, Proceedings. ICRA'04. 2004 IEEE International Conference, 5, 2004a, 4393-4398

[2] S. Bouabdallah, A. Noth, R. Siegwart, PID vs LQ control techniques applied to an indoor micro quadrotor. Technical report, Swiss Federal Institute of Technology, 2004b

[3] P. Castillo, A. Dzul, R. Lozano. Real-Time stabilization and tracking of a Four-Rotor mini rotorcraft. IEEE Transactions on Control Systems Technology, 12(4), 2004, 510-516

[4] P. Castillo, R. Lozano, A. Dzul, Experimental implementation of linearand nonlinear control laws. IEEE Control Systems Magazine, 2005, 11

[5] J. Dvorak, Micro quadrotor, Design, modelling, identi_cation and control. Master's thesis, Czech Technical University in Prague, 2011

[6] T. Hamel, R. Mahony, R. Lozano, J. Ostrowski. Dynamic Modelling and Configuration Stabilization for An X4-Flyer. IFAC 15th Triennial World Congress, 2002, 6

[7] G. M Hoffmann, H. Huang, S. L Waslander, C. J Tomlin, Quadrotor helicopter high dynamics and control: Theory and experiment. Technical report, American Institute of Aeronautics and Astronautics, 2007

[8] T. Kim, K. Stol, V. Kecman. Control of 3 DOF quadrotor model. Robot Motion andControl 2007, 29-38

[9] R. Krishnan, Permanent Magnet Synchronous and Brushless DC Motor Drives. CRC Press, 2010

[10] F. L. Lewis, V. L. Syrmos, Optimal Control. John Wiley & Sons, 1995

ISBN 978-93-5156-328-0
International Conference of Advance Research and Innovation (ICARI-2015)

Sustainability Analysis in Terms Energy and Exergy Evaluation of Two-Stage Vapour Compression Refrigeration System Using Eight Ecofriendly Refrigerants

Kapil Chopra [a], V. Sahni [b], R. S. Mishra [c]
[a] Department of Mechanical Engineering, M V D.V. Katra, Jammu, India
[b] Department of Mechanical Engineering, SLIT Longowal, Punjab, India
[c] Department of Mechanical Engineering, Delhi Technological University, Delhi, India

Article Info

Article history:
Received 3 January 2015
Received in revised form
10 January 2015
Accepted 20 January 2015
Available online 31 January 2015

Keywords

First law Analysis,
Coefficient of Performance,
Irreversibility Minimization,
Exergetic Efficiency,
Entropy Generation,
Second law Analysis,
Vapour Compression Refrigeration System

Abstract

Comparative thermodynamic analysis using first and second law of eight ecofriendly R152a, R600, R600a, R410a, R290, R1234yf, R404a and R134a refrigerants in the two stage vapour compression refrigeration system on the basis of energetic and exergetic performances is presented in this paper. The thermal performance parameters such as entropy generations, first law efficiency in terms of COP, second-law efficiency in terms of exergetic efficiency, sustainability index were investigated at different ambient condition. It is found that that both energy and exergy efficiencies of R134a is 8.97% and 5.38% lower than R152a and R600 respectively. Numerical computation was carried out using ecofriendly refrigerants and It was also observed that the irreversibility was minimal at higher evaporator temperatures while condenser temperature was responsible for highest irreversibility in terms of thermal energy losses in the two stage vapour compression refrigeration system. Sustainability index for R152a (1.96) was highest compared to other ecofriendly refrigerants.

Nomenclature

CFC	chlorofluorocarbon	**Subscripts**	
HCFC	hydrochlorofluorocarbon	Evap	evaporator
Q	rate of heat transfer (kW)	Cond	condenser
W	work (kW)	Amb	ambient conditions
T	temperature (^oC)	WI	water intercooler
s	specific entropy (kJ/kgK)	H	high temperature
h	specific enthalpy(kJ/kg)	L	low temperature
$\dot{S}$	entropy (kJ/s.K)	LP	low pressure
ODP	ozone depletion potential	EV	expansion valve
GWP	global warming potential	Gen	generation
m	mass flow rate (kg/s)	HP	high pressure
η	efficiency (non-dimensional)	FC	flash chamber
		Ex	exergetic

1. Introduction

Refrigeration technology based on the principle of rejection of heat to the surrounding at higher temperature and absorption of heat at low temperature [1].evaporator, expansion valve, condenser and compressor are the main four components of single stage vapour compression system

Corresponding Author,
E-mail address: professor_rsmishra@yahoo.co.in
All rights reserved: http://www.ijari.org

Vapour compression refrigeration systems consume large amount of electricity. This difficulty can be removed by improve the performance parameters of system. Coefficient of performance and exergetic efficiency are main two parameters to calculate the performance of refrigeration systems. Coefficient of performance can be enhanced either by minimizing power consumption of compressor or increasing of refrigeration effect. Refrigeration effect can be increased by adoption of multi-stage throttling .On the other hand power consumption of compressor can be enhanced by incorporation of multi-stage compression and flash chamber. Collective effect of these two factors improves overall performance of vapour compression system.

It is presented that irreversibility in system components take place due to large temperature difference between system and surrounding. In order to improve the system performance Irreversibility should be measured in the cycle because Exergy losses are responsible for degradation of system performance. Coefficient of performance is commonly used to calculate the performance of vapour compression system but COP provides no information regarding thermodynamic losses in the system components. Using exergy analysis one can be quantify the exergy losses in vapour compression refrigeration systems. Exergy losses increase with increasing of temperature difference between systems and surrounding. Exergy is the available or useful energy and loss of energy means loss of exergy in the system. Exergy losses are useful to improve the performance of system and better utilization of energy input given to the system which is beneficial for environmental conditions and economics of energy technologies. Utilization of green energy can be increased by this method.

[2-4] In past decades, refrigerants such as R12, R02, R22 etc. used in vapour compression refrigeration system responsible for increasing of global warming and ozone depletion potential. An international society named Montreal protocol discussed and signed on the refrigerants having higher global warming and ozone depletion potential values for all countries. In order to control the emission of green house gases one more committee was formed named as Kyto protocol [5].After 90's a program was ran to phase out the higher GWP and ODP refrigerants (CFC and HCFC) for the purpose of environmental problems..To replace "old" refrigerants with "new" refrigerants lots of researches has been b lots of researches has been carried out [6-11].Selladurai and Saravanakumar [12] evaluated performance parameters such as COP and exergetic efficiency with R290/R600 hydrocarbon mixture on a domestic refrigerator designed to work with R134a and observed that performance of same system is higher with R290/R600a hydrocarbon mixture compared to R134a. In their analysis condenser, expansion valve and evaporator showing lower exergy destruction compared to compressor. Reddy et al.[13] presented theoretical analysis of R134a, R143a, R152a, R404A, R410A, R502 and R507A in vapour compression refrigeration system and effect on coefficient of performance and second law efficiency with variation of superheating of evaporator outlet, evaporator temperature and degree of sub cooling at condenser outlet, vapour liquid heat exchanger effectiveness and degree of condenser temperature was discussed. They reported that COP and exergetic efficiency significantly affected with change of evaporator and condenser temperatures and also observed that R134a and R407C show highest and lowest performance in all respect. Kumar et al.[14] they carried out energy and exergy analysis of single stage vapour compression refrigeration system using R11 and R12 as working fluids. Evaluation in terms of COP, exergetic efficiency and exergy losses in different components (compressor, evaporator, expansion valve and condenser) was done. Cornelissen [15] proposed that non-renewable energy sources are useful for minimizing the irreversibility of the system for sustainable development of systems. He also observed that emissions of gases put adverse effect on environmental conditions. Nikolaidis and Probert [16] effect of condenser and evaporator temperatures on two-stage vapour compression refrigeration system using R22 was studied and suggested that there is requirement to optimize the condenser and evaporator conditions.

Many researchers carried out researches on different proportion of hydrocarbons as working fluid in vapour compression refrigeration systems. Fatouh and Kafafy [17] suggested replacing R134a with hydrocarbon mixtures such as propane, propane/ isobutene /n-butane mixtures, butane, and various propane mass fractions in domestic refrigerator. Pure butane showed high operating pressures and low coefficient of performance among considered refrigerants. Wongwises et al.[18] did experimental investigation on automotive air-conditioners with isobutene, propane, butane and suggested to replace R134a with these hydrocarbon mixtures. They observed that mixture of propane 50%, butane 40%, and isobutane 10% was best hydrocarbon mixture to replace R134a.Jung et al.[19] , Arcaklioglu [20] and Arcaklioglu et. Al [21] suggested to use of pure hydrocarbon instead of their mixtures due variation in condenser and evaporator temperature during phase changing at constant pressure. These Changes in condenser and evaporator temperature cause for problem in vapour compression refrigeration cycle. Liedenfrost et al. [22] investigated freon as refrigerant on the performance of a refrigeration cycle Through above literature, it was found that energy, exergy and sustainable analysis of single stage vapour compression refrigeration systems have been done. But no literature contributed for energy and exergy analysis of two-stage vapour compression refrigeration system. Present works analyze the system in terms of energy and exergy efficiencies and explain the effect of exergy losses on two-stage vapour compression refrigeration system with hydrocarbons and R134a.

2. Numerical Computations

Some mathematical calculations are required to analyze the two-stage vapour compression refrigeration system based on energy and exergy method. Two stage vapour compression refrigeration system consist of low and high pressure compressor, condenser, evaporator, expansion valves, water-intercooler and flash chamber. Energy and exergy efficiencies are different for different refrigerants for same system. Following assumptions are taken for thermodynamic analysis of the system:

1. Temperature and pressure losses are not considered.
2. All components are running under steady state conditions.
3. Energy and exergy losses due to potential and kinetic energy are neglected.
4. Mechanical efficiencies of low and high pressure compressors are assumed to be 80%.

Two stage vapour compression refrigeration system and its P-H plot shown in Fig 1 and Fig 2 respectively. Exergy, energy and sustainability analysis can be done as follow:

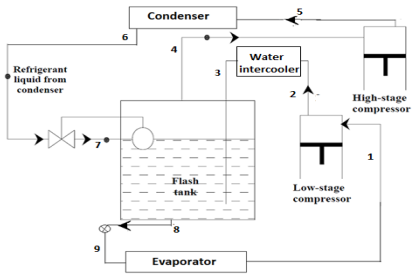

Fig: 1. Schematic Diagram of two-stage Vapour Compression Refrigeration System

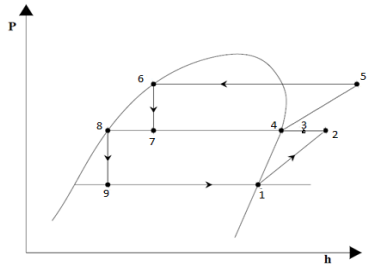

Fig: 2 Pressure Enthalpy Diagram of two-stage Vapour Compression Refrigeration System

ISBN 978-93-5156-328-0

Exergy at any point, $EX = (h - h_{amb}) - T_{amb}(s - s_{amb})$

For high and low temperature compressors

$$(T_{amb}\dot{S}_{gen})_{HP} = W_{HP} + m_{HP}((h_1 - h_2) - T_{amb}(s_1 - s_2))$$

$$(T_{amb}\dot{S}_{gen})_{LP} = W_{LP} + m_{LP}((h_4 - h_5) - T_{amb}(s_4 - s_5))$$

For evaporator

$$(T_{amb}\dot{S}_{gen})_{Evap} = \dot{m}_{LP}((h_9 - h_1) - T_{amb}(s_9 - s_1)) + Q\left(1 - \frac{T_{amb}}{T_L}\right)$$

For condenser

$$(T_{amb}\dot{S}_{gen})_{Cond} = \dot{m}_{HP}((h_5 - h_6) - T_{amb}(s_5 - s_6)) - Q_{Cond}\left(1 - \frac{T_{amb}}{T_H}\right)$$

For expansion valves

$$(T_{amb}\dot{S}_{gen})_{EV} = \dot{m}_{HP}((h_6 - h_7) - T_{amb}(s_6 - s_7)) + \dot{m}_{LP}((h_8 - h_9) - T_{amb}(s_8 - s_9))$$

For water-intercooler

$$(T_{amb}\dot{S}_{gen})_{WI} = \dot{m}_{LP}((h_2 - h_3) - T_{amb}(s_2 - s_3))$$

For flash chamber

$$(T_{amb}\dot{S}_{gen})_{FC} = \dot{m}_{LP}((h_3 - h_4) - T_{amb}(s_3 - s_4)) + (\dot{m}_{HP}h_7 - \dot{m}_{LP}h_8) - T_{amb}(\dot{m}_{HP}s_7 - \dot{m}_{LP}s_8)$$

Exergetic efficiency

$$\eta_{ex} = \frac{Q\left(1 - \frac{T_{amb}}{T_L}\right)}{W_{LP} + W_{HP}}$$

Coefficient of Performance (COP)

$$COP = \frac{\dot{m}_{LP}((h_1 - h_9)}{W_{LP} + W_{HP}}$$

Sustainability index (SI)

$$SI = \frac{1}{1 - \eta_{ex}}$$

Total entropy generation

$$(T_{amb}\dot{S}_{gen})_{TOTAL} = \sum(T_o\dot{S}_{gen})_{HP} + (T_o\dot{S}_{gen})_{LP} + (T_o\dot{S}_{gen})_{Evap} + (T_o\dot{S}_{gen})_{Cond} + (T_o\dot{S}_{gen})_{EV} + (T_o\dot{S}_{gen})_{WI} + (T_o\dot{S}_{gen})_{FC}$$

3. Results and Discussion

The effect of change of evaporator and condenser temperature on performance parameters like coefficient of performance, exergy loss, exergetic efficiency and sustainability index was studied for considered refrigerants by change of coefficient of performance with change in evaporating temperature for considered refrigerants. As cleared from Table.1 (a)-(b) respectively.

Table: 1a. Variation of COP at Different Evaporating Temperature for Different Refrigerants

T_{Evap} (°C)	R152a	R600	R134a	R600a
-50	1.457	1.409	1.337	1.33
-45	1.59	1.54	1.466	1.458
-40	1.74	1.689	1.611	1.603
-35	1.911	1.857	1.775	1.767
-30	2.105	2.05	1.964	1.956
-25	2.328	2.273	2.181	2.175
-20	2.587	2.533	2.433	2.429
-15	2.89	2.838	2.73	2.729
-10	3.251	3.202	3.083	3.086
-5	3.686	3.641	3.509	3.519
0	4.219	4.182	4.033	4.052
5	4.889	4.863	4.691	4.723

Table: 2(b) . Variation of COP at Different Evaporating Temperature for Different Refrigerants

T_{Evap} (°C)	R410a	R290	R1234yf	R404a
-50	1.314	1.303	1.197	1.123
-45	1.437	1.429	1.321	1.24
-40	1.576	1.571	1.461	1.371
-35	1.732	1.733	1.62	1.521
-30	1.91	1.917	1.802	1.691
-25	2.115	2.129	2.013	1.887
-20	2.351	2.376	2.259	2.115
-15	2.627	2.666	2.548	2.383
-10	2.955	3.01	2.894	2.702
-5	3.348	3.425	3.312	3.086
0	3.831	3.936	3.827	3.558
5	4.436	4.578	4.476	4.151

The coefficient of performance of R134a is 4.2-8.9% and 3.6-5.3% lower than R152a and R600 respectively or in other words R134a consumes more electricity than R152a and R600.Ambient condition play an important role in electricity consumption of vapour compression refrigeration systems because higher the temperature difference between system and surrounding higher will be compressor work that's why COP of vapour compression refrigeration system increase with increase in evaporator temperature and decrease with decrease in evaporator temperature.COP of considered system with R152a, R600, R134a, R600a, R290, R410a, R1234yf and R404a varied between 1.45-4.88, 1.40-4.86, 1.33-4.69, 1.33-4.72, 1.30-4.57, 1.31-4.43, 1.30-4.47 and 1.12-4.15 respectively between –50 °C to 5 °C evaporator temperature. As shown in Fig.3 exergy destructions or exergy losses decreases with increase of evaporator temperature. This is because that if evaporating temperature decreases the heat exchange between working fluid entered into the evaporator tubes and space being cooled also decreases, which finally decrease the cooling effect and therefore exergy destruction increases

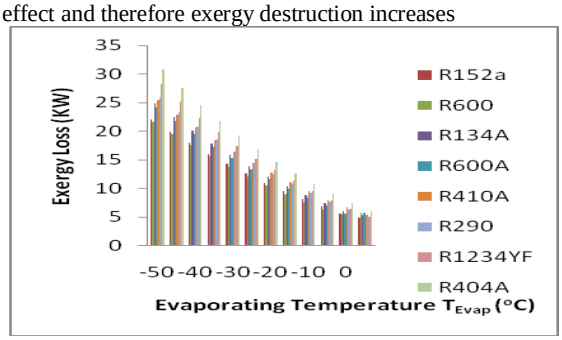

Fig: 3. Variation of Exergy Loss (KW) at Different Evaporating Temperature for Different Refrigerants

ISBN 978-93-5156-328-0

Among selected refrigerants R404a (6.02-30.83 KW) and R152a (4.94-22.06 KW) shows higher and lower exergy loss for selected evaporator temperature range respectively. It was also observed that flash chamber, compressor, condenser, expansion valve, water-intercooler and evaporator are in increasing order of exergy loss for different refrigerants. As shown in Fig.3 exergy destructions or exergy losses decreases with increase of evaporator temperature. This is because that if evaporating temperature decreases the heat exchange between working fluid entered into the evaporator tubes and space being cooled also decreases, which finally decrease the cooling effect and therefore exergy destruction increases. Among selected refrigerants R404a (6.02-30.83 KW) and R152a (4.94-22.06 KW) shows higher and lower exergy loss for selected evaporator temperature range respectively. It was also observed that flash chamber, compressor, condenser, expansion valve, water-intercooler and evaporator are in increasing order of exergy loss for different refrigerants. Fig.4 shows the variation of exergy loss for individual component with change in evaporating temperature with R152a used as working fluid. Behaviour of exergy destruction in different components of two stage vapour compression refrigeration system for rest of refrigerants are also observed similar. Flash chamber responsible for highest and evaporator shows lowest exergy destruction compared to other components. The exergy destruction in the components increase with the decrease of evaporating temperature. Yumrutas et al. [23] observed the effect on exergy loss with change of evaporation and condenser temperature. Khan [24] studied that due to the low expansion process and compressor efficiency most of the irreversible losses occurred in the system. He also found that with increase in difference between evaporator and condenser temperatures exergy losses increases with R12, R134a, R22, and R502 used as refrigerants.

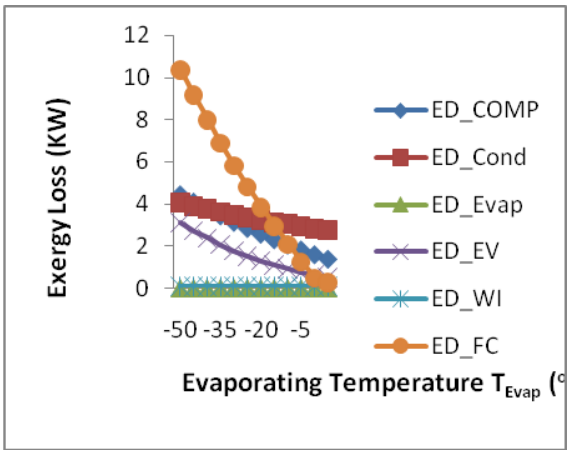

Fig: 4. Variation of Exergy Loss (KW) at Different Evaporating Temperatures for R152a

It is observed from Fig.5 that for all considered refrigerants exergy destructions increased with increase of condensing temperature. This is due to increase of temperature difference between condenser and surrounding .It is found that exergy losses decreases with increase of evaporating temperature for considered refrigerants. It was observed that R152a gives highest exergetic efficiency

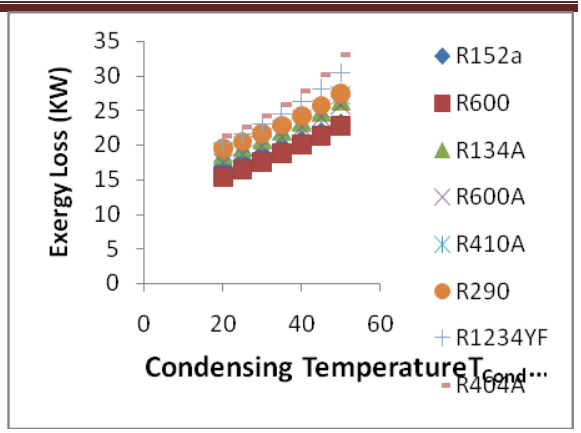

Fig: 5. Variation of Exergy Loss (KW) at Different Condensing Temperatures for Different Refrigerants

among selected refrigerants. The purpose of condenser to take out the heat produced by compressor in discharge line and carried by refrigerant during cooling effect in evaporator. This heat in refrigerant removed by transferring heat to the wall of condenser tubes due to convection and then transfer of heat due to conduction from tubes wall to surrounding.

As shown in Fig.6 with increase in evaporator temperature sustainability index increases for selected refrigerants. R152a shows higher sustainability index than R134a for selected evaporating temperature range. It is also found that R152a and R600 have higher sustainability index and low impact on surrounding compared to R134a.

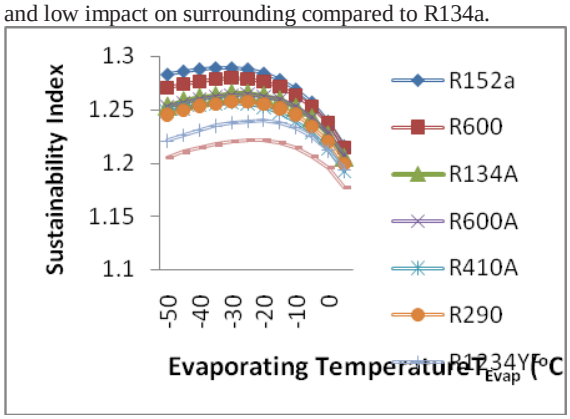

Fig: 6. Variation of Sustainability Index at Different Evaporating Temperatures for Different Refrigerants

4. Conclusions and recommendation

Energetic and exergetic analysis of two stage refrigeration system was carried out with different refrigerants and following conclusion and recommendation are presented below:

(i) R404a shows lowest performance among selected refrigerants

(ii) Exergy destruction for R134a is higher than R152a and R600 but lower than R600a, R410a, R290, R1234yf and R404a.

(iii) Exergetic and energetic efficiency of R152a is highest among selected refrigerants. Flash chamber responsible

for highest exergy destruction for all refrigerants taken under consideration

(iv) Sustainability index of the R152a and R600 are higher than that of R134a at every evaporator temperature. It indicates also less environmental impact for hydrocarbons. However the performance of R152a and R600 is higher than R134a but hydrocarbons are flammable in nature and can be used in limited applications using safety measures. Therefore R134a recommended for all kind of applications.

References

[1] K. Chopra, V. Sahni, R. S. Mishra, Thermodynamic analyses of multiple evaporators vapour compression refrigeration systems with R410A, R290, R1234YF, R502, R404A and R152A.International Journal of Air-conditioning and Refrigeration 21(1), 2014, 1-14

[2] Z. Oktay, I. Dincer, Energetic, exergetic, economic and environmental assessments of the bigadic geothermal district heating system as a potential green solution. International Journal of Green Energy 4 (5), 2007, 549–569

[3] M. A. Rosen, I. Dincer, M. Kanoglu, Role of exergy in increasing efficiency and sustainability and reducing environmental impact. Energy Policy, 36, 2008, 128–37

[4] S. Genoud, J. B. Lesourd, Characterization of sustainable development indicators for various power generation technologies. International Journal of Green Energy 6 (3), 2009, 257–267

[5] E. Johnson, Global warming from HFC, Environ. Impact Asses, 18, 1998, 485–492

[6] M. Padilla, R. Revellin, J. Bonjour, Exergy analysis of R413A as replacement of R12 in a domestic refrigeration system, Energy Convers. Manag. 51, 2010, 2195–2201

[7] H. O. Spauschus, HFC 134a as a substitute refrigerant for CFC 12, Int. J. Refrig, 11, 1988, 389–392

[8] J. U. Ahamed, R. Saidur, H. H. Masjuki, A review on exergy analysis of vapor compression refrigeration system, Renew. Sustain. Energy Rev. 15, 2011, 1593–1600

[9] R. Llopis, E. Torrella, R. Cabello, D. S_anchez, Performance evaluation of R404A and R507A refrigerant mixtures in an experimental double-stage of vapour compression plant, Appl. Energy 87, 2010 1546–1553

[10] A. Arora, S. C. Kaushik, Theoretical analysis of a vapour compression refrigeration system with R502, R404A and R507A, Int. J. Refrig. 31, 2008, 998–1005

[11] V. Havelsky, Investigation of refrigerating system with R12 refrigerant replacements, Appl. Therm. Eng. 20, 2000, 133–140

[12] R. Saravanakumar, V. Selladurai, Exergy analysis of a domestic refrigerator using eco-friendly R290/R600a refrigerant mixture as an alternative to R134a, J. Therm. Anal. Calorim, 2013

[13] V. S. Reddy, N. L. Panwar, S. C. Kaushik, Exergy analysis of a vapour compression refrigeration system with R134a, R143a, R152a, R404A, R407C, R410A, R502 and R507A, Clean Techn. Environ. Policy 14, 2012, 47–53

[14] S. Kumar, M. Prevost, R. Bugarel, Exergy analysis of a vapour compression refrigeration system, Heat Recovery Syst. CHP 9, 1989, 151–157

[15] R. L. Cornelissen, Thermodynamics and sustainable development. Ph.D. thesis. University of Twenty, the Netherlands, 1997

[16] C. Nikolaidis, D. Probert, Exergy method analysis of a two-stage vapour-compression refrigeration plants performance, Appl. Energy 60, 1998, 241–256

[17] M. Fatouh, E. I. M. Kafafy, Assessment of propane/commercial butane mixtures as possible alternatives to R134a in domestic refrigerators. Energy Conversion and Management 47, 2006, 2644–58

[18] S. Wongwises, A. Kamboon, B. Orachon, Experimental investigation of hydrocarbon mixtures to replace HFC-134a in an automotive air conditioning system. Energy Conversion and Management, 47, 2006, 1644–59

[19] D. Jung, C.B. Kim, K. Song, B. Park., Testing of propane, iso-butane mixture in domestic refrigerants. International Journal of Refrigeration, 23, 2000, 517–27

[20] E. Arcaklioglu, Performance comparison of CFCs with their substitutes using artificial neural networks. International Journal of Energy Research, 28(12), 2004, 1113–25

[21] E. Arcaklioglu, A. Cavosuglu, A. Erisen, An algorithmic approach towards finding better refrigerant substitutes of CFCs in terms of the second law of thermodynamics. Energy Conversion and Management 46, 2005, 1595–1611

[22] W. Liedenfrost, K. H. Lee, K. H. Korenic, Conversion of energy estimated by second law analysis of power consuming process. Energy, 5, 1980, 47–61

[23] R. Yumrutas, M. Kunduz, M. Kanoglu, Exergy analysis of vapor compression refrigeration systems. Exergy, an International Journal, 2, 2002, 266–72

[24] S. H. Khan, Second law based thermodynamics analysis of vapor compression system. M. S. Thesis in Engineering, Department of Mechanical Engineering, King Fahad University of Petrolium and Minerals, Saudi Arabia, 1992

Volume 3, Issue 1 (2015) 31-36 ISSN 2347 - 3258
International Journal of Advance Research and Innovation

Thermal Analysis & Optimization of Two Stages Vapour Compression Refrigeration Systems Using Sixteen Ecofriendly Refrigerants

R. S. Mishra
Department of Mechanical Engineering, Delhi Technological University, New Delhi, India

Article Info

Article history:
Received 02 February 2015
Received in revised form
20 February 2015
Accepted 28 February 2015
Available online 15 March 2015

Keywords

Irreversibility,
Exergetic Efficiency,
Two Stage Vapour Compression
Refrigeration Systems

Abstract

This paper mainly deals with comparative computation performance evaluation of sixteen ecofriendly refrigerants used in the two stage vapour compression refrigeration system based on energetic and exergetic principles for findingsystem and components irreversibilities . Performance parameters have been evaluation using entropy generation concept. The numerical computation was carried out for finding rational exergy destruction ratio based on system exergy input in terms of total work dene by compressors as will as exergy destruction ratio based on exergy of product out and first law efficiency in terms of COP . The second law efficiency in terms of exergetic efficiency is also computed at different input variations . It was found Flash chamber responsible for highest exergy destruction for all refrigerants taken under consideration . R123 shows best first law efficiency and R125 shows lowest first law performance among selected sixteen ecofriendly refrigerants The first and second law performance of using R1234ze (of GWP =6) is better than R1234yf (of GWP=4) for higher temperature applications. The exergy destruction using R134a is higher than R152a. R1234yf refrigerant has (GWP = 4) can be used for high temperature applications which can replace R134a around 2030 and R152a, R600a, , R290, R600 are flammable in nature can be used by using safety measures. Therefore R134a recommended for all kind of applicationsbefore 2030.

Nomenclature

CFC	Chlorofluorocarbon
HCFC	Hydrochlorofluorocarbon
Q	rate of heat transfer (kW)
W	work (kW)
T	temperature (oC)
s	specific entropy (kJ/kgK)
h	specific enthalpy(kJ/kg)
S	entropy (kJ/s.K)
ODP	ozone depletion potential
GWP	global warming potential
m	mass flow rate (kg/s)
η	efficiency (non-dimensional)

Subscripts

Evap	Evaporator
Cond	Condenser
amb	ambient conditions
WI	water intercooler
H	high temperature
L	low temperature
LP	low pressure
EV	expansion valve
gen	Generation
HP	high pressure
FC	flash chamber
ex	Exergetic

Corresponding Author,
E-mail address: professor_rsmishra@yahoo.co.in
All rights reserved: http://www.ijari.org

1. Introduction

In past decades, refrigerants such as R12,R02,R22 etc. used in vapour compression refrigeration system responsible for increasing of global warming and ozone depletion potential. An international society named Montreal protocol discussed and signed on the refrigerants having higher global warming and ozone depletion potential values for all countries. In order to control the emission of green house gases one more committee was formed named as Kyto protocol [5].After 90's a program was ran to phase out the higher GWP and ODP refrigerants(CFC and HCFC) for the purpose of environmental problems.

To replace "old" refrigerants with "new" refrigerants lots of researches has been lots of researches has been carried out[]. Coefficient of performance can be enhanced either by minimizing power consumption of compressor or increasing of refrigeration effect. Refrigeration effect can be increased by adoption of multi-stage throttling .On the other hand power consumption of compressor can be enhanced by incorporation of multi-stage compression and flash chamber. Collective effect of these two factors improves overall performance of vapour compression system as reported by several investigators [1-11].

2. Literature Review

Selladurai and Saravanakumar [12] evaluated performance parameters such as COP and exergetic efficiency with R290/R600 hydrocarbon mixture on a domestic refrigerator designed to work with R134a and observed that performance of same system is higher with R290/R600a hydrocarbon mixture compared to R134a. In their analysis condenser, expansion valve and evaporator

showing lower exergy destruction compared to compressor. Reddy et al. presented theoretical analysis of R134a, R143a, R152a, R404A, R410A, R502 and R507A in vapour compression refrigeration system and effect on coefficient of performance and second law efficiency with variation of superheating of evaporator outlet, evaporator temperature and degree of subcooling at condenser outlet, vapour liquid heat exchanger effectiveness and degree of condenser temperature was discussed. They reported that COP and exergetic efficiency significantly affected with change of evaporator and condenser temperatures and also observed that R134a and R407C show highest and lowest performance in all respect. Kumar et al. they carried out energy and exergy analysis of single stage vapour compression refrigeration system using R11 and R12 as working fluids. Evaluation in terms of COP, exergetic efficiency and exergy losses in different components (compressor, evaporator, expansion valve and condenser) was done. Cornelissen proposed that non-renewable energy sources are useful for minimizing the irreversibility of the system for sustainable development of systems vapour compression refrigeration systems. Fatouh and Kafafy suggested to replace R134a with hydrocarbon mixtures such as propane, propane/isobutane/n-butane mixtures, butane, and various propane mass fractions in domestic refrigerator. Pure butane showed high operating pressures and low coefficient of performance among considered refrigerants. Wongwises et al. did experimental investigation on automotive air-conditioners with isobutene, propane, butane and suggested to replace R134a with these hydrocarbon mixtures.They observed that mixture of propane 50%, butane 40%, and isobutane 10% was best hydrocarbon mixture to replace R134a.Jung et al., Arcaklioglu, and Arcaklioglu et. al suggested to use of pure hydrocarbon instead of their mixtures due variation in condenser and evaporator temperature during phase changing at constant pressure. These Changes in condenser and evaporator temperature cause for problem in vapour compression refrigeration cycle. Liedenfrost et al. investigated freon as refrigerant on the performance of a refrigeration cycle Through above literature, it was found that energy, exergy and sustainable analysis of single stage vapour compression refrigeration systems have been done. But no literature contributed for energy and exergy analysis of two-stage vapour compression refrigeration system. Present works analyze the system in terms of energy and exergy efficiencies and explain the effect of exergy losses on two-stage vapour compression refrigeration system with hydrocarbons and R134a.

3. Methods for Improving Thermal Performances of Two Stages Refrigeration Systems

Refrigeration technology based on the principle of rejection of heat to the surrounding at higher temperature and absorption of heat at low temperature [1]. Evaporator, expansion valve, condenser and compressor are the main four components of single stage vapour compression system. Vapour compression refrigeration systems consume large amount of electricity. This difficulty can be removed by improve the performance parameters of system. Coefficient of performance and exergetic efficiency are main two parameters to calculate the performance of refrigeration systems. The irreversibility in system components take place due to large temperature difference between system and surrounding. In order to improve the system performance Irreversibility should be measured in the cycle because Exergy losses are responsible for degradation of system performance .Coefficient of performance is commonly used to calculate the performance of vapour compression system but COP provides no information regarding thermodynamic losses in the system components. Using exergy analysis one can be quantify the exergy losses in vapour compression refrigeration systems. Exergy losses increase with increasing of temperature difference between systems and surrounding. Exergy is the available or useful energy and loss of energy means loss of exergy in the system. Exergy losses are useful to improve the performance of system and better utilization of energy input given to the system which is beneficial for environmental conditions and economics of energy technologies. Utilization of green energy can be increased by this method. [2-4]

Two stage vapour compression refrigeration system consist of low and high pressure compressor, condenser, evaporator, expansion valves, water-intercooler and flash chamber. Energy and exergy efficiencies are different for different refrigerants for same systemTo analyzed the two-stage vapour compression refrigeration system based on energy and exergy method following assumptions are taken in the thermodynamic analysis:

1. Effect of temperature and pressure losses arenegligible.
2. All components of two stages vapour compression refrigeration system are working under steady state conditions.
3. Energy and exergy losses due to potential energyand kinetic energy are neglected.
4. Thermal efficiencies of low and high pressure compressors are assumed to be 80%.

Two stage vapour compression refrigeration system and its P-H plot shown in Figure 1 and Figure 2 respectively.

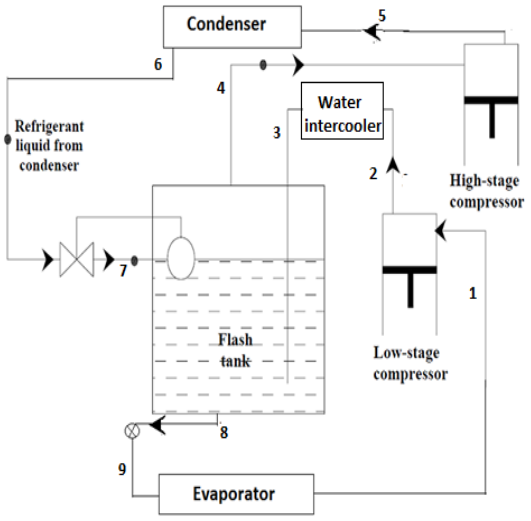

Fig: 1. Schematic Diagram of Two-Stage Vapour Compression Refrigeration System

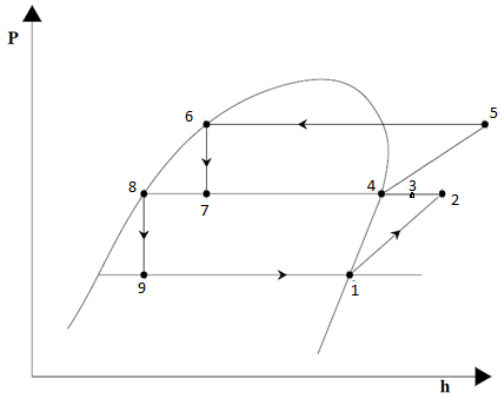

Fig: 2. Pressure Enthalpy Diagram of Two-Stage Vapour Compression Refrigeration System

4. Irreversibility Evaluation Using Entropy Generation Principle

Exergy at any point, $EX = (h - h_{amb}) - T_{amb}(s - s_{amb})$ (1)

For high and low temperature compressors

$(T_{amb}\dot{S}_{gen})_{HP} = \dot{W}_{HP} + \dot{m}_{HP}((h_1 - h_2) - T_{amb}(s_1 - s_2))$ (2)

$(T_{amb}\dot{S}_{gen})_{LP} = \dot{W}_{LP} + \dot{m}_{LP}((h_4 - h_5) - T_{amb}(s_4 - s_5))$ (3)

For evaporator

$(T_{amb}\dot{S}_{gen})_{Evap} = \dot{m}_{LP}((h_9 - h_1) - T_{amb}(s_9 - s_1)) + Q\left(1 - \frac{T_{amb}}{T_L}\right)$ (4)

For condenser

$(T_{amb}\dot{S}_{gen})_{cond} = \dot{m}_{HP}((h_5 - h_6) - T_{amb}(s_5 - s_6)) - Q_{Cond}\left(1 - \frac{T_{amb}}{T_H}\right)$ (5)

For expansion valves

$(T_{amb}\dot{S}_{gen})_{EV} = \dot{m}_{HP}((h_6 - h_7) - T_{amb}(s_6 - s_7)) + \dot{m}_{LP}((h_8 - h_9) - T_{amb}(s_8 - s_9))$ (6)

For water-intercooler

$(T_{amb}\dot{S}_{gen})_{WI} = \dot{m}_{LP}((h_2 - h_3) - T_{amb}(s_2 - s_3))$ (7)

For flash chamber

$(T_{amb}\dot{S}_{gen})_{FC} = \dot{m}_{LP}((h_3 - h_4) - T_{amb}(s_3 - s_4)) + (\dot{m}_{HP}h_7 - \dot{m}_{LP}h_8) - T_{amb}(\dot{m}_{HP}s_7 - \dot{m}_{LP}s_8)$ (8)

Exergetic efficiency

$$\eta_{ex} = \frac{Q\left(1 - \frac{T_{amb}}{T_L}\right)}{W_{LP} + W_{HP}} \quad (9)$$

Coefficient of Performance (COP)

$$COP = \frac{\dot{m}_{LP}((h_1 - h_9)}{W_{LP} + W_{HP}} \quad (10)$$

Total entropy generation in the two stage vapour compression system is

$(\dot{S}_{gen})_{TOTAL} =$

$\sum(\dot{S}_{gen})_{HP} + (\dot{S}_{gen})_{LP} + (\dot{S}_{gen})_{Evap} + (\dot{S}_{gen})_{Cond} + (\dot{S}_{gen})_{EV} + (\dot{S}_{gen})_{WI} + (\dot{S}_{gen})_{FC}$

Total exergy losses based on the entropy generation in the two stage vapour compression system is

$(T_{amb}\dot{S}_{gen})_{TOTAL} =$

$\sum(T_o\dot{S}_{gen})_{HP} + (T_o\dot{S}_{gen})_{LP} + (T_o\dot{S}_{gen})_{Evap} + (T_o\dot{S}_{gen})_{Cond} + (T_o\dot{S}_{gen})_{EV} + (T_o\dot{S}_{gen})_{WI} + (T_o\dot{S}_{gen})_{FC}$

Exergy destruction in the two stage vapour compression refrigeration system based on the exergy input (i.e. total two compressor work in the system) is expressed as Rational exergy destruction ratio $EDR_{Rational}$ is a ratio of total exergy losses based on the entropy generation in the two stage vapour compression system to the exergy input.

$EDR_{Rational} = \{(T_{amb}\dot{S}_{gen})_{TOTAL}/(W_{LP}+W_{HP})\}.$

Similarly exergy destruction ratio in the two stage vapour compression refrigeration system is also based on exergy output can expressed as a ratio of total exergy losses based on the entropy generation in the two stage vapour compression system to the exergy of product can be expressed as

COPsystem=

$(T_{amb}\dot{S}_{gen})_{TOTAL}/(T_{amb}\dot{S}_{gen})_{TOTAL} =$

$\sum(T_o\dot{S}_{gen})_{HP} + (T_o\dot{S}_{gen})_{LP} + (T_o\dot{S}_{gen})_{Evap} + (T_o\dot{S}_{gen})_{Cond} + (T_o\dot{S}_{gen})_{EV} + (T_o\dot{S}_{gen})_{WI} + \frac{(T_o\dot{S}_{gen})_{FC}}{\left(\frac{Q_{eva}\left(1-\frac{T_{amb}}{T_L}\right)}{}\right)}$

5. Results and Discussions

The effect of change of evaporator and condenser temperature on performance parameters like coefficient of performance, exergy loss in terms of Exergy destruction ratio based on input and exergy destruction ratio based on output exergy, exergetic efficiency was investigated as shown in Table-1 for for sixteen ecofriendly refrigerants.

As cleared from Table.1 that highest coefficient of performance of R123is found and lowest COP is using R125. R717 is toxic in nature while R152a, R290 and R600a, R600 are found to be flammable nature. Although R134a consumes more electricity than R152a and R600. COP of vapour compression refrigeration system increase with increase in evaporator temperature and decrease with decrease in evaporator temperature in the considered system with R152a, R600, R134a, R600a, R290, R410a, R1234yf and R404a Ambient condition play an important role in electricity consumption of vapour compression refrigeration systems because higher the temperature difference between system and surrounding higher will be compressor work. For all considered refrigerants exergy destructions ratio is higher for R125 and lowest for R717 and next lowest is R134a. R1234yf has global warming potential of six can be used for high temperature circuit while exergy input in terms of total work of compressors is higher for using R404 than R717. From Table-2, 3 & 4 shows the variation of condenser temperature with performance parameters using R1234yf, R134a and R717 refrigerant. The purpose of condenser to take out the heat produced by compressor in discharge line and carried by refrigerant during cooling effect in evaporator. This heat in refrigerant removed by transferring heat to the wall of condenser tubes due to convection and then transfer of heat due to conduction from tubes wall to surrounding. From Table-2-4 , the EDR and exergy of fuel is also increases with increases with increasing condensing temperature. This is due to increase of temperature difference between condenser and surrounding and cop and exergetic efficiency is decreases with increases condenser temperature Table-5 to Table-7 is representing the variation of evaporator temperature with performance parameters using R1234yf, R134a and R717 refrigerants. .From Table-4-6, exergy destructions or exergy losses decreases with increase of evaporator temperature. This is because that if evaporating temperature decreases the heat exchange between working fluid entered into the evaporator tubes and space being cooled also decreases, which finally decrease the cooling effect and therefore exergy destruction increases. It was also observed that flash chamber, compressor, condenser, expansion valve, water-

intercooler and evaporator are in increasing order of exergy loss for different refrigerants. Exergy losses decrease with increase of evaporating temperature for considered refrigerants. The R123 gives highest exergetic efficiency among selected refrigerants.

Table: 1. Performance evaluation of sixteen eco-friendly of two stage two compressor single evaporator vapour compression refrigeration system for condenser temperature =40^{o}C and evaporator temperature of -40^{o}C and computed exergy output =9.764 "KJ/kg) and Carnot coefficient of performance. 3.585

Refrigerant	COP	EDR	ETA_{Second}	Exergy-input (Kj/Kg)	EDR_Rational
R1234yf	1.623	8.027	0.4529	21.56	0.5471
R134a	1.769	7.847	0.4934	19.79	0.5066
R717	1.988	7.626	0.5546	17.60	0.4454
R404a	1.537	8.149	0.4289	22.77	0.5711
R410a	1.743	7.876	0.4862	20.08	0.5138
R407c	1.607	8.045	0.4482	21.79	0.5518
R507a	1.552	8.127	0.4330	22.55	0.5670
R152a	1.894	7.714	0.5283	18.48	0.4717
R125	1.429	8.326	0.3986	24.50	0.6014
R123	1.931	7.68	0.5386	18.13	0.4614
R290	1.730	7.892	0.4826	20.23	0.5174
R600	1.843	7.766	0.5142	18.99	0.4858
R600a	1.760	7.857	0.4910	19.89	0.5090
R245fa	1.873	7.735	0.5226	18.68	0.4774
R235fa	1.696	7.933	0.4732	20.64	0.5268
R227ea	1.497	8.211	0.4177	23.37	0.5823

Table: 2. Variation of Performance parameters with condenser temperature using R1234yf eco-friendly in the two stage two compressor single evaporator vapour compression refrigeration system for condenser temperature =40^{o}C and evaporator temperature of -40^{o}C, HP compressor efficiency=0.80, LP compressor efficiency=0.80

Condenser temperature (^{o}C)	COP	COP_{carnot}	EDR	$Exergy_{product}$	$Exergy_{fuel}$	ETA_{Second}	EDR Rational
30	2.006	3.589	7.607	9.764	17.45	0.5597	0.4403
35	1.804	3.589	7.804	9.764	19.40	0.50.32	0.49.68
40	1.623	3.589	8.027	9.764	21.57	0.4529	0.5471
45	1.461	3.589	8.272	9.764	23.96	0.4074	0.5926
50	1.312	3.589	8.548	9.764	26.68	0.366	0.6340
55	1.175	3.589	8.865	9.764	29.79	0.3278	0.6722
60	1.047	3.589	9.236	9.764	33.41	0.2922	0.7078

Table: 3. Variation of Performance parameters with condenser temperature using R134a eco-friendly in the two stage two compressor single evaporator vapour compression refrigeration system for condenser temperature =40^{o}C and evaporator temperature of -40^{o}C, HP compressor efficiency=0.80, LP compressor efficiency=0.80

Condenser temperature (^{o}C)	COP	COP_{carnot}	EDR	$Exergy_{product}$	$Exergy_{fuel}$	ETA_{Second}	$EDR_{Rational}$
30	2.142	3.585	7.495	9.764	16.34	0.5974	0.4026
35	1.944	3.585	7.664	9.764	18.0	0.5424	0.4576
40	1.769	3.585	7.847	9.764	19.79	0.4934	0.5066
45	1.611	3.585	8.044	9.764	21.73	0.4494	0.5506
50	1.468	3.585	8.261	9.764	23.85	0.4094	0.5906
55	1.336	3.585	8.50	9.764	26.19	0.3728	0.6272
60	1.275	3.585	8.776	9.764	28.82	0.3388	0.6612

Table: 4. Variation of Performance parameters with condenser temperature using R717eco-friendly in the two stage two compressor single evaporator vapour compression refrigeration system for condenser temperature =40^{o}C and evaporator temperature of -40^{o}C, HP compressor efficiency=0.80, LP compressor efficiency=0.80

Condenser temperature (^{o}C)	COP	COP_{carnot}	EDR	$Exergy_{product}$	$Exergy_{fuel}$	ETA_{Second}	EDR Rational
30	2.327	3.585	7.364	9.764	15.04	0.6493	0.3507
35	2.147	3.585	7.493	9.764	16.30	0.5989	0.4011
40	1.988	3.585	7.626	9.764	17.60	0.5546	0.4444
45	1.847	3.585	7.763	9.764	18.95	0.5153	0.4847
50	1.721	3.585	7.905	9.764	20.33	0.4802	0.5198
55	1.608	3.585	8.052	9.764	21.77	0.4485	0.5515
60	1.504	3.585	8.204	9.764	23.26	0.4197	0.5803

Table: 5. Variation of Performance parameters with evaporator temperature using R1234yf eco-friendly in the two stage two compressor single evaporator vapour ompression refrigeration system for condenser temperature =40^{o}C and evaporator temperature of -40^{o}C HP compressor efficiency=0.80, LP compressor efficiency=0.80

Evaporator Temperatur	COP	COP_{carnot}	EDR	Exergy product	$Exergy_{fuel}$	ETA_{Second}	EDR Rational

e (^{o}C)							
-30	2.015	4.418	10.29	7.9222	17.37	0.456	0.544
-35	1.805	3.967	8.991	8.824	19.39	0.455	0.545
-40	1.623	3.585	8.027	9.764	21.56	0.4529	0.5471
-45	1.465	3.257	7.283	10.75	23.89	0.4498	0.5502
-50	1.326	2.973	6.696	11.27	26.40	0.4459	0.5541
-55	1.203	2.725	6.222	12.84	29.10	0.4410	0.5590
-60	1.094	2.506	5.833	13.97	32.0	0.4364	0.5636

Table: 6. Variation of Performance parameters with evaporator temperature using R134a eco-friendly in the two stage two compressor single evaporator vapour compression refrigeration system for condenser temperature =40^{o}C and evaporator temperature of -40^{o}C, HP compressor efficiency=0.80, LP compressor efficiency=0.80

Evaporator temperature (^{o}C)	COP	COP$_{carnot}$	EDR	Exergy$_{product}$	Exergy$_{fuel}$	ETA$_{Second}$	EDR$_{Rational}$
-30	2.171	4.418	10.13	7.922	16.12	0.4914	0.5086
-35	1.956	3.967	8.823	8.824	17.9	0.4930	0.5070
-40	1.769	3.585	7.847	9.764	19.79	0.4934	0.5066
-45	1.605	3.257	7.091	10.75	21.81	0.4928	0.5072
-50	1.461	2.973	6.483	11.77	23.95	0.4914	0.5086
-55	1.334	2.725	6.001	12.84	26.24	0.4894	0.5106
-60	1.220	2.506	5.598	13.97	28.68	0.4869	0.5131

Table: 7. Variation of Performance parameters with condenser temperature using R717 eco-friendly in the two stage two compressor single evaporator vapour compression refrigeration system for condenser temperature =40^{o}C and evaporator temperature of -40^{o}C, HP compressor efficiency=0.80, LP compressor efficiency=0.80

Evaporator Temperature (^{o}C)	COP	COP$_{carnot}$	EDR	Exergy$_{product}$	Exergy$_{fuel}$	ETA$_{Second}$	EDR$_{Rational}$
-30	2.421	4.418	9.923	7.922	14.46	0.5479	0.4521
-35	2..19	3.967	8.609	8.824	15.98	0.5521	0.4479
-40	1.988	3.585	7.626	9.764	17.60	0.5546	0.4454
-45	1.81	3.257	6.864	10.75	19.33	0.5558	0.4442
-50	1.653	2.973	6.257	11.77	21.18	0.5558	0.4442
-55	1.512	2.725	5.764	12.84	23.45	0.5549	0.4451
-60	1.386	2.506	5.356	13.97	25.26	0.5530	0.4470

6. Conclusions and Recommendations

Using first and second law analysis on two stage refrigeration system was carried out using sixteen ecofriendly refrigerants and following conclusions and recommendation are presented below:

(i) R123 shows best first law efficiency and R125 shows lowest first law performance among selected sixteen ecofriendly refrigerants refrigerants.
(ii) Exergy destruction for R134a is higher than R152a.
(iii) R152a, R600a, R290, R600 are flammable in nature can be used by using safety measures. Therefore R134a recommended for all kind of applications.
(iv) R1234yf refrigerant has (GWP = 4) can be used for high temperature applications
(v) The first and second law performance of using R1234ze (of GWP =6) is better than R1234yf (of GWP=4) for higher temperature applications
(vi) Flash chamber responsible for highest exergy destruction for all refrigerants taken under consideration.

References

[1] K. Chopra, V. Sahni, R. S. Mishra, Thermodynamic analyses of multiple evaporators vapour compression refrigeration systems with R410A, R290, R1234YF, R502, R404A and R152A.International Journal of Air-conditioning and Refrigeration, 21(1), 2014, 1-14
[2] Z. Oktay, I. Dincer, Energetic, exergetic, economic and environmental assessments of the bigadic geothermal district heating system as a potential green solution. International Journal of Green Energy, 4(5), 2007, 549–569
[3] M. A. Rosen, I. Dincer, M. Kanoglu, Role of exergy in increasing efficiency and sustainability and reducing environmental impact. Energy Policy 36, 2008, 128–37
[4] S. Genoud, J. B. Lesourd, Characterization of sustainable development indicators for various power generation technologies. International Journal of Green Energy, 6(3), 2009, 257–267
[5] E. Johnson, Global warming from HFC, Environ.Impact Asses. 18, 1998, 485–492
[6] M. Padilla, R. Revellin, J. Bonjour, Exergy analysis of R413A as replacement of R12 in a domestic refrigeration system, Energy Convers. Manag. 51, 2010, 2195–2201
[7] H. O. Spauschus, HFC 134a as a substitute refrigerant for CFC 12, Int. J. Refrig., 11, 1988, 389–392
[8] J. U. Ahamed, R. Saidur, H. H. Masjuki, A review on exergy analysis of vapor compression refrigeration system, Renew. Sustain. Energy Rev., 15, 2011, 1593–1600

[9] R. Llopis, E. Torrella, R. Cabello, D. S_anchez, Performance evaluation of R404A and R507A refrigerant mixtures in an experimental double-stage of vapour compression plant, Appl. Energy, 87, 2010, 1546–1553
[10] A. Arora, S. C. Kaushik, Theoretical analysis of a vapour compression refrigeration system with R502, R404A and R507A, Int. J. Refrig., 31, 2008, 998–1005
[11] V. Havelsky, Investigation of refrigerating system with R12 refrigerant replacements, Appl. Therm. Eng., 20, 2000, 133–140
[12] R. Saravanakumar, V. Selladurai, Exergy analysis of a domestic refrigerator using eco-friendly R290/R600a refrigerant mixture as an alternative to R134a, J. Therm. Anal. Calorim., 2013
[13] V. S. Reddy, N. L. Panwar, S. C. Kaushik, Exergy analysis of a vapour compression refrigeration system with R134a, R143a, R152a, R404A, R407C, R410A, R502 and R507A, Clean Techn. Environ. Policy, 14, 2012, 47–53
[14] S. Kumar, M. Prevost, R. Bugarel, Exergy analysis of a vapour compression refrigeration system,Heat Recovery Syst. CHP, 9, 1989, 151–157
[15] R. L. Cornelissen, Thermodynamics and sustainable development. Ph.D. thesis. University of Twenty, the Netherlands, 1997
[16] C. Nikolaidis, D. Probert, Exergy method analysis of a two-stage vapour-compression refrigeration plants performance, Appl. Energy, 60, 1998, 241–256
[17] M. Fatouh, E. I. M. Kafafy, Assessment of propane/commercial butane mixtures as possible alternatives to R134a in domestic refrigerators. Energy Conversion and Management, 47, 2006, 2644–58
[18] S. Wongwises, A. Kamboon, B. Orachon, Experimental investigation of hydrocarbon mixtures to replace HFC-134a in an automotive air conditioning system. Energy Conversion and Management, 47, 1644–59
[19] D. Jung, C. B. Kim, K. Song, B. Park, Testing of propane, iso-butane mixture in domestic refrigerants. International Journal of Refrigeration, 23, 2000, 517–27
[20] E. Arcaklioglu, Performance comparison of CFCs with their substitutes using artificial neural networks. International Journal of Energy Research, 28, 12, 1113–25
[21] E. Arcaklioglu, A. Cavosuglu, A. Erisen, An algorithmic approach towards finding better refrigerant substitutes of CFCs in terms of the second law of thermodynamics. Energy Conversion and Management, 46, 2005, 1595–1611
[22] W. Liedenfrost, K. H. Lee, K. H. Korenic, Conversion of energy estimated by second law analysis of power consuming process. Energy, 5, 1980, 47–61
[23] R. Yumrutas, M. Kunduz, M. Kanoglu, Exergy analysis of vapor compression refrigeration systems. Exergy, an International Journal, 2, 2002, 266–72
[24] S. H. Khan, Second law based thermodynamics analysis of vapor compression system. M.S.Thesis in Engineering, Department of Mechanical Engineering, King Fahad University of Petrolium and Minerals, Saudi Arabia, 1992

Engineering Science and Technology, an International Journal xxx (2015) 1–9

HOSTED BY

Contents lists available at ScienceDirect

Engineering Science and Technology, an International Journal

journal homepage: http://www.elsevier.com/locate/jestch

Full length article

Time-domain UWB transmission model for three-dimensional environments with low-loss obstacles

Bajrang Bansal*, Sanjay Soni [1]

Department of Electronics and Communication Engineering, Delhi Technological University, Delhi 110042, India

ARTICLE INFO

Article history:
Received 18 October 2014
Received in revised form
12 January 2015
Accepted 26 January 2015
Available online xxx

Keywords:
Ultra wideband
Propagation model
Transmission
Diffraction
Frequency-domain
Time-domain

ABSTRACT

In this work, time-domain (TD) solution is presented for ultra wideband (UWB) transmission through three dimensional (3-D) scenarios made up of low-loss dielectric materials. Considering soft and hard polarizations, propagation through different structures like building and wedge is analyzed with arbitrary position of the receiver (Rx). Further the presented TD solution for transmission has been compared with TD UWB diffraction; single diffraction, double diffraction and diffraction followed by reflection when both transmitter (Tx) and Rx are in a plane normal to the edge. A detailed analysis of attenuation and distortion of transmitted and diffracted pulse waveforms through lossy obstacles is presented. It is observed that transmitted pulse waveform suffers comparatively lesser attenuation and distortion in shape as compared to diffracted pulse for low-loss obstacles. The TD results have been validated with the inverse fast Fourier transform (IFFT) of the corresponding exact frequency-domain (FD) results.

Copyright © 2015, Karabuk University. Production and hosting by Elsevier B.V. This is an open access article under the CC BY-NC-ND license (http://creativecommons.org/licenses/by-nc-nd/4.0/).

1. Introduction

In recent years, research in ultra wideband (UWB) propagation through indoor scenario has received great attention because of unique features of UWB communication like resilient to multipath phenomena, good resolution, high bit rates, accurate positioning and ranging, low power density, low complexity and low cost [1,2]. In radio propagation of UWB signals, especially in non-line-of-sight (NLOS) communication in deep shadow regions, transmitted field component proves to be very significant [3,4]. Considering the huge bandwidth (3.1−10.6 GHz) of UWB signals [5], it is more efficient to study UWB propagation directly in time-domain (TD) than applying numerical inverse fast Fourier transform (IFFT) to frequency-domain (FD) solutions to convert them into TD. Also TD solutions appear to be more efficient as all the frequencies are treated simultaneously [1].

In the TD, diffraction and reflection have been well studied [6,7]. Considering the importance of transmission in the deep shadow regions, the TD solution of transmitted field through a dielectric slab was presented in Ref. [8]. The measurements characterizing the different materials within UWB range along with the discussion about dispersion suffered by UWB signals due to penetration through the walls were presented in Refs. [9,10]. A simplified TD model for UWB signals transmitting through a dielectric slab was presented in Refs. [11,12]. The TD solutions for the reflection and transmission through a dielectric slab were presented in Ref. [13]. The TD solutions for transmission through a multilayer wall structure were presented in Ref. [14]. The TD solutions for transmission of UWB signals in microcellular and indoor scenario were presented in Ref. [15].

To design the receiver (Rx) for wireless communication system optimally, the accurate channel characterization is an important aspect. The Knowledge of the significant multipath components and pulse distortion helps in optimal design of the UWB Rx [16]. An analysis of attenuation and distortion of UWB transmission through lossy obstacles has not been well studied before. This work gives a comprehensive TD analysis of attenuation and distortion of UWB transmission. The motivation behind this analysis is that the pulse distortion significantly affects the performance of UWB Rx and thus it needs to be analyzed properly [16]. In Ref. [16], it is explained how pulse distortion would affect the system performance if no compensation for this kind of distortion is included. It is known that a matched filter Rx yields maximum signal to noise ratio (SNR) if it is matched to the transmitted pulse. For the narrow band case, it is not the problem as the transmitted pulse suffers no distortion or negligible distortion. In UWB communication, due to the channel being frequency-selective, UWB pulse suffers significant distortion

* Corresponding author. Tel.: +91 8826435527.
E-mail addresses: bajrangbnsl@gmail.com (B. Bansal), sanjoo.ksoni@gmail.com (S. Soni).

Peer review under responsibility of Karabuk University.

[1] Tel.: +91 9540390146.

http://dx.doi.org/10.1016/j.jestch.2015.01.005
2215-0986/Copyright © 2015, Karabuk University. Production and hosting by Elsevier B.V. This is an open access article under the CC BY-NC-ND license (http://creativecommons.org/licenses/by-nc-nd/4.0/).

Please cite this article in press as: B. Bansal, S. Soni, Time-domain UWB transmission model for three-dimensional environments with low-loss obstacles, Engineering Science and Technology, an International Journal (2015), http://dx.doi.org/10.1016/j.jestch.2015.01.005

and hence after convolved with matched filer yields lower SNR output. Thus, the accurate knowledge of pulse distortion at the Rx helps in optimal design of the Rx.

Propagation is considered through low-loss obstacles because most of the building materials used in construction work are of low-loss types like glass, wood, brick, dry concrete, etc [9]. The propagation environments considered in our work are of great significance in various scenarios such as offices, residential structures and outdoor scenarios. A detailed list of these environments with the corresponding range is given in Ref. [17, Table 1]. In Ref. [18], UWB Propagation measurements in typical indoor scenarios, including line-of-sight (LOS), NLOS, room-to-room, within-the-room and hallways have been considered. In Ref. [16], UWB propagation in renowned Bertoni's urban environment consisting of high rise buildings is investigated. In other available literature, UWB propagation modeling has been considered inside the room [19,20] and inside the home [21] that includes transmitter (Tx) and Rx positioned on different floors also. In Refs. [1,8,11–15,22,23], scattering objects have been modeled as slabs, buildings, half-planes and wedges.

The goal of this work is to present TD solution for UWB transmission through three-dimensional (3-D) scenarios and carry out the comparison with UWB diffraction when both Tx and Rx are in a plane normal to the edge. In-depth analysis of physics behind the distortion in UWB pulse waveform has been presented which helps to understand the nature of distortion.

The paper is organized as follows: In Section 2, the 3-D propagation environments and TD formulations for transmitted and diffracted field are presented. Diffraction covers single diffraction, double diffraction, and diffraction followed by reflection. Next in the result section, a detailed TD analysis of UWB propagation is presented. The TD results are validated against the IFFT [24,25] of the corresponding exact FD results. Further the comparison of computational efficiency of the two approaches (IFFT-FD and TD) is performed to emphasize the significance of the TD solutions presented. Finally the comparative analysis of normalized mean and mean square error between TD and IFFT-FD solutions is performed for transmission through all considered scenarios for different loss-tangent values to show the accuracy of low-loss assumption.

2. Propagation through 3-D scenarios

2.1. Propagation environments

Figs. 1 and 2 show 3-D and 2-D (side view) view for different propagation mechanisms through the building (with low-loss materials) scenario with Tx height h_t greater and lower than the building height h_b respectively. The plane along which the ray propagates from Tx to Rx through the building, changes with the movement of Rx along the y direction (can be seen in Figs. 1 and 2). Thus the 3-D scenario gets converted to 2-D for a particular Rx position.

The intersection points of ray path at roof-top and side-walls of the building (e.g. points P and S in Fig. 1) are found out using the parametric form of equation of line [26]. For $h_t > h_b$, transmission is through the corner of the building comprising roof-top and side-wall transmission. Side-wall width d_2 changes with the change in plane containing Tx and Rx. While for $h_t < h_b$, transmission is through the side-walls of the building and both d_1 and d_2 changes with Rx movement along the y direction.

Fig. 3 shows 3-D and 2-D (front view) propagation through the wedge structure. Similarly to building scenario, Rx is fixed along x and z direction while moving along the y direction. Parameters d_1, d_2 and internal wedge angle a_i change with Rx movement along the y direction.

2.2. Formulations

For a signal transmitting through the building or wedge structure in a particular plane, the FD transmitted field at Rx is given as [4,27]

$$E_{RX,s,h}(\omega) = (E_{inc}(\omega)/r_{total}(\omega))\left(\prod_{i=1}^{N} T_{i,s,h}(\omega)\right) L_{total,s,h}(\omega) \quad (1)$$

where E_{inc} is the relative amplitude of the spherical source [22], $r_{total}(\omega) = \sum_{i=1}^{J} r_i$ represents the total distance traversed by the transmitted field from Tx to Rx (J is equal to 5 for the building and 3 for the wedge structures). $T_{total,s,h}(\omega) = \prod_{i=1}^{N} T_{i,s,h}(\omega)$ represents the total FD transmission coefficient [27], which is equal to the product of all the FD transmission coefficients occurring along the transmission path between Tx and Rx with 's' and 'h' subscripts referring to the soft and hard polarizations respectively. The parameter N corresponds to 4 and 2 for the building and wedge structures respectively. $L_{total,s,h}(\omega)$ [11,12] represents the total propagation path-loss suffered by the transmitted field during transmission between Tx to Rx.

The corresponding TD transmitted field through the building or wedge structure is given as

$$e_{RX,s,h}(t) \approx \left(\frac{e_{inc}(t)}{r_{total}}\right) * \Gamma_{total,s,h}(t) * l_{total,s,h}(t) \quad (2)$$

with '*' representing the convolution operator. $\Gamma_{total,s,h}(t)$ and $l_{total,s,h}(t)$ [11,12] are TD counterparts of $T_{total,s,h}(\omega)$ and $L_{total,s,h}(\omega)$

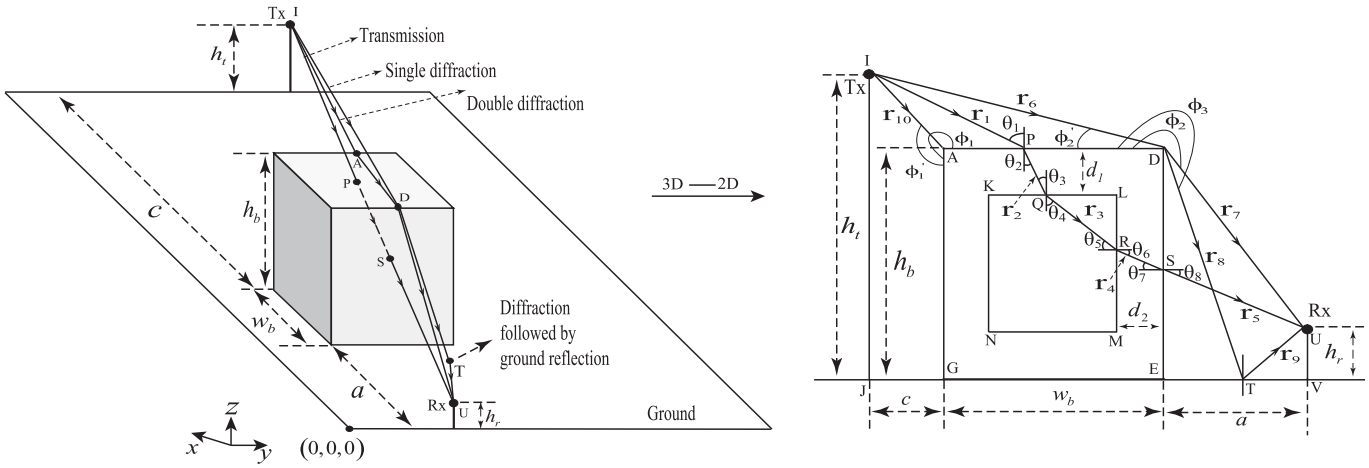

Fig. 1. Propagation through the building scenario with $h_t > h_b$.

Please cite this article in press as: B. Bansal, S. Soni, Time-domain UWB transmission model for three-dimensional environments with low-loss obstacles, Engineering Science and Technology, an International Journal (2015), http://dx.doi.org/10.1016/j.jestch.2015.01.005

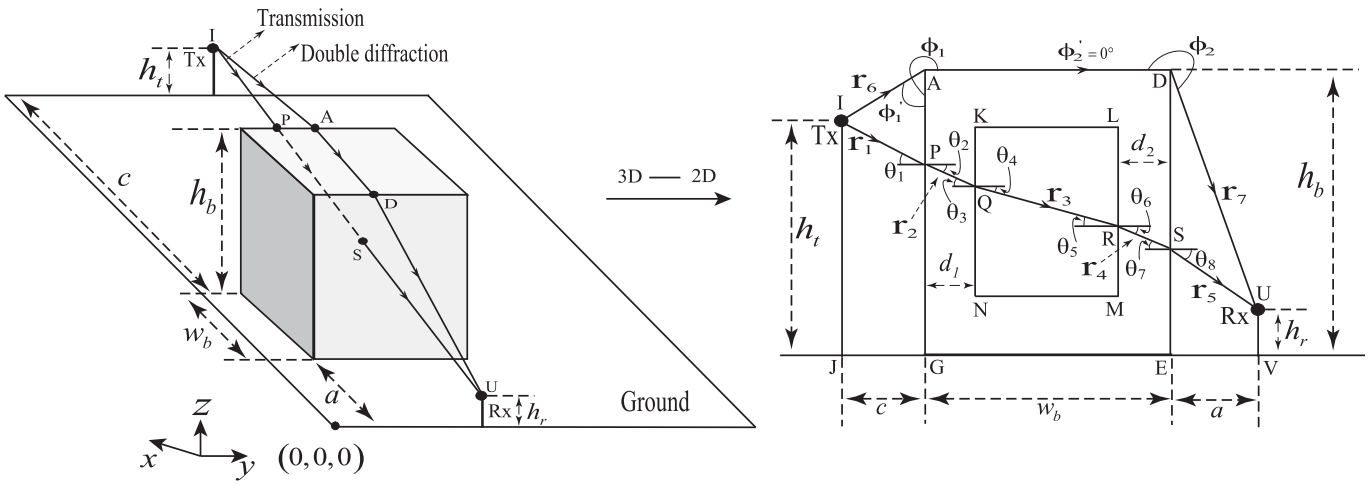

Fig. 2. Propagation through the building scenario with $h_t < h_b$.

respectively. Considering low-loss assumption, TD transmission coefficient for hard and soft polarizations, are given by [7,11,15]

$$\gamma_h(t) \approx \delta(t) - r_h(t) \tag{3}$$

$$\gamma_s(t) \approx [\delta(t) - r_s(t)]\left(\frac{\cos\theta_i}{\cos\psi_t}\right) \tag{4}$$

where $\delta(t)$ is the impulse function [24] and $-r_{h(s)}(t)$ is the TD reflection coefficient for hard (soft) polarization, $r_{h,s}(t) = [K_{h,s}\delta(t)] + 4k_{h,s}/(1-k_{h,s}^2)e^{-pt}[K_{h,s}/2X_{h,s} + (1-X_{h,s})/2K_{h,s} - (pt)X_{h,s}/4]$ with $X_{h,s} = e^{-(K_{h,s}pt/2)}$, $K_{h,s} = (1-k_{h,s}/1+k_{h,s})$, $k_h = (\cos\theta_i/\cos\psi_t)(1/\sqrt{\varepsilon_{r2}})$, $k_s = (\cos\psi_t/\cos\theta_i)(1/\sqrt{\varepsilon_{r2}})$, $p = \tau/2$ and $\tau = \sigma/\varepsilon_2$. θ_i is the incident angle and ψ_t is the true refracted angle [15]. σ is the conductivity of the dielectric medium with ε_2 and ε_{r2} as the dielectric permittivity and relative dielectric permittivity respectively.

For loss-tangent much less than unity ($\sigma/\omega\varepsilon << 1$), the FD path-loss expression $L_{total,s,h}(\omega)$ for building scenario, is given as [14,15] (derived in the Appendix at the end of the paper)

$$L_{total,s,h}(\omega) \approx \exp\left[-j\omega\sqrt{\mu\varepsilon}\left(1+\frac{\sigma}{2j\omega\varepsilon}\right) \times \left(\sum_{i=0}^{1} d_{i+1}\sqrt{\frac{\varepsilon_r}{\varepsilon_r - \sin^2\theta_{(4i+1)}}}\right)\right] \times \exp\left(-jk\left(\sum_{i=1}^{3} r_{(2i-1)}\right)\right)\exp(-\alpha_b r_3) \tag{5}$$

where α_b is the assumed specific attenuation constant [3] of the interior of the building $k = \omega/c$, with ω as the angular frequency and c as the speed of light. Corresponding TD expression is given by

$$l_{total,s,h}(t) \approx \exp\left\{(-\sigma/2)\sqrt{\frac{\mu}{\varepsilon}}\left(\sum_{i=0}^{1} d_{i+1}\sqrt{\frac{\varepsilon_r}{\varepsilon_r - \sin^2\theta_{(4i+1)}}}\right)\right\} *\delta\left\{t - \sqrt{\mu\varepsilon}\left(\sum_{i=0}^{1} d_{i+1}\sqrt{\frac{\varepsilon_r}{\varepsilon_r - \sin^2\theta_{(4i+1)}}}\right)\right\} *\delta\left(t - \frac{\sum_{i=1}^{3} r_{(2i-1)}}{c}\right)\exp(-\alpha_b r_3) \tag{6}$$

Similarly, following the Appendix, the FD path-loss expression for wedge structure can be given as

$$L_{total,s,h}(\omega) \approx \exp\left[-\sqrt{\mu/\varepsilon}\left(\sigma/2\right)r_2\right]\exp[-j\omega\sqrt{\mu\varepsilon}r_2] \times \exp[-jk(r_1+r_3)] \tag{7}$$

The TD expression corresponding to Eq. (7) is then given by

$$l_{total,s,h}(t) \approx \exp\left[-\sqrt{\mu/\varepsilon}\left(\sigma/2\right)r_2\right]\delta[t-\sqrt{\mu\varepsilon}r_2] *\delta\left(t - \frac{r_1+r_3}{c}\right) \tag{8}$$

These approximated TD path-loss expressions are used to compute the TD transmitted field through the building or wedge structure and the accuracy is proved by the comparison with the IFFT-FD results.

Now the TD single diffracted field through building (path *I–D–U* in Fig. 1) or wedge (path *W–D–Y* in Fig. 3) structure, is given by [1]

$$e_{RX,s,h}(t) = A(r_m)\left(\frac{e_{inc}(t)}{r_l}\right) * d_{s,h}(t) * \delta\left(t - \frac{r_l + r_m}{c}\right) \tag{9}$$

where $d_{s,h}(t)$ is the TD diffraction coefficient for lossy obstacles and is given as [1]

$$d_{s,h}(t) = d_1(t) + r_{0,s,h}(t) * r_{n,s,h}(t) * d_2(t) + r_{0,s,h}(t) * d_3(t) + r_{n,s,h}(t) * d_4(t) \tag{10}$$

where the parameters l, m correspond to 6,7 for building scenario and 4,5 for wedge structure. $r_{0,s,h}(t)$, $r_{n,s,h}(t)$ are TD reflection coefficients for 0-face and n-face of the wedge with $A(r_m)$ as the spreading factor. The details of $A(r_m)$, $d_i(t)$ can be found out in Ref. [1]. The TD double diffracted field at Rx through the building structure (path *I–A–D–U* in Fig. 1), is given as [1]

$$e_{RX,s,h}(t) = \left[e_2(t) * d_{2,s,h}(t) + \frac{e_2^{der}(t)}{2} * d_{2,s,h}^{der}(t, \phi_2')\right] A_2(r_7) * \delta\left(t - \frac{r_7}{c}\right) \tag{11}$$

where $e_2(t)$ is the TD single diffracted field at point D with $e_2^{der}(t)$ as the corresponding TD derivative. $d_{2,s,h}(t)$, $d_{2,s,h}^{der}(t, \phi_2')$ are TD diffraction coefficient and derivative of the diffraction coefficient respectively, with respect to ϕ_2' [1,23]. The TD field expression for

Please cite this article in press as: B. Bansal, S. Soni, Time-domain UWB transmission model for three-dimensional environments with low-loss obstacles, Engineering Science and Technology, an International Journal (2015), http://dx.doi.org/10.1016/j.jestch.2015.01.005

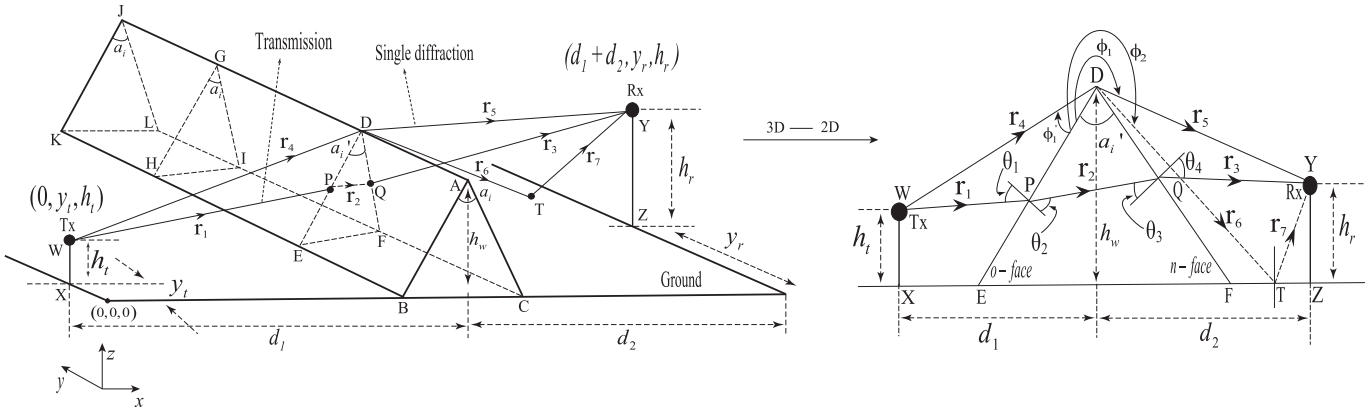

Fig. 3. Propagation through the wedge structure.

Table 1
Electromagnetic properties of different dielectric materials.

Material	Relative permittivity	Conductivity σ (S/m)
Glass [9,31]	6.7	0.001
Dry concrete [11]	5	0.016
Brick [13]	4.4	0.018
Wood [11]	2	0.01
Ground [7]	10	0.01

diffraction followed by reflection (path *I–D–T–U* in Fig. 1) is given as

$$e_{RX,s,h}(t) = \left[\frac{e_{inc}(t)}{r_6} * d_{2,s,h}(t) * r_{s,h}(t)\right] A_2(r_8+r_9) * \delta\left(t - \frac{r_6+r_8+r_9}{c}\right) \quad (12)$$

Similarly the TD field expression for diffraction followed by refection can be written for wedge structure (Fig. 3). Next in the result section, the TD transmitted and diffracted fields are computed for different scenarios considered in Section 2.

3. Results and discussions

In all results, the Gaussian doublet pulse [22] is used as the excitation UWB signal with 0.1 ns to be the full width half maximum pulse duration. As UWB communication spans a large frequency range (3.1–10.6 GHz), the worldwide regulatory groups have issued rulings concerning the UWB emitted power spectral density to enable UWB signals to coexist with current radio services with minimal or no interference [28]. According to the Federal Communications Commission (FCC) (United States frequency regulator), the maximum permissible power spectral density in the complete UWB frequency range is −41.3 dBm/MHz (75 nW/MHz), which is below the noise floor of a typical narrow band Rx [29] and put the UWB systems in the category of unintentional radiators, such as TVs and computer monitors. The software tool MATLAB 7.1 is used and all the cases are run on an Intel Core-i5 2.5 GHz computer, with 8 GB of RAM. In all results, the thickness of the walls of building is considered to be 10 cm. Considering all propagation profiles discussed above, if conductivity becomes zero, then the transmitted field computed through IFFT approach is supposed to exactly match the transmitted field computed through TD approach. But in MATLAB simulation, it is observed that some offset value in time-axis still remains between TD and IFFT-FD results and that was noted due to MATLAB limitations. In all the following results, this offset has been compensated.

As our presented TD analysis is purely based on the assumption of low-loss obstacles, so the electrical parameters such as permittivity and conductivity are chosen which correspond to low loss-

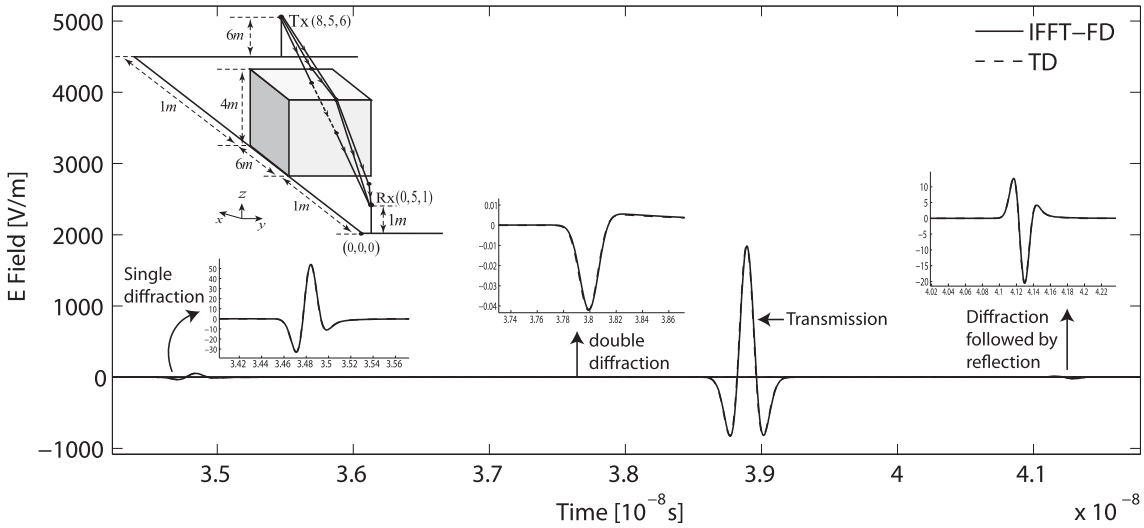

Fig. 4. Transmitted and diffracted field for Fig. 1 (Tx and Rx in same planes), with dry concrete [11].

Please cite this article in press as: B. Bansal, S. Soni, Time-domain UWB transmission model for three-dimensional environments with low-loss obstacles, Engineering Science and Technology, an International Journal (2015), http://dx.doi.org/10.1016/j.jestch.2015.01.005

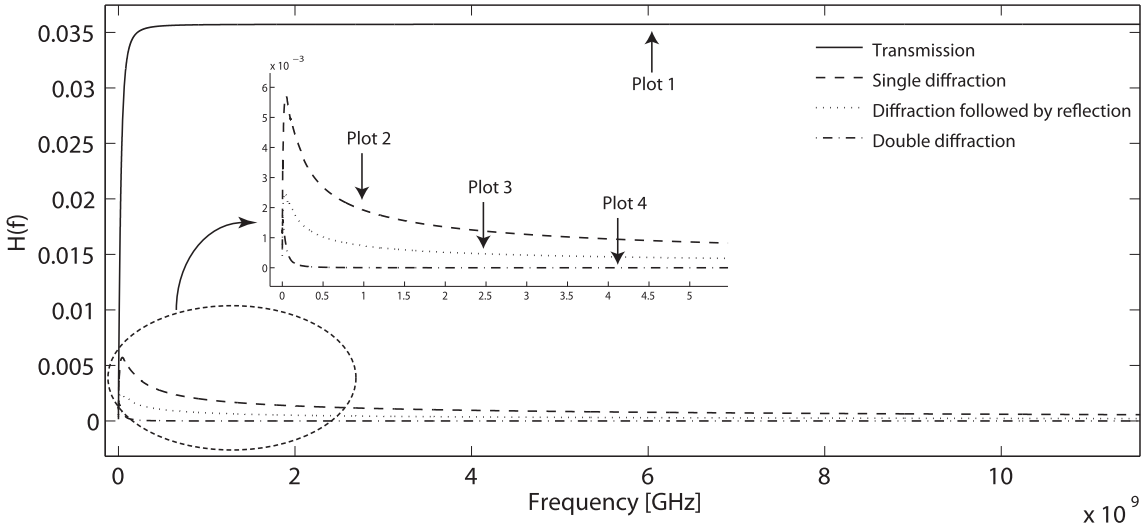

Fig. 5. Frequency response of different propagation mechanisms for geometry considered in the inset of Fig. 4.

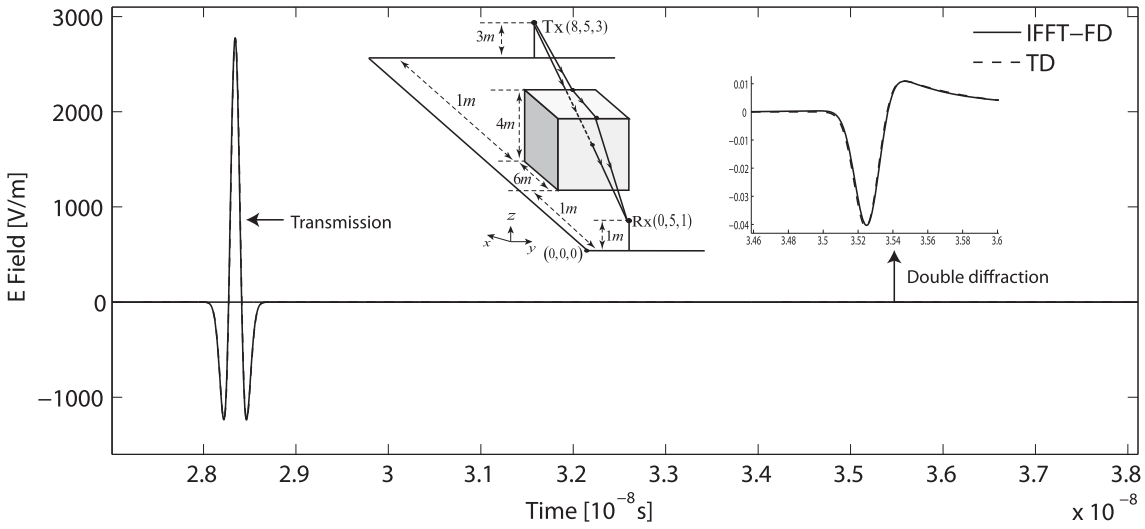

Fig. 6. Transmitted and diffracted field for Fig. 2 (Tx and Rx in same planes), with dry concrete [11].

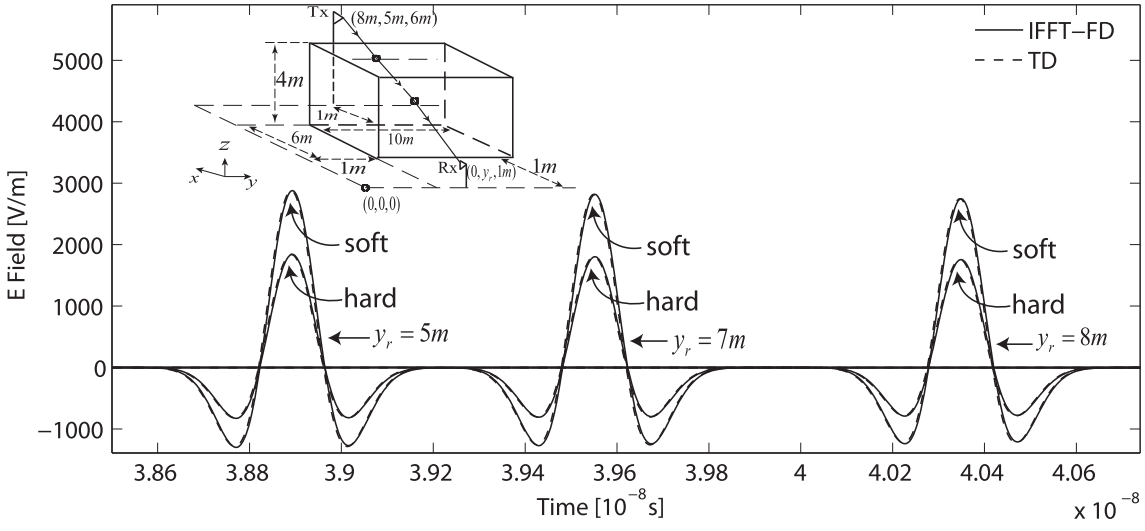

Fig. 7. Transmitted field through the building structure (Fig. 1) for different Rx positions, with dry concrete [11].

Please cite this article in press as: B. Bansal, S. Soni, Time-domain UWB transmission model for three-dimensional environments with low-loss obstacles, Engineering Science and Technology, an International Journal (2015), http://dx.doi.org/10.1016/j.jestch.2015.01.005

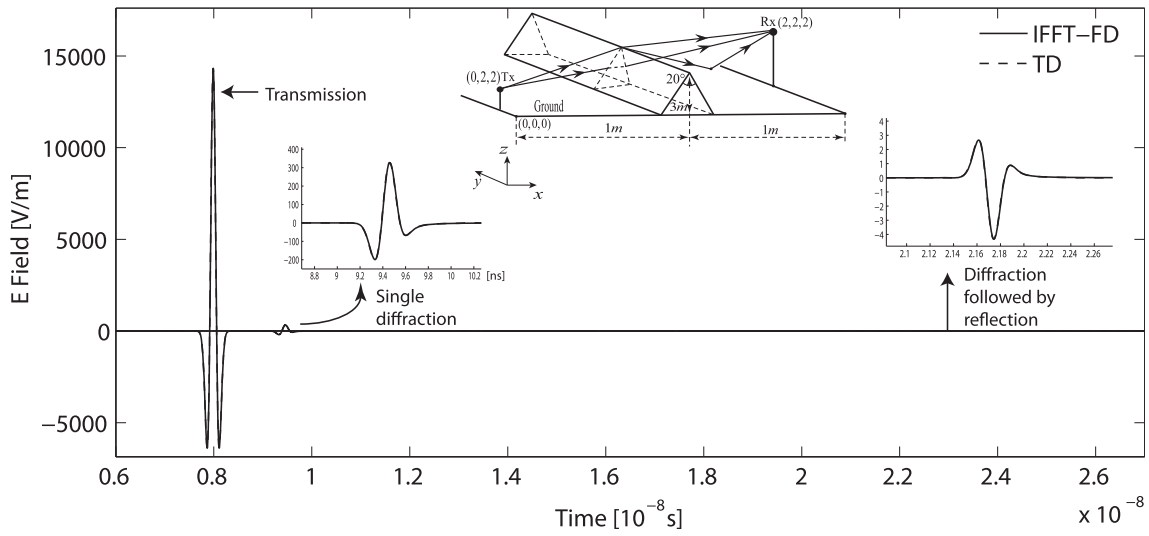

Fig. 8. Transmitted and diffracted field for Fig. 3 (Tx and Rx in same planes), with dry concrete [11].

tangent which is generally true for various structures such as dry-concrete/dry-wall, brick-wall etc [2,7,9]. In many results from literature [9,18,30], it is evident that for many common building materials, the value of relative permittivity and conductivity are almost constant for a wide frequency range including the FCC approved UWB bandwidth. Other results [9] also show that the value of conductivity for some commonly used materials in indoor scenario such as dry-wall, Styrofoam, wallboard, cloth partition and door is very small and doesn't vary much with frequency in the UWB range. The values for dielectric properties chosen in our work closely resemble with the measured and established standard values and satisfy our low-loss assumption which is the prime requirement of our presented model. Table 1 shows the electromagnetic properties of the considered materials.

Fig. 4 shows transmitted and diffracted field at Rx for propagation scenario considered in Fig. 1 for hard polarization. As it can be seen, the transmitted field is more significant than the diffracted field whether it is single diffracted or double diffracted. Also the transmitted field at Rx suffers no distortion in shape in comparison to the shape of the excited UWB pulse. On the other hand, the diffracted UWB pulse waveform shows larger attenuation and distortion. The TD results for the transmitted or diffracted field are in excellent agreement with corresponding IFFT of exact FD results, thus providing validation to the TD solutions.

Table 2
Average ratios of the computation time of the two methods.

Propagation profile	$T_{IFFT-FD}/T_{TD}$
Building 3-D roof-top and side-wall propagation	~165
Building 3-D side-walls propagation	~315
Wedge 3-D propagation	~275

The transmitted field is undistorted due to very small magnitude of the loss-tangent with respect to unity. However, the amplitude of the transmitted field is attenuated because of the transmission loss through the dielectric mediums. Fig. 5 shows frequency response of different propagation mechanisms for geometry considered in the inset of Fig. 4, generally occurring in indoor scenarios. Considering

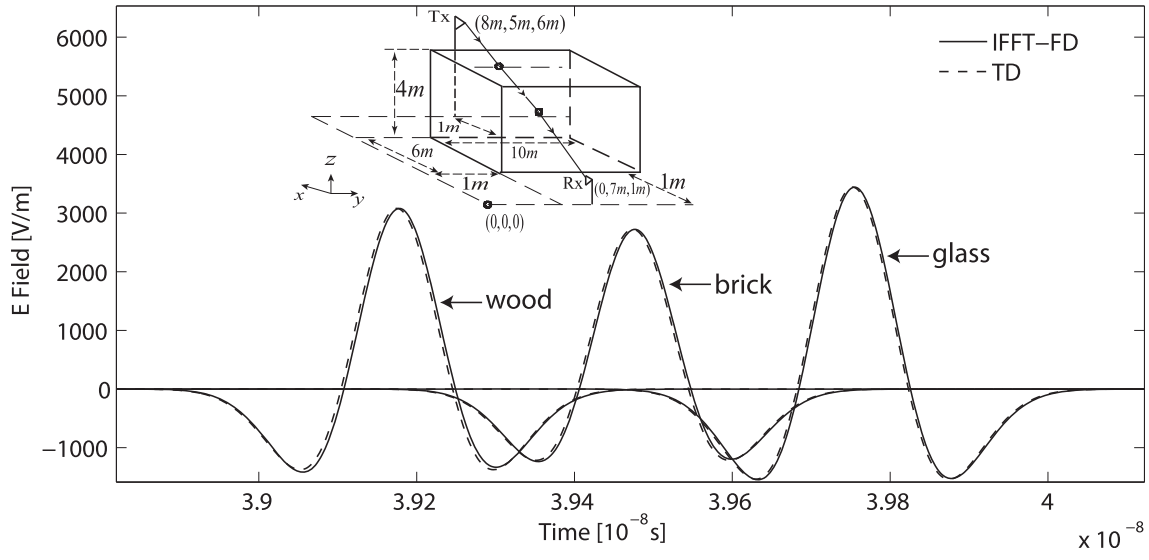

Fig. 9. Transmitted field through the building structure (Fig. 1) for soft polarization, with glass [9,31], brick [13] and wood [11].

Please cite this article in press as: B. Bansal, S. Soni, Time-domain UWB transmission model for three-dimensional environments with low-loss obstacles, Engineering Science and Technology, an International Journal (2015), http://dx.doi.org/10.1016/j.jestch.2015.01.005

Table 3
Error variation with loss-tangent.

Loss-tangent	→	0.01918	0.02452	0.03997	0.08269	0.13114	0.17128	0.18734	0.19983	0.23663	0.25478
Building ($h_t > h_b$)	Mean error	1.388E−3	1.642E−3	3.244E−3	6.612E−3	1.465E−2	2.54E−2	2.712E−2	3.047E−2	3.906E−2	4.327E−2
	Mean square error	3.877E−5	5.561E−5	2.256E−4	8.547E−4	3.694E−3	1.027E−2	1.139E−2	1.425E−2	2.318E−2	2.845E−2
Building ($h_t < h_b$)	Mean error	7.507E−4	6.308E−4	2.121E−4	5.269E−4	1.931E−3	4.029E−3	5.383E−3	6.223E−3	9.438E−3	1.104E−2
	Mean square error	1.154E−5	8.158E−6	7.595E−7	3.878E−6	5.032E−5	2.376E−4	4.582E−4	6.155E−4	1.444E−3	1.954E−3
Wedge	Mean error	6.078E−4	6.223E−4	4.465E−4	1.542E−3	4.55E−3	6.142E−3	9.533E−3	1.04E−2	1.808E−2	2.154E−2
	Mean square error	4.852E−6	4.849E−6	2.935E−6	2.656E−5	2.374E−4	4.131E−4	1.021E−3	1.189E−3	3.277E−3	4.328E−3

low-loss obstacles, the channel shows flat response for transmission (plot 1), i.e. impulse response of transmitted path is constant for low-loss obstacles. Thus the shape of transmitted pulse at Rx remains undistorted. On the other hand, for diffraction, the channel is frequency dependent (plots 2, 3, 4), i.e. impulse response is varying in nature. This is mainly because of stronger frequency dependency of diffraction coefficient [32]. Thus the diffracted pulse waveform at Rx shows larger distortion in shape. Also shown in Fig. 5, the magnitude of frequency response is very small for double diffraction. Thus double diffracted field at Rx is almost negligible as shown in Fig. 4. For diffraction followed by reflection, the received pulse waveform gets inverted in shape and that is because of ground reflection.

Fig. 6 shows transmitted and diffracted field at Rx for propagation scenario considered in Fig. 2 for hard polarization. Again the transmitted field is larger than the diffracted field showing the significance of transmitted field in the shadow regions. The diffracted UWB pulse waveform shows larger attenuation and distortion in shape for the same reasons discussed above. The TD and IFFT-FD results are in good agreement, thus validating the TD solutions.

Fig. 7 shows transmitted field at Rx for propagation scenario considered in Fig. 1 with different Rx positions, for both soft and hard polarizations. The received field varies slightly with the movement of Rx. The TD results for the transmitted field for both polarizations are in good agreement with corresponding IFFT of exact FD results.

Fig. 8 shows transmitted and diffracted field at Rx for propagation scenario considered in Fig. 3 for hard polarization. Same as in the building case, transmitted field is less distorted and stronger in magnitude than the diffracted field and also the TD results are in good agreement with corresponding IFFT-FD results, thus providing validation to the TD solutions.

Fig. 9 shows transmitted field at Rx for Fig. 1 with building structure made up of different dielectric materials, for soft polarization. The TD results are in good agreement with the IFFT-FD results. It is observed that TD and IFFT-FD results match better with decrease in loss-tangent, thus validating our low-loss assumption for transmission of UWB signals.

A comparison between the computational times of the IFFT-FD method and the TD solution for transmission through different scenarios is presented in Table 2 which establishes that the TD analysis is computationally very efficient in comparison to the IFFT-FD solution.

The two main reasons for such a significant reduction in the computational time in TD are: (i) the efficient convolution technique (Section 10.1, Fig. 10.1 and 10.2 in Ref. [24]) due to which few number of time samples suffice to provide accurate results. (ii) Approximation of the multiple transmission paths in FD by a single effective path for low-loss dielectric case.

Table 3 shows the variation of normalized mean error and mean square error (for transmitted field) with increasing loss-tangent for all the considered scenarios. It can be concluded from this table that error tends to increase for larger values of loss-tangents or in other words, the TD solution performs better for low loss-tangent values. Also it is observed that presented TD solution for transmission through low-loss obstacles is accurate for loss-tangent value up to the order of 10^{-2}.

Given the excellent agreement between the TD and the IFFT-FD solution, it can be concluded that the presented TD approach is accurate for low loss-tangent values in the UWB bandwidth. The presented work also establishes that the TD solution is computationally more efficient than the conventional IFFT-FD method.

4. Conclusion

In this work, TD solution has been presented for transmission through 3-D scenarios with low-loss dielectric properties. The different structures like building and wedge are considered with arbitrary position of the Rx. Both soft and hard polarizations are considered and the height of Tx is considered to be above and below the obstacle height. Accuracy of the TD solution is confirmed by comparison with IFFT of the corresponding exact FD solution. Further the presented TD transmitted field has been compared with the diffracted field components when both Tx and Rx are in a plane normal to the edge. It is observed that the transmitted UWB waveform shows lesser attenuation and distortion. Distortion in diffracted field is observed due to frequency selective nature of diffracted path. The solution given in the work is useful in the design of optimal UWB Rx.

Acknowledgment

The authors are thankful to Mr. Piyush Tewari for his continuous support, guidance and valuable suggestions.

Appendix

This appendix contains the derivation of the path-loss expressions for transmission through the building (shown in Fig. 1 or Fig. 2) and wedge structure (shown in Fig. 3).

First, considering transmission through the building structure, the path loss expression is written as:

$$L_{total,s,h}(\omega) = \sum_{i=1}^{5} \exp(-\gamma_i r_i) \tag{13}$$

where $\gamma = \alpha + j\beta$ is the propagation constant with α as the attenuation constant and $\beta = k = 2\pi/\lambda$ as the phase shift constant. λ is the wavelength and $r_i\,(i = 1–5)$ are propagation distances. Now Eq. (13) can be written as:

$$L_{total,s,h}(\omega) = \exp(-jk(r_1 + r_3 + r_5))\exp(-\gamma_2 r_2)\exp(-\gamma_4 r_4) \times \exp(-\alpha_b r_3) \tag{14}$$

Please cite this article in press as: B. Bansal, S. Soni, Time-domain UWB transmission model for three-dimensional environments with low-loss obstacles, Engineering Science and Technology, an International Journal (2015), http://dx.doi.org/10.1016/j.jestch.2015.01.005

where α_b is the assumed specific attenuation constant [3] of the interior of the building and

$$\gamma_2 = \gamma_4 = \sqrt{j\omega\mu(\sigma + j\omega\varepsilon_0\varepsilon_r)} = j\omega\sqrt{\mu\varepsilon_0\varepsilon_r\left(1 + \frac{\sigma}{j\omega\varepsilon_0\varepsilon_r}\right)} \tag{15}$$

with $\gamma_1 = j\omega\sqrt{\mu\varepsilon_0}$. Considering low-loss assumption (i.e. $\sigma/\omega\varepsilon << 1$ [27]), Eq. (15) can be written as:

$$\gamma_2 = \gamma_4 \approx j\omega\sqrt{\mu\varepsilon}\left(1 + \frac{\sigma}{2j\omega\varepsilon}\right) \tag{16}$$

where $\varepsilon = \varepsilon_0\varepsilon_r$. Now using Eq. (16) and $r_2 = d_1\sec(\theta_2)$, $\exp(-\gamma_2 r_2)$ in Eq. (14) is given as:

$$\exp(-\gamma_2 r_2) \approx \exp\left(-j\omega\sqrt{\mu\varepsilon}\left(1 + \frac{\sigma}{2j\omega\varepsilon}\right)d_1\sec(\theta_2)\right) \tag{17}$$

Using Snell's law of refraction, i.e. $\gamma_1 \sin\theta_1 = \gamma_2 \sin\theta_2$, $\sec(\theta_2)$ in Eq. (17) can be written as:

$$\sec(\theta_2) = 1/\cos(\theta_2) \approx \sqrt{\frac{\varepsilon_r}{\varepsilon_r - \sin^2\theta_1}} \tag{18}$$

Now using Eq. (18), Eq. (17) is given as:

$$\exp(-\gamma_2 r_2) \approx \exp\left(-j\omega\sqrt{\mu\varepsilon}\left(1 + \frac{\sigma}{2j\omega\varepsilon}\right)d_1\sqrt{\frac{\varepsilon_r}{\varepsilon_r - \sin^2\theta_1}}\right) \tag{19}$$

In the same way, $\exp(-\gamma_4 r_4)$ can be written as:

$$\exp(-\gamma_4 r_4) \approx \exp\left(-j\omega\sqrt{\mu\varepsilon}\left(1 + \frac{\sigma}{2j\omega\varepsilon}\right)d_2\sqrt{\frac{\varepsilon_r}{\varepsilon_r - \sin^2\theta_5}}\right) \tag{20}$$

Finally using Eqs. (19) and (20), Eq. (14) is given as:

$$\begin{aligned} L_{total,s,h}(\omega) \approx \exp&\left[-j\omega\sqrt{\mu\varepsilon}\left(1 + \frac{\sigma}{2j\omega\varepsilon}\right)\right. \\ &\left.\times\left(\sum_{i=0}^{1} d_{i+1}\sqrt{\frac{\varepsilon_r}{\varepsilon_r - \sin^2\theta_{(4i+1)}}}\right)\right] \\ &\times\exp\left(-jk\left(\sum_{i=1}^{3} r_{(2i-1)}\right)\right)\exp(-\alpha_b r_3) \end{aligned} \tag{21}$$

Summarizing, Eq. (21) presents path-loss expression for transmission through the building structure made up of low-loss material.

Now considering transmission through the wedge structure (Fig. 3), the path loss expression is given as:

$$L_{total,s,h}(\omega) = \sum_{i=1}^{3}\exp(-\gamma_i r_i) \tag{22}$$

Now Eq. (22) can be written as:

$$L_{total,s,h}(\omega) = \exp(-jk(r_1 + r_3))\exp(-\gamma_2 r_2) \tag{23}$$

where

$$\gamma_2 = \sqrt{j\omega\mu(\sigma + j\omega\varepsilon_0\varepsilon_r)} = j\omega\sqrt{\mu\varepsilon_0\varepsilon_r\left(1 + \frac{\sigma}{j\omega\varepsilon_0\varepsilon_r}\right)} \tag{24}$$

Considering low-loss assumption (i.e.$\sigma/\omega\varepsilon << 1$ [27]), Eq. (24) can be written as:

$$\gamma_2 \approx j\omega\sqrt{\mu\varepsilon}\left(1 + \frac{\sigma}{2j\omega\varepsilon}\right) \tag{25}$$

Now using Eq. (25), Eq. (23) is given as:

$$L_{total,s,h}(\omega) \approx \exp(-jk(r_1 + r_3))\exp\left(-j\omega\sqrt{\mu\varepsilon}\left(1 + \frac{\sigma}{2j\omega\varepsilon}\right)r_2\right) \tag{26}$$

which can be further written as:

$$\begin{aligned} L_{total,s,h}(\omega) \approx &\exp\left[-\sqrt{\mu/\varepsilon}\left(\sigma/2\right)r_2\right]\exp\left[-j\omega\sqrt{\mu\varepsilon}r_2\right] \\ &\times\exp[-jk(r_1 + r_3)] \end{aligned} \tag{27}$$

Thus, Eq. (27) presents path-loss expression for transmission through the wedge structure made up of low-loss material.

References

[1] A. Karousos, C. Tzaras, Multiple time-domain diffraction for UWB signals, IEEE Trans. Antennas Propag. 56 (5) (2008) 1420–1427.
[2] A.M. Attiya, A. Safaai-jazi, Simulation of ultra-wideband indoor propagation, Microw. Opt. Technol. Lett. 42 (2) (2004) 103–108.
[3] Y.L.C.D. Jong, H.J.L. Koelen, M.H.A.J. Herben, A building-transmission model for improved propagation prediction in urban microcells, IEEE Trans. Veh. Technol. 53 (2) (2004) 490–502.
[4] S. Soni, A. Bhattacharya, An analytical characterization of transmission through a building for deterministic propagation modeling, Microw. Opt. Technol. Lett. 53 (8) (2011) 1875–1879.
[5] FCC First Report and Order: In the Matter of Revision of Part 15 of the Comparison's Rules Regarding Ultra-Wideband Transmission System, April 2002. FCC 02-48.
[6] P.R. Rousseau, P.H. Pathak, Time-domain uniform geometrical theory of diffraction for a curved wedge, IEEE Trans. Antennas Propag. 43 (12) (1995) 1375–1382.
[7] P.R. Barnes, F.M. Tesche, On the direct calculation of a transient plane wave reflected from a finitely conducting half space, IEEE Trans. Electromagn. Compat. 33 (2) (1991) 90–96.
[8] Z. Chen, R. Yao, Z. Guo, The characteristics of UWB signal transmitting through a lossy dielectric slab, in: Proceedings of the IEEE 60th Vehicular Technology Conference (VTC2004-Fall) Los Angeles, CA, USA, 2004, pp. 134–138.
[9] A. Muqaibel, A. Safaai-Jazi, A. Bayram, A.M. Attiya, S.M. Riad, Ultrawideband through-the-wall propagation, IEE Proc.-Microw. Antennas Propag. 152 (6) (2005) 581–588.
[10] A. Muqaibel, A. Safaai-Jazi, Characterization of wall dispersive and attenuative effects on UWB radar signals, J. Frankl. Inst 345 (6) (2008) 640–658.
[11] W. Yang, Z. Qinyu, Z. Naitong, C. Peipei, Transmission characteristics of ultra-wide band impulse signals, in: Proceedings of the IEEE International Conference on Wireless Communications Networking and Mobile Computing (WiCom 2007) Shanghai, 2007, pp. 550–553.
[12] W. Yang, Z. Naitong, Z. Qinyu, Z. Zhongzhao, Simplified calculation of UWB signal transmitting through a finitely conducting slab, J. Syst. Eng. Electron. 19 (6) (2008) 1070–1075.
[13] A. Karousos, G. Koutitas, C. Tzaras, Transmission and reflection coefficients in time-domain for a dielectric slab for UWB signals, in: Proceedings of the IEEE Vehicular Technology Conference (VTC Spring 2008) Singapore, 2008, pp. 455–458.
[14] B. Bansal, S. Soni, A new time-domain solution to transmission through a multilayer low-loss wall structure for UWB signals, Wireless Pers. Commun. 79 (2014) 581–598.
[15] P. Tewari, S. Soni, B. Bansal, Time-domain solution for transmitted field through low-loss dielectric obstacles in a microcellular and indoor scenario for UWB signals, IEEE Trans. Veh. Technol. (2014), http://dx.doi.org/10.1109/TVT.2014.2323699.
[16] R.C. Qiu, C. Zhou, Q. Liu, Physics-based pulse distortion for ultra-wideband signals, IEEE Trans. Veh. Technol. 54 (5) (2005) 1546–1555.
[17] A.F. Molisch, Ultrawideband propagation channels-theory, measurement, and modeling, IEEE Trans. Veh. Technol. 54 (5) (2005) 1528–1545.
[18] A. Muqaibel, Characterization of UWB Communication Channels (Ph.D. dissertation), Virginia Polytechnic Institute and State University, Blacksburg, VA, USA, 2003.
[19] R. Yao, G. Gao, Z. Chen, W. Zhu, UWB multipath channel model based on time-domain UTD technique, in: Proceedings of the IEEE International Conference on Global Telecommunications (GLOBECOM), 2003, pp. 1205–1210.
[20] R. Yao, W. Zhu, Z. Chen, An efficient time-domain ray model for UWB indoor multipath propagation channel, in: Proceedings of the IEEE International

Please cite this article in press as: B. Bansal, S. Soni, Time-domain UWB transmission model for three-dimensional environments with low-loss obstacles, Engineering Science and Technology, an International Journal (2015), http://dx.doi.org/10.1016/j.jestch.2015.01.005

Vehicular Technology Conference (VTC) Orlando, FL, USA, 2003, pp. 1293–1297.
[21] R. Yao, Z. Chen, Z. Guo, An efficient multipath channel model for UWB home networking, in: Proceedings of the IEEE International Radio and Wireless Conference (RAWCON), 2004, pp. 511–516.
[22] P. Liu, J. Tan, Y. Long, Time domain UTD-PO solution for the multiple diffraction of spherical waves for UWB signals, IEEE Trans. Antennas Propag 59 (4) (2011) 1420–1424.
[23] P. Liu, J. Wang, Y. Long, Time-domain double diffraction for UWB signals, in: PIERS Proceedings Beijing, China, 2009, pp. 848–852.
[24] E.O. Brigham, The Fast Fourier Transform and Its Applications, Prentice-Hall, Englewood Cliffs, New Jersey, 1988.
[25] L. Sevgi, Numerical Fourier transforms: DFT and FFT, IEEE Antennas Propagat. Mag. 49 (3) (2007) 238–243.
[26] P.S. Chauhan, S. Soni, Y. Shanker, A novel approach to predict field strength in the shadow of a 3-D building scenario, Wireless Pers. Commun. 70 (4) (2013) 1683–1695.
[27] C.A. Balanis, Advanced Engineering Electromagnetic, Wiley, New York, 1989.
[28] APT Report on Ultra Wideband (UWB), August 2007. No. APT/AWF/REP-1, edition.
[29] F. Nekoogar, Ultra-Wideband Communications: Fundamentals and Applications, Prentice Hall, NJ, USA, 2005.
[30] International Telecommunication Union, ITU-R Recommendation P.1238–7, Propagation Data and Prediction Methods for the Planning of Indoor Radio Communication Systems and Radio Local Area Networks in the Frequency Range 900 MHz to 100 GHz, February 2012.
[31] M. Jing, Z. Qinyu, Z. Naitong, Impact of IR-UWB waveform distortion on NLOS localization system, in: Proceedings of the IEEE International Conference on Ultra-Wideband (ICUWB 2009) Vancouver, BC, 2009, pp. 123–128.
[32] W. Yang, Z. Qinyu, Z. Jie, Z. Naitong, Analysis of UWB pulsed field diffracted by a perfectly conducting wedge, in: Proceedings of the Second IEEE Conference on Industrial Electronics and Applications (ICIEA 2007) Harbin, 2007, pp. 1539–1542.

Please cite this article in press as: B. Bansal, S. Soni, Time-domain UWB transmission model for three-dimensional environments with low-loss obstacles, Engineering Science and Technology, an International Journal (2015), http://dx.doi.org/10.1016/j.jestch.2015.01.005

Author's Accepted Manuscript

Visible, up-conversion and NIR (~ 1.5μm) luminescence studies of Er^{3+} doped Zinc Alumino Bismuth Borate Glasses

K. Swapna, Sk. Mahamuda, M. Venkateswarlu, A. Srinivasa Rao, M. Jayasimhadri, Suman Shakya, G. Vijaya Prakash

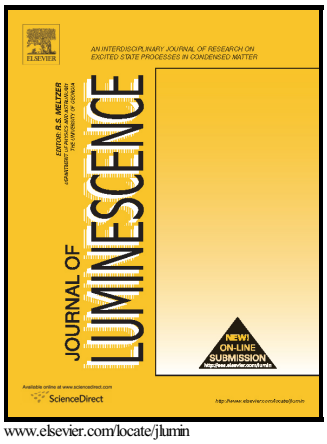

www.elsevier.com/locate/jlumin

PII: S0022-2313(15)00108-8
DOI: http://dx.doi.org/10.1016/j.jlumin.2015.02.036
Reference: LUMIN13222

To appear in: *Journal of Luminescence*

Received date: 26 September 2014
Revised date: 4 February 2015
Accepted date: 18 February 2015

Cite this article as: K. Swapna, Sk. Mahamuda, M. Venkateswarlu, A. Srinivasa Rao, M. Jayasimhadri, Suman Shakya and G. Vijaya Prakash, Visible, up-conversion and NIR (~ 1.5μm) luminescence studies of Er^{3+} doped Zinc Alumino Bismuth Borate Glasses, *Journal of Luminescence,* http://dx.doi.org/10.1016/j.jlumin.2015.02.036

This is a PDF file of an unedited manuscript that has been accepted for publication. As a service to our customers we are providing this early version of the manuscript. The manuscript will undergo copyediting, typesetting, and review of the resulting galley proof before it is published in its final citable form. Please note that during the production process errors may be discovered which could affect the content, and all legal disclaimers that apply to the journal pertain.

ACCEPTED MANUSCRIPT

Visible, Up-Conversion and NIR (~ 1.5 µm) Luminescence Studies of Er^{3+} doped Zinc Alumino Bismuth Borate Glasses

K. Swapna[1], Sk. Mahamuda[1], M.Venkateswarlu[1], A. Srinivasa Rao*[1, 2], M.Jayasimhadri[2], Suman Shakya[3]and G. Vijaya Prakash[3]

[1]Department of Physics, K L University, Green Fields, Vaddeswaram-522 502, Guntur (Dt). A P, India.
[2]Department of Applied Physics, Delhi Technological University, Bawana Road, New Delhi-110 042, India.
[3]Nanophotonics Laboratory, Department of Physics, Indian Institute of Technology-Delhi, KauzKhaz, New Delhi-110016,India.

Corresponding author, E-mail: drsrallam@gmail.com, Tel: +91 85860 39007, Fax:+91 01127871023.

Abstract

Er^{3+} doped Zinc Alumino Bismuth Borate (ZnAlBiB) glasses with composition 20 ZnO+10 Al_2O_3+(10-x) Bi_2O_3+60 B_2O_3+xEr_2O_3 (where x=0.1, 0.5, 1.0 and 2.0 mol %) were prepared by using melt quenching technique to study their luminescence efficiency in different regions of electromagnetic spectrum using absorption, emission, up-conversion and time resolved photoluminescence spectral studies at room temperature. The Judd-Ofelt (JO) parameters evaluated by applying JO theory to the absorption spectra of Er^{3+} doped ZnAlBiB glasses were used to calculate the radiative properties such as transition probability (A_R), Branching ratios (β_R), radiative lifetimes (τ_R), stimulated emission cross-section (σ_{se}), gain band width ($\sigma_{se} \times \Delta\lambda_P$) and optical gain ($\sigma_{se} \times \tau_R$) parameters for the prominent luminescent levels of Er^{3+}. Visible and near infrared (NIR) emission spectra have been recorded by exciting the glass samples at 486 nm and 980 nm respectively. Quantum efficiency (η) values for the prepared glasses were evaluated from the decay curves recorded for the NIR transition $^4I_{13/2} \rightarrow {}^4I_{15/2}$. The up-conversion luminescence shown by these glasses were recorded and analysed to understand utility of these glasses as up-conversion lasers by exciting them with 980 nm laser diode. The visible, up-conversion and NIR luminescence studies indicates that Er^{3+} ions doped ZnAlBiB glasses are aptly suitable for solid state lasers and optical amplifiers.

Key words:

Glasses, Erbium, JO parameters, up-conversion, radiative properties, emission cross-section

Accepted manuscript

ACCEPTED MANUSCRIPT

1. Introduction

In quite recent years, there has been an intense search for the materials which can up-convert the near infrared light to visible light. Such materials are very important because of their versatile applications in diversified fields such as fibre amplifiers, optoelectronic devices, lasers, colour displays, optical data storage and under water optical communication [1]. In recent year's wavelength division multiplexing (WDM) technology gained so much of attention as it increases the information carrying capacity of communication network used in telecommunication systems [2-4]. Since broadband fibre amplifiers are the key devices in such systems, tremendous work has been dedicated in fabricating the optical materials possessing broad bandwidths of luminescence particularly in the wavelength range from 1200-2600 nm [5, 6]. For such near infrared and mid infrared applications, the materials in general are activated by rare earth (RE) ions. Quite recently, RE ions doped glasses are found to be potential in the development of luminescent devices suitable for Infrared (IR) lasers, infra-red to visible up-convertors, fibre and waveguide amplifiers for optical transmission network [2-4].

The glasses doped with RE ions became superior than crystals because of several advantages such as easy preparation, large RE^{3+} ion doping capacity, large inhomogeneous line broadening etc. [7]. Glasses doped with RE ions are also playing a significant role in producing highly efficient up-conversion lasers. It is well known that a host material with low phonon energies can suppress the non-radiative decay loss produced by multi-phonon relaxation and increases the luminescence efficiency. Strong up-conversion luminescence is possible in such systems having phonon energies considerably less. Since from the last few decades, the borate glasses are being investigated so extensively because of their novel properties such as high transparency, large refractive index and good rare earth ion solubility [8, 9]. It is well known that boric acid (B_2O_3) is one of the best glass former among the known good glass formers [10]. But most of the oxide glasses are having large phonon energies (~1100cm^{-1}) due to stretching vibrations of network forming oxides [11] and decreases the luminescence efficiency. On the other hand in recent years lot of research was done on heavy metal oxide (HMO) glasses owing to their low phonon energies. Hence, the addition of HMO such as Bi_2O_3 to a borate glass can definitely reduce the phonon energies considerably and increases the luminescence efficiency [12]. In addition to this, glasses based on Bi_2O_3 are possessing considerably high linear and non-linear refractive index with high density. Because of these remarkable features, the HMO based glasses got several

Accepted manuscript

ACCEPTED MANUSCRIPT

applications in diversified fields such as ceramics technology and optoelectronic devices [13, 14]. Addition of Bi_2O_3 to a borate glass can augment its chemical durability and thermal stability. Addition of Al_2O_3 and ZnO to bismuth borate glasses can increase mechanical strength and further enhances the chemical durability of the glasses [15]. Al_2O_3 plays an important role in the geometric distribution of RE elements to prevent the clustering of the RE ions, which in turn improves the quality of the optical devices [16- 18]. On the other hand ZnO plays an important role in RE doped glasses due to its unique electronic and optical properties and have potential applications in solar energy conversion, nonlinear optics, photo electrochemical cells and heterogeneous photo catalysis [19, 20]. Hence in the present investigation, using B_2O_3, Bi_2O_3, ZnO and Al_2O_3 chemicals as constituent elements we prepared a germane optical system namely Zinc Alumino Bismuth Borate (ZnAlBiB) glass in which Er^{3+} ions were placed with different concentrations to study the luminescence efficiency of these glasses in different regions of the electromagnetic spectrum. Excellent luminescent properties possessed by ZnAlBiB glasses doped with Dy^{3+}, Sm^{3+}, Ho^{3+}, Tb^{3+} and Eu^{3+} ions have also motivated us to take up the present investigation [21-25].

Among all the RE ions, Er^{3+} ions are considered to be the most important because of their potential applications in the fields of optical fibre amplifiers, infrared lasers, microchip lasers, erbium doped fibre amplifiers (EDFA) in wavelength division multiplexing (WDM) system, eye-safe lasers in medical fields [26]. This EDFA is one of the key devices for use in 1.5μm wavelength optical communication window. The broadening of optical communication window system becomes very important because of the rapid increase of information carrying capacity and the need of flexible networks [27]. Recently, up-conversion emission studies of Er^{3+} ions in different mediums have been increased because of its visible green and red emissions. In Er^{3+} ions doped materials, the red up-conversion emission increases due to energy transfer (ET) between neighbouring RE ions, whereas the green up-conversion emission is due to ET and excited state absorption (ESA) [28, 29]. On the other hand, at higher concentration of RE ions, the local surroundings of RE ions and the optical properties of host glass matrix are influenced by clustering of RE ions. Such aggregation and clustering of RE ions will augment the interaction between RE ions, resulting in luminescence quenching [30, 31]. The present work reports the results of our systematic investigation on the luminescence properties of ZnAlBiB glasses doped with different concentrations of Er^{3+} ions in different regions of the

Accepted manuscript

ACCEPTED MANUSCRIPT

electromagnetic spectrum using absorption, emission, up-conversion and decay spectral measurements.

2. Experimental

Glasses with molar composition of 20 ZnO + 10 Al_2O_3 + (10-x) Bi_2O_3+60 B_2O_3+ x Er_2O_3 (where x=0.1, 0.5, 1.0 and 2.0 mol %) were prepared by using melt quenching method. For convenience these glasses are labelled as ZnAlBiBEr01, ZnAlBiBEr05, ZnAlBiBEr10 and ZnAlBiBEr20 depending on the RE ion concentration present in the glass. The analar grade (high purity) starting materials ZnO, Al_2O_3, Bi_2O_3, B_2O_3 and Er_2O_3 were weight, mixed in an agate mortar and melted in an alumina crucible at 1200°C for 30 min in an electric furnace. After that, the bubble free melt was casted on a pre-heated brass mould and subsequently annealed at 400°C. The obtained glass samples were cut and polished for optical measurements. The refractive indices of prepared glasses have been determined by employing Brewster's law using He-Ne Laser which can operate at a wavelength of 650 nm. The densities of the prepared samples were measured using Archimedes' principle with water as an immersed liquid. By using the measured densities and refractive indices, several other physical properties were evaluated by using the expressions collected from literature [32] and are given Table 1. The absorption spectra of these glasses were recorded by using JASCO V-670 UV-vis-NIR spectrophotometer in the range of 300-1800 nm. The luminescence spectra of these glasses have been recorded using Schimadzu RF-5301 PC type spectrofluorophotometer. Fluorescence in NIR region was detected through an ANDOR SR-500i-B2 monochromator coupled to InGaAs detector through 750 nm short pass filter and plano convex lenses assembly of focal length 5 and 10 cm. The up-conversion and fluorescence decay measurements were recorded using a monochramator (Acton SP2300) coupled to CCD (charge coupled detector) through 750 nm short pass filter and plano convex lenses assembly of focal length 5 and 10 cm by employing 980 nm diode laser having 1 w output power (from Shanghai Dream Lasers) as an excitation source.

Result and Discussion

3.1. Optical Absorption spectra analysis

Fig 1 shows the optical absorption spectrum of ZnAlBiBEr20 glass in the range 300-1800 nm. It has various inhomogeneous broadened bands due to f-f transitions which originate from $4f^9$ configuration of Er^{3+} ions. The absorption occurs due to 4f-4f electric dipole transitions from the $^4I_{15/2}$ ground state to various excited state of Er^{3+} ions. The absorption spectrum shown in Fig 1,

Accepted manuscript

ACCEPTED MANUSCRIPT

consists eleven absorption bands at wavelengths 1530 nm, 977 nm, 798 nm, 658 nm, 547 nm, 522 nm, 486 nm, 449 nm, 405 nm, 376 nm and 372 nm corresponding to the transitions $^4I_{15/2} \rightarrow {}^4I_{13/2}$, $^4I_{11/2}$, $^4I_{9/2}$, $^4F_{9/2}$, $^4S_{3/2}$, $^2H_{11/2}$, $^4F_{7/2}$, $^4F_{5/2}$, $^2G_{9/2}$, $^4G_{11/2}$ and $^2G_{7/2}$ respectively [33]. With Er^{3+} ion concentration in ZnAlBiB glasses, no change is observed in peak positions except some intensity variations. The intensities of the absorption bands known as oscillator strengths (f_{exp}) are measured from the relative areas under the absorption bands using relevant expression [15]. The Judd - Ofelt (JO) theory [34, 35] has been used to estimate the oscillator strengths (f_{cal}) of the absorption transitions from the ground level (ΨJ) to various excited state (Ψ'J') of Er^{3+} ions by using the following relation.

$$f_{cal} = \frac{8\pi^2 mc\vartheta}{3h(2J+1)} \frac{(n^2+2)^2}{9n} \sum_{\lambda=2,4,6} \Omega_\lambda \, (\Psi J \| U^{(\lambda)} \| \Psi' J')^2 \qquad (1)$$

Where n is the refractive index of the medium, J is the total angular momentum of the ground state, ϑ is the energy of the transition in cm^{-1} and Ω_λ (λ=2, 4 and 6) are the JO parameters, which are the characteristics of the RE ion-host combination. $\|U^{(\lambda)}\|^2$ are the square reduced matrix elements of the unit tensor operator of rank λ= 2, 4 and 6 and are collected from the Carnal et al.[33]. The JO intensity parameters ($\Omega_{\lambda=2, 4, 6}$) were estimated by using the least square fitting approximation method, which can provide the essential information about the symmetry and bonding of the active ions within ligand fields [34, 35]. The experimental and calculated oscillator strengths (f_{exp}, f_{cal}) along with root mean square (δ_{rms}) deviation for Er^{3+} ion in ZnAlBiB glasses are given in Table 2. The JO intensity parameters ($\Omega_{\lambda=2, 4, 6}$) obtained through least square fitting analysis are listed in Table 3. From Table 3, it is observed that the JO intensity parameters for all the ZnAlBiB glasses follow the same trend $\Omega_2 > \Omega_4 > \Omega_6$. In general the JO parameters are very sensitive to the structural change in the host matrix. In the present case, the Ω_2 value is increasing with increase in Er^{3+} concentration up to 1 mol % and decreasing beyond as shown in Fig 2. Usually Ω_2 relates to the degree of the covalency of the RE-O bond and asymmetry around RE ions, which in turn depends on the short range effects. From Table 3, it is observed that the Ω_2 value is high for ZnAlBiBEr10glass which results because of the superior oscillator strength of hypersensitive transitions. Hence ZnAlBiBEr10 glass has the strong covalency of RE-O bond and highest asymmetry of the sites in the surrounding area of the dopant ion. Among the JO parameters, Ω_6 has least influence and Ω_4 has moderate influence on the structure of the host matrix due to the small values of $\|U^2\|^2$square reduce matrix elements.

Accepted manuscript

ACCEPTED MANUSCRIPT

The Ω_4 and Ω_6 JO parameter values depend on the bulk properties of the medium such as viscosity and dielectric constant of the media and are also affected by the vibronic transitions of the RE ions bounded to the ligand atoms [36-38]. As given in Table 3, the JO parameter values obtained for the present glass systems are comparable with the values reported for other Er^{3+} doped glassy systems [26, 39-47]. The JO parameters obtained in the present work suggest that different concentrations of Er^{3+} ion in ZnAlBiB glasses possess strong asymmetry and/or covalency of the RE ion sites.

3.2. Absorption Edge

An investigation on an optical absorption spectra gives very useful information about optically induced electronic transitions, energy gap and band structure of various crystalline and amorphous materials [48]. It is well known that, a material exposed for photons will absorb the energy continuously if the energy supplied is greater than the band gap energy of that material [49, 50]. Such energy absorption made by the glasses in UV-vis-NIR regions can be used to study the short-range structure of glasses which in turn gives the information of immediate surroundings of the absorbing atom [51]. Optical absorption edge is one of the important parameters used to describe solid state disordered materials and can be interpreted in terms of indirect transitions across optical band gap. According to Mott and Devis [45] the absorption coefficient is given by

$$\alpha(\upsilon) = \frac{B(h\upsilon - E_{opt})^n}{h\upsilon} \qquad (2)$$

Where n is the index number used to specify the type of transition causing the absorption and E_{opt} is the optical band gap energy. Fig 3 represents the tauc's plot indicating the variation of $(\alpha h\upsilon)^{1/2}$ with photon energy ($h\upsilon$) obtained by substituting the value n=1/2 in equation (2) corresponding to a transition. By extrapolating the linear region of the curves shown in Fig 3 at $(\alpha h\upsilon)^{1/2} = 0$, the band gap energy values for all the glasses under investigation were obtained. From Fig 3 it is observed that, the fundamental absorption edge slightly shifts toward the blue region with decreasing in Bi_2O_3 content which may be due to some structural rearrangement in glass brought by network former and modifier [52]. The optical band gap energy values for Er^{3+} ions doped ZnAlBiB glasses are found to be increasing with increase in Er^{3+} ion concentration (ZnAlBiBEr01-2.32eV, ZnAlBiBEr05-2.44eV, ZnAlBiBEr10-2.92eV and ZnAlBiBEr20-3.44

Accepted manuscript

ACCEPTED MANUSCRIPT

eV). Such results obtained for the present glasses suggests that the covalent nature of the glass matrix increases with increase in Er^{3+} ion concentration in the present titled glasses.

3.3 Visible, NIR Luminescence &Decay curve analysis:

In order to record the photoluminescence spectra, it is essential to identify the excitation bands for the prepared Er^{3+} ions doped ZnAlBiB glasses. Fig 4 shows the excitation spectra which consists of the three excitation peaks at 349 nm, 445 nm, 486 nm corresponding to the transitions $^4I_{15/2} \rightarrow {}^2G_{7/2}$, $^4I_{15/2} \rightarrow {}^4F_{3/2}$ and $^4I_{15/2} \rightarrow {}^4F_{7/2}$ respectively. Among the three excitation peaks shown in Fig.4, it is observed that $^4I_{15/2} \rightarrow {}^4F_{7/2}$ transition at 486 nm is more intense and is used to record the photoluminescence spectra for all the ZnAlBiB glasses under investigation. Such visible luminescence spectra obtained for Er^{3+} ion in the ZnAlBiB glasses under 486 nm excitation wavelength is shown in Fig 5. In general at around 488 nm excitation, the atoms excited to $^4F_{7/2}$ energy level will reach to $^4S_{3/2}$ energy level through non-radiative emission process and from there the main emission corresponds to green one due to $^4S_{3/2} \rightarrow {}^4I_{15/2}$ transition. In some cases, multiphonon relaxation from $^4S_{3/2}$ energy level populates $^4F_{9/2}$ energy level causing very weak $^4F_{9/2} \rightarrow {}^4I_{15/2}$ red emission transition [53, 54]. In the present work we have not noticed any red emission, may be all most all the atoms reaching to $^4S_{3/2}$ energy level are coming down to $^4I_{15/2}$ ground state directly through radiative emission process and none have preferred to reach to $^4F_{9/2}$ energy state through multiphonon relaxation. Moreover, the strong absorption from the glass host seen as a featureless broad absorption band at about 450 nm also may involve in the below 500 nm excitation, which may directly involve in the attenuation of green emission and other radiative channels. From Fig. 5 it can also be seen that, the intensity of the emission band increases with increase in Er^{3+} ion concentration from 0.1 to 1.0 mol % and then decreases beyond showing concentration quenching at 1 mol% of Er^{3+} ion concentration. The quenching in luminescence intensity may be due to a non-radiative energy transfer [55] mechanism. From this luminescence spectra and JO parameters obtained from the absorption spectra, the important radiative properties such as radiative transition probabilities (A_R),radiative branching ratios (β_R), stimulated emission cross sections (σ_{se}), radiative lifetime (τ_R), gain band width ($\sigma_{se} \times \Delta\lambda_P$) and optical gain parameters ($\sigma_{se} \times \tau_R$) are determined by using the relevant expressions given in our previous paper [56] and are given in Table 4. From the data presented in Table 4, it can be seen that the stimulated emission cross-sections and branching ratios values are high for

Accepted manuscript

ACCEPTED MANUSCRIPT

ZnAlBiBEr10 glass suggesting that ZnAlBiBEr10 glass is quite suitable to act as a good luminescent device in visible green region (535 nm).

The near infrared (NIR) luminescence spectra of Er^{3+} doped ZnAlBiB glasses have been recorded by using 980 nm diode laser and are shown in Fig 6. The NIR luminescence spectra show a strong emission peak at 1530 nm corresponding to the transition $^4I_{13/2} \rightarrow {}^4I_{15/2}$.The intensity of this emission transition increases with increase in Er^{3+} ion concentration up to 1 mol% and then decreases beyond. To have a comprehensive picture on the emission characteristics of the Er^{3+} ions in in ZnAlBiB glasses, we have evaluated the important radiative parameters such as full width at half maxima (FWHM) ($\Delta\lambda_p$), stimulated emission cross-section (σ_{se}), gain band width ($\Delta\lambda_p$x σ_{se}) and optical gain parameters (τ_R x σ_{se}) [57] and are given in Table 5. Large values of FWHM are very much useful in optical fiber amplifiers to enhance the number of possible optical channels that can be multiplexed without the usage of any gain compensation technique in WDM systems [58]. The product of full width at half maxima and stimulated emission cross section (FWHM x σ_{se}) is often used to calculate the bandwidth of optical fiber amplifier [59]. From Table 5 it is observed that among all the titled glasses, the ZnAlBiBEr10 glass possesses maximum values for all these parameters. The stimulated emission cross-section and gain band width values of ZnAlBiBEr10 glass are comparable to the other reported glass hosts [24, 47, 60-64].

In order to understand the 1.50 μm emission property, the absorption and emission cross-sections were also measured. These cross-sections tell us about the ability of the doped rare earth ions to absorb or emit light. It is well known that large stimulated emission cross-section gives high gain coefficient with low threshold energy needed for effective pumping action in lasers. Thus, in order to have a host aptly suitable for lasing action and optical fiber amplification, it is necessary to enhance the emission cross-section as high as possible [65]. The absorption and emission cross-sections of ZnAlBiBEr10 glass has been calculated from the absorption spectrum and McCumber theory [66]. Fig 7 shows the absorption and emission cross-sections of ZnAlBiBEr10 glass. The absorption cross-sections of $^4I_{15/2} \rightarrow {}^4I_{13/2}$ transition have been evaluated from the absorption spectrum using the following expression

$$\sigma_a(\lambda) = \frac{2.303\ \mathrm{OD}(\lambda)}{Nl} \quad (3)$$

Accepted manuscript

ACCEPTED MANUSCRIPT

Where OD (λ), N, l represents the optical density (obtained from the absorption spectrum), Er^{3+} doping concentration and sample thickness, respectively. The stimulated emission cross-section of $^4I_{13/2} \rightarrow {}^4I_{15/2}$ transition is calculated using the equation given by McCumber theory [66].

$$\sigma_e(\lambda) = \sigma_a(\lambda) exp^{\frac{(\varepsilon - h\upsilon)}{KT}} (4)$$

Where ε is the net free energy required to excite Er^{3+} from $^4I_{15/2}$ to $^4I_{13/2}$ state at temperature T. It can be calculated by the simplified procedure provided in Ref [67]. $\sigma_a(\lambda)$and $\sigma_e(\lambda)$are absorption and emission cross-sections respectively, h is the Planck constant, K the Boltzmann constant and υ is the phonon frequency. The emission and absorption cross-sections shown in Fig.7 are in consistent with the figures reported in literature [68-70]. Our intension behind drawing Fig. 7 is just to know the trends and shapes of absorption and emission cross-sections and to compare the emission cross-section obtained from McCumber theory with that of the JO theory. The calculated peak emission cross-section for ZnAlBiBEr10 glass is 10.417 X 10^{-22} cm^2 from the MCcumber theory is in good agreement with the emission cross-section calculated from JO theory (11.4 x 10^{-22} cm^2). Hence this glass can be used for optical fiber amplification.

The transient photoluminescence behaviour of $^4I_{13/2} \rightarrow {}^4I_{15/2}$ emission transition measured for Er^{3+} ions in ZnAlBiB glasses is shown in Fig 8. From Fig 8, It is interesting to see that the photoluminescence decay of $^4I_{13/2}$ level is found to be single exponential in nature for all the glasses studied irrespective of the Er^{3+} ion concentration. The effective decay time (τ_{eff}), which is also called as experimental lifetime (τ_{exp}) has been evaluated from the recorded decay profiles using the following expression [71]

$$\tau_{eff} = \tau_{exp} = \frac{\int tI(t)dt}{\int I(t)dt} \qquad (5)$$

The obtained experimental lifetime (τ_{exp}) values are given in Table 5. In general, the lifetime of $^4I_{13/2}$ level of Er^{3+} ion is strongly influenced by both radiative and non-radiative emission processes. In the present investigation the experimental lifetime (τ_{exp}) values measured from decay curves are found to be smaller than the radiative lifetimes (τ_{rad}) obtained from JO analysis. The smaller values obtained for experimental lifetimes for the present glasses indicate that the relaxation mechanism from $^4I_{13/2}$ level is a combination of both radiative and non-radiative emission processes. The decrease in measured lifetimes with increase in Er^{3+} ion concentration in the present study may be attributed to the energy transfer among the neighbouring Er^{3+} ions and

Accepted manuscript

ACCEPTED MANUSCRIPT

also energy transfer from Er^{3+} ions to quenching centers like OH - groups [36, 72]. The Quantum efficiency (η) of $^4I_{13/2}$ level can be estimated by using the following relation, and are given in Table 5.

$$\eta = \frac{\tau_{exp}}{\tau_{rad}} \times 100 \qquad (6)$$

From Table 5 it can be observed that, among all the Er^{3+} doped ZnAlBiB glasses, ZnAlBiBEr10glass possess highest values of stimulated emission cross-section, gain parameters and quantum efficiency values for the transition $^4I_{13/2} \rightarrow {}^4I_{15/2}$ (1530 nm). Hence ZnAlBiBEr10 glass can be suggested as a good host to generate efficient lasing action at 1530 nm and also highly useful for optical fibre amplification.

3.4 Up-Conversion Luminescence Spectral analysis:

Fig 9 shows the up-conversion luminescence spectra of Er^{3+} ions doped ZnAlBiB glasses under 980 nm laser excitation. The up-conversion luminescence spectra consist of two intense luminescence bands at 543 nm (green region) and 656 nm (red region) corresponding to the transitions $^4S_{3/2} \rightarrow {}^4I_{15/2}$ and $^4F_{9/2} \rightarrow {}^4I_{15/2}$ respectively. Among the two emission bands, a band observed in red region is more intense than green region. The intensity of this red band ($^4F_{9/2} \rightarrow {}^4I_{15/2}$) increases with increase in the concentration of Er^{3+} ions up to 1 mol% and then decreases beyond showing the concentration quenching. The possible up-conversion mechanism for the observed emission bands can be clearly understood from the energy levels diagram of ZnAlBiBEr10 glass shown in Fig 10. The mechanism of up-conversion observed in the present Er^{3+} ions doped ZnAlBiB glasses can be explained as follows.

Generally, in up-conversion phenomenon, two photon processes populates the atoms from ground state to the desired higher energy levels. Initially under 980 nm laser excitation, Er^{3+} ions reaches to the $^4I_{11/2}$ excited state from $^4I_{15/2}$ ground state through the ground state absorption (GSA) mechanism [73].

Ground state absorption (GSA): $^4I_{15/2}$ (Er^{3+} ion) + hν (a photon) → $^4I_{11/2}$ (Er^{3+} ion)

From $^4I_{11/2}$ level the same ions by absorbing a second photon will move to $^4F_{7/2}$ level by excited state absorption (ESA) and Energy transfer (ET) which can be represented by the simple processes as follows [73]

Excited State Absorption (ESA): $^4I_{11/2}$ (Er^{3+} ion) + hν (a photon) → $^4F_{7/2}$ (Er^{3+} ion)

Energy Transfer (ET): $^4I_{11/2}$ (Er^{3+} ion) + $^4I_{11/2}$ (Er^{3+} ion) → $^4F_{7/2}$ (Er^{3+} ion) + $^4I_{15/2}$ (Er^{3+} ion)

Accepted manuscript

ACCEPTED MANUSCRIPT

Simultaneously Er^{3+} ion at $^4F_{7/2}$ level decays very rapidly to $^4S_{3/2}$ level through non radiative (NR) decay process and thereby $^4S_{3/2} \rightarrow {}^4I_{15/2}$ transition emits an intense green up-conversion at 543 nm [73].

For the 656 nm red emission, Er^{3+} ions are excited to $^4I_{11/2}$ state through the GSA and energy transfer (ET) between adjacent Er^{3+} ions under 980 nm excitation. The populated Er^{3+} ions from $^4I_{11/2}$ state then decays to the long-living $^4I_{13/2}$ state via multi-phonon relaxation (MPR) and ultimately excited to the $^4F_{9/2}$ state by one of the following processes [73].

Multi-Phonon Relaxation: $^4I_{13/2}$ (Er^{3+} ion) + hν (a photon) → $^4F_{9/2}$ (Er^{3+} ion)

Energy Transfer: $^4I_{13/2}$ (Er^{3+} ion) + $^4I_{13/2}$ (Er^{3+} ion) → $^4I_{15/2}$ (Er^{3+} ion) + $^4F_{9/2}$ (Er^{3+} ion)

Finally, the $^4F_{9/2} \rightarrow {}^4I_{15/2}$ transition gives bright red colour emission at 656 nm.

Table 6 gives the information pertaining to several important radiative properties such as peak wavelength, FWHM, stimulated emission cross-section, gain band widths and optical gain parameters evaluated from the up-conversion luminescence spectra. From Table 6 it is observed that among all the Er^{3+}ions doped ZnAlBiB glasses investigated in the present work, the ZnAlBiBEr10 glass possess highest stimulated emission cross-section, gain band width and optical gain parameters for the transition $^4F_{9/2} \rightarrow {}^4I_{15/2}$ (656 nm) in bright red region. Hence ZnAlBiBEr10 glass can be suggested as a good host for giving up-conversion luminescence in the red region corresponding to the transition $^4F_{9/2} \rightarrow {}^4I_{15/2}$ at 656 nm under 980 nm laser excitation. It is interesting to see that the green up-conversion emission observed (543 nm) under 980 nm laser excitation is in close agreement with the visible green emission observed (535 nm) under 486 nm excitation. It is a known fact that the up-conversion mechanism being a nonlinear phenomenon, involves several non-radiative transitions as shown in Fig. 10 than the down conversion emission. This may cause the minor difference in the green emission band positions and their relative intensities observed in both visible emission and up-conversion spectra.

Accepted manuscript

4. Conclusion

In the present study, Zinc Alumino Bismuth Borate (ZnAlBiB) glasses doped with different concentrations of Er^{3+} ions were prepared and characterized for their effective usage in different regions of the electromagnetic spectrum using luminescence spectral studies. The visible luminescence under 486 nm excitation wavelength has shown one emission band at 535 nm corresponding to the transition $^4S_{3/2} \rightarrow {}^4I_{15/2}$, for which the luminescent parameters such as

ACCEPTED MANUSCRIPT

branching ratio, stimulated emission cross-section and optical gain parameters have been evaluated and found to be maximum for ZnAlBiBEr10 glass. Hence ZnAlBiBEr10 glass can be suggested as good optical material to emit green luminescence. The NIR photoluminescence spectra recorded under 980 nm laser excitation show one broad peak at 1530 nm corresponding to the transition $^4I_{13/2} \rightarrow {}^4I_{15/2}$ for which the luminescent parameters have been evaluated and found to be maximum for ZnAlBiBEr10 glass. The nearly broad and flat nature of 1530 nm NIR emission and the other favourable radiative optical properties possessed by ZnAlBiBEr10 glass suggests the possibility of using this glass for broadband optical fiber amplification applications. The up-conversion luminescence under 980 nm laser excitation gives two emission bands, one in green (543 nm) and the other one in red (656 nm) regions corresponding to the transitions $^4S_{3/2} \rightarrow {}^4I_{15/2}$ and $^4F_{9/2} \rightarrow {}^4I_{15/2}$ respectively. Among these two, a transition observed in red region found to be more intense than green and the luminescent parameters for this transition also found to be highest for ZnAlBiBEr10 glass. Hence this glass can be suggested as a suitable material for visible up-conversion laser applications. Our systematic spectroscopic analysis on Er^{3+} doped ZnAlBiB glasses allows us to contemplate that these glasses are potential candidates for luminescent applications in different regions of the electromagnetic spectrum. Especially, ZnAlBiB glass doped with 1mol% of Er^{3+} ions can act as an efficient luminescent device among all the glasses studied in visible and NIR regions. The same glass can also acts as good up-converting luminescent device under 980 nm laser excitation.

Accepted manuscript

Acknowledgements

Two of the authors Swapna Koneru (File No: SR/WOS-A/PS-35/2011) and Mahamuda Shaik (SR/WOS-A/PS-53/2011) are highly grateful to the Department of Science and Technology (DST), Govt. of India,, New Delhi for the financial support given to them under DST/WOS-A scheme. This work is also partly supported by High-impact Research initiative of IIT-Delhi, UK-India Education Research Initiative (UKIERI) and DST, Govt. of India, New Delhi.

References

[1] Shiqing Xu, Zhongmin yang, Junjie Zhang, Guonian Wang, Shixun Dai, Lili Hu, Zhonghong Jiang, Chem. Phys. Lett. 385 (2004) 263-267.

[2] W. J. Miniscalco, M. J. F Digonnet Ed, Marcel Dekker, New York (2001) pp. 17-112.

ACCEPTED MANUSCRIPT

[3] H. Lin, X. Y. Wang , L. Lin, C. Li, D. Yang, S. Tanabe , J. Phys. D: Appl. Phys. 40 (2007) 3567-3572.

[4] Y. Z. Li, Q.Y. Zhang, D. M. Shi, Q. Qian, S. H. Xu, Opt. Mater.32 (2009) 334-338.

[5] B. J. Chen, G. C. Righini, M. Bettinelli, A. Speghini, J. Non-Cryst. Solids 322 (2003) 319-323.

[6] C. Zhao, G.F. Yang, Q. Y. Zhang, Z. H. Jiang, J. Alloys. Compd. 461 (2008) 617-622.

[7] M. Sreenivasulu, A. S. Rao, J. Mater. Sci. Lett. 20(8) (2001) 737-740.

[8] L. R. Moorthy, T. S. Rao, K. Janarthanam, A. S. Rao, Y. Subramanyan, Opt. Mater. 12 (4) (1999) 459-465.

[9] Sk. Mahamuda, K. Swapna, P. Pakiyaraj, A. Srinivasa Rao, G. Vijaya Prakash, J. Lumin. 153 (2014) 382-392.

[10] P. Becker, Adv. Mater. 10 (1998) 979-992.

[11] D. Rajesh, Y. C. Ratnakaram, M. Seshadri, A. Balakrishna, T. Satya Krishna, J. Lumin, 132 (2012) 841-849.

[12] K.Swapna, Sk. Mahamuda, A. Srinivasa Rao, T. Sasikala, L. Rama Moorthy, J. Lumin 146 (2014) 288-294.

[13] D. W. Hall, M. A. Newhouse, N. F. Borelli, W. H. Dumbaugh, D. L. Weidman, Appl. Phys. Lett. 54 (1989) 1293-1295.

[14] C. Stehle, C. Vira, D. Hogan, S. Feller, M. Affatigato, Phys. Chem. Glasses 39 (21) (1998) 83-86.

[15] Sk. Mahamuda, K. Swapna, A. Srinivasa Rao, M. Jayasimhadri, T. Sasikala, K. Pavani, L. Rama Moorthy, J. Phys. Chem. Solids 74 (2013) 1308 – 1315.

[16] K. Arai, H. Namikawa, K. Kumata, T. Honda, Y. Ishii, T. Handa, J. Appl. Phys. 59 (1986) 3430-3436.

[17] Sk. Mahamuda, K. Swapna, A. Srinivasa Rao, T. Sasikala, L.Rama Moorthy, Physica B 428 (2013) 36-42.

[18] S. Sen and J. F. Stebbins: J. Non-Cryst. Solids 188 (1995) 54-62.

[19] K. Swapna, Sk. Mahamuda, A. Srinivasa Rao, M. Jayasimhadri, T. Sasikala, L. Rama Moorthy, Ceramic Int. 39(7) (2013)8459-8465.

[20] H. Weller, Angew. Chem., Int. Ed. Engl. 32 (1993) 41-53.

Accepted manuscript

ACCEPTED MANUSCRIPT

[21] K. Swapna, Sk. Mahamuda, A. Srinivasa Rao, M. Jayasimhadri, T. Sasikala, L. Rama Moorthy, J. Lumin.139 (2013) 119–124

[22] K. Swapna, Sk. Mahamuda, A. Srinivasa Rao, T. Sasikala, L. Rama Moorthy, J. Lumin 146 (2014)288-294

[23] Sk. Mahamuda , K. Swapna, P. Packiyaraj, A. Srinivasa Rao, G. Vijaya Prakash, Opt. Mater. 36 (2013) 362–371

[24] K. Swapna, Sk. Mahamuda, A. Srinivasa Rao, T. Sasikala, P. Packiyaraj, L. Rama Moorthy, G. Vijaya Prakash, J. Lumin.156 (2014)80–86

[25] K. Swapna, Sk. Mahamuda, A. Srinivasa Rao, M. Jayasimhadri, Suman Shakya, G. Vijaya Prakash , J. Lumin. 156 (2014)180–187

[26] L. R. Moorthy, M. Jayasimhadri, S. A. Saleem, D. V. R. Murthy, J. Non-Cryst. Solids 353 (2007) 1392 -1396.

[27] Q. Qiah, C. Zhao, G. F. Yang, Z. M. Yang, Q. Y. Hang, Z. H. Jiang, Spectro. Chim. Acta part A 71 (2008) 280-285.

[28] C. J. da Silva, M. T. de Araujo, Opt. Mater. 22 (2003) 275-282.

[29] M. Takahashi, M. Shojiya, R. Kanno, Y. Kawamoto, K. Kadono, T. Ohtsuki, N. Peyghambarian, J. Appl. Phys. 81 (1997) 2940-2945.

[30] A. J. Kenyon, Progr. Quant. Elect. 26 (2002) 225-284.

[31] M.Venkateswarlu, M.V.V.K.S.Prasad, K.Swapna, Sk.Mahamuda, A.Srinivasa Rao, A.Mohan Babu, D.Haranath, Ceramics International 40(4) (2014) 6261-6269.

[32] A. S. Rao, Y. N. Ahammed, R. R. Reddy, T.V.R. Rao, Opt. Mater. 10 (1998) 245-252.

[33] W.T. Carnall, P.R. Fields, K. Rajnak, J. Chem. Phys. 49 (1968) 4424-4442.

[34] B. R. Judd, C. K. Jorgensen Mol. phys. 8 (1964) 281-290.

[35] G. S. Ofelt, J. Chem. Phys 37 (1962) 511-520.

[36] H. Desirena, E.D. la Rosa, L. A. Diaz-Torres, G. A. Kumar, Opt. Mater. 28 (2006) 560-568.

[37] P. Nachimuthu, R. Jagannathan, J. Am. Ceram. Soc. 82 (1999) 387-392.

[38] R. Reisfield, C. K. Jorgensen, Lasers and excited states of Rare-earths, Springer Verlag NY, 1975.

[39] J. Azevedo, J. Coelho, G. Hungerford, N. Sooraj Hussain, Physics B 405 (2010) 4696 - 4701.

Accepted manuscript

ACCEPTED MANUSCRIPT

[40] N. Sooraj Hussain, G. Hunger ford, R. El-Mallawany, M. J. M. Gomes, M. A. Lopes, N. Ali, J. D. Santos, S. Buddhudu, J. NanoSci, Nanotechnol. 9(6) (2009) 3672-3677.

[41] Tao Wei, Fangze Chen, Ying Tian, Shiqing XU, Opt. Com 315 (2014) 199-203.

[42] Y. Tian, R. Xu, L. Zhang, L. Hu, J. Zhang Opt. Lett. 36 (2011) 109-111.

[43] Y. Tian, R. XU, L. HU, J. Zhang, Opt. Mater 34 (2011) 308-312.

[44] M. Hamzaoui, M. T. Soltani, M. Baazouzi, B. Tioua, Z.G. Ivanova, R. Lebullenger, M. Poulain, J. Zavadil, J. Phys. Staus Solids B (2012) 1-9.

[45] H. Takebe, Y. Nageno, K. Morianga, J. Am. Ceram. Soc 78 (1992) 1161-1164.

[46] J. Yang, S. Dai, N. Dai, L. Wen, L. Hu, Z. Jiang, J. Lumin 101 (2004) 9-14.

[47] D. Ramachari, L. Rama Moorthy, C. K. Jayasankar, Opt. Mater. 36 (2014) 823- 828.

[48] Altaf, M. Chaudhry M. A, Maria Z, J. Res. Sci 2003, 14, 253-259.

[49] Abd El-Ati M. I, Higazy A. A, J. Mater. Sci. 2000, 35, 6175- 6180.

[50] L. R. Moorthy, M. Jayasimhadri, S.A. Saleem, D.V. R. Murthy, J. Non. Cryst. Solids. 353 (2005) 1392-1396.

[51] X. L. Zou, T. Izumitani, J. Non-Cryst. Solids 162 (1993) 68–80.

[52] Y. Gangfeng, L. Tao, J. Rare Earths 26 (2008) 924–927.

[53] K.Linganna, M.Rathaiah, N.Vijaya, Ch.Basavapoornima, C.K.Jayasankar, S.Ju, W.T.Han, V.Venkatramu. Ceramic Int. (2015) (In Press)

[54] N.Vijaya, P.Babu, N.Venkatramu, C.K.Jayasankar, S.F.Leon-Luis, U.R.Rodriguez-Mendoza, I.R.Martin, V.Lavin, Sensors and Actuators B: Chemical 186(2013)156-164.

[55] P. Nandi, G. Jose, Physica B 381 (2006) 66–72.

[56] Y. G. Choi, K. H. Kim, J. Heo, J. Am. Ceram. Soc. 82 (1999) 2762–2768.

[57] M. Liao, L. Hu, Z. Duan, L. Zhang, L. Wen, Appl. Phys B 86 (2007) 83–89.

[58] G. A. Kumar, J. Thomas, N. George, N.V. Unni krishnan, P. Radha krishnan, V.P.N. Nampoori, C. P. G. Vallabhan, J. Mater. Sci. 35 (2000) 2539–2542.

[59] Doremus, H. R. Glass Science, 2nd ed.; Wiley: New York, NY, USA, 1994.

[60] R. P. Sreekanth Chakradhar, K. P. Ramesh, J. L. Rao, J. Rama Krishna , J. Phys. Chem. Solids 64 (2003) 641-650.

[61] N. Jaba, H. Ben Mansour, A. Kanoun, A. Brenier, B. Champagnon, J. Lumin. 129 (2009) 270-276.

[62] J. Yang, S. Dai, Y. Zhou, J. Appl. Phys. 93 (2003) 977-983.

Accepted manuscript

ACCEPTED MANUSCRIPT

[63] R. Balda, R. I Merino, J. I Pena, V. M. Orera, M. A. Arriandiaga, J. Fernandez, Opt. Mater. 31 (2009) 1105-1108.

[64] J. Yang, S. Dai, Y. Zhou, L. Wen, L. Hu, Z. Jiang, J. Appl. Phys. 9 (2003) 977- 983.

[65] H. Desirena, E. De la Rosa, V. H. Romero, J. F. Castillo, L. A. Diaz-Torres, J. R. Oliva, J. Lumin. 132 (2012) 391-397.

[66] D. E. MCcumber, Phys. Rev 136 (1964) 954-957.

[67] W. J. Miniscalco, R. S. Quimby, Opt. Lett. 16 (1991) 258-260.

[68] G. Bilir, G. Ozen, D. Tatar, M.L. Öveçoğlu, Opt.Comm. 284 (2011) 863-868.

[69] P. Babu, Hyo Jin Seo, C. R. Kesavulu, Kyoung Hyuk Jang, C. K. Jayasankar, J. Lumin. 129 (2009) 444-448.

[70] I. Jlassi, H. Elhouichet, M. Ferid, R. Chtourou, M. Queslati, Opt. Mater. 32 (2010) 743-747.

[71] C.C. Santos, I. Guedes, C. K. Loong, L. A. Boatner, A. L. Moura, M. T.D Araujo, C. Jacinto, M. V. D. Vermelho, J.Phys.D: Appl. Phys. 43 (2010) 025102-025109.

[72] Y. Yan, A. J. Faber, H. de Waal, J. Non-Cryst. Solids 181 (1995) 283-290.

[73] D. M. Shi, Y. G. Zhao, X. F. Wang, Physica B 406 (2011) 2588-2593.

Accepted manuscript

ACCEPTED MANUSCRIPT

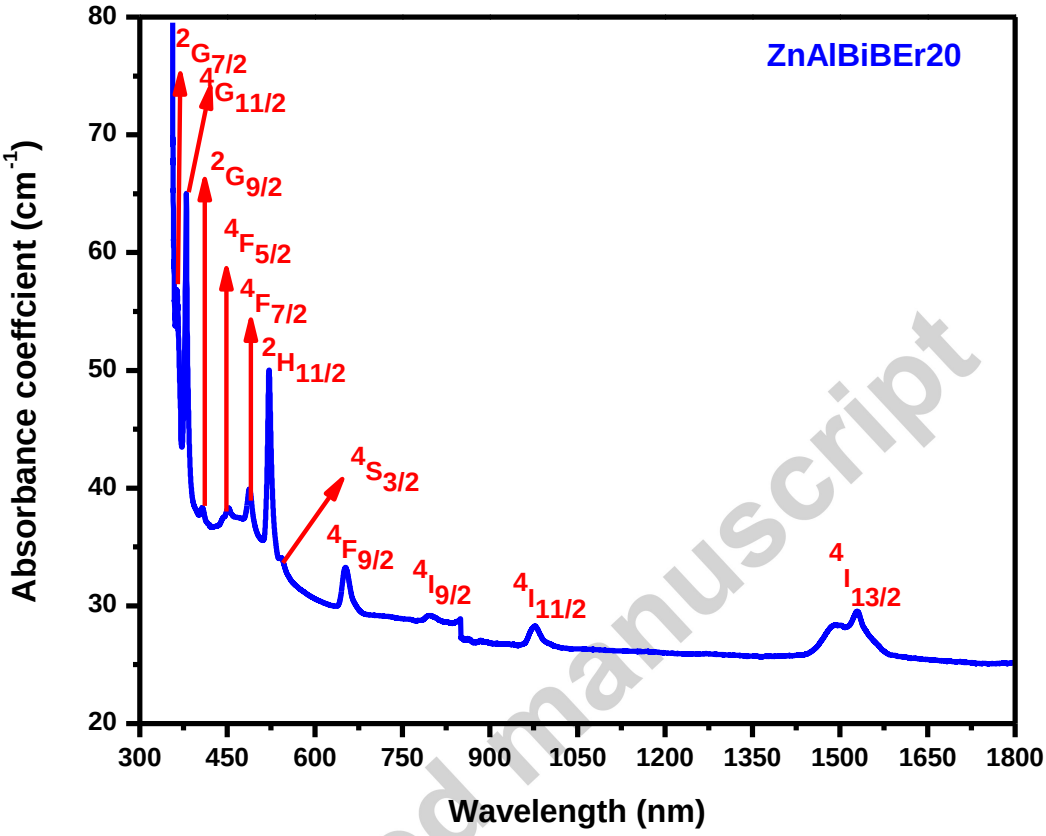

Fig 1: UV-vis-NIR absorption spectrum of ZnAlBiBEr20 glass.

Accepted manuscript

ACCEPTED MANUSCRIPT

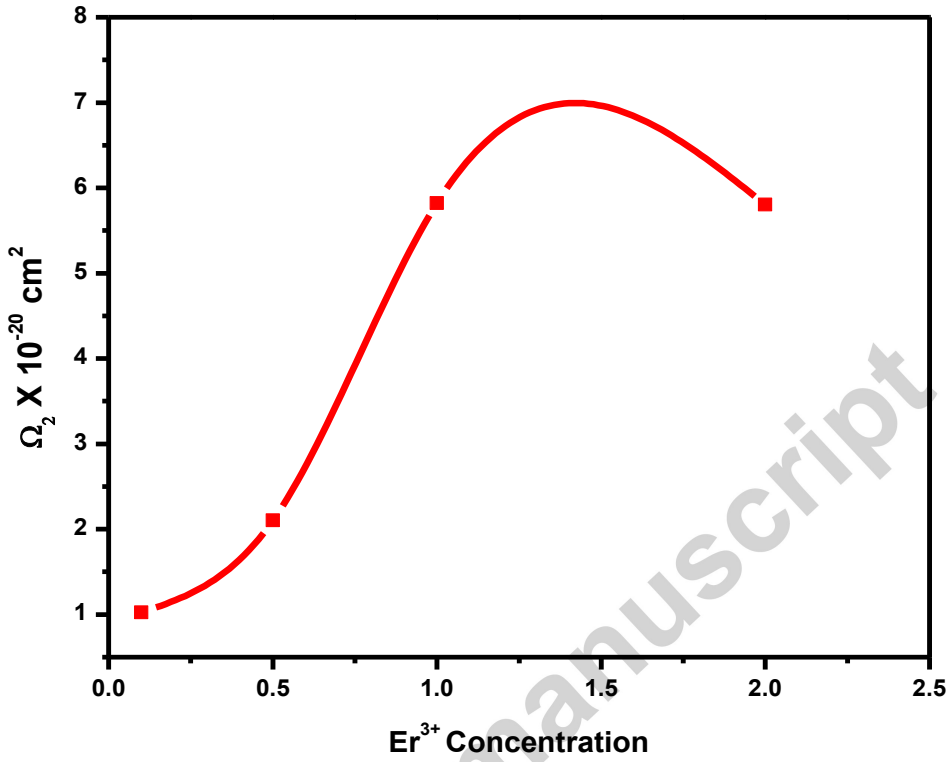

Fig 2: Variation of Ω_2 with respect to the Er^{3+} ion concentration in ZnAlBiB glasses.

Accepted manuscript

ACCEPTED MANUSCRIPT

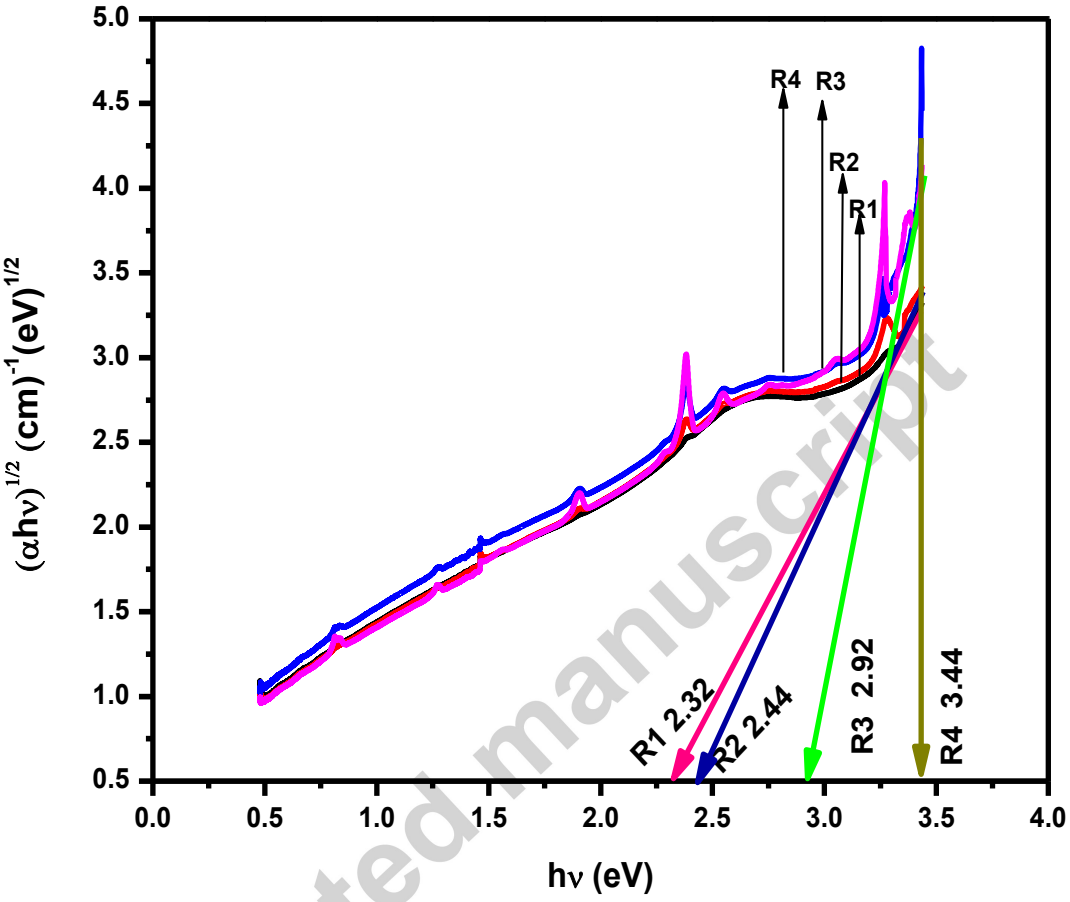

Accepted manuscript

Fig 3: Variation of $(\alpha h\upsilon)^{1/2}$ with photon energy ($h\upsilon$) in Er^{3+} ions in ZnAlBiB glasses.

ACCEPTED MANUSCRIPT

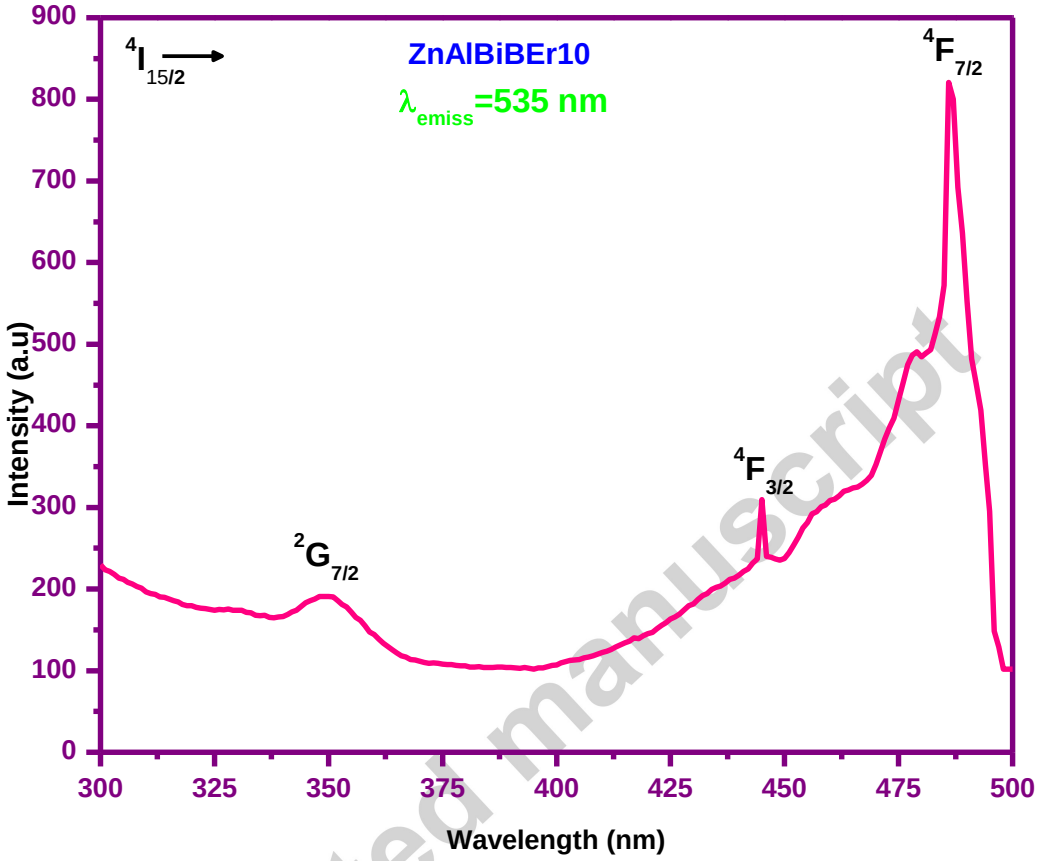

Fig 4: PL excitation spectrum of Er^{3+} ions in ZnAlBiBEr10 glass.

Accepted manuscript

ACCEPTED MANUSCRIPT

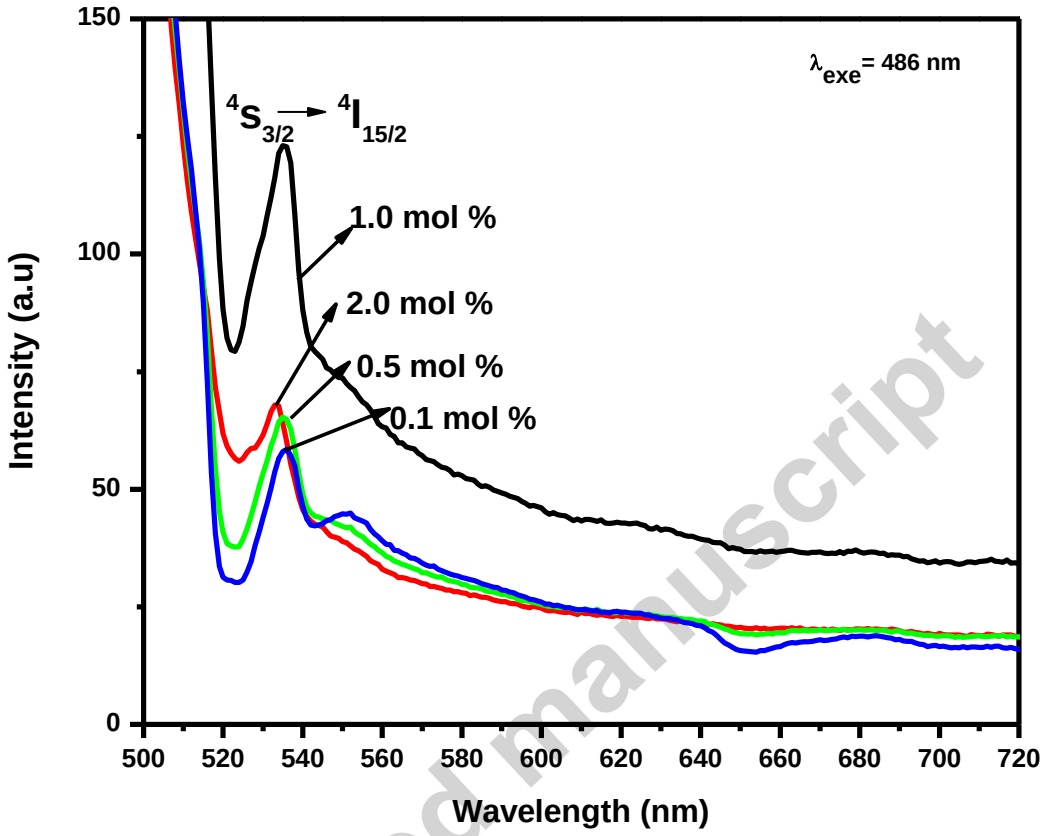

Fig 5: PL Emission Spectra of Er^{3+} ions in ZnAlBiB glasses.

Accepted manuscript

ACCEPTED MANUSCRIPT

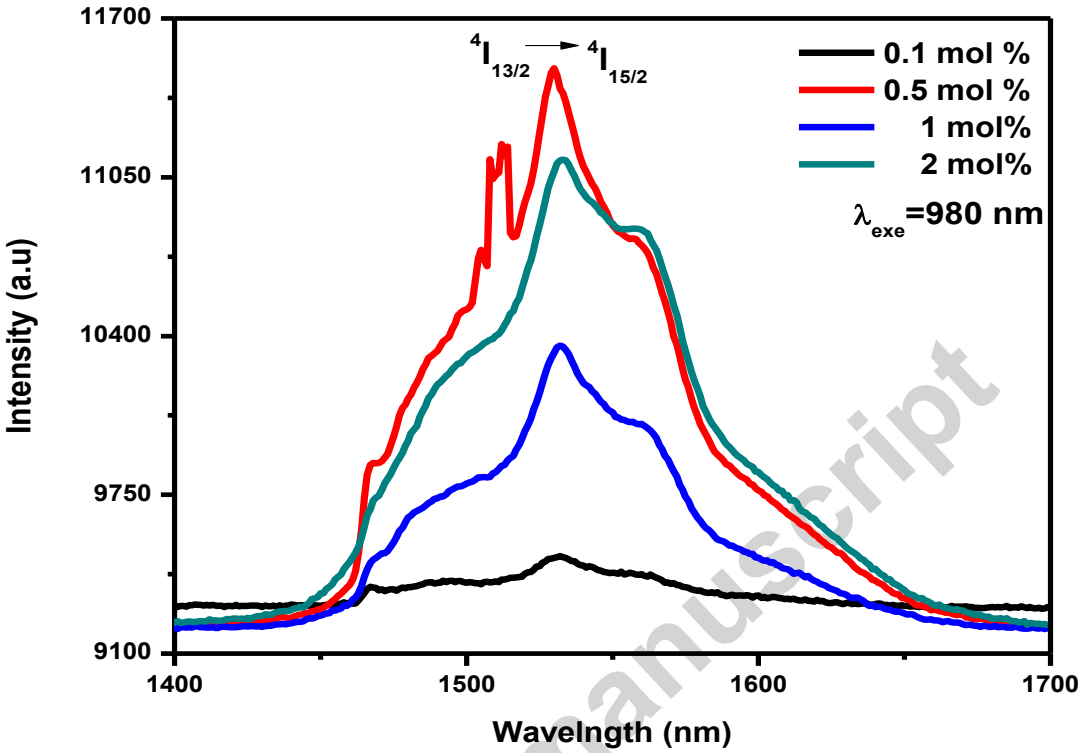

Fig 6: NIR fluorescence spectra of Er^{3+} ions in ZnAlBiB glasses.

Accepted manuscript

ACCEPTED MANUSCRIPT

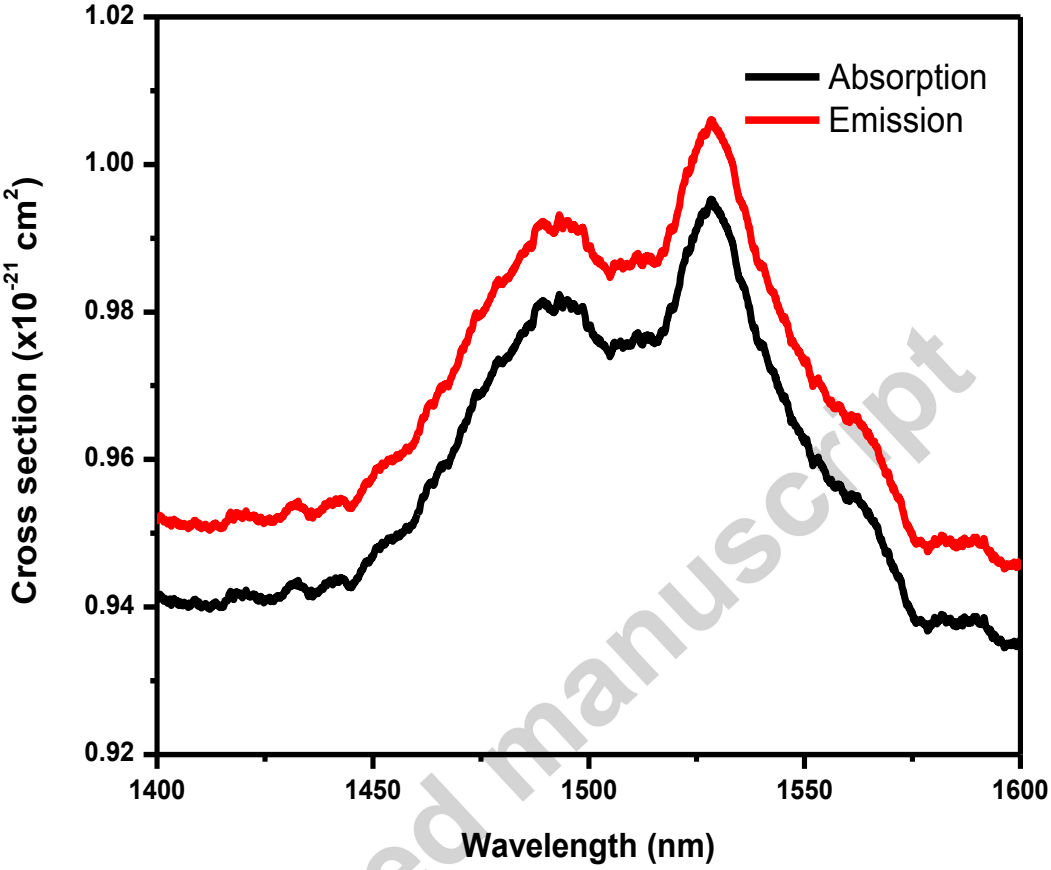

Fig 7: Absorption and emission cross-sections of ZnAlBiBEr10 glass.

Accepted manuscript

ACCEPTED MANUSCRIPT

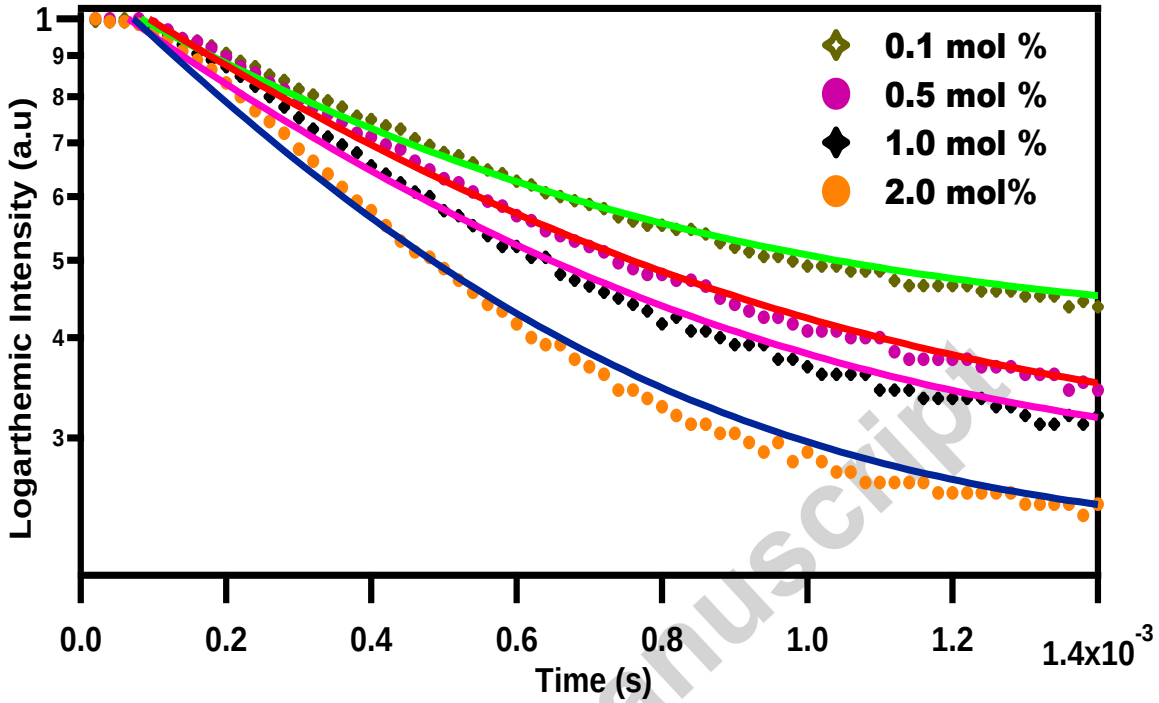

Fig 8: Decay curves of $^4I_{13/2} \rightarrow {}^4I_{15/2}$ (1530 nm) emission transition of Er^{3+} ions in ZnAlBiB glasses under 980 nm Laser excitation.

Accepted manuscript

ACCEPTED MANUSCRIPT

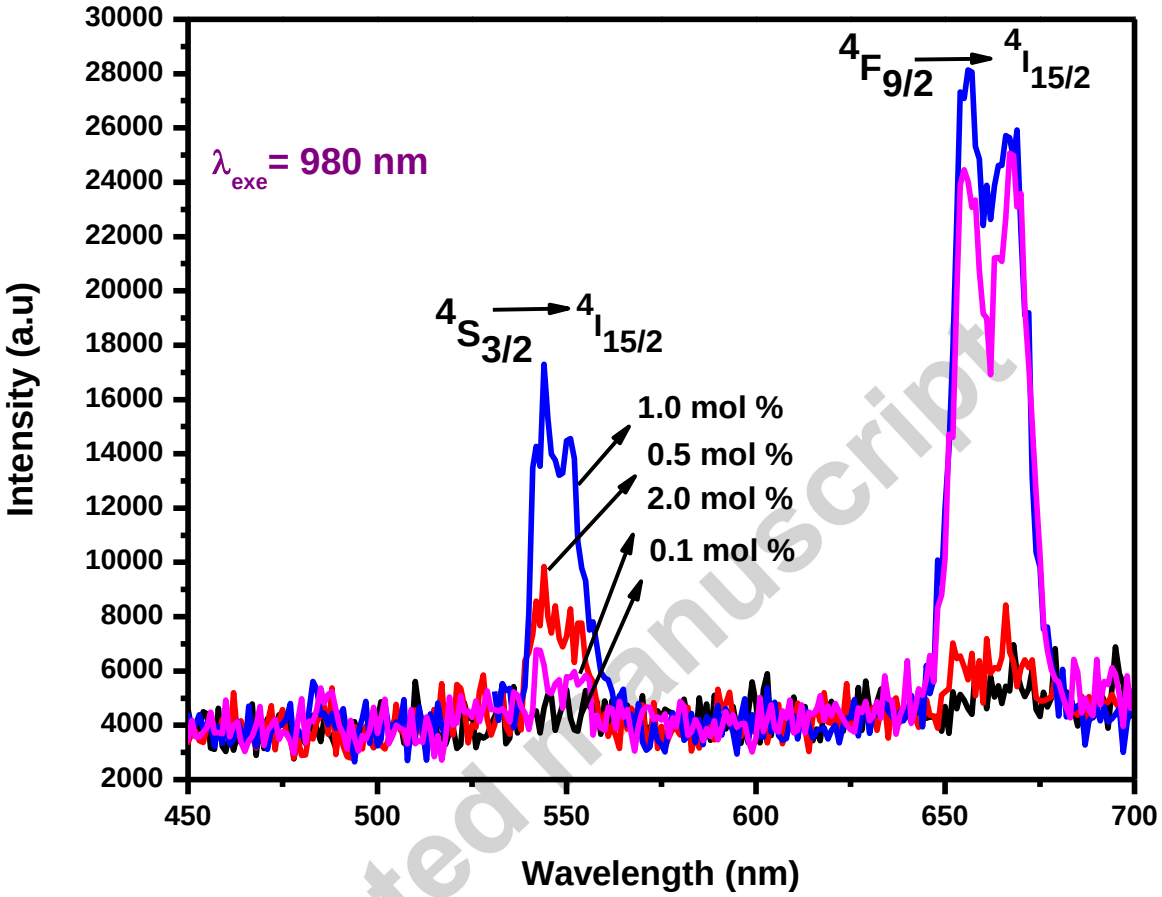

Fig 9: Up-conversion emission spectra of Er^{3+} ions in ZnAlBiB glasses.

Accepted manuscript

ACCEPTED MANUSCRIPT

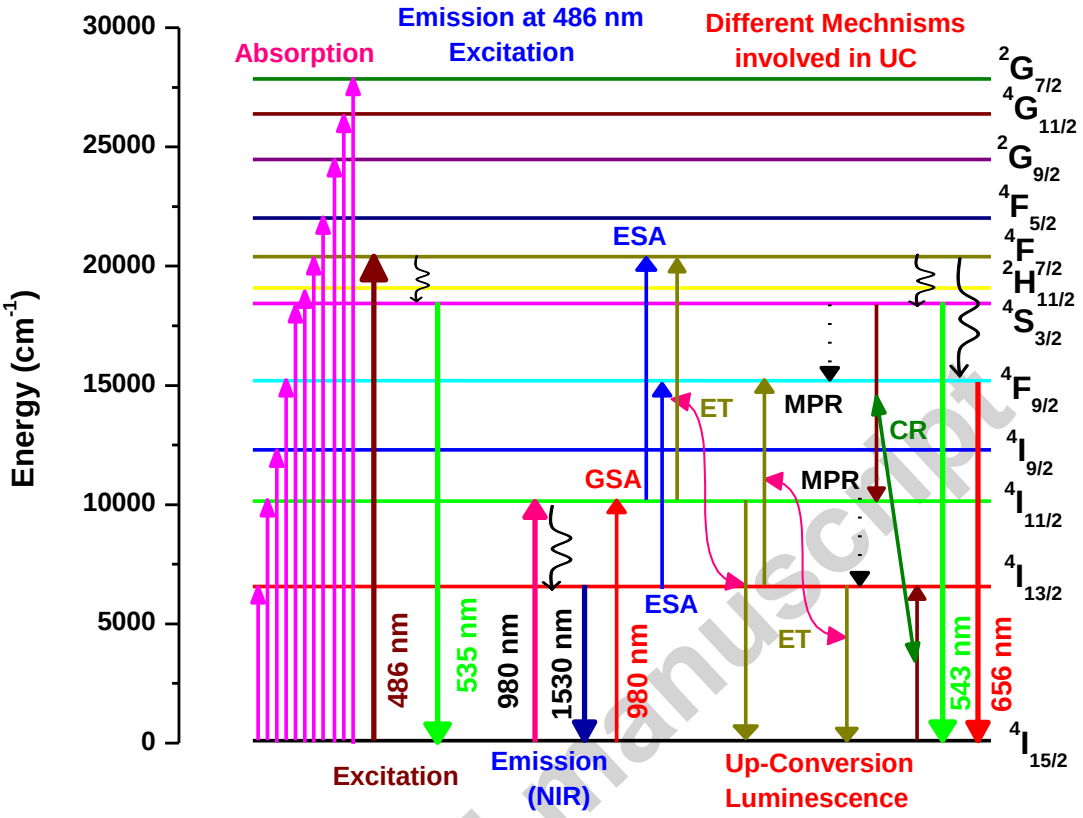

Fig 10:Energy level diagram of ZnAlBiBEr10 glass showing the mechanism of absorption, excitation, emission under 486 nm excitation and up-conversion emission under 980 nm laser excitation.

Table 1:

Physical properties of Er^{3+}ions in ZnAlBiB Glasses

Physical properties	**ZnAlBiBEr01**	**ZnAlBiBEr05**	**ZnAlBiBEr10**	**ZnAlBiBEr20**
Refractive index (n_d)	1.821	1.819	1.816	1.811
Density (d) (g/cc)	3.906	3.905	3.904	3.901
Average molecular weight ($\bar{M}$)(g)	114.7	114.4	114.4	114.0

Accepted Manuscript

ACCEPTED MANUSCRIPT

Er^{3+} ion concentration (x10^{22} ions/cm^3)	0.205	1.027	2.054	4.122
Mean atomic Volume (g/cm^3/atom)	6.676	6.658	6.660	6.640
Dielectric Constant (ϵ)	3.316	3.308	3.297	3.279

Transition	**Wave number**	**ZnAlBiBEr01**	**ZnAlBiBEr05**	**ZnAlBiBEr10**	**ZnAlBiBEr20**
Optical Dielectric constant ($\epsilon - 1$)		2.316	2.308	2.297	2.279
Reflection losses (R %)		0.084	0.084	0.083	0.083
Molar Refraction (R_m)(cm^{-3})		12.79	12.74	12.71	12.61
Polaron radius (r_p) (Å)		3.224	1.885	1.496	1.187
Interionic distance (r_i) (Å)		8.001	4.677	3.714	2.945
Molar electronic polarizability α (x$10^{-3}cm^3$)		5.075	1.010	0.504	0.250
Field Strength (x $10^{15}cm^{-2}$)		2.884	8.441	13.39	21.28
Optical basicity (Λ_{th})		0.438	0.439	0.441	0.445

Accepted manuscript

Table 2:

Experimental (f_{exp}) (x 10^{-06}) and calculated oscillator strength (f_{cal}) (x 10^{-06}) of Er^{3+}ions in ZnAlBiB glasses.

ACCEPTED MANUSCRIPT

		f_{exp}	f_{cal}	f_{exp}	f_{cal}	f_{exp}	f_{cal}	f_{exp}	f_{cal}
$^4I_{13/2}$	6535	-	-	1.800	1.734	2.310	2.196	2.170	2.047
$^4I_{11/2}$	10121	-	-	0.836	0.741	0.962	0.987	0.911	0.934
$^4I_{9/2}$	12515	0.210	0.193	0.31	0.409	0.491	0.755	0.369	0.674
$^4F_{9/2}$	15337	1.240	1.242	2.772	2.658	3.220	4.172	3.200	3.780
$^4S_{3/2}$	18484	0.251	0.315	0.295	0.684	0.386	0.810	0.364	0.757
$^2H_{11/2}$	19193	2.44	2.445	5.62	5.074	10.00	12.29	9.180	11.91
$^4F_{7/2}$	20491	1.18	1.245	2.22	2.691	2.880	3.560	2.620	3.283
$^4F_{5/2}$	21929	0.578	0.377	0.80	0.820	1.910	0.970	1.580	0.906
$^2G_{9/2}$	24630	0.530	0.468	0.783	1.014	1.360	1.258	0.694	1.169
$^4G_{11/2}$	26315	4.31	4.304	8.34	8.933	24.10	21.66	23.90	21.00
$^2G_{7/2}$	27624	-	-	-	-	7.540	2.926	5.860	2.638
δ_{rms}		± 0.081		± 0.334		± 1.784		± 1.595	

Accepted manuscript

Table 3:

Comparison of JO Parameters (Ω_2, Ω_4, Ω_6) (x 10^{-20} cm^2), and their trend for Er^{3+} ions in ZnAlBiB glasses with other reported glass systems.

Glass System	Ω_2	Ω_4	Ω_6	Trend	References

ACCEPTED MANUSCRIPT

ZnAlBiBEr01	1.02	0.72	0.66	$\Omega_2 > \Omega_4 > \Omega_6$	Present system
ZnAlBiBEr05	2.10	1.53	1.43	$\Omega_2 > \Omega_4 > \Omega_6$	Present system
ZnAlBiBEr10	5.82	2.90	1.70	$\Omega_2 > \Omega_4 > \Omega_6$	Present system
ZnAlBiBEr20	5.80	2.59	1.60	$\Omega_2 > \Omega_4 > \Omega_6$	Present system
KTFP	5.09	0.69	1.47	$\Omega_2 > \Omega_6 > \Omega_4$	[26]
YB25	3.86	1.52	1.17	$\Omega_2 > \Omega_4 > \Omega_6$	[39]
LiBO	3.24	0.92	0.82	$\Omega_2 > \Omega_4 > \Omega_6$	[40]
Germa-silicate	3.4	2.11	1.56	$\Omega_2 > \Omega_4 > \Omega_6$	[41]
Fluorphosphate	5.14	1.02	0.91	$\Omega_2 > \Omega_4 > \Omega_6$	[42]
Fluoride	3.08	1.46	1.69	$\Omega_2 > \Omega_4 > \Omega_6$	[43]
SNZE0.5	4.46	1.21	0.71	$\Omega_2 > \Omega_4 > \Omega_6$	[44]
SiO_2+Na_2O	4.23	1.04	0.61	$\Omega_2 > \Omega_4 > \Omega_6$	[45]
SAL	5.59	1.42	0.87	$\Omega_2 > \Omega_4 > \Omega_6$	[46]
NKZLSEr10	5.82	2.35	2.37	$\Omega_2 > \Omega_6 > \Omega_4$	[47]

Accepted manuscript

Table 4:

Emission peak wavelength (λ_P) (nm), effective band widths (FWHM) ($\Delta\lambda_P$) (nm), Transition Probability (A_R) (s^{-1}), radiative branching ratio (β_R), stimulated emission cross-section (σ_{se}) ($\times 10^{20}$) (cm^2), radiative lifetime (τ_R) (ms), gain band width ($\sigma_{se} \times \Delta\lambda_P$) ($\times 10^{26}$) ($cm^3$) and

ACCEPTED MANUSCRIPT

optical gain ($\sigma_{se} \times \tau_R$) ($\times 10^{20}$) ($cm^2$ s) parameters evaluated from the visible emission spectra of Er^{3+} ions in ZnAlBiB Glasses.

Glass	$\Delta\lambda_p$	A_R	β_R	σ_{se}	τ_R	$\sigma_{se} \times \Delta\lambda_P$	$\sigma_{se} \times \tau_R$
$^4S_{3/2} \rightarrow {}^4I_{15/2}$ (λ_P= 535 nm)							
ZnAlBiBEr01	11.76	971	0.6641	27.0	0.68	31.7	18.5
ZnAlBiBEr05	10.58	2103	0.6646	65.3	0.31	69.1	20.7
ZnAlBiBEr10	8.234	2480	0.667	99.3	0.26	81.8	26.5
ZnAlBiBEr20	8.234	2306	0.667	93.1	0.28	76.7	26.8

Accepted manuscript

Table 5:

Comparison of Emission peak wavelength (λ_P) (nm), effective band widths ($\Delta\lambda_P$) (nm), stimulated emission cross-section (σ_{se}) ($\times 10^{22}$) (cm^2), radiative and experimental lifetimes

ACCEPTED MANUSCRIPT

(τ_R, τ_{exp}) (ms)), Quantum efficiency (η) (%), gain band width ($\sigma_{se} \times \Delta\lambda_P$) ($\times 10^{28}$) ($cm^3$) and optical gain ($\sigma_{se} \times \tau_R$) ($\times 10^{25}$) ($cm^2$ s) parameters for the NIR emission of Er^{3+} ions in ZnAlBiB glasses.

Glass System	λ_P	$\Delta\lambda_p$	σ_{se}	τ_R	τ_{exp}	η	$\sigma_{se} \times \Delta\lambda_P$	$\sigma_{se} \times \tau_R$	**References**
ZnAlBiBEr01	1530	81.9	3.89	0.68	0.41	59	31.9	2.67	Present Work
ZnAlBiBEr05	1530	67.5	7.99	0.40	0.37	74	54.0	3.25	Present Work
ZnAlBiBEr10	1530	57.0	11.4	0.34	0.31	91	64.9	3.87	Present Work
ZnAlBiBEr20	1530	65.5	9.38	0.36	0.30	82	61.5	3.39	Present Work
GaBPGe	-	58.0	1.03		-		5.97	-	[24]
NKZLSEr10	1540	93.0	0.74		-		6.94	-	[47]
LiTFP	1534	37.9	1.12		-		42.7	-	[60]
NaTFP	1534	39.3	1.17		-		45.9	-	[60]
KTFP	1534	36.4	1.24		-		45.2	-	[60]
Silicate	-	40.0	0.55		-		2.20	-	[61]
Tellurite	-	59.0	0.68		-		4.06	-	[62]
GaBP1	-	62.0	1.03		-		6.38	-	[63]
Phosphate	-	56.0	0.67		-		3.79	-	[64]

Accepted manuscript

Table 6:

Emission peak wavelength (λ_P) (nm), effective band widths ($\Delta\lambda_P$) (nm), stimulated emission cross-section (σ_{se}) ($\times 10^{-21}$) (cm^2), gain band width ($\sigma_{se} \times \Delta\lambda_P$) ($\times 10^{28}$) ($cm^3$) and optical

ACCEPTED MANUSCRIPT

gain ($\sigma_{se} \times \tau_R$) ($\times 10^{20}$) (cm^2 s) parameters for the up-conversion emission transitions of Er^{3+} ions in ZnAlBiB Glasses.

Glass	λ_P	$\Delta\lambda_p$	σ_{se}	$\sigma_{se} \times \Delta\lambda_P$	$\sigma_{se} \times \tau_R$
		$^4S_{3/2} \rightarrow {}^4I_{15/2}$ (Green)			
ZnAlBiBEr01	543	26.92	1.25	33.7	0.859
ZnAlBiBEr05	543	23.07	3.18	73.3	1.01
ZnAlBiBEr10	543	13.46	6.44	86.8	0.172
ZnAlBiBEr20	543	21.15	3.85	81.4	0.111
		$^4F_{9/2} \rightarrow {}^4I_{15/2}$ (Red)			
ZnAlBiBEr01	656	28.8	2.69	77.6	2.30
ZnAlBiBEr05	656	25.0	6.67	167	2.68
ZnAlBiBEr10	656	21.2	12.4	262	0.319
ZnAlBiBEr20	656	23.1	10.3	238	0.295

High lights

- ZnAlBiB glasses were prepared by conventional melt quenching technique.
- Emission spectral data coupled with JO analysis were used to measure various radiative properties such as branching ratios and emission cross-sections.
- The mechanism of up-conversion observed in the present Er^{3+} ions doped ZnAlBiB glasses.
- Emission decay spectral measurements were used to measure quantum efficiency.

Accepted manuscript